

**ASSESSMENT OF TEMPORAL TREND-DYNAMICS OF WATER FLOW AND
SEDIMENT FLUX FOR CHÓKWÈ IRRIGATION SCHEME IN GAZA PROVINCE,
MOZAMBIQUE**

LATEIRO SALVADOR DE SOUSA

**A Thesis Submitted to the Board of Postgraduate Studies in Partial Fulfillment of the
Requirements for the Doctor of Philosophy Degree in Agricultural Engineering of Egerton
University**


EGERTON UNIVERSITY

MAY, 2021

DECLARATION AND RECOMMENDATION

Declaration

I declare that this thesis is my original work and has not been presented in this university or any other for the award of a degree.

Signature:  Date: 21st May, 2021

Lateiro Salvador de Sousa

BD11/14690/16

Recommendation

This thesis has been submitted with our approval as official University supervisors.

Signature:  Date: 21st May, 2021

Prof. Dr.-Ing Benedict M. Mutua

Division of Planning, Partnerships, Research, and Innovation

Kibabii University

Signature:  Date: May 21st 2021

Dr. (Eng). James M. Raude

Department of Soil, Water and Environmental Engineering

Jomo Kenyatta University of Agriculture and Technology

Signature:  Date: 22nd May, 2021

Dr. Raphael M. Wambua

Department of Agricultural Engineering

Egerton University

COPYRIGHT

© 2021, de Sousa Lateiro Salvador

All rights reserved. No part of this thesis may be reproduced, stored in a retrieval system or transmitted in any form or by any means of electrostatic, magnetic tapes, mechanical, photocopying, recording, or otherwise, without permission in duly writing from the author or Egerton University.

DEDICATION

This work is dedicated to my wife Mariza Mateus César Sousa (for love, patience and care), and my children Líria Lateiro de Sousa, Elias Lateiro de Sousa, Liliana Lateiro de Sousa and Hadassa Lateiro de Sousa (for encouragement). I also dedicate this work to my father Salvador Inácio Lateiro de Sousa and my mother Catarina Bancue Tomossene (for their support and understanding). Extensively, this work is dedicated my Christian brethren at Bible Believers Fellowship in Chókwè (Branham Tabernacle) (for their love and care).

ACKNOWLEDGEMENTS

I thank The Lord Jesus Christ, God Almighty, my Creator, my Redeemer, my Healer and my Saviour, for enabling me to complete this work.

I would like to record my thanks to the Hidráulica de Chókwè, Empresa Pública (HICEP) for allowing access to the Chókwè Irrigation Scheme and to the relevant historical data set. I am also grateful to the Administração Regional das Águas do Sul (ARA-SUL) for allowing our access to useful information in their database. Further, I acknowledge Q-Point, B.V., for encouragement and support in undertaking this research work.

My thanks are also due to the Staff of Egerton University, Kenya, specifically the Faculty of Engineering and Technology, and to all my colleagues at Instituto Superior Politécnico de Gaza (ISPG), Mozambique, for their interest and support during this study.

Cordial thanks to my supervisors Prof. Dr.-Ing. Benedit M. Mutua; Dr. (Eng). James M. Raude and Dr. Raphael M. Wambua, for their valuable guidance and advices throughout this work.

Finally, I would like to express my sincere appreciation to my family and parents for their continuous encouragement and patience.

ABSTRACT

Sedimentation of irrigation canals is one of the major challenge that affects their hydraulic control and operation. The sedimentation reduces water conveyance capacity and may lead to overtopping in low land areas. A case in point is the Chókwè Irrigation Scheme (CIS) which has experienced sedimentation problems for decades. There is scanty information on water flow and sedimentation within the canals in the CIS which is crucial for proper management and operation of the scheme. To address this trend-dynamics of water flow and sediment flux for CIS was assessed. The study involved fieldwork at 9 stations during the dry (DS) and wet (WS) seasons, laboratory analysis and scenarios predictions. Bathymetric data were obtained for 2001, 2016 and 2019. Flow measurements and collection of the bed and suspended loads, were carried out using respective devices. The laboratory analysis for water and sediment's pH, turbidity, Total Dissolved Solids (TDS), Atterberg test and sodium, calcium, magnesium, and potassium concentrations analysis, were performed. Forecasting and trend analysis of water flow and sediment flux was conducted using ARIMA, Mann-Kendall and Fourier Transform tests. Simulation of best scenarios was achieved by use of Ackers and White, Brownlie, Engelund-Hansen, Van Rijn and Yang models. Results indicated significant differences in canal banks and centre canal bed bathymetric profile between 2001, 2016 and 2019. The inflow physico-chemical factors explained their effects on sediment influx and deposition. The concentration of TDS was found to be around 250-300 ppm and 380-500 ppm, for DS and WS, respectively. Sodium was the most predominant element in water and sediment samples, reaching 0.285 ppm. The Liquid Limit, Plasticity Limit and Plasticity Index, were 52%, 20% and 32%, respectively. A mean of 2.96 N/m² was obtained for the critical shear stress of erosion (τ_c). The main particle size in bed load sediments which were classified as saline were silt, fine sand and clay at 52%, 39% and 9%, respectively. The temporal water flow was found out to have a positive trend in majority of the stations. Sediment discharge recurrence was found out to be in every 2-4 and 1-2 years for DS and WS, respectively. At the offtake, the water flow and sediment flux magnitude was much lower. The results of this study show that there was a positive influence of water flow velocity on sediments settling time, which varied with time, grain sizes and canal depth. This study provides trends and scenarios of water flow and sediment flux that could be used for better management and operation of the CIS.

TABLE OF CONTENTS

DECLARATION AND RECOMMENDATION	ii
COPYRIGHT	iii
DEDICATION.....	iv
ACKNOWLEDGEMENTS	v
ABSTRACT.....	vi
LIST OF FIGURES	xi
LIST OF TABLES	xvi
LIST OF SYMBOLS	xvii
LIST OF ABBREVIATION AND ACRONYMS	xix
CHAPTER ONE	1
INTRODUCTION.....	1
1.1 Background Information.....	1
1.2 Statement of the Problem.....	4
1.3 Objectives	4
1.3.1 Main Objective	4
1.3.2 Specific Objectives	4
1.4 Research Questions.....	5
1.5 Justification	5
1.6 Scope and Limitation	6
1.7. Definition of Terms.....	6
CHAPTER TWO	9
LITERATURE REVIEW	9
2.1 Sedimentation in Irrigation Schemes	9
2.2 Sediment Deposition Management	9
2.3 Sediment Parameters.....	11

2.4 Temporal Trends-Dynamics in Water Flow and Sediment Flux	15
2.4.1 Hydraulic Functions	16
2.4.2 Sediment Models	16
2.4.3 Mann-Kendall	18
2.4.4 ARIMA Model	20
2.4.5 Fourier Transform.....	22
2.5 Water Flow and Sediments Settling Velocity	24
2.5.1 Driving Forces	26
2.5.2 Resisting Framework.....	27
2.5.3 Sediment Budget.....	29
2.5.4 Bed load Transport	29
2.5.5 Uniformity and Curvature Coefficients	32
2.5.6 Suspended Load Transport	33
2.6 Evaluation of Best Scenario Predicting Sediment Deposition.....	35
2.7 Statistical Analysis.....	39
2.7.1 Principal Components Analysis (PCA)	39
2.7.2 Holt-Winters Method.....	41
2.7.3 Statistical Parameters for Model Selection.....	42
2.8 Calibration and Validation of the Models.....	46
2.9 Sensitivity Analysis	47
CHAPTER THREE.....	49
MATERIALS AND METHODS	49
3.1 Study Area	49
3.1.1 Climate and Soils.....	51
3.1.2 Hydraulics in the Irrigation Scheme	51
3.1.3 CIS Operation Characteristics	52
3.1.4 Data Acquisition	52
3.2. Determination of the Effects of the Canal and Inflow Factors on Sedimentation Flux	57
3.2.1 Canal Channel Factors.....	57
3.2.2 Inflow Factors.....	63
3.3 Determination of the Temporal Trends-Dynamics	66

3.4 Determination of the Influence of Water Flow on the Sediments Settling Velocity	67
3.5 Evaluation of Best Scenario for Predicting Sediment Deposition	68
3.6 Data Analysis and Performance Criteria.....	72
3.6.1 Linear Regression	72
3.6.2 Holt-Winters Method.....	72
3.6.3 Statistical Parameters for Model Selection.....	73
3.7 Calibration and Validation of the Models.....	75
3.8 Sensitivity Analysis	76
CHAPTER FOUR.....	77
RESULTS AND DISCUSSION	77
4.1 Effects of Canal Channel and Inflow Factors on Sediments Flux	77
4.1.1 Canal Channel Factors	77
4.1.2 Inflow Factors.....	119
4.1.3 PCA analysis for Water and Sediment Characteristics	163
4.1.4 Cross-section Profiles and Sediments Flux	172
4.2 Temporal Trends-Dynamics of Water Flow and Sediment Flux.....	178
4.2.1 Water Flow	178
4.2.2 Sediment Flux.....	182
4.2.3 Fourier Transform.....	183
4.2.4 ARIMA Test.....	188
4.2.5 Mann-Kendall Trends.....	192
4.3 Influence of Water Flow on Sediment Settling Velocity.....	196
4.3.1. Sediment Settling Velocity	196
4.3.2 Sediment Settling Velocity and Particle Grain Sizes	201
4.3.3 Water Flow and Canal Depths.....	204
4.3.4 Sediment Settling Velocity and Canal Depths	208
4.4 Simulation of Changes in Sediment Deposition and Scenarios Analysis.....	213
4.4.1 Linear Regression	213
4.4.2 Non-parametric Regression Simulations	214
4.4.3 Goodness Fit Analysis for Scenarios.....	217
4.4.4 Sensory Data Analysis (SDA)	221

4.4.5 Best Predictions	224
4.4.6 Winters Method for Model Predictions	229
CHAPTER FIVE	237
CONCLUSION AND RECOMMENDATIONS	237
5.1. Conclusion	237
5.1.1 The effect of canal channel and inflow factors on sediment flux.....	237
5.1.2 The temporal trends-dynamics of water flow and sedimentation flux	237
5.1.3 Influence of water flow on sediments settling velocity at different depths.....	238
5.1.4 Best sediment deposition scenarios	238
5.2. Recommendations.....	239
REFERENCES.....	240
APPENDICES.....	274
A: Selected Photographs	274
B: The Velocity-Area Method of Streamflow Measurement	277
C: Chókwè Irrigation Canal Reaches and Cross-Sections.....	283
D: T-Student Test and PCA Analysis	290
E: Sediment Budget Analysis	300
F: Normality Test.....	301
G. ARIMA and MANN-KENDALL tests	309
H. Scenarios Formulation for Sediment Deposition in CIS.....	313
I. The Main Assumptions for the Scenarios Applications	318
J: ARIMA's ACF, PACF, ACFR and PACFR.....	319
K: Atterberg Test Procedures.....	328
L. Letter of Authorization for Field Data Collection.....	331
M. Published Articles.....	332

LIST OF FIGURES

Figure 2. 1: Typical water velocity curve at the vertical (a) and different shapes of velocity distribution curve in vertical (b).....	24
Figure 3. 1: Map of Chókwè District in Gaza Province, Mozambique	50
Figure 3. 2: The network of Chókwè Irrigation Scheme showing the Sampling Stations.....	56
Figure 3. 3: Schematic Bathymetry Measurements Points in each Station	58
Figure 3. 4: Schematic Representation of Canal Geometry and Profile Parameters	58
Figure 4. 1 (a, b & c): Bathymetry Variation of Cross-section at the Intake-Lionde Reach for 2001, 2016 and 2019 Periods	79
Figure 4. 2 (a, b & c): Bathymetry Variation of Cross-section at the Lionde-Conhane Reach for 2001, 2016 and 2019 Periods	80
Figure 4. 3 (a, b & c): Bathymetry Variation of Cross-section at the Lionde-Marrambajane Reach for 2001, 2016 and 2019 Periods	81
Figure 4. 4 (a, b & c): Longitudinal Profile for Banks and Canal Bed for Intake-Lionde Reach in 2001, 2016 and 2019	84
Figure 4. 5 (a, b & c): Longitudinal Profile for Banks and Canal Bed for Lionde-Conhane Reach in 2001, 2016 and 2019	85
Figure 4. 6 (a, b & c): Longitudinal Profile for Banks and Canal Bed for Lionde-Marrambajane Reach in 2001, 2016 and 2019.....	86
Figure 4. 7 (a & b): Trend Analysis and Residual Plots for Centre of Canal Base for Intake-Lionde Reach in 2001	88
Figure 4. 8 (a & b): Trend Analysis and Residual Plots for Centre of Canal Base for Lionde-Conhane Reach in 2001.....	89
Figure 4. 9 (a & b): Trend Analysis and Residual Plots for Centre of Canal Base for Lionde-Marrambajane Reach in 2001	90
Figure 4. 10 (a & b): Trend Analysis and Residual Plots for Centre of Canal Base for Intake-Lionde Reach in 2016	94
Figure 4. 11 (a & b): Trend Analysis and Residual Plots for Centre of Canal Base for Lionde-Conhane Reach in 2016.....	95
Figure 4. 12 (a & b): Trend Analysis and Residual Plots for Centre of Canal Base for Lionde-Marrambajane Reach in 2016	96

Figure 4. 13 (a & b): Trend Analysis and Residual Plots for Centre of Canal Base for Intake-Lionde Reach in 2019	99
Figure 4. 14 (a & b): Trend Analysis and Residual Plots for Centre of Canal Base for Lionde-Conhane Reach in 2019.....	100
Figure 4. 15 (a & b): Trend Analysis and Residual Plots for Centre of Canal Base for Lionde-Marrambajane Reach in 2019	101
Figure 4. 16 (a, b & c): Variation in Depth, Banks and Bed Profiles for Intake-Lionde Reach in 2001, 2016 and 2019	105
Figure 4. 17 (a, b & c): Variation in Depth, Banks and Bed Profiles for Lionde-Conhane Reach in 2001, 2016 and 2019	106
Figure 4. 18 (a, b & c): Variation in Depth, Banks and Bed Profiles for Lionde-Marrambajane Reach in 2001, 2016 and 2019	107
Figure 4. 19: Liquid Limit (LL) and Plasticity Index (PI) for Montante Sector Stations.....	111
Figure 4. 20: Liquid Limit (LL) and Plasticity Index (PI) for Sul Sector Stations.....	112
Figure 4. 21: Liquid Limit (LL) and Plasticity Index (PI) for Rio Sector Stations	112
Figure 4. 22: Particle Size Distribution Curve for DS and WS	117
Figure 4. 23 (a & b): Average Water Depth at Sampling Stations for the DS and WS.....	121
Figure 4. 24: Water Flow Velocity for Canal Cross-Sections at Sampling Stations During DS	122
Figure 4. 25: Water Flow Velocity for Canal Cross-Sections at Sampling Stations During Wet Season.....	126
Figure 4. 26 (a & b): A 3D Representation of Water Flow Velocity at Cross-Section During DS and WS	129
Figure 4. 27: Mean SSC as Function of Water Depths During DS and WS.....	131
Figure 4. 28: Mean SSC as Function of Sampling Weeks During DS and WS	133
Figure 4. 29: Water Turbidity as Function of the Suspended Sediment and Water Turbidity as Function of the Water Discharge	134
Figure 4. 30: Average Values for Water Turbidity Sampling Stations in Both Seasons at CIS	135
Figure 4. 31: Turbidity as Function of Water Depth for DS and WS	137
Figure 4. 32: Turbidity as Function of Sampling Dates for DS and WS	139

Figure 4. 33: Average Values for Water pH at Each Sampling Stations in Both Seasons at CIS.....	141
Figure 4. 34: pH Variation With Water Depths for DS and WS	142
Figure 4. 35: pH Variation With Sampling Weeks n for DS and WS	144
Figure 4. 36: Average Water Temperature at Sampling Stations for DS and WS.....	145
Figure 4. 37: Water Temperature as Function of Water Depths During for DS and WS.....	147
Figure 4. 38: Water Temperature as Function of Sampling Weeks for DS and WS	149
Figure 4. 39: TDS as Function of Sampling Depths for DS and WS	151
Figure 4. 40: Electrical Conductivity Given for Each Sampling Stations for DS and WS....	152
Figure 4. 41: Electrical Conductivity as Function of Sampling Weeks for DS and WS	153
Figure 4. 42: Electrical Conductivity as Function of Water Depths for DS and WS	155
Figure 4. 43: Water Electrical Conductivity as Function of the Water Total Dissolved Solids for DS	156
Figure 4. 44: Chemistry Analysis for Suspended Sediments During DS for Each Sampling Station.....	161
Figure 4. 45: Chemistry Analysis for Suspended Sediments During WS at Each Sampling Station.....	162
Figure 4. 46: Normal Q-Q Plots for Sediment Discharge Dataset.....	163
Figure 4. 47: Normal Q-Q Plots for the Water Discharge	164
Figure 4. 48: PCA Eigenvalue Plots for Canal (a&b) and Inflow (c&d) Factors for DS and WS.....	168
Figure 4. 49: PCA Variable Plots for Canal (a&b) and Inflow (c&d) Factors for DS and WS	170
Figure 4. 50: PCA Cluster Analysis for Canal (a&b) and Inflow (c&d) Factors for DS and WS.....	172
Figure 4. 51 (a-d): PCA Analysis in Biplots at Montante Sector for DS and WS.....	173
Figure 4. 52 (a-f): PCA Analysis in Biplots at Sul Sector for DS and WS	175
Figure 4. 53 (a-f): PCA Analysis in Biplots at Rio Sector for DS and WS	177
Figure 4. 54: Water Discharge for Montante Sector Sampling Stations.....	178
Figure 4. 55: Water Discharge for Sul Sector Sampling Stations.....	180
Figure 4. 56: Water Discharge for Rio Sector Sampling Stations	181

Figure 4. 57: Sediment Flow (Q_s) for DS and WS at Intake and Offtake, from 2004-2005 to 2018-2019 Period	182
Figure 4. 58: Fourier Transform for Water Discharge at Intake-Massawasse Reach.....	184
Figure 4. 59: Fourier Transform for Sediment Discharge for the Main Intake and Offtake Reaches.....	188
Figure 4. 60: ARIMA Test Analysis for Each Sampling Stations.....	190
Figure 4. 61: Mann-Kendall Test and Sen’s Slope Analysis for Water Discharge at CIS all Stations	194
Figure 4. 62: Mann-Kendall Test and Sen’s Slope Analysis of Sediment Discharge for Intake and Offtake	195
Figure 4. 63 (a, b & c): Sediment Settling Velocities Behaviour with Sampling Dates for Montante Sector During DS and WS	197
Figure 4. 64 (a, b & c): Sediment Settling Velocities Behaviour with Sampling Dates for Sul Sector During DS and WS	198
Figure 4. 65 (a, b & c): Sediment Settling Velocities Behaviour with Sampling Dates for Rio Sector During DS and WS	199
Figure 4. 66: Sediment Particle Size Given as Function of Settling Velocities at Sampling Station.....	203
Figure 4. 67: Water Flow Velocity at Montante Sampling Stations.....	205
Figure 4. 68: Water Flow Velocity at Sul Sampling Stations.....	206
Figure 4. 69: Water Flow Velocity at Rio Sampling Stations	207
Figure 4. 70: Sediment Particles Settling Velocity at The Depth of Sampling Stations Montante Sector	209
Figure 4. 71: Sediment Particles Settling Velocity at The Depth of Sampling Stations at Sul Sector.....	210
Figure 4. 72: Sediment Particles Settling Velocity at The Depth of Sampling Stations at Rio Sector.....	211
Figure 4. 73: Nonparametric regression for all simulated models during DS and WS	216
Figure 4. 74: RMSE and R2 for the Exponential and Linear Holt Models of Sensory Data Analysis.....	222
Figure 4. 75: RMSE and R2 for the Seasonal Aditive and Multiplicative Models of Sensory Data Analysis	223

Figure 4. 76: NSEC, R and RE for Best Predictions of the Models Scenarios.....	226
Figure 4. 77: PBIAS and RMSE for Best Predictions of the Models Scenarios	227
Figure 4. 78: Winters Plots for Sediment Prediction Using Ackers-White Model.....	231
Figure 4. 79: Winters Plots for Sediment Prediction Using Brownlie Model	232
Figure 4. 80: Winters Plots for Sediment Prediction Using Engelund-Hansen Model	233
Figure 4. 81: Winters Plots for Sediment Prediction Using Van Rijn Model.....	234
Figure 4. 82: Winters Plots for Sediment Prediction Using Yang Model	235

LIST OF TABLES

Table 2. 1: Sediment Particle Classification	12
Table 2. 2: Classification of Sediment Based on EC, pH, ESP and SAR Values.....	14
Table 2. 3: Fall Velocity for Sand-Size Sediment in Still Water at 20oC	34
Table 2. 4: Selected Empirical Formulas for Predicting of Sediments.....	38
Table 3. 1: Sampling Stations and Cumulative Distances from the Intake	53
Table 3. 2: Classification of Sediment Based on EC, pH, ESP and SAR Values.....	62
Table 3. 3: Models and Inputs Used to Predict Scenarios and their Approaches	70
Table 4. 1: Summary of t-test for the Slope Changes in the Canal Reaches for Selected Years	103
Table 4. 2: Atterberg Limit Test for the Bed load Particles of CIS.....	109
Table 4. 3: Erosion Critical Shear Stress for the Sediments at Canalbed of CIS	110
Table 4. 4: Average Grain Size Distribution of Bed load for Different Sampling Stations ..	115
Table 4. 5: Correlation matrix (Pearson) (r) for Inflow Factors-Water Depth in DS	158
Table 4. 6: Coef. of determination (Pearson) (R2) for Inflow Factors-Water Depth in DS ..	158
Table 4. 7: Correlation matrix (Pearson) for Inflow (r) Factors-Samp. Weeks in DS.....	158
Table 4. 8: Coef. of determination (Pearson) (R2) for Inflow Factors-Samp. Weeks in DS.	158
Table 4. 9: Correlation matrix (Pearson) for Inflow (r) Factors-Sampling Weeks in WS.....	159
Table 4. 10: Coef. determination (Pearson) (R2) for Inflow Factors-Samp. Weeks in WS ..	159
Table 4. 11: ARIMA Struct. and Parameters of Model for Sed. Discharge Based on AIC...	192
Table 4. 12: Winters' Method for Model Prediction of Sedimentation at CIS.....	236

LIST OF SYMBOLS

Symbol	Description	Units
A	Area	(m ²)
Q	Water discharge	(m ³ /s)
t	Time	(s)
x	Distance	(m)
h	Water depth	(m);
V	Mean velocity	(m/s)
C	Chezy's coefficient	(m ^{1/2} /s)
R	Hydraulic radius	(m)
z	Bottom level above datum	(m)
g	Gravity acceleration	(m ² /s)
Q_s	Sediment discharge	(m ³ /s)
B	Bottom width	(m)
d_{50}	Mean diameter of sediment	(m)
p	Porosity	(-)
S_o	Bed slope	(m/m)
n	Manning's roughness coefficient	(s/m ^{1/3})
S_f	Energy slope, due to uniform flow, it is equal with bed slope	(-)
Fr	Froude number	(-)
a, b, c	Parameters to be adjusted	(-)
P	Wetted perimeter	(m)
d	Sediment size	(m)
U	Mean velocity	(m/s)
f	Lacey's silt factor for sediment size d	(-)
τ	Shear stress	(N/m ²)
c	Correction factor depending upon the B/h ratio (B for canal width) and for wide canals $c=1$	(-)
ρ	Density of water	(kg/m ³)
W_s	Settling velocity	(m/s)
C	Concentration of sediment	(ppm or g/l)
Q_0^t	Observed discharges at time t	(m ³)

Q_s^t	Simulated discharges at time t	(m ³)
\bar{Q}_0	Mean of the observed data	(m ³)
n	Total number of observations	(-)
M_i	Measured values	(-)
S_i	Simulated values	(-)
M	Average of measured values	(-)

LIST OF ABBREVIATION AND ACRONYMS

1D	One - Dimensional (space dimensions and spatial orientation)
2D	Two – Dimensional
2DH	Two - Dimensional Horizontal
2DV	Two - Dimensional Vertical
3D	Three – Dimensional
A _d	Adequacy
ARA-SUL	Administração Regional das Águas do Sul (South-Regional Water Administration)
AT	Atterberg Test
AVIS	Downstream surface gate for water flow control
AVIO	Downstream orifice gate for water flow control
CBIO	Crop Based Irrigation Operation
CCB	Centre of the Canal Base
CIS	Chókwè Irrigation Scheme
CROPWAT	Crop Water Requirement software
DPR	Delivery Performance Ration
DUFLOW	Dutch Flow
E _{op}	Operational Efficiency
EB	East Bank
ELC	East Lower Corner
EMP	East Middle-Point
EX	Executable
FAO	Food and Agriculture Organization
HDC	Hydraulic Design Criteria
HEC-RAS	Hydrologic Engineering Corps - River Analysis System
HICEP	Hidráulica de Chókwè, Empresa Pública (Hydraulic of Chókwè, Public Company)
LL	Liquid Limit
LRB	Limpopo River Basin
MAD	Mean Absolute Deviation
MAPE	Mean Absolute Percent Error

MSD	Mean Square Deviation
MHU	Main Hydraulic Units
DNA	Direcção Nacional de Águas (National Water Directorate)
INAM	Instituto Nacional de Meteorologia (National Meteorology Institute)
ISPG	Instituto Superior Politécnico de Gaza (Higher Polytechnic Institute of Gaza)
PI	Plasticity Index
PR	Proprietary
PSD	Particle Size Distribution
PU	Public
SBO	Supply Based Operation
SC	Source Code
SHU	Secondary Hydraulic Units
SIC	Simulation of Irrigation Canals
SIC ²	Simulation and Integration of Control for Canals
SO	Specific Objective
SOBEK	Hydrodynamics, Rainfall Runoff and Real Time Control package for River, Urban or Rural management
SRC	Sediment Rating Curve
SSC	Suspended Sediment Concentration
THU	Tertiary Hydraulic Units
WB	West Bank
WLC	West Lower Corner
WMP	West Middle-Point

CHAPTER ONE

INTRODUCTION

1.1 Background Information

Sedimentation is a process by which sediment particles are transported and deposited in a given water body (Anger et al., 2019). There are different sources of sediment entering a given water body. But the most common is generated by water motion causing erosion towards downstream, carrying mixture of particles (Bravo & Grant, 2018; Mostern, 2016; Ramalingam & Chandra, 2018). Human-induced activities such as large-scale agriculture (Montgomery, 2007), deforestation (Horton et al., 2017), and sand extraction (Torres et al., 2017), at nearby source, especially at upstream sites of the stream, can cause soil erosion and subsequent deposition or sedimentation in the water streams. Erosion disturbs the growth of naturally preserved landscapes, and produces sediment that is mostly deposited into the rivers, which then finds its way into the irrigation canals when water is diverted from the sediment laden river (Chen et al., 2018; Cui et al., 2017). The amount of global sediment discharge to the ocean, rivers, and even irrigation canals, remains unknown and its measurement still presents a daunting challenge. Quantification of sediment requires continuous measurements of suspended and bed load sediment at the mouth of every river and irrigation canals, which is quite difficult and expensive (Ali & Sterk, 2015; Arabameri et al., 2021). Limpopo river basin, located in Gaza province of Mozambique conveys water into Chókwè Irrigation Scheme (CIS), where more than 33000 hectares are cropped by medium and smallholder farmers. Limpopo river stream generate erosion materials that are conveyed into the network of the irrigation scheme. The influx of such material is comprised of sediment particles of different sizes, predominantly composed of finer particles. Finer materials are easily transported towards the more downstream-end, compared to bigger particles, which are first to deposit (Kamble et al., 2018; Mazumder & Ojha, 2017). Sediment in canals causes reduction in water conveyance capacity in the scheme, affecting croppable land in the scheme (Oh et al., 2016). It also reduces water conveyance efficiency leading to inadequacy and inequity in water distribution to crops. In addition, sedimentation may cause increased risk of canal breach due to reduction in freeboard and waterlogging (Osman, 2015). Although a number of irrigation canals at the CIS have had their initial geometric shape design altered as a result of sedimentation, very little work has been done at the CIS to help minimize the problem. The only activity that has been common in the site is the mechanical desilting which

is only performed when there are demands by affected farmers. Therefore, there is a need to improve water and sediment managements in order to achieve adequate water supply and food production in irrigation schemes, such as CIS (Kisi, 2012; Kusku et al., 2009).

To solve problems in water resources management, early identification of the problem gives higher possibilities of successful application of efficient and effective measures (Muema et al., 2018). Sediment deposition adversely affects hydraulic and operational performances of CIS. The CIS predominantly comprises of unlined canals and as a result is highly affected by sedimentation that affects water flow processes (Bai et al., 2014; Lopez et al., 1998). Therefore, concerns have been raised on how to tackle the sedimentation challenges at the CIS (Islam et al., 2008). Sedimentation concerns worldwide researchers and managers as it affects the design of irrigation systems and their operational performance. The slope of an irrigation canal is designed in such a way that the head works is usually smaller than that of the parent stream. This is meant to allow water to reach the points below the stream where irrigation is required (Coleman, 2010). With such a small slope, the canal can hardly transport the entire load especially when heavy sediment load enters in the canal system. In most cases, part of the load is deposited in the canal itself (Cook, 2008). This has also been reported in other studies where a number of irrigation schemes and rivers are affected by sedimentation leading to significant reduction in their capacity of water conveyance and delivery as well as channel's blockage. Notable irrigation schemes with huge challenges of sedimentation include: Chashma Right Bank Canal and Chashma Jheluni Link Canal and D.G. Khan Canal in Pakistan (Belaud, 1996; Nawazbhutta et al., 1996; Sarwar et al., 2013), Coromandel region in New Zealand (Ballantine et al., 2014; Marden et al., 2015) and Khoshi river system and Sunsari Morang Irrigation Scheme in Nepal (Depeweg et al., 2003; Paudel, 2010). Additionally, sedimentation has been reported in Elkhorn Slough Watershed and Upper North Santiam River Basin, Oregon in USA (Ouellet-Proulx et al., 2016; Spear et al., 2008; Uhrich et al., 2003), in the Ontario river basin in Canada (Rudra et al., 2006), Yellow River in China (Ma et al., 2016; Ruiguang et al., 2004; Shi et al., 2008), and in Luzon river and Magat catchment in the Philippines (White, 1990). Furthermore, Jatiluhur irrigation system, case study at Bekasi Weir Irrigation Scheme in Indonesia (Sutama, 2010), in rivers of the Russian Arctic, namely the Anabar River at Saskylakh, the Lena River at Tabaga and the Indigirka River at Vorontsovo all in Russia (Tananaev, 2014), at Magdalena river in

Colombia (Higgins et al., 2015) and Iguatu Experimental Watershed in Brazil (Santos et al., 2017), have also faced sedimentation.

Sedimentation has been reported as one of the major problems affecting irrigation schemes in Africa and the south-east region, where Mozambique is located, is not an exception. A number of studies carried out in other irrigation schemes such as Southwest Kano Irrigation Scheme in Kenya (Ochiere et al., 2015), Metahara Scheme in Ethiopia (Ali et al., 2014; Bishaw et al., 2015; Munir, 2011), Gezira Irrigation Scheme in Sudan (Osman, 2015), in suburban tropical basin in Congo (Lootens et al., 1986) and irrigation schemes in South Africa (Ojo & Otieno, 2010) indicate that these irrigation schemes are experiencing similar problems. In CIS sedimentation has been reported to have compromised the canals' efficiency by lowering it to an average magnitude of around 50% (Chambal, 2017). This therefore, demands rehabilitation for the entire system. Additionally, having low efficiency due to sedimentation, compromises water supply in the canals, which is critical to match with population growth demanding for more food (Myers & Tanner, 1992; West & Myers, 1996). In order to cope with such high population growth, more food is needed to meet such a demand. Therefore, an efficient irrigation scheme is widely seen as a major solution whereby, establishment of a system with good performance is critical (Evans, 2008). To achieve this, it requires a deep understanding of the influence of canal channel and inflow factors on sedimentation, and water flow velocity on sediments settling time at different depths of the canal (Hoffmann et al., 2017; Muttashar et al., 2019). Furthermore, analysis of temporal trends and formulation of best sediment deposition scenarios, is critical at the site as a contribution for better performance (Tannaev, 2014). CIS's efficiency of water conveyance system should be enhanced and this is only achievable if canals hydrodynamics under sedimentation are well understood and described. Although extensive work has been done in this area of water flow and sedimentation, information on the effect of canal channel factors, inflow factors, and water flow characteristics on the sediment accumulation and settling velocity is scanty. Therefore, in this research, an assessment of temporal trends-dynamics of water flow and sedimentation flux is undertaken for CIS with a view to developing a sustainable management strategy for the scheme.

1.2 Statement of the Problem

The high sediment load carried by water coming from erosion in the upper basin of the Limpopo River enters in the Chókwè Irrigation Scheme (CIS) network, inducing a severe problem of sediment deposition in the main canal. The amount of sediment entering the network increases every year at the point of becoming a concern, as more than 35% of the scheme is affected (Chambal, 2017). The annual amount of sediment removal in CIS is around 240,000 m³ in average, having an estimated cost of more than USD\$ 184,504, corresponding to around 60% of the total company cost with maintenance. Sediment deposition at the canal outlets and along the normal flowing course of the canals inflicts serious problems to the network system such as blocking the passages and diversions points such as pipes and gates, raises canal beds, increases the field levels, reduces canal conveyance capacity and favours aquatic vegetation development. Aquatic vegetation may aggravate the sedimentation rate, by slowing water flow and increasing deposition. The sedimentation process in the main canal cause limited control capacity and operation disfunction in the system. In consequence there occur higher water levels against the designed pattern and may lead to frequent breaks or overtop of canal side banks in addition to inequity and inadequacy in water supply. This is reflected in the variation in crop yield in some cropped areas. Therefore, the productivity of the scheme reduces. Moreover, sustainable management of CIS has been challenged due to limited information on water flow and sediment flux dynamics in the canal system. Water flow and sediment distribution trends in time and space, and the influence of water flow on sediments settling velocity at different depths, has not been established. Prediction on future of sedimentation remains unknown. Therefore, this study assesses canal and inflow factors influencing sedimentation in the CIS and potential for its prediction.

1.3 Objectives

1.3.1 Main Objective

The main objective of this research was to assess the temporal trend-dynamics of water flow and sedimentation flux for Chókwè Irrigation Scheme, in Gaza Province, Mozambique.

1.3.2 Specific Objectives

The specific objectives of this study were to:

- i. Determine the effect of canal channel factors and the inflow factors on the sediment flux for Chókwè Irrigation Scheme;
- ii. Determine the temporal trends-dynamics of water flow and sedimentation flux for Chókwè Irrigation Scheme;
- iii. Determine the influence of water flow on sediments settling velocity at different depths of the main canal sections for Chókwè Irrigation Scheme; and
- iv. Evaluate the best sediment deposition scenario using prediction analysis for Chókwè Irrigation Scheme.

1.4 Research Questions

- i. How does canal channel factors and inflow factors affect on the sediment flux in Chókwè Irrigation Scheme?
- ii. How does the water flow and sediment flux distribution trends vary along the Chókwè Irrigation Scheme in time?
- iii. How does water flow influences the sediment deposition at Chókwè Irrigation Scheme?
- iv. How can different scenarios be used to predict sediment deposition in Chókwè Irrigation Scheme?

1.5 Justification

CIS covers around 33000 hectares of land sourcing water from sediment loaded Limpopo River, with an estimated annual sediment load of 33×10^6 tonnes (FAO, 2016). Given that Limpopo River Basin drainage area covers around 430,000 km², sediment yield is estimated at approximately 77 tonnes/km².year. Current situation in the site points out to a difficult situation on sedimentation, given the fact that some areas are already facing serious problems of sedimentation. More than 35% of CIS is affected by sedimentation (Chambal, 2017) and if urgent measures are not taken the problem may worsen, leading to a decline in water delivery and crop production capacity. Beside this, literature dealing with sedimentation problems in irrigation canals is very limited, in especial for cohesive sediment. This problem is worsened by complications imposed by physical processes behind descriptions of the cohesive sediment transport. Such knowledge gap demand for more research be undertaken to understand the behaviour of cohesive sediment under a variety of operation conditions.

Moreover, most of the models already developed to simulate the fine sediment transport are well fit to rivers or estuaries. There is, therefore, a need of a model for fine sedimentation in irrigation canals. Assessing the temporal trend-dynamics of water flow and sedimentation flux will contribute to reach that aim, by explaining effects of canal and inflow factors in the sediment settling velocity. Best scenarios predicting sedimentation can be tried, both for sediment transport and deposition in the irrigation system.

1.6 Scope and Limitation

This research work scope is oriented to canal channel factors, water inflow factors and sedimentation flux analysis at CIS. Potential effects of canal channel and inflow factors on sedimentation were established. The canal channel factors (bathymetry of the banks and channel, cross-sectional and longitudinal profiles, section geometry, canal depth, width, side slope and top width, and bed load and its physico-chemistry), were covered. Water inflow (water depth, water velocity, suspended load and its physico-chemistry), were also assessed. Physico-chemistry parameters included turbidity, pH, temperature, TDS, EC, PSD, PI, LL and PL, as well as SAR, ESP, SP, $\text{Ca}^{2+}+\text{Mg}^{2+}$, Na^+ and K^+ . Temporal trends-dynamics on water flow and sediments flux, were also taken into account. Sediment deposition scenarios were formulated. The research was limited to the main canal reaches of CIS.

1.7. Definition of Terms

Activity Number of a Soil Sample: Is the ratio of the plasticity index to the clay-size fraction, or sediment particles finer than $2\mu\text{m}$. Sediments with an activity number over 1.25 are considered active and will have a greater change of the volume in response to moisture conditions. They will expand in wet conditions and shrink in dry conditions.

Canal Channel Factors: These are the physical and chemical factors directly related to the channel of the canal and bed load. For the purpose of this work, it includes *canal bathymetry for banks and channel (separated into cross-sectional and longitudinal profiles)*, *canal depth*, *bed load and its physico-chemical characteristics*.

Consistency Index (CI) or Relative Consistency: Liquid limit of the soil, minus the natural moisture content, divided by the PI. It is related to the LI and is an indicator of the relative shear strength. As CI increases, the firmness, or shear strength of the soil also increases.

Flow Rate: Is the quantity of fluid passing through any section (pipe line or open channel) per unit time.

Inflow Factors: These are the physical and chemical factors directly related in the water inflow and the canal. In this research these factors include *water depth, water velocity, suspended sediment load and its physico-chemical characteristics.*

Liquid Limit (LL): Water content at which soil changes from a plastic to a liquid state when the soil specimen is just fluid enough for a groove to close when jarred in a specified manner (ASTM D4318 2011; Rezaee et al., 2019).

Liquidity Index (LI): Is determined by subtracting the plastic limit from the natural water content of the sample, then dividing by the PI. Sediments with a LI of 1 or more suggests that it is closer to the liquid state. A LI of 0 or lower indicates sediments that are harder and more brittle. The LI allows prediction of sediment properties at different moistures (ASTM D4318 2011; Rezaee et al., 2019).

Plastic Limit (PL): Is the amount of water content at the change from a plastic to a semi-solid state of the sediment sampling extract. This test involves repeated rolling of a sediment specimen into a thread until the point where it crumbles and breaks apart at a diameter of 3.2 mm (ASTM D4318 2011; Rezaee et al., 2019).

Plasticity Index (PI): Is the difference between PL and LL and indicates the size of the range between the two boundaries. Sediments with a high PI have a higher clay content. If the PI value is higher than the low to mid-20s, the sediment may be expansive under wet conditions or exhibit shrinkage in dry conditions (ASTM D4318 2011; Rezaee et al., 2019).

Sediment: Is a naturally occurring material that is broken down by processes of weathering and erosion, and is subsequently transported by the action of wind, water, or ice or by the force of gravity acting on the particles (Ding & Langendoen, 2018).

Sedimentation: Is the process by which different sized particles are transported and deposited into the water bodies. Sediment transport starts when shear forces applied by the flow overcome the weight of the particle and in the process, detaches and initiates down-slope motion (Rahman et al., 2018).

Sediment Discharge: Is the amount of sediment moved by a stream in a given time, measured by dry weight or by volume. Also known as sediment-transport rate.

Sediment Flux - Bed load: Is the solid volume of bed load particles crossing a vertical surface per unit time per unit width (Nowacki & Ganju, 2019; Wilcock et al., 2020).

Sediment Flux – Suspended Load: Is the volume of water loaded with sediment particles crossing a vertical surface per unit time per unit width (Nowacki & Ganju, 2019; Wilcock et al., 2020).

Sediment Rate: Is the mass of sedimentary material, both particulate and dissolved, that passes across a given flow-transverse cross section of a given flow in unit time (Roushangar & Shahnazi, 2020).

Shrinkage Limit (SL): Water content where the further loss of moisture does not cause a decrease in specimen volume.

Turbidity: The extent to which light is scattered and absorbed by suspended sediment, dissolved organic matter, and, to a lesser extent, plankton and other microscopic organisms (Borok, 2014).

Water Discharge: The amount of water and sediment flowing in a channel, expressed as volume per unit of time. The water contains both dissolved solids (Dissolved Load) and suspended sediment (Suspended Load) (Rahman et al., 2018).

Water Flow: Is the movement of water in a channel without reference to rate, depth, width or length (Perzyna, 2016).

CHAPTER TWO

LITERATURE REVIEW

2.1 Sedimentation in Irrigation Schemes

Water flow of a given system can be analysed in terms of its amount at its point of entry and exit at a given point, as well as its velocity, turbidity, flux, which in turn depends on the cross-section (Bagherimihab, 2012; Munir, 2011). Particles move in the form of bed load or suspended load depending on the hydrodynamic conditions and sediment characteristics. Firstly, bed load, refers to the mode of transport of sediments where the particles glide, roll or jump in constant contact with the surface of the water body bed (Graf & Cellino, 2002). The bed load, consisting of coarser particles, is a very important aspect in sediment transport, as it controls the shape, stability, and hydraulic characteristics of the channel. Equations describing bed load are found in different authors, and are grouped into the following three types: DuBoys-type equations that utilize a shear stress relationship; Schoklitsch-type equations, focused on the discharge relations; and Einstein-type equations, grounded in statistics of lift forces. Details on their distinctions are given by Munir (2011). Secondly, in suspended mode of sediment transport the sediment particles displace themselves by making large jumps, but remain (occasionally) in contact with the bed load and also with the bed (Graf & Cellino, 2002). The suspended load usually consists of finer particles, as silt and clay. There are two states of suspended sediment transport, equilibrium condition (Akkuzu et al., 2008; Alfonso & Price, 2012), with no deposition and no scouring processes, and non-equilibrium condition (Kuscu et al., 2009), when either of the phenomena can take place. The theoretical approaches applied to estimate suspended sediment discharge in water streams are majorly the energy approach and the diffusion-dispersion approach. The diffusion-dispersion theory is recommended over the energy approach because experimental evidence indicates that it better fits to observed data (Lawrence, 1996). Finally, the total load is the summation of the bed load and suspended load. A large number of relationships have been developed for total load prediction in the flow (Ouellet-Proulx et al., 2016).

2.2 Sediment Deposition Management

Sedimentation causes may include natural occurrence (when sediment particles are embodied in the water stream resulting from normal water motion), changes in gradient, erosion and

obstruction of canals. However, a thorough research work is required to ascertain the real causes of occurrence. As a result, numerous studies related to sedimentation in irrigation canals have been carried out worldwide. Jinchi et al. (1993) found that sediment degradation and aggregation processes in irrigation canals depend to a large extent upon the hydrograph of water and sediment discharge. These authors concluded that adjustments in intervals of the processes, sediments can be transported into further areas for deposition. Nawazbhutta et al. (1996) investigated clearance works in Pakistan and found that if the desilting campaign is done in the upper two-thirds of the canal, it can greatly improve hydraulic performance of the canals. Belaud and Baume (2002) developed a methodology based on numerical modelling and successfully applied it on secondary network in Pakistan while proposing improvements in the design and desilting processes as a tool for longer preservation of equity. These findings can be useful for the CIS sediment management options. Depeweg and Paudel (2003), on the other hand, studied the design of irrigation system in Nepal for different operation and maintenance plans and their effectiveness on sediment transport. It was found that the system performance for sediment transport, depends on the management of the system, including the water delivery schedules, the operation of flow control structures and the maintenance conditions of the canals. Sherpa (2005) used SETRIC model to analyse sediment transport in irrigation scheme in Nepal, while Sutama (2010) applied the same model in an irrigation scheme in Indonesia. Both studies dealt with how applicable and versatile the model were for different conditions of operation and sediment input in the irrigation canals. Shi et al. (2008) developed a mathematical model and applied it to simulate sediment in irrigation canals and found that it predicts the non-uniform sediment movement in irrigation canals precisely. Paudel (2010) concluded that sediment deposition problem can be reduced by proper design and management of the system. These models may play considerable role in sediment prediction and improve its management in the CIS.

Munir (2011) suggested an improvement in the canal operation in a study of irrigation schemes in Pakistan. The author found out that sediment deposits during low crop water requirement periods can be re-entrained during peak water requirement periods. Osman (2015) studied the impact of improved operation and maintenance on cohesive sediment transport in Sudan and found that the absence of proper maintenance activities and water management counted for increased deposition along the irrigation canals. Noteworthy, these studies have

not been performed in Mozambique though they dealt with non-cohesive sediments, except work by Osman (2015) which considered cohesive sediment. In addition, settling velocities at different depths of a given canal are either not covered or inadequately covered in the literature presented. Moreover, Julaia (2009) tested different scenarios for improvement of operational performance in Chókwè Irrigation Scheme (CIS) in Mozambique, through DUFLOW model and found that by lowering the water level in the main system improved the efficiency indicator. The study did not deal with sediment analysis and therefore, no information was presented. Consequently, there is still a gap in research that deals with sediment analysis, both non-cohesive and cohesive, to improve on management practices. Therefore, this work sought to address the influence of canal channel factors, inflow factors, and water flow on sediments settling velocity at different depths of canal sections for temporal trend-dynamics, which is responsible for deposition, and formulate scenarios for sediment occurrence across the irrigation scheme.

2.3 Sediment Parameters

Different components of water flow system are thought to comprise sediment parameters, including bed and suspended loads, which both make the total load. Water turbidity, sediment concentration and its settling velocity, grain size distribution, depth of occurrence, Atterberg limits and relevant physico-chemical characteristics (Wei et al., 2016), are also included in sediment parameters. Additionally, analysing these parameters require carrying different methods and procedures that may cover techniques to determine sediment concentration, specific weight of sediment, sieve analysis and hydrometric analysis for sediment sizes, carried out in a laboratory (Uhrich & Bragg, 2003). In general, the physico-chemical analysis, Atterberg limits tests and water column test are relevant, and aims at studying the properties of sediment (Stergiopoulou et al., 2013). The suspended sediment concentration, can be performed either by evaporation (for finer materials) or by filtration (for coarser grain sizes and lower concentration). Grain size distribution, on the other hand, for both bed load and suspended load transport can be determined using sieves analysis. The sieve analysis is used for grain sizes greater than 0.063 mm (limit between sand and silt) (Uhrich & Bragg, 2003). The hydrometer test is conducted for fine materials, such as silt and clay. In order to perform separation of the colloids and remove the organic matter, a dispersing agent, a solution of sodium hexametaphosphate (40 grams/litre of solution) can be used. The sizes of sediments

are classified by the United State Geological Survey (USGS) as follows: Clay sized particles (<0.002 mm); Silt sized particles (from 0.002 mm to 0.0625 mm); Sand sized particles (from 0.0625 mm to 2 mm); and Gravel sized particles (2 mm to 64 mm) and Cobbles (>64 mm), as presented in Table 2.1 (Dearnaley et al., 1995; Mehta & Lee, 1994).

Table 2. 1: Sediment Particle Classification

Type	Texture	Diamter (mm)
Clay		<0.002
Silt	Fine	0.002-0.006
	Medium	0.006-0.02
	Coarse	0.02-0.0625
Sand	Fine	0.0625-0.2
	Medium	0.2-0.6
	Coarse	0.6-2
Gravel	Fine	2-6
	Medium	6-20
	Coarse	20-64
Cobbles		>64

Source: Adapted from Dearnaley et al. (1995); Mehta and Lee (1994).

This work used the Atterberg limits test, to classify unconsolidated sediments and distinguish between cohesive and non-cohesive sediment as well to determine cohesive sediment mechanical behaviour, in accordance with the procedure proposed by Osman (2015). The LL and PL helped obtain water content for sediment samples and, hence, the Plasticity Index (PI = LL-PL). In case of high PI may suggest cohesiveness of the sediments, due to presence of clay particles, which retain more water. When there is observed silty cohesive sediments the LL ranges 24-35% and the PL can vary around 14-25%. In case of clayey cohesive sediments the LL ranges between 14-25% and the PL is over 20%. Further, physico-chemistry test seeks at assessing sediment properties such as saturation percentage (SP), pH, EC, Ca+Mg, Na, K, SAR, Exchangeable Na⁺ and ESP. SP indicates sediment capacity for water retention, therefore, high SP indicates high capacity of sediment to store water. Sediments extracts with low pH (≤ 5.5) values imply a stratified sediment bed exhibiting a high erosion rate near the

surface. In another hand, sediments samples with intermediate pH ($5 \leq \text{pH} \leq 7$) results in a weaker bed structure due to lack of surface contact, which leads to more susceptibility to erosion. Additionally, at high pH (>7), sediment particle orientation predominates, the surface attraction forces become significant and form denser aggregates (Stone et al., 2009). Additionally, the total amount of sediments soluble ions, is another measure, which is estimated by measuring the electrical conductivity (EC) of a sediment in water extract. This is an important factor for the susceptibility analysis of cohesive sediment to erosion. Sediment with $\text{EC} > 4 \text{ dS/m}$ is saline and the increase of the change in the fluid pore of clay of a higher value de-flocculates (Munir, 2011).

Sodium Adsorption Ratio (SAR), stands for the ratio of dissolved ions of sodium to the calcium and magnesium cations. When the SAR value is high then particles repulsive forces become dominant, produce significant swelling and lead clay into de-flocculation process. Dispersion and flocculation, both aggregate stability processes depends on the balance (SAR) between calcium (Ca^{2+}) and magnesium (Mg^{2+}), and sodium (Na^+) as well as the amount of soluble salts (EC) in the sediments. The SAR can be obtained from Equation 2.1. Sediment particles will flocculate if concentrations of $\text{Ca}^{2+} + \text{Mg}^{2+}$ is incremented in relation to the concentration of Na^+ (SAR is decreased). The sediment will be classified as normal sediment according to Table 2.2, as adapted from Osman (2015).

$$\text{SAR} = \frac{\text{Na}^+}{\sqrt{(\text{Ca}^{2+} + \text{Mg}^{2+})/2}} \quad (2.1)$$

Where:

SAR = Sodium Adsorption Ratio (-)

Na^+ = Sodium concentration (mg/L)

Ca^{2+} = Calcium concentration (mg/L)

Mg^{2+} = Magnesium concentration (mg/L)

Table 2. 2: Classification of Sediment Based on EC, pH, ESP and SAR Values

Sediment Classification	EC (dS/m)	pH (-)	ESP (%)	SAR (-)	Condition
Normal	<4	<8.5	<15	<13	Flocculation
Saline	>4	<8.5	<15	<13	Flocculation
Sodic	<4	>8.5	>15	>13	Dispersed
Saline-Sodic	>4	<8.5	>15	>13	Flocculation

> = greater than and < = less than.

Source: Adapted from Osman et al. (2016); Osman (2015) and Rahimi et al. (2019).

The exchangeable sodium percentage (ESP), represents the presence of excessive amounts of exchangeable sodium that affects in reverse order the aggregation process and causes sediment aggregates to disperse into their constituent individual particles. Such process is called de-flocculation and can occur in sodic sediments. The ESP can be computed based on the following relation:

$$ESP = Exchangeable \left(\frac{Na^+}{Ca^{2+} + Mg^{2+} + K^+ + Na^+} \right) \times 100 \quad (2.2)$$

Where:

ESP = Exchangeable Sodium Percentage (%)

Na⁺ = Sodium concentration (mg/L)

K⁺ = Sodium concentration (mg/L)

Ca²⁺ = Calcium concentration (mg/L)

Mg²⁺ = Magnesium concentration (mg/L)

Water column is essential in estimating the time needed for the sediment to settle. In these tests different water columns with different cylinder heights are used. In case of different sediment concentrations, the test must be repeated. The aim of the tests is to understand the mechanism of sedimentation in canal and to investigate the relationship between the concentration and time for the sediment to be deposited. Consequently, the test makes it

possible to know quantity of sediment that can be deposited if water is stored in the minor canals for a certain period and also, to determine the optimum time for the operation with less sediment. It is advisable that samples for further analysis are taken from upstream and downstream of a canal reach.

2.4 Temporal Trends-Dynamics in Water Flow and Sediment Flux

Water flow and sediments flux behave differently on the canal stream depending on the level of changes observed in space and time. Changes in space can be assessed in two levels, across distance from one point to the other and depths at water at surface, middle and bed points (Rovira et al., 2012). On the other hand, changes in time include days, months, season, years or even decades. There are different studies that have been carried out to analyse spatial and temporal variability of water flow and sediment flux. In a study, Clayton and Pitlick (2007) found that intensity of transport varies with location of channel, and that coarser particles in bed load were differentially transported in some canals areas than on others. Moreover, research work by Bai and Duan (2014) found that the presence of vegetation in canals increases the grain resistance that transport sediment. The authors suggested that the grain resistance is a function of vegetation density. Therefore, denser vegetation cause less erosion. Indeed, the variation of sediment concentration in canals depends on the time and location. Some canals present very little or have sediments absence, while others suffer from high concentrations throughout the year or in certain months (Osman, 2015). There are two aspects considered in dealing with water flow in the irrigation canals, operational and sediment transport. The operational aspects relates to where the water flow becomes non-uniform and unsteady due to changing water requirements and gates operation to fulfil the water demand and to keep water level as it is required for the fields needs. The sediment transport aspects deals with changes in water flow over time and space, and assesses how faster it is compared to changes in morphology of sediment. Therefore, the interrelation between these two aspects can be illustrated as one-dimensional event without changing the cross sectional shape (Sutama, 2010). In addition, trends-dynamics of water and sediment fluxes can also be expressed as in the following equations:

2.4.1 Hydraulic Functions

The following continuity equation for water movement has been put forth by Sutama (2010):

$$\frac{\partial A}{\partial t} + \frac{\partial Q}{\partial x} = 0 \quad (2.3)$$

Where:

A = area (m^2)

Q = discharge (m^3/s)

t = time (s)

x = distance (m)

Additionally, a dynamic equation for water movement has been presented by the same author as:

$$\frac{\partial h}{\partial x} + \frac{V^2}{C^2 R} + \frac{\partial z}{\partial x} + \frac{V}{g} \times \frac{\partial V}{\partial x} + \frac{1}{g} \times \frac{\partial V}{\partial t} = 0 \quad (2.4)$$

Where:

h = water depth (m)

V = mean velocity (m/s)

C = Chezy's coefficient ($\text{m}^{1/2}/\text{s}$)

R = hydraulic radius (m)

z = bottom level above datum (m)

g = gravity acceleration (m^2/s)

t = time (s); and

x = distance (m)

The Equations (2.3 and 2.4) describe the conservation of mass and momentum which is also known as Saint-Venant equations for continuity and dynamic unsteady flows and water flow related. For sediment related, the equations are presented as follows:

2.4.2 Sediment Models

In this case, the friction factor predictor is given as a function of:

$$C = f(d_{50}, V, h, S_o) \quad (2.5)$$

And the continuity equation for sediment transport as:

$$(1 - p) \times B \times \frac{\partial z}{\partial t} + \frac{\partial Q_s}{\partial x} = 0 \quad (2.6)$$

Where:

- t = time (s)
- Q_s = sediment discharge (m³/s)
- B = bottom width (m)
- d_{50} = mean diameter of sediment (m)
- p = porosity (-)
- S_o = bed slope (m/m)

Finally, the sediment transport equation is presented as a function of:

$$Q_s = f(d_{50}, V, h, S_o) \quad (2.7)$$

These equations are related to each other since sediment transport and water flow are interrelated; given, for example, the roughness coefficient is influenced by water flow while sediment transport is affected by the water flow (Méndez V., 1998). The unsteady flow condition, on the other hand, in irrigation canal is assumed to be quasi-steady; hence $\partial A/\partial t$ and $\partial V/\partial t$ can be neglected. The continuity and dynamic equations become:

$$\frac{\partial Q}{\partial x} = 0 \quad (2.8)$$

$$\frac{dh}{dx} = \frac{S_o - S_f}{1 - Fr^2} \text{ with } Fr = \frac{V}{\sqrt{g \times h}} \quad (2.9)$$

For the uniform flow, there is no change in water depth. Hence:

$$\frac{dh}{dx} = 0 \longrightarrow S_o = S_f \quad (2.10)$$

Making the uniform flow new equation as:

$$v = \frac{1}{n} \times R^{1/3} \times S_f^{2/3} \text{ or } v = C \sqrt{R \times S_f} \quad (2.11)$$

Where:

- A = area (m²)
- Q = water discharge (m³)
- h = water depth (m)
- V = mean velocity (m/s)

C = Chezy's coefficient ($\text{m}^{1/2}/\text{s}$)

R = hydraulic radius (m)

z = bottom level above datum (m)

g = gravity acceleration (m^2/s)

t = time (s)

Q_s = sediment discharge (m^3/s)

B = bottom width (m)

d_{50} = mean diameter of sediment (m)

p = porosity (-)

n = Manning's roughness coefficient ($\text{s}/\text{m}^{1/3}$)

S_f = energy slope, due to uniform flow, it is equal with bed slope

Fr = Froude number

2.4.3 Mann-Kendall

Trend detection in hydrology and water flow time series has received attention in the recent years. In a number of studies on water quality data in lakes and streams (Bouchard & Haemmerli, 1992; Yu et al., 1993; Zetterqvist, 1991) and streamflow data (Burn, 1994; Chiew & McMahon, 1993; Mitosek, 1992; World Meteorological Organization [WMO], 1988) a number of parametric and non-parametric tests were applied for detection of trends. Both parametric and non-parametric tests are commonly used. Parametric trend tests are powerful and more trustfull compared to non-parametric ones, but they require data to be independent and normally distributed. On the other hand, non-parametric trend tests only require independent data and tolerate outliers. One of the most used non-parametric tests in the time series is the Mann Kendall test (Kendall, 1955; Mann, 1945). The Mann-Kendall trend test derives from a rank correlation test for two groups of observations proposed by Kendall (1955). In the Mann-Kendall trend test consideration is given to the correlation between the observed rank order and their order in time. The null hypothesis is that the data are independent and randomly ordered, meaning that there is no trend or serial correlation structure in the observations. However, observed data in many real situations are in somehow autocorrelated.

The presence of autocorrelated observed data results in misinterpretation of trend tests results. Cox and Stuart (1955) suggest that the presence of positive correlation in observations may mislead into conclusion about data significancy. This fact has attracted attention to fix such problem of existence of seasonality in data (Hirsch et al.,1982). To eliminate seasonality observations are divided into separate classes according to seasons and then performing the Mann-Kendall trend test on the sum of the statistics from each season, in a process called seasonal Kendall test (Hirsch et al.,1982; Hirsch & Slack, 1984; Zetterqvist, 1991). Although technic eliminates the seasonal test, it does not affects the correlation in the series within seasons (Hirsch & Slack, 1984). When yearly data are analyzed there is large possibilities for seasonality, since they are often significantly autocorrelated.

The rank correlation test (Kendall, 1955) for two sets of observations $X = x_1, x_2, \dots, x_n$ and $Y = y_1, y_2, \dots, y_n$ is formulated as follows. The statistic S is calculated as in Equation (2.12):

$$S = \sum_{i < j} a_{ij} \times b_{ij} \quad (2.12)$$

Where:

$$a_{ij} = \text{sgn}(x_j - x_i) = \begin{cases} 1 & x_i < x_j \\ 0 & x_i = x_j \\ -1 & x_i > x_j \end{cases} \quad (2.13)$$

and b_{ij} is similarly defined for the observations in Y . Under the null hypothesis that X and Y are independent and randomly ordered, the statistic S tends to normality for large n , with mean and variance given by:

$$E(S) = 0 \quad (2.14)$$

$$\text{var}(S) = n(n-1)(2n+5)/18 \quad (2.15)$$

If the values in Y are replaced with the time order of the time series X , *i.e.* $1, 2, \dots, n$, the test can be used as a trend test (Mann, 1945). In this case, the statistic S reduces to that given in equation (2.16):

$$S = \sum_{i < j} a_{ij} = \sum_{i < j} \text{sgn}(x_j - x_i) \quad (2.16)$$

with the same mean and variance as in Equation (2.14) and (2.15). Kendall (1955) provides information proving an asymptotic normality of the statistic S . The trends significance is

found when comparison between standardized test statistic $Z = S/[var(S)]^{0.5}$ with the standard normal variate, is performed at the desired significance level. More details on the derivation of the mean and variance of S is given by Kendall (1955). If X is normally distributed with mean g and variance σ^2 , then $(x_j - x_i)$ will also be normally distributed with mean zero and variance $2\sigma^2$. Further detailed information on the Mann-Kendall can be sought in different sources including Hirsch et al. (1982); Hirsch and Slack (1984); Kendall (1955); and Zetterqvist (1991).

2.4.4 ARIMA Model

ARIMA are models used for forecasting time-series and are vastly used in this scope. An ARIMA model, requires to be stationarized in most cases. To do so, transformations such as differencing and logging are commonly applied. Improving ARIMA prediction quality can be attained by fine-tuning consisting of adding lags of the differenced series and/or lags of the forecast errors to the prediction equation. This will help remove persisting traces of autocorrelation from the forecast errors. In the ARIMA models, lags of the differenced series in the forecasting equation are ‘autoregressive’ terms, and lags of the forecast errors are ‘moving average’ terms. In addition, time-series which requires to be differenced to stationarity is an ‘integrated’ version of a stationary series (Huang, 2004). A non-seasonal ARIMA model is referred to as an ‘ARIMA (p, d, q)’ model, where: p represents the number of autoregressive terms, d represents the number of non-seasonal differences and q indicates the number of lagged forecast errors in the prediction equation (Box & Jenkins, 1976). The identification of the appropriate ARIMA model for a given time-series, begins by identifying the order(s) of differencing needed to stationarize the series and to remove the gross features of seasonality, perhaps in conjunction with a variance-stabilizing transformation such as logging or deflating. If it stop at this point and predict that the differenced series is constant, it will have merely fitted a random-walk or random-trend model. However, the best random-walk or random-trend model may still have autocorrelated errors, suggesting that additional factors of some kind are needed in the prediction equation. ARIMA model forecasting includes three basic steps: model identification, parameter estimation and forecasting. ARIMA model parameter selection is based on the autocorrelation -function linear relation between observation pairs; and partial-autocorrelation-function conditional correlation with intervening observations removed. According to Hamilton (1994), the general procedure for

ARIMA model selection and calibration includes: (i) stationarity conditions checking; (ii) autocorrelation function checking to choose the P value; (iii) partial autocorrelation function checking to choose the Q value (iv) identifying the ARIMA (p, q) model; (v) estimation; (vi) residual diagnostics. In this study, several trials were made to choose the optimal ARIMA model parameters. The model parameters that meet the statistical residual diagnostic checking were chosen in the ARIMA forecasting model (Huang, 2004).

Generally, for the Box-Jenkins methodology (Box & Jenkins, 1976), the auto-regressive moving average (ARMA (p, q)), or auto-regressive integrated moving average (ARIMA(p, d, q)) models are often applied for time series forecasting. However, the application of ARMA model requires the time series to be stationary; that is to say, the algorithm of ARMA assumes that the process remains in equilibrium about a constant mean level. If the series are nonstationary or have obvious trend variability, the ARIMA model based on difference process can be used (Box et al.,1994). In this work, the augmented Dickey–Fuller (ADF) test (Elliott et al., 1996) is used to test the stationarity in the original annual runoff time series and the decomposed annual runoff time series (Wang, 2015). As it is known, the ARMA model consists of three main steps: model identification, parameter estimation and application. Among these three steps, the identification step is important, and includes two stages: (1) if it is necessary, appropriate differencing of the series is performed to achieve stationary and normality, (2) the order of the AR and MA parts of ARMA model is identified. Box and Jenkins (1976) employed the autocorrelation function (ACF) and the partial autocorrelation function (PACF) of the sample data as the basic tools to identify the order of the ARIMA model. If sample data is an AR (p) model, the PACF cut-off is at lag p , On the other hand, if sample data is a MA (q) process, the ACF has a cut-off at lag q . However, the PACF and ACF method is not very useful when dealing with mixed ARMA processes. Simple inspection of the graphs of the ACF and the PACF would not, in general, give clear values of p and q for mixed models (Chan, 1999). Some other identification methods have been presented based on the information-theoretic approaches, such as the Akaike’s Information Criterion (AIC) (Shibata, 1976), the Bayesian Information Criterion (BIC) (Gideon, 1978), the final prediction error criterion (FPE) (Akaike, 1969) and others. In this work, the best fitted model is selected according to AIC. Once an appropriate model is chosen, the

parameters of the model must be estimated. This can be accomplished using a nonlinear optimization procedure. The application and analysis is presented as follows:

The MA(1) model is in the form off:

$$x_i = e_t + \theta e_{t-1} \quad (2.17)$$

where e_t is $N(0, \sigma_e^2)$. In this case the autocorrelation function $\rho(i)$ is given by:

$$\rho(i) = \begin{cases} 1 & i = 0 \\ \frac{\theta}{(1+\theta^2)} & i = 1 \\ 0 & i > 1 \end{cases} \quad (2.18)$$

The AR(1) model is of the form of:

$$x_t = \varphi x_{t-1} + e_t \quad (2.19)$$

In this case, the autocorrelation function is given by:

$$\rho(i) = \varphi^{|i|} \quad (2.20)$$

2.4.5 Fourier Transform

The Fourier Transform (FT) is a mathematical function that takes a time-based pattern as input and determines the overall cycle offset, rotation speed and strength for every possible cycle in the given pattern. The FT is normally applied to waveforms that are a function of time, space or some other variable. The FT decomposes a waveform into a sinusoid and thus provides another way to represent a waveform (Ding et al., 2016; Lin, 2018; Rosenberg & Abookasis, 2020). FT theorem establishes that any complex periodic function will be decomposed into periodic functions with varying amplitude, period, and phase shift. The FT as an decomposition technique uses sinusoidal basis functions. While there are various techniques to derive unit hydrographs from discharge and precipitation data, most are either illposed or require assumptions about system behavior (Yang & Han, 2006). The FT deconvolution will produces a quick and deterministic unit hydrographs that are useful in the analysis process. The total time-series response of a linear system to a forcing input can be derived by the convolution of the system unit response and the input time-series as follows (Lin, 2018; Oganegov et al., 2018; Xu & Zhang, 2020):

$$q(t) = \int_0^{\infty} h(\tau) \times p(t - \tau) d\tau \quad (2.21)$$

Where:

q = total time-series response (i.e. stream discharge)

h = the unit response (for the case of stream discharge, this unit response has the special name of “unit hydrograph”)

p = the input sedimentation time series.

According to the convolution theorem,

$$Q(k) = H(k)P(k) \quad (2.22)$$

Where $Q(k)$, $H(k)$, and $P(k)$ are the FTs of $q(t)$, $h(t)$, and $p(t)$, respectively, where k is the spectral frequency. The unit hydrograph time-series is then,

$$h(t) = F^{-1} \left[\frac{Q(k)}{P(k)} \right] (t) \quad (2.23)$$

where $F^{-1}[\dots](t)$ denotes the inverse Fourier Transform. Thus the hydrograph for unit-response will be the inverse FT of the ratio of the discharge and sedimentation spectra. Though not strictly necessary, the analysis is simplified if the sampling frequency and units of the sedimentation and discharge time-series are identical. The data would require resampling so that the number of samples, n , and the sampling frequency, f , become equivalent. The n is the length of unit-response function $h(t)$, which is only valid to the point where it is negative, since sedimentation can not directly produce a decrease in stream discharge (Yang & Han, 2006). The negative response is therefore the signature of some other process related to the studied variable. If baseflow separation is used, this issue can be avoided, though some small uncertainties will remain due to the data itself, and may result in negative calculated unit responses. The resultant unit-response hydrograph is not an invariant property of the water flow, as it is sensitive to variations in runoff generating processes. These processes can be studied by directly comparing different unit-response hydrographs (Tan et al., 2020; Widjaja et al., 2020). Differences in response curve timing, peak, and shape can all be used to infer the activity and relative influence of various water flow processes. Applying data subset selection with these process differences in mind can allow for a quantitative sensitivity analysis of system sub-processes. For further information on FT Lin (2018); Oganessov et al. (2018); Yang and Han (2006); and Xu and Zhang (2020), can be sought.

2.5 Water Flow and Sediments Settling Velocity

Water flow has direct influence on the sedimentation process. High velocity leads to low rate of sedimentation and vice-versa. Hydraulic theory indicate that non-turbulent streams present water flow velocity typically varying in the vertical in a parabolic manner as shown in Figure 2.1 (a). It is called a typical velocity profile, as suggested by Perzyna (2016). From the profile it can be viewed that at lower depths of a given canal, there are possibilities for higher deposition of sediments, if compared to the upper sides, where water tend to flow with more velocity. In case of pre-existing conditions be found occurring in a given water body, such as the type of bottom material, weed growth on the streambed, large boulders within the cross-section, turbulence and other factors, may alter this pattern and a velocity profile usually will differ from the “ideal” velocity profile. Different forms on the velocity profile can be seen in Figure 2.1 (b), after Perzyna (2016). Whereby, it is expected that the shape profile with low velocity will be more susceptible to sediment deposition notwithstanding other factors influencing such processes.

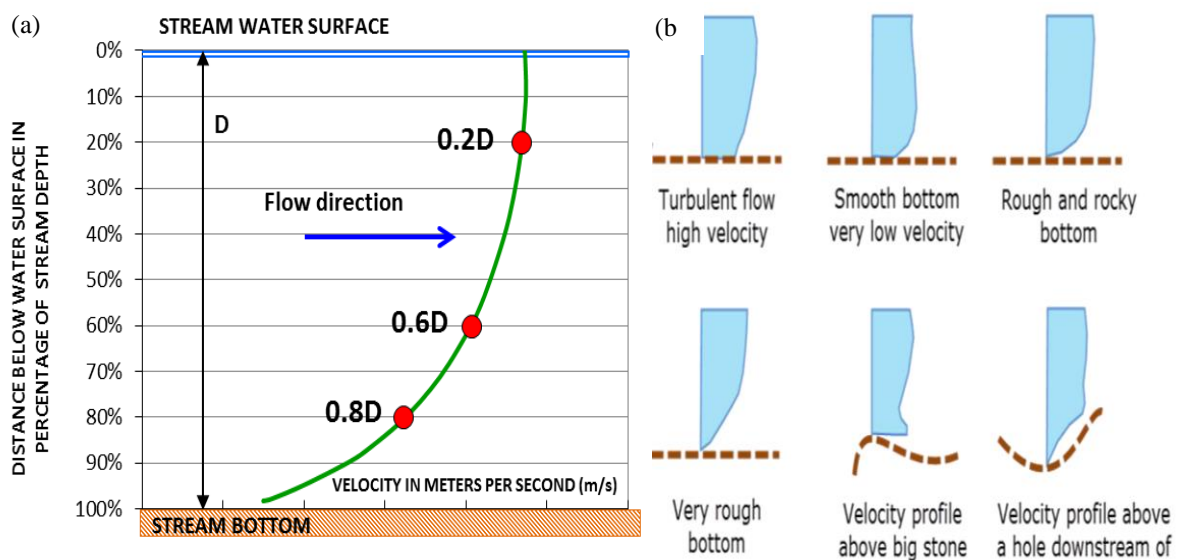


Figure 2. 1: Typical water velocity curve at the vertical (a) and different shapes of velocity distribution curve in vertical (b)

To predict the susceptibility of sedimentation within a given reach one needs to know the capacity of the channel to transport sediment through the reach (Gericke, 2013).

Sedimentation process may be studied in one of two ways: a forward physical approach or an inverse morphological approach (Burge et al., 2014). The forward physical approach uses known physics to predict sedimentation. The inverse morphological approach is an inverse approach using observed properties of the stream channel to infer sedimentation process. After many years of research in this field no universally applied bed load transport function exists. However, different approaches describing bed load transport have been brought up are considered in this work. Furthermore, deposition of suspended sediment will occur when the fall velocity of the sediment is greater than the turbulent eddies suspending the sediment within the water column (Faghihirad et al., 2015).

The forward approach is used to predict susceptibility of a canal section to bed sediment accumulation. Moreover, estimations on the size and volume of background sediment supplied to the channel and its capacity to transport sediment downstream can be performed. Sediment within canal is transported through two main mechanisms: as bed load and suspended load (Knighton, 1998). Suspended load is material transported within the water column; while bed load is transported on the channel bed. The transport mechanics and therefore the fate of bed load and suspended load differ and are considered separately (Galappatti & Vreugdenhil, 2010). Better understanding on the mechanics of sedimentation, allow predict downstream sedimentation (Kirkbride, 1999). The inverse approach makes use of channel morphology to inform the antecedents conditions of the channel (Ma & Huang, 2016). Channel morphology provides an integration of past conditions of sediment input, discharge, etc. It also provides information on the transport capacity of the channel: supply limited channels have greater transport capacity than transport limited channels. Canal beds are considered stable when driving forces and the factors (framework) resisting that erosion, are in balance. Sedimentation or erosion will occur the driving forces and the resisting framework within a stream channel, are imbalanced. Einstein (1942) proposed a function to describe the balance as:

$$Q \times S \propto Q_s \times D^{5/3} \quad (2.24)$$

Where:

Q = water discharge (m³/s)

S = bed slope (m/m)

Q_s = sediment discharge (m³/s) and

D_{50} = median sediment size

This function is termed Lane's Law and balances the driving forces on one side against the resisting framework on the opposite side. The concept of Lane's stability equates the product of a canal's sediment load and sediment size with the product of the same canal's slope and discharge. The estimation of each component can be described as follows:

2.5.1 Driving Forces

Lane's Law illustrates that the driving forces in channels increase with larger slope and greater discharge (Burge et al., 2014). Bank full discharge (Q_{bf}) is commonly used as the dominant channel forming flow, occurring when the canal stage reaches the floodplain level (Clayton & Pitlick, 2007). The energy at the channel bed available to do work, calculated using the channel slope and discharge, is represented by stream power (Ω , W/m):

$$\Omega = \rho \times g \times Q \times S \quad (2.25)$$

Where:

Q = water discharge (m^3/s)

ρ = density of water (Kg/m^3) and

g = gravitational constant (m^2/s)

S = bed slope (m/m)

A related energy term is specific stream power (ω , W/m^2):

$$\omega = \frac{\rho \times g \times Q \times S}{w} = \frac{\Omega}{w} \quad (2.26)$$

Where:

ω = specific stream power (W/m^2)

Ω = is normalized by channel width (w) (m)

w = is the flow width (m).

An additional term describing the driving force is the shear stress at the bed (τ_o , Pa):

$$\tau_o = \rho \times g \times R \times S = \frac{\omega}{v} \quad (2.27)$$

Where:

R = hydraulic radius (m) ($R = A/P$, where A is the channel area (m²), P is the wetted perimeter (m)) and;

v = cross-sectional average velocity (m/s).

Then, a related variable to driving force is velocity (v , m/s) because as velocity increases, shear stress and stream power generally increase. Velocity can be estimated using Manning's equation:

$$v = \frac{R^{2/3} \times S^{1/2}}{n} \quad (2.28)$$

2.5.2 Resisting Framework

The resisting framework balances against the driving forces to limit sediment entrainment and transport (Kim et al., 2013). One important aspect of the resisting framework is grain size of the bed sediment. Material with larger grain size offers more resistance to transport than smaller material. Lane's Law uses the median grain size (D_{50}) to describe this effect. However, several other measurable parameters are used to describe the grain size, including D_{16} and D_{84} (the 16th and 84th percentile of the cumulative grain size distribution, respectively). For areas where it is impractical to measure grain size directly, like downstream of all crossings, grain size (D_{50}) can be estimated using a technique developed by Buffington et al. (2004), using:

$$D_{50} = \frac{(\rho \times \alpha \times A^\beta \times S)^{1-n}}{(\rho_s - \rho) \times k \times g^n} \quad (2.29)$$

Where:

k and n = empirical values that vary with channel type and local catchment conditions;

A = drainage basin area covered by the canal stream (m²);

α and β = empirical values representing local physiography (geology, topography and climate), basin hydrology and sediment supply, and

g = gravitational constant (m/s²).

The critical shear stress (τ^*) is the threshold of shear stress on the bed required to initiate motion of a particle. The most common method used to relate particle grain size to the critical shear stress is the Shields equation (Buffington et al., 2004):

$$\tau^* = \frac{\tau_c}{(\gamma_s - \gamma) \times D_{50}} \quad (2.30)$$

Where:

τ^* = the Shields parameter

γ_s = is the specific weight of sediment (N/m^3)

γ = is the specific weight of water (ρg) (N/m^3)

For gravel bed rivers the Shields parameter typically ranges from 0.03 to 0.073.

To estimate the suspended-sediment concentration by the interpolation method, USGS proposed the following equation:

$$Q_s = Q_w \times C_s \times k \quad (2.31)$$

Where:

Q_s = suspended-sediment discharge (tonnes per day)

Q_w = water discharge (m^3/s)

C_s = mean concentration of suspended sediment in the cross-section (mg/L)

k = a coefficient based on the unit of measurement of water discharge that assumes a specific weight of 2.65 for sediment, and equals 0.0864 in SI units.

The other factor from Lane's Law (Burge et al., 2014) is the sediment load (Q_s) or the total volume of sediment transported by a stream channel, applying the transport-curve method also referred as rating curve. A simple relation using the sediment discharge (Q_s) as a function of discharge (Q) is called a sediment rating curve (Peter et al., 2009):

$$Q_s = a \times Q^b \quad (2.32)$$

Where:

Q_s = suspended-sediment discharge (tonnes per day)

Q_w = water discharge (m^3/s)

a and b = are coefficients for the intercept and the slope, respectively.

A dimensionless rating curve has been developed by dividing Q_s by bank full discharge (Q_{bf}). Assuming that the coefficient a does not vary with Q_{bf} , this eliminates a from the equation. Some authors have suggested average values for the exponent b , however b varies from one canal to another and is not predictive but may be calibrated for individual sites.

2.5.3 Sediment Budget

Sediment load is not constant downstream and the effect of increasing sediment input to a stream bed can be assessed through the development of a sediment budget for a reach. The sediment budget can be defined as:

$$\Delta Q_s = Q_{s \text{ in}} - Q_{s \text{ out}} \quad (2.33)$$

Where:

ΔQ_s = change in sediment volume within a reach (m^3)

$Q_{s \text{ in}}$ = volume of sediment entering a reach (m^3) and

$Q_{s \text{ out}}$ = volume of sediment exiting a reach (m^3)

Where ΔQ_s is equal to zero, the bed is stable (termed in grade), ΔQ_s is positive when the bed is aggrading (bed level increasing/sedimentation) and where ΔQ_s is negative when the bed is degrading (bed level decreasing/erosion).

2.5.4 Bed load Transport

Sedimentation on a channel bed depends on the dynamics of sediment transport in a given reach. More than a century of research on sedimentation, bed load transport remains not fully described and there is no universal equation that provides a reliable estimate of the transported bed sediment in a flood or water flow. The sediment size transported in the channel depends on its input, and distribution and energy characteristics of the channel. But, the bed load fraction represents the sediment moving in contact with the channel bed (Downing, 2008). In gravel-bed canals, displacement of particles occurs by different means depending on the duration of the contact between the river bed and the particle. Generally, sediment particles can move by saltation (little jumps in the water column), rolling or sliding (Cislaghi et al., 2015).

Most theories on bed load transport were generated based on flume experiments in laboratories, where flow is steady and uniform (Burge et al., 2014). These experiments, normally use a reductionist approach and do not translate well the natural environment. This is especially true in gravel-bed canals where bed forms affect the flow at different spatial scales (Peter et al., 2005). The scientific community has persistently attempted a diversified

approach to bed load transport (Cislaghi et al., 2015) and it is argued that a combination of a deterministic approach and a stochastic process is better suited to the understanding of bed load transport processes (Jain & Kothyari, 2000). Because of the non-cohesive nature of the bed load sediments in riverbeds, the resistance to entrainment offered by the particle depends on its physical characteristics such as size, shape, mass, particles shape around it and the canal bed structure. The particle remains on the bed by its weight while the forces that lead to the incipient motion are a combination of the drag that acts tangentially to the particle and the lift force. Sediment drag is result of the friction of water and sediment lift takes place by pressure differences around the particle. The entrainment characteristics has been found to be proportional to the shear velocity, μ^* where:

$$\mu^* = \sqrt{\frac{\tau_o}{\rho}} = \sqrt{g \times R \times S} \quad (2.34)$$

Gravel-bed canals presents wide range of particle sizes in their bed sediments composition. The structure of the bed and the presence of various particle sizes creates complex relationships between particle size and the force needed for particle entrainment. In normal situations, small particles require higher force than expected to be entrained, when they are under large particles shield, while larger particles requires lower entraining force when they are protruding in the flow (Hicks et al., 2000). Bed load transport can be divided into three phases (Peter et al., 2005). Each phase of transport is a function of bed load transport intensity and exceeding the critical threshold of particle entrainment of the median particle size. Bed load transport tends to follow a power relationship with a mean hydraulic variable. However, the response of the bed load is highly variable within a flood and from one flood to another (Mueller & Pitlick, 2005), which is explained by the intermittent nature of bed load sediment transport. Bed armour, sediment supply and sediment waves are variables responsible for intermittency of gravel-bed canals. Because of these variables, bed load transport is discontinuous even in steady flow conditions; one set of hydraulic conditions does not lead to one transport response. These intermittencies are characterized by moments of intense transport rates and of low transport rates that return periodically, over various time scales, from seconds to a season. Haschenburger (2003), successfully related the peak of the pulsation to the movement of bed forms. The bed load transport signal is composed of movement at different time scales caused by the movement of individual particles and the

displacement of bed forms where the amplitude is higher at the lower frequency point of the bed load process. The nature of bed load transport intermittency changes in accordance with flow conditions (Church & Hassan, 2002). At low flow conditions, bed load transport becomes very intermittent and it tends to be less intermittent at higher flow conditions.

Gravel-bed canals present particles over a wide size range, therefore, canals with such characteristics their bed load rate is calculated for different sizes in the mixture. Bed sediment size is typically characterized using a cumulative frequency distribution of grain-size. In sedimentation studies, it is common to use the proportions of the size fractions to predict the transport rate. When the bed mixture of the gravel-bed canal is comprised of >40% sand, it is designated matrix-supported, and when it has < 25% sand, the bed is framework-supported (Burge et al., 2000). In addition, gravel-bed canals presents vertical sorting. Surface material is coarser than the sub-surface material. The surface layer is then designated the armour layer because it has the effect of increasing the critical shear stress necessary for entrainment. The composition of the transported sediment is generally finer than the surface layer and closer to that of the sub-surface sediment (Buffington et al., 2004). Bed load transport rate is generally defined as the volume of sediment transport per unit of channel width (Méndez V., 1998). The unit sediment discharge (q_s), is influenced by both flow and bed material variables. Generally, q_s is given as a function of the force of the water (τ_o), water depth (d or y), grain size (D), specific water density (γ), sediment density (γ_s) and water viscosity (μ). Almost all bed load formulae belong to one of three types in which the unit transport rate is related to either, the excess shear stress (Du Boys type), the excess discharge/unit width (Schoklitsch type) or the excess stream power/unit width (Bagnold type), respectively are presented in the Equations 2.35, 2.36 and 2.37 respectively:

$$(\tau_o - \tau_c) \quad q_s = X' \times \tau_o \times (\tau_o - \tau_c) \quad (2.35)$$

$$(q_o - q_c) \quad q_s = X'' \times S^{3/2} \times D^{-1/2} \times (q_o - q_c) \quad (2.36)$$

$$(w_o - w_c) \quad q_s \cong (w_o - w_c)^{2/3} \times d^{-3/2} \times D^{-1/2} \quad (2.37)$$

Where:

X' and X'' = are sediment coefficients (dimensionless)

d = is flow depth (m)

S = is slope (m/m) and

$D =$ is grain size (mm)

2.5.5 Uniformity and Curvature Coefficients

The uniformity coefficient (C_u), and curvature coefficient (C_c) and the effective size (D_{10}) are the grading characteristics of the sediment. These factors indicate the geometric properties of a grading curve describing a particular sediment type. The features and determination of uniformity coefficient, curvature coefficient and the effective size are applied for sediments grading curve characteristics. A grade size distribution curve can be evaluated using different particle sizes, such as D_{60} , D_{30} , and D_{10} . The grading curve represents the graph plotting between the percentage finer in y-axis to the particle size in x-axis on a logarithmic scale. This curve is plotted based on the observations from results of sieve analysis conducted on the soil sample. D_{10} is normally designated effective particle size, which means that 10% percent of the particles are finer and 90% of the particles are coarser than D_{10} . This is the size at 10% finer by weight. Similarly, D_{60} is the particle size at which 60% of the particles are finer and 40% of the particles are coarser than D_{60} size. D_{30} is the size at which 30% is finer by weight and remaining 70% particles are coarser than D_{30} size. Hence, D_{10} , D_{30} and D_{60} are used to determine the measures of gradation.

Measures of Gradation

The uniformity coefficient (C_u) and the coefficient of gradation (C_c) are used to measure sediment gradation of bed load samples. These coefficients help to classify the sediment as either well graded or poorly graded. The uniformity coefficient (C_u) represents the ratio of D_{60} to D_{10} . A value of C_u greater than 4 to 6 is interpreted to mean that the sediment is well graded. When C_u is less than 4, it is classified as poorly graded or uniformly graded sediment. Uniformly graded sediments have been considered to suggest identical particles with C_u value approximately equal to 1. A uniformity coefficient value of 2 or 3 suggest that the sediments are classified as poorly graded. Sand sediments comes under this category. Higher value of C_u indicates that the sediment mass consists of sediment particles with different size ranges. A well graded sediment has the C_c value ranging between 1 and 3. For any single sized sediment mass, the value of both C_u and C_c is 1. C_u is always greater than 1 (equal to 1 is possible only theoretically). If C_u is closer to 1 (this is, D_{60} and D_{10} sizes are close to each other, which means that there are more particles in the same size range), the sediment is said

to be uniformly graded. If C_u is away from 1, the sediment is well graded (this means that, it has a variety of size range distributed well). For gravel, if $C_u > 4$, it is well graded. For sand, if $C_u > 6$, it is well graded. C_c is also greater than 1 (equal to 1 is only possible theoretically). For a well graded sediment C_c ranges between 1 to 3. So, C_u and C_c gives an idea about particle size distribution of a sediment. These values are used in the sediment classification. Equations for C_u and C_c are presented as the following:

$$C_u = \frac{D_{60}}{D_{10}} \quad (2.38)$$

$$C_c = \frac{(D_{30})^2}{D_{10} \times D_{60}} \quad (2.39)$$

Where:

D_{10} = effective particle size which 10% of the particles are finer and 90% of the particles are coarser than D_{10} .

D_{60} = effective particle size which 60% of the particles are finer and 40% of the particles are coarser than D_{60} .

D_{30} = effective particle size which 30% of the particles are finer and 70% of the particles are coarser than D_{30} .

2.5.6 Suspended Load Transport

Suspended sediment transport occur within the water column and generally consists of relatively fine sediment (sand to clay). Cohesion may be important as it leads to aggregation of particles (Jain & Kothyari, 2000). Fundamentally, suspended sediment is moved as upward turbulent water motion supports suspended sediment in the water column (Church, 2006). Deposition occurs where the fall velocity of a particle is greater than the turbulent motion holding the sediment within suspension. The fall velocity of a particle can be calculated using:

$$V_o = \frac{1}{18} \times D^2 \times g \times \frac{\rho_s - \rho}{\mu} \text{ for silt and clay } < 0.0063 \text{ mm (Stokes' Law)} \quad (2.40)$$

$$V_o = \sqrt{\frac{2}{3} D \times g \times \frac{\rho_s - \rho}{\rho}} \text{ for gravel } > 2 \text{ mm} \quad (2.41)$$

Where:

V_o = is the settling velocity (m/s);

D = is the grain size (mm);

ρ_s = is the sediment density (assumed to be 2650 kg/m³);

ρ = is the water density (1000 kg/m³) and;

μ = is the dynamic viscosity (affected by temperature) (N.s/m²)

For sand, a composite law can be derived based on particle *size*, as presented in Table 2.3, as adapted from Wilcock et al. (2009).

Table 2. 3: Fall Velocity for Sand-Size Sediment in Still Water at 20°C

Grain Size D (mm)	Wentworth Scale	Fall velocity V _o (m/s)
0.089	Very fine sand	0.005
0.147	Fine sand	0.013
0.25	Medium sand	0.028
0.42	Medium sand	0.050
0.76	Coarse sand	0.10
1.8	Very course sand	0.17

Source: Adapted from Wilcock et al. (2009).

Water velocity and grain size were related to the entrainment, transport and deposition of suspended sediment by Hjulstrøm (1939) through the development of two curves: one for entrainment and one for deposition. The depositional curve is set to help find velocities at which sediment of a given size would be deposited. There is large difference between the entrainment curve and the depositional curve for fine sediment, indicating that sediment will be entrained at a much higher velocity than it would be deposited. This leads to the suspended sediment being often deposited far away from the water source area (Church, 2006). However, sediment can deposit at downstream pool or riffle and depends on the local velocities at the time. The concentration of suspended sediment is generally several orders of magnitude below its sediment transport capacity (Knighton, 1998). Therefore, the dominant control on suspended sediment concentration is given by the rate of supply. Concentration of suspended sediment may change throughout a storm hydrograph and also throughout the year. These temporal changes can cause hysteresis due to the fact that the rate of fine sediment supplied to the flow is greater during the rising limb of the hydrograph compared to the falling limb (Knighton, 1998; Ma & Huang, 2016). Sediment that are deposited on the

channel bed between storms is entrained by the increasing velocities during the rising limb, leaving less sediment supplied to the flow during the falling limb (Knighton, 1998).

2.6 Evaluation of Best Scenario Predicting Sediment Deposition

The amount of water and sediment load, entering into an irrigation canal, may change with crop growing season and life time of the irrigation system. Such change can be managed by different tools. Different factors such as the water supply, water requirements to the crop, size of the area-to-be-irrigated, planned cropping pattern and concentration of sediment can vary in disproportional magnitude, and this can frequently occur during the life time of a given irrigation system. The design of the irrigation canals and flow controlling structures allows to some extent, flexibility in the delivery of different water flows. To achieve this fixed water levels and the incoming sediment conveyance is made possible under equilibrium condition assumptions for the entire sediment load transport (Partheniades, 2009; Paudel, 2010; Peizhen et al., 2001). When flow conditions is found with slight deviations in relation to values of designed canal, then the flow velocity and its capacity for transporting the sediment load may change in time and space in the irrigation canal. Then, the assumption at the initial period related to the conveyance of the sediment load in equilibrium condition is not longer relevant in such changing flow conditions. The process of the sediment transport in an irrigation canal is then characterised by conditions of non-equilibrium for such changes in the operations situations (Perk, 2008). Therefore, the sediment transport become entirely relying on the changes of the initial conditions of the water inflow and sediment load at the irrigation season or the life span of that canal. Because of such conditions the sediment transport in an irrigated canal is viewed in a more broader context taking into consideration the time and place of such changes in the system. To attain such desired situation models may be necessary to be applied and scenarios analysed as predicting factors for sedimentation in the irrigation scheme (Shi, 2008). Additionally, sediment transport models allow predicting the behavioural conditions of the sediment deposition in time and space, for particular inflow condition and incoming sediment load. Such models are supposed to give detailed applicabilities and improved understandings on the processes of the sediment transport in the irrigation systems (Perk, 2008). Different models can be used to run simulations for a certain period of time in given irrigation canal, whereby their initial geometrical and hydraulic conditions and the incoming sediment characteristics, are given.

Based on these results the sediment load are often either transposed with none deposition along the whole canal or it is often adjusted from a non-equilibrium condition to the sediment transport capacity of the canal. The adjustment for assessing the capacity of the sediment transport is predicated on the Gallapatti's depth-integrated model. A sediment mass balance in each reach of the canal gives either net deposition or net entrainment between the two boundaries of that specific canal reach. Just in case the incoming sediment load is a smaller amount than the transport capacity of the canal, two possibilities can occur counting on whether motion of sediment occurs or not. Within the first case, entrainment of the previously deposited sediment occurs until the difference to the sediment transport capacity of the canal is observed. For the second case, the sediment load is conveyed with none change. The effect of changes within the incoming sediment load on the sediment transport will include the effect of variations within the incoming sediment concentration and within the median sediment size during the irrigation season. These changes are associated with the sediment concentration and sediment size as assumed for the equilibrium conditions. As sediment deposition and therefore the removal of the sediment belong to the foremost important problems in irrigation canals, the effect of controlled deposition of sediment by deepening or widening of one or some reaches of the canal are often simulated. From a study by Mendez (1998) different sediment predictors are described and compared for equilibrium conditions. That study, the effect of the varied sediment transport predictors, like Ackers and White, Brownlie and Engelund and Hansen, on the sediment deposition were compared. Further, sediment deposition during a particular period and under non-equilibrium conditions were simulated. Adaptation of the non-equilibrium condition to the equilibrium condition were also performed for each sediment transport predictor. Hence, this approach was adopted for this study, to seek out how applicable it can be for the CIS characteristics.

All this may be done considering that an irrigation canal has got to deliver water at the proper amount, at the specified time and at the right elevation to the command area. There the quantity of water must be kept at the proper level for varying discharges by flow control structures, which may be divided into two main groups, namely undershot and overflow structures. The choice of the structure depends on various operational aspects, one among which is that the ability of the structure to pass sediment. The influence of the two sorts of

structures on the sediment deposition and therefore the distribution of the sediment deposition along the whole canal are often compared by using the model. Among these methods include by Ackers and White (1973), Bagnold (1966), Bishop et al. (1965), Brownlie (1981), Colby (1964), Einstein (1950), Engelund and Hansen (1967), Toffaletti (1969), Yang (1973), Van Rijn (1984), and whatmore. But, the extent of accuracy of those methods in predicting sedimentation remains poor. Van Rijn (1984) stated that it's hardly possible to predict any sediment transport without an inaccuracy, which may be found between 0 and 100%. In fact, it's quite difficult to form firm recommendations about which formula to use in practice. However, a comparison of sediment transport methods under the standard flow conditions and sediment characteristics of irrigation canals could become a strong tool to scale back inevitable errors and inaccuracy. Given the restrictions to see all the prevailing methods to predict sediment transport, only few models are often tested. During this work five of the foremost widely used methods to compute sediment transport are evaluated. These methods are of Ackers and White, Brownlie, Engelund and Hansen, Van Rijn and Yang, as presented in the following Table 2.4.

Table 2. 4: Selected Empirical Formulas for Predicting of Sediments

Formula	Name	Equation
$q_s = G_{gr} \times s \times d_{35} \times \left(\frac{V}{u_*}\right)^n$	Ackers-White (1973)	(2.42)
$q_s = 727.6 \times c_{f\ gr} \times (F_g - F_{gcr})^{1.978} \times S^{0.6601} \times \left(\frac{R}{d_{50}}\right)^{-0.3301}$		(2.43)
Grain Froude number: $F_g = \frac{V}{[(s-1) \times g \times d_{50}]^{0.5}}$		(2.44)
Critical Grain Froude number: $F_{gcr} = 4.596 \times \tau_{*o}^{0.5293} \times S^{-0.1405} \times \sigma_s^{-0.1696}$	Brownlie (1981)	(2.45)
Critical dimensionless shear stress: $\tau_{*o} = 0.22 \times Y + 0.06 \times (10)^{-7.7 \times Y}$		(2.46)
The Y value is computed from: $Y = (\sqrt{s-1} \times R_g)^{-0.6}$		(2.47)
Grain Reynolds number: $R_g = \frac{(g \times d_{50}^3)^{0.5}}{31620 \times \nu}$		(2.48)
$q_s = \frac{0.05 \times V^5}{(s-1)^2 \times g^{0.5} \times d_{50} \times C^3}$	Engelund-Hansen (1967)	(2.49)
$q_b = 0.053 \times (s-1)^{0.5} \times g^{0.5} \times d_{50}^{1.5} \times D_*^{-0.3} \times T^{2.1}$	Van Rijn (1984a & 1984b)	(2.50)
$q_s = 0.001 \times c_t \times V \times h$	Yang (1973)	(2.51)

Where:

D^* = Dimensionless grain parameter

or particle parameter (-)

s = Relative density (-)

ν = Kinematic viscosity (m^2/s)

g = Gravitational acceleration (m/s^2)

d_{35} = Representative particle diameter (mm)

d_{50} = Median diameter (mm)

F_g = Grain Froude Number (-)

F_{gcr} = Critical grain Froude number (-)

R_g = Grain Reynolds number (-)

u^* = Shear velocity or bed shear velocity related to grains (m/s)

T = Bed Shear parameter (-)

u^*_{cr} = Critical bed shear velocity (m/s)

n = Exponent in the dimensionless mobility parameter F_{gr} (-)

h = Water depth (m)

G_{gr} = Dimensionless transport parameter (-)

c = Coefficient in the transport parameter (-)

$q_b=q_s$ = bed, suspended and total sediment transport rate per unit width (m^2/s)

Y = Y value (-)

S = Bottom slope (m/m)

G_{Stdev} = Geometric standard deviation (-)

C_f = Coef of transport rate for field conditions (-)

)

R = Hydraulic radius (m)

C = Chezy coefficient ($m^{1/2}/s$)

c_t = Total sediment transport expressed in ppm

by mass

V = Mean velocity (m/s)

2.7 Statistical Analysis

2.7.1 Principal Components Analysis (PCA)

PCA is a data reduction technique aimed at reducing the dimensionality of any given data set, and finding important spectral features which hold a significant influence on the spectral variance and to identify subtle relationship within data which contains a large number of variables (Varmuza & Filzmoser, 2009). The technique performs dimension reduction, data modeling, detection of outliers, and selection of main variables, classification, validation and prediction of samples (Miao & Lv, 2020; Shen et al., 2019). For this, the PCA rotates the original variables within the data set and transforms into new variables which lie in new planes of maximum variance, such that the first few axes reflect most of the variations within the data. The new variables are referred to as principal components (PCs). PCs are orthogonal to each other to ensure that each of the new variables are not related. The PCs are computed in order of maximum variance, which means that PC 1 represents the largest amount of

variance followed by PC 2 and PC 3. The PCs are sorted out in decreasing order of importance as dictated by their associated eigenvalues (Setiawan et al., 2020). This technique is applied for data exploratory analysis, this is, to search for underlying similarities or differences in the data set, and hence also referred to as unsupervised method. The common method for determination of the optimum PCs number is through plotting the PCA eigenvalues, which in turn represents the PC variances, versus the PC number to obtain a scree plot (Setiawan et al., 2020). The amount of the total variance of a principal component is generally represented by the eigenvalues (Landgraf & Lee, 2020; Shen et al., 2019; Wang & Aelst, 2020; Zakhem et al., 2017; Zhang et al., 2020). The principal component breaks or drops in the scree plot points out to components to be considered in subsequent analyses, since they indicate components that represent significant amount of variance in the data set. The flat region in the graph represents components with a small amount of variance, which is not optimum for subsequent analyses, and thus should not be retained (Varmuza & Filzmoser, 2009). The eigenvalue criterion refers that only the PCs with eigenvalues greater than one unit should be taken into account as important (Gyimah et al., 2020; Souza et al., 2020).

The relationship between the old and new variables is demonstrated by the loadings plot. This plot essentially illustrates the contribution of the old variables, such as the water discharge at differing canal depths in spectra, to the principal component. This allows the regions of the spectra which account for the greatest amount of variance (largest contribution) to be distinguished from noise, the spectroscopic structures which are not relevant to the structure of the PC. Each analyzed sample is assigned a score with respect to a particular PC. By plotting two PCs against each other, samples will be separated based on their scores for each PC. This plot is referred to as the scores plot and is the method by which the subtle differences in spectra due to differing constituent concentrations can be used to distinguish the sample. Factor loadings indicate both the contribution of the variable to PC and how well the PC takes into account the variation of the same variable over the whole points in the data. In geometrical terms, factor loadings are simply the cosine of the angle lying between the variable and the current PC. Therefore, smaller angle has a larger loading. Hence factor loadings can only vary from -1 to +1.

2.7.2 Holt-Winters Method

Holt (1957) and Winters (1960) has expanded the Holt's method so that this can be used to capture seasonality in observations data. The Holt-Winters seasonal method can be reduced into the forecasting equation and other three smoothing equations, where one is related to the level ℓ_t , another to the trend b_t , and the last one into the seasonal component s_t , having corresponding smoothing parameters α , β^* and γ , respectively. In these equations, m denotes the seasonality frequency, such as the number of seasons in a year. If the frequency seasonality as to do with a quarterly data within a year, then $m=4$, and in case of monthly data $m=12$. Normally, there are two degrees of variations to consider in this method, that differ in the nature of their components seasonality. First, is the additive method, recommended when the variations in seasonality are roughly constant through the series, and secondly, the multiplicative method, recommended when the variations in seasonality change in proportions to the level of the series. The additive method provides relations of the seasonality components in absolute terms, in the scale of the observed series, as well as, in the level equation the series is seasonally adjusted by subtracting the seasonal components. In each and every year, component seasonality adds up to zero, approximately, whilst for multiplicative method, the seasonal component expresses in relative terms (percentages), and the series are seasonally adjusted by dividing through by the seasonal component. In each year, the components seasonality sums up to approximately m . The level equation shows a weighted average between the seasonally adjusted observation $(y_t - s_{t-m})$ and the non-seasonal forecast $(\ell_{t-1} + b_{t-1})$ for time t . The trend equation is identical to Holt's linear method. The seasonal equation shows a weighted average between the current seasonal index, $(y_t - \ell_{t-1} - b_{t-1})$, and the seasonal index of the same season of year before (it is, m time periods ago). Equations for both components are presented in the following:

The component form for the additive method is:

$$\hat{y}_{t+h|t} = \ell_t + h \times b_t + s_{t+h-m \times (k+1)} \quad (2.52)$$

$$\ell_t = \alpha \times (y_t - s_{t-m}) + (1 - \alpha) \times (\ell_{t-1} + b_{t-1}) \quad (2.53)$$

$$b_t = \beta^* \times (\ell_t - \ell_{t-1}) + (1 - \beta^*) \times b_{t-1} \quad (2.54)$$

$$s_t = \gamma \times (y_t - \ell_{t-1} - b_{t-1}) + (1 - \gamma) \times s_{t-m} \quad (2.55)$$

The component form for the multiplicative method is:

$$\hat{y}_{t+h|t} = (l_t + h \times b_t) \times s_{t+h-m \times (k+1)} \quad (2.56)$$

$$l_t = \alpha \frac{y_t}{s_{t-m}} + (1 - \alpha) \times (l_{t-1} + b_{t-1}) \quad (2.57)$$

$$b_t = \beta^* \times (l_t - l_{t-1}) + (1 - \beta^*) \times b_{t-1} \quad (2.58)$$

$$s_t = \gamma \frac{y_t}{l_{t-1} - b_{t-1}} + (1 - \gamma) \times s_{t-m} \quad (2.59)$$

Where:

k = integer part of $(h-1)/m$, which ensures that the estimates of the seasonal indices used for forecasting come from the final year of the sample.

2.7.3 Statistical Parameters for Model Selection

Beside the aforementioned parameters, other statistical indicators can be used, among them, is the Adjusted Coefficient of Determination (Adj. R^2 , R^2_{adj} . or \bar{R}^2), Mean Absolute Percentage Error (MAPE), Root Mean Square Error (RMSE), Durbin-Watson statistic (DW), Mallows coefficient (Cp), Akaike's Information Criterion (AIC), Schwarz's Bayesian Criterion (SBC) and Amemiya's Prediction Criterion (PC) (Charnigo et al., 2011; Chen, 2018; Goyal et al., 2017; Fujikoshi et al., 2005; Luo et al., 2006; Momber & Marquardt, 2019; Yurekli & Ozturk, 2003). When assessed in terms of their importance, Adj. R^2 appears to be more important followed by MAPE and RMSE. On the other side, AIC and SBC, are most important models followed by DW, Cp and PC.

Adjusted Coefficient of Determination (\bar{R}^2)

Adj. R^2 refers to the adjusted value of the coefficient of determination in which the number of variables of the data set is taken into consideration. This coefficient determines the fitting of the multiple regression equations for the sample data, and the proportion of variation which is determined by the estimated line of regression. The Adj. R^2 takes the values between 0 and 1, and it explains the percentage of variation of the independent variables that affect the dependent variables. If the Adj. R^2 is closer to 1, it indicates that the estimated equation of regression fits the data. The value of the Adj. R^2 increases only when new independent variables are added which in turn increases the power of the regression equation. Hence, the adjusted coefficient of determination is widely used in multiple regression analysis. In this

way, it is a very useful measure than the coefficient of determination (R^2). The formula for the Adj. R^2 from the obtained value of the R^2 is defined as,

$$\bar{R}^2 = 1 - (1 - R^2) \left[\frac{n-1}{n-(k+1)} \right] \quad (2.60)$$

Where:

n = sample size

R^2 = coefficient of determination

k = number of independent variables in the equation of regression.

The adjusted coefficient of determination is always less than or equal to the coefficient of determination. The addition of independent variables that do not fit the model will be penalized by the adjusted coefficient of determination. If the adjusted coefficient of determination is negative, it indicates that the model does not fit the data.

Mean Absolute Percentage Error (MAPE)

The Mean Absolute Percentage Error (MAPE), also known as Mean Absolute Percentage Deviation (MAPD), is a measure of accuracy prediction of a forecasting method in statistics. It is used in trend estimation, also in loss function for regression analysis in Machine Learning. The MAPE is also used to measure the size of the error in percentage terms, and it is calculated as the average of the unsigned percentage error, as shown in the equation:

$$MAPE = 100 \times \frac{1}{n} \times \sum_{i=1}^n \left| \frac{Obs_i - Model_i}{Obs_i} \right| \quad (2.61)$$

Where:

Obs = observation value

Model = forecast value

Root Mean Square Error (RMSE)

Analysis based on the Root Mean Square Error (RMSE) and Durbin-Watson statistic (DW) were also performed (Boylan & Cho, 2013; Goyal et al., 2017; Ingrassia & Morlini, 2005; Yurekli & Ozturk, 2003). RMSE measures the average error performed by the model in predicting the outcome for an observation, and the lower the RMSE, the better the model. The RMSE give description about the sample standard deviation of the differences between the predicted and observed values. Such differences are referred as residuals, when the

calculations are done over the data sample that was used to estimate, and referred as prediction errors, when it is calculated out of sample. The RMSE constitutes the aggregation of the errors magnitude in predicting different times into a single measure of predictive power.

$$RMSE = \sqrt{\sum_{i=1}^n \frac{(X_i - Y_i)^2}{n}} \quad (2.62)$$

Where:

n = number of data

X_i = observed value

Y_i = predicted value

Durbin-Watson statistic (DW) and Amemiya's Prediction Criterion (PC)

Durbin-Watson statistic (DW) and Amemiya's Prediction Criterion (PC) are useful parameters in model selection. The first, DW, is used to test autocorrelation in residuals from a given regression analysis. Normally, the DW test statistic ranges in between 0 to 4, and when it has a value of 2 it indicates that there is no autocorrelation in the dataset. Value nearing 0 (and below 2) indicates positive autocorrelation and value towards 4 (and over 2) indicates negative autocorrelation (Fujikoshi et al., 2005). On the other hand, the Amemiya's Prediction Criterion (PC), is based on the Adjusted R², and therefore, the bigger value for PC implies a better model (Srinivas et al., 2019).

Mallows coefficient (Cp)

Mallows coefficient (Cp) is used to help choose between regression models, as it makes comparisons of the precision and bias of the full model to models with a subset of the predictors (Charnigo et al., 2011; Mallows, 2000). In applying Mallows' Cp, it is recommended to look for models where its value is small and close to the number of predictors in the model plus the constant (p). When the Mallows' Cp value is small it suggests that the model is relatively precise, that is, has small variance, being used in estimating the true regression coefficients and predicting future responses (Aydın & Memmedli, 2012; Bhattacharyya & Sengupta, 2009; Fujikoshi et al., 2005). The Mallows' Cp value that is close to the number of predictors plus the constant, elucidates that the model is relatively unbiased

in estimating the true regression coefficients and predicting future responses. Models having lack-of-fit and bias presents values of Mallows' Cp greater than p.

Akaike’s Information Criterion (AIC) and Schwarz’s Bayesian Criterion (SBC)

Akaike’s Information Criterion (AIC) and Schwarz’s Bayesian Criterion (SBC) are widely used in model selection criteria. AIC serves to compare quality of a set of statistical models to each other. The AIC takes each model and rank them from the best to the worst. In this case, the “best” model is the one that neither under-fits nor over-fits. Although the AIC will help in choosing the best model from a set, it won’t indicate their absolute quality. Therefore, the best model is identified, it is recommended that a hypothesis test is run in order to figure out the relationship between the variables in the model and the outcome of interest. Akaike’s Information Criterion is usually calculated with software application. The basic formula is defined as:

$$AIC = -2(\log - likelihood) + 2K \tag{2.63}$$

Where:

K= number of model parameters (the number of variables in the model plus the intercept).

Log-likelihood = measure of model fit. The higher the number, the better the fit. This is usually obtained from statistical output.

For small sample sizes ($n|K \leq 40$), it is used the second-order AIC:

$$AIC = -2(\log - likelihood) + 2K + \left(\frac{2K(K+1)}{n-K-1}\right) \tag{2.64}$$

Where:

n = sample size

K = number of model parameters

Log-likelihood = measure of model fit

SBC, Bayesian Information Criterion (BIC) or SBIC, is an statistical criterion for model selection among a class of parametric models with different numbers of parameters. Choosing a model to optimize SBC is a form of regularization. SBC uses maximum likelihood to estimate model parameters estimation to increase the likelihood by adding parameters, which may result in overfitting. The SBC solves such cases by introducing a

penalty term for the number of parameters in the model. SBC penalty for additional parameters appears to be stronger than that of the AIC. The SBC is asymptotic result derived under the assumptions that the data distribution is in the exponential family.

$$-2 \times \ln p(x|k) \approx SBC = -2 \times \ln L + k \ln(n) \quad (2.65)$$

Where:

x = the observed data;

n = the number of data points in x , the number of observations, or equivalently, the sample size;

k = the number of free parameters to be estimated. If the estimated model is a linear regression, k is the number of regressors, including the constant;

$p(x|k)$ = the likelihood of the observed data given the number of parameters;

L = the maximized value of the likelihood function for the estimated model.

Under the assumption that the model errors or disturbances are normally distributed, this becomes (up to an additive constant, which depends only on n and not on the model):

$$SBC = n \ln \left(\frac{RSS}{n} \right) + k \ln(n) \quad (2.66)$$

Where:

RSS = residual sum of squares from the estimated model.

Note that the term for $-2 \times \ln L$ used in this specialization is equal to the rescaled normal loglikelihood up to an additive constant that depends only on n .

2.8 Calibration and Validation of the Models

Model calibration involves checking the model results with the observed data and adjusting the parameters until the model results fall within acceptable range of accuracy. Calibration of the model is accomplished by matching the computed and measured water levels and discharges of the off-takes for the same flow conditions at the head of distributary. After calibration of the model for typical situations observed in the field, the model is validated with another data set to recheck the results simulated from the model. Different procedures are available for model validation, being one of them the technique of cross validation (leave-one-out cross-validation year method or jack-knife technique) (Laanaya et al., 2017). Additionally, to further check the calibration and validity of the model Root Mean Square Error (RMSE), Nash-Sutcliffe Efficiency Coefficient (NSE) and Percent bias (PBIAS) are

used for criteria. NSEC values ranging between 0 and 1.0 are generally viewed as acceptable levels of performance, whereas values ≤ 0.0 indicate unacceptable performance (Mutua & Klik, 2007).

Some parameters can be determined to evaluate the performance of a given model. These include the Correlation Coefficient (R), Nash–Sutcliffe Efficiency Coefficient (NSEC), Root Mean Square Error (RMSE) and Relative Error (RE). The larger values of the NSEC and R and smaller one of RMSE indicate the higher accuracy of the model (Roushangar & Shahnazi, 2020). The Percent bias (PBIAS) measures the average of the tendency of simulated data to be larger or smaller than their observed counterparts. The optimal value of PBIAS is zero and lower values indicate better simulation. A positive value indicates a tendency of the model for underestimation while negative values indicate overestimation (Mutua & Klik, 2007; Tariq & Latif, 2010). In the following is presented the Equations 2.67-2.70 commonly used to determine R, NSEC, RE and PBIAS, respectively:

$$R = \frac{\sum_{i=1}^N (X_i - \bar{X}) \times (Y_i - \bar{Y})}{\sqrt{\sum_{i=1}^N (X_i - \bar{X})^2 \times \sum_{i=1}^N (Y_i - \bar{Y})^2}} \quad (2.67)$$

$$NSEC = 1 - \left\{ \frac{\sum_{i=1}^N (X_i - Y_i)^2}{\sum_{i=1}^N (X_i - \bar{X})^2} \right\} \quad (2.68)$$

$$RE = \sqrt{\sum_{i=1}^N \frac{|(X_i - Y_i)/X_i|}{N}} \quad (2.69)$$

$$PBIAS = \left\{ 100 \times \frac{\sum_{t=1}^n X_t - \sum_{t=1}^n Y_t}{\sum_{t=1}^n X_t} \right\} \quad (2.70)$$

Where:

n = number of data

X_i = observed value

Y_i = predicted value

\bar{X} and \bar{Y} = mean values of the observed and predicted values

2.9 Sensitivity Analysis

A sensitivity analysis can be performed in order to evaluate the effects of various inputs, such as water flow, sediment inflow and sediment particle size on the model's output. The canals downstream of the irrigation system can be simulated using the design discharge data with a certain sediment concentration and mean particle diameter. The parameters like water inflow

discharge, mean sediment inflow, median diameter and canal roughness may change and the effects observed on the sediment deposition volume in the canals. Simulations can also be performed for a given period and applied in a model. From the results, normally the most and the least influential parameters can be identified (Ding & Langendoen, 2018; Roushangar & Shahnazi, 2020).

CHAPTER THREE

MATERIALS AND METHODS

3.1 Study Area

This study was undertaken at Chókwè Irrigation Scheme (CIS) which is located in the Limpopo River Basin (LRB), Chókwè District, Gaza Province in Mozambique. The scheme is located at the Lower Limpopo River Sub-Basin (LLRSB), covering approximately 84 981 km² and lies between latitudes 24°04'32'' to 25°01'35''South and longitudes 32°40'11'' to 33°37'14''East. The area is largely dry, with rainfall around 500-600 mm/year. Rainfall events are concentrated between October and March. The population density is 88.78 inhabitants/km² (INE, 2019) according to 2017 Census results (City Population 2019; de Sousa et al., 2020). The Limpopo River originates in central southern Africa and flows generally eastwards to the Indian Ocean, traversing a terrain encompassing an altitude of 1,600 m in South Africa (Drakensberg Mountains) to the sea level in Mozambique (WMO, 2012). Its length and drainage area are estimated at 1,750 km long and 430,000 km², respectively, while the mean annual discharge at its mouth in Mozambique is 170 m³/s (Magombeyi et al., 2013 and 2016). The CIS is the main irrigation scheme in Mozambique and abstracts water from Limpopo River at a flow of approximately 45 m³/s. Water is diverted to unlined canals benefiting more than 12000 farmers tilling approximately 33,000 hectares for food production (HICEP, 2012; Munguambe et al., 2013). CIS is used to deviate, store, manage and distribute water to the local agricultural producers, for which relies on Massingir dam and Macarretane weir, at the upstream. Agriculture is the main economic activity in the region and constitutes the backbone of the district, producing rice, maize and vegetables. Gravity flow system is the main form of water supply through furrow and flood methods. The main crops in the region are rice (for WS), vegetables (DS) and maize (in both seasons). Chókwè district is located South of Gaza Province in the middle reaches of the Limpopo River, into the North. Limpopo River separates Chókwè from the Massingir district, Mabalane and Guijá. At the South is Bilene district and Mazimuchope River that separates it from the district of Magude. To the East, Chókwè confines with Bilene district and Chibuto, and to the West with the districts of Magude and Massingir. Figure 3.1 shows map of the Chókwè district, as adapted from HICEP, E.P (2012).

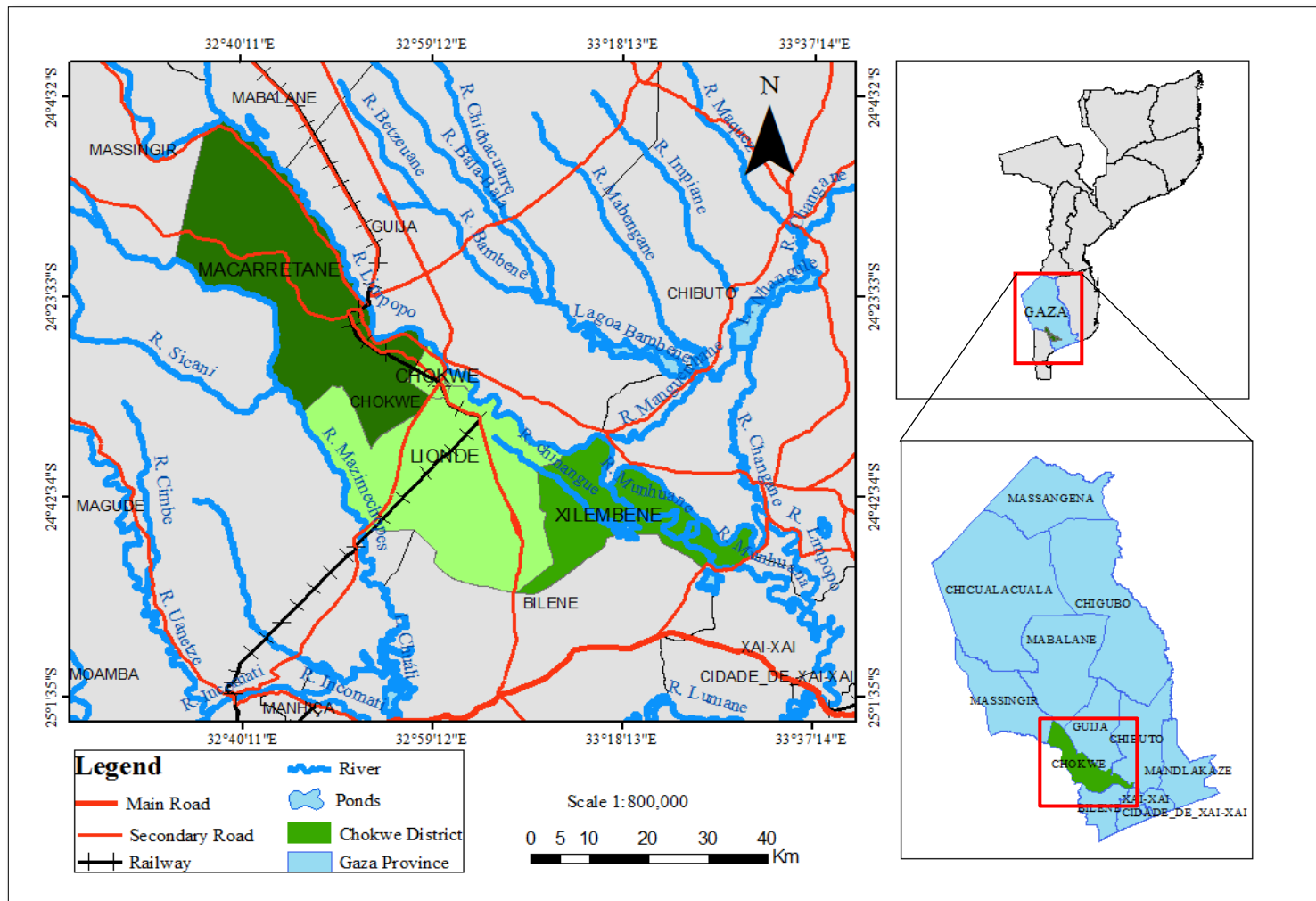


Figure 3. 1: Map of Chókwe District in Gaza Province, Mozambique

3.1.1 Climate and Soils

The climate of the area is classified by Köppen (Munguambe et al., 2013) as BSW (semi-arid, mega thermal), that is, a steppe climate with a dry period in winter. In the area, the average rainfall is 530 mm/year and the annual average temperature is 23.6° C, the wind speed is around 153 km/day and insolation is 7.9 hr/day. The relative humidity has an average of 65%/year (Sousa, 2012). The reference evapotranspiration based on Penman-Monteith method exceeds the rainfall in every month, and is about 1400 mm (Munguambe et al., 2013). The soils in the region consist mostly of marine formation, often with saline-sodic underground, which requires efficient drainage. In addition, the soils consist of river terraces, which is rich in fertility. CIS has very fertile land due to deposition of materials transported by the river, a fact that leads to good yields without use of fertilizers, in most areas. In general, soils are predominantly clayey to clay-loam, heavy, compact, impenetrable and very abrasive, tending to alkalinity (Munguambe et al., 2013). They are also considered to be deep (with an effective thickness greater than 1 m), with clay content of around 35%. The internal permeability is moderately rapid (7-10 mm/hr) with a usable fraction of water ranging between 10 and 13% which varies with the content of organic matter and clay. These soils achieve high yields, but require careful monitoring (Munguambe et al., 2013). The pH ranges from 7.0 to 7.3.

3.1.2 Hydraulics in the Irrigation Scheme

The hydraulic structure of the irrigation scheme as illustrated in Appendix C, includes the Massingir dam, Macarretane weir, the main, secondary and tertiary canals, as well as the drainage networking. Massingir dam is located nearly 130 km from Chókwè city and has a role to store water and convey it through Limpopo River stream to the Macarretane weir, at 30 km from Chókwè city. Here water level is managed before continuing its course to the CIS. These two structures play an important role on flood and drought management in the area. The CIS is composed of three main hydraulic sectors, namely Montante, Sul and Rio, which involves three levels of water conveyance: Main Hydraulic Units (MHU), Secondary Hydraulic Units (SHU) and Tertiary Hydraulic Units (THU). MHU includes a protection dike that is 75 km on the west bank of Limpopo River; Main unlined canals (*Geral, Rio, Direito* and *Nwachicoloane*), operating under upstream command. The total nominal discharges are between 4 and 45 m³/s, having a total length of 98.710 km; Main drains (of 125 km length)

covering a surface of 30,000 hectares and the remaining 3,000 hectares of MHU are naturally drained; and has Main roads connecting to the National Road of nearly 155 km in length. Additionally, the SHU includes 107 secondary zones, with 42 secondary canals (off-takes) directly supplied by the MHU. Its discharges varies between 0.1 to 4 m³/s, with a total length of 270 km; Pumping equipment's and water distribution directly connected to the MHU canals; Secondary drains (of 450 km), covering 27,000 hectares, and the remaining 6,000 hectares of the SHU are naturally drained; and feeder roads over these secondary's networking of 175 km. Finally, the THU, has prefabricated tertiary canals supplying water to the irrigation extensions, with unitary discharge of 32 l/s, and a total of 1,050 km of length; and Trenches draining the extensions; and accessing ways to the plots.

3.1.3 CIS Operation Characteristics

The CIS is operated by a public company known as Hydraulic of Chókwè, Public Company (Hidráulica of Chókwè, E.P). It observes a fixed mode of operation: Supply Based Operation (SBO) and running flexible operation model (Crop Based Irrigation Operations (CBIO)). In SBO the canals are operated always at full supply discharge depending on the water availability at the source. Whereas, in case of CBIO, when it is considered, the canals would be operating according to the crop water requirement, mostly applied at periods of lower water availability. This work gathered relevant data from the CIS, taking into account its current operation characteristics. The sampling stations for data collections as obtained from Google Map (Google Earth Pro, 2019) are presented in Figure C.3 of the Appendix C.

3.1.4 Data Acquisition

The primary data on physical and hydraulic parameters were obtained from fieldwork whereby consideration was given to the canal bathymetry, its depth, and cross-section and longitudinal slope profiles. Additionally, water discharge and water depths, water temperature, water electric conductivity, water turbidity and water pH, were also collected and analysed. Field data on suspended and bed sediment were sampled from different stations within the study area. Nine sampling points were established across the main canal of CIS. Three at each section of the canal, namely; upstream (Montante section), midstream (Sul section) and downstream (Rio section). At the upstream of the CIS (at the Montante section), three sampling points were established, namely Macarretane Weir Intake, Railways-Node and

FIPAG bridges. In the midstream of the irrigation scheme (at Sul section), other three sampling stations were established as; Lionde, Massawasse and Conhane bridges. At the downstream point (at Rio section), samplings were done at Nico, Muianga and Marrambajane bridges. Table 3.1 presents all sampling stations, coordinates and their cumulative distances from the Intake.

Table 3. 1: Sampling Stations and Cumulative Distances from the Intake

Sampling station code	Station name	Cumulative Distance from Intake (km)	Coordinates		Elevation* (m)
			Latitude	Longitude	
P0G	Intake	0.000	S24°24'12.10"	E032°52'05.90"	42
P1G	Railways bridge	1.527	S24°24'53.21"	E032°51'37.89"	41
P1O	Node	14.102	S24°28'23.29"	E032°56'37.34"	36
P1D	Node bridge	14.154	S24°28'25.30"	E032°56'37.80"	36
P3D	Chókwè bridge (FIPAG)	23.359	S24°31'26.30"	E033°00'15.40"	33
P2O	River canal	33.889	S24°34'55.70"	E033°03'45.62"	31
P6D	Lionde bridge	33.960	S24°34'57.30"	E033°03'47.50"	31
P7D	Massawasse bridge	40.031	S24°38'08.40"	E033°04'39.10"	26
P9D	Conhane bridge	44.312	S24°40'10.10"	E033°05'35.60"	25
P2O	River canal	33.889	S24°34'55.70"	E033°03'45.62"	31
P2R	Nico bridge	44.339	S24°37'28.30"	E033°08'60.90"	27
P3R	Muianga bridge	47.244	S24°38'11.10"	E033°09'98.20"	26
P6R	Marrambajane bridge	58.872	S24°41'30.30"	E033°15'65.50"	23

**Elevation obtained by GPS placed at the top of the sampling station bridge.*

The study covered an estimated distance of more than 80 km, leaving out some parts of the CIS, such as Canal Esquerdo, Canal of Nwachicoluane and the most downstream of Rio section, below Marrambajane bridge towards the Chiguidela region. The choice of the sampling stations were based on the hydrodynamics and history of the canal hydraulic

characteristics and properties relevant to sedimentation taking place in the scheme. Sediment inflow and outflow, as well as alluvial adjustments can have effect on the sediment transport rates computation. Moreover, the fact that the scheme reaches are lengthy, abstracting water from the Limpopo river mainstream, conveying water into an transnational boundary, and occurrence of steep slope from the country entering point to the Indian Ocean, exacerbates the watershed risk and vulnerability to sedimentation. Furthermore, having the scheme entirely unlined, makes the site highly prone for sediment accumulation at any point of the scheme. Additionally, the main canal shape and geometry design, and its alterations in result to inflow and human kind activities, presence of meanders and vegetation, which can trap large fraction of the sediment supply, served as basis in choosing the reaches and specific locations for samplings. Therefore, due to their potentials to influence hydrodynamics changes in transport and bed loads composition in the reach, sampling stations were picked to better represent the entire affected sites in the scheme. The fact that this study is the first of its kind in the site, also played a role to use the opportunity to bring up a grasp of the real picture about the problem in the whole CIS. The presence of bridges in the site, for convenience and sampling safety, was an extra factor in the sampling stations choice. Figure 3.2. presents the CIS sectors and main canal, sampling stations and bridges as per adaptation from BRL Engénierie (2003) and HICEP (2012).

Fieldwork for primary data collection was conducted between the months of June and August in 2018, for dry season and, between January and March in 2019, for wet season. The data collection started in 2018 during dry season and lasted eight weeks in row. It started on the 11th June and ended on the 01st August, 2018. Then, it continued for the wet season for another eight weeks in row. Starting on the 23rd January and ending on the 26th March, 2019, period in which heavy rainfall was expected. The secondary data on physical and hydraulic parameters for historic information (cross-section, depth, bottom width, side slope and top width, reach length and longitudinal bed slope, water flow, water level, flow velocity) as well as for temporal discharge variation were obtained from Hidráulica de Chókwè (HICEP) for the period between 2004-2005 and 2018-2019 periods. Sediment data, was collected from the fieldwork on suspended and bed load. Google Earth Pro, Global Mapper, Q-GIS 3.10 and AUTOCAD (Civil 3D 2016) were also used as input for data processing, analysis and

presentation. Statistical models namely R (i386 3.5.3), MATLAB (R2009), Minitab 18.1, Origin (2020) and XLSTAT (2020) were used for further data analysis.

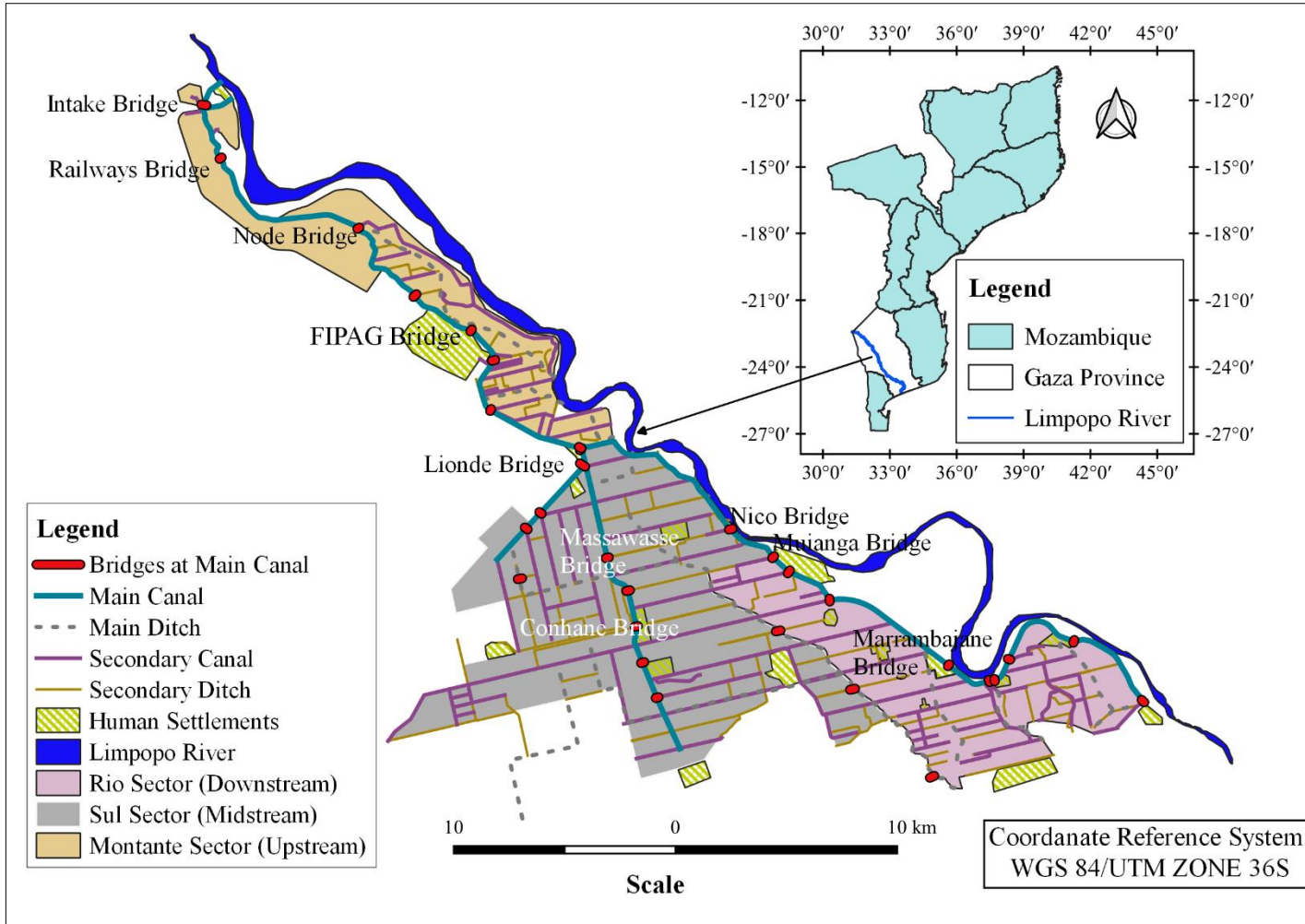


Figure 3. 2: The network of Chókwe Irrigation Scheme showing the Sampling Stations

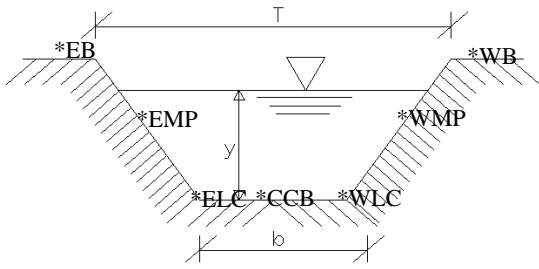
3.2. Determination of the Effects of the Canal and Inflow Factors on Sedimentation Flux

The hydraulic characteristics of the canal channel and inflow factors were determined as described in the following sub-sections. For canal channel factors, the canal bathymetry, including its banks and channel bed or centre canal base, were considered separately in terms of cross-sectional and longitudinal profiles. Additionally, canal depth changes, bed load and its physico-chemical characteristics, were also considered. On the other hand, for inflow factors, water depth, water velocity, suspended load and its physico-chemistry, were covered. Analysis seeking to assess these group of factors on the sediment flux, were performed. Lastly, supporting data on upstream of CIS infrastructure, water intake, regulators structures types, their functions and current operation status, canals length, width and depth; and number of distributaries (off-takes), helped shape this sub-section. The details on these characteristics were collected at the beginning of the fieldwork and the data recorded down.

3.2.1 Canal Channel Factors

Bathymetry and Canal Depth Changes

Assessment of the effect of change in bathymetry of the canal on the water level was carried out, with the aim of determining changes in the bed profile and canal cross-sections and longitudinal profiles, and finally, assess the sediment volume deposited or scoured. Bathymetric data were measured by surveying in intervals of 100 m in the main canal using GPS-Rover, for three data sets (i) 2001- after CIS rehabilitation; and (ii) 2016 - during severe drought occurrence when the whole scheme was totally dry; and (iii) 2019 - after drought. The data allowed comparisons of the bathymetry for these years. Readings for east and west banks, and the canal bed, were carried out, including two in-between points on either sides. The use of GPS-Rover entailed recording the geographical positioning of each reading station as well as the longitudinal slope and the canal cross-sectional dimensions. The canal cross-section presents seven points, namely: East Bank (EB), East Middle-Point (EMP), East Lower Corner (ELC), Centre of the Canal Base (CCB), West Lower Corner (WLC), West Middle-Point (WMP) and West Bank (WB) as presented in Figure 3.3.



* = Readings with GPS-Rover
 T = canal top width (m)
 b = canal base width (m)
 y = water depth or level (m)

Figure 3. 3: Schematic Bathymetry Measurements Points in each Station

The width of the canal bottom, side slope, with at the top, velocity of water flow at the upstream and downstream of the canal reach, depth of the canal and canal water level were considered. All these profile and water flow parameters are presented in Figure 3.4, where b=shape, bottom width (m), Z:1= side slope, T=top width (m), V_1 and V_2 = water flow velocity (m/s) at the upstream and downstream of the canal reach, d_1 and d_2 = canal depths (m), y_1 and y_2 = water level in the canal (m) (Shi et al., 2008).

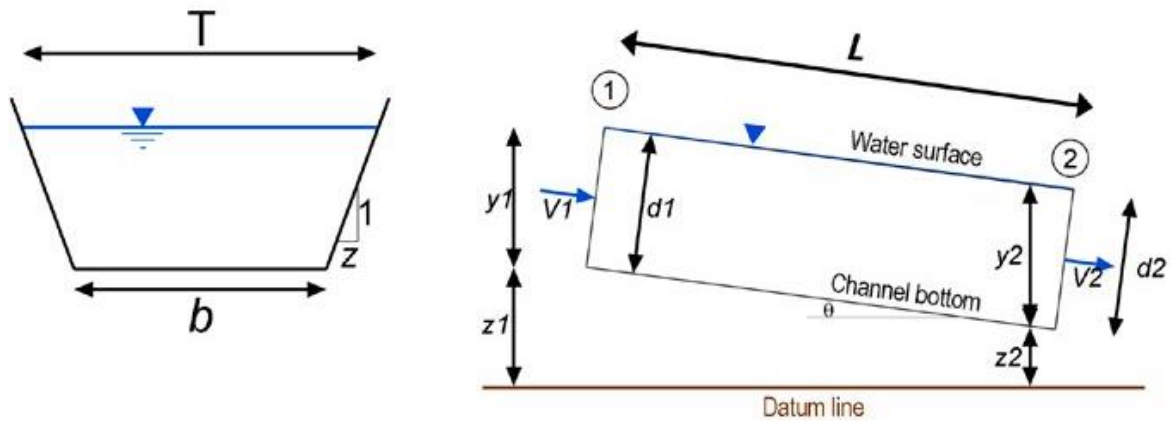


Figure 3. 4: Schematic Representation of Canal Geometry and Profile Parameters

$$S_o = \frac{-(Z_1 - Z_2)}{L} \quad (3.1)$$

Where:

S_o = canal slope (m/m)

Z_1 = canal height above datum at upstream (m)

Z_2 = canal height above datum at downstream (m)

L = is the reach length (m) and longitudinal bed slope

Once data collection on the bathymetry, canal geometry and profile, was over, then the analysis on the effect of these canal factors on sedimentation, was carried out. Canal depth changes were also captured making further usage of the previous bathymetric data, but applying it in terms of cross-section for each sampling stations covered in the study. Density plots were generated showing changes in distribution of depth across reaches, from east to west banks and for the centre of canal base. Information on the canal depth variation was compared for 2001, 2016 and 2019.

Bed load Physical Characteristics

Bed load sampling was performed using Van Veen grab device coded Eijkelkamp 043002, with capacity of 2 litres. Collections were performed at the centreline of the canal bottom towards downstream side of the main canal. After collection, samples were dried for 7-10 days in a natural atmosphere, and then, worked on in the laboratory. Atterberg limits test was used to classify unconsolidated sediments and to distinguish cohesive from non-cohesive sediment, as well as to determine cohesive sediments mechanical behaviour (Osman, 2015). Atterberg test on the bed load may provide the basis for a simple and effective unconsolidated sediments classification (Hunt & Jones, 2019; Osman, 2015; Rezaee et al., 2019). The Atterberg limits were determined in accordance to McBride (2002); and Rubinić et al. (2020) descriptions. The liquid limit obtained with use of the Casagrande apparatus and standard test method for liquid limit (LL), plasticity limit (PL) and plastic index (PI) of sediments was applied, following ASTM D 4318-00 guidelines. The level of water contained in the cohesive sediment samples was obtained from the difference between liquid and plastic limits, which also provides the plasticity index (PI). In case where PI is high this suggests presence of clay particles in the extract and may lead to conclusion that the sediments are cohesive. Normally, in silt cohesive sediments LL is found ranging from 24-35% and the PL varies between 14-25%. For clay cohesive sediments LL ranges from 14-25% and PL is over 20%.

$$PI = LL - PL \quad (3.2)$$

Where:

PI = Plasticity Index

LL= Liquid Limit

PL= Plastic Limit

The techniques used for determining particle size distribution (PSD) for particles were based on the fraction types or sieve analysis and using Stokes' law and pipetting method. The sieves analysis were performed for the grain sizes with diameters greater than 0.063 mm, which is the limit between sand and silt (Masoodi et al., 2017; Molinas & Wu, 2001; Zhu et al., 2018). Under the assumption of the techniques of pre-treatment, the methods of pipette and hydrometer, both thought to give comparable results (Jiang et al., 2020; Meraj et al., 2018), were applied. However, for the pipette method clay and silt fraction (<0.063 mm) required separation from the sand fraction using wet sieving (Ferro & Mirabile, 2009). The pipette or the hydrometer method was used to define a particle diameter as corresponding to that of a sphere settling in the same liquid with the same speed as the unknown sized particles, also called as the "Stoke's diameter" (Masheane et al., 2018; Orhan & Kılınc, 2020; Sahib & Robinson, 2020). The sphere is usually assigned to the density of quartz (Ferro & Mirabile, 2009). The hydrometer test was conducted for those fine materials (silt and clay) as described by Glendon and Doni (2002). The solution of sodium hexametaphosphate (40 grams/litre of solution) was used as dispersing agent to separate colloides and remove the organic matter contained in the samples. Sizes of sediment were characterized by the United States Geological Survey (USGS) method as follows: Clay sized particles (<0.002 mm); Silt sized particles (from 0.002 mm to 0.0625 mm); Sand sized particles (from 0.0625 mm to 2 mm); and Gravel sized particles (2 mm to 64 mm) and Cobbles (>64 mm), as presented in Table 2.1 (Dearnaley et al., 1995).

Measures of Bed load Gradation

The sediment uniformity coefficient (C_u) and the coefficient of gradation (C_c) are two measures of gradation. These two coefficients can help classifying sediments as either well or poorly graded. In first case, C_u can be determined from the ratio of D_{60} to D_{10} . When there is a value of C_u varying from 4 to 6 units it is interpreted to mean that the sediments are well graded. But when the values for $C_u < 4$, the sediments are referred to be poorly graded or uniformly graded sediment. Uniformity in graded sediments were considered as to suggesting identical particles with C_u value approximately equal to unit. When the uniformity coefficient value of 2 or 3 is is found it can be used to classify the sediments as poorly graded. Sandy sediments, normanly comes under this category. When C_u presented higher values this suggestes that the sediment mass is comprised of particles with different size ranges. In order

for the sediment to be well graded, the value of C_c must range between 1 and 3. For any single sized sediment mass, the value of both C_u and C_c is 1. C_u is always greater than 1 (equal to 1 is possible only theoretically). If C_u is closer to 1 (this is, D_{60} and D_{10} sizes are close to each other, which means that there are more particles in the same size range), the sediment is considered as uniformly graded. If C_u is away from 1, the sediment is well graded (this means that it has a variety of size range distributed well). For gravel, if $C_u > 4$, it is well graded. For sand, if $C_u > 6$, it is well graded. C_c is also greater than 1 (equal to 1 is only possible theoretically). A well graded soil will have its C_c ranging between 1 and 3. So, C_u and C_c gives an idea about particle size distribution of a sediment sample. These values are used in sediment classification. Equations for C_u and C_c are presented in the following:

$$C_u = \frac{D_{60}}{D_{10}} \quad (3.3)$$

$$C_c = \frac{(D_{30})^2}{D_{10} \times D_{60}} \quad (3.4)$$

Where:

D_{10} = effective particle size which 10% of the particles are finer and 90% of the particles are coarser than D_{10} .

D_{60} = effective particle size which 60% of the particles are finer and 40% of the particles are coarser than D_{60} .

D_{30} = effective particle size which 30% of the particles are finer and 70% of the particles are coarser than D_{30} .

Bed load Chemistry Characteristics

The amount of total dissolved ions in a sediment sample extract was estimated from its electrical conductivity (EC). Sherard et al. (1972) and Osman (2015) consider it to be significant factor for assessment of the erosion susceptibility of cohesive sediment. When $EC > 4$ dS/m the sediment extract is referred to be saline. Additionally, when SAR value is found to be high, sediment clay particles tend to de-flocculate. Therefore, the aggregate stability, either dispersing or flocculating, rely on the SAR balance and can be given by the relation between calcium (Ca^{2+}), magnesium (Mg^{2+}), and sodium (Na^+) quantity, including soluble salts (EC). Sediment particles flocculate when SAR decreases. The exchangeable sodium percentage (ESP), on the other hand, indicate excess exchangeable sodium causing sediment particle disaggregation and dispersion, known to be deflocculation, and is commonly

observed in sodic sediments. Some sediment parameters were considered in this work (A. Estabragh et al., 2019; K. Estabragh et al., 2019; Recking, 2013; Sulaiman et al., 2017; Wegen et al., 2011): saturation percentage (SP), potential for hydrogen (pH), sediment electric conductivity (EC), exchangeable of calcium and magnesium ($Ca^{2+}+Mg^{2+}$), sodium (Na^+), potassium (K^+), sodium adsorption ratio (SAR), and exchangeable sodium percentage (ESP). SP is an indicator of sediment water retention. High SP indicates high capacity of sediment to store water. Where low pH (≤ 5) is found, there are large possibilities that stratified bed sediment will present high erosion rate, whilst for intermediate pH (5-7), it may indicate a weaker bed structure and highly erosion prone sediments. On the other hand, high pH (> 7) sediment particles will predominate as denser aggregates can be formed (Stone et al., 2009). The SAR can be calculated from the Equation 3.5.

$$SAR = \frac{Na^+}{\sqrt{(Ca^{2+}+Mg^{2+})/2}} \quad (3.5)$$

The EC, pH, ESP and SAR values were used to classify sediment in normal, saline, sodic and saline-sodic, either with flocculation or dispersion, as presented in the Table 3.2.

Table 3. 2: Classification of Sediment Based on EC, pH, ESP and SAR Values

Sediment Classification	EC (dS/m)	pH (-)	ESP (%)	SAR (-)	Condition
Normal	<4	<8.5	<15	<13	Flocculation
Saline	>4	<8.5	<15	<13	Flocculation
Sodic	<4	>8.5	>15	>13	Dispersed
Saline-Sodic	>4	<8.5	>15	>13	Flocculation

> = greater than and < = less than.

Source: Adapted from Osman et al. (2016); Osman (2015); and Rahimi et al. (2019).

The ESP measures the quantity of exchangeable sodium that affect the aggregation of sediments and cause dispersion of loosen particles. Such process is called de-flocculation in sodic sediments and the ESP can be obtained from the Equation:

$$ESP = Exchangeable \left(\frac{Na^+}{Ca^{2+}+Mg^{2+}+K^++Na^+} \right) \times 100 \quad (3.6)$$

Sediment pH was determined with a pH-meter, whilst the electrical conductivity (EC) was measured with an EC-meter. Combination of exchangeable $\text{Ca}^{2+} + \text{Mg}^{2+}$ were determined by applying the complexometric titration method, while Na^+ and K^+ were determined by flame photometry using a flame-photometer in accordance with Embrapa Manual of Soil Analysis Method, Third Edition, Revised and Expanded (Teixeira et al., 2017).

3.2.2 Inflow Factors

Water Depth Variation

Water depth or water level in the canal, was measured, using staff gauge with 6 meters length, in the all 9 sampling stations during DS and WS, with purpose to compare the findings and correlate with sediments depositions. Water depth or level was compared to the full supply levels of the canal at a given time. These comparison took place at the upstream, mid section, downstream of the main canals. The maximum, mean and minimum levels were considered, including the full supply level (FSL), standard deviation, mean level above FSL and peak level above FSL was also taken into account for comparisons of the different locations.

Water Flow Velocity

Water flow measurements and flow velocities took place using a current-meter OTT C31 employed at different depths in an integrated method, during DS and WS, at all the 9 sampling stations. The flow velocity at the stations was converted into discharge by computing the product of cross-sectional area and the velocity as per the continuity flow equation (Equations 2.3 and 2.4). The canal cross-sections were divided into vertical sections depending on the width of the surface water. For each section, the flow velocity was measured at surface or 0 cm, then, next at depth of 20 cm, up to maximum depth of 160 cm of water, with spaced difference of 20 cm intervals in depths. (for water depth greater than 1.5 m). This method is consistent with the U.S. Geological Survey (USGS) procedure and Perzyna (2016). All measurements, were undertaken on a weekly basis for two months at normal flow period (dry season: June-August in 2018) and two months at peak flow period (wet season: January-March in 2019).

Suspended Load Physical Characteristics

Suspended sediment load physical characterisation was performed using samples from all sampling points located along the main canal. The readings were performed on weekly basis during two months at normal flow period (dry season, June-August of 2018) and at expected peak flow period (wet season, January-March of 2019). In both seasons samples were collected at water surface up to 160 cm depth. Suspended load sampler “Water trap” type standard Eijkelkamp 1202 able to collect up to 25 m of depth, was used. Measurement on water turbidity on every suspended sediment sample was performed for data comparisons. Then, the determination of suspended sediment concentrations (SSC) took place at ISPG Soil and Water Laboratory. Oven dry at 105° C was used for weighted sample of water contained in a capsule with sediments particles. After dried, the sediment particles were weighted in a scale for differences of the sediments. Event loads were estimated by predicting SSC from regression on turbidity. Using simple linear regression the collected loads were estimated using root mean square errors for sediment rating curve estimates based on the same sample.

Suspended Load Chemistry Characteristics

Parameters such as water turbidity, potential for hydrogen (pH), total dissolved solids (TDS) and electrical conductivity (EC), as well as concentrations of calcium (Ca^{2+}), sodium (Na^+) and potassium (K^+), were taken into consideration, in all the 9 sampling stations, for DS and WS. Water turbidity was measured using turbidimeter. The pH was measured with resource to pH-meter and temperature, with thermometer. In addition, TDS and EC were measured using mutiparameter and conductivimeter, respectively.

Water and Sediment Characteristics

Attempting to assess characteristics of water in relation to sediment, a multivariate statistical analysis (PCA analysis) was employed, for water flow and sediment flux, during DS and WS, at all the 9 sampling stations. Given the fact that the purpose of using PCA in this case was oriented to reductionist and exploratory analysis, normality test was performed under expectation of further usage of the data for the modelling purposes, either for subsequent gradient or regression analyses. Normality test allowed check data distribution, which then indicated their suitability for type of test to be used. In case the data are normally distributed,

parametric tests, such as T-test, ANOVA, Pearson's coefficient of correlation, Z-test and Multivariate Regression, can be used. But, in case non-normal distribution or distribution-free data is found, it is recommended to use non-parametric tests, as Kruskal-Wallis Test, Friedman Test, 1-Sample Sign Test, Mood's Median Test, Spearman Rank Correlation, Mann-Kendall Trend Test and Mann-Whitney Test. Due to the large number of samples, PCA was employed to evaluate useful information in the water flow and sediment flux that could not be manifest by univariate analysis. Therefore, multivariate statistical analysis using PCA in XLSTAT 2020 package was used to differentiate among sampling points data profiles from DS to WS water and sediments in the canal depths. The PCA was used to reduce the original dimensions of the flow and flux data and represent the original data using new principal component (PC) scores that capture the maximum variance in the data. In such case, the transportation matrix was applied to the flow and flux. The main components that describe majority of the variations were extracted from the data as PCA loadings. These loadings were plotted as a function of sampling points in order to reveal the most important diagnostic sampling point related with the differences found in the scheme. Peaks with large amplitudes were identified as the most influential in the differentiation.

PCA was performed in accordance to the description in section 2.7, whereby canal channel characteristics and inflow factors were considered factors or components influencing the CIS sedimentation. The Principal Components (PCs) were computed in order of maximum variance, where F1 represented the largest amount of variance followed by F2 and F3, successively. The PCs or F were sorted out in decreasing order of importance as dictated by their associated eigenvalues (Setiawan et al., 2020). A common method for determining the optimum number of PCs was by plotting the PCA eigenvalues, which corresponded to the PC or F variances, versus the PC number to obtain a scree plot (Landgraf & Lee, 2020; Shen et al., 2019; Wang & Aelst, 2020; Zakhem et al., 2017; Zhang et al., 2020). According to the eigenvalue criterion, only the PCs with eigenvalues greater than one were considered important (Gyimah et al., 2020; Souza et al., 2020). The relationship between canal and inflow factors focused on their effects and association. The PCA plot essentially illustrates the contribution of the canal channel factors at different sampling stations in spectra, to the principal component. This allowed the regions of the spectra which account for the greatest amount of variance (largest contribution) to be distinguished from noise (the spectroscopic structures which were not relevant to the structure of the PC). Each analyzed factor was

assigned a score with respect to a particular PC. By plotting two PCs against each other, factors were separated based on their scores for each PC.

3.3 Determination of the Temporal Trends-Dynamics

The determination of temporal water flow distribution trends at CIS was performed using historical data on the water flow from 2004-2005 to 2018-2019 seasons, available at HICEP. Given that these recorded data does not include sediment information, for the determination of temporal sediments distribution trends the outputs on the water flow and sedimentation data from the first specific objective were adopted. The historical data on water flow obtained in the HICEP, was used for calibration of the collected fieldwork data. A correlation was established in an attempt to generate a relation function between both data (water flow and sediment). These outcomes were used to generate the temporal sediment amounts at CIS. For determination of water flow and sediment the study considered different distances from the main intake toward the lowest point in the canals. The system reliability and performance were conducted based on the findings of the specific objective (i) and compared to the initial design characteristics and parameters of the CIS, then the outputs were used to run simulations in their hydrodynamics. Mann-Kendall test, ARIMA test and Fourier Transform were also considered for determination of temporal trends, whilst the spatial trends provided insight maps and density plots for sampling stations. Two hypothesis where tested for MK: null hypothesis (H_0), there was no trend in the series, and the alternative hypothesis (H_a), there was a trend in the series. When the computed p-value showed to be greater than the significance level $\alpha=0.05$, null hypothesis (H_0) was not rejected. And when the computed p-value was lower than the significance level $\alpha=0.05$, the null hypothesis H_0 , would be rejected, and the alternative hypothesis (H_a) accepted.

The Fourier transform was performed with autocorrelation using the Hamed and Rao (1998) method. When transforming the water discharge function, using Fourier transform, it resulted into the frequency domain function. The new function generally consists of a real and an imaginary part. The real part gives information about the frequencies and their magnitude, and the imaginary part determines the phase shift of the corresponding frequencies. For an real signal the imaginary part must be zero, and vice-versa. Prior to implementing any time series analysis, the data must be evaluated for any dominating trend signals. A bars/column, autocorrelogram function (ACF) and partial autocorrelogram function (PACF) technique was

employed to determine the linear trend, if any, and the seasonality of the data. If present, the linear trend was removed by a simple linear regression technique. Since seasonality can easily be identified in the domain, it was not necessary to remove the seasonal signal prior to further analysis. Therefore, the time domain and frequency domain analyses were performed using the linear detrended data to quantify the persistence of total water discharge in the scheme. The fact that the main canal of the CIS is regulated infrastructure, a stochastic model like ARIMA, wouldn't be commendable to apply. However, the study considered the length, width, and the level of natural characteristics that remain in the system, including very limited human intervention, which is mostly related to regulators. Throughout the year, CIS main canal is used to store water, besides serving mainly for its conveyance. Spillways gates at Macarretane weir remain open at a certain level, for more than 9 months per year, until rainy season, when high demand for regulation sets in. Lastly, distances between regulators are separated apart for more than 10-15 km, giving the hydraulic processes time and space to behave naturally, in most of cases. Although CIS main canal is an regulated canal, there is much of natural process taking place in terms of water flow. For these reasons, ARIMA was applied in the study.

3.4 Determination of the Influence of Water Flow on the Sediments Settling Velocity

Once collected, water and sediment samples were processed and analysed at the ISPG soil and water laboratory. The laboratory work involved measuring settling velocity, especially on its temporal variations with the concentration, which is particularly important in cohesive sediment transport. The physical sediment properties such as size, shape and specific weight were used to determine the settling velocity. Measurements of settling velocity were carried out at different concentrations of suspended sediment. The correlation between measured settling velocity of the mean concentration and the mean settling velocity for the sediment fraction were calculated using the following adjusted calibrated equation (Wilcock et al., 2009):

$$W_s = 1.68 \times 10^{-7} \times C^{0.62} \quad (3.7)$$

Where: W_s = settling velocity (m/s)

C = concentration of sediment (ppm)

Sediment budget for the canals were measured through load and mass balance analysis, as detailed steps are presented in the Appendix E. This technique allowed for the study of the hydraulic and sediment transport functions of the canals and the interdependence between hydraulic, morphologic and sediment parameters. The total discharge and average sediment concentration at the inlet and outlet of the canal's reach were measured and summarized on weekly basis. The analysis of the influence of water flow on the sediment settling velocity was performed by generating and comparing the flow curves for each sampling station with the respective sediment settlings. The sediment settling velocity was assessed for sampling stations and the particle sizes, specifically d_{10} , d_{30} , d_{50} , d_{60} , and d_{90} , where d_x is a characteristic particle size such that $x\%$ of the sediment (in volume) is finer than d_x (Ancy, 2020). Similarly, water flow and sediments settling velocity were assessed against the canal depths (at 0 to 20 cm intervals up to 160 cm). Relation graphs of settling velocity with grain size were generated taking into account the particle size distribution predominant in the sampling station, for the sampling date.

3.5 Evaluation of Best Scenario for Predicting Sediment Deposition

Best scenarios for sediment deposition as tool for CIS was generated from the outcomes of the previous specific objectives and different predictors. For most of the above described simulation cases, assumptions were made for a single irrigation canal. On the other hand, for the application case of operational activities, it was assumed that an irrigation canal composed of several reaches. Additionally, several assumptions for the hydraulic conditions and sediment characteristics during the simulation period were made. The main assumptions for these applications are listed in Appendix I. Owing to the need to characterise models and scenarios, this study assumed the observed and actual situation taking place at CIS, as the base for the predictions. Performance criteria was used to compare actual condition to the proposed scenarios. Prediction scenarios for sediment deposition were generated using five models, namely, Ackers-White (1973), Brownlie (1981), Engelund-Hansen (1967), van Rijn (1984) and Yang (1973) as per Mendez_V (1998). Multivariate Linear Regression (MLR) and Sensory Data Analysis (SDA) were used and applied to the models. SDA procedure included Exponential and Holt-Winters models (Holt, 1957 and Winters, 1960) as per Blázquez-García et al. (2020); JafariKhasragh et al. (2019); Kuo & Kusiak (2019); and Wu et al. (2018), whereby within the Holt-Winters, Linear Holt (LH), Seasonal Additive (SA) and

Seasonal Multiplicative (SM) were included. The first scenario (S_1) considered parameters of flow conditions and the second scenario (S_2) considered the suspended sediment load conditions. The last scenario (S_3) observed the bed load conditions. All scenarios were computed using all predictors, Ackers-White (A-W), Brownlie (BRO), Engelund-Hansen (E-H), Van Rijn (VR) and Yang (YAN) models. Different combinations of input variables were developed after a trial and-error process according to flow conditions and sediment properties. The input models for predicting scenarios are presented in Table 3.2.

Table 3. 3: Models and Inputs Used to Predict Scenarios and their Approaches

Models	Input variables	Inputs for trial and error	Actual	Scenarios			Approach
			S ₀	S ₁	S ₂	S ₃	
Ackers-White	D [*] , s, v, g, d ₃₅ , F _{gr} , u [*] , n, V, h, G _{gr} , c, A, m and q _s	d ₃₅ , u [*] and V	√	√	√	√	Energy Balance Concepts
Brownlie	Fg, V, s, g, d ₅₀ , Rg, v, Y, ss, Fg _{cr} , S, G _{Stdev} , C _f , R and q _s	V, d ₅₀ and S	√	√	√	√	Energy Balance Concepts
Engelund-Hansen	V, s, g, d ₅₀ , C, h, S _o , q _s	V, d ₅₀ and S _o	√	√	√	√	Energy Balance Concepts with regression method
Van Rijn	D [*] , s, g, v, d ₅₀ , C, h, d ₉₀ , , T, u [*] _{cr} , and q _b	d ₅₀ , V and u [*] _{cr}	√	√	√	√	Deterministic equal mobility method
Yang	V _{cr} , Ws, I, J, d ₅₀ , v, u [*] , c _t , V, S, h and q _s	Ws, d ₅₀ and S	√	√	√	√	Regression Method

Where:

D^* = Dimensionless grain parameter or particle parameter (-)

s = Relative density (-)

ν = Kinematic viscosity (m^2/s)

g = Gravitational acceleration (m/s^2)

d_{35} , d_{50} , d_{90} = Representative particle diameter (mm), Median diameter (mm) and Particle diameter; 90% of the sample is finer (mm), respectively

F_g , F_{gr} , F_{grcr} = Grain Froude Number (-), Dimensionless mobility parameter (-) and Critical grain Froude number (-), respectively

R_g = Grain Reynolds number (-)

u^* = Shear velocity or bed shear velocity related to grains (m/s)

T = Bed Shear parameter (-)

u^*_{cr} = Critical bed shear velocity (m/s)

n = Exponent in the dimensionless mobility parameter F_{gr} (-)

V = Mean velocity (m/s)

h = Water depth (m)

G_{gr} = Dimensionless transport parameter (-)

c = Coefficient in the transport parameter (-)

A = Value of F_{gr} at the nominal, in initial movement (-)

m = Exponent in the transport parameter G_{gr} (-)

$q_b=q_s$ = bed, suspended and total sediment transport rate per unit width (m^2/s)

Y = Y value (-)

τ_{ss} = Critical dimensionless shear stress (-)

$S = S_o$ = Bottom slope (m/m)

G_{Stdev} = Geometric standard deviation (-)

C_f = Coef of transport rate for field conditions (-)

R = Hydraulic radius (m)

C = Chezy coefficient ($m^{1/2}/s$)

V_{cr} = velocity for initiation of motion (m/s)

W_s = Fall velocity (m/s)

I and J = Coefficient in Yang's function for the total sediment transport (-)

c_t = Total sediment transport expressed in ppm by mass

3.6 Data Analysis and Performance Criteria

3.6.1 Linear Regression

To identify the statistical significance of observed differences of physical properties among the water flow and sediment flux, as well as for the best scenarios prediction, a Multivariate Linear Regression (MLR) was employed. This aimed at determining the extent to which the dependent variable was explained by the independent variable. Differences were counted and denoted as “significant” when $p < 0.05$, with higher significance for smaller p values.

3.6.2 Holt-Winters Method

This study used the Holt (1957) and Winters (1960) extended Holt’s method in order to capture the seasonality. This Holt-Winters seasonal method comprises the forecasting equation and three smoothing equations, one dedicated to the level l_t , one oriented to the trend b_t , and one last specifically for the seasonal component s_t , with corresponding smoothing parameters α , β^* and γ , respectively. It is used m is used to denote the frequency of the seasonality, it represents the number of seasons in a year. With reference to section 2.7, this method was used to assess seasonal component in the scenario predictions.

The component form for the additive method is:

$$\hat{y}_{t+h|t} = l_t + h \times b_t + s_{t+h-m \times (k+1)} \quad (3.8)$$

$$l_t = \alpha \times (y_t - s_{t-m}) + (1 - \alpha) \times (l_{t-1} + b_{t-1}) \quad (3.9)$$

$$b_t = \beta^* \times (l_t - l_{t-1}) + (1 - \beta^*) \times b_{t-1} \quad (3.10)$$

$$s_t = \gamma \times (y_t - l_{t-1} - b_{t-1}) + (1 - \gamma) \times s_{t-m} \quad (3.11)$$

The component form for the multiplicative method is:

$$\hat{y}_{t+h|t} = (l_t + h \times b_t) \times s_{t+h-m \times (k+1)} \quad (3.12)$$

$$l_t = \alpha \frac{y_t}{s_{t-m}} + (1 - \alpha) \times (l_{t-1} + b_{t-1}) \quad (3.13)$$

$$b_t = \beta^* \times (l_t - l_{t-1}) + (1 - \beta^*) \times b_{t-1} \quad (3.14)$$

$$s_t = \gamma \frac{y_t}{l_{t-1} - b_{t-1}} + (1 - \gamma) \times s_{t-m} \quad (3.15)$$

Where:

k = integer part of $(h-1)/m$, which ensures that the estimates of the seasonal indices used for forecasting come from the final year of the sample.

3.6.3 Statistical Parameters for Model Selection

Model simulations were generated in Multiple Linear Regression (MLR) for DS and WS and all five predictors. The values of performance criteria were based on simulations of the observed CIS sedimentation fluxes. Analysis of statistical parameters such as Adjusted Coefficient of Determination (Adj. R^2), Root Mean Square Error (RMSE), Durbin-Watson statistic (DW), Mallows coefficient (Cp), Akaike's Information Criterion (AIC), Schwarz's Bayesian Criterion (SBC), Amemiya's Prediction Criterion (PC), Prediction error sum of square (Presse) and the fraction of total variation of dependent variables that can be predicted by a component (Q^2), were performed in order to find the best fitting models for the simulations. Beside the aforementioned parameters, other statistical indicators can be used, among them, is the Adjusted Coefficient of Determination (Adj. R^2 , R^2_{adj} . or \bar{R}^2), Mean Absolute Percentage Error (MAPE), Root Mean Square Error (RMSE), Durbin-Watson statistic (DW), Mallows coefficient (Cp), Akaike's Information Criterion (AIC), Schwarz's Bayesian Criterion (SBC) and Amemiya's Prediction Criterion (PC) (Charnigo et al., 2011; Chen, 2018; Fujikoshi et al., 2005; Luo et al., 2006; Goyal et al., 2017; Momber & Marquardt, 2019; Yurekli & Ozturk, 2003). Section 2.7 provides theoretical base of each parameters used and the respective equations are preented as follows:

Adjusted Coefficient of Determination (\bar{R}^2)

The formula for the Adjusted Coefficient of Determination (Adj. R^2) from the obtained value of the R^2 is defined as,

$$\bar{R}^2 = 1 - (1 - R^2) \left[\frac{n-1}{n-(k+1)} \right] \quad (3.16)$$

Where:

n = sample size

R^2 = coefficient of determination

k = number of independent variables in the equation of regression.

Mean Absolute Percentage Error (MAPE)

The Mean Absolute Percentage Error (MAPE) was determined using the following relation:

$$MAPE = 100 \times \frac{1}{n} \times \sum_{i=1}^n \left| \frac{Obs_i - Model_i}{Obs_i} \right| \quad (3.17)$$

Where:

Obs = observation value

Model = forecast value

Root Mean Square Error (RMSE)

The Root Mean Square Error (RMSE) was calculated using the following equation:

$$RMSE = \sqrt{\sum_{i=1}^n \frac{(X_i - Y_i)^2}{n}} \quad (3.18)$$

Where:

n = number of data

X_i = observed value

Y_i = predicted value

Durbin-Watson statistic (DW), Amemiya's Prediction Criterion (PC) and Mallows coefficient (Cp)

Durbin-Watson statistic (DW), Amemiya's Prediction Criterion (PC) and Mallows coefficient (Cp) were used as for model selection also, respecting the criteria established in section 2.7.

Akaike's Information Criterion (AIC) and Schwarz's Bayesian Criterion (SBC)

Akaike's Information Criterion (AIC) and Schwarz's Bayesian Criterion (SBC) were used in model selection criteria. AIC basic formula was defined as:

$$AIC = -2(\log - likelihood) + 2K \quad (3.19)$$

Where:

K= number of model parameters (the number of variables in the model plus the intercept).

Log-likelihood = measure of model fit. The higher the number, the better the fit. This is usually obtained from statistical output.

For small sample sizes ($n|K \leq 40$), it is used the second-order AIC:

$$AIC = -2(\log - likelihood) + 2K + \left(\frac{2K(K+1)}{n-K-1} \right) \quad (3.20)$$

Where:

n = sample size

K = number of model parameters

Log-likelihood = measure of model fit

The SBC is an asymptotic result derived under the assumptions that the data distribution is in the exponential family.

$$-2 \times \ln p(x|k) \approx SBC = -2 \times \ln L + k \ln(n) \quad (3.21)$$

Where:

x = the observed data;

n = the number of data points in x , the number of observations, or equivalently, the sample size;

k = the number of free parameters to be estimated. If the estimated model is a linear regression, k is the number of regressors, including the constant;

$p(x|k)$ = the likelihood of the observed data given the number of parameters;

L = the maximized value of the likelihood function for the estimated model.

Under the assumption that the model errors or disturbances are normally distributed, this becomes (up to an additive constant, which depends only on n and not on the model):

$$SBC = n \ln \left(\frac{RSS}{n} \right) + k \ln(n) \quad (3.22)$$

Where:

RSS = residual sum of squares from the estimated model.

Note that the term for $-2 \times \ln L$ used in this specialization is equal to the rescaled normal loglikelihood up to an additive constant that depends only on n .

3.7 Calibration and Validation of the Models

Water flow historical data were used for calibration and collected fieldwork data were used for verification and validation. Models were validated by the technique of cross validation (leave-one-out cross-validation year method or jack-knife technique) (Laanaya et al., 2017). This procedure consists of temporarily removing the data on water flow for one year from the database and using the rest of the database for calibration. Then, the water values of the year removed are estimated. This operation is repeated for all years to find an estimate for all the

water flow values for comparison between the estimated values and the observed values using five criteria: correlation coefficient (R), Nash–Sutcliffe Efficiency Coefficient (NSEC), Root Mean Square Error (RMSE), Relative Error (RE) and Percent bias (PBIAS), as depicted in Equations 3.23–3.26. These criteria were also used as statistical parameters for evaluating performance of the Multivariate Linear Regression (MLR) and Holt-Winters sensory analysis models.

$$R = \frac{\sum_{i=1}^N (X_i - \bar{X}) \times (Y_i - \bar{Y})}{\sqrt{\sum_{i=1}^N (X_i - \bar{X})^2 \times \sum_{i=1}^N (Y_i - \bar{Y})^2}} \quad (3.23)$$

$$NSEC = 1 - \left\{ \frac{\sum_{i=1}^N (X_i - Y_i)^2}{\sum_{i=1}^N (X_i - \bar{X})^2} \right\} \quad (3.24)$$

$$RE = \sqrt{\sum_{i=1}^N \frac{|(X_i - Y_i)/X_i|}{N}} \quad (3.25)$$

$$PBIAS = \left\{ 100 \times \frac{\sum_{i=1}^n X_i - \sum_{i=1}^n Y_i}{\sum_{i=1}^n X_i} \right\} \quad (3.26)$$

Where:

n = number of data

X_i = observed value

Y_i = predicted value

\bar{X} and \bar{Y} = mean values of the observed and predicted values

3.8 Sensitivity Analysis

A sensitivity analysis was performed in order to evaluate the effects of various inputs, such as water flow, sediment inflow and sediment particle size on the model's output. The canals downstream of the irrigation system were simulated using the design discharge data with a certain sediment concentration and mean particle diameter. The parameters like water inflow discharge, mean sediment inflow, median diameter and canal roughness were changed and the effects observed on the sediment deposition volume in the canals. Most reliable model for each scenario was identified (Ding & Langendoen, 2018; Roushangar & Shahnazi, 2020).

CHAPTER FOUR

RESULTS AND DISCUSSION

4.1 Effects of Canal Channel and Inflow Factors on Sediments Flux

Effects of canal channel factors and inflow factors on sedimentation are presented in the following sub-sections. Firstly, for canal channel factors, bathymetric profiles for different reaches in 2001, 2016 and 2019 on sedimentation is given, followed by the canal depths changes, bed load physical and chemistry characteristics. Secondly, for inflow factors, water depth variation, water velocity, followed by suspended load physical and chemistry characteristics, are presented.

4.1.1 Canal Channel Factors

Bathymetric Changes in Terms of Cross-sectional Profile

The cross-sectional bathymetric profile of CIS main canal appeared to be seriously affected by sedimentation as was noted from the changes of the bed profile along the canal width. In 2001, the bathymetric profile varied from more than 35 m at the Intake-Lionde reach to less than 20 m in Lionde-Marrambajane. The centre of the canal profile seemed to maintain its profile overtime, whereby, it remained in lower depth as compared to the other points along the cross-section. However, similar observations were not made at the Intake-Lionde and Lionde-Marrambajane reaches. Probably, this variation was caused by material deposition along canal length or some kind of deviation occurred in the modelling design. The Intake-Lionde reach in 2001, measured 37.5 to 40 m in depth in the first 200 metres. The central point of the canal appeared to be lower than the banks, which is obvious and acceptable. In Lionde-Conhane reach, the depth at first 120 metres had heights of 28-29 m and 25-28 m for a distance of 12-600 m, and 22-34 m at a distance of 122-1000 m. There seemed to be fewer variations from East to West banks of canal cross-sections in this reach. In Lionde-Maarambajane, similar pattern was observed, whereby, the canal centre was deeper than the lateral points and banks. In 2016 and 2019, there was less variation in the cross-section and profile depths as compared to 2001. In 2001, Lionde-Conhane and Lionde-Marrambajane reaches had their depths for the central canal base above 22 m in most parts of the canal. This was likely caused by sediment deposition. Figures 4.1, 4.2 and 4.3 present the variation of canal level at cross-section points for the Intake-Lionde, Lionde-Conhane and Lionde-Marrambajane reaches over 2001, 2016 and 2019 periods. Where, 1=WB=West Bank,

2=WMP=West Medium-Point, 3=WLC= West Lower Corner, 4=CCB=Centre Canal Base,
5=ELC= East Lower Corner, 6=EMP=East Medium-Point and 7=EB=East Bank.

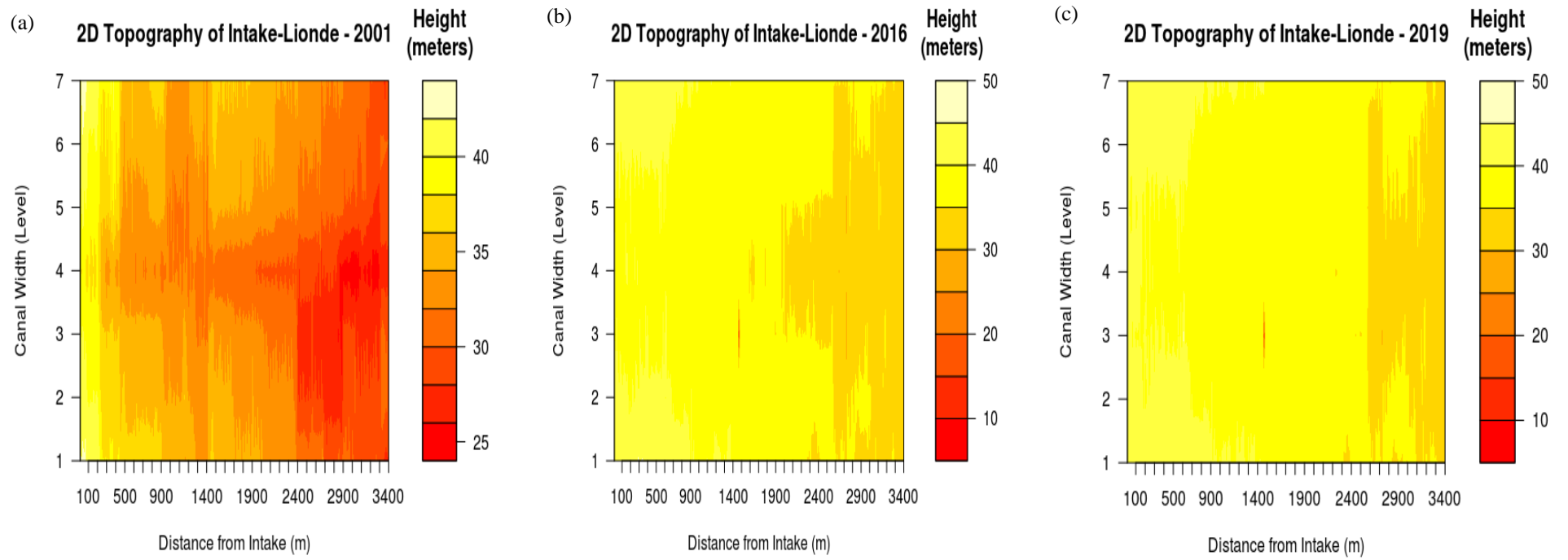


Figure 4. 1 (a, b & c): Bathymetry Variation of Cross-section at the Intake-Lionde Reach for 2001, 2016 and 2019 Periods

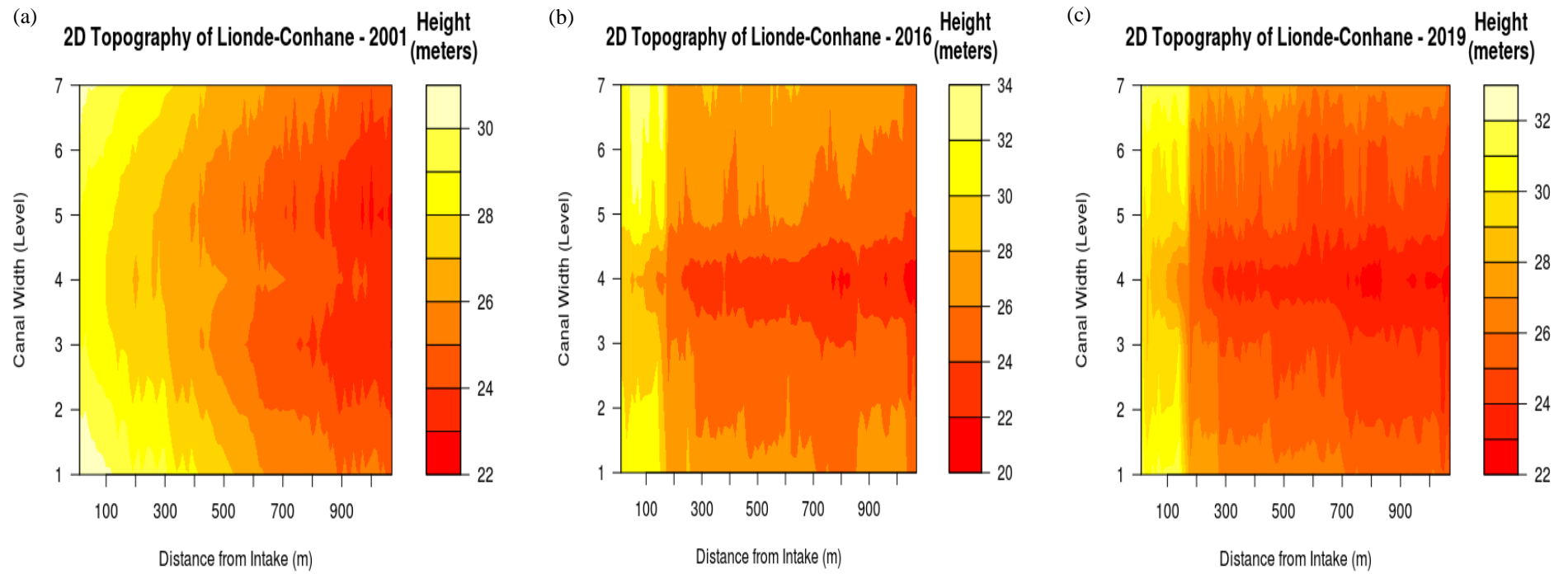


Figure 4. 2 (a, b & c): Bathymetry Variation of Cross-section at the Lionde-Conhane Reach for 2001, 2016 and 2019 Periods

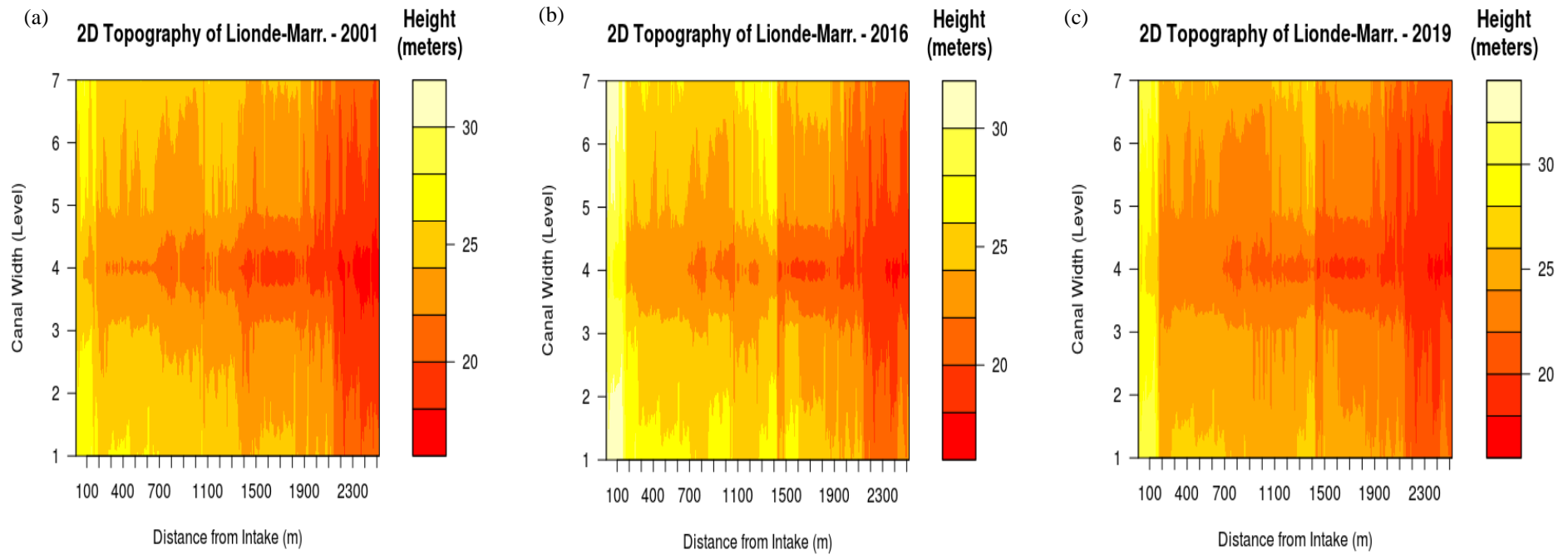


Figure 4. 3 (a, b & c): Bathymetry Variation of Cross-section at the Lionde-Marrambajane Reach for 2001, 2016 and 2019 Periods

Bathymetric Changes in Terms of Longitudinal Profile

In 2001, it was observed that the intake-Lionde reach measured above 40 m high at the starting point and decreased to nearly 24 m, 34 km away from the starting point. Within this distance, variations were observed, whereby east bank shifted from low to high heights against west bank. Canal bed profile remained stable, but with some variations. At a distance of 27 km, 29 km, 30 km and 33 km from the Intake, there were visible changes on the height of the banks. This can be due to changes of sediment deposition or even erosion on the canal bed through entrainment and aggradation processes. For the Lionde-Conhane reach in 2001, the heights varied between 23.5 and 31 m at an approximate distance of 10 km. The East Bank (EB) showed increased and decreased height points at the first 5 km and the West Bank (WB) at the last 2 km. These changes may influence the detachment of soil particles and allow them to enter into the canal flow and contribute to changes in the distribution of sediment particle sizes. It was also observed that at the start of the reach, the height differences between canal centre base and the banks were higher than at the end of the reach. In 2001, the reach heights at Lionde-Marrambajane varied between 17.5 and 28.0 m at a distance of approximately 25 km apart. The EB and WB runs in a relatively smooth line of topography, though some increments and reductions were noted as it runs through. Reach height at the upstream was 28 m but decreased to 22.5 m. Similar pattern was observed for the canal central baseline, which started at 25 m and dropped to 17.5 m. Changes at the bank of this reach seemed not to be caused by an external factor which would cause soil particles to be detached, transported and deposited in the canal. It was also observed that at the beginning of the reach, the height differences between canal centre base and the banks were less than what was observed at the middle and end of the reach.

Similar analysis was done for 2016, whereby the canal WB, EB and bed profiles were considered. It was observed that changes in the bathymetric profile start at an height of above 41 m high and decreases to nearly 32 m at a distance of 34 km. Within this distance, variations were observed, whereby EB and WB run together at relatively same level, except at some points where either of them was higher or lower than the other. Canal bed profile seemed to remain stable, but with some variations, such as what was observed at distances of 5 km (37.7 m), 7 km (37.4 m), 17 km (35.8 m), 27 km (30.3 m) and 33.5 km (31.3 m). These

changes could be attributed to variation in sediment deposition or erosion at the canal bed brought about by entrainment and aggradation processes.

Intake-Lionde reach in 2019, started at a height of above 42 m high and decreased to about 32 m at an approximate distance of 34 km away. Within this distance, minimal variations were observed between the banks. Canal bed profile remained stable, but with slight variations. At a distances of 6.0 km (37.7 m), 16.5 km (36.6 m) and 29 km (32.2 m) there were visible changes on the height of the canal base. This could be attributed to material deposition in the canal bed.

In the case of Lionde-Conhane reach in 2019, the heights varied between 22.0 and 33.0 m at an approximate distance of 10 km between the two furthest points. The EB height appeared slightly under the WB throughout the canal extension. It was also observed that at the start of the reach (at around 35.5 km), the height differences between canal centre base and the banks are slightly smaller (0.7 m or just 70 cm) compared to the end of the reach (3.4 m). Central base of the canal started with steep decreasing slope (from 0.3% to 0.21%) and maintained a small variation (0.013%) as it runs to the end of the reach, similarly to the banks. This is a potential reason for the relatively high water velocity (0.763 m/s in DS and 0.913 m/s in WS) at the upstream of the reach and lower water velocity at the downstream (0.125 m/s in DS and 0.300 m/s in WS) in Conhane region. Centre of the canal base appeared to be stable and with few changes towards the end of the reach.

Overally, all the reaches and years presented changes in banks and centre of canal base heights. For the canal EB and WB, bathymetric differences were seen between 2001 and 2016, as well as for 2001 and 2019. On the other hand, very small difference was observed between 2016 and 2019, with banks presenting very close heights and canal bed depths. Similar pattern was also observed for the centre of canal base, where 2001 was outstandingly different from the years 2016 and 2019. These patterns were also exhibited in all the three reaches and years, as changes were observed as having potential effect on the canal bed profile over time. Figures 4.4, 4.5 and 4.6 present canal banks and bed profiles for Intake-Lionde, Lionde-Conhane and Lionde-Marrambajane reaches in 2001, 2016 and 2019.

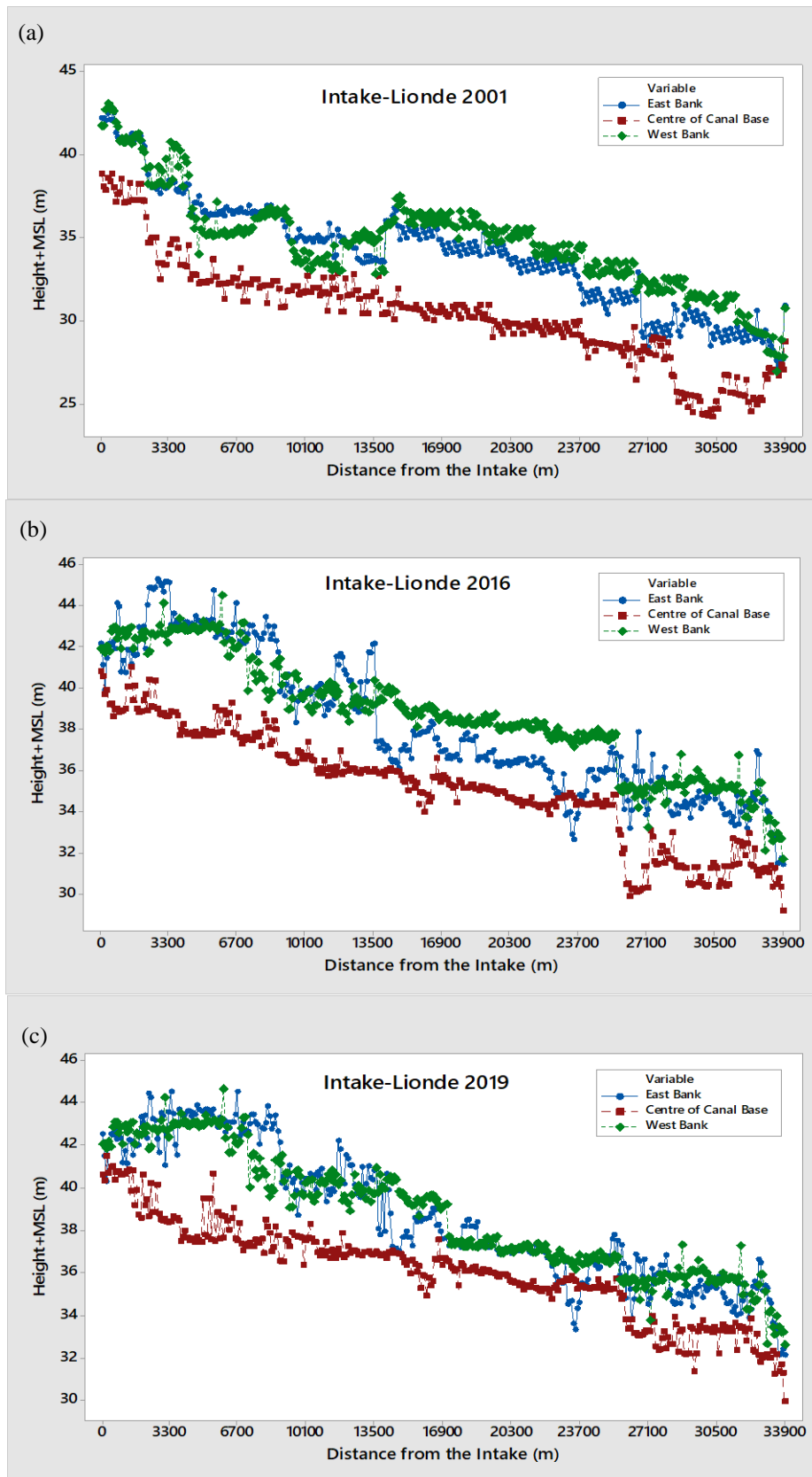


Figure 4. 4 (a, b & c): Longitudinal Profile for Banks and Canal Bed for Intake-Lionde Reach in 2001, 2016 and 2019

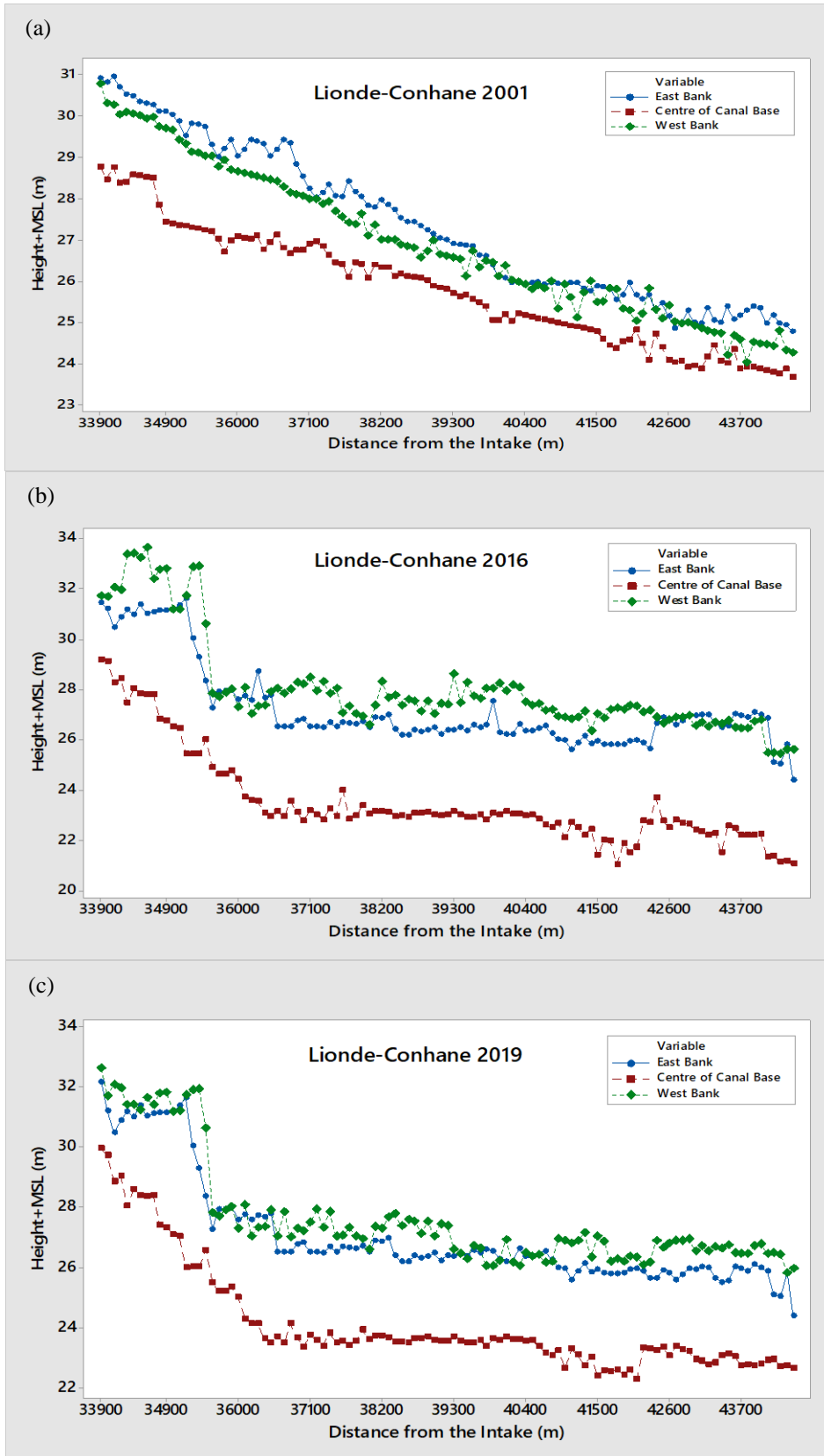


Figure 4. 5 (a, b & c): Longitudinal Profile for Banks and Canal Bed for Lionde-Conhane Reach in 2001, 2016 and 2019

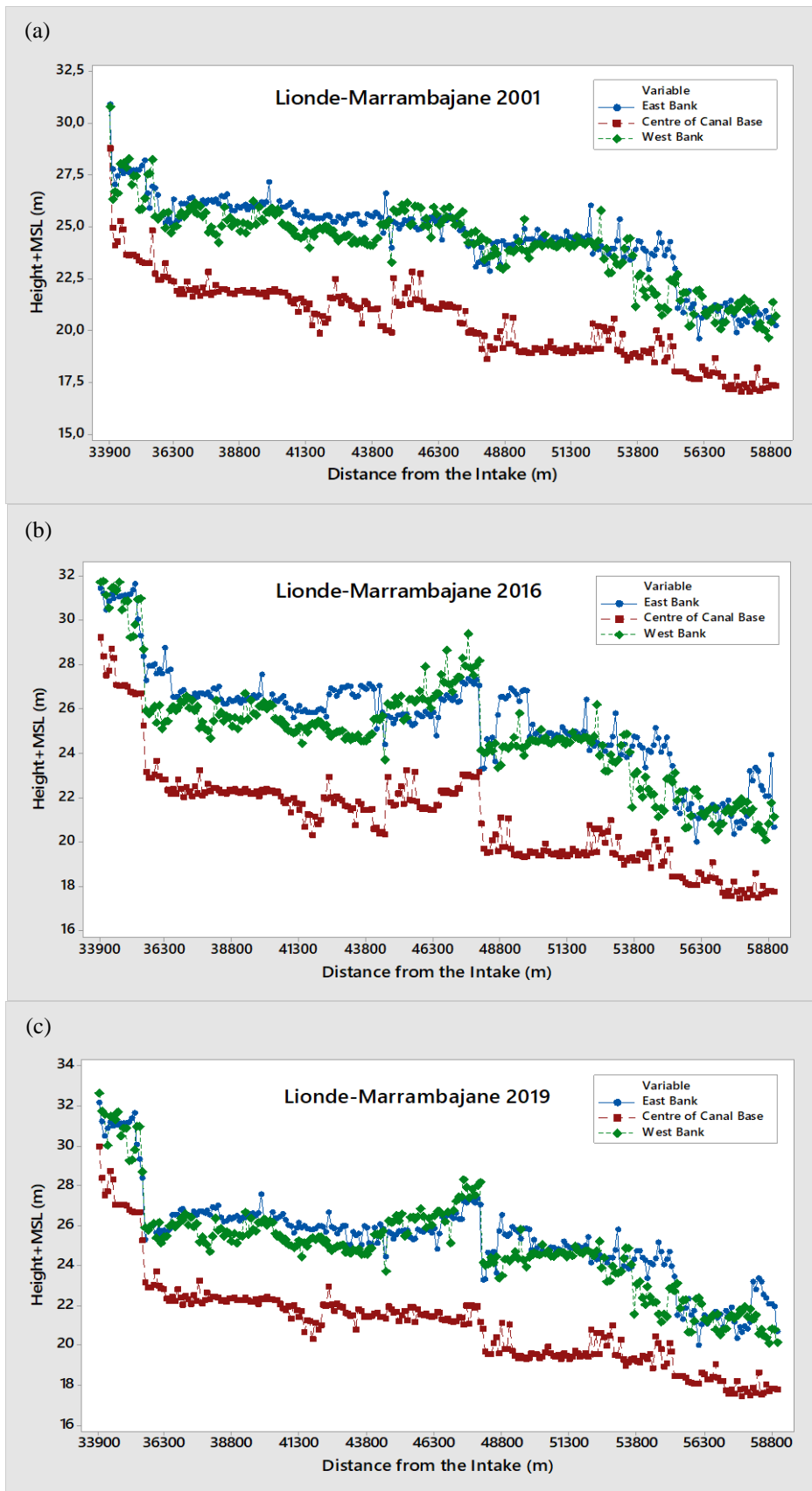


Figure 4. 6 (a, b & c): Longitudinal Profile for Banks and Canal Bed for Lionde-Marrambajane Reach in 2001, 2016 and 2019

Bathymetric Changes in Terms of Trend Analysis of Centre Canal Base

The results of trend profiles as per Mean Absolute Percent Error (MAPE), Mean Absolute Deviation (MAD) and Mean Square Deviation (MSD) are presented in Figures 4.7, 4.8 and 4.9, respectively.

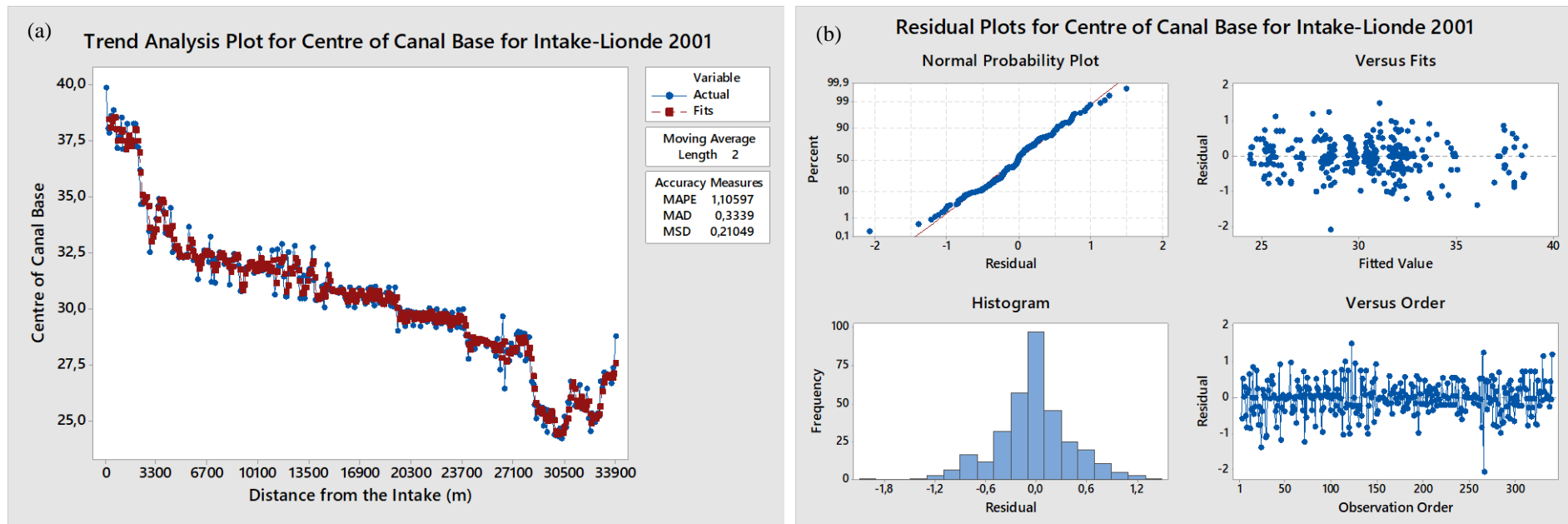


Figure 4. 7 (a & b): Trend Analysis and Residual Plots for Centre of Canal Base for Intake-Lionde Reach in 2001

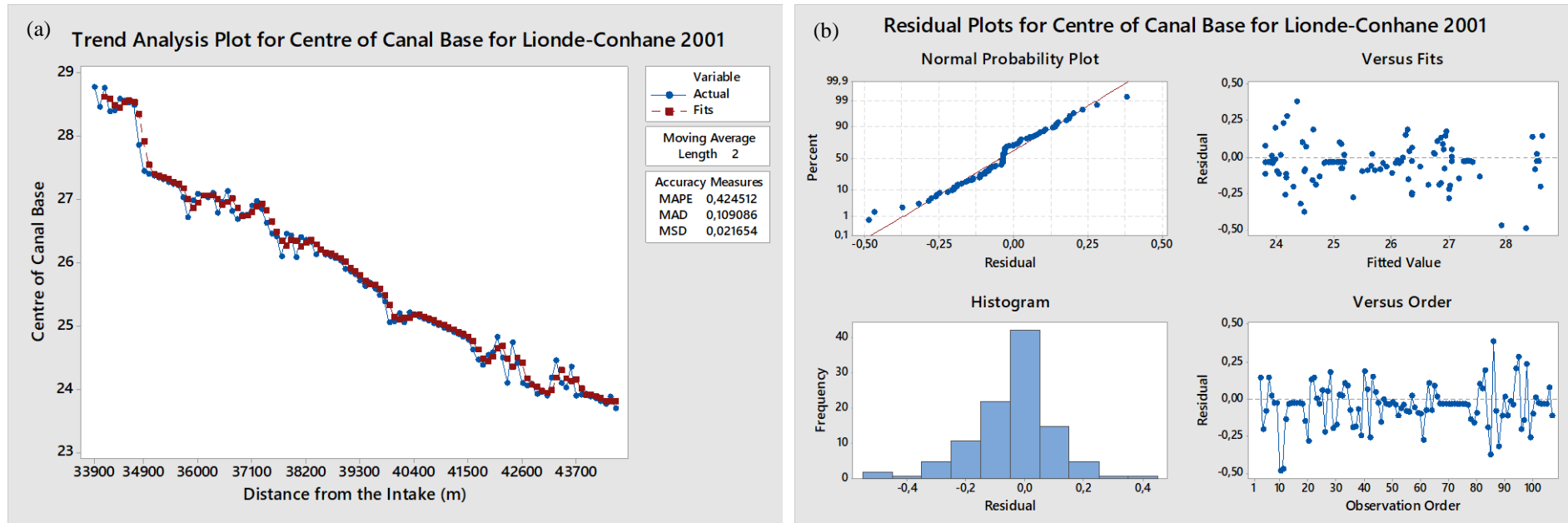


Figure 4. 8 (a & b): Trend Analysis and Residual Plots for Centre of Canal Base for Lionde-Conhane Reach in 2001

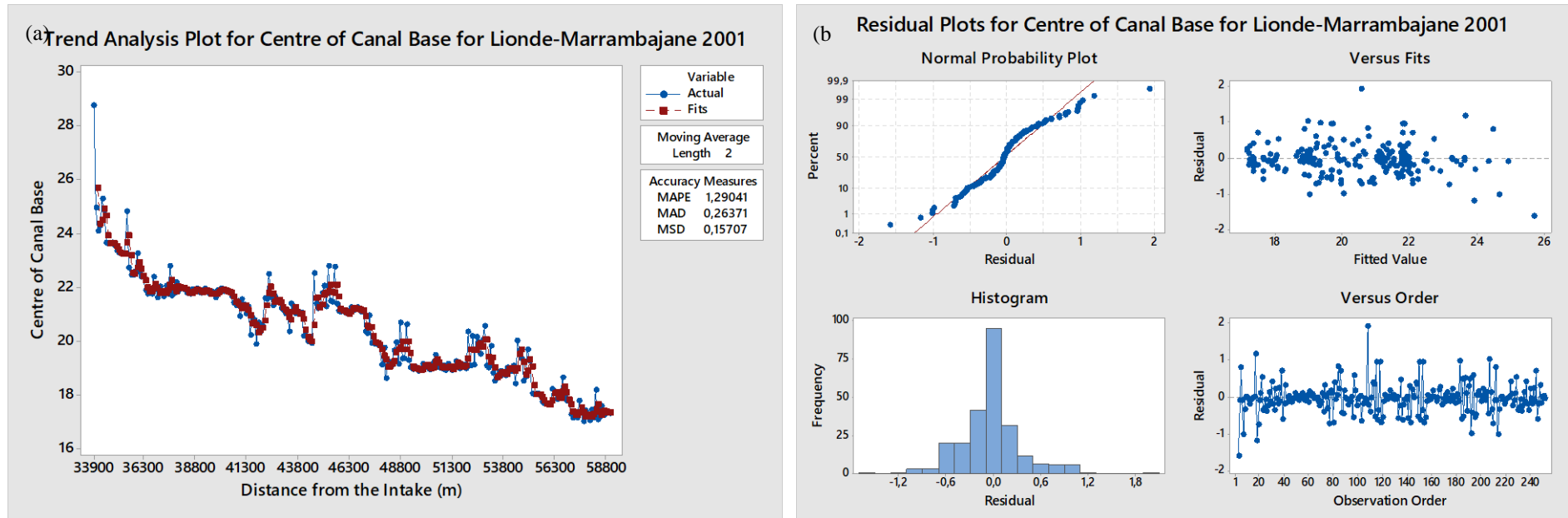


Figure 4. 9 (a & b): Trend Analysis and Residual Plots for Centre of Canal Base for Lionde-Marrambajane Reach in 2001

A decreasing profile was observed from the upstream towards the downstream. This is consistent with the standard canal profile for an irrigation scheme; especially where water is gravity driven as is the case at CIS. The actual or observed data had consistent fits. In this case, for the Intake-Lionde reach, the MAPE value was 1.11, meaning that the forecast was off by nearly 1.5%. Accuracy less by about 3.0% is acceptable as per Perk et al. (2008). MAD, which expresses accuracy in the same units as the data, helps conceptualize the amount of error. Outliers have less of an effect on MAD than on the MSD. MAD is used to compare the fits of different time series models. In this case, MAD was 0.33, which is a good accuracy indication, as the smaller values indicate a better fit. On the other hand, MSD was equal to 0.21, which also gives better fitting or prediction (Hamed & Rao, 1998; Kendall, 2007). In Lionde-Conhane reach the MAPE, MAD and MSD values were 0.42, 0.11 and 0.02, respectively. Accuracy results in this reach was less than 1% and 1, which is an indication of a good accuracy prediction. The Lionde-Marrambajane values for MAPE, MAD and MSD were 1.29, 0.26 and 0.16, respectively. Accuracy in this reach was less than 1.5% and 1, which is also an indication of a good accuracy prediction. Overall, the actual dataset for all three reaches in 2001 showed good accuracy to fits, as confirmed by the measures of forecast accuracy predictors MAPE, MAD and MSD, for which all the values were acceptable because they were very low and found to be below 3.0%, 1.0 and 2.0, respectively.

Residual plots of all the three reaches in 2001 are shown in previously presented Figures 4.7, 4.8 and 4.9. For the normal probability plot, where percentage was plotted against residual, they appeared to be well fitted in, clearly showing marginal differences from the straight line, which indicates that the residuals of the reaches were normally distributed. Residuals for the Intake-Lionde ranged between -2 and +2, and good fit was found between intervals of -1 and 1. Good fits were observed between 15 and 99% of probability, while in the remaining data the fits were slightly outside the line. Residuals for the Lionde-Conhane reach were in between intervals of -0.25 to +0.25, and good fit was found between the same interval, between 10-97% of probability. Residuals for Lionde-Marrambajane were in between intervals of -0.7 to +0.7, and good fit was found in between same interval, which in terms of percentage were between 15 and 90% of probability. This tendency was observed in other three graphs, respectively for residuals versus fitted values, histogram for frequency and residuals and, residuals versus observation order.

On the residuals versus fitted values graph, large amount of fits points were closer to the zero residuals and others were spread out away from it. Similarly, histogram graph presented frequency of between 0 and 100, and residuals from -1.4 to +1.4. Large amount of fits, for Intake-Lionde, Lionde-Conhane and Lionde-Marrambajane, were above 20, 10 and 20 respectively, and less than 10% of fits were below these values. Residuals versus observation order, for Intake-Lionde, shown residuals in between -2 to +2 and observation order from 1 to 350, with large amount of data gathering around zero, for the entire order. As per the data set was found normally distributed, as shown from the plots in Figure 4.7(b), 4.8(b) and 4.9(b), the accuracy measures predictors were well established, and therefore, accepted, given that it is of a low value. For Lionde-Conhane, residuals were in between -0.5 to +0.5 and observation order from 1 to 110, with some data gathering around zero in most orders. For Lionde-Marrambajane, residuals were in between -2 to +2 and observation order from 1 to 250, with large amount of data gathering around zero for the entire order. Data set is normally distributed and the accuracy measures predictors were well established, and therefore, accepted, given small number for MAPE, MAD and MSD.

In 2016, for Intake-Lionde reach, MAPE, MAD and MSD values were 0.73, 0.25 and 0.14, respectively, which represent good fits. For Lionde-Conhane, the values for MAPE, MAD and MSD were 0.94, 0.22 and 0.097 respectively. While for Lionde-Marrambajane, the values were 1.28, 0.27 and 0.17, respectively. Accuracy in this reach was less than 2.0%, 1 and 1, which is an indication of acceptable accuracy prediction (Mueller and Pitlick, 2005; Lima *et al.*, 2011). The residual plots for the centre of the canal base at the Intake-Lionde reach in 2016 indicate normal distributed plot, as the data has large amount of data fitting the linear graph, although with slight deviations close to zero point, in both left and right sides. Similar pattern is present for Lionde-Marrambajane reach. Residuals at the Intake-Lionde reach were in between -1 to +2 interval, and a good fit was observed between -0.75 to +0.75 intervals. On the other hand, the good fit was also observed to range from 3 to 92% of probability, fitting within the line pattern. For Lionde-Conhane the residuals were in between -0.5 to +0.5 intervals, and good fit is found in the same interval, between 10-90% of probability, while in the remaining data the fits were outside the straight line graph. Lionde-Marrambajane, instead, residuals were in between -1 to +1 interval, and good fit found along

the central points. In terms of percentage, the good fit is observed at 7 and 92% of probability respectively, while minority of data are outside the linearity. Similar tendency was observed in the other three graphs for residuals versus fitted values respectively, histogram form frequency and residuals and, residuals versus observation order. Figures 4.10. 4.11 and 4.12 present the trend analysis for the canal bed profile at its centre in 2016.

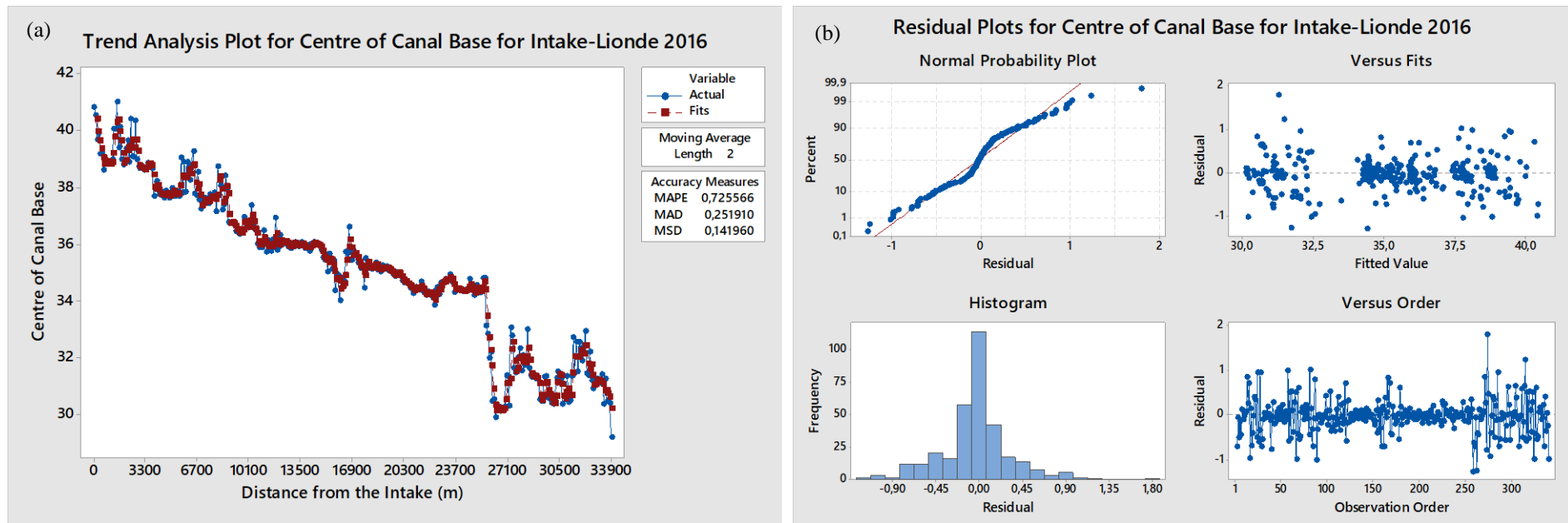


Figure 4. 10 (a & b): Trend Analysis and Residual Plots for Centre of Canal Base for Intake-Lionde Reach in 2016

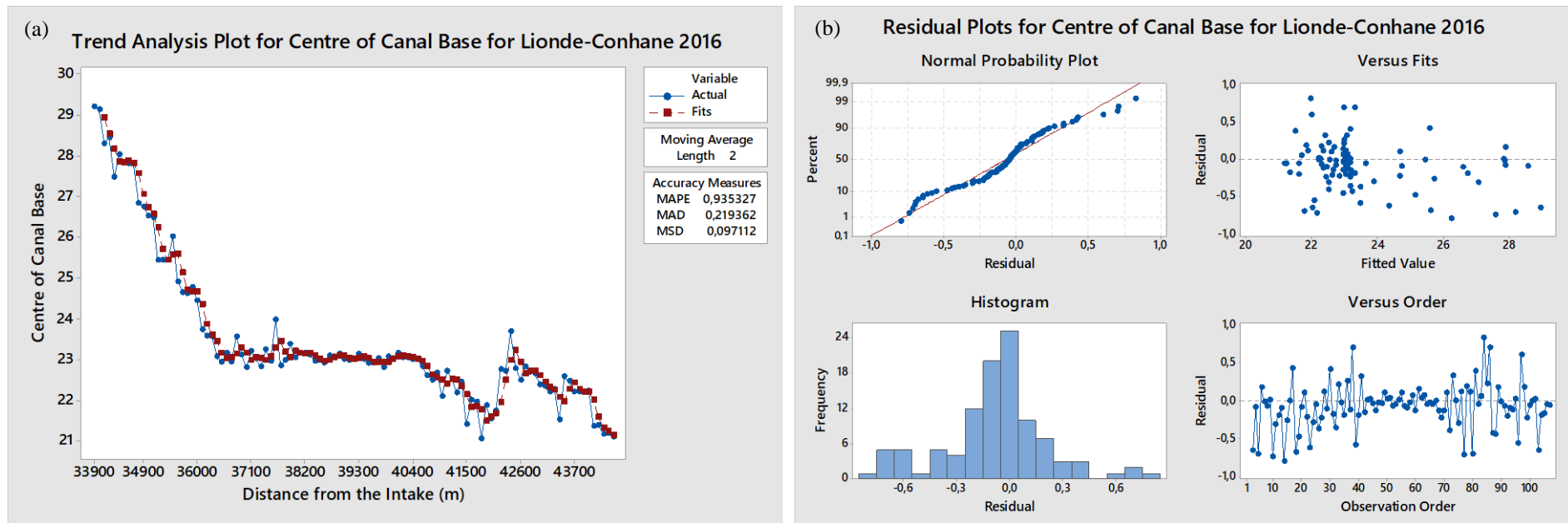


Figure 4. 11 (a & b): Trend Analysis and Residual Plots for Centre of Canal Base for Lionde-Conhane Reach in 2016

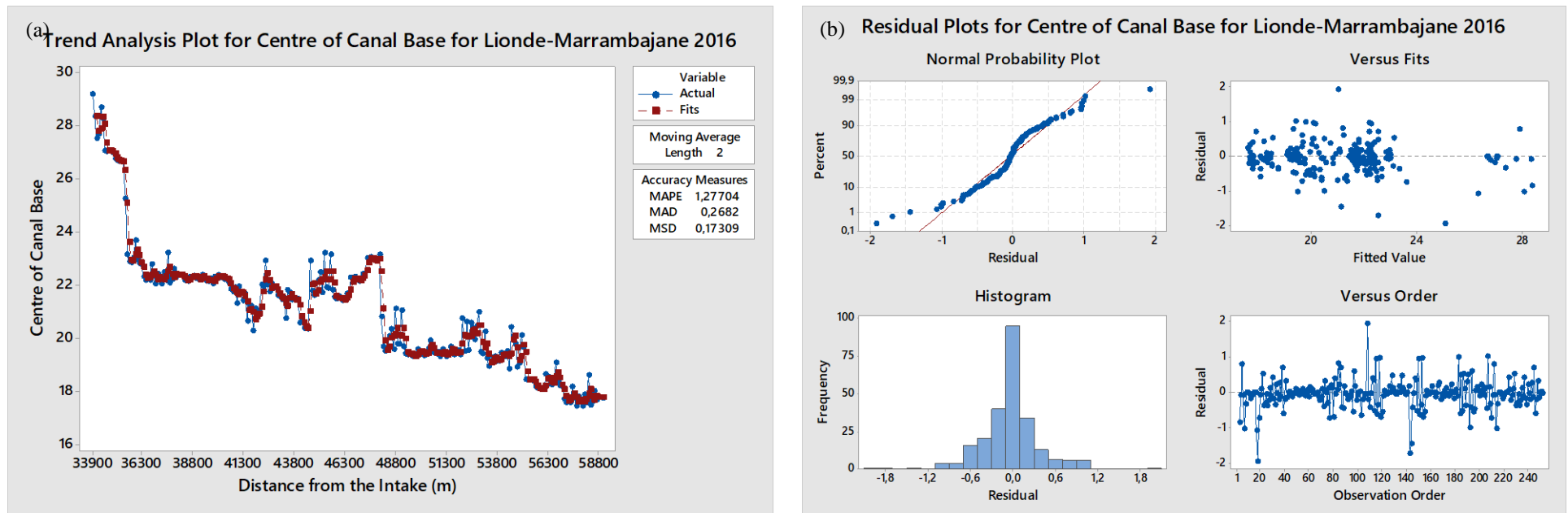


Figure 4. 12 (a & b): Trend Analysis and Residual Plots for Centre of Canal Base for Lionde-Marrambajane Reach in 2016

Intake-Lionde reach for 2019, presented MAPE, MAD and MSD values of 0.75, 0.27 and 0.17, respectively. Lionde-Conhane reach values for MAPE, MAD and MSD were 0.68, 0.17 and 0.06, respectively. Similarly, for Lionde-Marrambajane the MAPE, MAD and MSD values were 1.18, 0.25 and 0.13, respectively. In all cases, these values give better fitting (Lawrence and Edmund, 1998). The residual plots for the centre of the canal base of Intake-Lionde reach in 2019 were close to normally distributed. Residuals were in between interval of -2 and +2, and good fit was between an interval of -1 to 1, between 2 and 99% of probability. This tendency was observed in the other three plots within Figure 4.13(a). In general, the bathymetry dataset for Intake-Lionde reach in 2019 does follow normal distribution, as can be seen in Figure 4.13(b), which presents the trend analysis for the canal bed profile at its centre in 2019.

From the graph of residuals versus fitted values, a large number of fits points were closer to zero residuals and others were spread out away from it. Similarly, histogram graph presented frequencies between 0 and 120, and residuals from -1.6 to +1.8, for Intake-Lionde reach. Large amount of fits were above 20 and few were below it. The plot for residuals versus observation order has shown residuals values between -2 to +2 and observation order varied from 1 to 350, with considerable amount of data gathering around zero. The data set appears to be normally distributed, as shown from the plots and the accuracy measures predictors were well established, and therefore, accepted; given it was a small number. But, for Lionde-Conhane reach in 2019, residuals were in between -1.0 to +1.0 interval, and good fit was found between -0.5 to +0.5 interval. Good fit was observed between 10-90% of probability, while for the remaining data the fits were outside the straight line graph. In general, the data does follow normal distribution. On the plot related to the residuals versus fitted values graph, majority fitting points were closer to zero and some were spread out. Similarly, histogram graph presented frequency between 0 to 30, and residuals from -0.8 to +0.8. Large amount of fits were between 8 to 25. Moreover, the plots for the residuals versus observation order, showed residuals in between -1.0 to +0.5 and observation order from 1 to 110, with some data gathering around zero.

In the case of Lionde-Marrambajane reach in 2019, the residual plots for the centre of the canal base indicate close to normality of residuals distribution, despite slight deviation around

zero. Residuals were in between -1 to +1 interval, where good fit can be found. In terms of percentage, the good fit was observed between 8 and 90% of probability. Histogram graph presented frequency between 0 and 100, and residuals from -1.2 to +1.0. Large amount of fits were between 20 and 90. Residuals versus observation order, showed residuals in between -2 to 1 and observation order from 1 to 250, with large amount of data gathering around zero. The accuracy measures predictors were well established, and therefore, accepted, given the small values for MAPE, MAD and MSD.

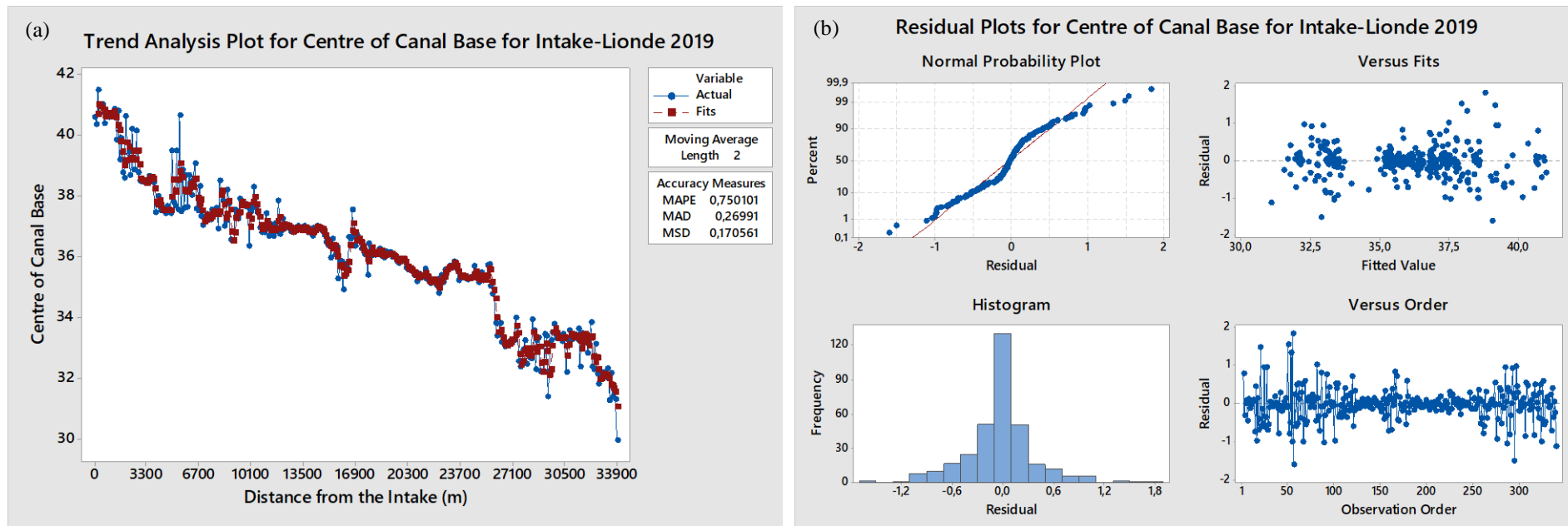


Figure 4.13 (a & b): Trend Analysis and Residual Plots for Centre of Canal Base for Intake-Lionde Reach in 2019

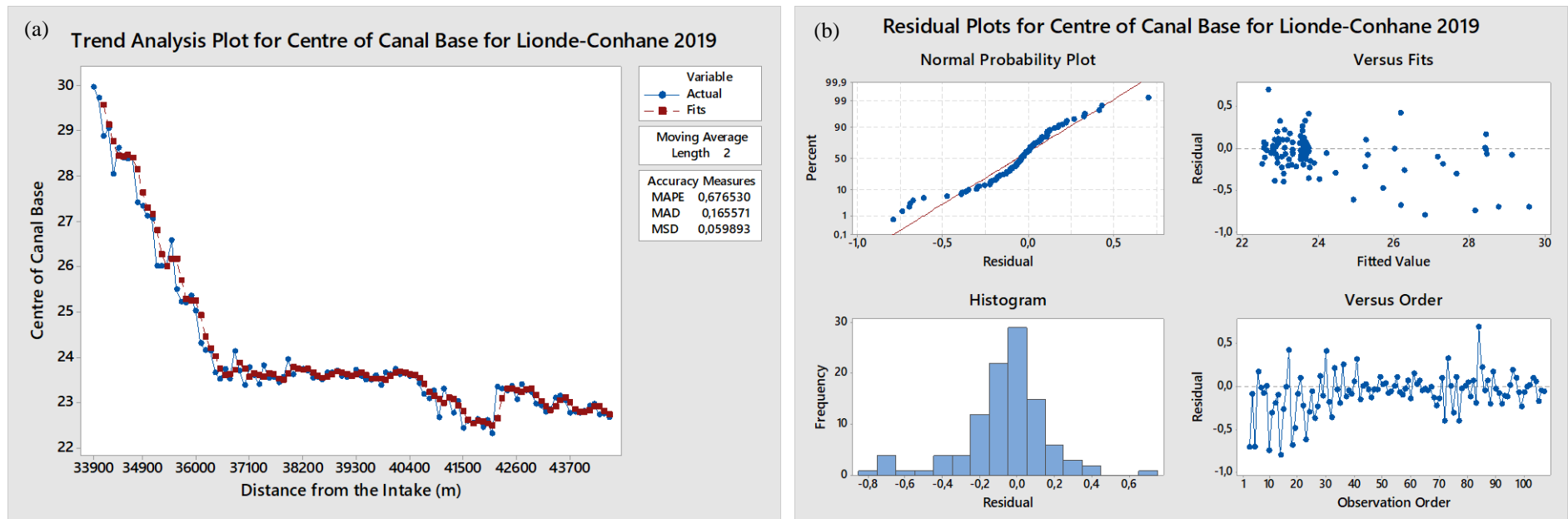


Figure 4. 14 (a & b): Trend Analysis and Residual Plots for Centre of Canal Base for Lionde-Conhane Reach in 2019

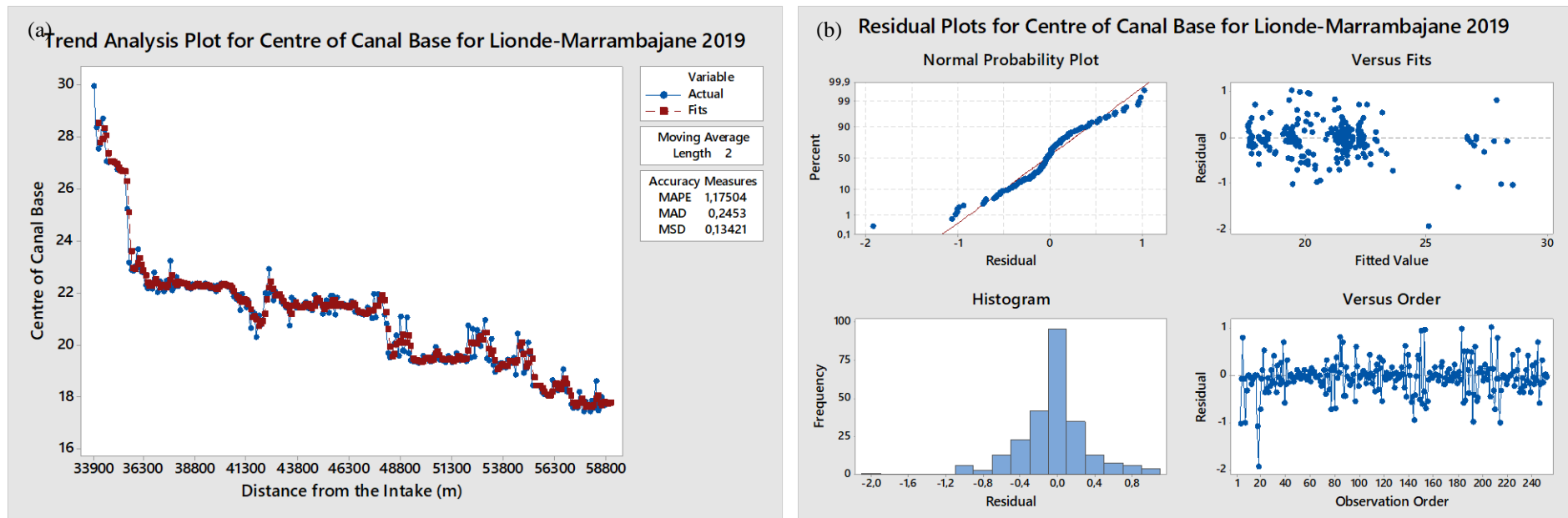


Figure 4. 15 (a & b): Trend Analysis and Residual Plots for Centre of Canal Base for Lionde-Marrambajane Reach in 2019

Different studies have been carried out on bathymetry and slope changes in canals. Some infer that such changes in canal bed profile may be due to a number of reasons, such as erosion, but mainly sediment deposition (Chen et al., 2018; Ghomeshi et al., 2019; Li et al., 2020). Throughout the studied years, changes were noted in all the reaches, among them changes in the banks, lateral slopes and centre of canal base. The canals East and West banks (EB and WB) showed bathymetric differences between 2001 and 2016, as well as for 2001 and 2019. On the other hand, very small differences were observed between 2016 and 2019, with banks presenting heights of 39 m and 27 m and 24 m for the canal bed depths. Similar pattern was also observed for the centre of canal base, where 2001 is outstandingly different from the years 2016 and 2019. These changes indicate potential sediment accumulation affecting the canal bed profile with time (Chen et al., 2018; Ghomeshi et al., 2019; Li et al., 2020).

In the Table 4.1 a summary of the Student t-test is presented for all three reaches where significant slope changes were observed, except for the most downstream site, in 2016 & 2019 variables. A two-sample t-test and z-test was conducted, having the hypothesized difference of zero and a significance level of 5%. Equality was assumed in population variances for the t-test. Comparison for the Intake-Lionde in 2001 & 2016, 2001 & 2019, and 2016 & 2019, was found to be statistically different, as the p-values were lower than the significance level alpha of 0,05. This means that one should reject the null hypothesis H_0 , and accept the alternative hypothesis H_a , whereby there is difference between the means is different from 0, or that, the slope of the centre of canal base, for 2001, 2016 and 2019, were different. Therefore, it appears that the slope has been significantly changing with time in the site. Potential reason for the changes in slope may be due to sedimentation. Similar results were found for Lionde-Conhane reach for the same time variables (2001 & 2016, 2001 & 2019, and 2016 & 2019) and Lionde-Marrambajane reach, in 2001 & 2016 and 2001 & 2019. However, Lionde-Marrambajane reach for 2016 & 2019 variable, the slope changes were not statistically significant. This means that despite some variations on the slope values, they were not sufficiently different one from the other, in both years. Lionde-Marrambajane, being the most downstream in the CIS may explain reason why this point did not indicate significant differences in the canalbed slope, over these three years.

Table 4. 1: Summary of t-test for the Slope Changes in the Canal Reaches for Selected Years

Reach	Variables	Difference	t (Observed value)	t (Critical value)	DF	p-value (Two-tailed)	alpha	Test Interpretation †
Intake - Lionde	2001 & 2016	-4.723	-20.917	1.963	678	<0.0001	0.050	Reject H0 & Accept Ha
	2001 & 2019	-5.613	-26.754	1.963	678	<0.0001	0.050	Reject H0 & Accept Ha
	2016 & 2019	-0.890	-4.660	1.963	678	<0.0001	0.050	Reject H0 & Accept Ha
Lionde - Conhane	2001 & 2016	2.316	10.320	1.971	212	<0.0001	0.050	Reject H0 & Accept Ha
	2001 & 2019	1.679	7.653	1.971	212	<0.0001	0.050	Reject H0 & Accept Ha
	2016 & 2019	-0.637	-2.574	1.971	212	0.011	0.050	Reject H0 & Accept Ha
Lionde - Marrambajane	2001 & 2016	-0.718	-3.797	1.965	502	0.000164	0.050	Reject H0 & Accept Ha
	2001 & 2019	-0.642	-3.422	1.965	502	0.000673	0.050	Reject H0 & Accept Ha
	2016 & 2019	0.076	0.370	1.965	502	0.712	0.050	Can't Reject H0

Where: DF = Degree of Freedom.

† Test interpretation based on the tests hypothesis:

Null Hypothesis (H0): The difference between the means is equal to 0.

Alternative Hypothesis (Ha): The difference between the means is different from 0.

For $p\text{-value} < \alpha$ (as the computed $p\text{-value}$ is lower than the significance level $\alpha=0.05$), one should reject the null hypothesis H0, and accept the alternative hypothesis Ha.

For $p\text{-value} > \alpha$ (as the computed $p\text{-value}$ is greater than the significance level $\alpha=0.05$), one cannot reject the null hypothesis H0.

Canal Depth Changes

The variations in canal depth is presented in Figures 4.16, 4.17 and 4.18, whereby the first reach, Intake-Lionde, in 2001, presents the changes in the depth profile as it moves from the WB to the EB points at cross-section, including the centre canal base (CCB). From the 25th to 40th m depth, material was accumulated at the bottom of the canal base. In 2016, however, the sediment material accumulated within the 10 m interval, at 30-40 m depth. Similar pattern was observed in 2019.

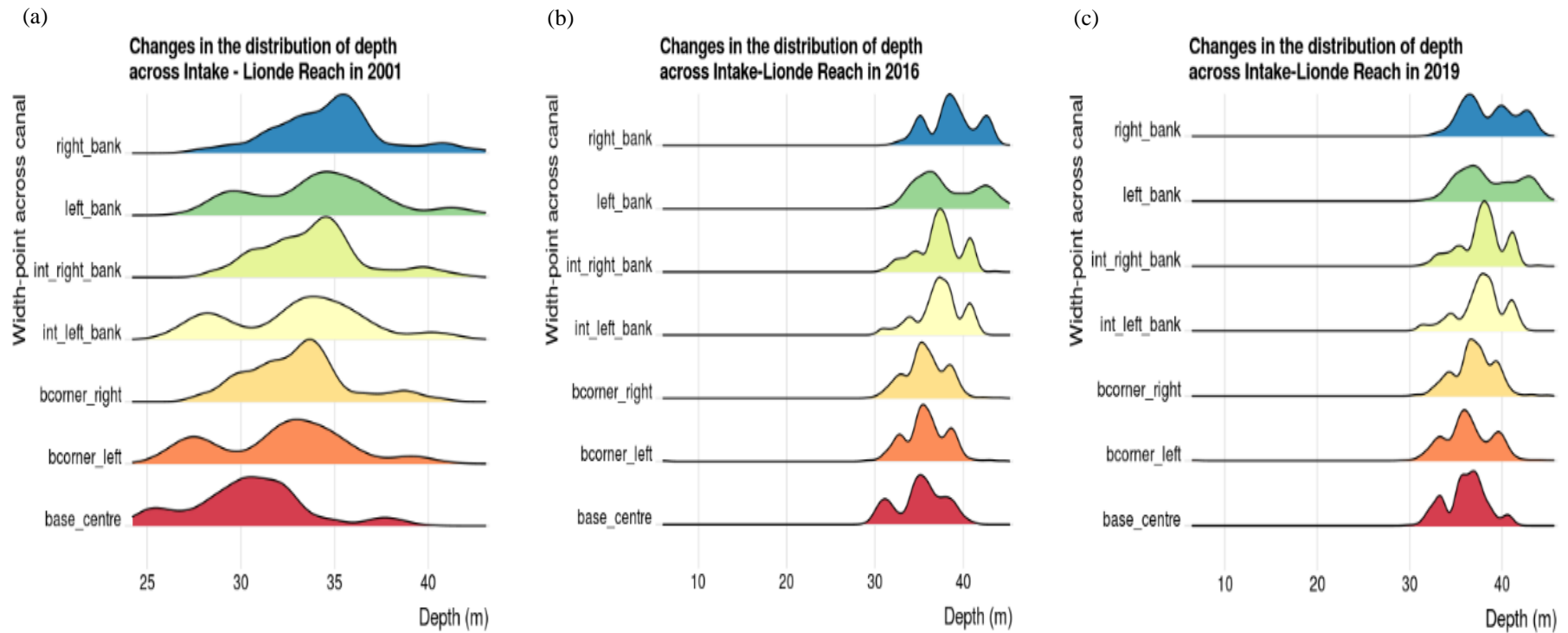


Figure 4. 16 (a, b & c): Variation in Depth, Banks and Bed Profiles for Intake-Lionde Reach in 2001, 2016 and 2019

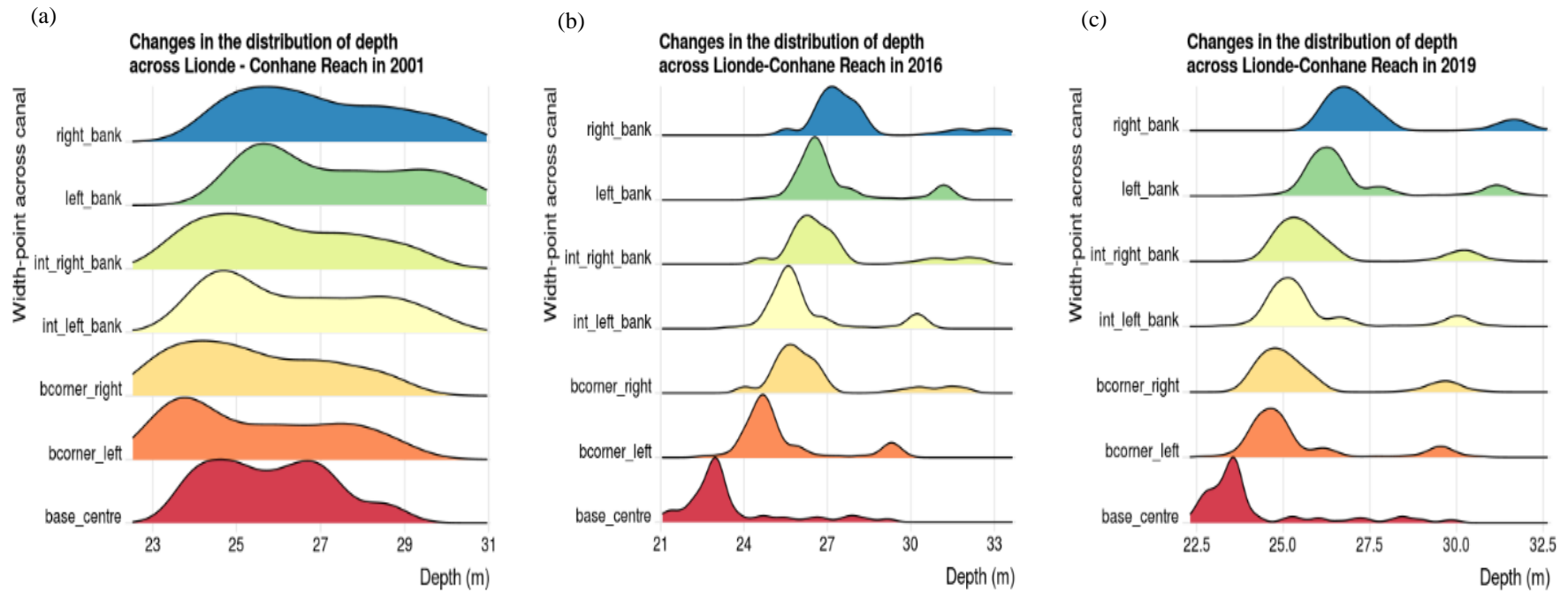


Figure 4. 17 (a, b & c): Variation in Depth, Banks and Bed Profiles for Lionde-Conhane Reach in 2001, 2016 and 2019

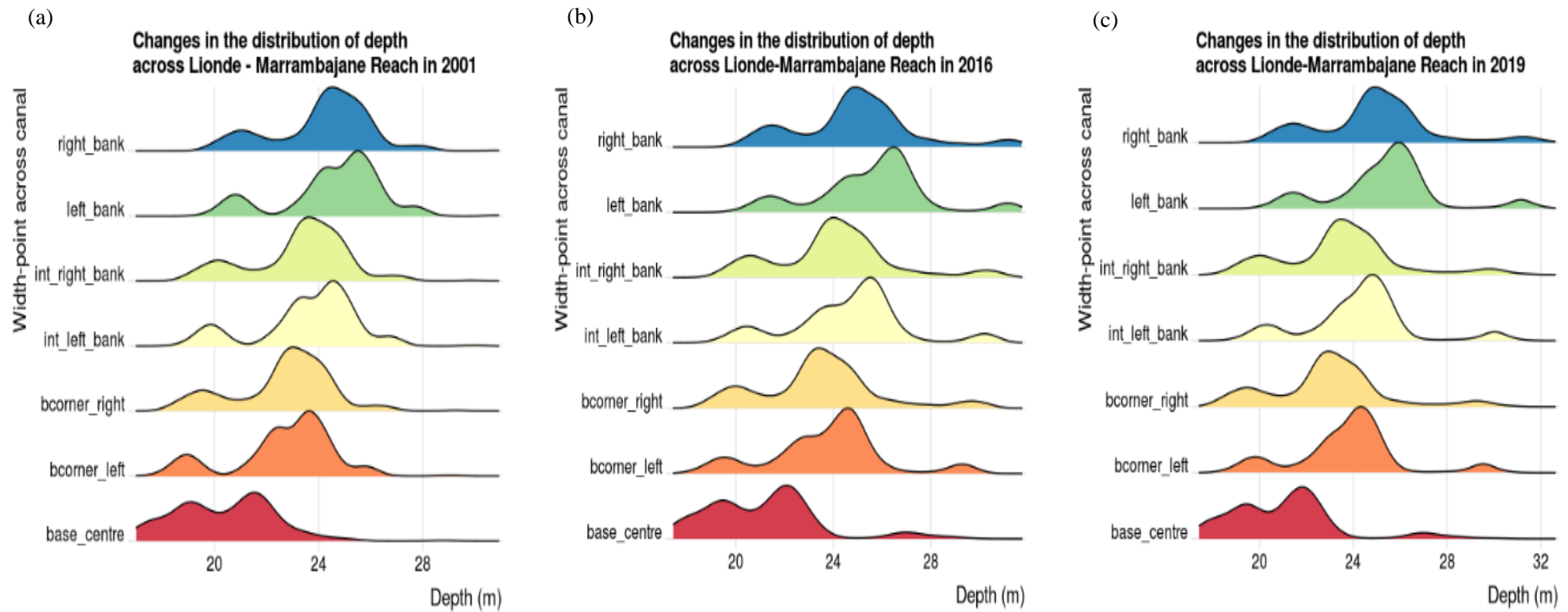


Figure 4. 18 (a, b & c): Variation in Depth, Banks and Bed Profiles for Lionde-Marrambajane Reach in 2001, 2016 and 2019

For Lionde-Conhane reach, in 2001, significant amount of accumulated material was observed at WB and EB, their intermediate points and CCB. From the upstream to downstream, the material tends to accumulate more at the downstream. For 2016, WB and EB accumulated material at the 24th-30th m depth, while the intermediate points, both west and east, had material piled up at the 23rd - 27th m depth. The CCB, on the other hand, has the bed material accumulated at the 21st-24th m depth. Same pattern was observed in 2019. At the Lionde-Marrambajane reach, in 2001, the sediment accumulation was found at the 20th-28th m depth for the WB and EB and the intermediate points. The canal base depth was found to vary between the 16th to 24th m. In 2016, the sediment material accumulated at the 20th-28th m depth, moving from the surface towards the bottom. This could be explained by the fact that at the canal surface is where the banks are normally laden by erodible materials, that in turn, are moved to lower points, such as canal bed, where sediments materials tend to accumulate (Fent et al., 2019; Terefe & Singh, 2020; Yokoyama et al., 2018). The results from 2019 do not differ considerably from what was observed in 2016.

Bed load Physical Characteristics

The CIS seems to be mainly comprised of silt and fine sand on its canal bed loads. Details on this are presented in the following sub-sections, with results of the Atterberg Test (AT), Liquid Limit (LL) and Plasticity Index (PI) and the Particle Size Distribution (PSD) given accordingly and sequentially.

Atterberg Test

Atterberg test was used to classify unconsolidated sediments (Osman, 2015), allowing to distinguish between cohesive and non-cohesive sediment and to determine the mechanical behaviour of cohesive sediments. Here, the LL and PL yielded water content of cohesive sediment samples, and the difference in water content between the LL and PL resulted in the Plasticity Index (PI). From the results, it was observed that the sediment is cohesive, since it has medium to high plasticity, which holds relatively significant amounts of water. Despite the fact that some stations presented some silt and sand particles, these remained majorly cohesive. Table 4.2 shows the results of the Atterberg test analysis.

Table 4. 2: Atterberg Limit Test for the Bed load Particles of CIS

Sampling stations	Liquid Limit (%)	Plasticity Limit (%)	Plasticity Index (%)
Railways-Node	54.473	21.755	33.717
FIPAG	53.958	20.175	34.241
Lionde	50.345	18.194	30.655
Massawasse	34.364	14.441	20.956
Conhane	37.655	14.327	23.475
Nico	60.908	22.260	35.283
Muianga	57.692	21.956	33.979
Marrambajane	69.811	26.631	40.849
Mean	52.401	19.967	31.644

All sampling stations presented LL above 50%, except Massawasse and Conhane, which had about 34% and 38%, respectively. Similar pattern was also observed for the PL and PI. These findings, according to Partheniades (2009), Ye (2012) and Osman (2015), allow for the classification of the sediment samples as silt and organic clay, with high plasticity. Overall averages for CIS for LL, PL and PI, were 52%, 20% and 32%, respectively.

Atterberg limits provide additional information on the plastic behaviour of the sediment as a whole and on the clay fraction of the sediment, in particular. When PI increases, the cohesion increases (Ye, 2012; Ampomah, 2014). However, the utility of these measures for predicting the erodibility of superficial sediment is questionable (Partheniades, 2009). The mechanical soil properties can be linked to erosive properties of cohesive sediments. Some authors correlated the critical shear stress of erosion to the PI of bed material (Decrop et al., 2015; González et al., 2017; Hoffmann et al., 2017; Recking, 2013; Tadesse & Dai, 2019; Zhu et al., 2018). Table 4.3 shows values of the critical shear stress of the sediment particles for the canal bed of the main canal in CIS, which ranged from 2.0 to 4.0 N/m². Sampling stations of Massawasse and Conhane presented the lowest values, while Marrambajane reached the highest value of critical shear stress. The mean value on the entire CIS was found to be equal to 2.960 N/m². These values indicate that the critical shear stress exceeded the bed shear stress (Partheniades, 2009), suggesting that no erosion does occur in the canal bed of the irrigation scheme.

Table 4. 3: Erosion Critical Shear Stress for the Sediments at Canabed of CIS

Sampling stations	Erosion critical shear stress, τ_c (N/m ²)
Railways-Node	3.130
FIPAG	3.171
Lionde	2.890
Massawasse	2.099
Conhane	2.309
Nico	3.252
Muianga	3.151
Marrambajane	3.678
Mean	2.960

Liquid Limit and Plasticity Index

The relationship between the LL and PI were also assessed. From the samples analysed, it is evident that the LL positively explains the PI for almost all the stations. For the Montante Sector sampling stations the LL (also coded as WL) and PI (also coded as Ip) resulted in the regression fitting line, given for Railways-Node and for FIPAG for dry and wet seasons, as presented in Figure 4.19. For all the relationships in analysis, the coefficient of determination is above 80%, providing high level of confidence that the LL well explains the PI for the sampling stations. Having water content of more than 50% for the majority of observations, the PI is relatively high, confirming the expectation that the soil particle composing the sediment at Railways-Node and at FIPAG bridges sampling stations are mainly composed of fine material, with a capacity to hold moisture. Similar tendency is observed for the next two sectors, Sul and Rio, respectively. Regression fittings for the sampling stations at Montante, Sul and Rio sectors, are presented in Figures 4.19, 4.20 and 4.21, respectively.

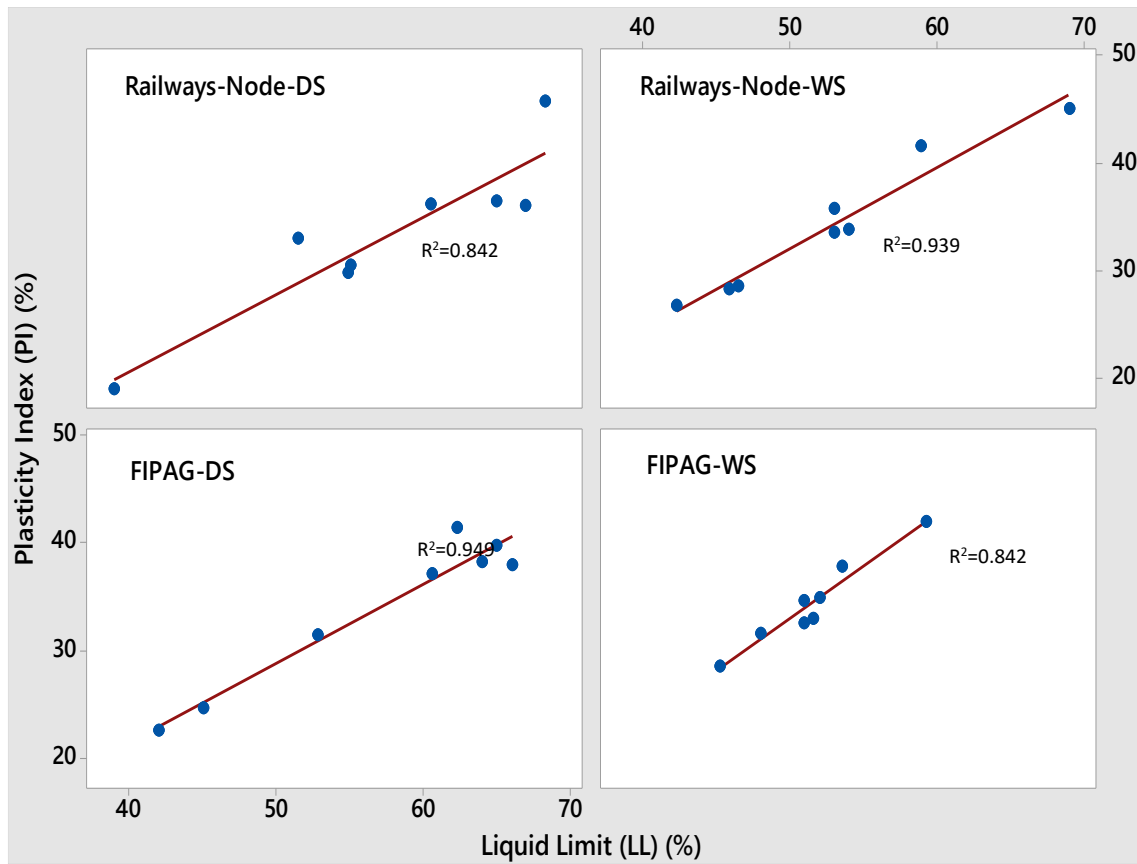


Figure 4. 19: Liquid Limit (LL) and Plasticity Index (PI) for Montante Sector Stations

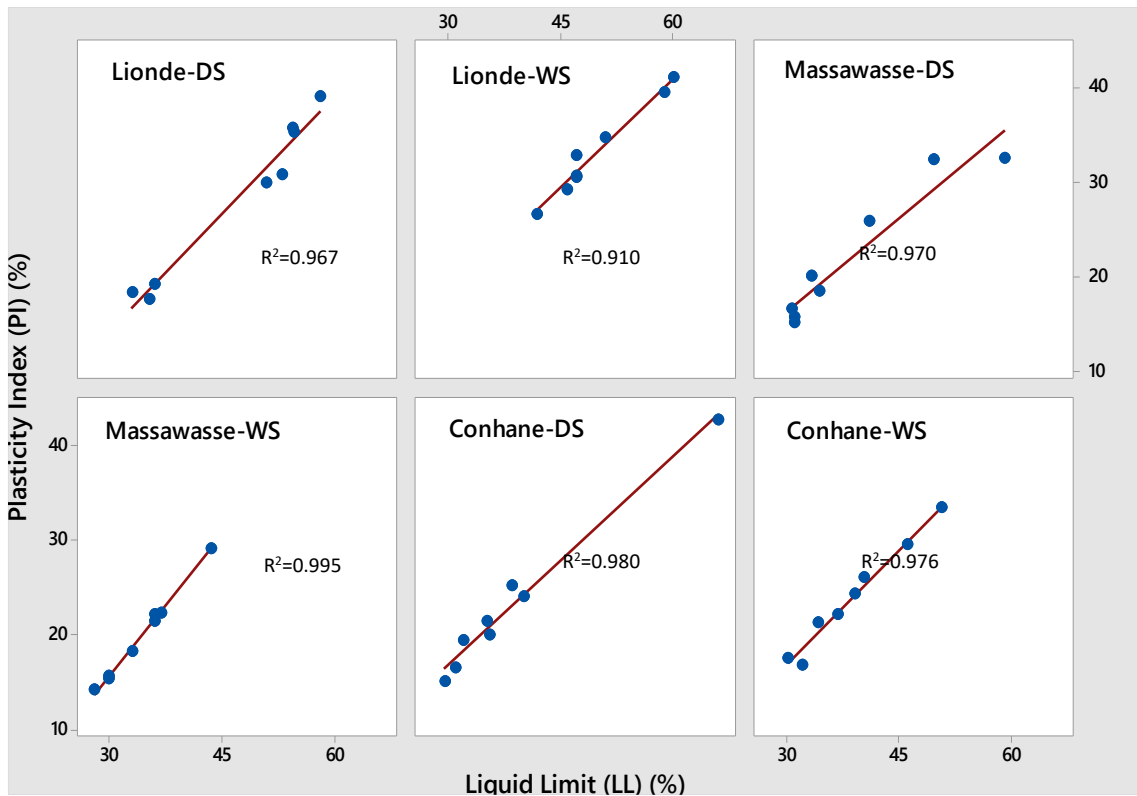


Figure 4. 20: Liquid Limit (LL) and Plasticity Index (PI) for Sul Sector Stations

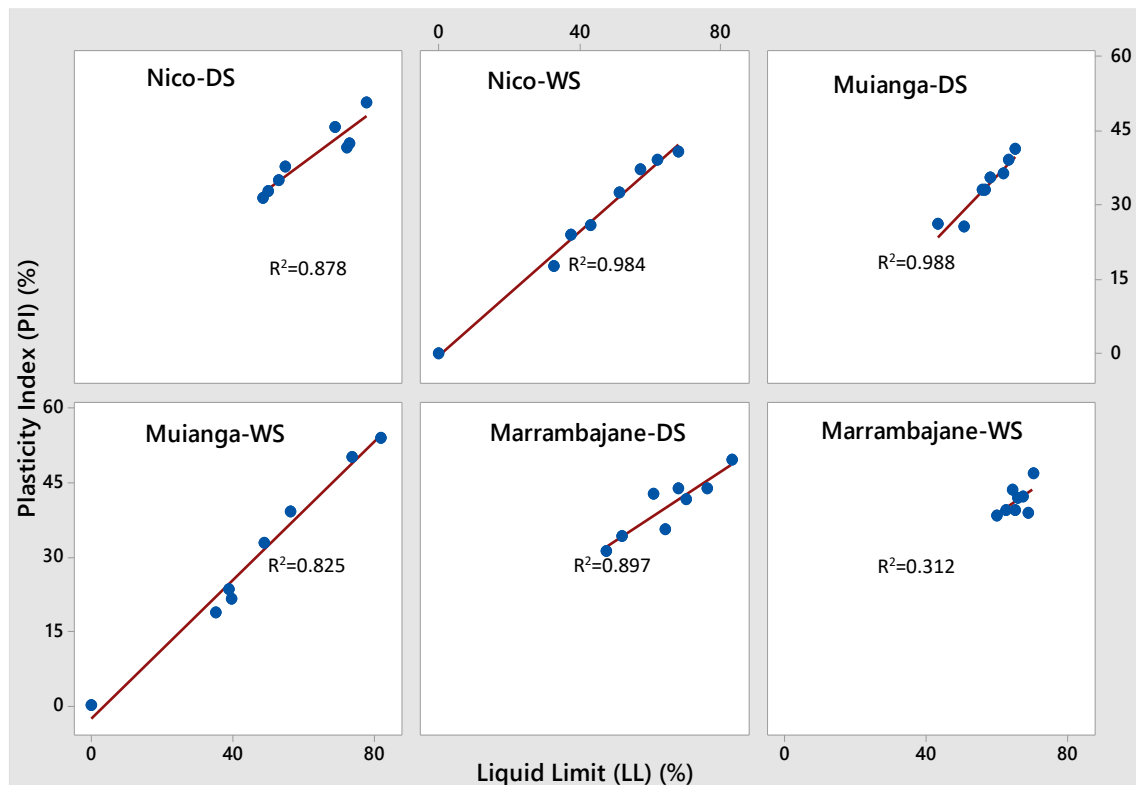


Figure 4. 21: Liquid Limit (LL) and Plasticity Index (PI) for Rio Sector Stations

Particle Size Distribution

Particle size is an fundamental sediment physical property for bed load and its characterization is seen as a keystone in the bedload studies. Measuring grain size distribution for sediment classification remains essential. In this work, the grain size distribution was performed for the bed loads and average specific weight of the sediment in CIS was found to be equal to 2.63. Normally, at CIS when comparing DS and WS, there is less rainfall during DS than the WS. In consequence, low flow and water flux was recorded during the DS. In contrast, WS recorded some rainfall and no significant floods, in opposite to what is commonly expected in this season. Theoretically, sediments particles with different sizes behave differently with less or more water flow and water depth in the system. At the beginning of the WS, the fine materials are washed from the river basin and transported through the irrigation canals, where transport or deposition may occur. The analysis of bed material at Intake was not considered since the canal bed at this point is lined with concrete and sediment is barely collectable.

During DS, the Railways-Node and FIPAG stations, both located in the Montante Sector produced around 60% silt, and significant quantity of fine sand and very low amount of clay. Similar pattern was found at the Sul Sector, whereby Lionde, Massawasse and Conhane stations, presented silt accounting for more than 60%, except in Massawasse, where more fine sand was recorded. For the Nico, Muianga and Marrambajane stations, all located in the Rio Sector, considerable presence of fine sand was recorded, at more than 60%, except in Muianga, where silt amounted for more than 70% of sediments. According to Ye (2012), sediment particles having particle diameter of less than $75\mu\text{m}$ are charged with positive and negative forces that cause them to stick to other particles, generating aggregated sediments. Therefore, the silt and clay presence in the stations, seems to facilitate flocculation, and even, where fine sand was found abounding, the silt and clay presence still appeared to influence aggregation process among the particles. These results agree with findings by other authors who did similar studies and reported similar outcomes (Kiani-Harchegani et al., 2018; Armanini et al., 2020). Analysis during WS, Montante Sector stations produced silt amount above 55% and large quantity of fine sand and clay. In contrast, the Sul Sector stations, resulted in opposite pattern than DS. Here, there was observed that fine sand accounts for more than 50%, except in Lionde, where silt contributed with around 68%. Rio Sector, on the

other hand, seemed to generate more than 50% of silt in all the three stations, hence indicating cohesiveness of the sediments.

The general overview for the CIS particle size distribution on the bed materials show sediment containing around 52% silt, 39% fine sand and 9% clay. For this reason, based on the particle size distribution of the sediment occurring in the CIS, it is referred to as cohesive sediment (Mehta et al., 2013). Higher clay contents, such that in between 4% and 10%, the framework of the sediment structure changes from a fine sand grain framework to a clay mineral one. This therefore, corresponds to a shift from a non-cohesive to a cohesive sediment (van Ledden et al., 2004; Winterwerp & van Kesteren, 2004). The classification of the sediment has been made based on the proportions of sand, silt and clay particles, in accordance with Shepard's diagram, which is the basis for sediment distribution map (Shepard, 1954). The sediment tend to be finer towards the CIS downstream-end, as coarser materials are deposited first, although Massawasse station registered high quantity of fine sand, this remained true in other stations. Despite this, silt effect appears to play relevance in role for cohesiveness at this points and stations. Table 4.4 presents the average grain size distribution for the sampling stations at CIS. According to Burge et al. (2000), when the bed mixture of the gravel-bed canal contains more than 40% sand, it is referred that the bed is matrix-supported, whilst, when the bed has less than 25% sand, the bed is said to be framework-supported. Matrix-supported bed suggests coarser predominance of composition, in opposition to framework supported canal bed. Therefore, given that the presence of sand particles comprising the bed load in the main canal of CIS is around 39%, which is situated in between 25% and 40%, the bed canal is said to be in transitional (Wu & Chou, 2003; Yao et al., 2018).

Table 4. 4: Average Grain Size Distribution of Bed load for Different Sampling Stations

Sampling stations	Fine Sand (%)	Silt (%)	Clay (%)	Classification according to Shepard 1954
Railways-Node	19.75	67.50	12.75	Silty Sand
FIPAG	40.00	56.00	4.00	Silty Sand
Lionde	21.00	69.00	10.00	Silty Sand-Clay
Massawasse	67.75	25.00	7.25	Sandy Silt
Conhane	42.75	49.00	8.25	Silty Sand
Nico	52.50	43.00	4.50	Sandy Silt
Muianga	17.50	60.75	21.75	Silty Clay-Sand
Marrambajane	48.00	45.50	6.50	Sandy Silt
Mean	38.66	51.97	9.38	-

Analysis of the PSD allowed for assessment of d_{10} , d_{30} , d_{50} , d_{60} and d_{90} for both seasons, where d_x is a characteristic particle size such that $x\%$ of the sediment (in volume) is finer than d_x (Ancey, 2020). It also show the coefficient of curvature (C_c) and the coefficient of uniformity (C_u), being the former an indication of how well or bad the curve is graded, and the later, serves to assess how uniform the curve is. Well graded curve, is the one presenting all the diameters of particles or clay, silt and sand sizes. According to Dearnaley et al. (1995) and Mehta and Lee (1994), particle size can be classified as clay ($<0.002\text{mm}$), silt ($0.002\text{-}0.0625\text{mm}$), sand ($0.0625\text{-}2.0\text{ mm}$) and gravel ($2.0\text{-}64.0\text{ mm}$). Coefficient of uniformity (C_u) indicates a well graded sand sediments when $C_u > 6$ and coefficient of curvature (C_c) indicates well graded curve when $1 < C_c < 3$, and not well graded curve if $C_c < 1$. In regard to the C_u all the stations presented $C_u > 6$, being well graded sand sediments, except for the Lionde station during DS and WS, and Muianga and Marrambajane, in WS. When it is referred to the C_c , only Lionde, Massawasse, Nico and Muianga, in DS, and Railways in WS, presented well graded curve (Nyika et al., 2019; Orhan & Kılınç, 2020). These results can be used to predict canal bed behaviour across all sampling stations.

Study by Wilcock et al. (2009) and Wilcock et al. (2020), where a persistence of armor layers in gravel-bed streams were investigated, a similar finding is reported, though their study considered bed layers divided into three, against just one in this study. The PSD curves are shown in Figure 4.22 for all sampling stations for both seasons.

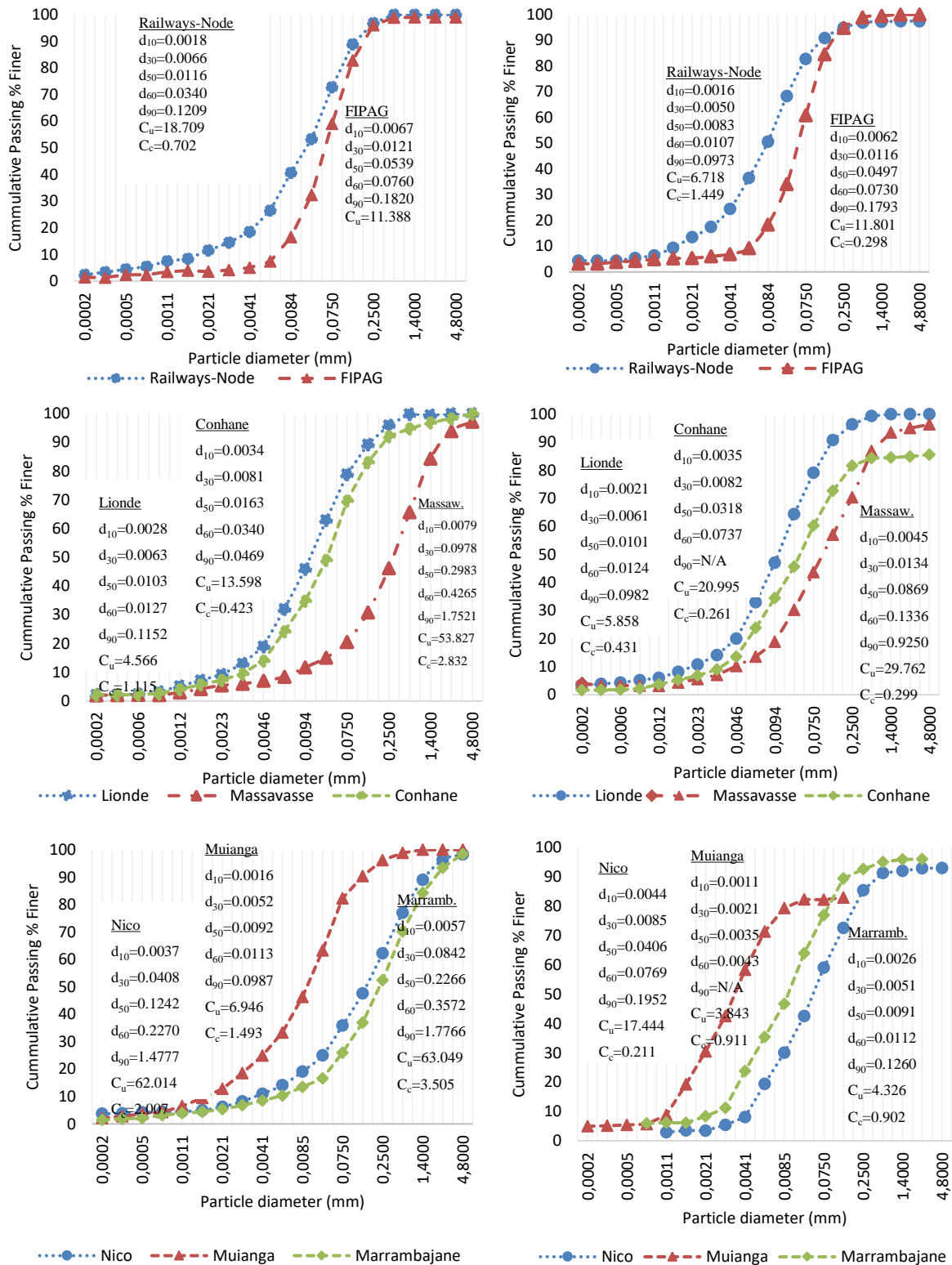


Figure 4. 22: Particle Size Distribution Curve for DS and WS

Bed load Chemistry Characteristics

The chemistry characteristics of the sediments are herein analysed for the laboratory results. The ponds between sediment particles appeared to be influenced by pH of the fluid found in the pore of the sediment matrix, which does affect the orientation of particles when bonding occurs by changing the surface or edge charges of the sediment particles. When the pH is found to be tendentially acidic (≤ 5.2), it results in an stratified sediment bed, which in turn, may exhibit high rate of erosion at near the surface. Additionally, when an intermediate pH is observed to be around or close to neutrality ($5 \leq \text{pH} \leq 7$), it causes a weaker bed structure in consequence of lack of surface contact, which may lead to more susceptibility to erosion. But, pH tendentially alkaline (>7), which is considered to be high enough, as was the case in this study, particle orientation will predominate and cause attraction forces to be present in the surface forming denser sediment aggregates. These findings suggest that the site conditions will favour stronger sediments as referred by Ravisangar et al. (2005) whose work showed that lower pH water has high possibilities to generate stronger sediments, with less risk to erosion due to excess shear stress. The total soluble amount of sediment ions, measured from the electrical conductivity (EC) of a sediment water extract, is considered a significant factor in the susceptibility of cohesive sediment to erosion (Sherard et al., 1972, Osman, 2015). Sediment with $\text{EC} > 4$ dS/m was classified to be saline. Chemistry analysis for the DS showed high values of EC, which suggests that the sediment is majorly saline. The increase in the electrolytic concentrations or variations in the fluid pore of clay with higher value tends to cause de-flocculation. The ratio of sodium ions dissolved in relation to the other main basic cations, such as calcium and magnesium, provides the Sodium Adsorption Ratio (SAR). When SAR presents high values, repulsive forces between particles become dominant, with considerable swelling and cause clay particles to de-flocculate. Partheniades (2009) suggested that decreases in SAR values cause decreased erosion rate. Results showed high values of SAR, reaching 98 in DS and around 70 in WS. The level of dispersion and flocculation, which accounts for the sediment aggregate stability, depends on the balance (SAR) between calcium (Ca^{2+}) and magnesium (Mg^{2+}), and sodium (Na^+), as well as the amount of soluble salts (EC) in the sediment extract. Sediment particles tend to flocculate if concentrations of $\text{Ca}^{2+} + \text{Mg}^{2+}$ increase relative to the concentration of Na^+ (SAR decreases). The classification of sediment was performed in accordance with Table 2.2, and is termed as saline-sodic and sodic sediment.

The exchangeable sodium percentage (ESP), explains the presence of excessive amounts of exchangeable sodium that reverse the process of aggregation and cause sediment aggregates to disperse into their constituent individual particles. This process is known as deflocculation and occurs in sodic sediment. The study results showing $ESP > 6\%$ was found, and is considered to have a very high percentage (Semenov et al., 2018), and that the sediment is sodic to saline-sodic. For this reason, one can state that the type of sediment in CIS presents properties of cohesive sediment and is fairly resistant to erosion. The saturation percentage (SP), which indicates sediment water retention capacity, presented high values of above 75%. This is an indication that the sediments can store water due its particle size distribution mainly made of fine materials. Corroborating factors were found to this as high value of the plasticity index were observed, prompting conditions to infer that no deep percolation occurs in CIS main canal, as consequence of sediment properties covering the canal bed layer. Indeed, highly retained water in the sediment leads to consolidation of individual particles and formation of sizeable aggregation (Kouzegaran et al., 2021; Zheng et al., 2020). High water retainers usually are comprised of silt and clay materials (Belal et al., 2019; Iyer, Joseph, Lopes, et al., 2018; Iyer, Joseph, Shetty, et al., 2018). These materials, in general, has high potential to generate cemented layers due to their properties of filling in the empty pores and allow water move to further points in the stream (Driss et al., 2021). Sediment aggregations with fine particle and high potential to retain water, will under water percolation (Iyer et al., 2018). The physio-chemical properties of the sediments are presented in Tables C1 (DS) and C2 (WS), in the Appendix C.

4.1.2 Inflow Factors

Water Depth Variation

Water depth in the canal has shown considerable variations within each sampling point, across the sampling points and sampling stations. Overall, less water was observed in the canal during the DS, with an average of 2.5 m, except at FIPAG station, where water level reached nearly 3.5 m. This shallow water depth of 2.5 m, on average, may be of significant influence on the water velocity and therefore, on the sedimentation process. Less water in the canal was a result of different reasons, some of which include increased demand for water by

farmers, and reduced inflow due to lack of rainfall during this season. The lowest height was found at Conhane-bridge station, with less than 1.2 m, as presented in Figure 4.23(a). During the dry season (DS), higher water level was observed from East to the West side of the canal cross-section at the most upstream side of CIS, in the Montante Sector, comprising Intake, Railways-Node and FIPAG sampling stations. The opposite scenario was observed for Conhane sampling station, which had the lowest water levels. Interestingly, at this sampling station, contrarily from the others, the lowest water levels were observed at their extremes points, respectively, East and West sides of the cross-section.

On the other hand, it was expected that higher water levels would be observed during the WS as compared to the DS. In a normal hydrologic year, this would be very true and observable in the region. Times have passed when WS used to bring significant amount of water into CIS on regular basis, either coming from runoff off Limpopo River or rainfall. However, in the past decade, and much towards the end of it, the region has received much reduced rainfall. From an average of approximately 650 mm, the region is now receiving less than 400 mm, all concentrated within 6 weeks (mid-January to mid-March), if lucky. Therefore, due to the reduced inflow and rainfall, the increase in water level was not so significant in the system. For example, as shown in Figure 4.23(b), the highest water level for WS was again observed at FIPAG sampling station and the lowest at Conhane station, with 3.5 m and 1.6 m, respectively. In general, during WS, in every sampling point, water level in the canal has a uniformly patterned behaviour, all along the canal, from the main intake to the outlet. That behaviour, although uniform, presents some differences among the levels at each point, even though small. Water level variation across the canal cross-section in this season, however, remains evenly and steadily distributed, from the East to West sides of the canal.

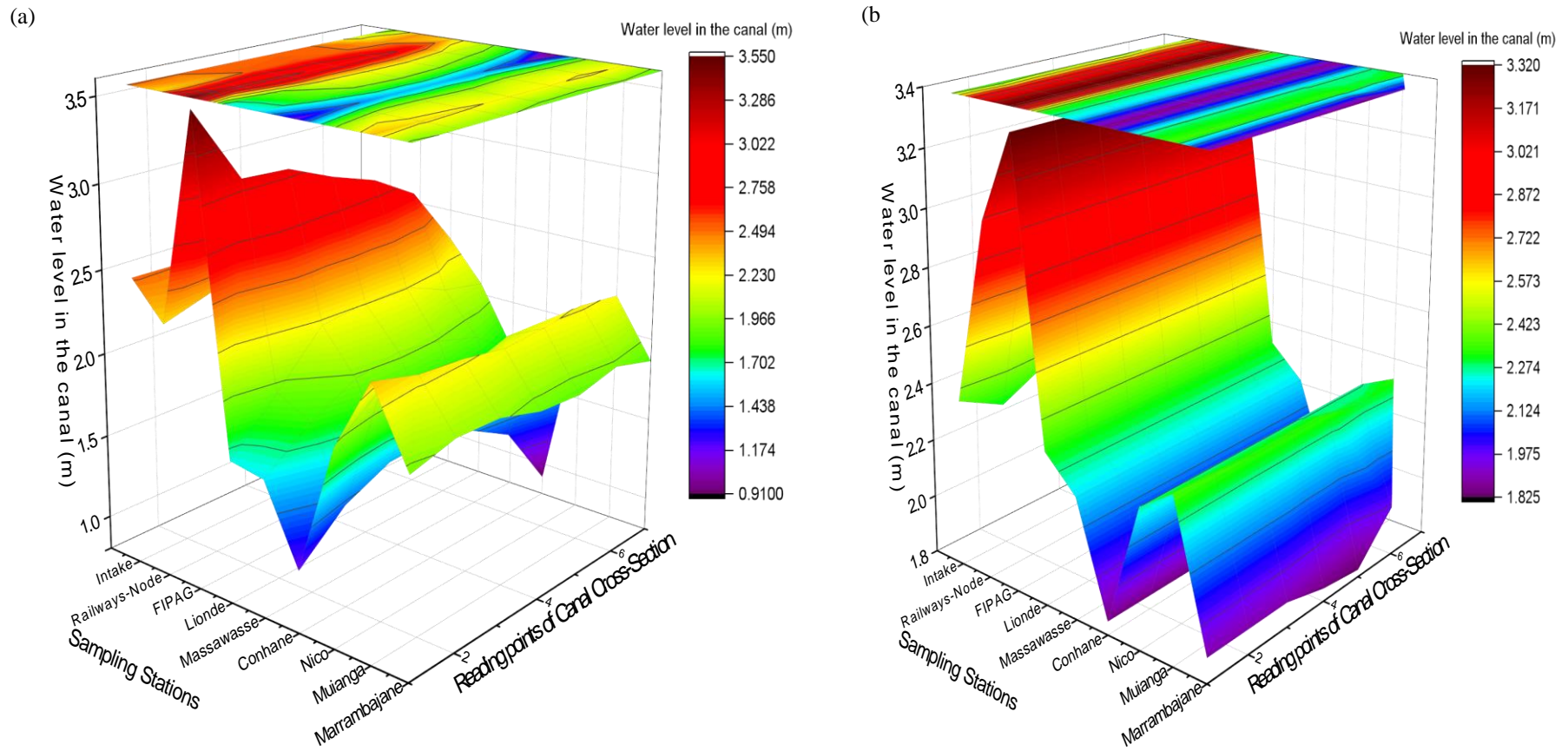


Figure 4. 23 (a & b): Average Water Depth at Sampling Stations for the DS and WS

Water Velocity

The changes in water velocity in the main CIS canal during DS is plotted against water depth, as shown in Figure 4.24.

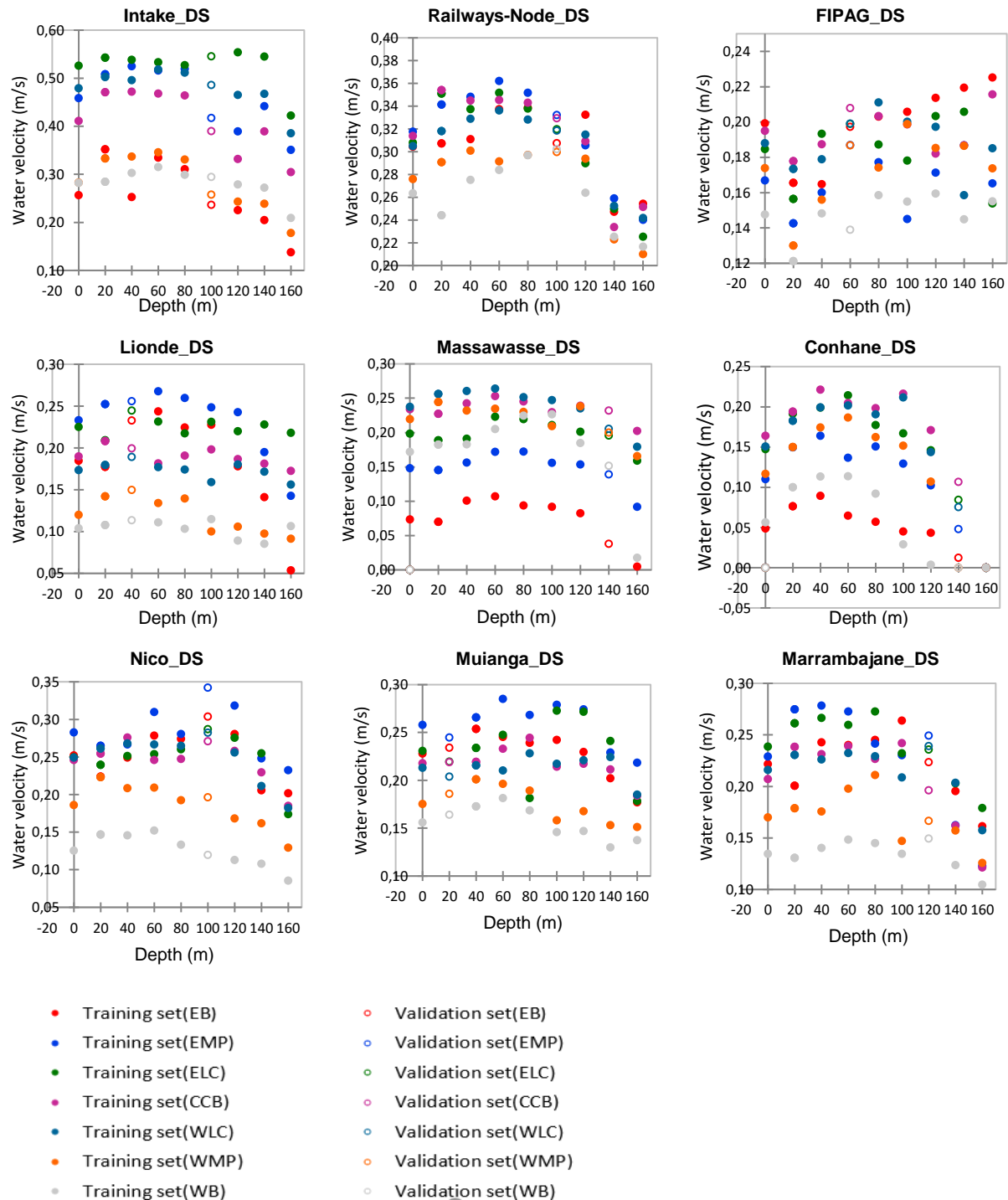


Figure 4. 24: Water Flow Velocity for Canal Cross-Sections at Sampling Stations During DS

In general, the whole CIS presented higher water velocity at the EB of the trapezoidal shaped canal, and this (high water velocity) continues towards the CCB and ends at the most WB side. Figures are presented in terms of water velocity and the respective percentage error. Percentage error equation is approximately presented in Equation 2.70, also referred to as PBIAS. In this work, PBIAS was used to indicate how far or close the theoretical values measured in the field work were. Intake station showed significant water velocity at the EMP and at the ELC, ranging from 0.40 ± 0.02 to 0.50 ± 0.03 m/s. Considerable high water velocity was also observed at the CCB and low velocity at the WB, with 0.35 ± 0.02 to 0.45 ± 0.02 m/s. Referring to Figure 2.1, shapes of velocity profile, it can be suggested that at the Intake station, water flow produces a form of turbulent flow with high velocity from water surface to the bottom. At the surface, the water velocity ranges from approximately 0.30 ± 0.02 to 0.60 ± 0.03 m/s, and at the bottom point which is at a depth of about 160 cm, it ranged from approximately 0.15 ± 0.01 to 0.40 ± 0.02 m/s. This makes this station less prone to sedimentation, as water velocity tends to transport the particles to further locations due to, relatively, high velocity (Fent et al., 2019; Quick et al., 2019; Rath & Swain, 2020; Sukhodolov, 2015; Terefe & Singh, 2020; Yokoyama et al., 2018; Zahidi et al., 2018).

The Railways-Node station has water velocity also directed from EB to WB of the canal cross-section, despite the fact that the CCB also has significant velocity. At the surface of water flowing through the canal, water velocity varied from approximately 0.25 ± 0.01 to 0.35 ± 0.02 m/s, while at the bottom; it ranged from between 0.22 ± 0.01 to 0.26 ± 0.01 m/s. The forms of the water velocity shape tend to be typical, allowing sediment particles to be carried towards the downstream points. This shape contrasts with the one found at FIPAG sampling station, whereby at the surface, water had a low velocity ranging from 0.12 ± 0.01 to 0.18 ± 0.01 m/s and at the bottom of the canal, water velocity was fairly high, ranging from 0.14 ± 0.01 to 0.22 ± 0.01 m/s, potentially allowing particles deposition at the bottom, even if the particles are rolled for some distances (Abhari et al., 2018; Rath & Swain, 2020; Sukhodolov, 2015). Moreover, at the Lionde site, similar patterns as observed in the Montante Sector were noted, whereby water velocity was higher at the EB of the canal cross-section and decreases as it reaches the extreme of the WB. Velocity varies from 0.1 ± 0.01 m/s to 0.25 ± 0.01 m/s at the surface and from 0.05 ± 0.003 m/s to 0.22 ± 0.01 m/s at the canal base, which is approximately 160 cm deep. Lionde velocity profile form is an approximate smooth

bottom with very low water velocity, which in turn, has potential to deposit sediment particles. Massawasse presented a different pattern from what was observed in Lionde. Here, the velocity tends to increase from WB to the EB of the canal, which is in the opposite direction compared to previous sites where the water velocity was very low. For example, at the water surface, it ranged from 0.06 ± 0.003 m/s to 0.25 ± 0.01 m/s and up to 0.2 ± 0.01 m/s at the canal bottom. Similar to the Lionde canal cross-section shape for water velocity, Massawasse had a smooth bottom with very low water velocity. The Conhane sampling station presents a very different pattern too. At this station, water velocity is higher at the CCB and decreases in both directions from the middle to the extreme, both to the EB and WB. Velocity ranges from 0.07 ± 0.004 m/s to 0.20 ± 0.01 m/s at the surface and to 0.1 ± 0.005 m/s at the bottom. This site presents a velocity shape of between very rough bottom and velocity profile above a hole downstream of the cross-section. For both cases, there is not too much risk of sedimentation at this site in DS as was found by Khan et al. (2018); Sanchez et al. (2020); Sun & Ma (2019); Yokoyama & Kitada (2019).

For the sampling stations located at the Rio Sector, Nico, Muianga and Marrambajane, the velocity decreases from EB to WB of the canal cross-section, despite their differences in shape of velocity profiles. An outstanding fact in this sector is that at the middle of the canal depths, between 80 and 120 cm, high water velocity was observed. Nico site has velocity varying from 0.15 ± 0.01 m/s to 0.26 ± 0.01 m/s for the surface and up to 0.23 ± 0.01 m/s at the bottom. For Muianga, the velocity ranges from 0.16 ± 0.01 m/s to 0.24 ± 0.01 m/s at the water surface to 0.14 ± 0.01 to 0.22 ± 0.01 at the bottom. In Marrambajane, at the surface, velocity varies from 0.13 ± 0.01 m/s to 0.28 ± 0.01 m/s, and from 0.1 ± 0.005 m/s to 0.16 ± 0.01 m/s at the bottom. Some studies corroborate with these findings (Sanchez et al., 2020; Sun & Ma, 2019; Yokoyama & Kitada, 2019).

During the WS, a slight difference was found from the DS. At the Intake station, for example, water velocity is high at the WMP, followed by the WLC and WB, with 0.65 ± 0.03 m/s, 0.55 ± 0.03 m/s and 0.54 ± 0.03 m/s, respectively. From CCB to the EB, water velocity orientation was from 0.56 ± 0.03 m/s to 0.45 ± 0.02 m/s, respectively. At the surface, water velocity was from approximately 0.45 ± 0.02 m/s to 0.65 ± 0.03 m/s and at the bottom of the canal it was from 0.40 ± 0.02 m/s to 0.60 ± 0.03 m/s. The sampling station has an approximated

shape of turbulent flow with high velocity, providing a very low potential for sediment deposition. However, at Railways-Node station, velocity tends to increase towards the right, ranging from 0.40 ± 0.02 m/s to 0.66 ± 0.03 m/s. A very small difference between the surface and the bottom velocity was observed and a smooth bottom with very low velocity form of the water velocity pattern, where potential for sedimentation does exist. In addition, for the FIPAG station, again the velocity increments were from the left to right, varying from 0.20 ± 0.01 m/s to more than 0.35 ± 0.02 m/s, at the same time that the surface water velocity drops from 0.35 ± 0.02 m/s to 0.20 ± 0.01 m/s. While at the bottom of the canal the velocity varies from 0.37 ± 0.02 m/s to 0.25 ± 0.01 m/s. This means that water velocity is somewhat influenced by canal depth (Afessa and Yosef, 2019; Vargas-Luna et al., 2019). Figure 4.25 shows the water flow velocity for canal cross-sections at sampling stations during WS.

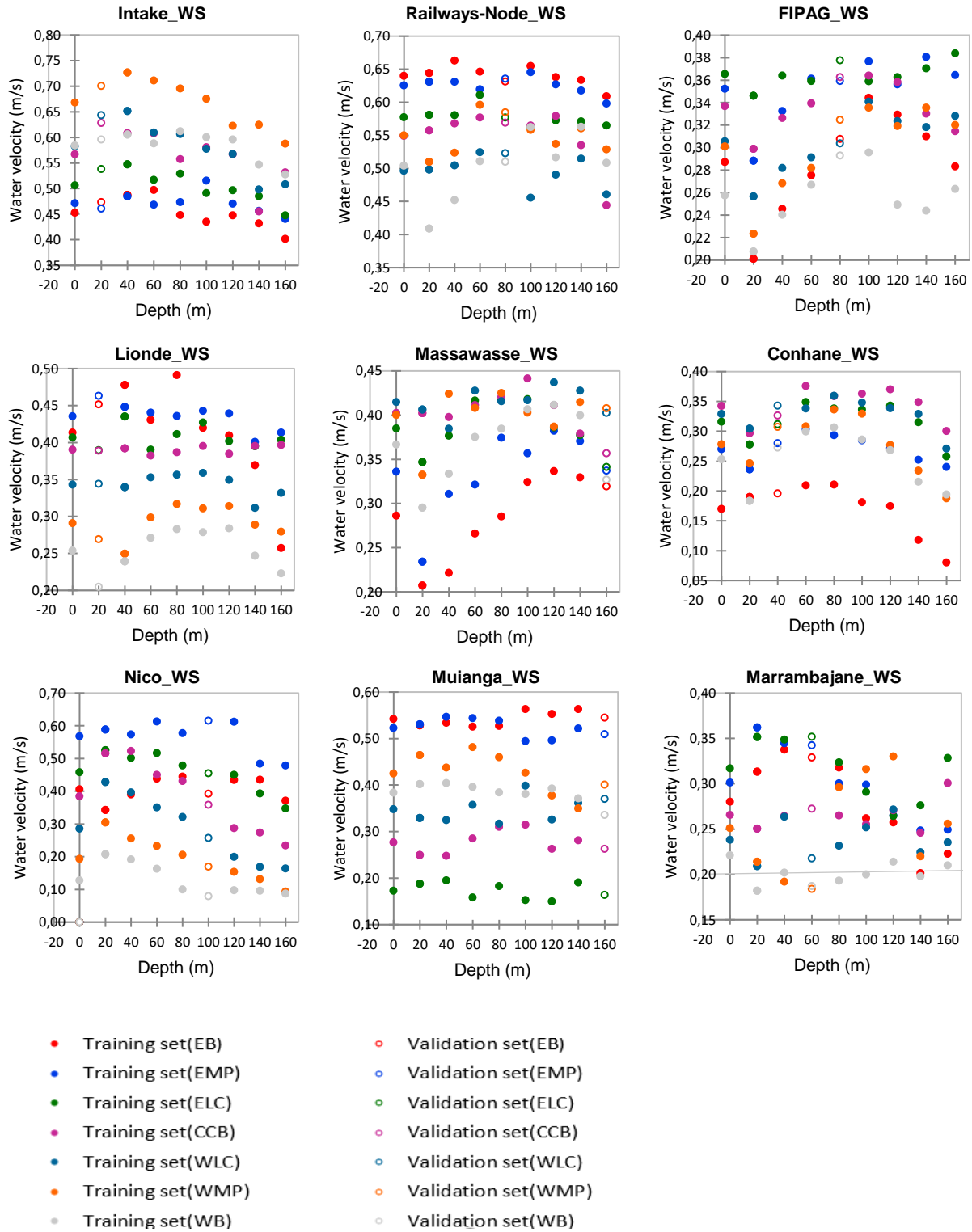


Figure 4. 25: Water Flow Velocity for Canal Cross-Sections at Sampling Stations During Wet Season

The Lionde sampling station presents water velocity from the EB to the right of the canal cross-section, varying from 0.20 ± 0.01 m/s to approximately 0.5 ± 0.03 m/s, with the surface and bottom having similarities on the values of velocities. The form shape of the velocity may imply stable velocity and therefore high risk of sedimentation. Massawasse station, in turn, has the velocity increasing from the WB to the EB of the canal. This may be due to the presence of vegetation on the surface of the water stream at the EB. Vegetation is known to reduce the rate of water flow by slowing down water flow downstream (Dearnaley et al., 1995; Ellison et al., 2010). Velocity was found to range between 0.20 ± 0.01 m/s and 0.42 ± 0.02 m/s. Being a WS, it would be expected to have higher velocity and less sedimentation at this station. However, the fact that water level was relatively high during this season, may have contributed to filling of the entire canal and therefore reducing the velocity and augmenting sedimentation risk. The Conhane station, on the other hand, presented fluctuation of velocities from the EB to the WB and vice-versa, with no clear orientation of water flow velocity. For example, at EB and WB the velocities were relatively low, while at the middle of canal cross-section, the velocities were high. This fluctuation may be due to the bottom profile which may contain holes and sand bumps (Afessa & Yosef, 2019; Vargas-Luna et al., 2019). Varying from 0.08 m/s to more than 0.35 ± 0.02 m/s, water flow velocity was relatively stable both at the surface and canal bottom.

At the Rio sector, specifically at Nico sampling station, water flow velocity tends to be higher at the EB of the canal and reduces at the WB, ranging from 0.10 ± 0.01 m/s to 0.60 ± 0.03 m/s. Similar pattern was observed at Muianga station, despite the centre of canal bed having a low velocity value. Lastly, Marrambajane station clearly presents a different velocity orientation where higher values were found on the EB and low values at the WB, between 0.15 ± 0.001 m/s and 0.37 ± 0.02 m/s. Comparing the upstream, midstream and the downstream sectors, it can be inferred that in all stations, water velocity decreases from the EB to the WB of the canal cross-section, except at Intake, Massawasse and Conhane sampling stations. Moreover, this allows for the prediction that sediment particles were more prone to deposit at the bottom of the canal on the WB, where there was low velocity.

Generally, water flow velocity across the Chókwè Irrigation Scheme tends to be high at the upstream and low at the downstream side, which is in agreement with the findings of other

authors (Afessa & Yosef, 2019; Sharif & Kabiri-Samani, 2018; Vargas-Luna et al., 2019). Velocity at Montante Sector is higher than at Sul and Rio sectors, respectively. Reading points at each sample station always started from the EB of canal to the WB, in an attempt to assess the water flow velocity at each cross-section point. For both DS and WS, water flow velocity tends to decrease as it moves towards the WB of canal cross-section, producing a potential to deposit more material at this side. As shown in Figure 4.26(a), during DS, the velocity falls significantly at Massawasse and Conhane sampling stations, with approximately 0.1 m/s, regaining speed at Rio sectors stations, with around 0.25 m/s. These outcomes were anticipated given the fact that water distribution in this scheme is gravity driven and flows under an accepted longitudinal slope towards downstream. Similar pattern is observed in the WS, as presented in Figure 4.26(b), despite changes in the water direction EB-WB orientation, and vice-versa. Higher velocities were observed at the EB than on the WB, varying from more than 0.60 m/s to 0.07 m/s. These findings are consistent with the findings from other similar studies (Afessa & Yosef, 2019; Vargas-Luna et al., 2019).

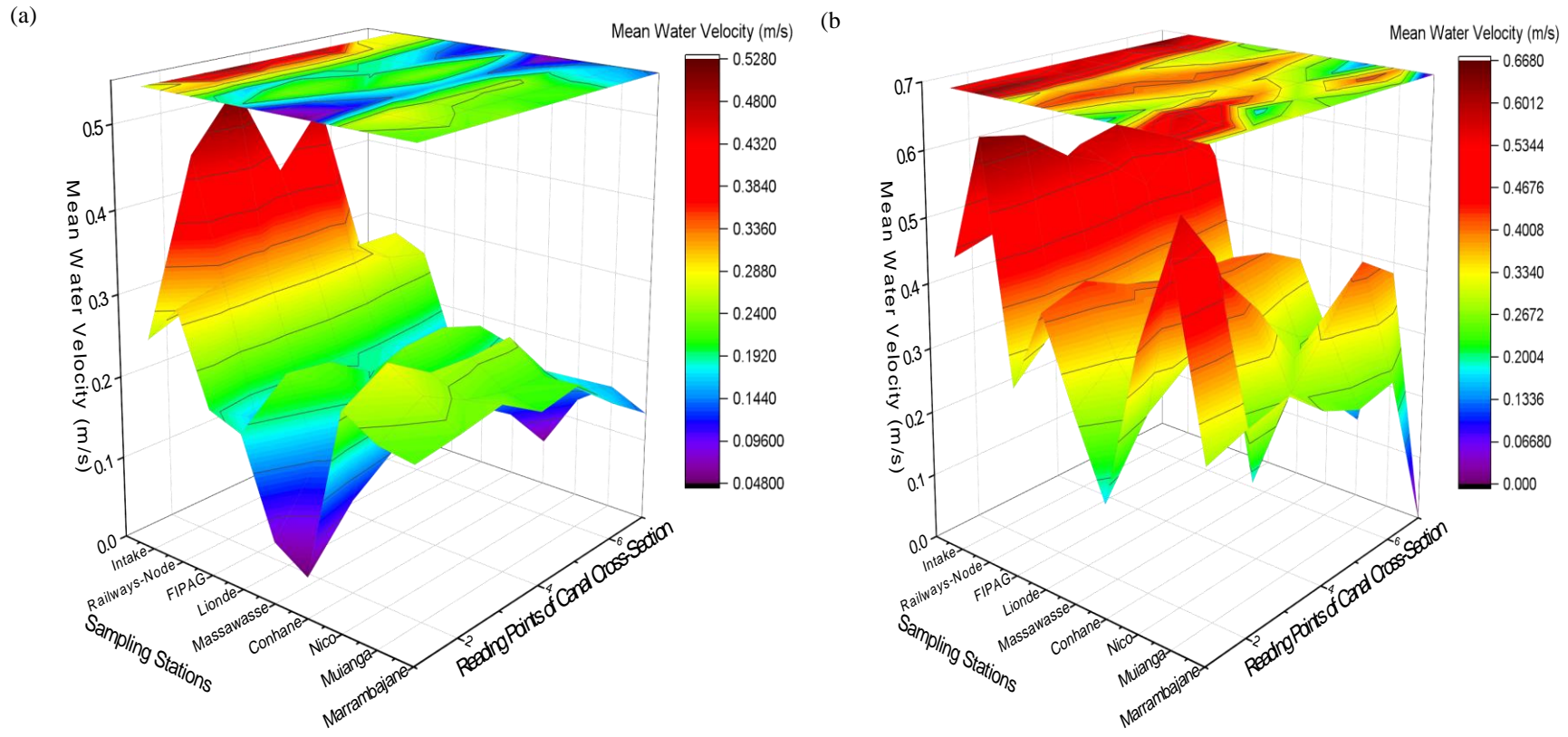


Figure 4. 26 (a & b): A 3D Representation of Water Flow Velocity at Cross-Section During DS and WS

Suspended Load Physical Characteristics

Suspended sediment concentration (SSC), given in mg/L or just ppm, at Intake station (in the Montante Sector) presented the highest SSC of above 3500 mg/L at 60 cm depth, during DS, while for the WS it falls sharply to merely 750 mg/L. This is unexpected situation, given that WS, being rainy season, would usually present high SSC, than DS. Study by Wu et al. (2004) suggest that wetter season are more prone to generate sediments than the drier. The lowest SSC was found at FIPAG bottom, with less than 250 mg/L, for DS, and at Railways-Node station for WS, with slightly above 200 mg/L. For this sector, during DS, Intake and FIPAG stations had considerable SSC at a depth interval of 20-100 cm. At Railways-Node station, attention was given to the 20-80 cm depths, whereby more than 400 mg/L were registered. The remaining depths had very small SSC below 400 mg/L. Water surface in the canal also presented very low SSC for the whole sector. Meanwhile, WS offered considerable SSC for all the water depths in all the three sampling stations at Montante.

In general, SSC behaved differently with season for water depth. During dry season SSC tend to decrease with water depth, exception was found for Massawasse station. This means that, as water depth increases, the amount of sediment reduces. Opposite scenario is observed during wet season, when the sediment concentration increased as water depth increased, except for Railways-Node and Lionde stations. This may be a result of wet season water inflow be loaded with sediments, under circumstances of high rates. Figure 4.27 presents SSC as function of water depths for all the three sectors, namely Montante, Sul and Rio, for both DS and WS.

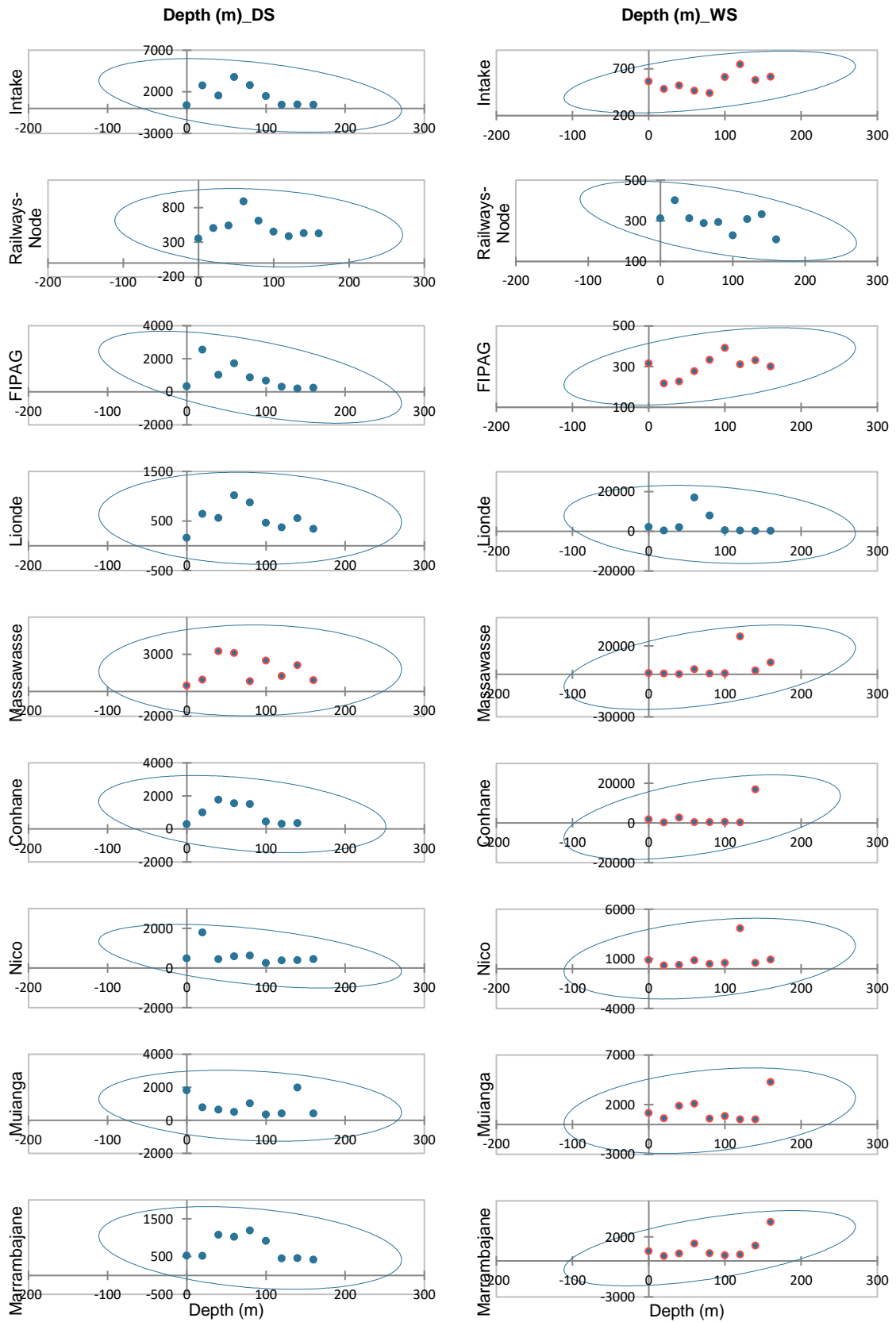


Figure 4. 27: Mean SSC as Function of Water Depths During DS and WS

In the Sul Sector, Massawasse station had the highest SSC recorded at 40 cm deep, with more than 3000 mg/L and more than 2500 mg/L, for DS and WS, respectively. The lowest concentration was found at Lionde water surface and at 140 cm deep, with less than 300 mg/L, during both seasons, respectively. Within all water depths studied, some presented very small SSC values than others. In Lionde, reasonable amount of SSC was found at 20-80 cm and 60-80 cm depths, for both seasons, DS and WS, respectively. While for Massawasse, consideration was given to all the depths of the sampling station and 60, 120 and 160 cm, respectively, on DS and WS. In Conhane, instead, only 20-80 cm provided reasonable amount of SSC, in DS, against just one depth point of 140 cm, on the WS. Other depth points had very small amounts of SSC. For Rio Sector, though, Muianga station was the highest SSC with approximately 2000 mg/L at 140 cm deep, during DS and, approximately 4300 mg/L at 160 cm, during WS. And the lowest was Nico with approximately 250 mg/L at 100 cm, and less than 400 mg/L at 20 and 40 cm, during WS. All the depths were considerable in this sector, whereby SSC had more than 400 mg/L, for both seasons. These findings were also observed in previous studies by Lu (2013) and Yu (2017), where wet and rainy season generated more SSC than drier season.

WS is by far the most loaded with SSC in the water stream. These findings were also observed in previous studies by Lu (2013) and Yu (2017), where WS and rainy period provided much greater amount of SSC in China. During DS, sampling stations of Intake, Massawasse, Muianga and Marrambajane, appeared heavily loaded with suspended sediments than others, in some weeks. On the other hand, during WS, Massawasse, Lionde, Conhane and Muianga were well much loaded. This fact sheds light on sedimentation occurring differently according to space and time. Neither the sampling stations nor the sampling weeks, showed uniformity in SSC. This can be due to canal design, canal shape, canal length, canal depth, canal meanders, water turbidity, inflow, and outflow, as well as, sampling collection season and time itself. In general, SSC varied in pattern for each sampling stations and seasons, with sampling weeks. During DS, Intake, Lionde, Massawasse, Muianga and Marrambajane stations presented SSC increase as sampling weeks added. This means that as time went on, the amount of sediment accumulated in the canal. During WS, this same pattern was observed for Intake, Railways-Node, Conhane and Marrambajane

stations. This suggest that the SSC is high at the intake of the scheme and at it's most downstream part, at Marrambajane, for both seasons, as presented Figure 4.28.

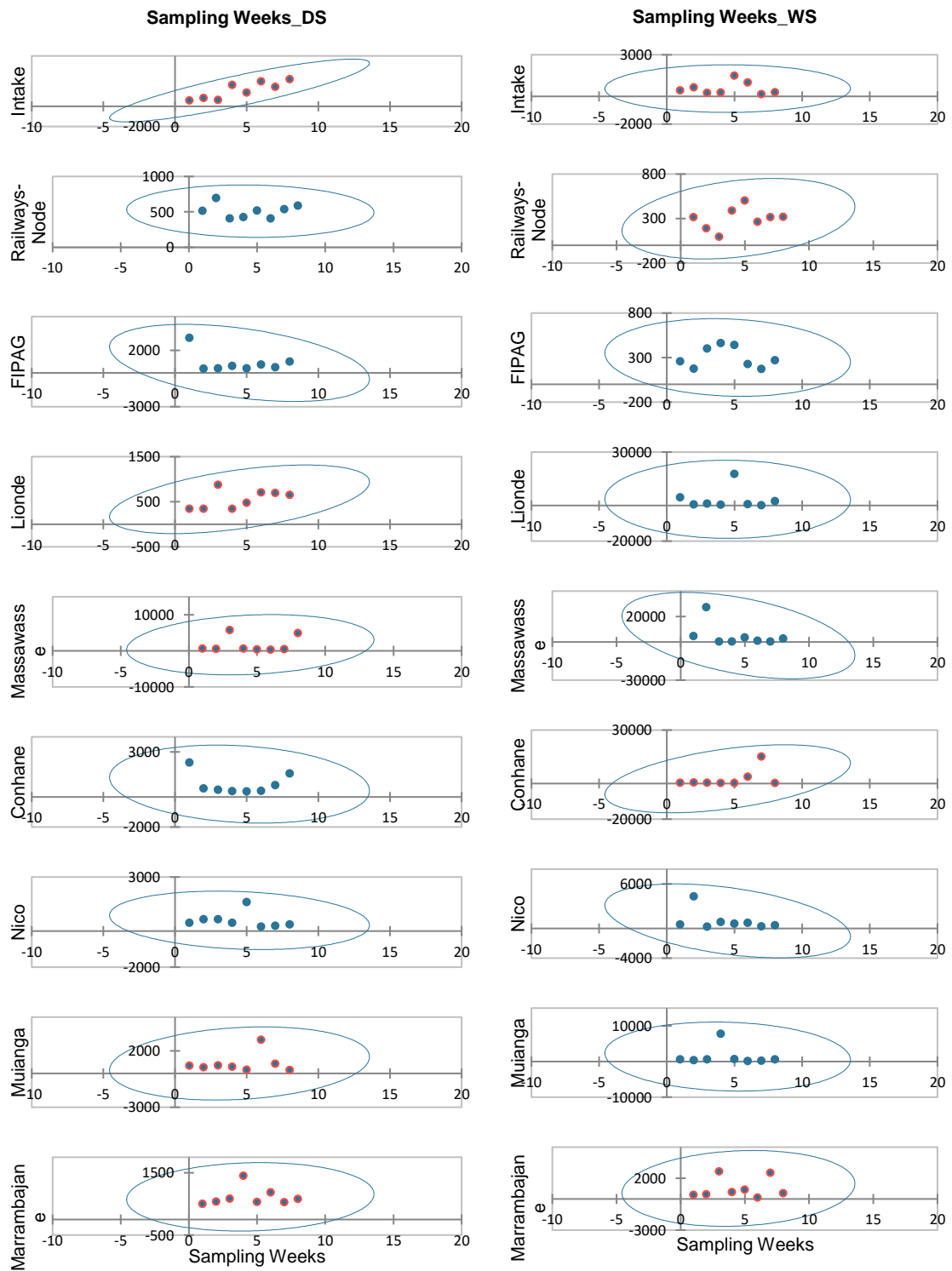


Figure 4. 28: Mean SSC as Function of Sampling Weeks During DS and WS

The relationship between water turbidity and the SSC was very weak for both seasons, as shown in Figure 4.29 (a & b), whereby just nearly 14% of coefficient of determination was found. This means that 14% of variance in turbidity was due to SSC in water. There was no evidence to affirm that water turbidity was due to SSC occurrence in the canal. Similar analysis was performed to assess the regression fit of turbidity and water discharge, as shown in Figure 4.29 (c & d). DS showed very weak relationship for both variables, with coefficient determination of 29.2%, whilst WS with 72.4%. This indicated a positive relationship between turbidity and water discharge. This is to infer that turbidity can be explained by water discharge.

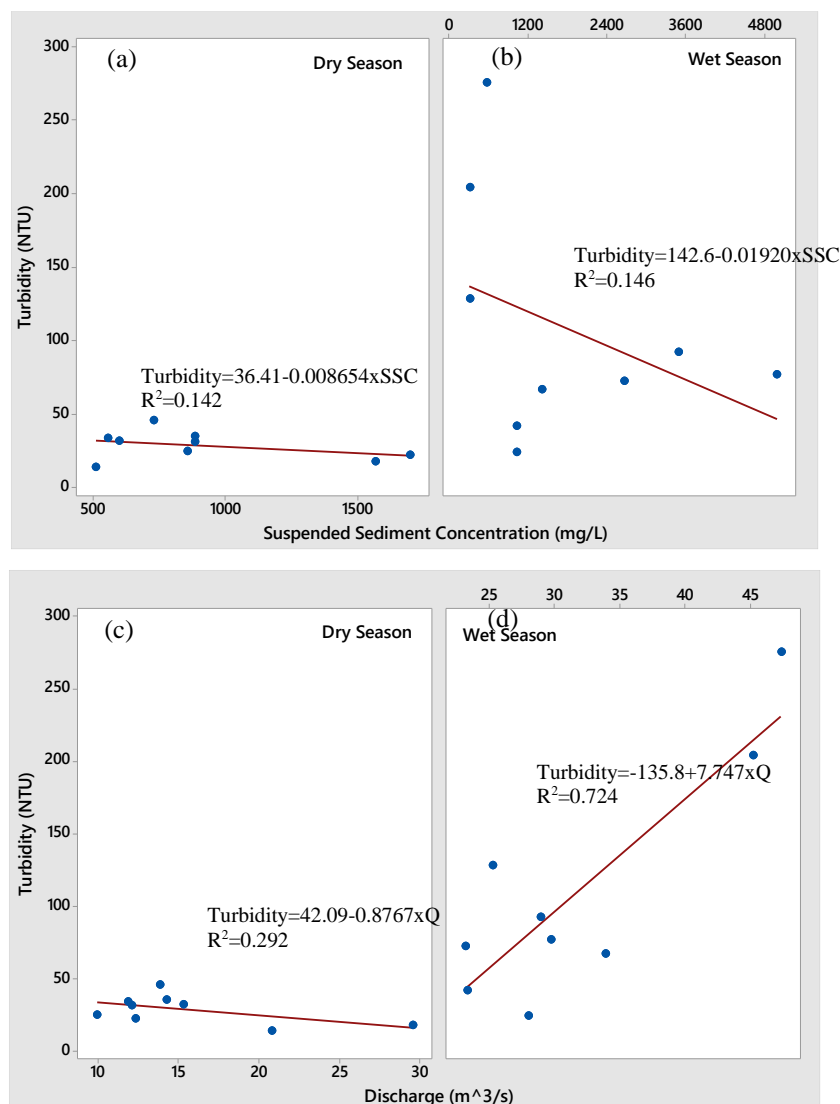


Figure 4. 29: Water Turbidity as Function of the Suspended Sediment and Water Turbidity as Function of the Water Discharge

Turbidity

Water turbidity for samples containing suspended sediments is presented in Figure 4.30, whereby DS had its maximum turbidity below 50 NTU (Nephelometric Turbidity Units) and in WS maximum turbidity reached 250 NTU.

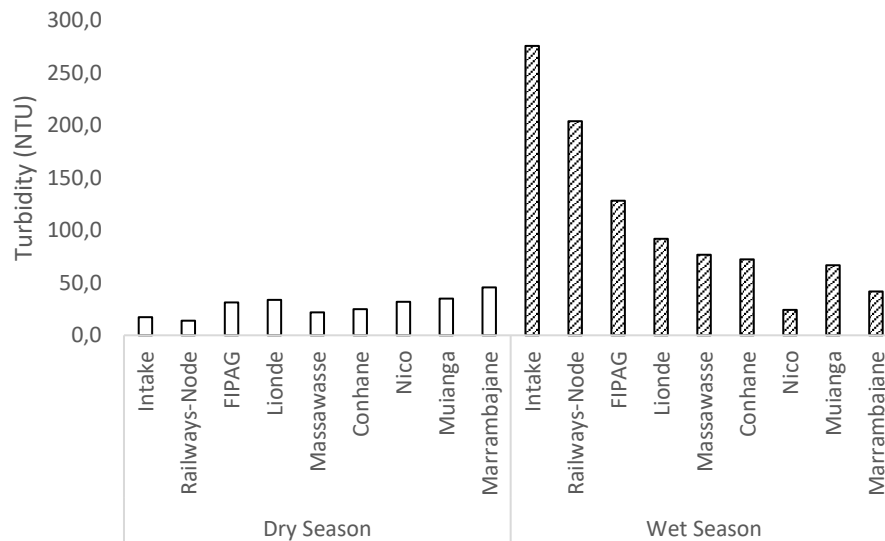


Figure 4. 30: Average Values for Water Turbidity Sampling Stations in Both Seasons at CIS

The highest turbidity during DS was found at Marrambajane, followed by Muianga and Lionde stations, with 45.7, 35 and 33.9 NTUs respectively. The lowest was found at Railways-Node, followed by Intake, with 13.9 and 17.4 NTUs respectively. Turbidity is known to make water to appear cloudy or opaque. These results infer that during periods of low flow, with predominance of base flow, the water in the canal appears to be very clear, and turbidity is less than 50 NTU. These findings are consistent with the USGS (2015) who analysed turbidity of Colorado River in Arizona (USA), whereby they recorded turbidity of less than 10 NTU. The slight difference in turbidity values of two sites may be due to the inflow entering the scheme from the Intake which causes water moving toward downstream, stirring it up and increasing the turbidity. During WS, however, as result of rainstorm, particles from the surrounding land are washed into the canal stream making the water to have a muddy brown colour, indicating higher turbidity values. Also, according to Abhari et al. (2018); and Soemitro et al. (2020), during high flows, water velocities are faster and water volumes are higher, which can more easily stir up and suspend sediments from the stream bed, causing higher turbidity.

Turbidity increased with water depth at Intake and Railways-Node, during dry and wet seasons, respectively, in the upstream of the scheme, whilst, same pattern was observed at Muianga and Marrambajane stations, in both seasons. In the remaining stations, turbidity decreased with water depth. Turbidity as function of water depth at each sampling station is presented in Figure 4.31, whereby DS presents turbidity between 10 and 50 NTU, with exception for 140 and 160 cm of depth in Marrambajane, which achieved 83 and 74.3 NTU, respectively. Lionde had the highest turbidity, for the first three depths (surface, 20 and 40 cm), followed by Marrambajane station with the highest thence to the bottom, from 40 to more than 80 NTU. Intake, Railway-Node, Massawasse and Conhane presented lowest turbidity values ranging between 10 and 30 NTU, respectively. These four stations appeared to have stable turbidity values across the entire water depth, from surface to the canal bottom. WS had stable turbidity between water surface and canal bottom. Intake and Railways-Node presented highest turbidity than others, recording 285 and 200 NTU, against 23 and 133 NTU, recorded in the other stations.

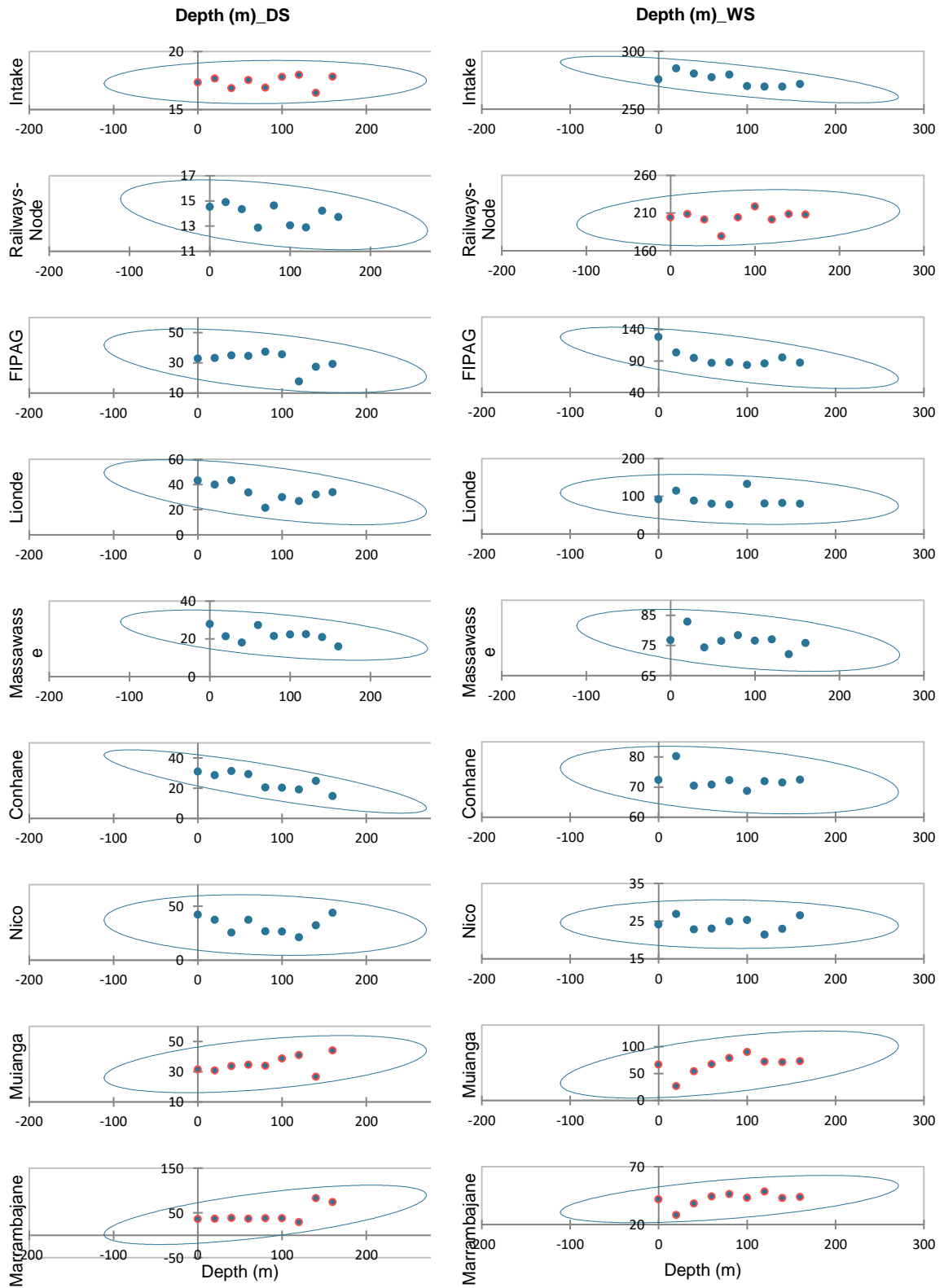


Figure 4. 31: Turbidity as Function of Water Depth for DS and WS

In WS, the fifth and sixth weeks presented highest turbidity rate, varying from 471 to 1000 NTU. The highest turbidity recorded was 1000 NTU and this was observed within these two weeks, when the region had heavy rainfall for more than 3 consecutive days. In general, turbidity had decreased trend during dry season, for the Montante and Sul sectors, whilst for Rio sector the opposite trend was found. Rivo sector is located at downstream, and this may explain why even during dry season, sediment accumulated most in this part of the CIS. On the other hand, wet season turbidity increased with sampling weeks. This means that, as the samplings went on, the level of turbidity increased. This is result of the sediment influx that took place during wet season with rain occurring in this season and runoff generated at upstream Limpopo river, in the neighboring countries, becoming so significant. Turbidity as a function of sampling dates for each sampling station during DS and WS is presented in Figure 4.32, with maximum of 250 and 1000 NTU, respectively for the two seasons.

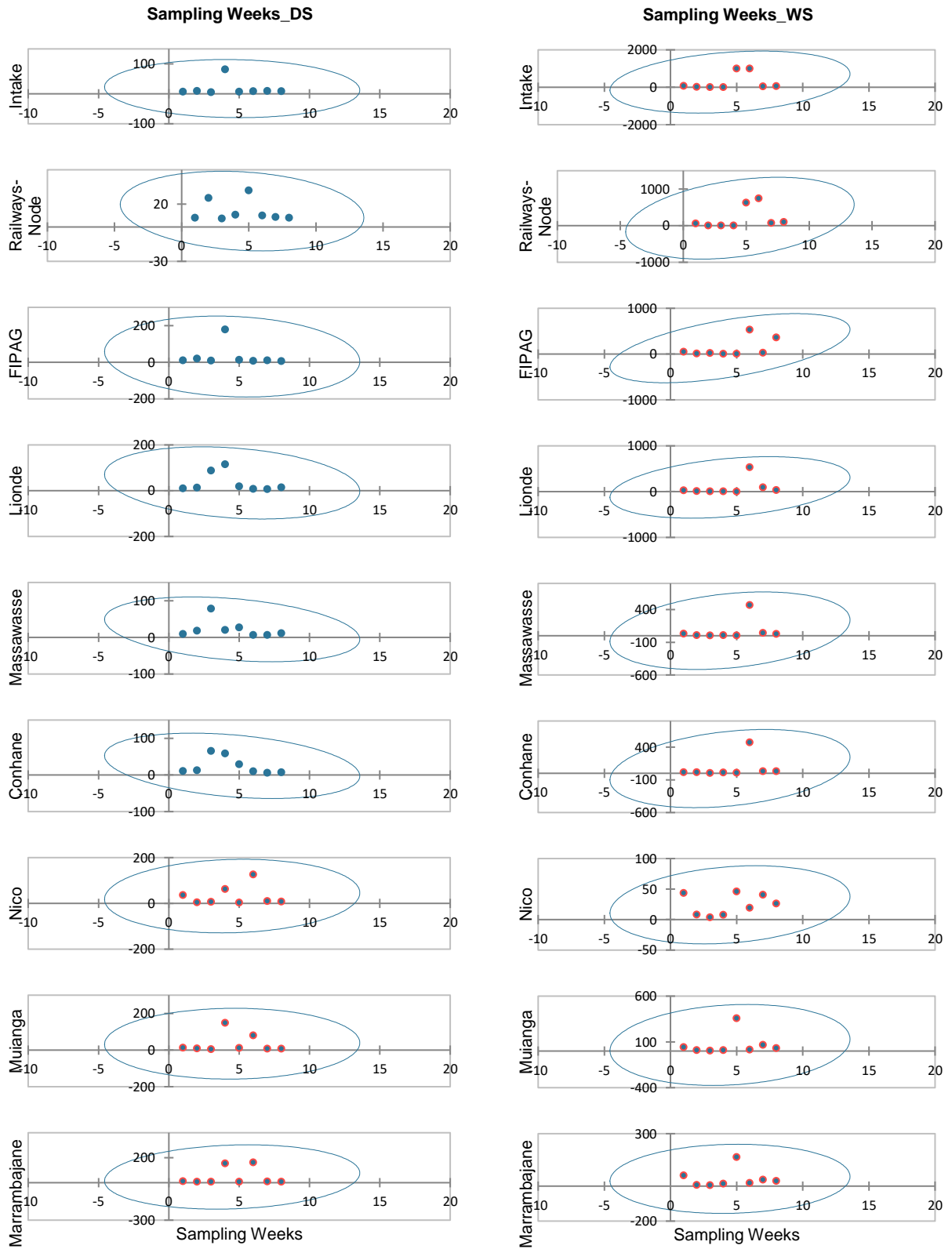


Figure 4. 32: Turbidity as Function of Sampling Dates for DS and WS

From Figure 4.32, it can be seen that turbidity as a function of sampling dates elucidates an increasing trend from the upstream at Intake to the downstream at Marrambajane, although in some sampling points and dates high turbidity rates were observed. From approximately 5 NTU at Intake to more than 160 NTU at Marrambajane. These sampling stations include Lionde, Massawasse and Conhane in 26th June, Intake, FIPAG, Lionde, Conhane, Nico, Muianga and Marrambajane on the 3rd July, Nico, Muianga and Marrambajane on the 25th February. Contrasting trend was observed for the WS, whereby high turbidity was observed at the upstream and it decreases towards the downstream. For example, from 1000 NTU at Intake turbidity falls sharply to around 20 NTU. These findings are consistent with authors advocating that turbidity tends to increase from upstream to downstream in accordance with flow direction (Léziart et al., 2019; Oke et al., 2019), which is verified in this work during DS. This is true as water motion creates energy that detaches soil particles responsible for reduction in water clarity because of the presence of suspended matter absorbing or scattering downwelling light (Adams et al., 2014; Faustino et al., 2019; Rahman et al., 2010; Yuan et al., 2013). On the other hand, during WS turbidity is relatively high due to increased water flow resulting from runoff and rainfall. Therefore, the behaviour becomes different from what takes place in DS.

Potential for Hydrogen (pH)

The potential for hydrogen (pH) for water samples containing suspended sediments showed DS as having higher pH than during WS, varying between 8.5 and 8.6 and from 7.6 to 7.9, respectively. pH is an indicator of the acidity or basicity of water, but is seldom a problem by itself. The main use of pH in water analysis is for detecting abnormality in water depending on the intended use of the water. The normal pH range for irrigation water is from 6.5 to 8.4 (Bauder et al., 2014; FAO, 2014; Flynn, 2009). An abnormal value is a warning that the water needs further evaluation. Irrigation water with a pH outside the normal range may cause a nutritional imbalance or may contain a toxic ion. Results show normal pH values during WS, despite abnormal pH reported in DS, with 7.8 and 8.5, respectively. Difference in pH for DS and WS is caused by the presence of high amount of free carbonates present in surrounding soils, which indicates alkalinity in water and sediment which are reported to form under dry climatic conditions (El-Amier et al., 2015; Sofi et al., 2018). During DS Nico sampling station had the highest pH value and FIPAG the lowest, of 8.6 and 8.5, respectively.

On the other hand, WS maximum pH value was found at Intake station and the lowest at Conhane, with 7.9 to 7.6, respectively. In general terms, the average pH of the CIS was found to be alkaline for water and sediments (Qiao et al., 2016). The slight decrease in pH values during WS can also be linked to the pollutants entering the scheme when rain water increases considerably at the upstream (El-Amier et al., 2015; Golui et al., 2019). Details related to pH are provided in Figure 4.33.

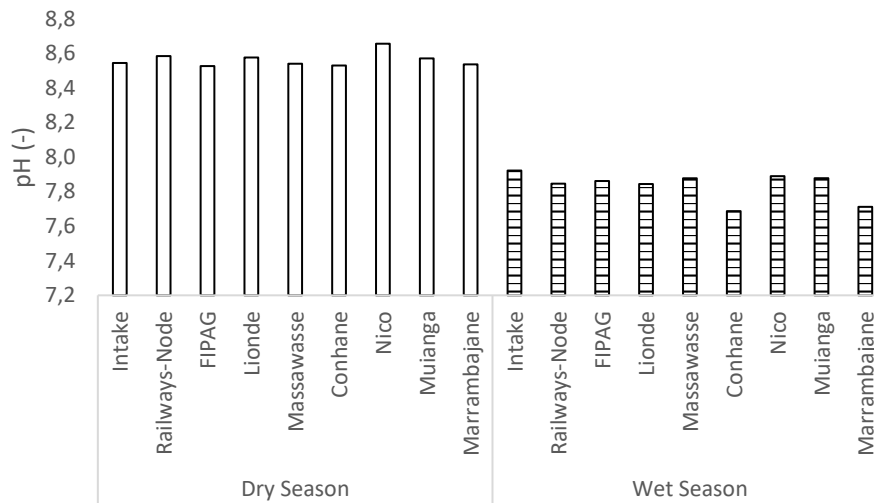


Figure 4. 33: Average Values for Water pH at Each Sampling Stations in Both Seasons at CIS

The pH of a waterbody reflects its water inputs and the chemical characteristics of surrounding land. The pH of runoff from the land, or of groundwater inputs to surface water, depends on the minerals and soils in contact with the water as it moves through the land. Water draining from forests and swamps may be acidic, having dissolved weak organic acids from the organic matter there, whereas water moving through limestone deposits may be slightly alkaline. During DS the pH showed considerable variation from the water surface to the canal bottom. In general, water pH shown steadfast augment with water depth in both seasons, for all sampling stations, except for Lionde and Nico during wet season. Figure 4.34. can be seen the variation of water pH with water depths in the nine sampling stations.

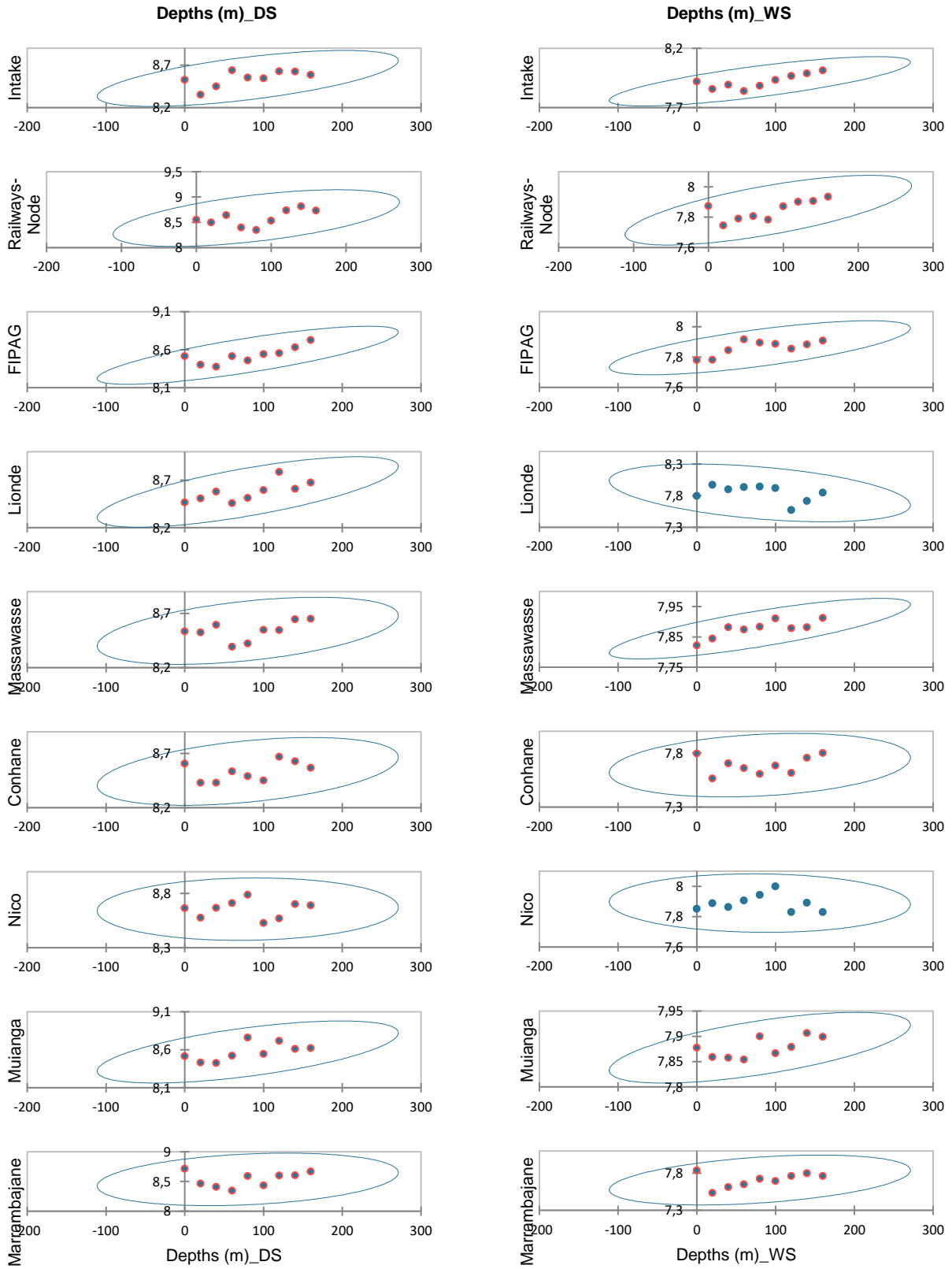


Figure 4. 34: pH Variation With Water Depths for DS and WS

The highest pH at the surface was found in Marrambajane, while the highest pH for the mid-depth at 80 cm was found at Nico station. The highest pH at the canal bottom was observed in Railways-Node station, with 8.72, 8.78 and 8.8, respectively. This is owed to the fact that points with relatively considerable presence of organic matter tend to have high pH, which was the case at Rio (Oss & Giese, 2005). The presence of organic matter stimulates the release of chemical elements which influences pH (Riaza et al., 2015). The lowest pH values were recorded at Lionde, Railways-Node and Conhane, for the surface, mid-depth and bottom, respectively, with 8.45, 8.35 and 8.55. The variation in pH was very small, varying between 8.3 and 8.8. During WS, a relatively low pH was recorded than in the DS, which is owed to the fact that organic waste material is commonly fluxed into the water body during this period of WS. Different types of minerals also have high concentration during the WS than DS. This could be explained by the fact that considerable amount of runoff get into the scheme during the WS, carrying sediment particles into Limpopo River Basin, even from neighbouring countries located upstream (Akinyemi et al., 2015; Asadi et al., 2011; Kawai *et al.*, 2003; Léziart et al., 2019; Manassis & Constantinos, 2003). Intake and FIPAG stations presented the highest and the lowest pH values at water surface, 7.92 and 7.79, respectively. At 80 cm mid-depth of canal, the highest and the lowest pH values were recorded at Nico and Conhane, with 7.94 and 7.61, respectively. And at canal bottom, highest pH was recorded at Intake and the lowest at Marrambajane, with 8.0 and 7.76, respectively. Here, in WS, from the water surface to the bottom, pH varies less. According to Oss and Giese (2005) and Oke et al. (2019), temperature and pH of water have an inverse relationship. DS has low temperature and WS higher, it is expectable that as temperature increases, the pH level decreases and vice-versa. Therefore the hotter it gets, the more acidic the water will be. On the other hand, pH decreased with sampling weeks, for both seasons in all stations, except for Intake, Massawasse, Conhane, Nico and Muianga during dry season. This means that as time went on, during sampling weeks, water pH decreased. In other words, wet season is hotter than dry, and therefore, pH decreased with temperature, which in turn depend on the season of the year. Figure 4.35 shows the observed pH variation with sampling dates during data collection at CIS.

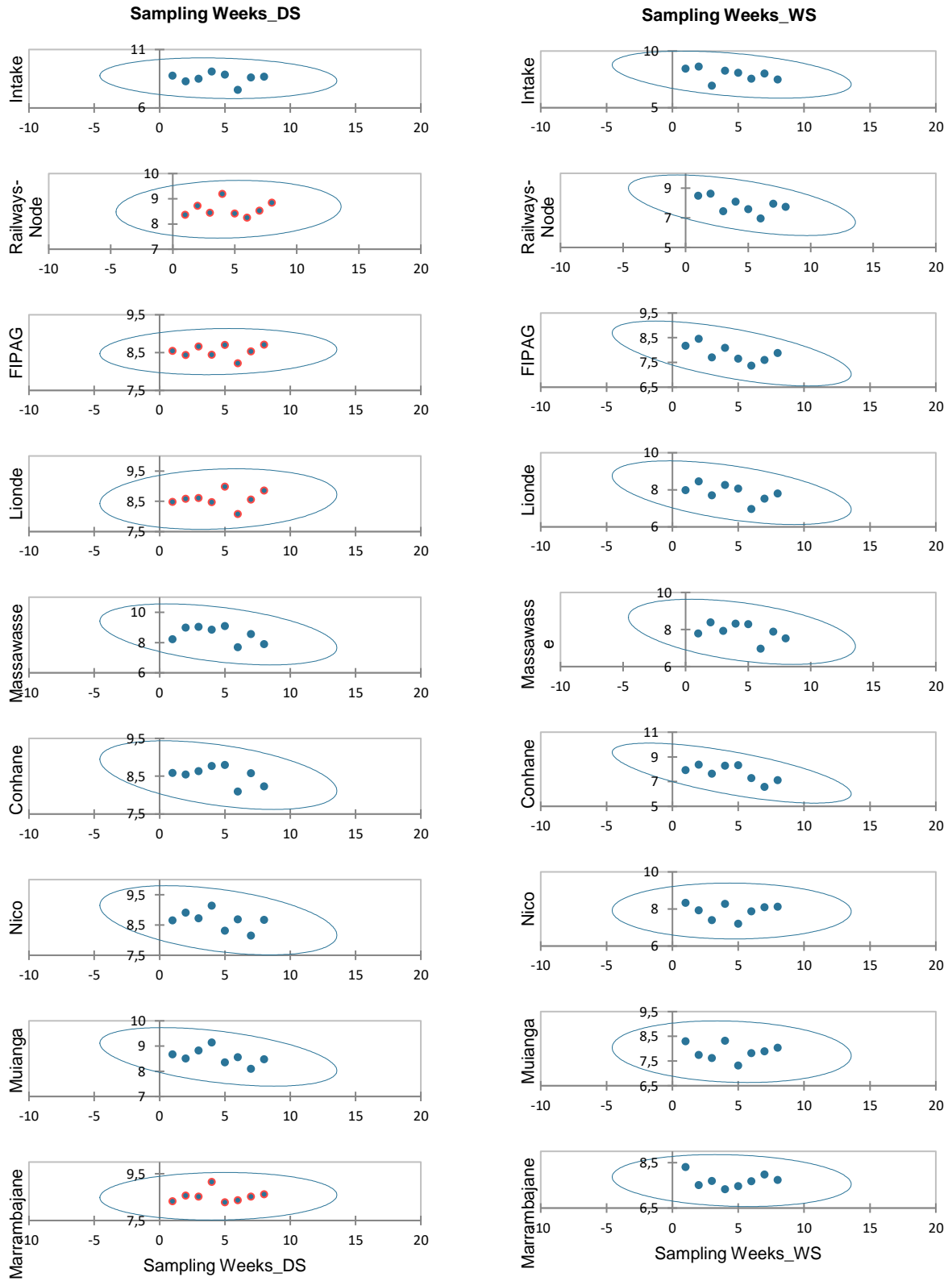


Figure 4. 35: pH Variation With Sampling Weeks n for DS and WS

During the DS, pH decreased slightly and considerable variation was found from the first week to the last one. The highest pH was found at the third week and the lowest at the sixth week. On the other hand, during the WS, the highest pH was observed at the second week and the lowest at seventh week. Overall, the pH maintained a stable state of about 8.5 and 8.0, for both DS and WS, respectively. The fact that the WS in that particular year of sampling, was too dry and with very low rainfall may have contributed for the slight variation in pH. The trend would indicate that at WS pH is significantly lower than during the DS.

Temperature

Water temperature for the samples containing suspended sediments was found to be, on average, 21°C and 26°C for DS and WS, respectively. Water temperature in CIS appears to be suitable for local aquatic fauna, including Nile tilapia, both in DS and WS. Furthermore, water density and stratification, can also depend on temperature. Water is most dense at 4°C. Differences in water temperature, and hence density, between layers of water lead to stratification and seasonal turnover in water streams. Fortunately, in the CIS this fact was not the case. Water appeared to have temperature normally and evenly distributed with depths as seen in Figure 4.36. Temperature of water also provides environmental cues for life-history stages, whereby, for example, changes in water temperature may act as a signal for aquatic insects to emerge or for fish to spawn. This can be true enough for the CIS main canal, where Nile tilapia and catfish (*Clarias gariepinus*) are common.

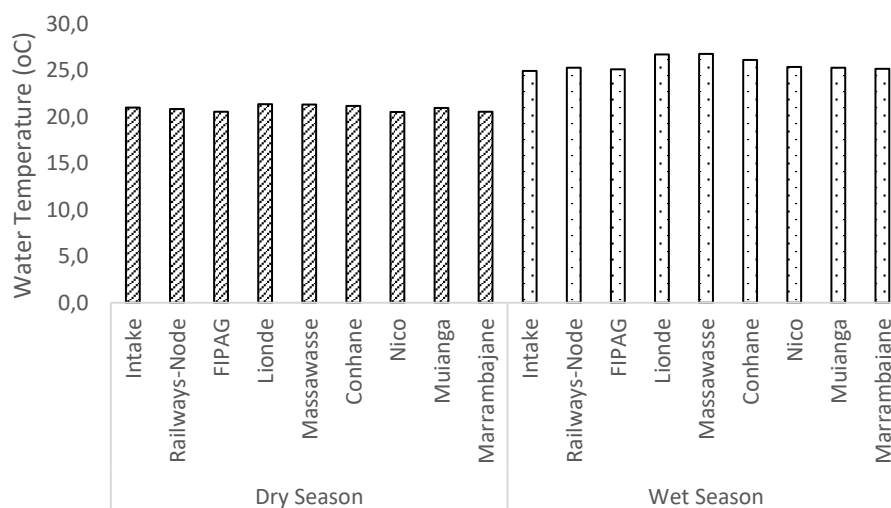


Figure 4. 36: Average Water Temperature at Sampling Stations for DS and WS

The most important source of heat for fresh water is the sun, although temperature can also be affected by the temperature of water inputs, such as precipitation, surface runoff, groundwater, and water from upstream tributaries (Khan et al., 2019; Robertson et al., 2018; Zhang et al., 2018). Heat exchanges with the air, and heat lost or gained by evaporation or condensation are other sources for water temperature rise or fall (Guo et al., 2019; Kim et al., 2018; Tharkar & Mahulikar, 2019). Water temperature fluctuates between day and night and over longer time periods. Water temperature varies along the length of a river with latitude and elevation, but can also vary between small sections only metres apart, depending on local conditions. For example, a deep, shaded pool is cooler than a shallow, sunny area. Study works by Haddout et al. (2018); Kim et al. (2018); Zhang et al. (2018) found that in lakes, temperature can vary with depth, according to mixing characteristics and the depth to which sunlight penetrates. Surface water is usually between 0°C and 30°C, although hot springs may exceed 40°C. The water temperature in DS appeared to have very small amplitude scale of variation, for minimum and maximum observed temperatures, from 20 to 21°C. Furthermore, comparison of temperature from the surface to the canal bottom, at each sampling station, temperature varies with similar small scale. For example, for Intake, temperature in the surface was 21.1°C, but at the bottom was 20.9°C. WS presented temperature higher than DS, varying from 24.5 to 27°C. Moreover, water temperature increased with water depth in all stations and seasons, except at Intake and Conhane, during dry season, and FIPAG, Lionde and Massawasse, during wet season. This means that as one descend to the canal bottom, water temperature does increase. Figure 4.37 offer detailed variation of temperature as function of water depths for DS and WS.

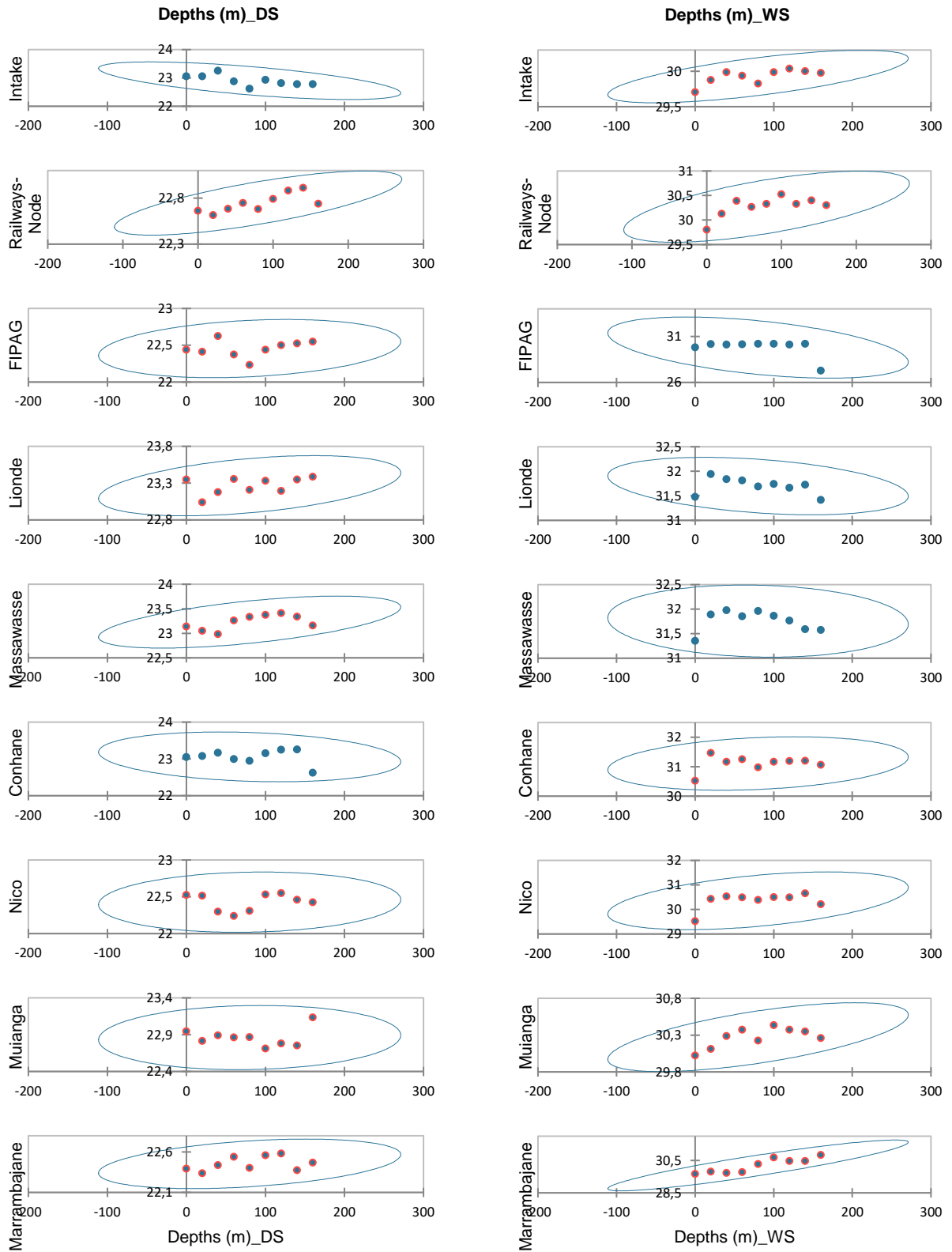


Figure 4. 37: Water Temperature as Function of Water Depths During for DS and WS

Water temperature varied with time, whereby during DS it was found to be between 17 and 25°C, in the whole sampling period. The highest water temperature was found in the last week at 31st July, 2018 and the lowest at the second last week, 18th July, 2018, respectively. June and July were the coolest months in Chókwè, therefore these findings are consistent with findings by Julaia (2009) and Munguange et al. (2013). Air temperature influences the water temperature, which also is affected by the depth of the canal. Therefore, in DS, water appears to be uniformly patterned, from Intake to Marrambajane, despite slight variation being observed. In the WS water temperature shown considerable variation across the entire irrigation scheme, reaching between 22 and 30°C. This is significantly high and under these conditions water was warmer than expected, although this fact has been observed in each week. In general, water temperature increased with sampling weeks during dry season, and decreased during wet season, except at Massawasse and Conhane stations. Differences of pattern for both seasons may be due to the fact that DS is tendentially cold in the region and WS is warmer. Therefore, colder seasons are normally steady than warmer ones, when atmospheric fluctuations take place more often. This is consistent with findings related to climate variation and influence on coffee production and sedimentation in Brazil, Portugal and Canada by Camargo (2010); Costa et al. (2018); and Vincent et al. (2018) who observed in that cold periods presented less variability in temperature, when compared to warmer seasons. Figure 4.38 presents the water temperature as function of sampling dates for both seasons.

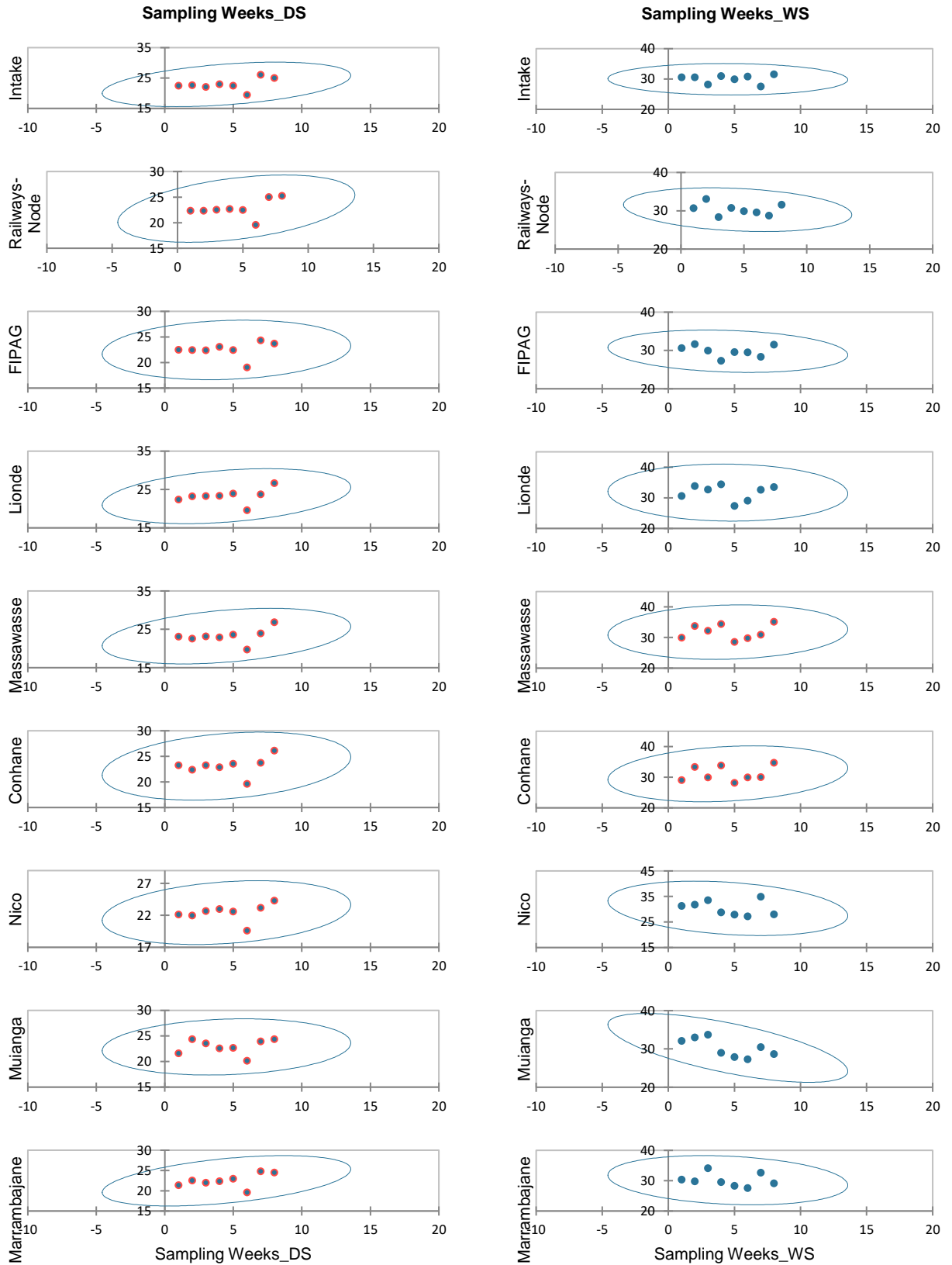


Figure 4. 38: Water Temperature as Function of Sampling Weeks for DS and WS

Total Dissolved Solids and Electrical Conductivity

TDS includes solutes such as sodium, calcium, magnesium, bicarbonate, chloride and others that remain as a solid residue after evaporation of water from the sample. Fresh water usually has TDS levels less than 1 000 mg/L (or ppm), depending on the geology of the region, climate and weathering, and other geographical features that affect sources of dissolved material and its transport and deposition into water bodies. The TDS varied from 250 to 300 ppm, approximately, except at the depth of 160 cm, where scarcely was above 100 ppm, in Marrambajane. The TDS behaviour in relation to water depth seems to be very variable and with no consistent pattern (Jukić & Denić-Jukić, 2004, 2008). For DS, there is decreasing trend for Railways-Node, FIPAG, Lionde and Nico, whilst for WS, decreasing trend occurred at Intake, Lionde, Massawasse and Marrambajane. The remaining stations presented increasing trends of TDS with water depth in the canal. Figure 4.39, shows TDS plotted against water depths sampling points, during the DS, for all the sampling stations.

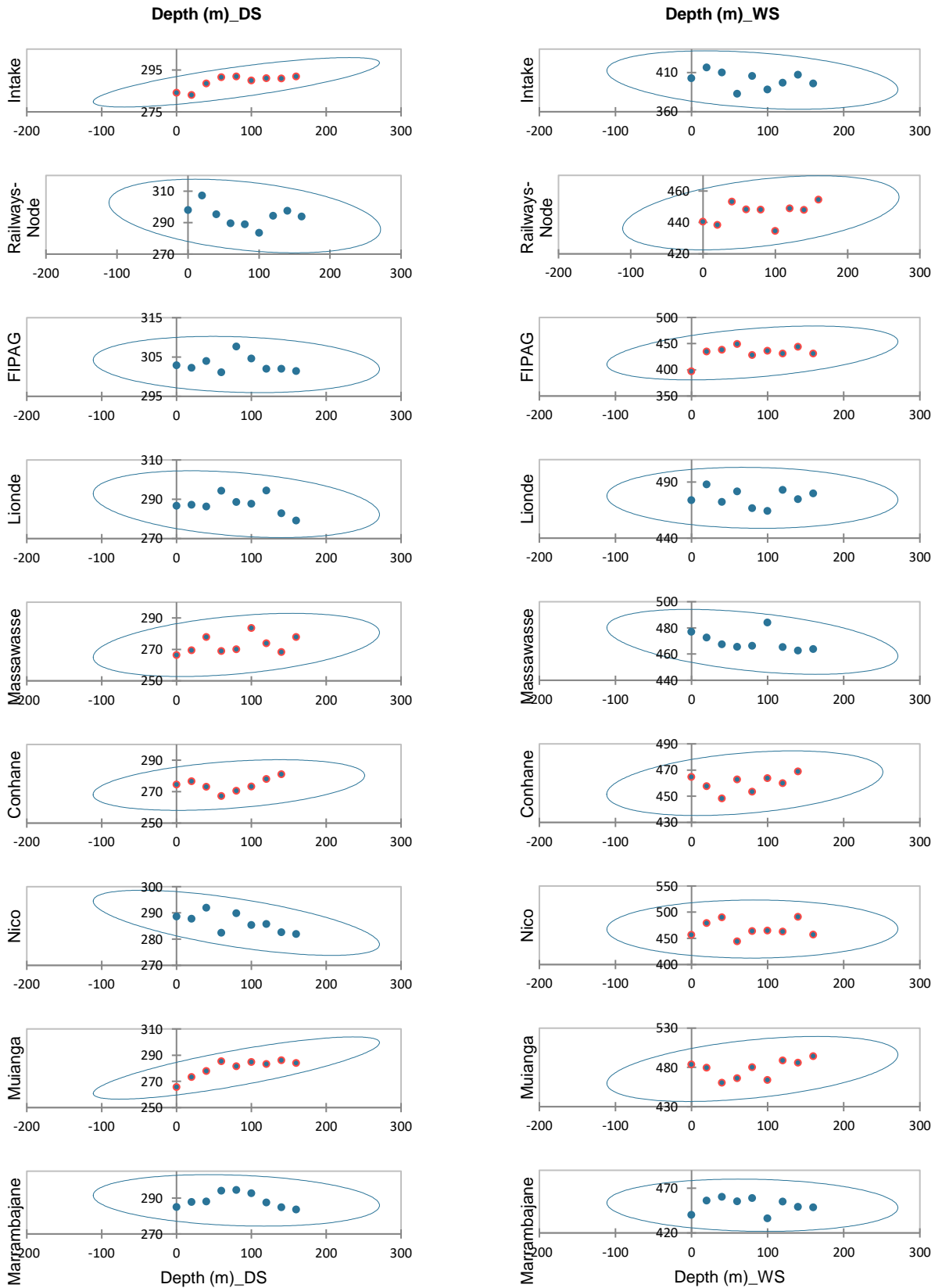


Figure 4. 39: TDS as Function of Sampling Depths for DS and WS

During DS very small variation amplitude in TDS was observed. Stations located in the upstream, namely Railways and FIPAG presented relatively high TDS than others, by being above 300ppm. At Massawasse and Conhane stations, located at midstream TDS values were the lowest. This may be related to steady flow in the season and high TDS observed in stations where the water level was relatively high. Contrary to this, the WS TDS values were relatively higher than during DS, with approximately 380 to nearly 500 ppm, except at 160 cm depth in Muianga. Stations located at the most downstream such as Nico and Muianga had highest TDS values, followed by the midstream stations of Lionde, Massawasse and Conhane, with TDS rounding 450 ppm.

Electrical Conductivity (EC), is a measure of the salinity and sodicity of irrigation water. EC is based on the ability of water to conduct an electric current, and is key in determination of water quality properties. The higher the concentration of ions in water, the more current it can conduct. Conductivity is therefore sensitive to the amount of dissolved solids - particularly mineral salts - in the water, and also depends on the amount of electrical charge on each ion, ion mobility, and temperature. EC in relation to sampling weeks varied in opposite direction in both seasons. During DS seems that EC increases with weeks and in WS, decreases. Exceptions are observed for Massawasse, Conhane and Muianga, in DS, and Nico, Muianga and Marrambajane, in WS. Seasons appears to influence the EC in scheme. Figures 4.40 and 4.41 presents EC as function of sampling stations and sampling weeks, respectively.

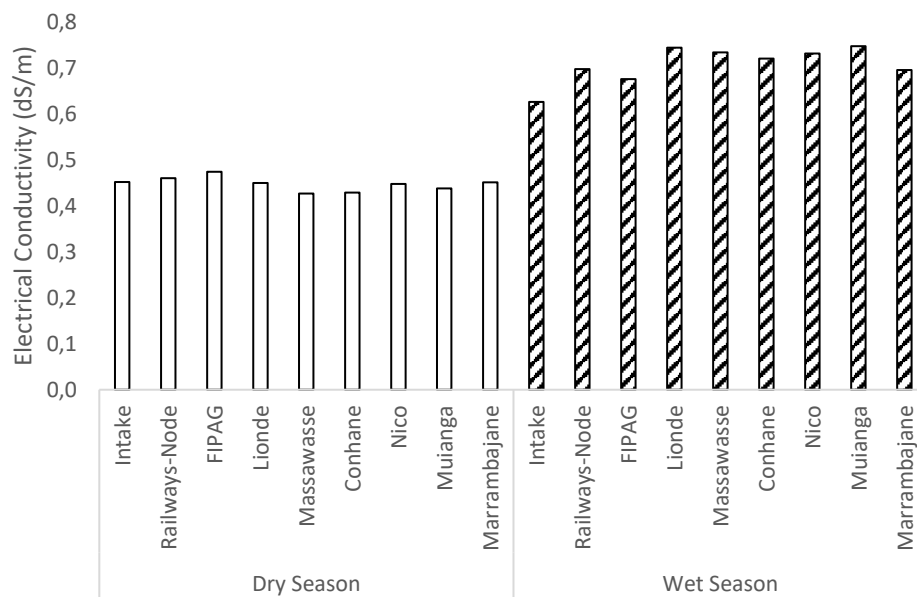


Figure 4. 40: Electrical Conductivity Given for Each Sampling Stations for DS and WS

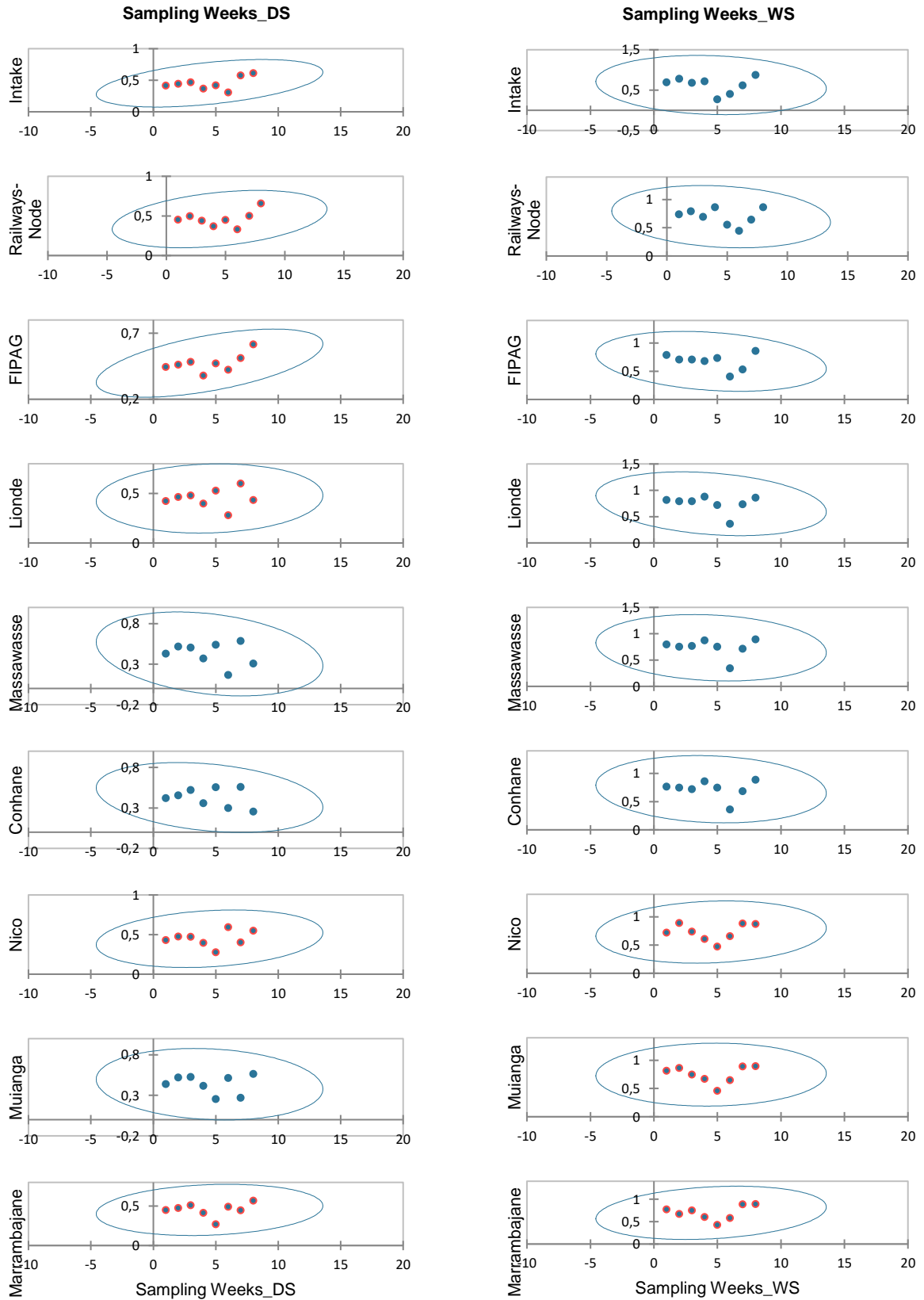


Figure 4. 41: Electrical Conductivity as Function of Sampling Weeks for DS and WS

The correlation between TDS and EC for water collected from specific region were found to be significant and consistent, whereby both parameters presents similar behaviour along CIS. Expressed in units of micro Siemens per centimetre ($\mu\text{S}/\text{cm}$), conductivity generally ranges between 10 and 1000 $\mu\text{S}/\text{cm}$ (or 0.01 and 1dS/m) in most rivers or lakes that have outflows. In Figure 4.41, EC varied with sampling weeks, from upstream to downstream. During the DS in the first four weeks, EC has a relatively uniform behaviour, increasing and decreasing with time at the fourth week of study, from 0.4 dS/m to more than 0.5 and again falling to 0.4 again. In the fifth and seventh weeks, midstream stations were higher, followed by upstream and downstream stations, respectively. During WS, on the other hand, downstream stations have been higher at the beginning of the sampling weeks, followed by a drastic fall in the fifth week and the rise on the following sixth and seventh weeks, with 0.9, 0.45 and again 0.85 dS/m, respectively. Midstream stations, had higher EC at fourth week and fallen at the sixth week, to approximately 0.25 dS/m. In the last week, all the stations recorded EC of around 0.85 dS/m. DS presented lower EC than WS, with an average of 0.45 dS/m and 0.7 dS/m, respectively (Hodlur et al., 2010; Park et al., 2011).

When looking at these results from the water depths perspective, one can see from Figure 4.41 that, during the DS, the EC varied from 0.41 to 0.48 dS/m. The FIPAG station presented the highest EC of 0.47 dS/m at all depths, followed by Railways-Node and Marrambajane, with 0.45 dS/m, respectively. Massawasse and Conhane had the lowest EC rate of around 0.42 dS/m. In the WS, however, EC varied between 0.6 and 0.8 dS/m. Lionde, Massawasse and Muianga had highest EC of nearly 0.75 dS/m, and the lowest EC was found at Intake, Railways-Node and FIPAG, all located at upstream (Thomas, 1986; Hrynkiw et al., 2003). Relating EC and water depth, no consistent trend is shown up. But in general, one can suggest that DS tend to have EC decreasing with water depth, while in WS, it decreases. Exception is found for Intake, Massawasse, Conhane and Muianga, for DS and, Intake, Lionde, Massawasse and Marrambajane, for WS. In Figures 4.42 is shown the EC as function of water depth for both seasons.

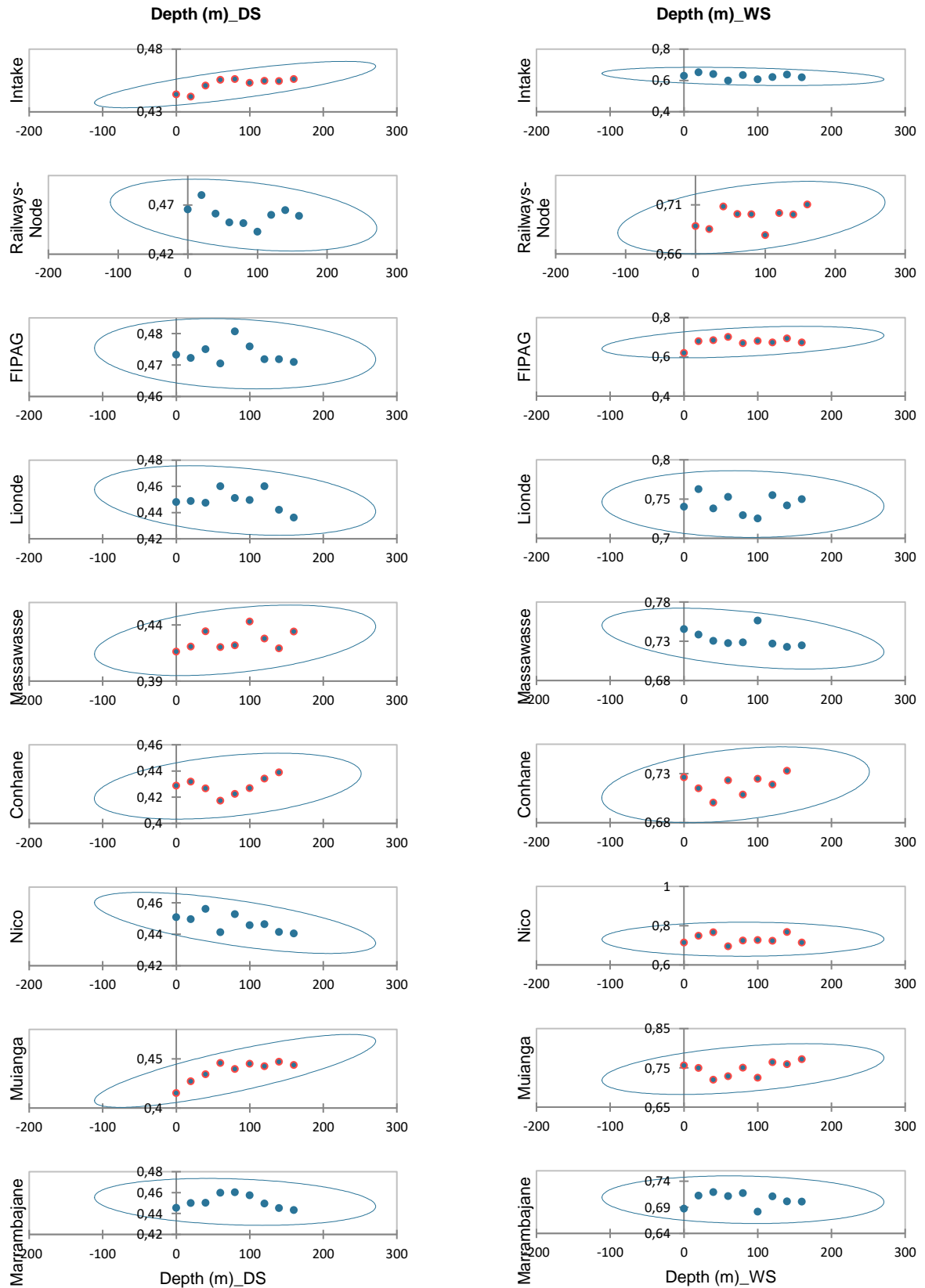


Figure 4. 42: Electrical Conductivity as Function of Water Depths for DS and WS

In general, considering the averages from the sampling stations depths and the whole two months data collection period, Electrical Conductivity (EC) of water containing the suspended sediments appeared to be very strongly influenced by the Total Dissolved Solids (TDS). During DS the positive regression fit is generated explaining EC from TDS was approximately 85%. In other words, TDS explains about 85% the EC occurring in the water stream in the DS. Similar pattern was observed during the WS, where EC was explained approximately 100% by TDS. These results are consistent with the findings of Stone et al. (1995). Additionally, Ye (2012) and Yu et al. (2014) found that EC increases with TDS increments. Zhang and Schilling (2004) found that the higher the temperature of water, higher is the electrical conductivity. As a rule of thumb, the electrical conductivity of water increases by 2-3% for each increase of 1°C in temperature. As observed from Figure 4.43 water EC seems to strongly be influenced by TDS and the regression fit for the plots were, 84% and 99%, for DS and WS, respectively.

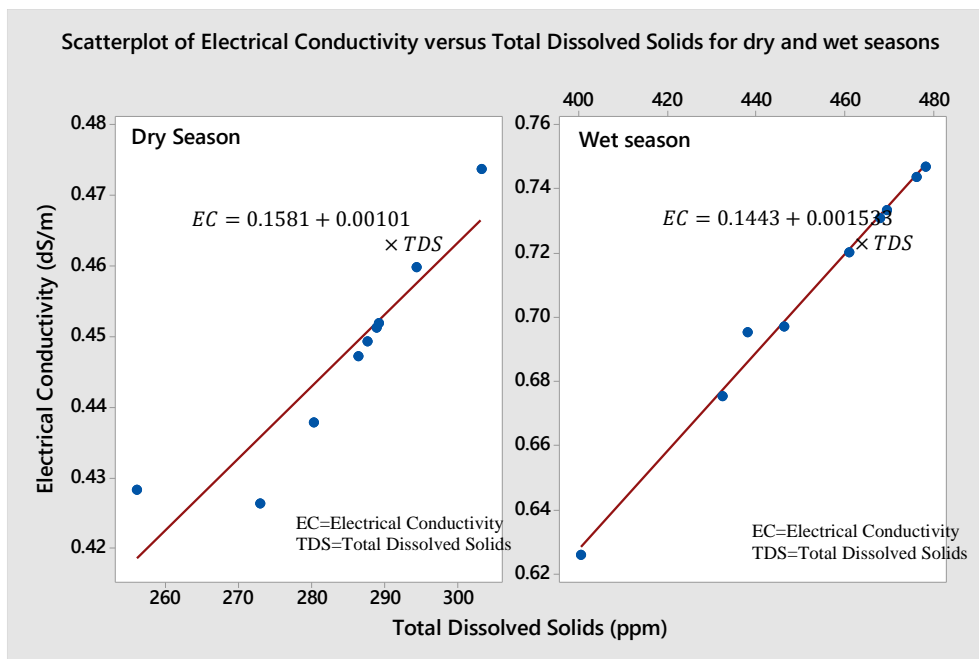


Figure 4. 43: Water Electrical Conductivity as Function of the Water Total Dissolved Solids for DS

Analysis of Correlation Matrices and Coefficient of Determination for Inflow Factors

Analyse of correlation between water depth in the canal and other different inflow factors was performed. Using Pearson correlation coefficient, which measures the linear association between two variables, for DS, it was found that TDS and EC has very strong positive correlation ($r=1.000$). These two factors may well be multicollinear, and therefore, one of this can be considered in the analysis and another left out. Water depth and water pH, showed strong positive correlation ($r=0.773$). This means that with increased water depth the pH value tend to increase, implying that as one descend from water surface to the canal depth, its become more alkaline. Additionally, water depth and suspended sediment concentration (SSC) showed strong negative correlation. Meaning that as the depth increase, the sediment concentration reduces. Coefficient of determination (R^2) of 59% was found for water depth and water pH, and around 65% for water pH and SSC. This serve to imply that 59% of water pH is explained by water depth, and that 65% of water pH by SSC occurring in the canal.

When analysis was performed in terms of the sampling weeks for DS, water temperature, EC and TDS appears to be correlated each other ($r=0.736$), with R^2 of 54%. But for WS, water temperature, turbidity and EC or TDS, have strong correlation. Water turbidity is strongly and negatively correlated to water temperature and EC (or TDS), with $r=-0.838$ and $r=-0.877$, respectively. This means that as water turbidity increases, water temperature and EC (or TDS) does decrease. Water temperature and EC (or TDS) have also shown strong positive correlation. This means that as water temperature increases, same happens with EC. Coefficient of determination (R^2) of 77% and 70% were found for EC (or TDS) and water temperature, during WS, respectively. This suggest that water turbidity is explained by EC (or TDS) in 77% and by water temperature in 70%. Water temperature and EC presented R^2 of 73%, indicating that EC is explained by water temperature in 73%. Tables 4.5-4.10 present the correlation matrix and coefficient of determination for inflow factors, both for water depth in the canal and sampling weeks.

Table 4. 5: Correlation matrix (Pearson) (r) for Inflow Factors-Water Depth in DS

Variables	EC-DS	TDS-DS	Depth	pH-DS	SSC-DS
EC-DS	1	1.000	0.593	0.136	0.067
TDS-DS	1.000	1	0.593	0.136	0.067
Depth	0.593	0.593	1	0.773	-0.462
pH-DS	0.136	0.136	0.773	1	-0.805
SSC-DS	0.067	0.067	-0.462	-0.805	1

Values in bold are different from 0 with a significance level $\alpha=0.05$

Table 4. 6: Coef. of determination (Pearson) (R^2) for Inflow Factors-Water Depth in DS

Variables	EC-DS	TDS-DS	Depth	pH-DS	SSC-DS
EC-DS	1	1.000	0.352	0.018	0.004
TDS-DS	1.000	1	0.352	0,018	0.004
Depth	0.352	0.352	1	0,598	0.213
pH-DS	0.018	0.018	0.598	1	0.648
SSC-DS	0.004	0.004	0.213	0.648	1

Table 4. 7: Correlation matrix (Pearson) for Inflow (r) Factors-Samp. Weeks in DS

Variables	Temp-DS	TDS-DS	EC-DS
Temp-DS	1	0.736	0.736
TDS-DS	0.736	1	1.000
EC-DS	0.736	1.000	1

Values in bold are different from 0 with a significance level $\alpha=0.05$

Table 4. 8: Coef. of determination (Pearson) (R^2) for Inflow Factors-Samp. Weeks in DS

Variables	Temp-DS	TDS-DS	EC-DS
Temp-DS	1	0.542	0.542
TDS-DS	0.542	1	1.000
EC-DS	0.542	1.000	1

Table 4. 9: Correlation matrix (Pearson) for Inflow (r) Factors-Sampling Weeks in WS

Variables	Turb-WS	EC-WS	TDS-WS	Temp-WS
Turb-WS	1	-0.877	-0.877	-0.838
EC-WS	-0.877	1	1.000	0.855
TDS-WS	-0.877	1.000	1	0.855
Temp-WS	-0.838	0.855	0.855	1

Table 4. 10: Coef. determination (Pearson) (R^2) for Inflow Factors-Samp. Weeks in WS

Variables	Turb-WS	EC-WS	TDS-WS	Temp-WS
Turb-WS	1	0.768	0.768	0.702
EC-WS	0.768	1	1.000	0.731
TDS-WS	0.768	1.000	1	0.731
Temp-WS	0.702	0.731	0.731	1

Values in bold are different from 0 with a significance level $\alpha=0.05$

Suspended Load Chemistry Characteristics

Water samples containing suspended sediments were analysed and sodium (Na^+), potassium (K^+) and calcium (Ca^{2+}) were considered in an attempt to assess the likelihood of the sediment particles to aggregate or disperse. The chemistry of the water appeared to be uniform, from surface to bottom and across the canal length at the sampling stations. Sodium was the most present element in terms of quantity compared to potassium and calcium, reaching 0.285 ppm. In some stations, sodium was found to be higher than in others. For example, FIPAG and Marrambajane, recorded approximately 0.300 ppm and 0.985 ppm, respectively. Potassium was relatively high in FIPAG, reaching 0.075 ppm, while other stations recorded approximately 0.06 ppm. Highest value for calcium was recorded at Nico station followed by Railways-Node station at 0.055 and 0.025 ppm, respectively. During the WS, low amounts of sodium were recorded in comparison to DS, whilst potassium and calcium did not vary considerably. In both seasons, sodium, potassium and calcium showed minimal variations at the sampling stations and varying water depths. This was more prominent during WS. Study by Verlicchi and Grillini (2020), on water quality at Limpopo river stream found significant amounts of sodium in the water body. Their findings corroborate with findings in this work, suggesting significant presence of sodium in the water

at the CIS, given that Limpopo is the source of water for this irrigation scheme. High presence of sodium in the canal could be attributed to runoff carrying fertilizers and biocides, given intense agriculture activities present in the region. Dumping of livestock waste into water bodies can be one of the sources, apart from the natural mineralogy of the soil formation (Huang et al., 2020; Xu, 2019). In Figures 4.44 and 4.45 are presented results of chemistry analysis for SSC during DS and WS, respectively.

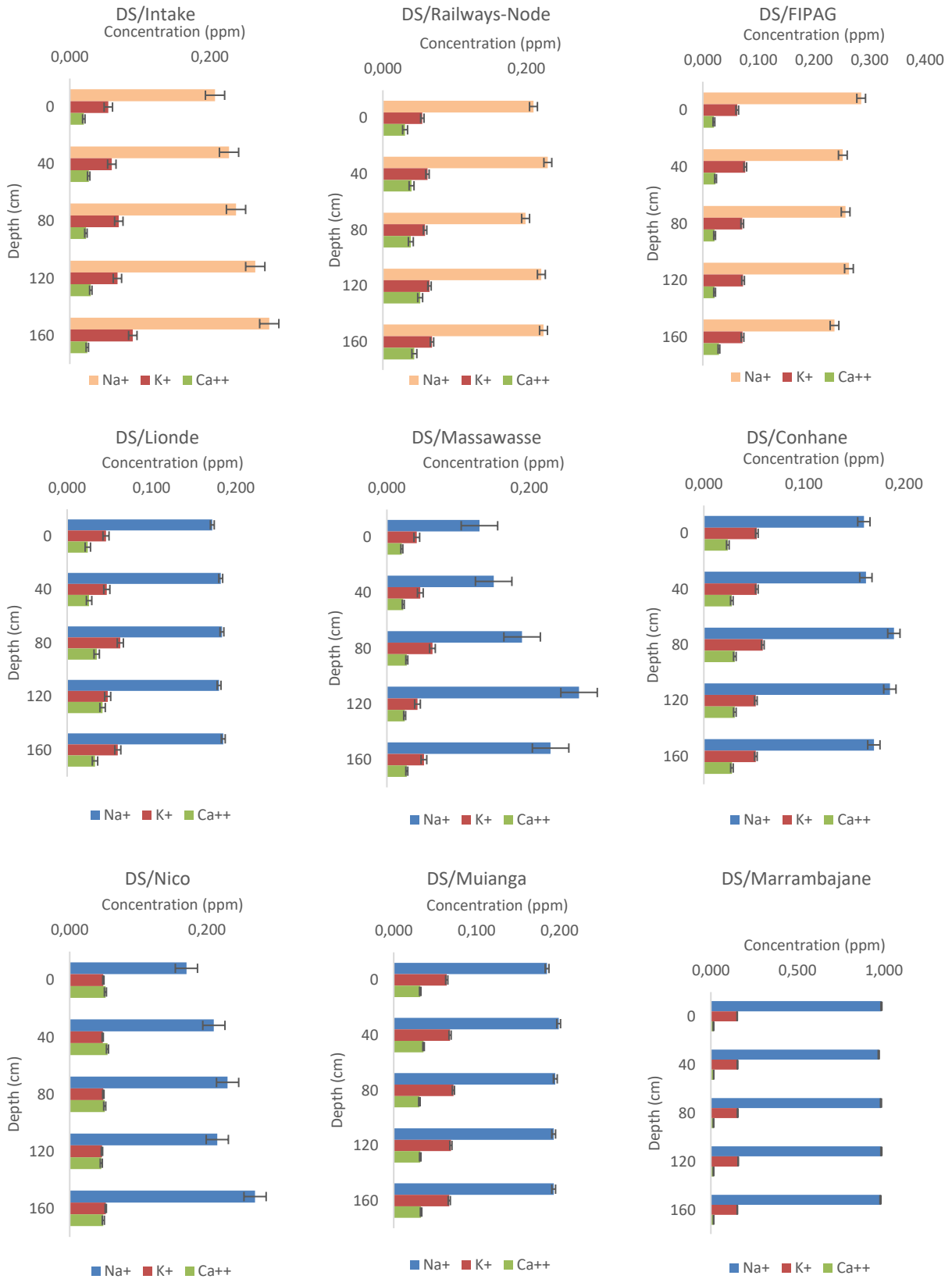


Figure 4. 44: Chemistry Analysis for Suspended Sediments During DS for Each Sampling Station

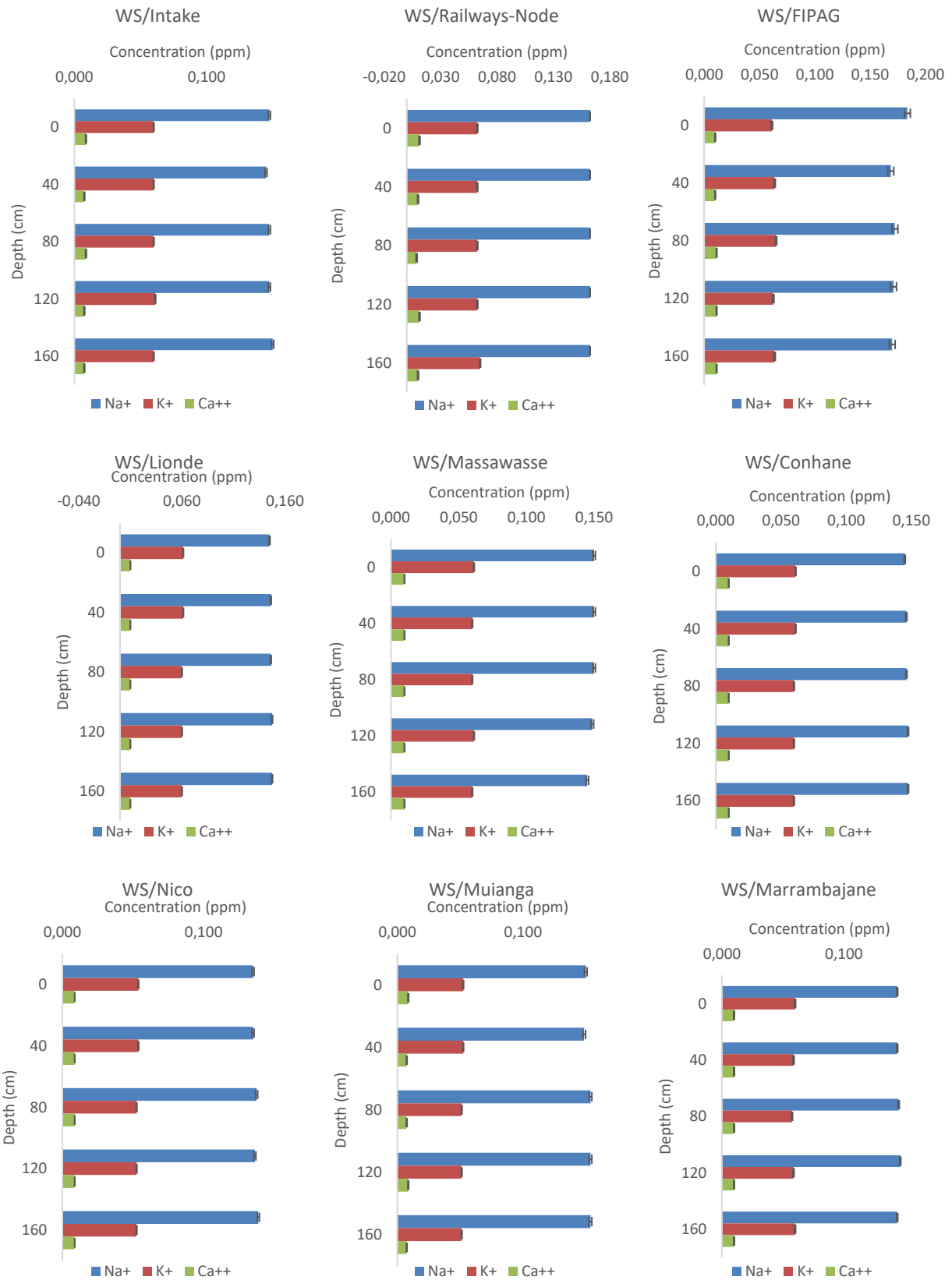


Figure 4. 45: Chemistry Analysis for Suspended Sediments During WS at Each Sampling Station

4.1.3 PCA analysis for Water and Sediment Characteristics

Normality Test

Dataset normality test was performed in an attempt to assess whether it followed normal distribution or not. Q-Q plots of sediment flux for the Offtake (DS) were the only dataset that presented normality. Different factors may have contributed to this end, including the length of data collection, changes of inflow and outflow, among others. Overall, majority of sampling points within each dataset appeared to be normally distributed. However, this was not the case for the water flow as it was observed that all stations presented normal distribution, with exception for the Intake, Nico and Muianga (both seasons), FIPAG and Conhane (DS), and Marrambajane (WS). Figures 4.46 and 4.47 present the normality results of test plots for sediment discharges and water flow in the CIS.

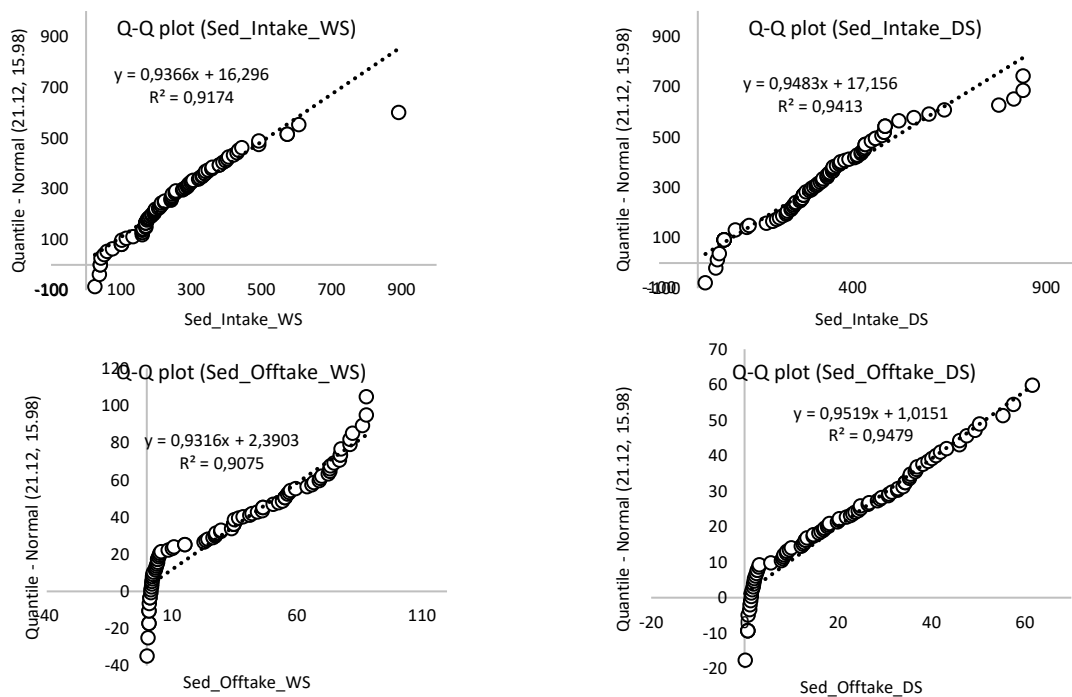


Figure 4. 46: Normal Q-Q Plots for Sediment Discharge Dataset

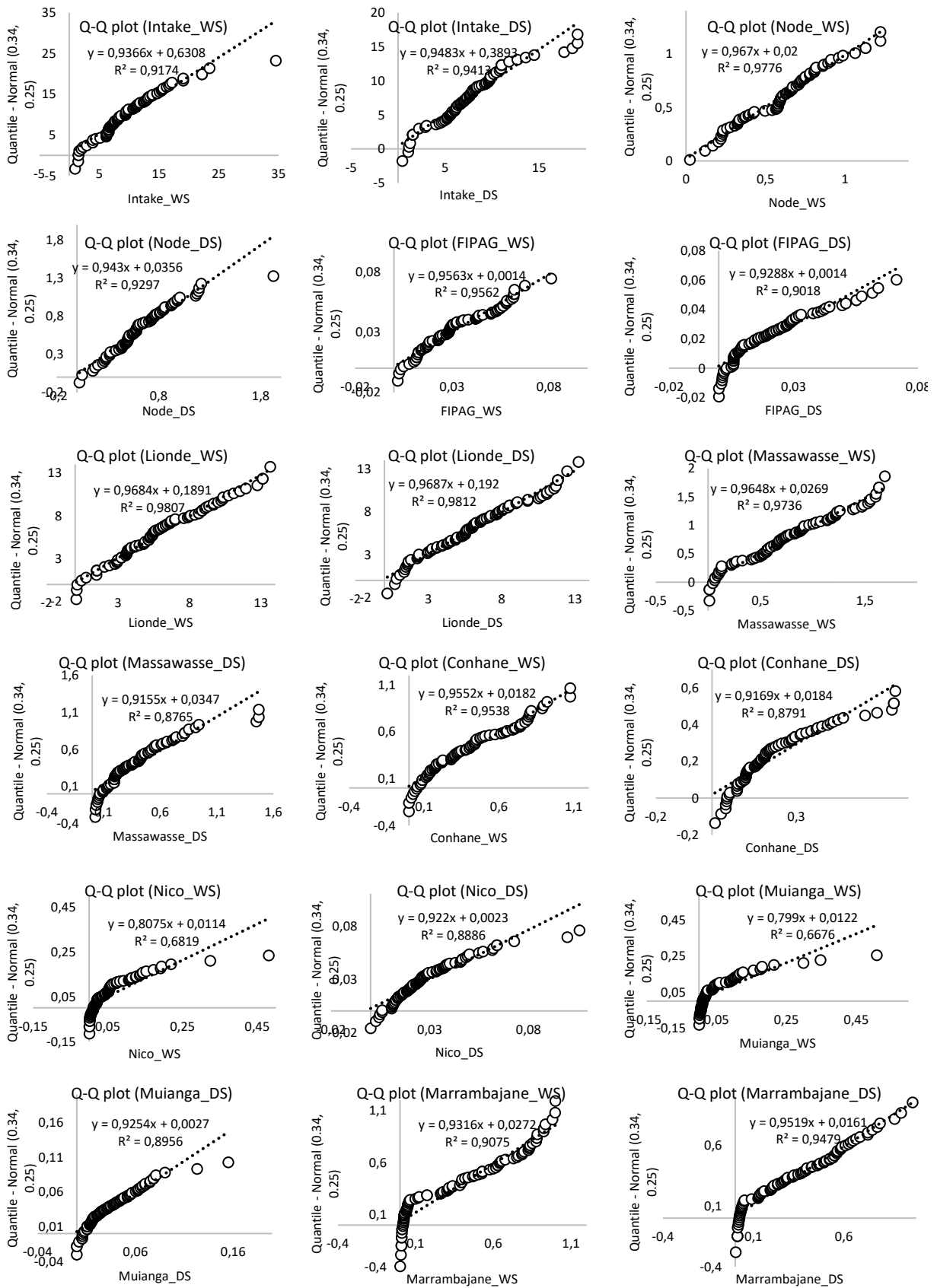


Figure 4.47: Normal Q-Q Plots for the Water Discharge

Correlation matrix

The PCA produces a correlation matrix including the correlation coefficient (r) between all variables. A correlation coefficient of $r \geq 0.5$ is considered significant (as highlighted in bold in Tables D.2-D.5 in the Appendix D.2.). The analysis was performed for canal channel factors and inflow factors, in both seasons, dry (DS) and wet (WS). Canal channel factors considered variables relevant to sedimentation processes, such as water flow (Q), water depth (WD), canal depth (CD), settling velocity (SV), critical shear stress (CSS), plasticity index (PI), electrical conductivity (EC), exchangeable sodium percentage (ESP), sodium adsorption ratio (SAR), sodium concentration (Na^+), potassium concentration (K^+) and combined concentration of calcium and magnesium ($\text{Ca}^{2+}+\text{Mg}^{2+}$). For the canal channel factors, during DS, a positive and high correlation coefficient is measured between CD and WD ($r = 0.88$), PI and CSS ($r = 0.96$), SAR and ESP ($r = 0.80$), Na^+ and SAR ($r=0.78$) and $\text{Ca}^{2+}+\text{Mg}^{2+}$ and PI ($r = 0.73$). A negative correlation coefficient was found for ESP and SV ($r=-0.75$). These correlations reflect the physico-chemical characteristics of the CIS main canal during dry season. The fact that some of the physical variables appear with positive correlation sustain the theory that in somehow these variables does exert influence on each other and at some extent, to the chemical variables in the system, as per relation between $\text{Ca}^{2+}+\text{Mg}^{2+}$ and PI. Moreover, sedimentation appears to be affected by canal channel factors in the CIS. Beside this, it may also indicate anthropogenic factors affecting the system. The diagonalization of the correlation matrix was produced by PCA to avoid the problems of different measurement units of the original variables, since the standardization of all variables is automatically applied. Similar analysis was performed for the canal channel factors, during WS, where a positive and high correlation coefficient was found between CD and WD ($r = 0.99$), WD and $\text{Ca}^{2+}+\text{Mg}^{2+}$ ($r=0.73$), CD and $\text{Ca}^{2+}+\text{Mg}^{2+}$ ($r=0.72$), CSS and PI ($r=0.96$), CSS and EC ($r=0.70$), PI and EC ($r=0.78$), ESP and SAR ($r=0.84$), ESP and Na^+ ($r=0.83$), SAR and Na^+ ($r=0.86$), Na^+ and $\text{Ca}^{2+}+\text{Mg}^{2+}$ ($r=0.81$) and K^+ and $\text{Ca}^{2+}+\text{Mg}^{2+}$ ($r=0.69$). A negative correlation coefficient was found for SV and CSS ($r = -0.75$) and SV and PI ($r=-0.69$).

Inflow factors considered water flow (Q), water depth (WD), water temperature (T), water velocity (WV), suspended sediment concentration (SSC), electrical conductivity (EC), total dissolved solids (TDS), turbidity (TURB), water pH (pH), sodium concentration in water (Na^+), potassium concentration in water (K^+) and calcium concentration in water (Ca^{2+}).

During DS, positive correlation coefficient was measured for Q and WV ($r=0.98$), WD and EC ($r=0.81$), WD and TDS ($r=0.86$), EC and TDS ($r=0.89$), pH and Ca^{2+} ($r=0.91$), and Na^+ and K^+ ($r=0.98$). No negative correlation coefficient is found in this season. But for WS, positive correlation coefficient was measured for Q and WV ($r=0.92$), Q and TURB ($r=0.85$), WD and Na^+ ($r=0.86$), T and SSC ($r=0.96$), WV and TURB ($r=0.90$), EC and TDS ($r=0.99$), and Ca^{2+} and K^+ ($r=0.74$). Negative correlation coefficient is found for EC and TURB ($r=-0.77$), and TDS and TURB ($r=-0.74$). From these correlations coefficients, one can see that sedimentation is affected by different inflow factors, in both seasons.

Factor loadings

Factor loadings, representing contributions of the original variables in the new factors, and the eigenvalues of each factor produced by PCA are summarized in Tables D.6-D.9 in the Appendix D.2. The amount of variance information explained by each PC depends on the relative eigenvalue with respect to the cumulative eigenvalues. Identification of the number of PCs (factors) to be selected is based on several criteria in order to analyse the data structure and understand the underlying information (Gyimah et al., 2020). The table of variance (%) of PCA factors, if a variance curve is plotted, a decrease in the slope can be observed after the sixth eigenvalue for canal channel factors and inflow factors during DS. For WS, decrease in the slope can be observed after fourth eigenvalue. This happens for both group of factors, for canal channel and inflow factors. According to the computed percentage of total cumulative variance of more than 98.11% and 99.58%, six factors were selected for DS canal channel and inflow factors, respectively. Similarly, total cumulative variance of more than 90.51% and 95%, four factors were selected for WS canal channel and inflow factors, respectively. Tables D.6-D.9 in the Appendix D.2, include factor loadings of 8 variables on these six and four PCs, respectively for DS and WS. Factor F1 for canal channel factor during DS, explains 33.24% of the variance and provides a positive correlation with variables such as WD, CD, CSS, PI, EC, ESP, Na^+ , and $\text{Ca}^{2+}+\text{Mg}^{2+}$, while correlating negatively with SV. Same F1 of canal channel factor, but for WS, explains 48.09% variance and provides also positive correlation with variables WD, CD, CSS, PI, EC, ESP, SAR, Na^+ , K^+ , and $\text{Ca}^{2+}+\text{Mg}^{2+}$. This factor represents high sedimentation potential through canal channel variables of water depth, canal depth, shear stress, plasticity index, sodium related parameters. It emphasizes that canal channel with sediment particles characterised by the

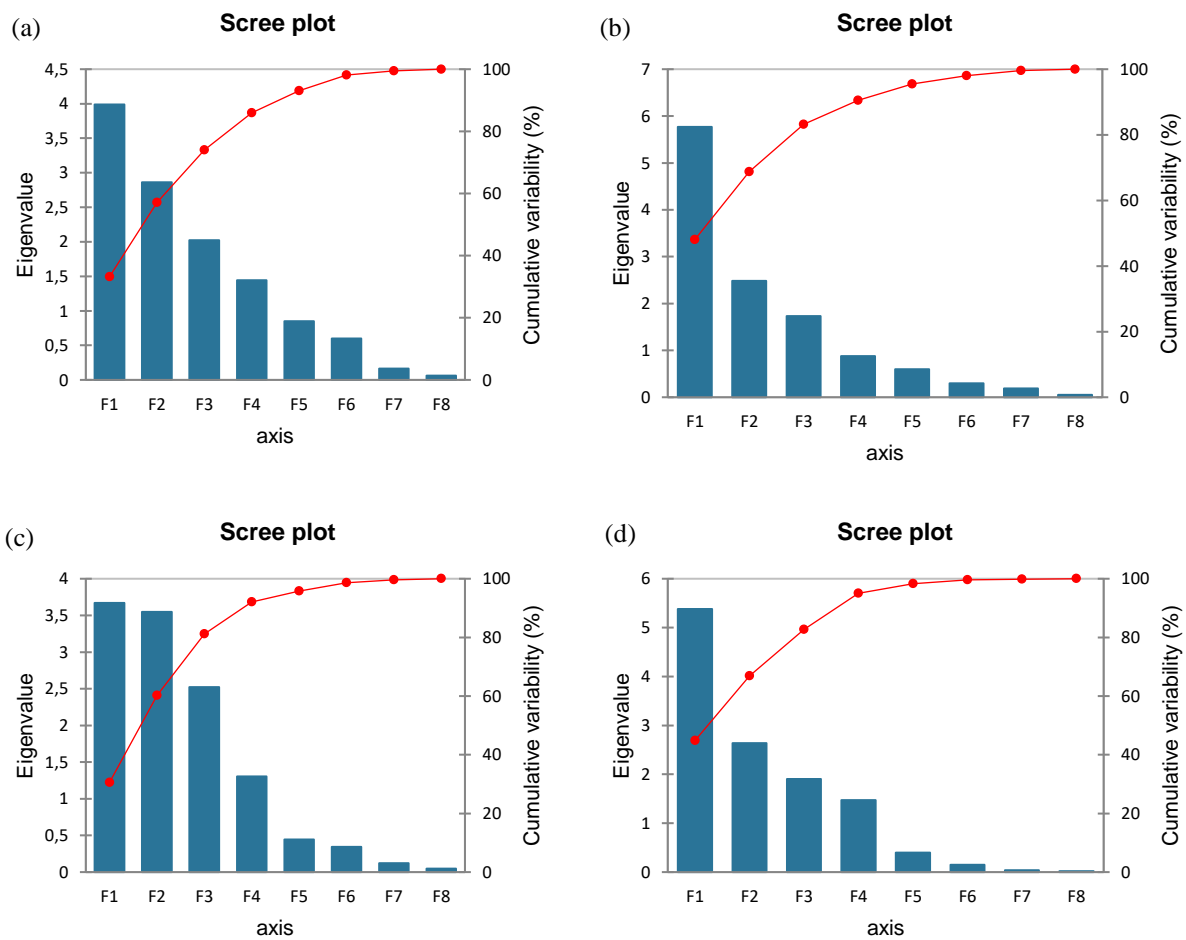
presence of sodium, has less possibilities to aggregate and precipitate thereafter, but remain suspended towards downstream. However, there are another part of flocculated particles depositing in the canal bed while the fine ones moves toward the scheme end (Croux et al., 2017; Kansara et al., 2015; Rokni et al., 2016; See & Porio, 2015).

In inflow factors, F1 explains 30.59% and 44.85, for DS and WS, respectively. F1 in DS, appears with positive correlation for variables of WD, EC, TDS, Na⁺ and K⁺, whilst a negative correlation with T. For WS, positive correlation was found for Q, WD, WV, TURB and Na⁺, while a negative correlation with T, WV, SSC, EC and TDS. These results suggest that sediment accumulating in the CIS are influenced by water flow, water depth, water velocity, turbidity and somehow the presence of sodium which impact on the particle susceptibility to flocculate. Water temperature, water volicity, suspended sediment concentration, electric conductivity and total dissolved solids appears to be less relevant in this factor.

F2 of canal chanel factors, counted to explain 57.10% and 68.78% for DS and WS, respectively. During DS, a positive correlation with ESP, SAR, and Na⁺ was found, while a negative correlation was found for SV. During WS, a positive correlation was found for CSS, PI and EC, whilst a negative correlation for Q and ESP. F2 appears to indicate that sodium concentration and its relation the potassium and calcium are critically relevant for this component and less of settling velocity. F2 for inflow factors explains 60.16% and 66.82% for DS and WS, respectively. During DS, it suggests a positive correlation with Q, WD, WV and Ca²⁺, and negative correlation with TURB, Na⁺ and K⁺. During WS, a positive correlation was observed for Na⁺, K⁺, and Ca²⁺. This seems that water discharge, water depth and velocity a concentration of calcium do affect sedimentation greatly, over water turbidity, calcium and potassium.

F3 of canal channel factors explains 73.98% and 83.19% for DS and WS, respectively. Positive correlation was found with K⁺, and negative correlation with EC, for DS. During WS, positive correlation was found for WD and CD. Inflow factors explained 81.16% and 82.72%, in DS and WS, respectively. A positive correlation was found with SSC, and a negative correlation with pH and Ca²⁺, in DS, whilst for WS, no significant correlation was found at

95% of significance level. DS for canal channel presented significance for F4 and F5, alike WS of canal channel factors, and both seasons of inflow factors. For F4, a positive correlation was found with WD and CD, and F5 presented positive correlation with Q. This serve to inform that, for these two factors, water depth and canal depth as well as, water discharge are important over any other variable in the system. The eigenvalue and respective cumulative (%) values are presented in the scree plots in the Figure 4.48, for canal factors (a&b) and inflow factors (c&d), both for DS and WS. From these figures one can see that the first three factors, F1, F2 and F3, count for above 80% of variance, except for the canal channel factors in DS (Figure a), with 74%.



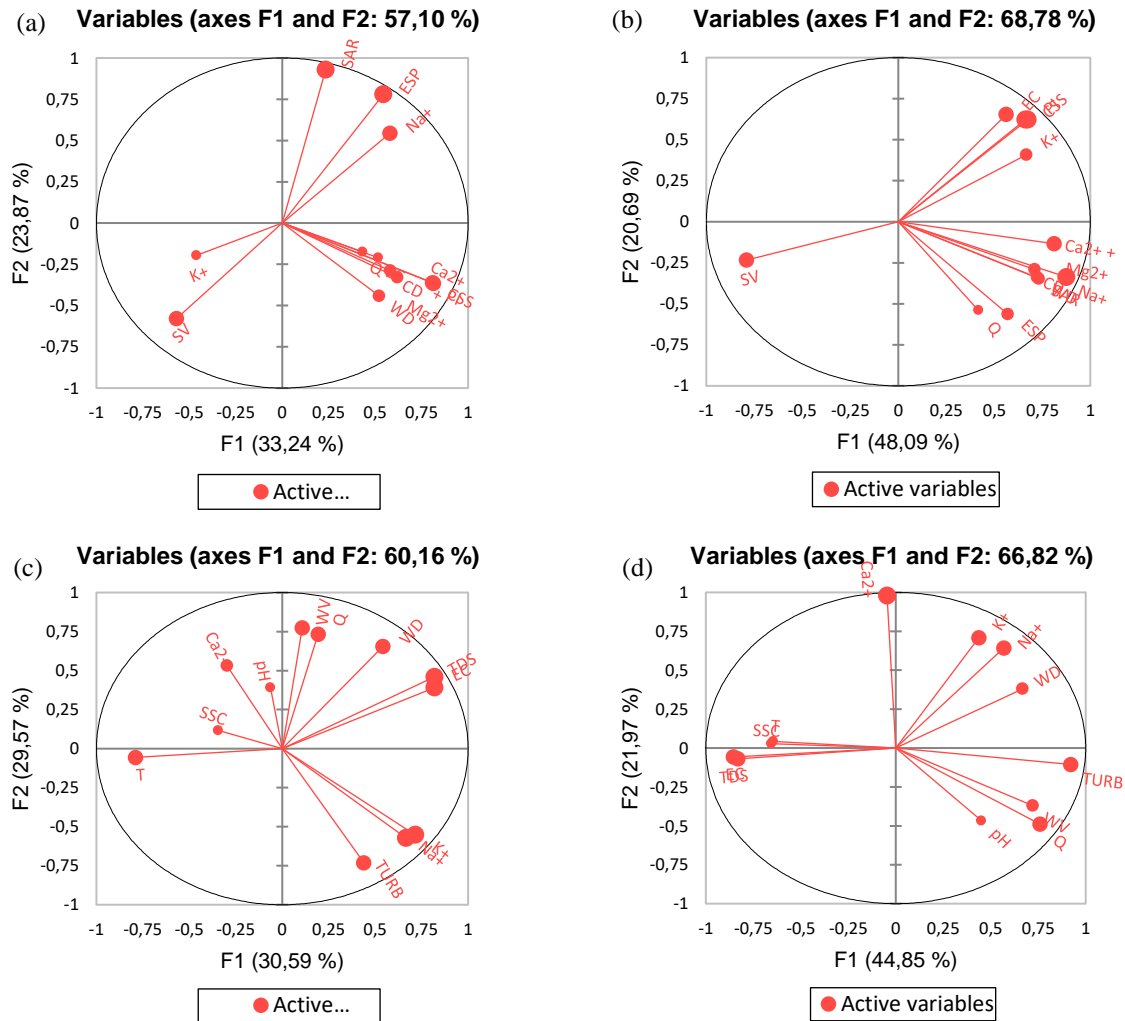
For Dry Season

For Wet Season

Figure 4. 48: PCA Eigenvalue Plots for Canal (a&b) and Inflow (c&d) Factors for DS and WS

From the variable plots for canal channel factors, both components explain 57.10% and 68.78%, for DS and WS, respectively. In DS (plot a), F1 is mostly associated with $WD > CD > Ca^{2+}+Mg^{2+} > CSS > Q > EC$ and PI . In turn, F2 seemed very much associated with $SAR > ESP$ and Na^+ , negative association is found for K^+ and SV . In WS (plot b), F1 appears very much associated with $ESP > SAR > Na^+ > CD > Ca^{2+}+Mg^{2+}$ and Q , whilst F2 associated with $CSS > PI > EC$ and K^+ , and negatively associated with SV . This suggest that for both seasons, F1 is mostly comprised of canal depth, combination of calcium and magnesium and water flow, whilst for F2, no common positively related variables were found for both seasons, but a negative effect coming from the settling velocity.

From inflow factors point of view, the components F1 and F2, explains in 60.16% and 66.82%, for DS and WS, respectively. For DS, F1 is well associated with $Na^+ > K^+$ and $TURB$, and negative association with $Ca^{2+} > SSC$ and pH . F2 is strongly associated with $TDS > EC > WD > WV$ and Q , and negatively related to T . For WS, F1 has strong association coming from $TURB > WV > Q$ and pH , while negative association with SSC and T . F2, is strongly associated with $Na^+ > K^+$ and WD , and negative association with EC and TDS . In general terms, for both seasons, strong associations between F1 and variables is found for turbidity and negative effect from suspended sediment concentration, meanwhile, for F2, positive association was found for water depth in the canal. Figure 4.49 present variables plots for canal channel (a & b) and inflow (c & d) factors for DS and WS.



For Dry Season

For Wet Season

Figure 4.49: PCA Variable Plots for Canal (a&b) and Inflow (c&d) Factors for DS and WS

Cluster Analysis

Cluster analysis explained the relationship between the sampling sites based on their similar sedimentation characteristics. The dendrogram in Figure 4.50 indicates that the sampling sites were grouped into two (plots a, b & d) and three (plot c) clusters, both for canal channel factors and inflow factors, during DS and WS. For canal channel factors, in DS, cluster 1 (C1) is comprised of Intake, Railways-Node, FIPAG, Nico, Muianga and Marrambajane sampling stations, and cluster 2 (C2) by Lionde, Massawasse and Conhane. For WS, C1 is composed of Railways-Node and FIPAG, while C2 by Intake, Lionde, Massawasse, Conhane, Nico, Muianga and Marrambajane. Additionally, for inflow factors, during DS, C1 comprise

Marrambajane station, C2 made of Lionde, Muianga, Massawasse and Conhane, and C3, include Intake, Railways-Node, FIPAG and Nico. Lastly, for WS, C1 is comprised of Nico, Muianga, Lionde, Massawasse, Conhane and Marrambajane, and C2, with Intake, Railways-Node and FIPAG.

The cluster analysis revealed that stations which fall in the same cluster have certain common water flow and sediment flux parameters. The cluster analysis showed different landscape characteristics at each site with respects to the physico-chemical parameters. This also may be used to assess the inflow sources. Intake station receives water directly from the Limpopo river mainstream, from which all system is then supplied. However, Railways-Node and Lionde stations also present diverting points, from where water is channelised to other downstream sites. This provide large possibilities for similarities in water and sediment processes taking place, and potential reason for differences may be due to sampling seasons. Considering factor loadings and their respective variables associations, one can see that clusters are in consistent agreement with loadings, as for the upstream stations, there are significant amount of sediment entering the scheme, which is transported downstream, accumulating there. Water depth tend to be higher at most upstream and less downstream, with opposite direction for sedimentation. Therefore, clusters for upstream sites are frequently combined together and same pattern for mid- and downstream sites.

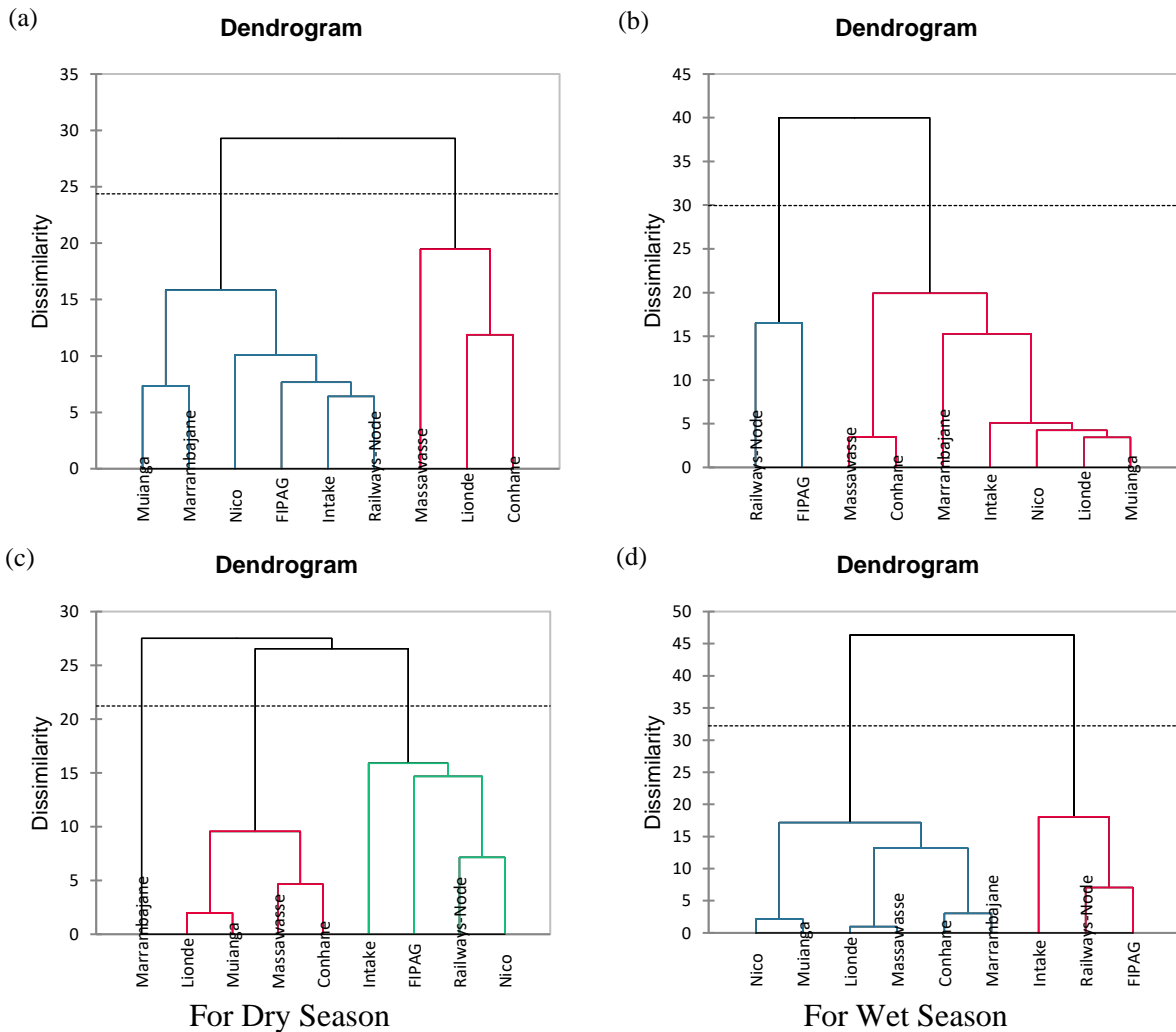


Figure 4. 50: PCA Cluster Analysis for Canal (a&b) and Inflow (c&d) Factors for DS and WS

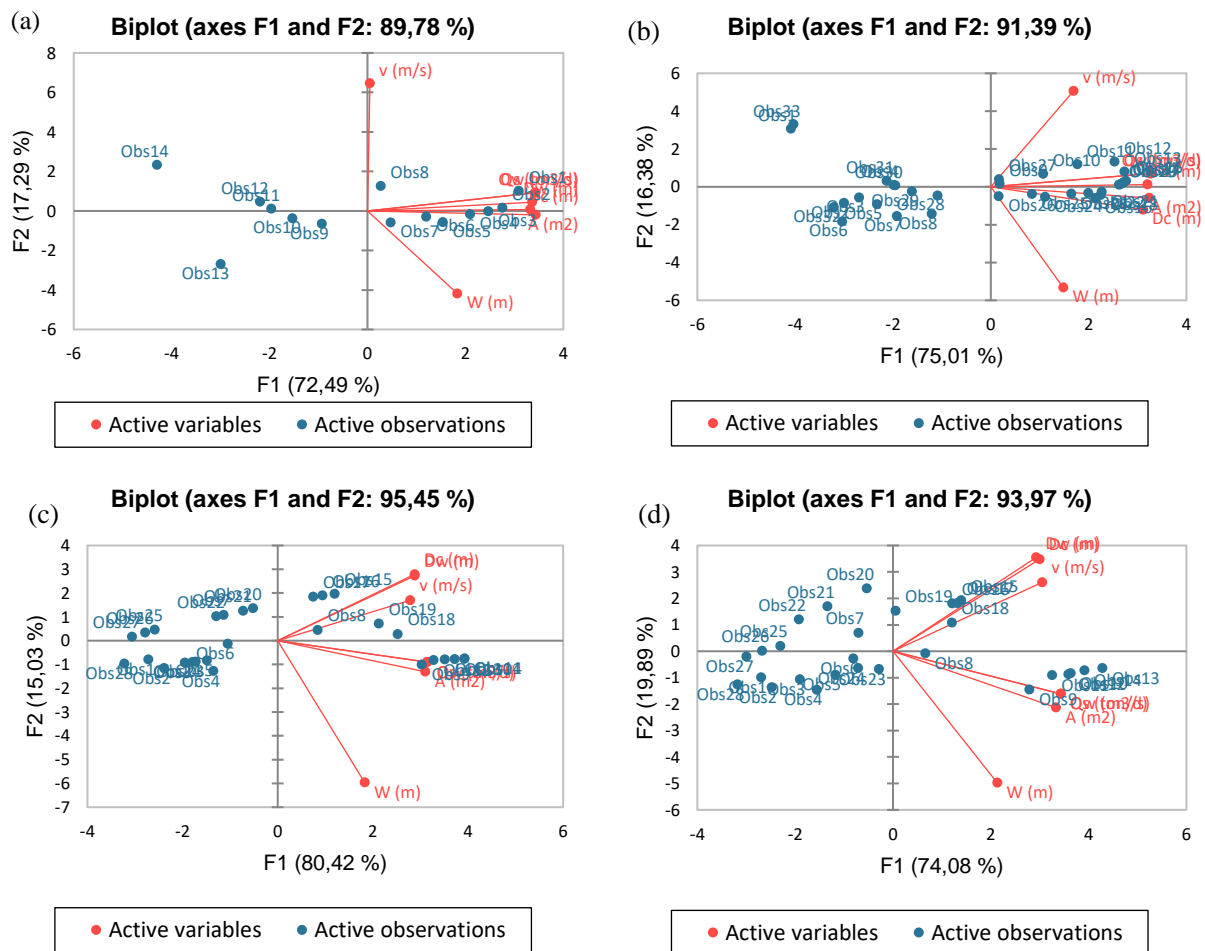
4.1.4 Cross-section Profiles and Sediments Flux

Montante Sector

At Railway-Node station, F1 explains 72.49% and 75.01% of variance, for DS and WS, respectively. Positive correlation for cross-section area (A), water (Qw) and sediment (Qs) discharges, canal (Dc) and water (Dw) depths were found. The most close correlated variables were A, Qw, Qs, Dc and Dw.

F2 explains 17.29% and it has a positive correlation with water velocity (v) and negative association with canal width (w). For FIPAG station, F1 explains 80.42% and 74.08% of variability for DS and WS, respectively. Both seasons show similarities in variables pattern.

Qs, Dw and A appear to be very closely positive correlated, and Dc, Qw and v, also are closely correlated. Canal width is counted in association to F2, in negative correlation. F2 explains 15.08%. This suggest that sedimentation at Railways-Node and FIPAG are very much associated to the canal cross-section profile and water depth. Figure 4.51 presents biplots for Montante Sector during DS and WS.



Dry Season (DS)

Wet Season (WS)

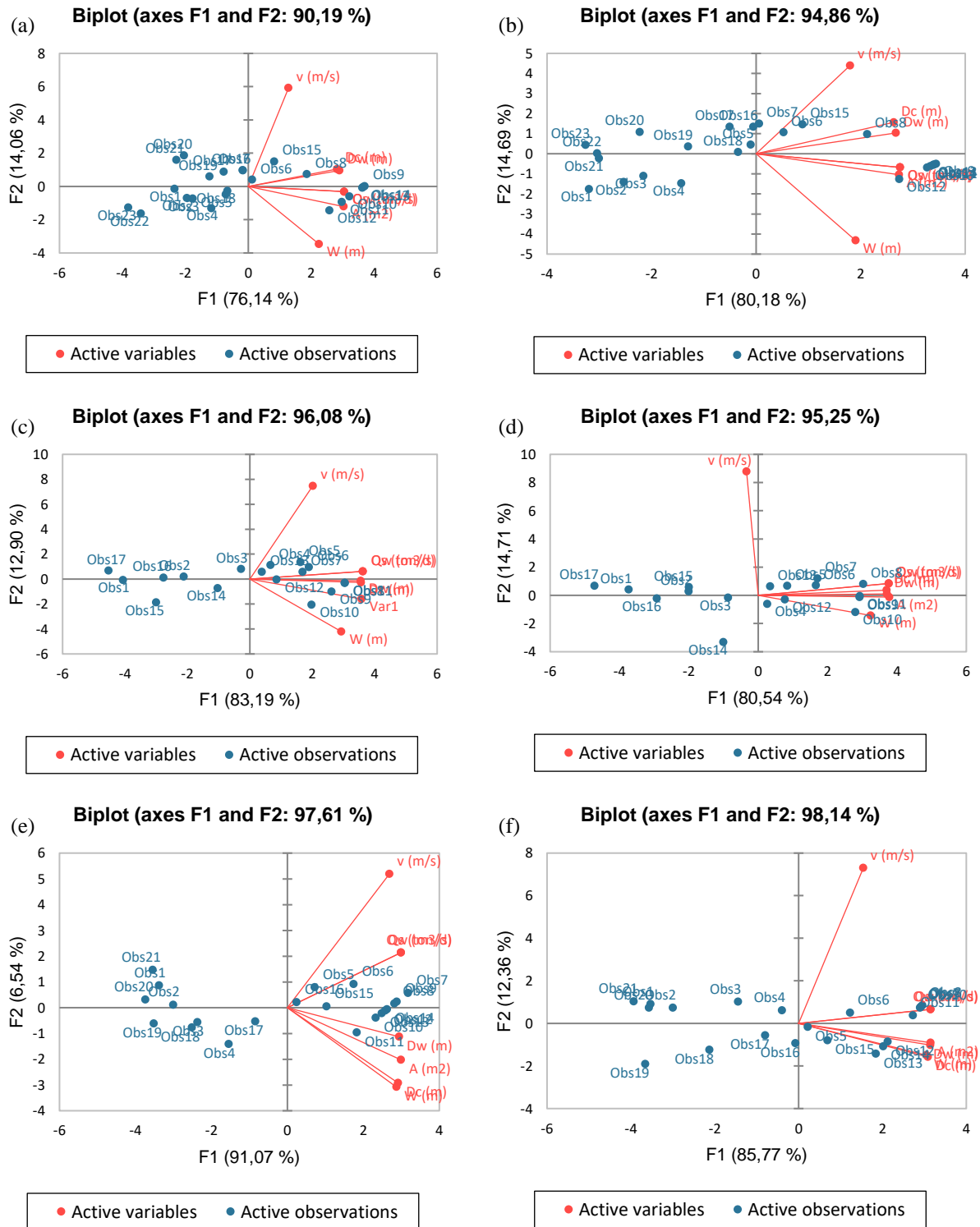
Figure 4. 51 (a-d): PCA Analysis in Biplots at Montante Sector for DS and WS

Water flow velocity, water discharge and sediment discharge followed similar pattern for DS and WS, despite some slight differences. For the cross-section profiles in relation to sedimentation, a slight increase in water discharge and sediment discharge were observed and this turned to be higher at the mid of the canal. Similar findings are reported by other works (Jaiyeola & Adeyemo, 2019; Lanzoni, 2008; Nokes et al., 2019). Additionally, the Node station showed similarities on the canal depth, in contradiction to the water depth and water

level, which were the same. WS had the highest water depth and level, and the canal shape presented changes in shape, possibly due to erosional pressure. At FIPAG though, the water depth went up to 3.0 m in DS and 3.5 m during the WS. Water velocity and discharge as well as the sediment discharge followed similar pattern, with water discharge and velocity having direct influence on the sediment discharge (Chen et al., 2018). At the Montante sector, the high water discharge and sediment discharge appeared to be higher at the centre of canal with slight leaning to the EB. For the Sul sector, Lionde station appeared to have a well stabilised canal cross-section, whereby during the DS, less water was recorded than in the WS. A positive relationship was established between water discharge and water sediment, for which it was observed that the higher the water discharge, the higher the sediment delivery (Kumar et al., 2018; Liu et al., 2017; Vargas-Luna et al., 2019; Wu et al., 2018).

Sul Sector

For Lionde sampling station, F1 explains 76.14% and 80.18% of variability, for DS and WS, respectively. Dw and Dc, Qs and Qw, are very closely correlated each other, similarly to A and w, in DS and WS, in general. F2 in this station, both for DS and WS, explains 14.06% and 14.69%, respectively. Water velocity (v) is positively correlated to F2. On the other hand, Massawasse station, has F1 explaining 83.19% and 80.54%, for DS and WS, respectively. Positive correlation was found, for DS, with w, Dc, Dw, A, Qw and Qs. F2 which explains 12.90% and 14.71%, in DS and WS, respectively, has positive correlation with water velocity (v). During WS, F1 presents positive correlation with w, Dc, Dw, A, Qw and Qs. F2 had a positive correlation with water velocity (v). In the Conhane station, F1 explain 91.07% and 85.77% of variance between variables. F1, in DS, have positive correlation with all variables in study, w, Dc, Dw, v, A, Qw and Qs. But for WS, F1 has positive correlation with variables, except with water velocity (v), which is well associated with F2. These findings allow to infer that sedimentation in the Sul Sector of CIS remain associated with hydraulic processes taking place in the main canal (Delleur, 2014), especially, water depth, canal width, water and sediment discharges. Figure 4.52 presents biplots for Sul Sector in both seasons.



Dry Season (DS)

Wet Season (WS)

Figure 4. 52 (a-f): PCA Analysis in Biplots at Sul Sector for DS and WS

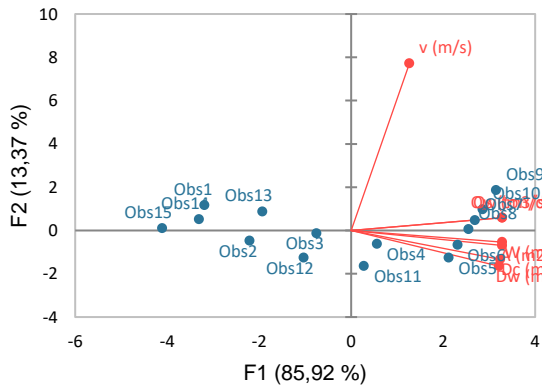
In Massawasse station, water velocity and water discharge were found to be very high, hence high sediment discharge. The depth of the water varied from 1.8 to 2.2 m, in DS and WS,

respectively. The canal cross-section seemed to be very stable as well. The Conhane station was the only one in the sector having lowest depth of water, as it ranged from 1.35 to 1.8 m, for DS and WS, respectively. Water discharge and sediment increased throughout the cross-section as it moved from one bank to the other. Similar pattern was found in the Rio sector, where Nico's water depth was almost the same at around 2 m, in both seasons. The water depth at Muianga and Marrambajane were approximately 2.2 m and 1.9 m respectively. From the graphs one can observe a linear relation between water flow and sediment, whereby as water flow increases, the amount of sediment also increases. Thus, the increment in water velocity led to increment in water flow.

Rio Sector

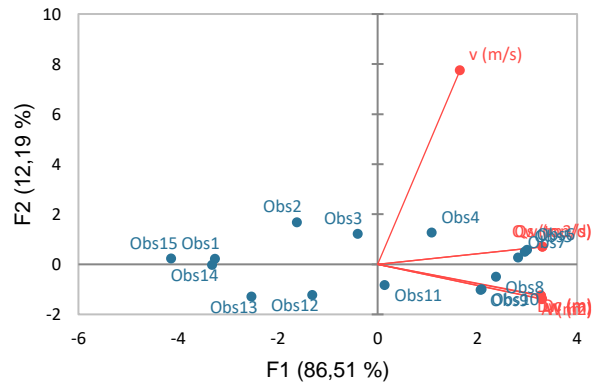
At Nico station, F1 contributes to explain 85.92% and 86.51% for DS and WS, respectively. F2 contribute with 13.37% and 12.19%, also for DS and WS, respectively. In both seasons, F1 presents positive correlation with w , D_c , D_w , A , Q_w and Q_s , and for F2, good correlation was found with water velocity (v), for Nico, Muianga and Marrambajane sampling stations. F1 in Muianga explains 86.23% and 85.55%, for DS and WS, respectively, and F2, explains 10.41% and 10.65%. But in Marrambajane, F1 was found explaining 83.12% and 85.85%, for DS WS, respectively, and F2 with 15.68% and 13.04%. In Figure 4.53 is presented the biplots at Rio Sector for both seasons.

(a) Biplot (axes F1 and F2: 99,28 %)



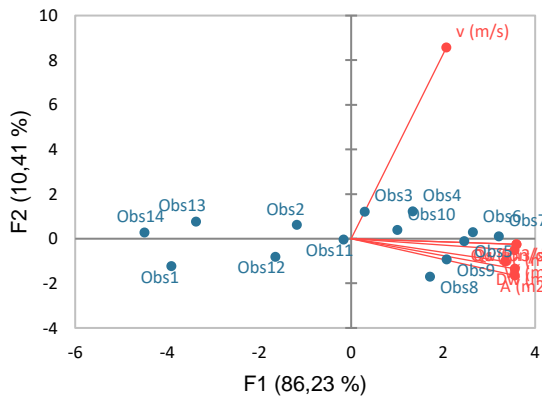
● Active variables ● Active observations

(b) Biplot (axes F1 and F2: 98,70 %)



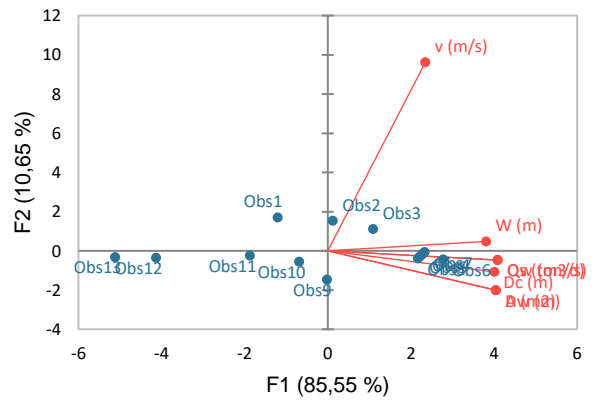
● Active variables ● Active observations

(c) Biplot (axes F1 and F2: 96,64 %)



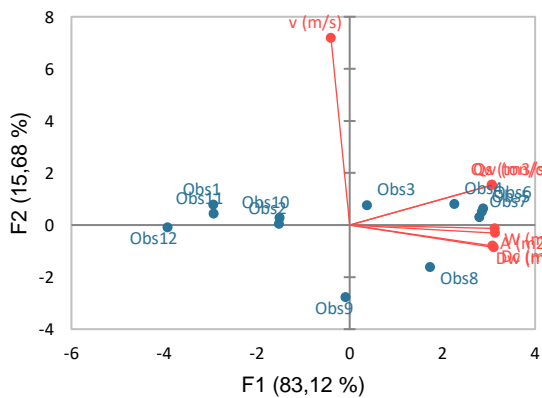
● Active variables ● Active observations

(d) Biplot (axes F1 and F2: 96,20 %)



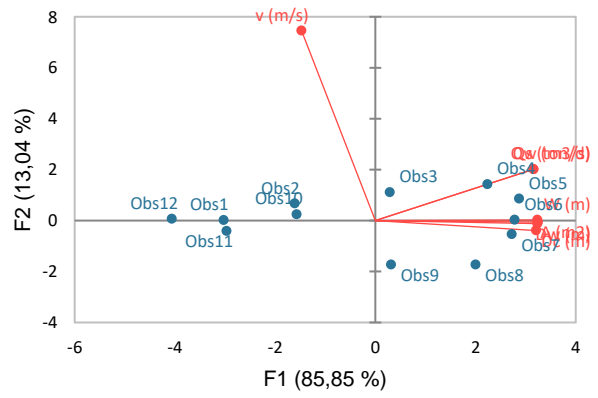
● Active variables ● Active observations

(e) Biplot (axes F1 and F2: 98,80 %)



● Active variables ● Active observations

(f) Biplot (axes F1 and F2: 98,89 %)



● Active variables ● Active observations

Dry Season (DS)

Wet Season (WS)

Figure 4. 53 (a-f): PCA Analysis in Biplots at Rio Sector for DS and WS

4.2 Temporal Trends-Dynamics of Water Flow and Sediment Flux

4.2.1 Water Flow

The temporal distribution of water discharge trends was recorded in all sampling stations from 2004-2005 and 2018-2019 period. Figure 4.54 shows the Montante sector water discharge distribution, at Intake, Railways-Node and FIPAG stations for both DS and WS.

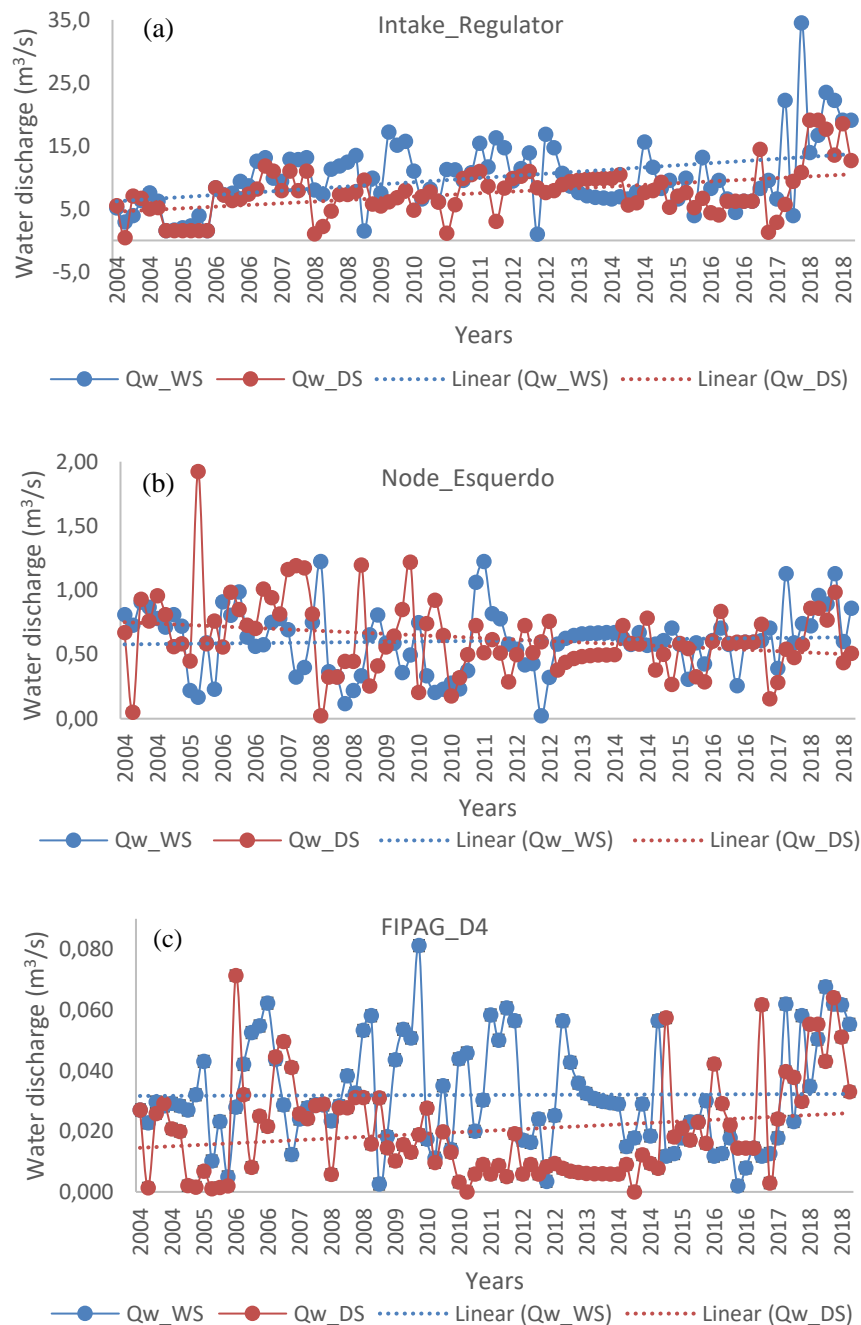


Figure 4. 54: Water Discharge for Montante Sector Sampling Stations

Samples for water discharges from the main Intake station were taken from the Regulator point, and for the Node station, at Esquerdo canal point. Whereas, for the FIPAG station, sampling took place at distributor 4 (D4). Results present Intake station as having higher water discharge values for every year during DS. Low peaks between 0-5 m³/s for DS were observed in 2004, 2005, 2008, 2010, 2011 and 2017. On the other hand, high peaks ranging from 10-35 m³/s for WS were recorded in 2011, 2012, 2013, 2017 and 2018. WS shows a positive trend as compared to the DS. Moreover, for Node station, the years of 2008 and 2017 presented considerable values of water discharge during WS, ranging from 1-2 m³/s. In 2005 during DS, about 1.9 m³/s was observed, being the highest. WS had a positive trend while the DS showed a negative trend. At the FIPAG station, water discharge above 0.03 m³/s for WS, and 0.015 m³/s for DS, were recorded. Both seasons had positive trends. Peaks were observed in 2006, 2007, 2010, 2011, 2012, 2014 and 2018, in both seasons. Water discharge was found to decrease as it flows downstream of the canal. These findings are consistent with findings from other similar works (Tena et al., 2012; Aksoy et al., 2013; Schmalz et al., 2015).

Sampling stations at Sul sector, presented positive trends for both seasons, whereby observed water discharge reached around 14 m³/s, 1.8 m³/s and 1.2 m³/s, for Lionde, Massawasse and Conhane, respectively. As it can be observed in Figure 4.55, similarly to the Montante sector, water discharge decreased with distance towards the downstream. Canal bed deformation due to sediment deposition, which in turn causes its flatness, is thought to be behind slowing the water flow and increasing sediment deposition (Salmasi et al., 2018), as the opportunity time for particle fall, increases. In general terms, water flow decrease at the downstream points of each reach is expectable, since during the flow process, irrigators are using water, and therefore causing reduction of flow downstream.

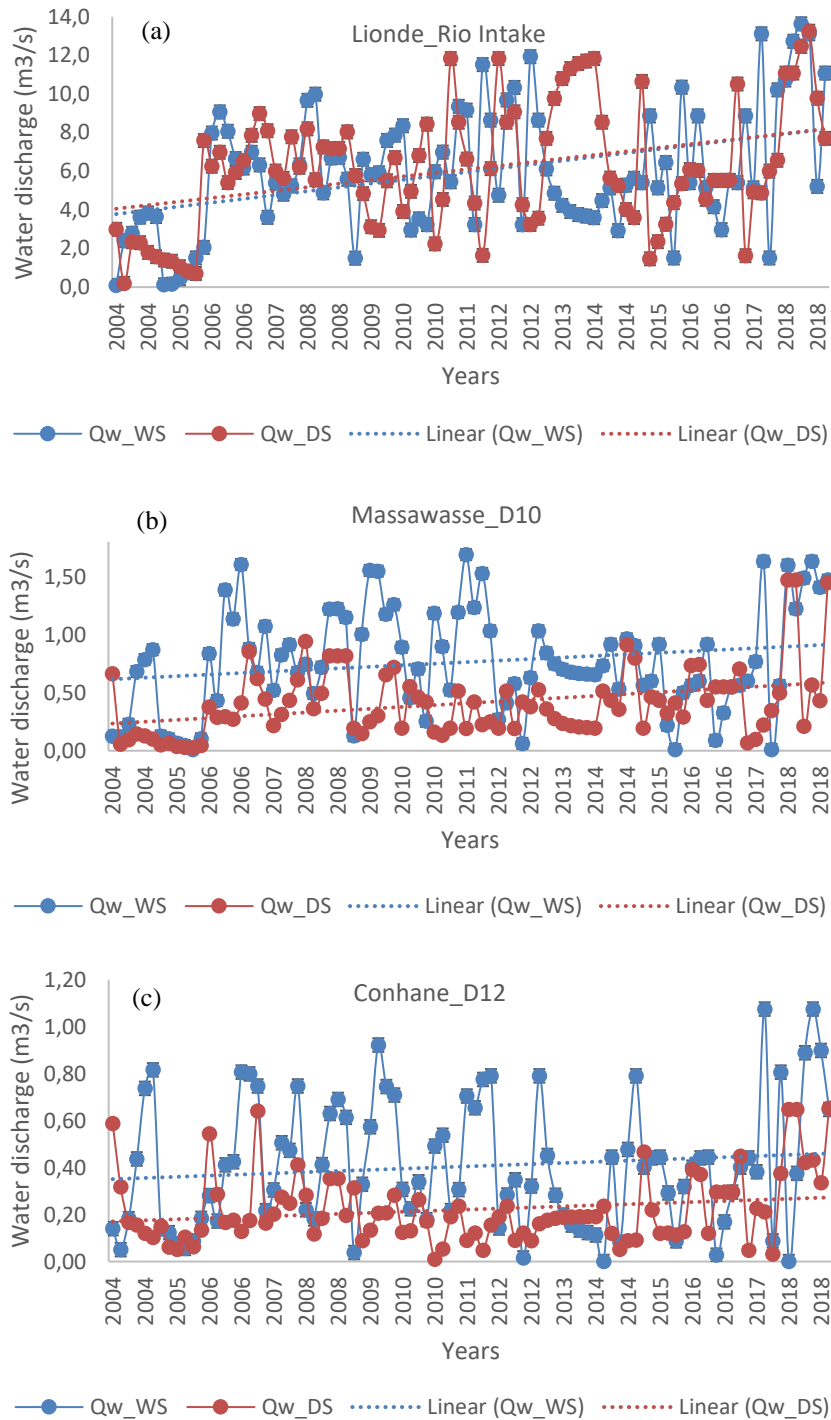


Figure 4. 55: Water Discharge for Sul Sector Sampling Stations

On the other hand, for the sampling stations located at the Rio sector, as shown in Figure 4.56, the trends exhibited a decrease in both seasons. Water discharge reached 0.5 m³/s for Nico and Muianga stations, and 1 m³/s at Marrambajane. An opposite trend was observed in

the other sectors. This is according to expectations, as water is withdrawn and used for irrigation, causing reduction of water flow in this part of the scheme, which happens to be the most downstream.

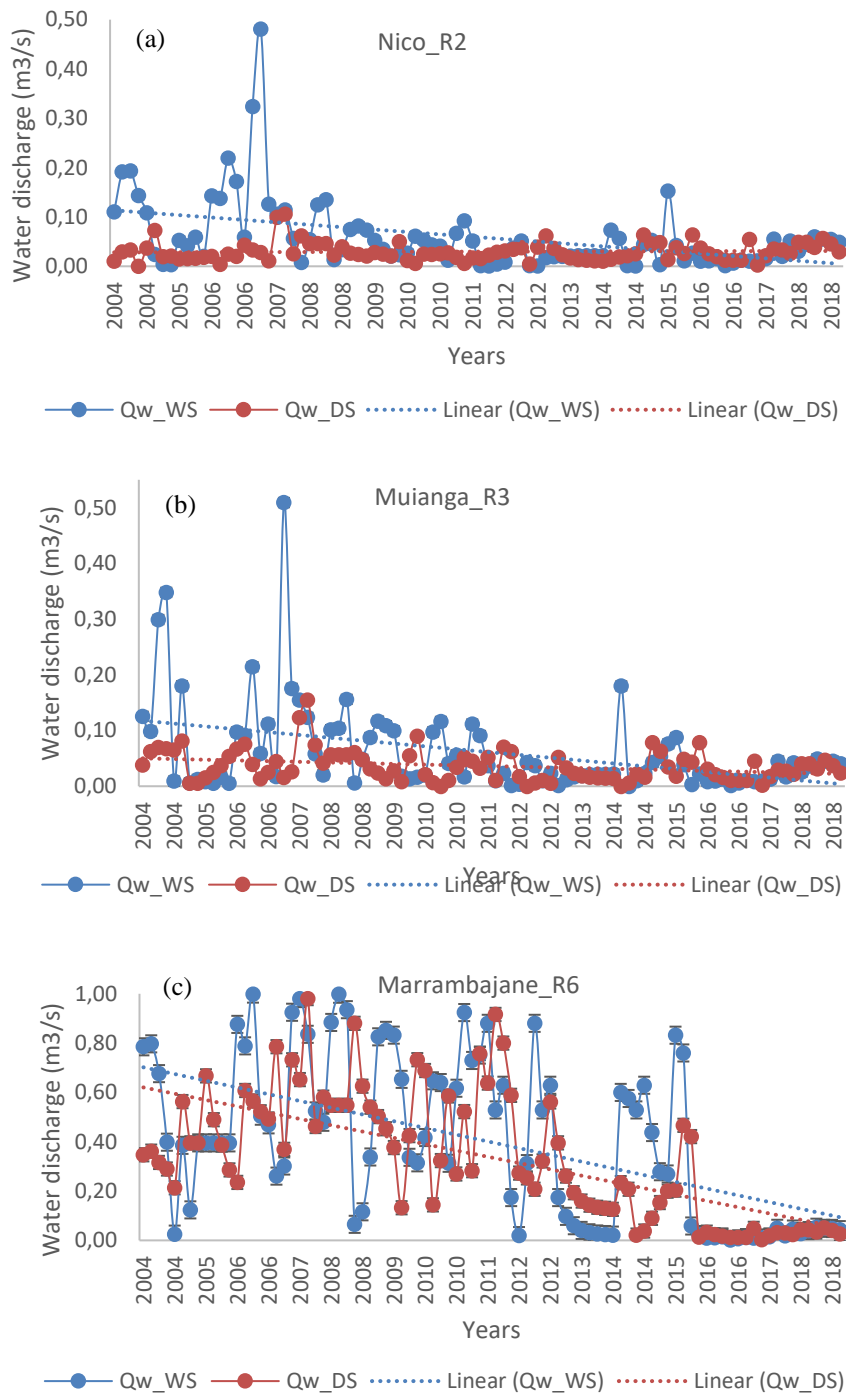


Figure 4. 56: Water Discharge for Rio Sector Sampling Stations

4.2.2 Sediment Flux

When assessing water discharge relationship with sediment flux, using a fitted line plot equation for the sampling station at Intake and Offtake, a close relationship was established. This means that the sediment flow was positively explained by water discharge, then the relationship generated was applied to predict sediment amount at the stations, from 2004-2005 season to 2018-2019. Figure 4.57 shows water discharge (Q_w) and sediment discharge (Q_s) for DS and WS at the Intake (a) and Offtake (b), from 2004-2005 to 2018-2019 period.

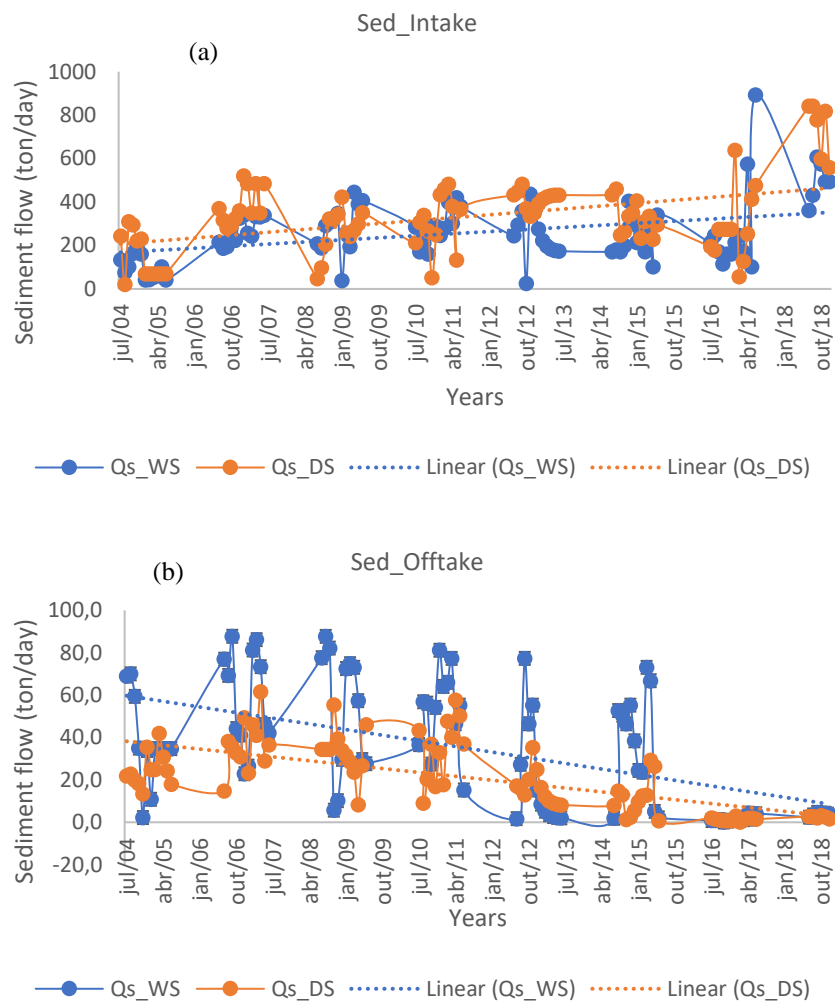


Figure 4. 57: Sediment Flow (Q_s) for DS and WS at Intake and Offtake, from 2004-2005 to 2018-2019 Period

At the Intake the sediment load flow is relatively high than at the offtake, while a direct proportionality between the water flow and sediment flow was also observed. The amount of

water flow and the respective sediment tend to increase. For example, from approximately 200 to more than 800 ton/day in WS, and from nearly 100 to 700 ton/day in DS, for the 2004-2005 and 2018-2019 period. On the other hand, at the Offtake, the sediment discharge presented a surge in peaks occurring with time. From 2015-2016 to 2018-2019 period, sharp decrease in sediment was observed at the most downstream of the system. This may be credited to the desilting activities in canal when the rice production program was relaunched in the CIS by the Government. This demanded increment in the areas and access to water by the farmers. Apart from this, in general terms, CIS is currently receiving less water inflow compared to the previous years. As a result, low water inflow in the CIS should be accounted for, given that less water inflow, lead to less turbulence and water motion which is responsible for sediment detachment and erosion.

In general, from the time series of both water flow and sediment discharge, it is clear that both present deterministic linear trends and periodicities or stochasticity. These models were carried out considering the fact that the CIS being a regulated canal flow artificial by virtue, and not natural water stream, the flow process is composed of deterministic events, in its large extent. However, given the fact that the main canal is used, not only to convey water, but also to store it, the models assumed occurrence of the stochastic events, too. Additionally, gravity-driven irrigation processes, are very much close to the ones taking place in the unregulated streams.

4.2.3 Fourier Transform

For Water Discharge

The Fourier Transforms (FT) were first employed to analyze the periodicities of the yearly water discharge series at CIS, for the three hydraulic sectors covered in this study. Results are shown in Figure 4.58.

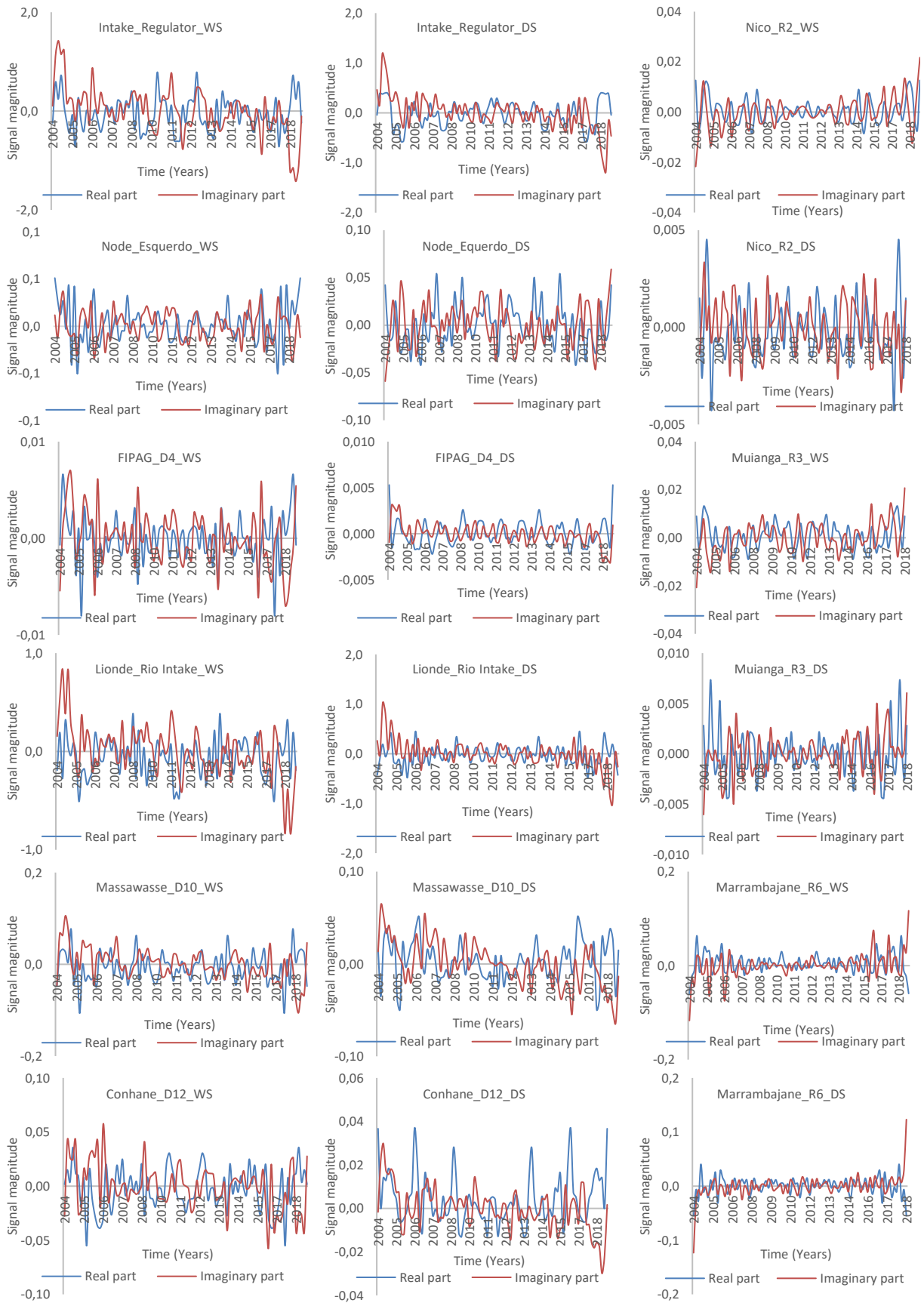


Figure 4. 58: Fourier Transform for Water Discharge at Intake-Massawasse Reach

Water discharge at Intake during WS has a presence of annual oscillations for 2004-2005 and 2018-2019 periods. During this period, high frequency of real signals appears to be above zero before 2010, and high imaginary signals is observed after that exact year. Similarly, for DS, both signals were closer to zero, except at the beginning and at the end of the two periods. The maximum signal amplitude in both seasons were around $2 \text{ m}^3/\text{s}$. This means that water flow varying in such magnitude may influence farming activities positively due to considerable amount of water made available. However, despite the dry years, in general at CIS, water availability is not a problem, as Macarretane dam offer some resilience capacity. But the water conveyance infrastructure, which are mostly degraded impose some degree of challenge, even during water abundance. During WS, at Intake station, on average, high amplitude of water occurred every 2-4 years, with a magnitude of $0.6\text{-}1.0 \text{ m}^3/\text{s}$. During DS a peak frequency was scarcely observed, except in some years, where significant streamflows were registered at almost every 3 years within the season, with a magnitude of $0.2\text{-}0.35 \text{ m}^3/\text{s}$ maximum. In the normal hydrologic year, during DS a normal flow of $0.22 \text{ m}^3/\text{s}$ is commonly observed.

The real and imaginary signals at Node sampling station, during both seasons, was found to have maximum signal amplitude of $0.1 \text{ m}^3/\text{s}$, which can be translated to 100 litres per second. This amount is relatively small for the size of the section, but could be as a result of the steep slope that allows water to flow rapidly downstream. In WS the real signal was relatively lower than the imaginary signal, except at the end of the period, in 2017. Similar pattern was observed during DS, except for 2007, 2009, 2010, 2016, 2017 and 2018. The phase (or frequency) of water discharge peak in the Node station, was found to be of nearly every 2 years in both seasons, but with differences in magnitudes. Water discharge magnitude in the WS ranged between $0.02\text{-}0.04 \text{ m}^3/\text{s}$, whilst in DS it was found to range between $0.04\text{-}0.08$. This peculiar fact at this station, where more water flow was observed during DS other than in WS, may have resulted from the fact that in this point there is water diverting structure transporting water for other areas covered by the scheme. So, during DS, normally there is relatively small inflow, and increased water demand in the referred downstream areas, made it to register more water.

For FIPAG, Lionde, Massawasse, Conhane, Nico, Muianga and Marrambajane sampling stations, the real signals appeared to be above the imaginary part and above zero line, for some years. The real and imaginary signals denounced the magnitude and yearly frequency of the data set, except for the start and the ending of the referred period which is considerably high. However, the magnitudes and frequency of water discharges varied considerably from station to station. The FIPAG magnitude and frequency ranged at 0.03-0.04 and 0.0018-0.0022 m³/s, 4-5 and 2-3 years, for WS and DS, respectively. For the Lionde station, from 0.2-0.55 m³/s and 2-4 years, for both seasons. The fact that Lionde station is located at a point where a diverting structure is, to convey water to the Rio sector water supply makes this point receiving significant amount of water, in both seasons, but significantly at DS, in order to cope with irrigation demands downstream. Therefore, the amount of water appears well high than from the previous two sampling stations.

For Massawasse sampling station, a magnitude and frequency of 0.04-0.09 and 0.04-0.07 m³/s, and 2 years, were registered, for WS and DS, respectively. While for Conhane, 0.02-0.045 and 0.015-0.035 m³/s, 2 years and 1-2 years, for WS and DS were observed respectively. Nico, on the other hand, presented 0.012-0.02 and 0.0015-0.0043 m³/s, and 1 year, for both seasons, respectively. While Muianga had 0.019-0.020 and 0.0002-0.00075, 1-2 years, for WS and DS, respectively. Finally, Marrambajane maximum magnitude was of 0.04-0.070 with an phase of approximately 10 years. Small peaks were found in this station as having high frequency and were found to be of 0.1-0.13 m³/s magnitude and 1-2 years of frequency for WS. During DS a magnitude of 0.03-0.05 and 1-2 years was observed. Here, attention should be paid to the fact that Marrambajane is an outlet point downstream of the entire irrigation scheme, and therefore accumulating significant amount of water from the upstream side.

Liu et al. (2012) investigated the spatial and temporal variability of water discharge in the Yellow River Basin over the past 60 years, using continuous wavelet transform (CWT) and Mann-Kendall (MK) test methods and identified spatial and temporal variation patterns at different levels of magnitudes and frequencies, within the basin. Their study also found that the periodic oscillations in water discharges had occurred at the temporal scales of 1-, 2- to 4-, 6- to 8- and 10- to 22-years. But this current study show that sediment load follows water

discharge pattern at a magnitude of around 2-, 3-, 4- to 5-years. Comparison between Yellow River basin and CIS may be seen as unreasonable given that Yellow River basin is a natural hydrological system whereas CIS is a controlled flow system. However, such comparison was performed with aim of only taking into consideration the application of the MK test method used in their study for analysis of water body behaviours and not much on the type of the system, which are different in size and water controlling regime and type.

For Sediment Flux

The Fourier Transform (FT) for the sediment discharge during WS indicated the Intake station as having the real part signal starting at around 5 ton/day and drops to a of magnitude of 20 ton/day. The waves phase also called the frequency, of 2-4 years recurrence was observed. For the DS, however, the magnitude ranged 0 to 18 ton/day with an observed frequency of 1-2 years. This can be an indication that the sediment discharges of such magnitude as 5 and 20 ton/day, for WS and DS, has a recurrence interval of 2-4 and 1-2 years respectively. At the Offtake, the magnitude was much lower, as result of water abstraction that causes reduction in the stream and consequently the sediment discharge. During WS, a maximum magnitude of 5 ton/day was reached with a frequency of approximated 3 years, while the DS had an magnitude of 2 ton/day maximum and frequency of 1 year. It was observed that the DS presented reduced frequency than the WS, as observed in Figure 4.59.

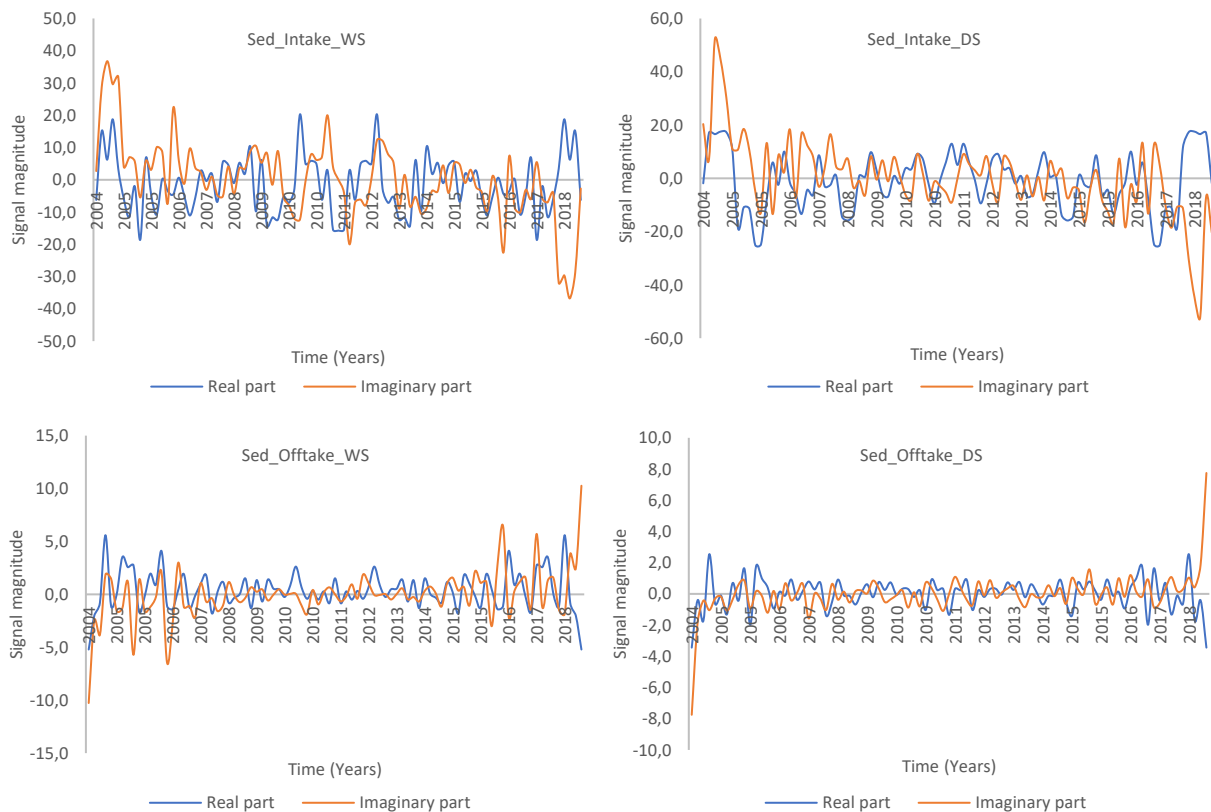
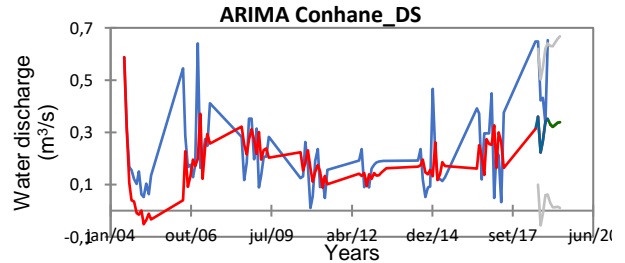
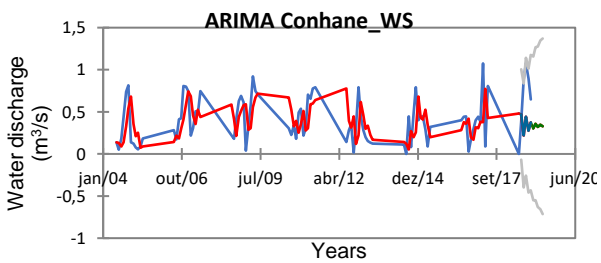
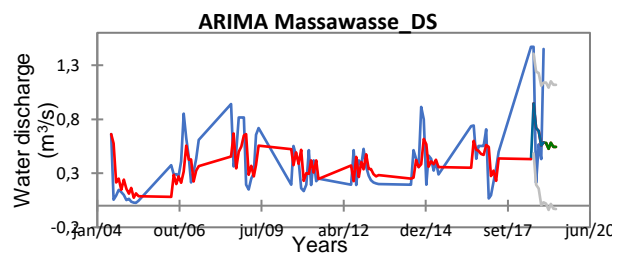
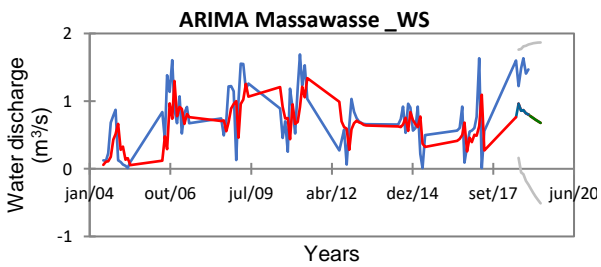
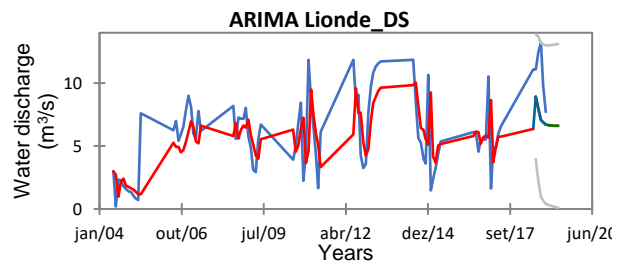
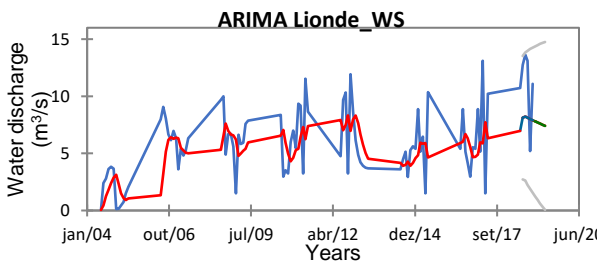
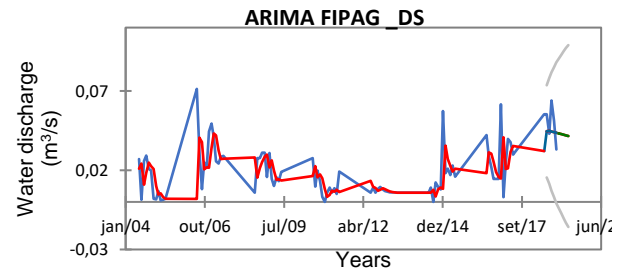
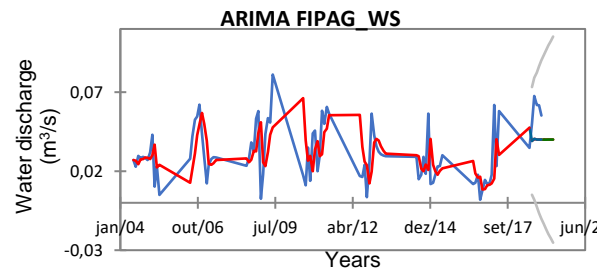
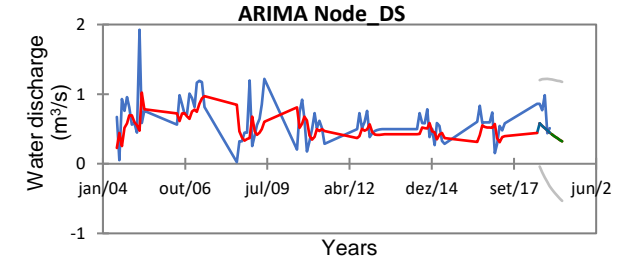
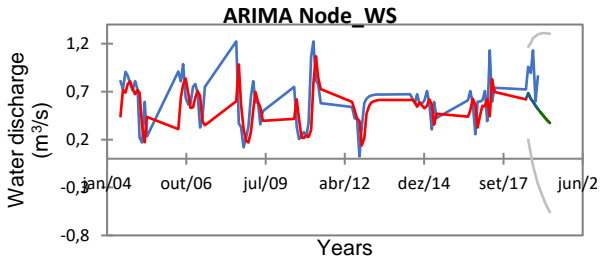
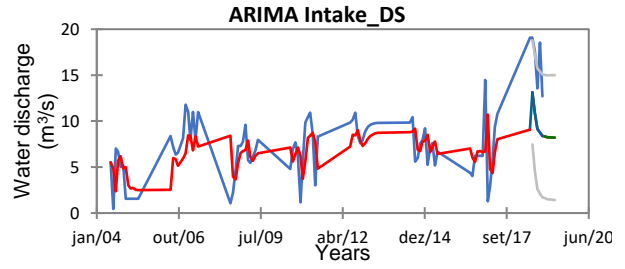
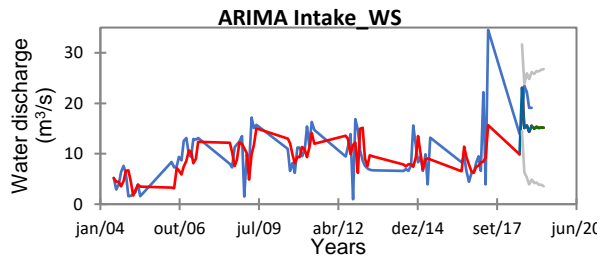


Figure 4. 59: Fourier Transform for Sediment Discharge for the Main Intake and Offtake Reaches

4.2.4 ARIMA Test

For Water Discharge

Apart from Fourier Transform (FT) that is used in assessing the spatial and temporal trends, a complementary analysis of Auto Regressive Integrated Moving Average (ARIMA (p,d,q)) was performed, using the model parameters of $p=1/d=0/q=0/P=0/D=0/Q=0/s=0$ for model training, at a confidence interval of 95%. Therefore, the performed analysis was ARIMA (1,0,0) also called first-order autoregressive model for pre-modeling. Where p is the number of autoregressive terms, d is the number of non-seasonal differences needed for stationarity, and q is the number of lagged forecast errors in the prediction equation. The test considered preliminary estimation based on Yule-Walker, with the optimization likelihood (Convergence=0.00001/Iterations=500). The number of validation and prediction was 5. Once the model training was performed, then the actual modelling was considered, the results are as presented in Figure 4.60.



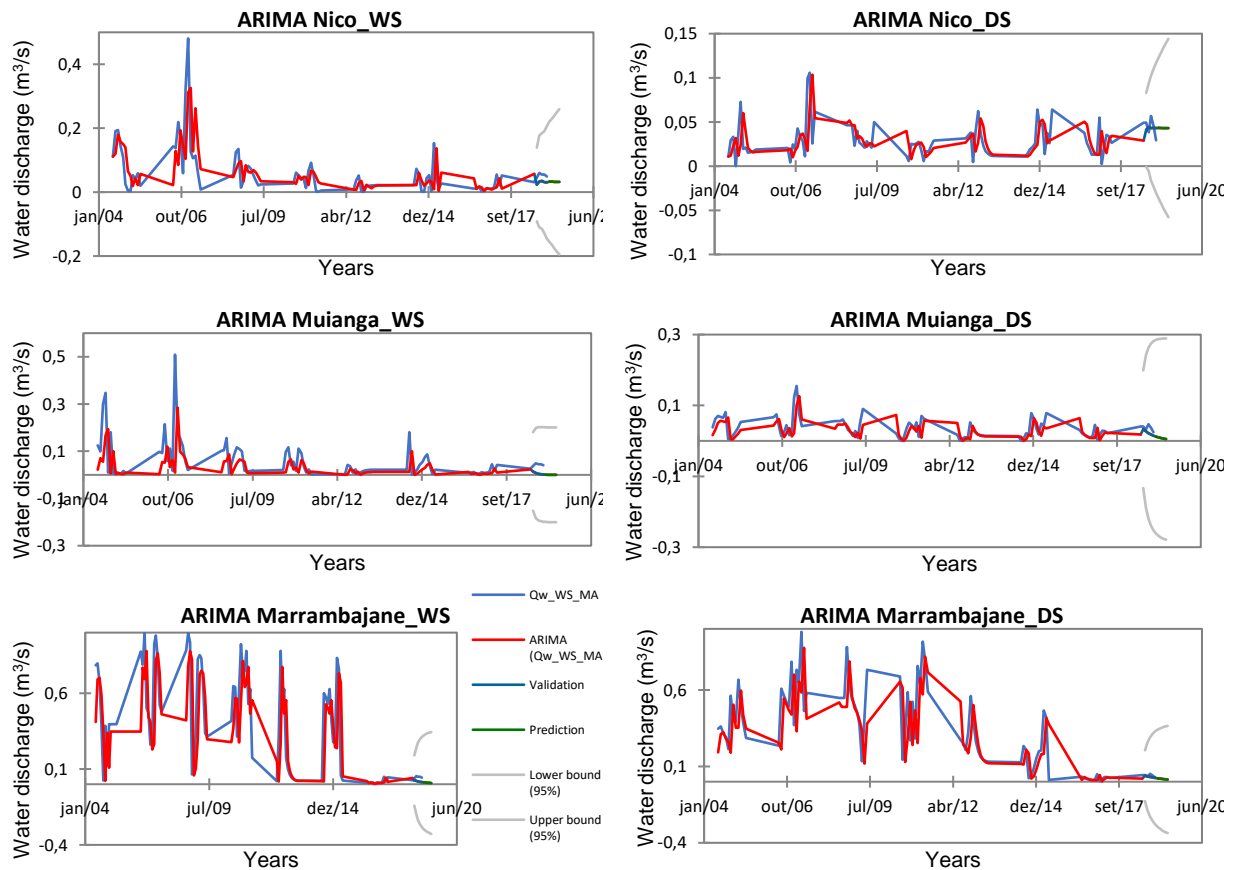


Figure 4. 60: ARIMA Test Analysis for Each Sampling Stations

In this work, the Augmented Dickey–Fuller (ADF) test was used to test the stationarity in the original annual water discharge time series and the decomposed annual water discharge series. It was observed that all the series were non-stationary. Therefore, these series were eligible for ARIMA modelling to be applied over them, except for series represented by Node and Muianga, in both seasons, and Lionde in the WS. This therefore indicate that, except for these five stations, all other dataset had no unit root effect in the sample dataset and it needed no differentiation in the original annual water discharge time series. Hence, requiring no decomposition of annual water discharge time series from nine of the sampling stations. They were suitable for ARMA model. After the first order difference of the original data of Node, Muianga and Lionde, the ADF test showed that the transformed data was stationary. Therefore, a process of model identification in the second stage was performed. Once the stationarity test was performed, then the following step was to identify the model for each time series, as shown on the Table G1 in Appendix G. The adopted structure and parameters for the ARIMA models for water discharge, are presented in Table G2 in Appendix G. More

details on ARIMA models can be found in plots presented in Figures J.1 to J.9 in the Appendix J, provided for each sampling stations and their respective seasons.

The ARMA model consisted of model identification, parameter estimation and application. Among these steps, the identification step is important, and includes two stages: (i) if it is necessary, appropriate differencing of the series is performed to achieve stationarity and normality, (ii) the order of the AR and MA parts of ARMA model is identified. Yurekli & Ozturk (2003) employed the autocorrelation function (ACF) and the partial autocorrelation function (PACF) of the sample data as the basic tools to identify the order of the ARIMA model. When the sample data is an AR (p) model, the PACF cut-off is at lag p . On the other hand, if sample data is a MA (q) process, the ACF has a cut-off at lag q . However, the PACF and ACF method was not very useful when dealing with mixed ARMA processes. Simple inspection of the graphs of the ACF and the PACF would not, in general, give clear values of p and q for mixed models (Yurekli & Ozturk, 2003). Some other identification methods have been presented based on the information-theoretic approaches, such as the Akaike's Information Criterion (AIC) (Aydın & Memmedli, 2012; Bozdogan, 1987; Fujikoshi et al., 2005), the Bayesian Information Criterion (BIC) (Yurekli & Ozturk, 2003), the Final Prediction Error criterion (FPE) (Akaike, 1969), among others. In this work, the best fitted model was selected according to AIC, whereby, the smaller the coefficient, the better the model. Once an appropriate model is chosen, the parameters of the model were estimated by reading the value of the best fitted p - and q -values, in a trial and error procedure. Appendix J presents the Autocorrelogram (ACF) and Partial Autocorrelogram (PACF) and Autocorrelogram Residuals (ACFR) and Partial Autocorrelogram Residuals (PACFR), all of them before the identification models. Once the models were identified, the next step produced new models and, therefore, new ACF, PACF, ACFR and PACFR, respectively for each sampling station during both seasons.

For Sediment Flux

After the ARIMA test for the sediment discharges, it was found that at the Intake, for DS and WS, sediments followed well the ARIMA model gave good results for the sediments, and indicated good fit between the observed and the predicted ARIMA model data. The adopted structure and parameters of ARIMA model for sediment discharge at CIS based on AIC has

good fit for AR ($p=1$), whereby, at the Intake the ARIMA p -value was 0.822 and 0.932, for WS and DS, respectively. Whilst for the Offtake, the ARIMA p -value was 0.877 and 0.893, respectively for WS and DS. As previously referred, the Appendix J also presents ACF, PACF, ACFR and PACFR for the ARIMA model at Intake and Offtake for sediment discharge, at confidence interval of 95%. These parameters were used to assess the ARIMA model structures and p , d and q variables calculation, by trial and error procedures, as shown in the Table 4.11.

Table 4. 11: ARIMA Struct. and Parameters of Model for Sed. Discharge Based on AIC

Variable	Model Identification	Model Structure		AIC
		AR (p)	MA (q)	
Intake_WS	ARIMA (1,0,0)	0.901	0.000	978.996
Intake_DS	ARIMA (1,0,0)	0.904	0.000	1017.932
Offtake_WS	ARIMA (1,0,0)	0.879	0.000	733.653
Offtake_DS	ARIMA (1,0,0)	0.897	0.000	633.478

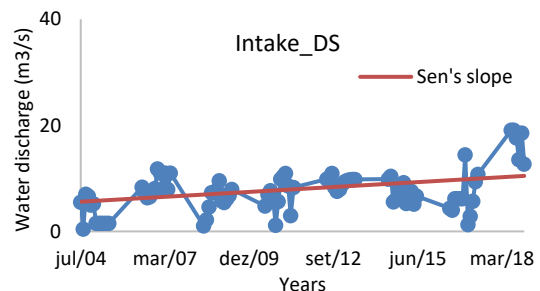
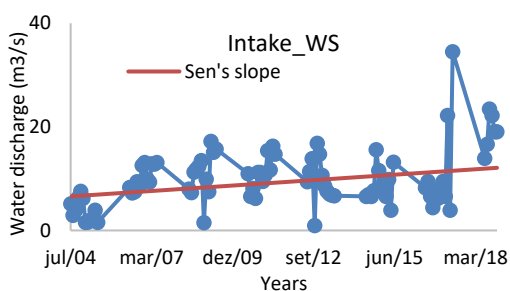
Test performed at confidence intervals of 95%

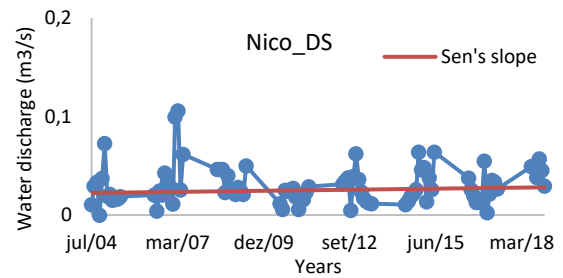
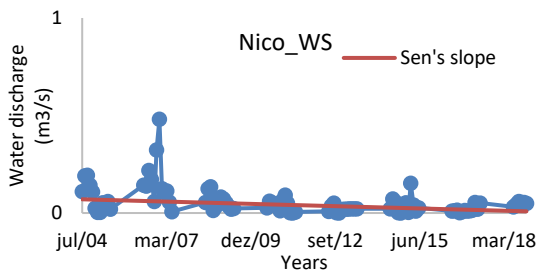
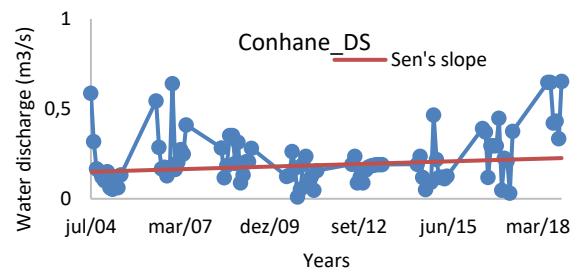
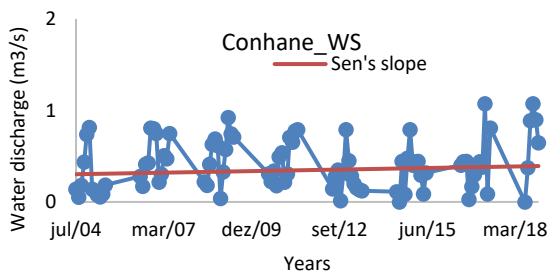
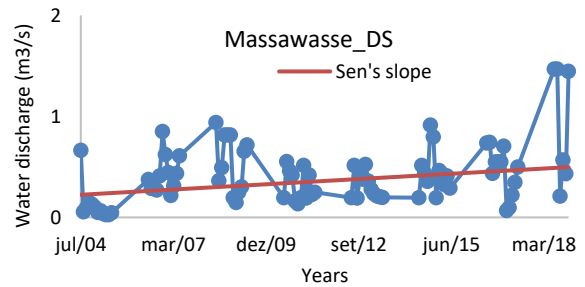
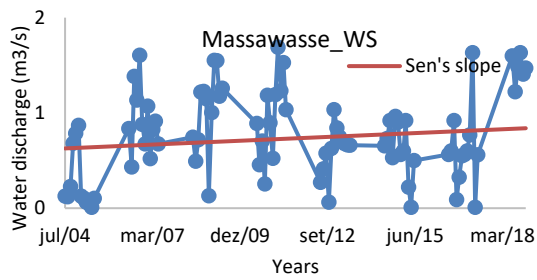
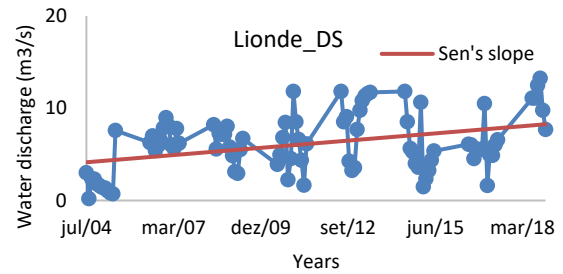
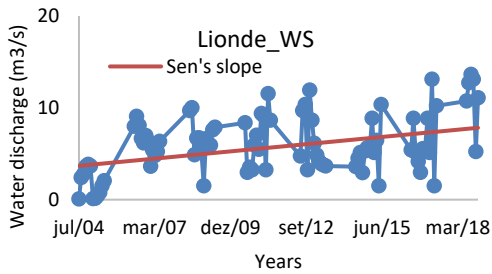
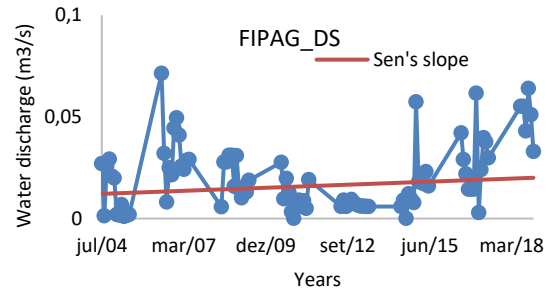
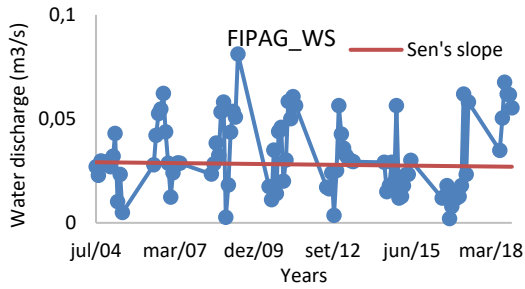
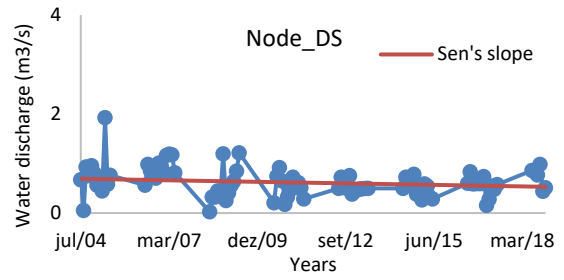
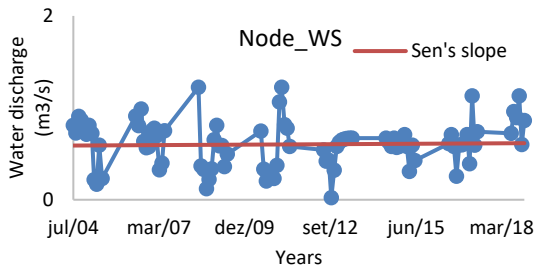
Optimization at Likelihood (Convergence = 0.00001 / Iterations = 500)

4.2.5 Mann-Kendall Trends

For Water discharge

Figure 4.61 presents Mann-Kendall (MK) test at 95% of confidence interval, whereby the Sen's slope and intercept are also given.





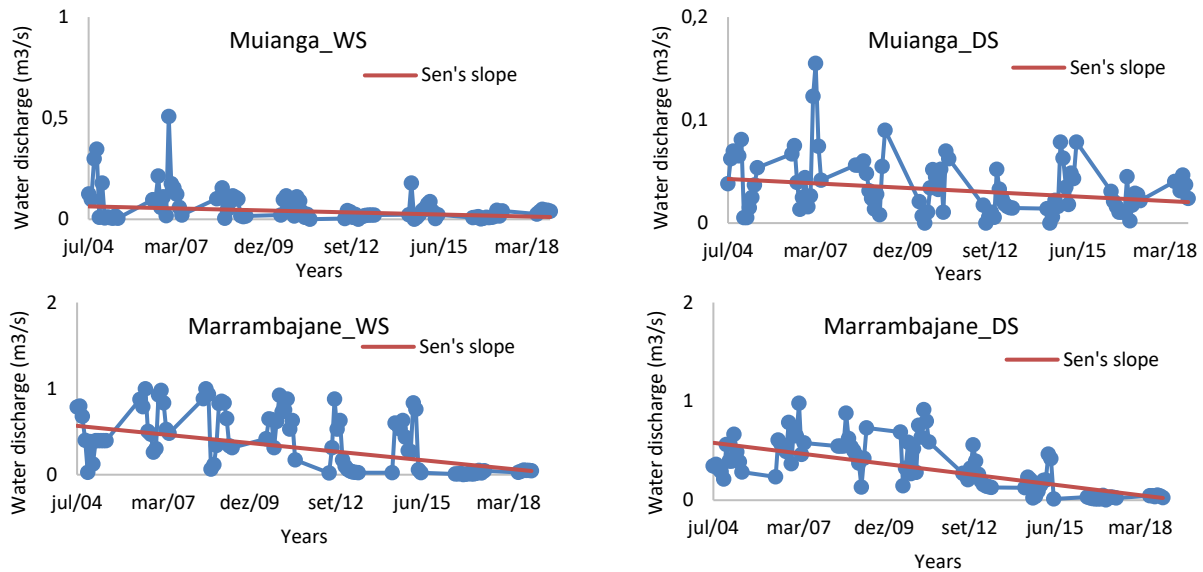


Figure 4. 61: Mann-Kendall Test and Sen's Slope Analysis for Water Discharge at CIS all Stations

The sampling stations that were tested performed well by presenting an indication of existence of trends. However, from the results it can be seen that only Lionde WS, Massawasse DS, Muianga WS and Marrambajane WS, showed trends that were statistically significant. Among the stations with significant trends, only Lionde and Massawasse presented increasing trend, whilst others exhibited decreasing trends.

Each MK plot present a Sen's slope, which captures the magnitude of the changes within the trends along the studied year. So, Sen's slope offers the insight of the magnitude of the trend with time. In this case, for the significant trends, they are either positive or negative. From the Table 4.16, it can be seen that at Lionde, Sen's slope was approximately $0.001 \text{ m}^3/\text{s}$ (1 l/s). While in Massawasse, Sen's slope was around $0.00005 \text{ m}^3/\text{s}$, which inclines towards zero (or 50 ml/s). The Muianga and Marrambajane, on the other hand, presented negligible value for their Sen's slope. This means that in these stations, changes in magnitude were very small and negligible in face of the total amount of water in the system. From these results, one can see that the increase in water discharge is of higher magnitude than the decrease in water discharge. Also, it shows the upstream of the scheme having increasing discharge while the downstream presents decreasing discharges.

For Sediment Flux

MK test for sediment discharge trends were not significant at 95% significance level, except for the Offtake in WS. However, though with no significant trend, the Sen's slope tend to increase at the Intake and decrease at the Offtake. The magnitude of these variations for Intake were 0.027 and 0.041ton/day (27 and 41 kg/day), during the WS and DS, respectively. However, for Offtake, the magnitudes were -0.009 and -0.007 ton/day (-9 and -7 kg/day), for WS and DS, respectively. Marrambajane station was the only station that presented significant trends for both water discharge and sediment. These results allow us to infer that in other stations such as Lionde in the WS, Massawasse in the DS, Muianga in the WS, significant trends could be observed as well. Figure 4.62 presents Mann-Kendall Test and Sen's Slope analysis of sedimente discharge for Intake and Offtake. Additional information is provided in Table G4 in Appendix G, which presents the MK analysis for sediment discharge.

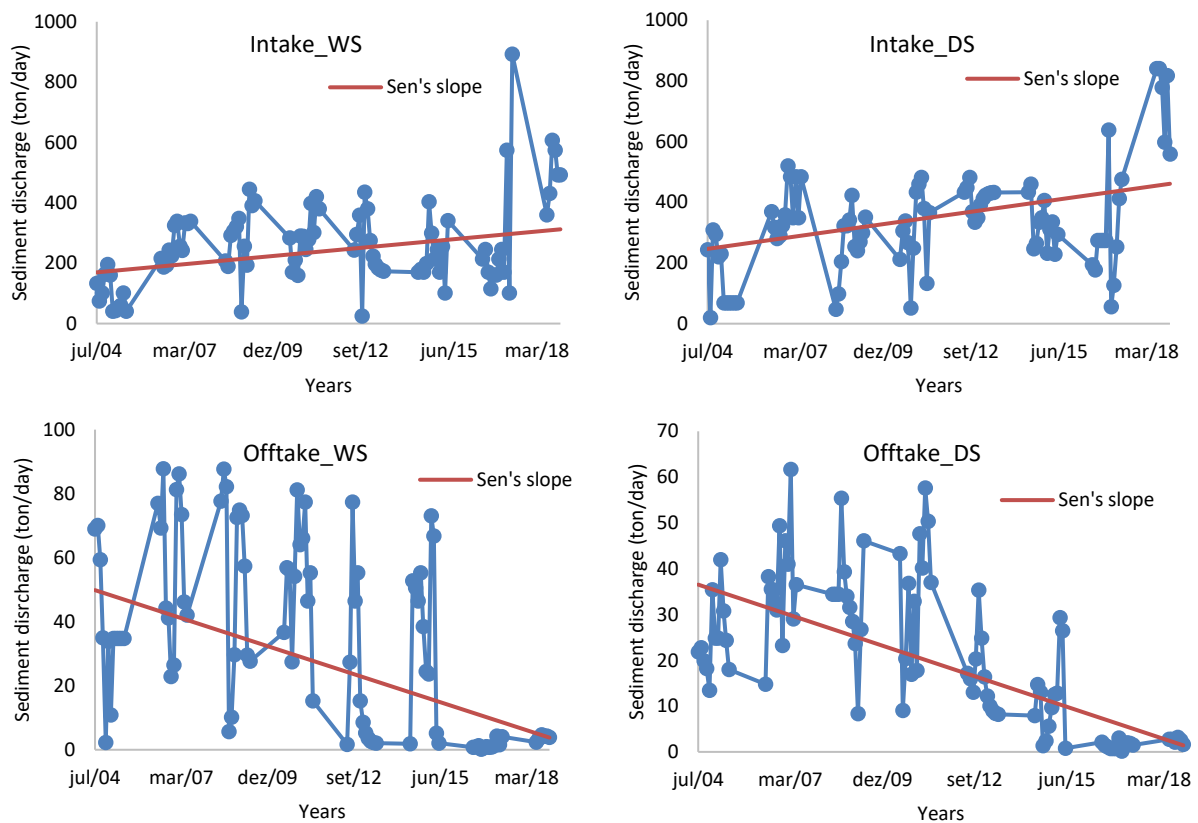


Figure 4. 62: Mann-Kendall Test and Sen's Slope Analysis of Sediment Discharge for Intake and Offtake

4.3 Influence of Water Flow on Sediment Settling Velocity

This section presents the influence of water flow on sediment settling velocity (SSV) at different depths of canal sections. Attention is paid to SSV as affected by sampling weeks, by particle grain sizes, water flow velocity versus canal depth, and canal depth.

4.3.1. Sediment Settling Velocity

The Figures 4.63, 4.64 and 4.65 show the sediment settling velocity for the sampling period for Montante, Sul and Rio sectors, respectively.

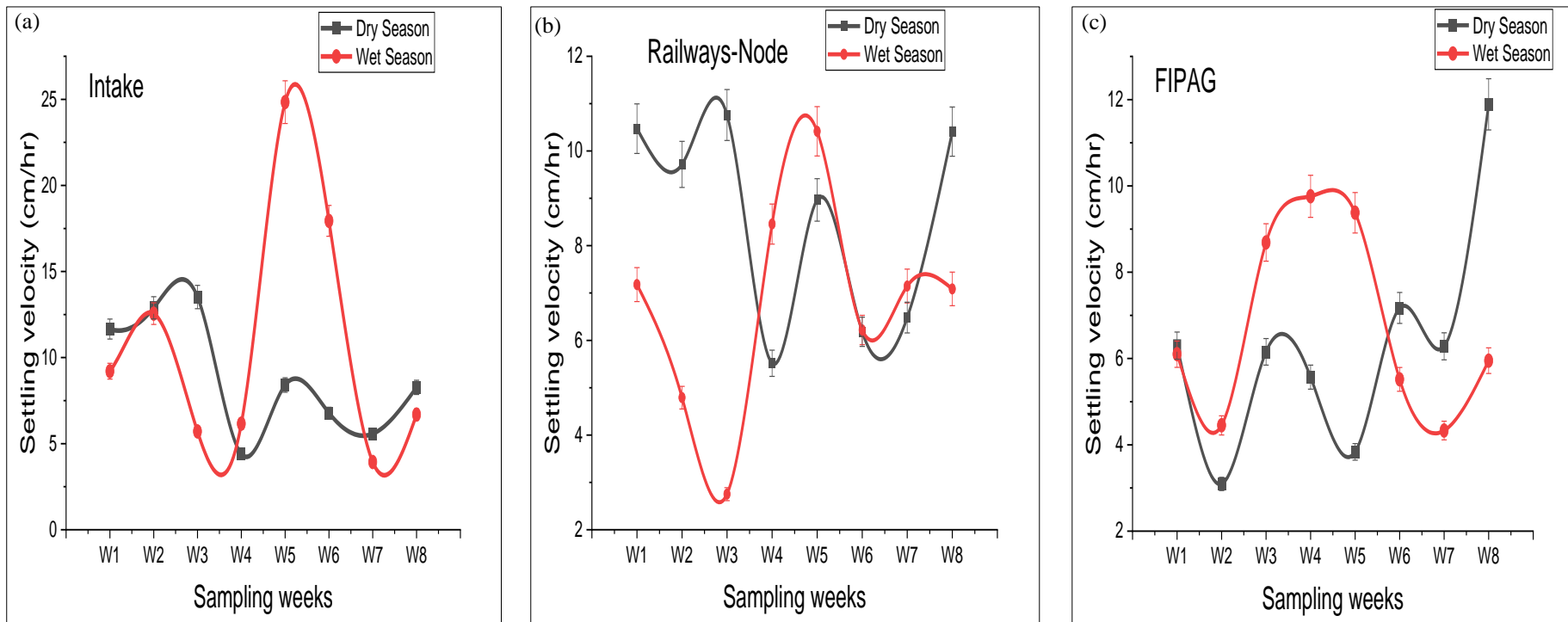


Figure 4. 63 (a, b & c): Sediment Settling Velocities Behaviour with Sampling Dates for Montante Sector During DS and WS

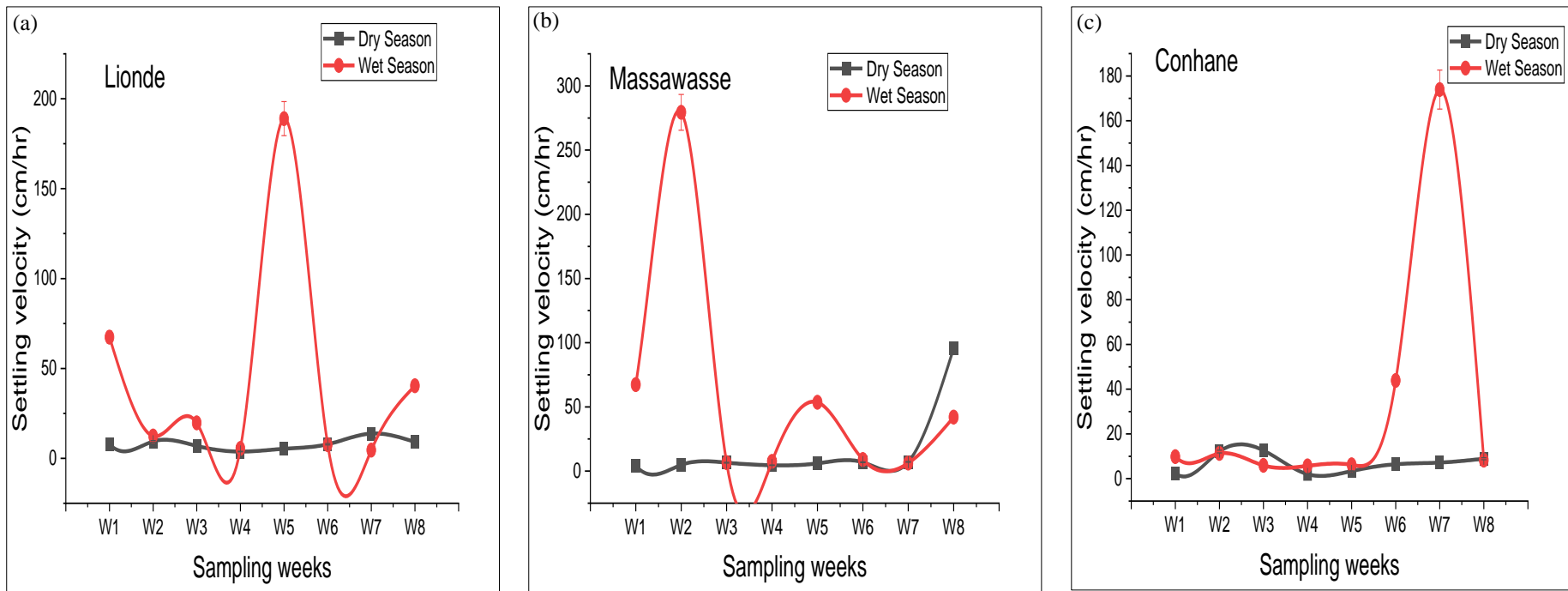


Figure 4. 64 (a, b & c): Sediment Settling Velocities Behaviour with Sampling Dates for Sul Sector During DS and WS

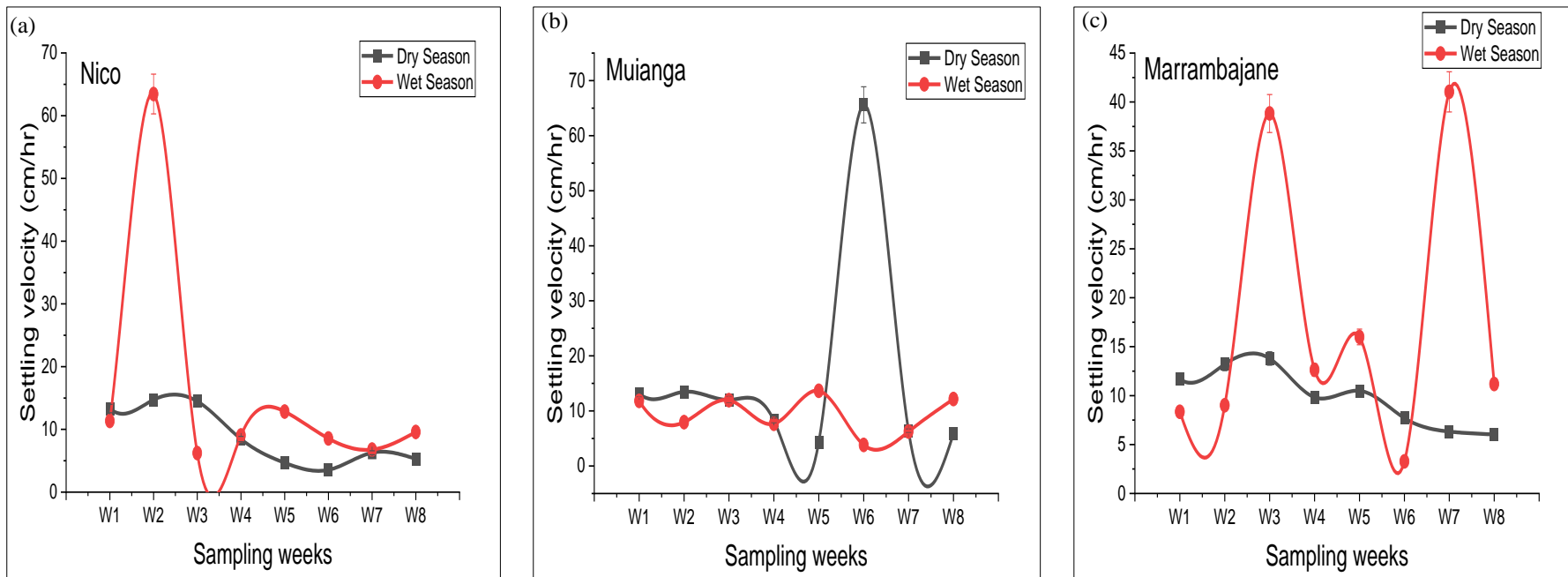


Figure 4. 65 (a, b & c): Sediment Settling Velocities Behaviour with Sampling Dates for Rio Sector During DS and WS

Plots a, b and c, in Figure 4.63, presents the sampling stations located in the upstream side of the scheme. Results suggest that SSV tend to be higher during WS than on DS, except for some weeks (W) at the Montante sector and also in Muianga station. The SSV varies temporally and spatially with the concentration and can be considered as one of the most important parameters in cohesive sediment transport. The physical sediment properties of sediment such as size, shape and specific weight are expressed as fall velocity. At Intake station, W1-W3 and the W7 and W8, presented higher SSV than the remaining weeks with values ranging from 5 to 15 cm/hr. The SSV was very high with 25 cm/hr in W3. A similar pattern was observed at Railways-Node, but the SSV during DS was higher than during the WS, in W4, when it registered a maximum of 11 cm/hr. The FIPAG station, on the other hand, had WS with high SSV of 10 cm/hr. Despite this, DS, which had higher SSV reached its new highest value in the W6-W8. The reason behind this is that during the DS there was less water flowing into the scheme, and reduced flow velocity increases the SSV speed towards the bottom of the canal. In Montante sector, the only case of higher SSV was observed during WS at the Intake, in W3. This can be explained by the fact that during that period, the gates were closed or in most cases reduced, therefore, decreasing water flow velocity and sharply increasing SSV (Effler & Brooks, 1998; Ramalingam & Chandra, 2018; Zhang et al., 2017).

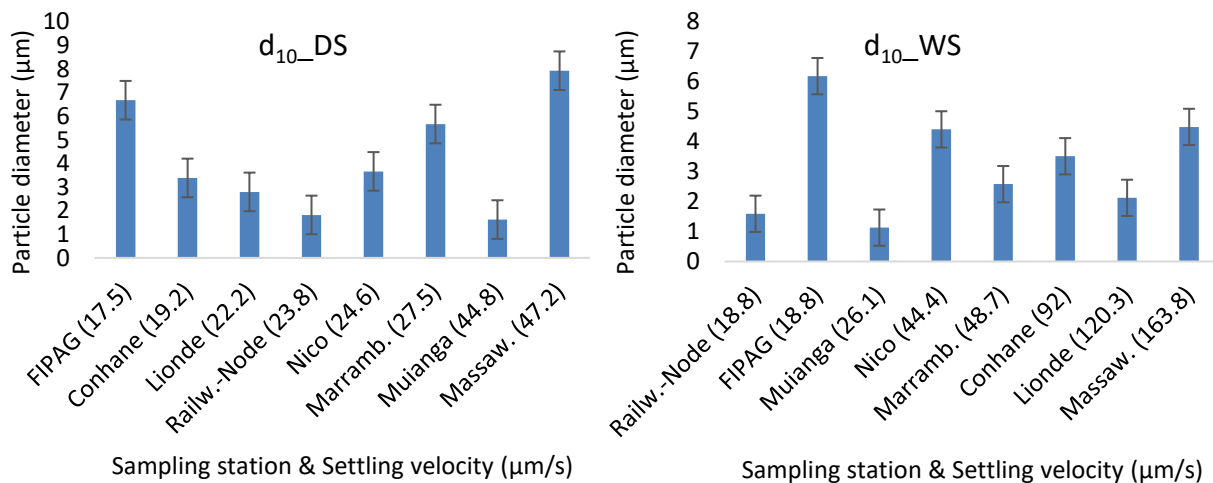
Additionally, plots a, b and c, in Figure 4.64, for the Sul sector, in every week presented higher SSV during WS, except for the W7, W8 and W3, at Lionde, Massawasse and Conhane, respectively. In Lionde, the SSV during DS was found to be around 10 cm/hr and in WS between 75 and 200 cm/hr. For Massawasse during WS the SSV reached 275 cm/hr and on the DS ranged 0 to 100 cm/hr. But in Conhane, the SSV fluctuated around 0-10 cm/hr, except for the W6-W8 when it reached 160 cm/hr. The high SSV observed in some weeks can be attributed to the increase in water flow and slowness of its velocity (Ahmed & Sato, 2003; Ali & Sterk, 2015; Ogston et al., 2017; Xiao et al., 2015).

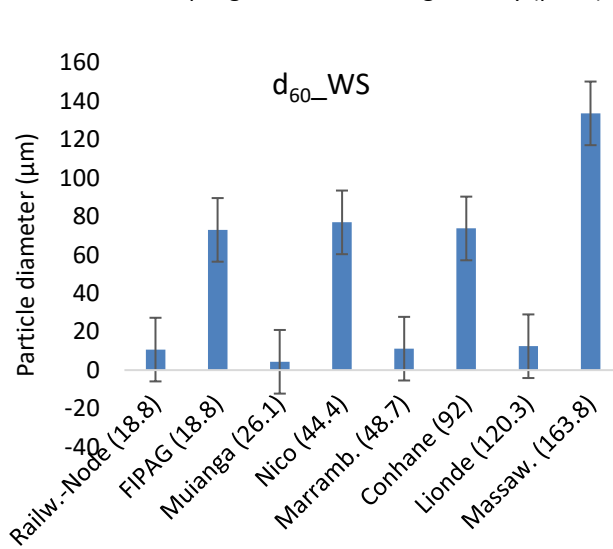
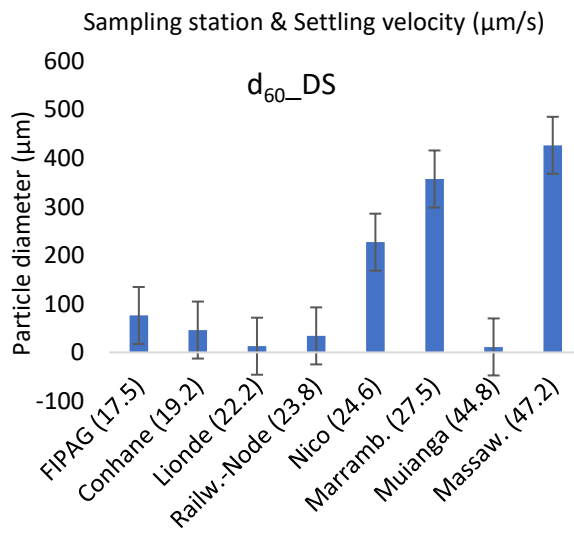
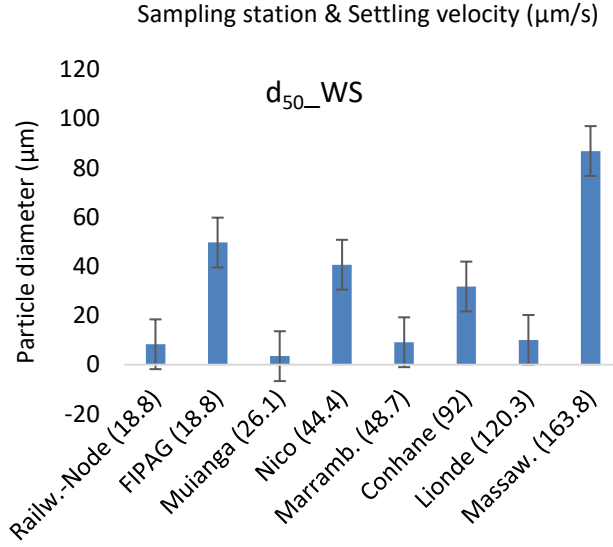
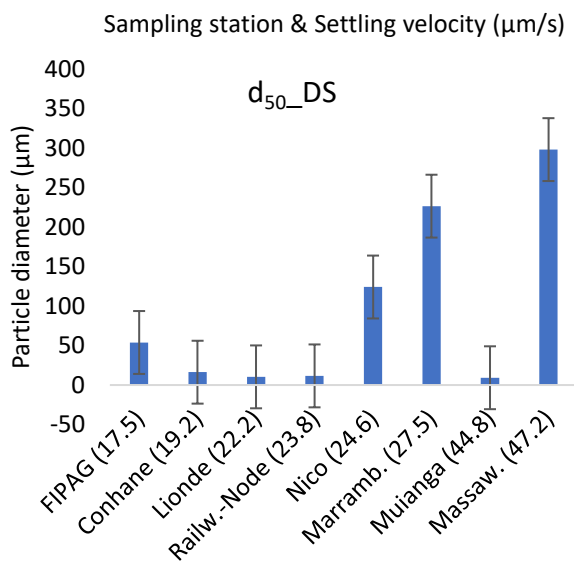
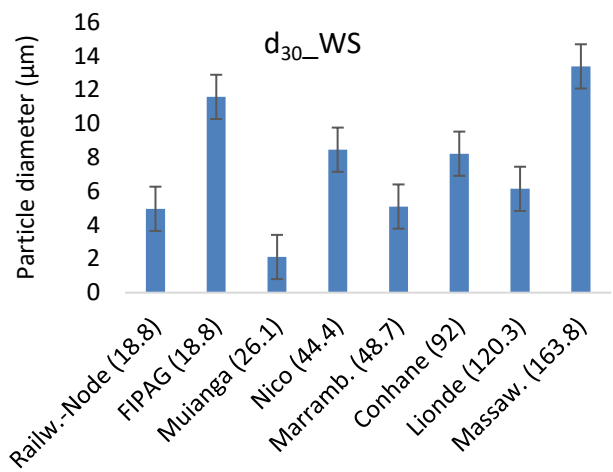
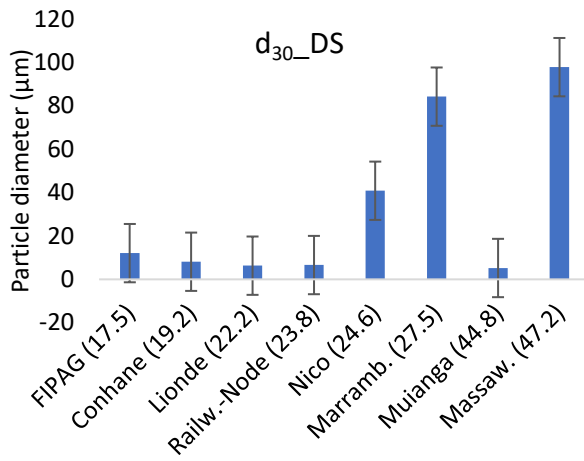
Plots a, b and c, in Figure 4.65, are for the Rio sector and presented higher SSV in W2, W5, W6 and W8 at Nico station, reaching maximum of more than 60 cm/hr. The DS did not reach more than 15 cm/hr. For Muianga station the highest SSV was observed at W2 and W6, reaching maximum of 65 cm/hr during DS. In Marrambajane, at the most endpoint

downstream showed higher SSV in all the weeks during WS, except in W6, reaching a maximum of 40 cm/hr. Overall, the SSV varied with sampling weeks period at a magnitude of 0-275 cm/hr, being the higher values observed during the WS, except for some weeks of the Intake, Railways-Node and Muianga sampling stations (Effler & Brooks, 1998; Ramalingam & Chandra, 2018; Zhang et al., 2017). Taking into consideration that the settling velocity of particles is a function of the particle shape, size, density and viscosity of the flow, one can infer that size and density count for main factors causing sediment particles to settle. Reason for this may have to do with considerable flocs generated in result to strong presence of cohesive sediments in the system, which easily aggregates and gain density and enlargement (Chen et al., 2021; Muttashar & Bryson, 2020). Therefore, special attention should be given to these two factors in all the sampling stations in order to minimize the aggregation of sediment particles, which is highly influenced by clay and silt present in the inflow.

4.3.2 Sediment Settling Velocity and Particle Grain Sizes

Sediment settling velocity (SSV) may vary with sediment particle grain sizes. Figure 4.66 shows the sediment particle grain size (PGS) given as a function of SSV at each sampling station.





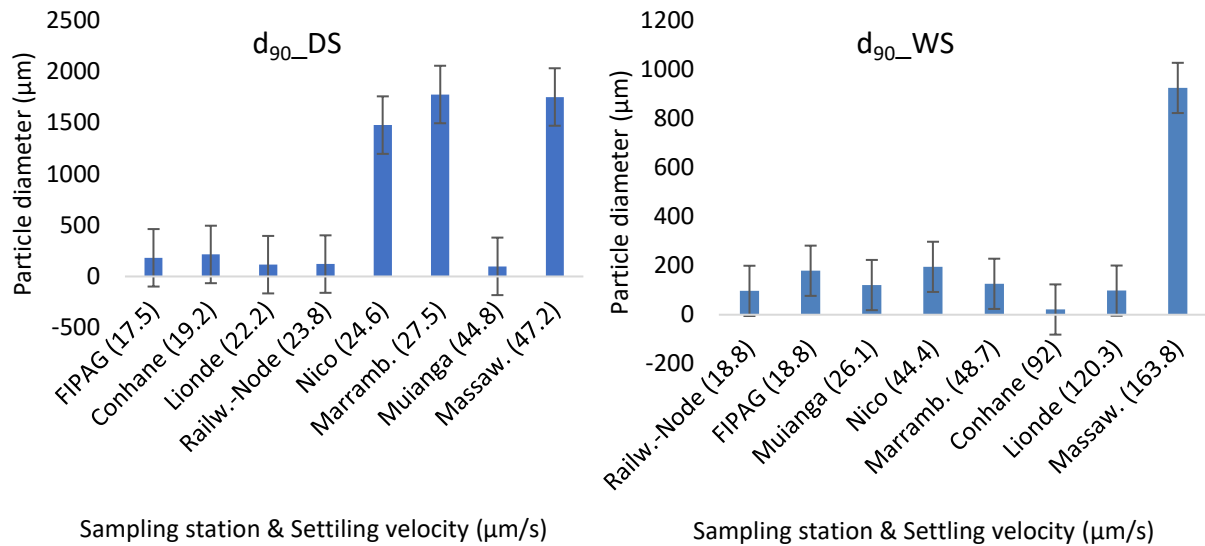


Figure 4. 66: Sediment Particle Size Given as Function of Settling Velocities at Sampling Station

SSV varied in accordance with the PGS. During DS the values of SSV for Railways-Node, FIPAG, Lionde, Massawasse, Conhane, Nico, Muianga and Marrambajane, were 23.8, 17.5, 22.2, 47.2, 19.2, 24.6, 44.8 and 27.5 μm/s, respectively. On the other hand, for WS the Railways-Node, FIPAG, Lionde, Conhane, Massawasse, Marrambajane, Nico and Muianga the SSV value corresponded to 8.8, 18.8, 120.3, 92, 63.8, 48.7, 44.4 and 26.1 μm/s, respectively. SSV is tentatively higher for sediments having higher PGS compared to those with smaller PGS. Numerous sources suggest that high SSV is also found at the downstream side of the water bodies where water velocity is commonly negligible (Liu & Sato, 2005; Yu & Lim, 2003).

In addition, different PGS were computed taking into account their respective characteristics for each sampling station's settling velocity. Having dx as a characteristic PGS such that x% of the sediment, in volume, is finer than dx (Ancy, 2020), then d₁₀, d₃₀, d₅₀, d₆₀, and d₉₀ were considered as good representation. Therefore, for the d₁₀, at DS it was observed that as it goes along the canal stream from the upstream Railways-Node to the downstream Marrambajane, the PGS varied from 2 to 8 μm. The higher the PGS, the quicker the SSV as observed in Massawasse, during DS and FIPAG during WS, at 6 μm. For the d₃₀, d₅₀, d₆₀, and d₉₀, Massawasse recorded a high SSV, for the DS and WS, and also Lionde during the WS. These findings are consistent with Ye (2012), who reported that the greater the particle size, the higher the settling velocity and vice-versa.

4.3.3 Water Flow and Canal Depths

Water flow velocity varied with the canal depth. All the sampling stations with high water flow velocity were reported during the WS. At the Intake the highest water flow velocity was found at 40 cm depth with a corresponding flow of about 0.6 m/s. Other depths recorded almost similar values with the flow velocity ranging between 0.5 and 0.6 m/s, while during the DS, the velocities ranged between 0.28 and 0.42 m/s. At the Railways-Node station, the highest velocity was found at a depth of 60 cm, while for FIPAG at a depth of 100 cm. In general, the peak of water velocity was observed during the WS. The highest water flow velocity of 0.383, 0.395, 0.315, 0.416, 0.390 and 0.292 m/s occurred at the depths of 80, 100, 80, 20, 60-100 and 40 cm at Lionde, Massawasse, Conhane, Nico, Muianga and Marrambajane stations, respectively. The water flow velocity has a tendency to increase from surface to the middle of the canal and then decrease relatively to the bottom. The majority of stations recorded high velocity at an interval of 40-100 cm. These outcomes may well be suggestive of the SSV as this factor is greatly influenced by water flow velocity. Consequently, SSV was observed to decrease from surface to the middle of the canal and then increase to the bottom. Inference can therefore be made that at the depth interval of 40-100 cm, less SSV would be verified (Ali & Sterk, 2015; Ramalingam & Chandra, 2018). Figures 4.67, 4.68 and 4.69 show water flow velocity at Montante, Sul and Rio. sampling stations, respectively.

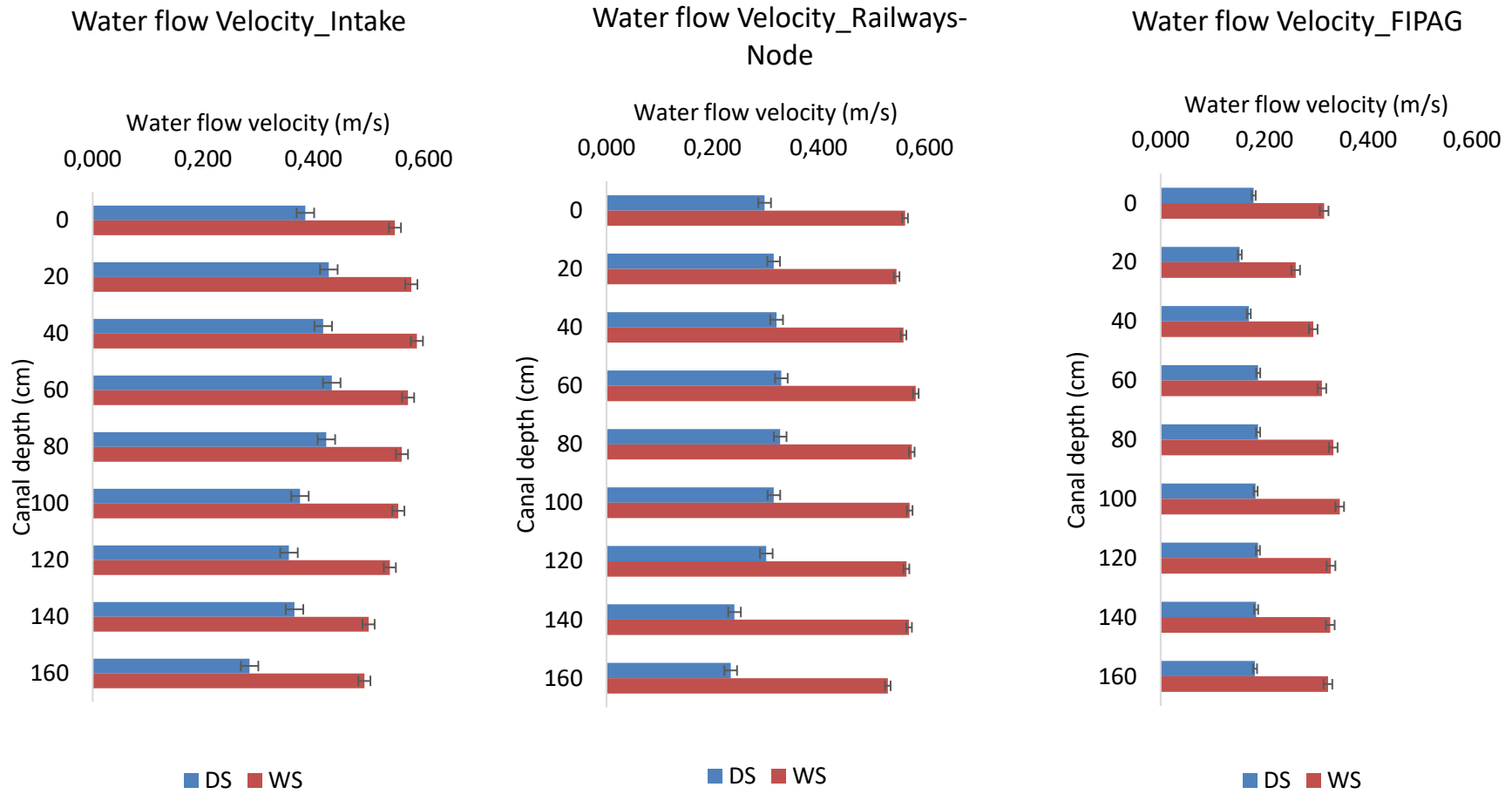


Figure 4. 67: Water Flow Velocity at Montante Sampling Stations

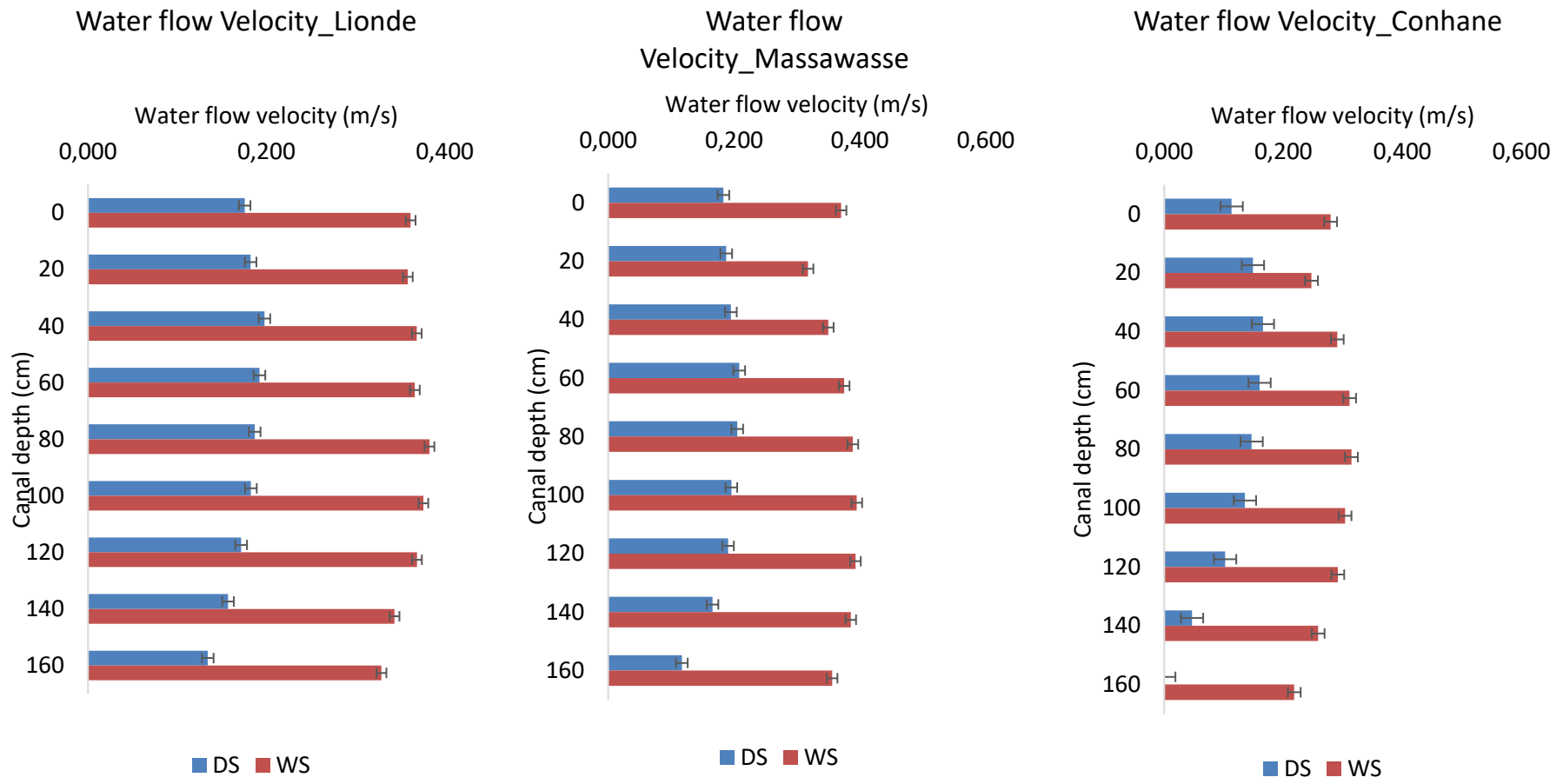


Figure 4. 68: Water Flow Velocity at Sul Sampling Stations

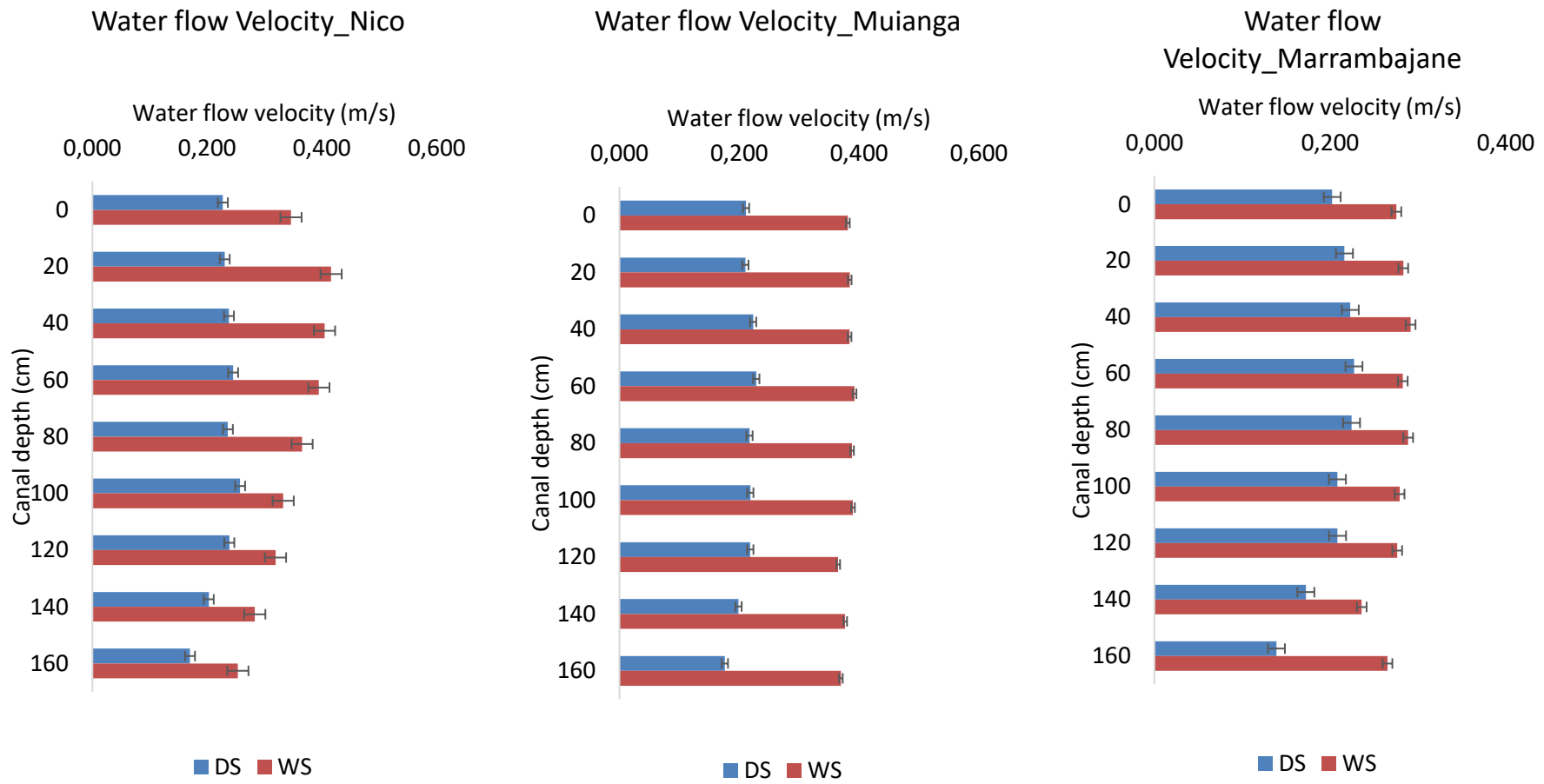


Figure 4. 69: Water Flow Velocity at Rio Sampling Stations

4.3.4 Sediment Settling Velocity and Canal Depths

Sediment settling velocity also varied with the canal depth. As it is shown in Figures 4.70, 4.71 and 4.72, all the sampling stations presented higher velocity during the WS than DS, except for Railways-Node, Muianga station and some points of the FIPAG stations.

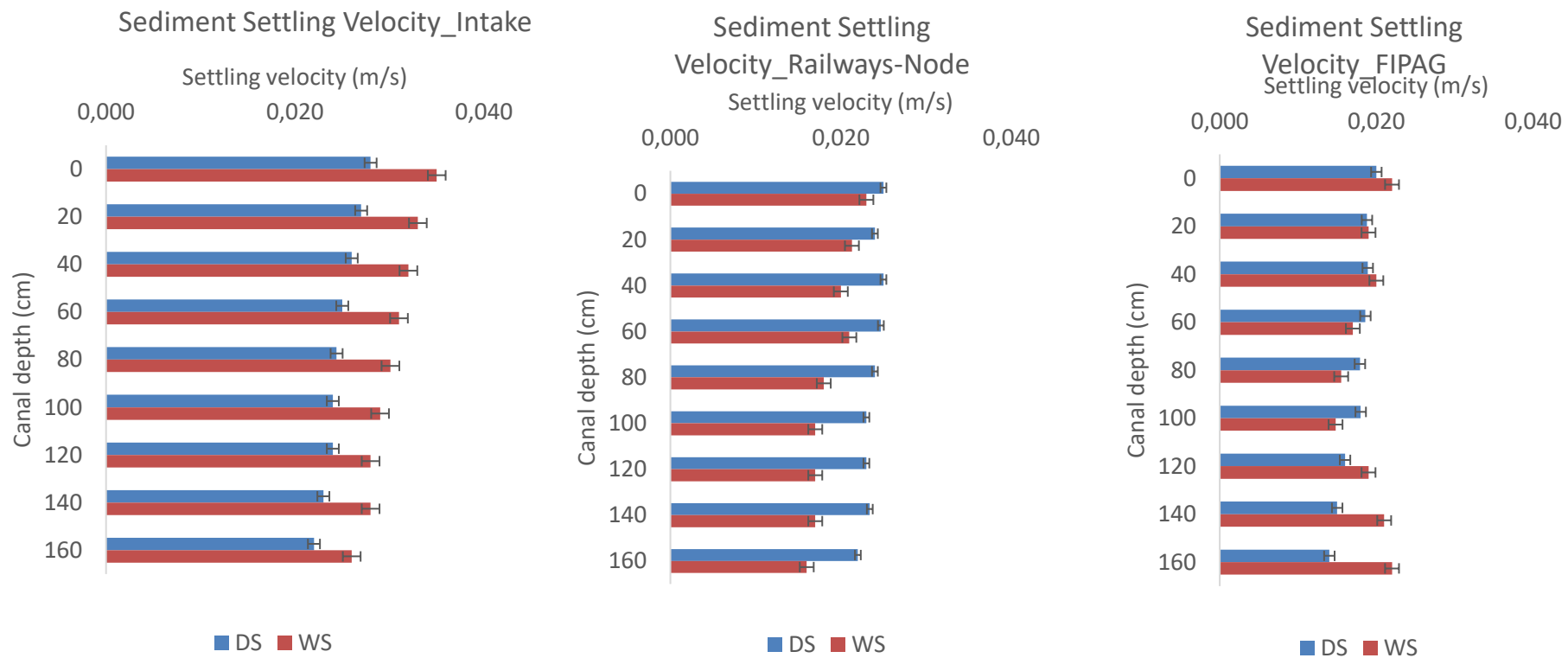


Figure 4. 70: Sediment Particles Settling Velocity at The Depth of Sampling Stations Montante Sector

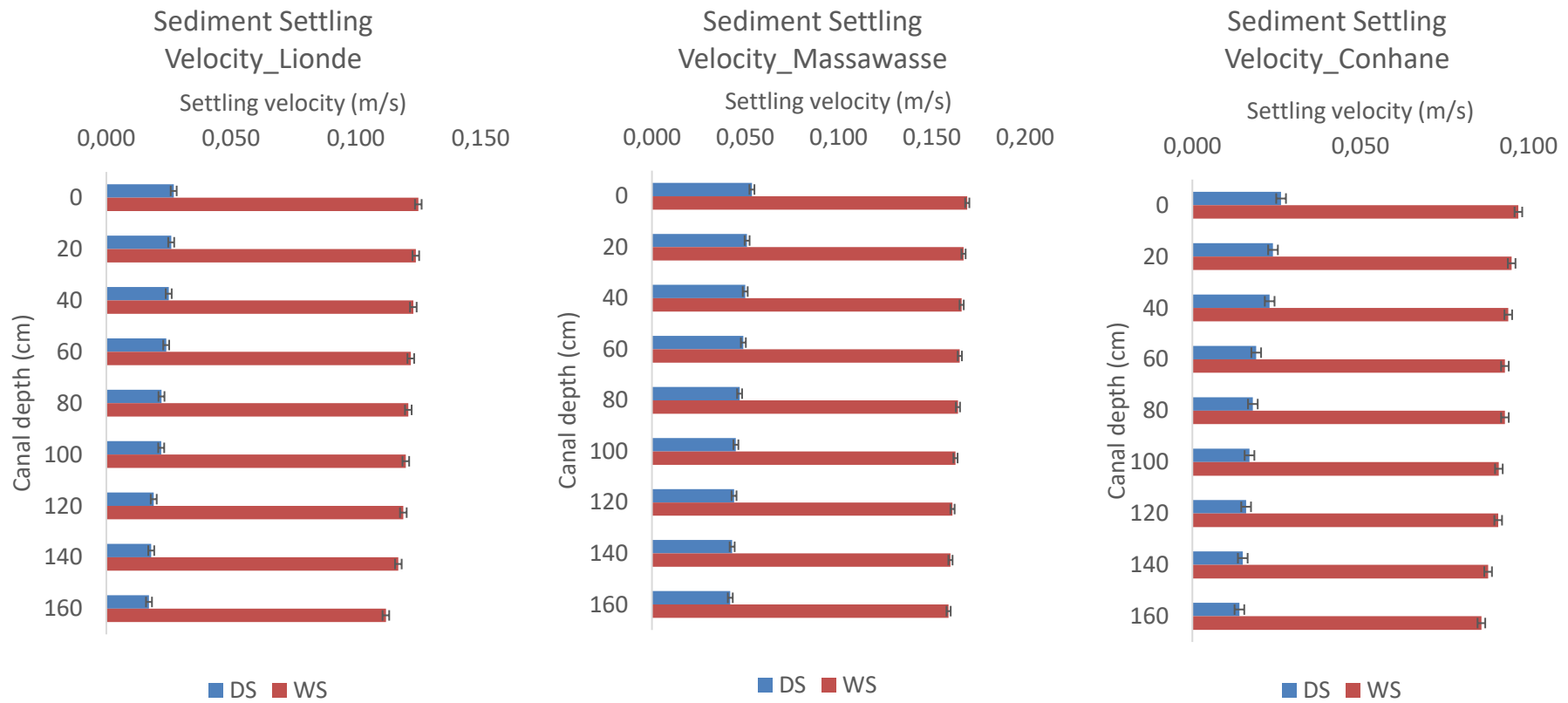


Figure 4. 71: Sediment Particles Settling Velocity at The Depth of Sampling Stations at Sul Sector

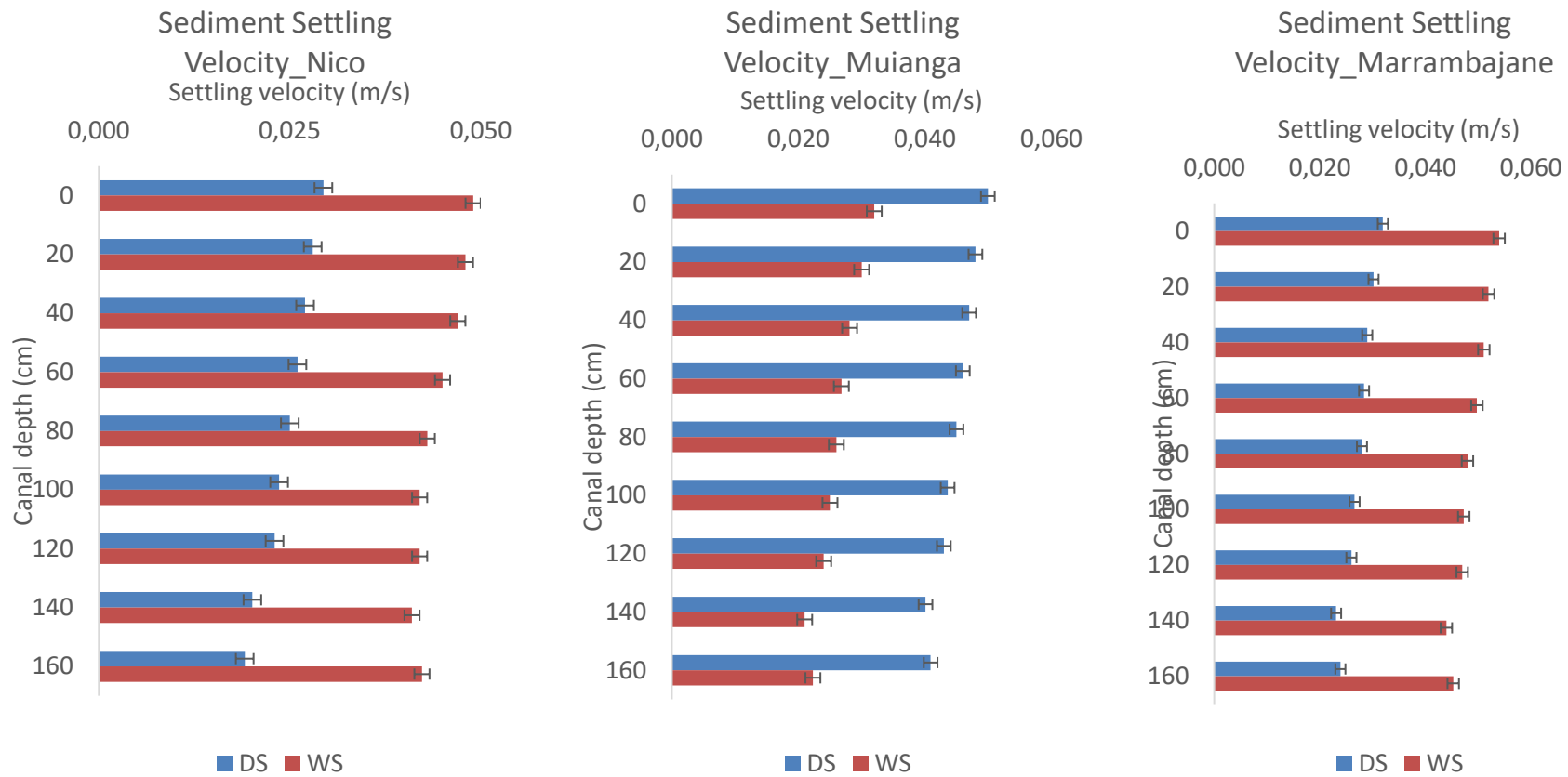


Figure 4. 72: Sediment Particles Settling Velocity at The Depth of Sampling Stations at Rio Sector

At the Intake, the highest sediment settling velocity was recorded at the canal surface, and it decreased considerably towards the bottom of canal, at a maximum magnitude of 0.040 m/s. Railways-Node station had the highest sediment settling velocity observed during the DS, with the maximum being 0.025 m/s at depths of 0, 40, 60 and 80 cm. FIPAG station observed the highest velocity during WS and had values ranging from 0.020 to 0.022 m/s, while in the DS, a value of 0.019 m/s was recorded at a depth of 60, 80 and 100 cm. In the Sul sector, Lionde, Massawasse and Conhane stations, the WS recorded the highest SSV than the DS, with a magnitude of 0.125, 0.169 and 0.097 m/s, respectively. The Rio sector, on the other hand, recorded low SSV, whereby, only Muianga recorded the highest value during the DS compared to the WS. This could be associated with the relatively high water volume entering the canal during the WS (Bravo & Grant, 2018; Mostern, 2016; Nitrouer et al., 2017; Ogston et al., 2017). The magnitude of SSV was around 0.05 and 0.06 m/s and presented a decrease from surface to the bottom of the canal. Overall, the settling velocity of the sediments were very low at Montante and Rio sectors, pointing out to the large occurrence of cohesive sediments (grain size $d_{50} < 62.5$ micrometers). But for the Sul sector the settling velocity was relatively high, due to presence of some large grain sizes within the sediments.

4.4 Simulation of Changes in Sediment Deposition and Scenarios Analysis

4.4.1 Linear Regression

Sediment transport and deposition were well predicted by Engelund-Hansen (E-H), Van Rijn 3, Van Rijn 1, Brownlie (BRO), and lastly, by Ackers-White (A-W), with coefficient of determination R^2 found between 60% and 99%. The Van Rijn 2 performed poorly with R^2 below 50%. Given the R^2 , 62% of the variability of the dependent variable total sediment transport per unit width for A-W during DS, is explained by the explanatory variable, water depth, in contrast to 65% found for WS. Moreover, for BRO predictor, 77% of the variability of the dependent variable total sediment discharge, in DS, is explained by the explanatory variable, hydraulic radius, against 72% of WS. Similarly, for E-H model, during DS, where R^2 of 98% was found, the variability of the dependent variable total sediment discharge is explained by the explanatory variable water depth, differently to the WS value of 99%. For Van Rijn predictor in result to its specific characteristics whereby different variables can affect sediment transport, three models were generated. First, Van Rijn 1 during DS, given the R^2 , 75% of the variability of the dependent variable critical bed shear velocity is explained by the explanatory variable, water depth, contrarily to 74% of WS. However, for bed load transport, in Van Rijn 2 model, 47% of the variability of the dependent variable is explained by the explanatory variable, water depth, against 48% from the WS. Lastly, in Van Rijn 3 during DS, 93% of the variability of the dependent variable bed load transport is explained by the explanatory variable, critical bed shear velocity, and 94% in WS. As can be seen, sedimentation is highly better explained in WS than in DS, except for BRO and VR (u^*) simulations.

Yang models gave R^2 of 100% of the variability of the dependent variable total load transport is explained by the explanatory variable, water depth, for both seasons. Due to high multicollinearity it did not offer good prediction, requiring different modelings. For all the predictors, given the p-value of the F statistic computed in the ANOVA table, and given the significance level of 5%, the information brought by the explanatory variables is significantly better than what a basic mean would bring. Appendix D provide some of statistics on these simulations. Table H10 in the Appendix H presents the goodness of fit statistics models for linear regression simulations.

When other performance parameters are assessed one can consider the best fitting simulation model to Engelund-Hansen, followed by Van Rijn 3, then Van Rijn 1, Brownlie and Ackers-White. All these predictors presented higher values of coefficient of determination (R^2) and the fraction of total variation of dependent variables that can be predicted by a component (Q^2), and lower values for error related parameters and coefficients such as MSE, RMSE, MAPE, DW, AIC and SBC, PC and Press. For example, Engelund-Hansen model presented R^2 of 99% (WS) and 98% (DS), Q^2 of 98% for both seasons. The MSE and RMSE were around zero, as well as the PC and Press values. Among the best fitting models, Engelund-Hansen, Van Rijn 3 and Ackers-White seems to be appropriate to model sedimentation during WS in the CIS, whilst Van Rijn 1 and Brownlie, for DS.

4.4.2 Non-parametric Regression Simulations

With exception for the E-H models, which reached R^2 above 90%, when linear regression was performed, majority of models presented R^2 between 60 and 70%, which suggest that models were not entirely explainable by linear regression modelling, thus requiring another level of analysis, such as non-parametric regression. When non-parametric regression was performed for both seasons, the R^2 improved for better, whereby models, that in linear regression where of weak correlation, had presented changes. Coefficient of determination for A-W model was found to be around 96%, but the SSE, MSE and RMSE are relatively high, with 647154.212, 22315.662, and 149.384, respectively. This indicate that in assuming this model, there is an estimated error of around 149. The BRO model presented R^2 of 90% and RMSE of 19, which is relatively good fit. Additionally, Van Rijn 1 (water depth versus bed shear velocity) had R^2 of around 93% and despicable error (RMSE of 0.004). Similarly, Van Rijn 2 (bed load transport versus bed shear velocity) had R^2 of around 95%, whilst Van Rijn 3 (water depth versus bed load transport) had R^2 of 69%. This means that even under non-parametric regression, the Van Rijn 2 model for water depth and bed load transport was relatively less performing that other models. Similar tendency was observed in the linear regression analysis. The last two models, Engelund-Hansen and Yang, presented R^2 of unit, indicating an improvement in E-H model, but not for YAN, as it was already unit in the linear regression. Non-parametric regression improves the fitness of models, when their R^2 is relatively low, in the linear regression, but requires large amount of data (Fan et al., 2018; Gu

et al., 2017; Hengade et al., 2018). Figure 4.73 presents nonparametric regression for simulations during DS and WS.

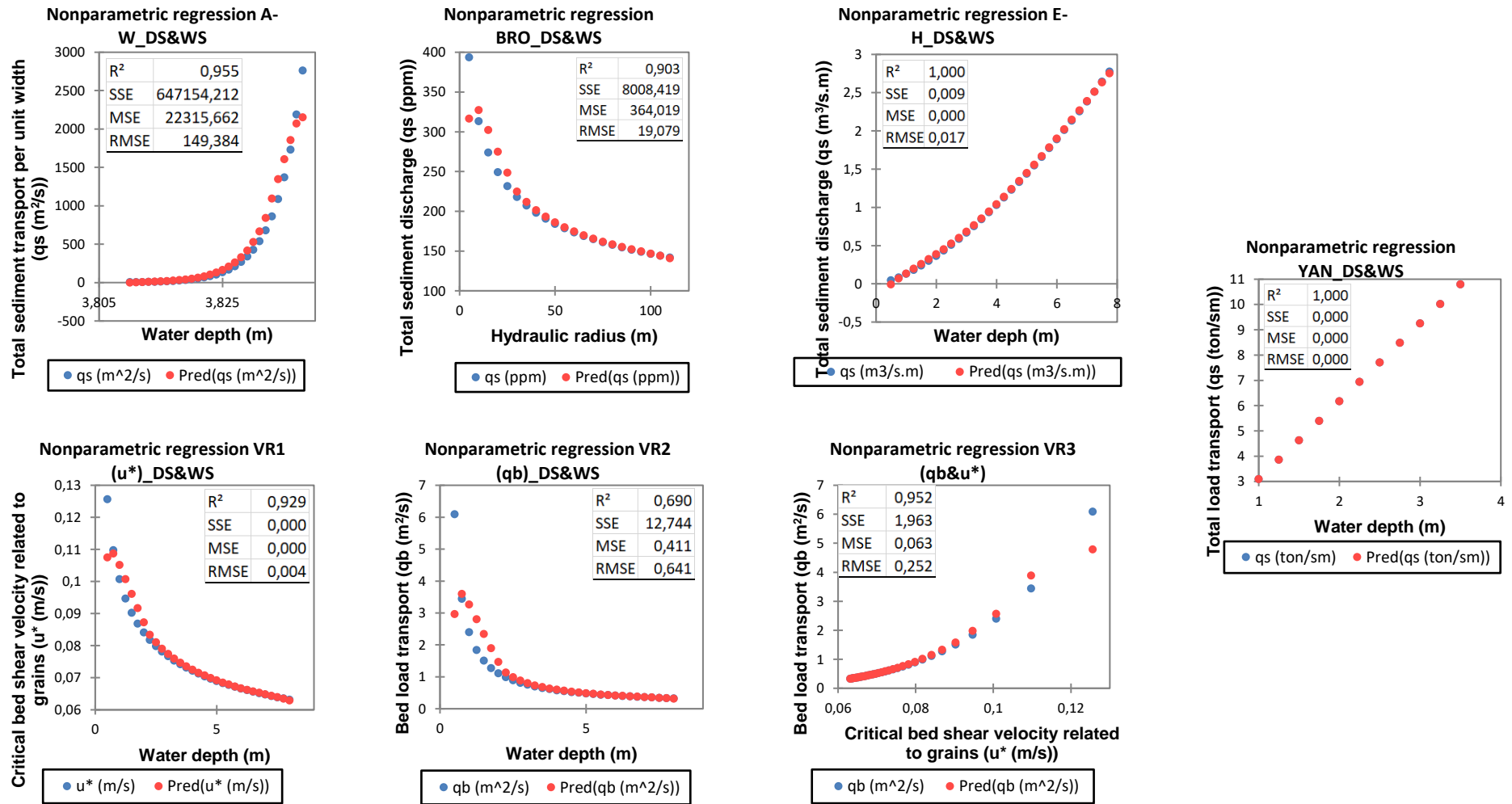


Figure 4. 73: Nonparametric regression for all simulated models during DS and WS

4.4.3 Goodness Fit Analysis for Scenarios

Apart from mere simulations to assess the fitness of the model to describe the sedimentation in the CIS main canal, scenarios were proposed to verify the potential to predict alternative measures in the scheme.

Adjusted coefficient of determination (Adj.R²)

From the Adj.R² plots, the higher the Adj.R² value, the better the model predictions (Goyal et al., 2017; Hu et al., 2020). It is observed that scenarios based on the Ackers-White (A-W), Brownlie (BRO), Engelund-Hansen (E-H) and Van Rijn (VR) models performed differently across the whole scheme in terms of accurately predicting the new situations in the CIS. With A-W model, all scenarios presented nearly maximum value of Adj. R² (99%) for DS and values between 50 and 72% for WS. This indicates that during the DS the conditions observed under the current situation (S₀) does not change. Therefore, this makes other scenarios (S₁ and S₂) to remain very close to S₀ in this season. The introduction of changes with scenarios is not bringing any improvement at all in the system, if compared to the WS, where S₂ reached 72% of Adj.R² which is less than the recommended 75%, in accordance with Srinivas et al. (2019). Further, according to Jerrett et al. (2007) and Günlü et al. (2019), Adj.R² is considered a good indicator for models performance, when compared to R² alone. When looking at the BRO model all scenarios performed better (>75%) at Lionde-Conhane (LC) and Lionde-Marrambajane (LM) reaches with Adj.R² around 84% during the WS. The Intake-Lionde (IL) reach performed relatively low (71%) during WS and the other reaches (LC and LM) performed relatively low (74% and 66%, respectively) during DS. Similar pattern was observed for the VR model, where poor performance was noted. On the other hand, under E-H model all the scenarios and reaches performed well, reaching above 98% of the Adj.R². Yang (YAN) model reached 100% of Adj.R² in all the reaches in both seasons, indicating that the model explains equally all the scenarios, independent of the conditions. Details on YAN can be seen in the Figure H.9 in Appendix H.

These results show that there is potential to improve the situation at CIS, if some assumptions are put in place, when introducing the proposed scenarios (S₁, S₂ and S₃). In considering the scenarios, assumptions include manipulating water level, hydraulic radius, mean water velocity and canal bed slope. However, manipulating canal system of an existing scheme

such as CIS, may be difficult task, therefore, the only plausible manipulation can be made for water level and its velocity, through regulation of the inflow head at the Intake and other regulators points. Sediment total loads in the models are in good agreement and it can be stated that it is possible to achieve a good approximation of sediment loads (S_2 and S_3) by using only hydraulic characteristics. Additionally, it seems that the inability of the S_1 in predicting the bed load transport rate is due to the fact that the bed load transport is more affected by characteristics of bed material, which happens to constitute the bed layer, such as median diameter of particles and using hydraulic characteristics as input parameters led to insufficient results (Boylan & Cho, 2013; Luo et al., 2006; Momber & Marquardt, 2019; Olive and Hawkins, 2005). Conversely, suspended load (S_2) appears to be more affected by flow conditions. Therefore, it can be deduced that different effective hydraulic parameters are the effective factors for prediction of total sediment loads in the models.

Root Mean Square Error (RMSE) and Durbin-Watson statistic (DW)

Analysis based on the Root Mean Square Error (RMSE) and Durbin-Watson statistic (DW) were also performed as in other similar studies by Boylan and Cho (2013) and Goyal et al. (2017), Ingrassia and Morlini (2005), Yurekli and Ozturk (2003). In A-W model the scenarios performed differently for either RMSE or DW, in both seasons. During DS the RMSE was almost null which is good for the model, compared to WS. Additionally, DW values were 0.16 and 1, for DS and WS, respectively. DW values indicates that the models presented positive autocorrelation. In this case, water flow, mean velocity and canal bed slope did positively autocorrelated.

The values of RMSE for all models, reaches and in both seasons were considered very low and therefore, indicative of good model predictions. RMSE values ranges from 0.2 to 5.2 (m^2/s , ppm or $m^3/s.m$) for A-W, BRO and E-H. VR model did not provide enough information for the analysis, despite the fact that a very large value was obtained for the RMSE around 140 m^2/s in DS. Similarly, DW values were between 0 and 1, a clear indication that the models has positive autocorrelation. This indicates that the models data are correlated with itself in its past. In this case, the model may require further analysis for better prediction (Bong & Liow, 2019; Günlü et al., 2019; Jerrett et al., 2007; Lee et al., 2019; Merikas et al., 2008; Park et al., 2017; Shekwa et al., 2017). These results suggest that

the models are consistent, despite the fact that results from DW indicate otherwise as observed from the autocorrelation values.

Akaike's Information Criterion (AIC) and Schwarz's Bayesian Criterion (SBC)

Akaike's Information Criterion (AIC) and Schwarz's Bayesian Criterion (SBC) were employed for further analysis of the models (Yurekli & Ozturk, 2003). For both parameters it is recommended to select a model with the lowest value of the criterion (Fujikoshi et al., 2005; Aydın & Memmedli, 2012). As expected both criteria are very close and offer similar values. For A-W model during DS the AIC and SBC values were around -303, -186 and -170, and -302, -184 and -168, respectively for S₀, S₁ and S₂. This indicates that during the DS, the best fitting model was S₀, which is the current actual situation. For WS, values of 23, 12 and 7.5, and 24, 12 and 8 for S₀, S₁ and S₂ respectively, were found for AIC and SBC. As per the aforementioned results, the good-fitting model was S₂. This means that the DS scenarios did not bring better options against S₀, as compared to WS for S₂.

For BRO model, S₁ appeared to offer good-fit in all the three reaches during DS, while during the WS, S₁ performed well for LC reach, and S₂ for IL and LM, with values around ±13, -129 and -142 respectively. When analysing VR model, it was observed that during DS the IL reach was better predicted for S₃ (bed load conditions), in the LC reach it was the S₁ that performed better and at LM, the S₃ again. This gives an alternative for the bed load situation that can be improved once the bed layer and its thickness have been manipulated to reduce the deposition of sediment. In the same model, but during WS, it was the S₁ scenario that offered better-fitting results, in favour of the water flow conditions, through water depth and mean velocity. Similar tendency is observed for VR model, where S₁ seems to fit well in both seasons. From the results S₁, S₂ and S₃ can be suggested as possible best fitting scenarios to the models, putting in consideration the main inputs used for the trial-and-error process (Chen, 2018; Fujikoshi et al., 2005; Hartless et al., 2003; Hu et al., 2020; Pervukhina et al., 2014).

Mallows coefficient (Cp)

Mallows Coefficient (Cp) was used to help choose between regression models. It compares the precision and bias of the full model for models with a subset of the predictors (Charnigo et al., 2011; Mallows, 2000). Usually, it is recommended to look for models where Mallows' Cp is small and close to the number of predictors in the model plus the constant (p). A small

Mallows' Cp value indicates that the model is relatively precise (has small variance) in estimating the true regression coefficients and predicting future responses (Aydın & Memmedli, 2012; Bhattacharyya & Sengupta, 2009; Fujikoshi et al., 2005). A Mallows' Cp value that is close to the number of predictors plus the constant indicates that the model is relatively unbiased in estimating the true regression coefficients and predicting future responses. Models with lack-of-fit and bias have values of Mallows' Cp larger than p. In this work all models, methods and reaches covered by the study the Cp was equal to 2.0, against the predictors value of 3 in each model. This means that the models are unbiased in their estimations (Luo et al., 2006). This is in agreement with several different studies (Aydın & Memmedli, 2012; Bhattacharyya & Sengupta, 2009; Bong & Liow, 2019; Shekwa et al., 2017).

Amemiya's Prediction Criterion (PC)

Amemiya's Prediction Criterion (PC) is based on Adjusted R^2 , bigger value means better model performance (Srinivas et al., 2020). In A-W model S_0 had the highest PC value of 66%, followed by S_1 with 55% and S_2 with 36%. Here, the scenarios did not offer improvements to the current situation (S_0). Looking at BRO model the highest value for PC was found at LM reach during the DS and the lowest at LC in the WS, with values of 40% and 20.8%, respectively. For E-H model, all the models presented PC values less than 10%, therefore, becoming negligible. VR model, on the other hand, presented 66 and 55%, respectively in the DS and WS. For this model, S_0 and S_1 performed equally in both seasons, meaning that the introduction of new scenario in terms of water flow brought some kind of change to improve the current conditions for better stage. From these results, it can be stated that the best-fitting models were A-W and VR which suggested that S_1 can be a scenario to consider in improving the sediment discharge in the CIS as an alternative to the current situation (Srinivas et al., 2020).

In general terms, Multiple Linear Regression has provided an explanation for the degree of the variability of the dependent variable by the explanatory variable, through different statistics goodness fits. The best fitting models in predicting suspended sediment and bed load sediments in the main canal of CIS were, in decreasing order, Engelund.-Hansen, Brownlie, Van Rijn and Ackers-White (Das et al., 2019; Goyal et al., 2017; Olive &

Hawkins, 2005; Yu et al., 2014). Given that some variables have their R^2 below 50%, a nonlinear analysis was performed to search for better fitted model.

4.4.4 Sensory Data Analysis (SDA)

This technique was used to assess the models performance through Root Mean Square Error (RMSE) after dataset were smoothed based on the statistic methods of Exponential (EXP), Linear Holton (LH), Seasonal Additive (SA) and Seasonal Multiplicative (SM) treatments. It was found that when all models were compared through EXP method, models of A-W, BRO and E-H in both seasons showed very low RMSE, and VR in WS presented similar tendency. In comparison to LH, SA and SM methods, the RMSE was very low for A-W, E-H in both seasons and VR during WS only.

Similar analysis was performed for the coefficient of determination (R^2), where EXP presented E-H model with 64% in DS followed by A-W with 50%. During WS, E-H reached 64% and A-W was around 33%. For LH method, both models A-W and E-H were above 90%, making it best fitting model followed by SM, because SA had a RMSE less than 30%. Overall, Linear Holt showed good performance of Ackers-White and Engelund-Hansen predictions of scenarios in both seasons, compared to the other models used. Seasonal Multiplicative method also singled out Ackers-White model as having good potential to accurately predict the sediment depositions in the canal. Both models being of energy balance concepts with regression method may have played considerable influence for their best fitting predictions (Bhattacharyya & Sengupta, 2009). Figures 4.74 and 4.75 present plots for EXP and LH models of sensory data analysis, as well as for the SA and SM models.

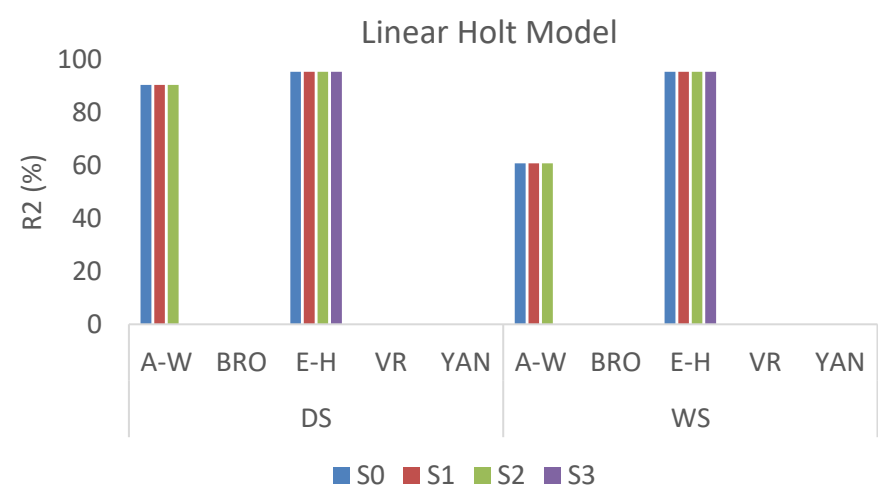
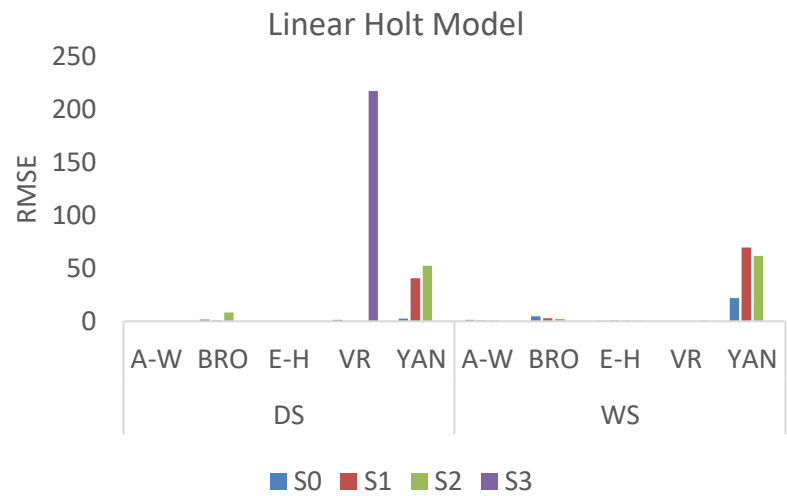
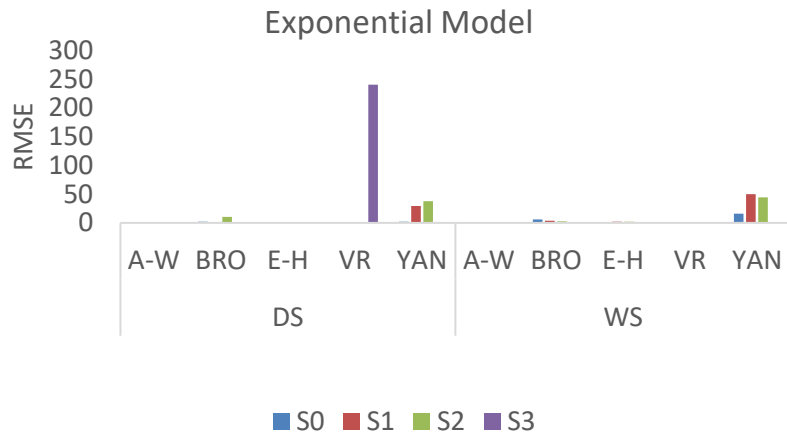


Figure 4. 74: RMSE and R² for the Exponential and Linear Holt Models of Sensory Data Analysis

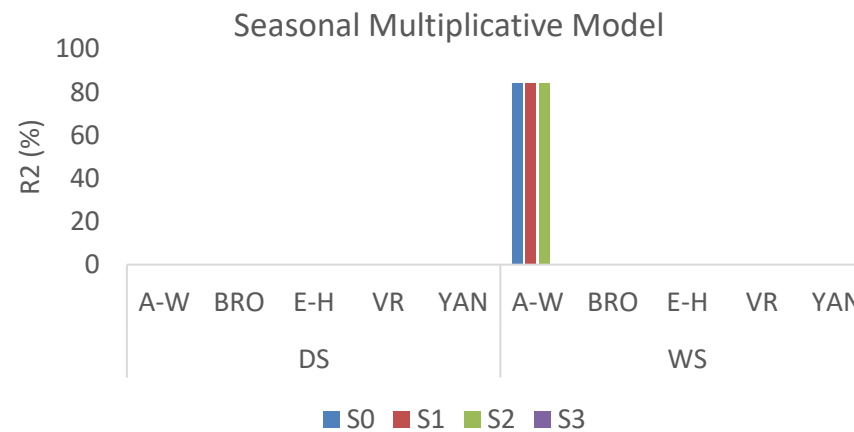
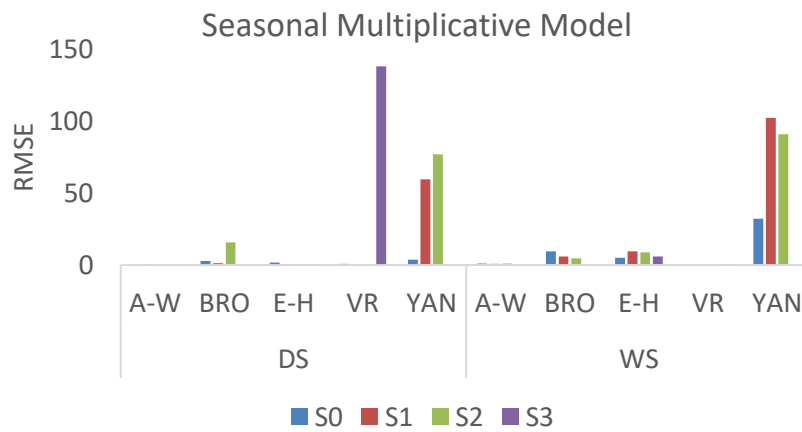
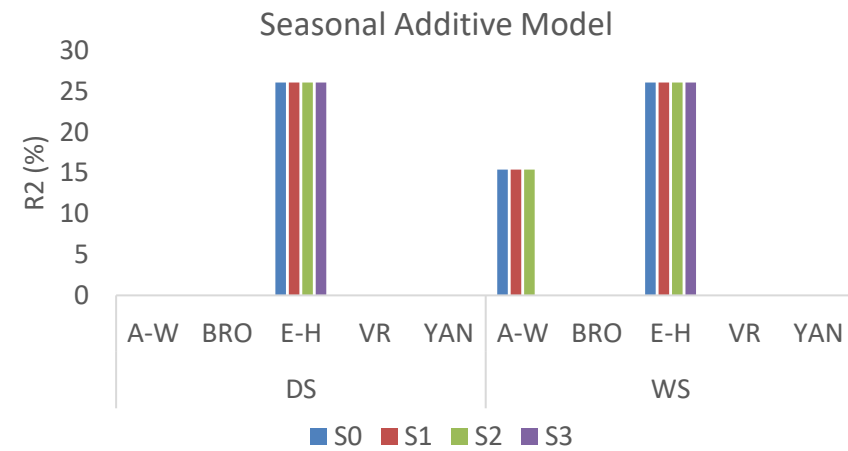
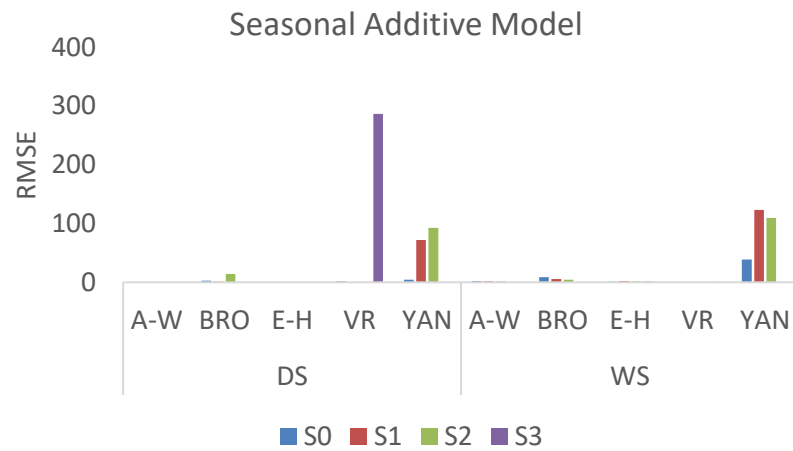


Figure 4. 75: RMSE and R² for the Seasonal Additive and Multiplicative Models of Sensory Data Analysis

4.4.5 Best Predictions

The prediction analysis was based on the Correlation Coefficient (R), Nash-Sutcliff Efficiency coefficient (NSE), Relative Error (RE), Percentage BIAS (PBIAS) and Root Mean Square Error (RMSE). Overall, the models presented different behaviour in regard to each sensitivity parameter. Looking at the NSEC parameter for S₁, it was found that A-W WS, E-H DS, E-H WS, VR DS and WS, resulted in values of 0.37, -28, -45, -21 and -44 respectively. These models seem to offer reliability owing to their closeness to zero values. Additionally, looking at R values it comes out that only BRO during the WS presented a positive value, which is in between zero and 0.24, as was expected. Being less than 50%, one cannot consider the model prediction as good fit for validation. Other models resulted in negative values. RE values were well situated below 30% for majority of the predictors, which is acceptable for tending to zero, except for YAN DS, which reached 70%. With regard to PBIAS, only A-W in the WS and BRO during the WS presented relatively low values of between 4 and 37 respectively. RMSE was observed to be close to zero, which is recommended in such cases. Overall, under scenario 1, only A-W and BRO appeared to offer better predictions worth of consideration for water flow under the conditions at CIS.

For S₂, positive NSEC was observed only for A-W during the WS, having a value of 0.40. The remaining models had a negative NSEC values (above -30), in particular E-H during the DS and during the WS, VR during the WS and YAN during the WS. R values between zero and unit were found for A-W WS, BRO DS and WS, with 0.01, 0.14, 0.32, respectively. Again, these values are below 50% and the models don't offer reliability. RE, on the other hand, are close to zero in all models, except for BRO during the DS and YAN during the DS, with 45% and 81%, respectively. The PBIAS values were found to be less than 100% for A-W DS, BRO WS and E-H DS with 94, 51 and 61%, respectively. The remaining models resulted in negative values, pointing to overestimation trends. RMSE values were found to be below 5, thus establishing a good fit of the models. In general, under S₂ A-W during the DS and during the WS, BRO during the DS and during the WS, E-H during the DS and during the WS can be good predictors to suspended sediment in CIS.

In S₃ it was found that R values strangely situated far below zero in most cases, except for A-W WS, BRO DS and BRO WS, with 5.2, 84.7 and 15.5 %, respectively. This means that only

BRO DS could offer good sensitivity value and therefore acceptable. A-W was the worse prediction sensitivity. NSEC values were negative for A-W DS, BRO both seasons, E-H WS and VR both seasons, with around -174, -128, -0.3, -1.0, -17 and -1.0, respectively. But A-W WS, E-H DS, and YAN had positive values of 0.99, 0.57, 0.89 and 0.92, respectively, being within the expected range of zero and unit. RE measures the level of uncertainty in the measurements, with the lowest being considered the best. In the models under evaluation in this work the RE was found to be between 0 and 0.2. This is an indication that the results offer high levels of trust. PBIAS were found to be around -34, -2.5, 11, 1.1, -8, -18, -25, -16, -7 and -22, respectively for both seasons (DS and WS) of A-W, BRO, E-H, VR and YAN. The optimal value of PBIAS is zero and lower values indicate better simulation. In this case, only BRO WS had good performance in relation to others. BRO DS being a positive value, indicates a tendency of the model to underestimate while the remaining models, with negative values, indicate the tendency to overestimate the values. The RMSE values were generally low values indicating that the models offered considerable level of trust, particularly, A-W DS, BRO in both seasons, VR WS and YAN both seasons. From the sensitivity analysis, it was found that despite some outfitting models, some offered acceptable predictions, such as A-W WS, BRO and E-H in both seasons and YAN.

Combining different sensitivity criteria, Correlation Coefficient (R), Nash-Sutcliffe Efficiency coefficient (NSEC), Relative Error (RE), Percentage BIAS (PBIAS) and Root Mean Square Error (RMSE), it is seen that S_1 for water flow in the canal, A-W and BRO can be considered reliable models. But in case of S_2 for suspended sediment A-W during the DS and during the WS, BRO during the DS and during the WS, E-H during wirtg DS and WS models appeared to give better predictions, whislit in S_3 for bed load sediments, A-W during the DS, BRO during the WS and E-H during the DS and during the WS, provided better predictions than the rest of models and seasons. Figures 4.76 and 4.77 presents plots for the best predictions models.

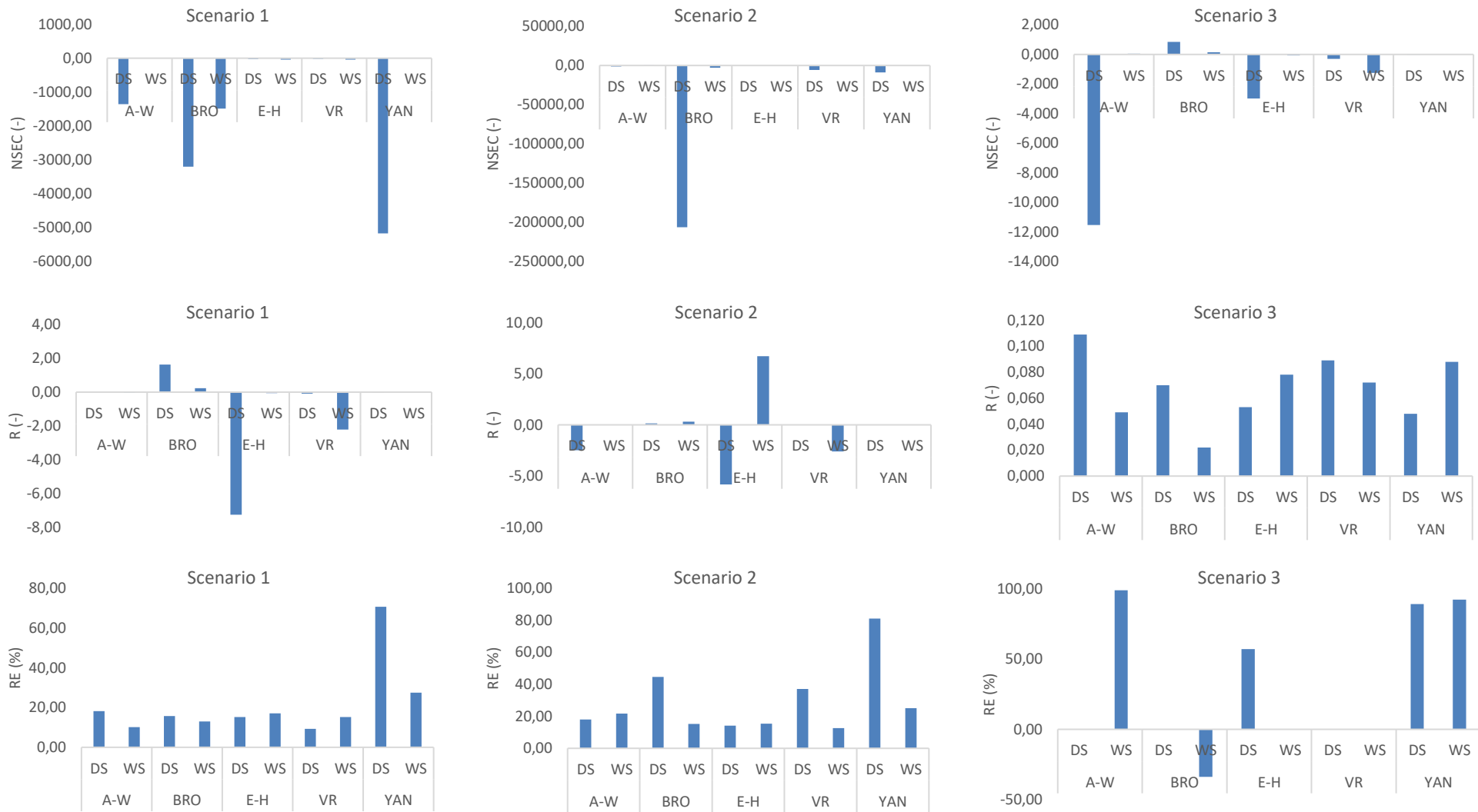


Figure 4. 76: NSEC, R and RE for Best Predictions of the Models Scenarios

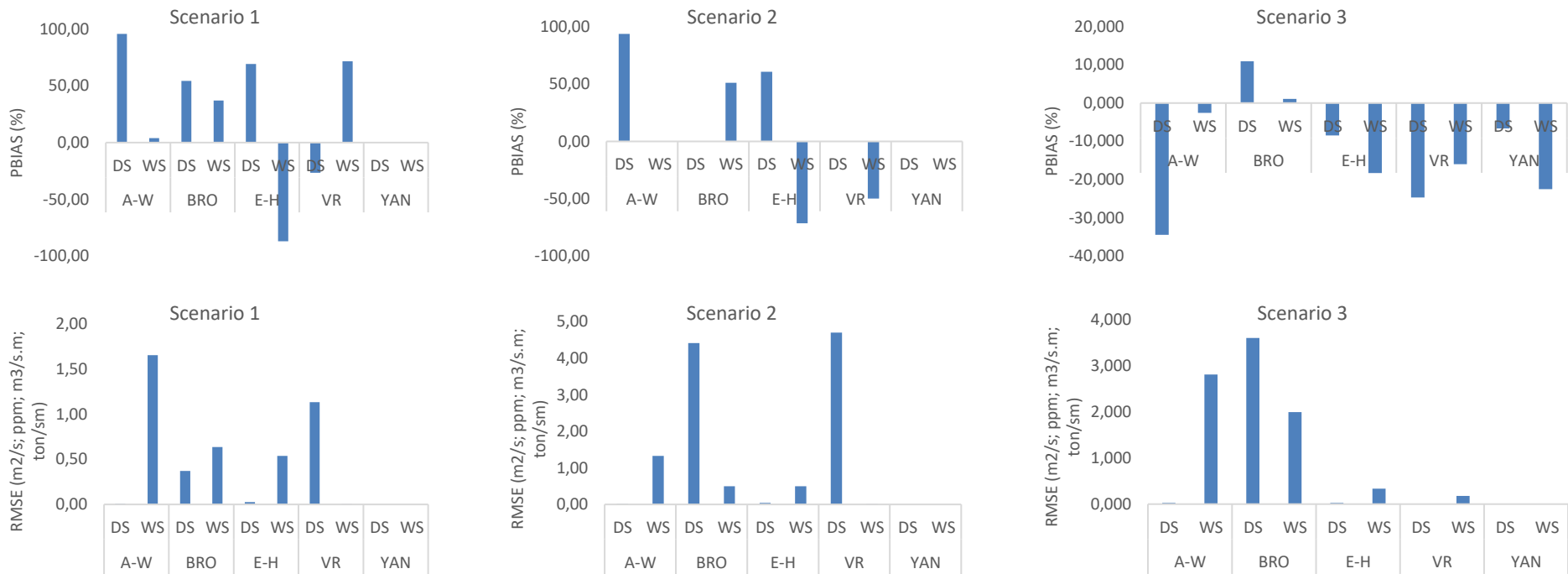


Figure 4. 77: PBIAS and RMSE for Best Predictions of the Models Scenarios

Model predictors for actual (S_0) and water flow (S_1) scenarios were generated for the DS and WS. In general terms, sediment transport and deposition was predicted to be higher during the WS as compared to the DS for all models, except Van Rijn's. However, despite the A-W model predicting more deposition in the WS than during the DS, it did not match the R^2 which was only 52% for the WS against 99% during the DS. Predictions for scenarios in DS indicated that S_0 experienced more sedimentation compared to scenario S_1 with 0.901 and 0.044 m^2/s of transported sediment, respectively. For the WS, the sediment transport per unit of square meter per second was approximately 2.108 and 1.427 for S_0 and S_1 respectively. The results show a relatively high amount of influx entering the scheme in both seasons due to considerable inflow during the DS and high rainfall in WS. Additionally, it was observed that the S_1 can lead to a reduction in sedimentation in CIS, if applied. These findings are in agreement with the assumption made that Ackers-White could be used to model the water flow suitably as was found by Roushangar and Shahnazi (2020). A R^2 value of 99% was found for both S_0 and S_1 scenarios during the DS, whilst in the WS, R^2 of approximately 59% and 52% for S_0 and S_1 , respectively was recorded. DS presented better prediction when using A-W for water flow conditions than WS.

When applying BRO predictor for S_1 , in both seasons, the R^2 was approximately 75%. However, more sediment was predicted to occur during the WS than in the DS. Similar results were observed for E-H in both seasons. Van Rijn model presented R^2 below 50% in both seasons, while YAN reached R^2 of unit. For the BRO model in the DS and in the WS, as well as for E-H model in the DS and VR in the WS, less sedimentation was found in comparison to S_0 . This can be an indication that the proposed simulation can offer a solution to the current situation in CIS. E-H in the WS, VR in the DS and YAN in the DS and in the WS, presented a contradicting pattern, whereby newly proposed simulation did not offer any improvements with regard to reduction in sedimentation. Similar results were found in this study. This can greatly be due to the fact that suspended sediment is entirely related to water flow. Again, S_1 presented less sedimentation in comparison to S_0 for A-W in the DS, BRO in the DS and in the WS, E-H in the DS and VR in the WS. A-W model had R^2 of 99% during the DS for both S_0 and S_1 , and 52% and 71% during the WS for S_0 and S_1 . BRO and E-H presented R^2 of about 75% and 98%, for S_0 and S_1 during the DS and WS, respectively. VR had R^2 less than 50% and YAN, despite reaching 100%, S_1 did not show reduction in

sedimentation. In this case, it can be rightly presumed that Van Rijn model did not provide scenarios alternative to the current situation. The use of water depth in the canal as the parameter for assessing sedimentation may have contributed to these findings. Many studies have found Van Rijn model explaining water flow and suspended sedimentation loads with good degree of accuracy (Mendez_V, 1998) in the laboratory experiments. The fact that each water body is unique, remains true and more trial and error tamptatives need to be performed more precisely using other parameters relevant for Van Rijn model, such as mean diameter (d_{50}), mean velocity (v), bed shear and critical bed shear velocity.

For A-W during both the DS and WS, it was observed that S_0 remained better than the proposed scenario S_1 . Therefore, the S_1 did not offer reduction in sedimentation. On the other hand, A-W for the WS S_1 , seemed to predict reduction in sedimentation and by this, becoming a potential solution for CIS sediment accumulation. Similar results were found using BRO for DS and WS, whereby S_1 presented reduction in sedimentation than S_0 . Even so, E-H, VR and YAN did not offer favourable predictions for DS and WS for S_1 compared to S_0 , although the graphs seems very close to one another. Prediction for bed load brought potential alternative to the current situation, if A-W in the WS, and BRO during the DS and WS are adopted. This agrees with findings by Roushangar and Shahnazi (2020), whose work looked at prediction of sediment transport rates in gravel-bed rivers using Gaussian process regression, whereby bed load predictors offer suitable results if slope and particle diameters are considered in the equations.

4.4.6 Winters Method for Model Predictions

Besides Horts-Withers and Linear Regression analysis, another analysis was performed as cross-checking procedure in order to assess the validity of the models used to predict sediment in CIS. The analysis was made possible through the Winters Method, which assumed that the results of observed sediment obtained from the differen models, could be extrapolated for a period of year. This allowed for prediction of the sedimentation in terms of month occurrence. A multiplicative method considering the smoothing constants of α (level) = 0.2, γ (trend) = 0.2 and δ (seasonality) = 0.2, was applied. The method provided an reinforced insight image of the prediction in CIS. A-W DS presented a positive trend with a quasi-linear plot for the actual model, while for the A-W WS, the positive trend appears to be

of an exponential model. This means that, as time increases, sedimentation in the canal, according to this model, also increases. Positively increasing patterns were also found for E-H and YAN models in both seasons. Additionally, for both seasons of the BRO model, the pattern appears to be negative and decreasing. Here, sedimentation decreases with time. A similar pattern was observed for the VR model. Few models presented normally distributed datasets, among which are A-W DS and E-H in both seasons. Some outliers were found in figures 4.78-4.82 in September, where an uncharacteristic outlier has been found in that same month. Non-normality was found for A-W WS, BRO and VR, in both seasons, as presented in Figures 4.78-82.

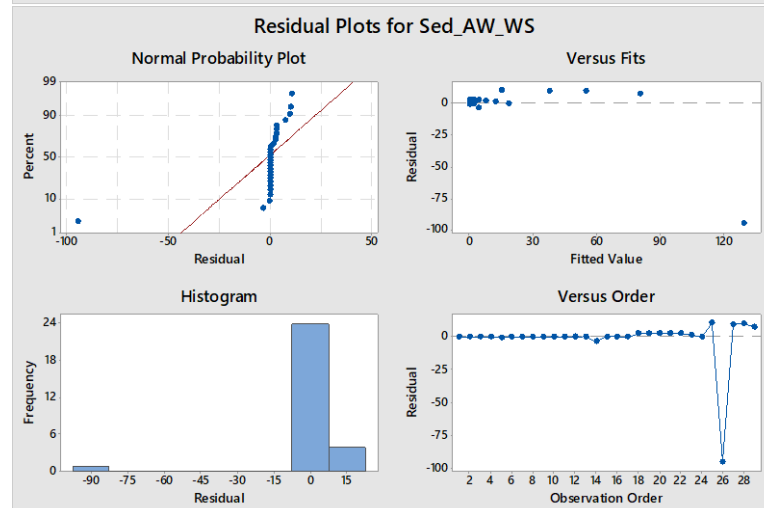
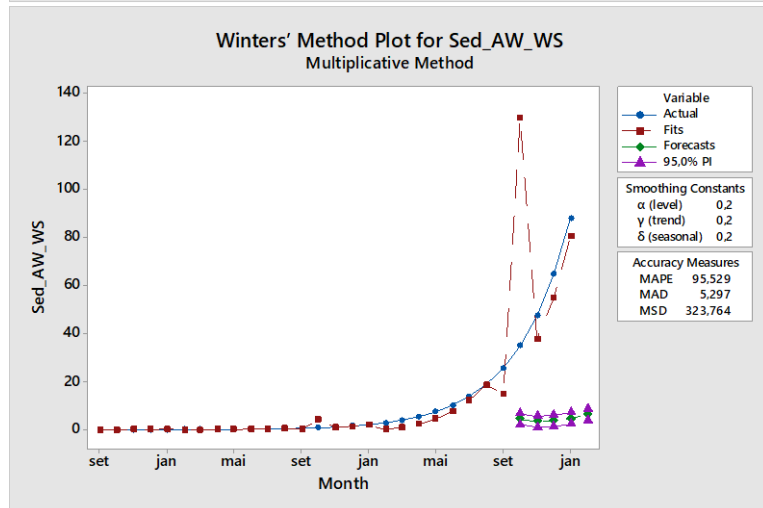
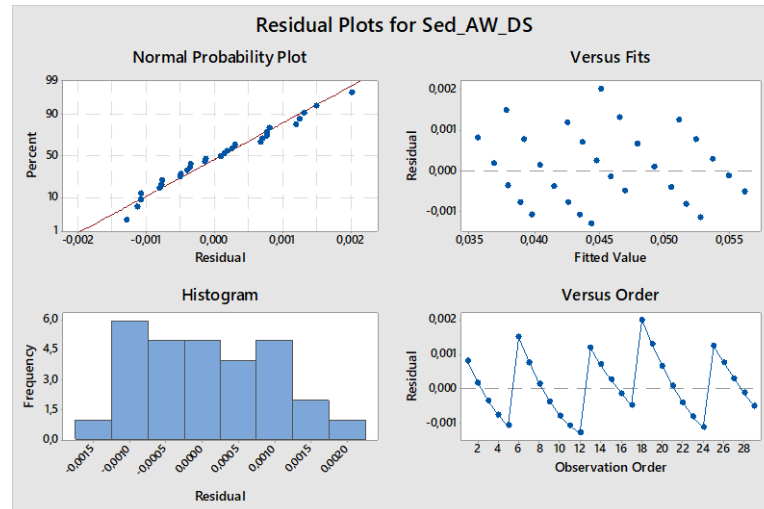
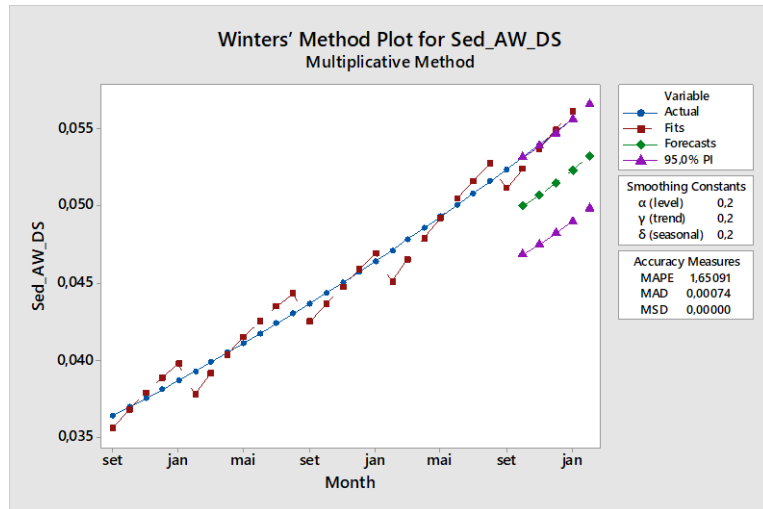


Figure 4. 78: Winters Plots for Sediment Prediction Using Ackers-White Model

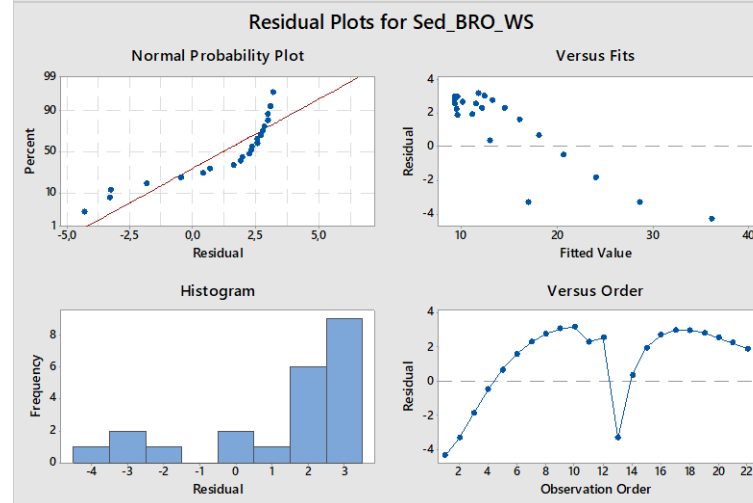
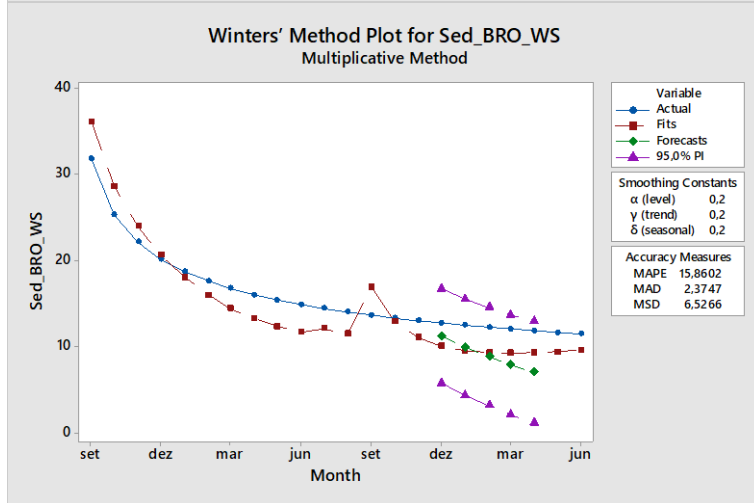
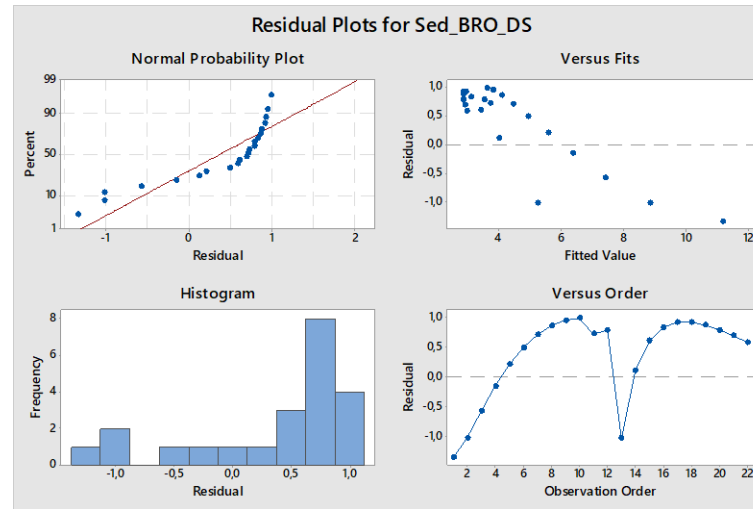
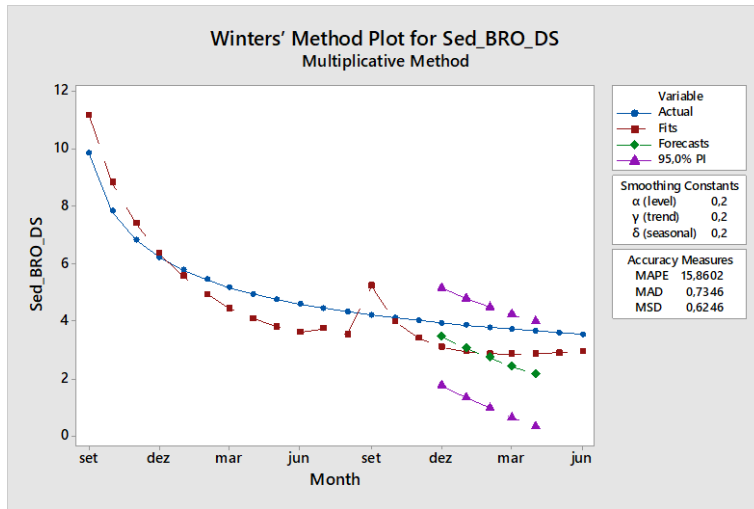


Figure 4. 79: Winters Plots for Sediment Prediction Using Brownlie Model

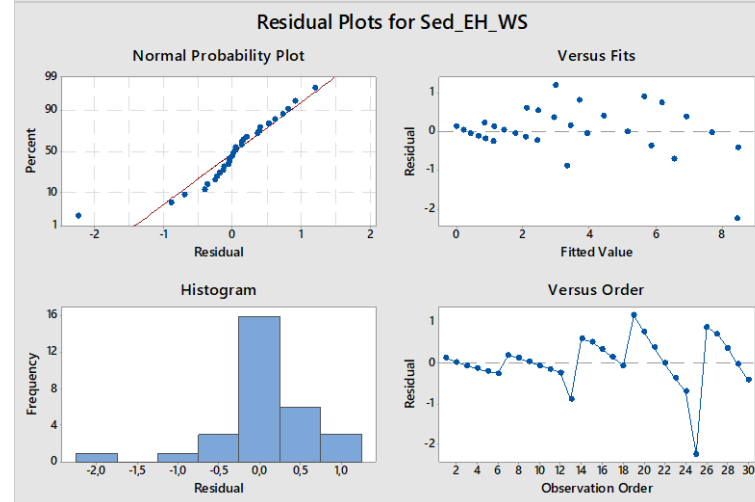
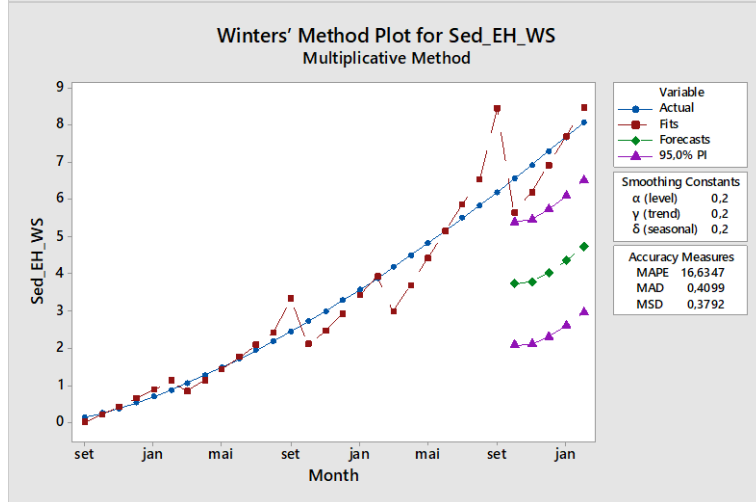
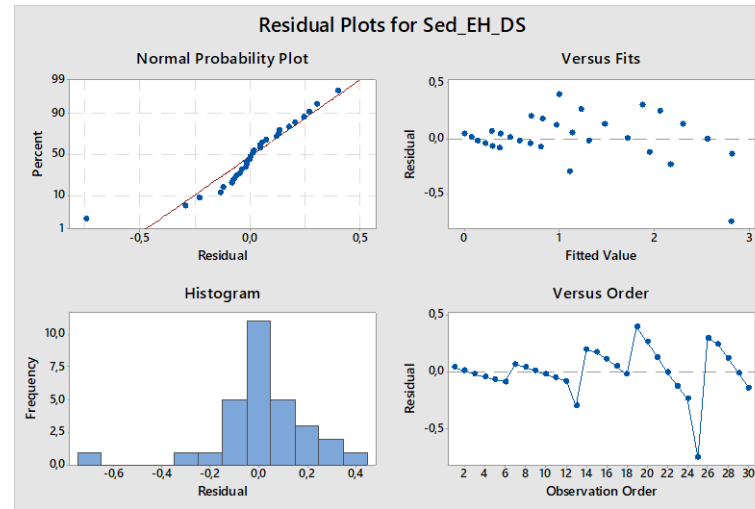
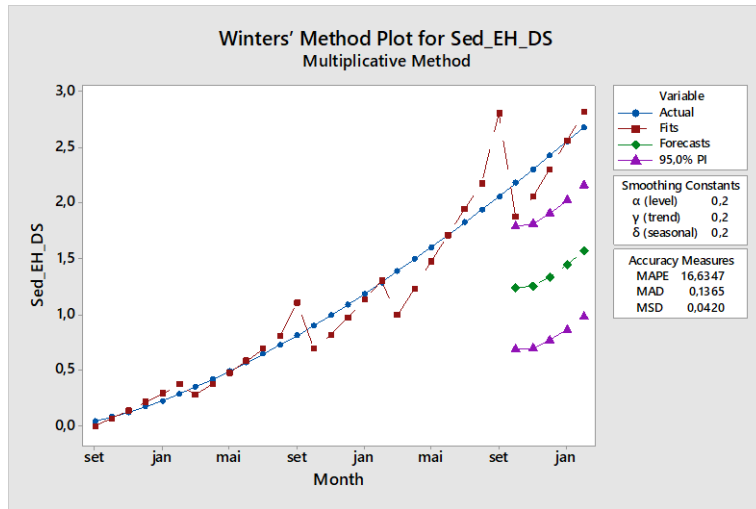


Figure 4. 80: Winters Plots for Sediment Prediction Using Engelund-Hansen Model

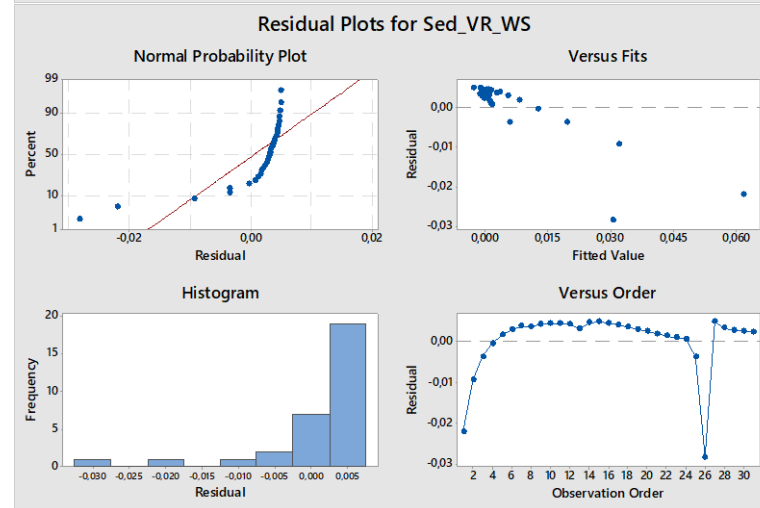
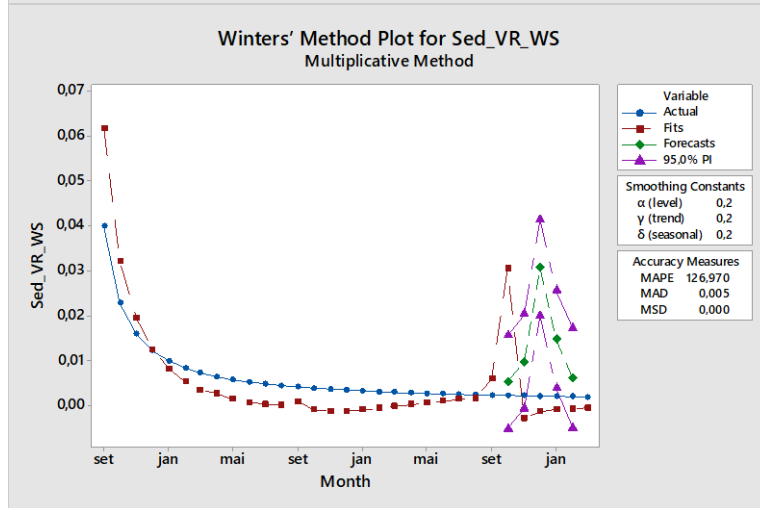
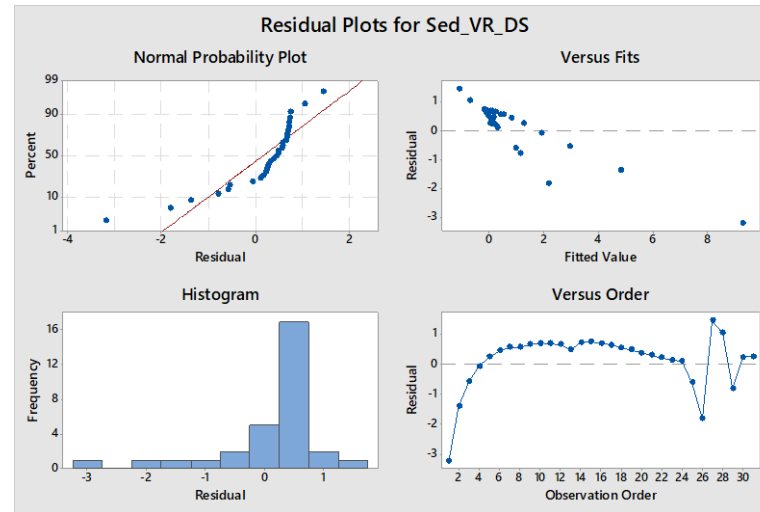
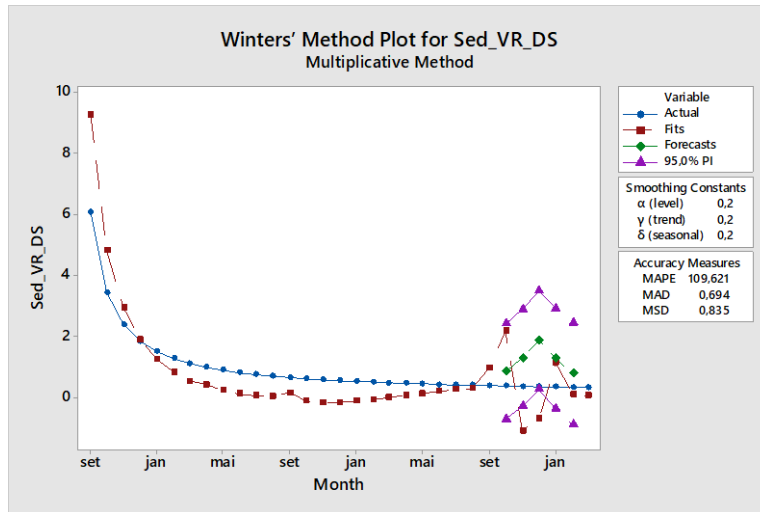


Figure 4. 81: Winters Plots for Sediment Prediction Using Van Rijn Model

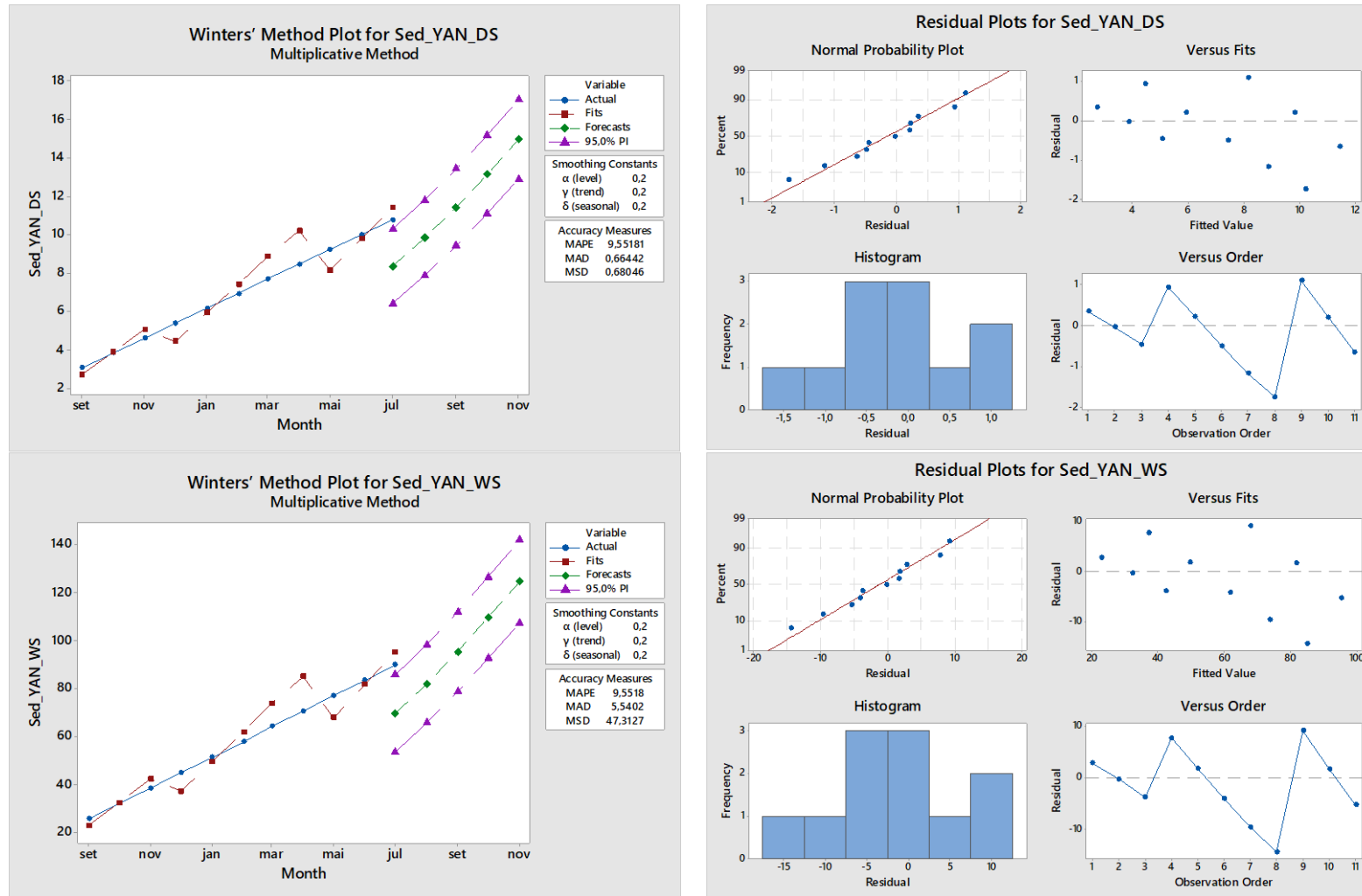


Figure 4. 82: Winters Plots for Sediment Prediction Using Yang Model

In Table 4.12 is presented in brief of the results of Winters' Method for each model prediction for sedimentation at CIS.

Table 4. 12: Winters' Method for Model Prediction of Sedimentation at CIS

Model Predictors	Season	MAPE	MAD	MSD	Observation
Acker's and White	DS	1.65091	0.00074	0.00000	Acceptable
	WS	95.5290	5.29700	323.764	
Brownlie	DS	15.8602	0.73460	0.62460	Acceptable
	WS	15.8602	2.37470	6.52660	Acceptable
Engelund and Hansen	DS	16.6347	0.13650	0.04200	Acceptable
	WS	16.6347	0.40990	0.37920	Acceptable
Van Rijn	DS	109.621	0.69400	0.83500	
	WS	126.970	0.00500	0.00000	
Yang	DS	9.55181	0.66442	0.68046	Acceptable
	WS	9.55180	5.54020	47.3127	

From the point of view of Winters Method, the best fitting model for sediment predictions at CIS were given by AW DS, YAN DS, BRO DS, BRO WS, E-H DS and E-H WS models, whereby their MAPE, MAD and MSD values were found to be low. These findings are consistent with Akasiadis and Georgogiannis (2018), Feizabadi (2020), Xie et al. (2019), and Zorndt and Schlurmann (2019) who refer that lower values of MAPE implies best fitting models.

CHAPTER FIVE

CONCLUSION AND RECOMMENDATIONS

5.1. Conclusion

5.1.1 The effect of canal channel and inflow factors on sediment flux

The key aspects causing sedimentation in the CIS can be divided into canal channel and inflow factors. Canal channel factors suggested canal slope changed considerably over time due to sediment accumulation. All three reaches and years of 2001, 2016 and 2019 presented significant variations, except for Lionde-Marrambajane, where no significance was found. Bed load characteristic at downstream had Atterberg limit test showing liquid limit, plasticity limit and plasticity index at magnitude of 52%, 20% and 32%, respectively. Erosion shear stress was found in 2.960 N/m². Beside this, particle size distribution in the scheme was found to be comprised by sand in 39%, silt 52% and clay 9%, leading to silt-sand to silt-clay-sand sediments classification. The canal bed is classified as transitional, as sand is found between 25% and 40%. High potential for occurrence of flocculation was found in the scheme for both seasons. Inflow factors suggested suspended sediment concentration decreases with water depth in dry season, whilst it increments during wet season. Similarly, sediment concentration accumulated with sampling weeks during dry season, and decreased in wet season, except for some stations. Moreover, water turbidity, pH, temperature, total dissolved solids and electric conductivity greatly influenced sediment flux.

5.1.2 The temporal trends-dynamics of water flow and sedimentation flux

A trend was observed for water flow and sediment flux from the upstream to downstream between 2004 and 2019. Tools for trend analysis such as Fourier transform, ARIMA test and Mann-Kendall indicated seasonality occurrence in the scheme. All stations showed higher magnitudes and peaks of water flow and sediment flux during wet season over dry season, for every year. Therefore, temporal trends-dynamic were found on water flow and sedimentation flux. Findings suggest higher values during DS for water discharge and sediment flux. Mann-Kendall test for sediment discharge trends was not significant at 95% significance level, except for the Offtake in WS. ARIMA test for the sediment discharges, at the Intake, for DS and WS, sediments were well described by the ARIMA model and gave a good result for the sediments. Good fit between the observed and the predicted ARIMA model was found. ARIMA model for sediment discharge at CIS based on AIC has a good fit for AR (p=1), whereby, at the Intake the ARIMA p-value was 0.822 and 0.932, for WS and DS,

respectively. Whilst in the Offtake, the ARIMA p-value was 0.877 and 0.893, respectively. Sediments discharges recurrence was found to be in every 2-4 and 1-2 years for DS and WS respectively. These results can be used to improve the CIS management, both for water flow and sediment flux. For example, the fact that the scheme has been built in the 50's points out to the need for a consistent and regular monitoring of water flow structures and sedimentation discharges.

5.1.3 Influence of water flow on sediments settling velocity at different depths

Different aspects of water flow related to sedimentation were assessed in this work. These included sediments settling velocity (SSV), which was seriously influenced by sampling weeks, particle grain size and canal depth. It also included water flow that was influenced by canal depth. SSV was higher during WS than on DS and varied considerably with particle grain size. Additionally, water flow velocity varied with the canal depth. The settling velocity of the sediments was low at Montante and Rio sectors than at the Sul sector. Therefore, the influence of water flow on the sediment settling velocity was thoroughly confirmed at different depths and lengths. These findings are important because they shed a light on the subject that can help project the effect of water flow every time the gates are opened at the most upstream in the Macarretane weir and other diverting structures located along the canal. Managers and developers will find great opportunity to improve the CIS operation and maintenance, with particular focus on the sediments transport and deposition.

5.1.4 Best sediment deposition scenarios

Sedimentation was best predicted in linear regressions by Engenlund-Hansen, Van Rijn 3, Van Rijn 1, Brownlie and Ackers-White, with coefficient of determination (R^2) between 60% and 90%. Non-parametric regression was successfully introduced for simulations to improve models accuracy, and $R^2 > 90\%$ was found, in majority of predictors. Predicting models were analysed in terms of goodness fit, and there favourably suggested that besides the current situation there is significant potential for improvements ($R^2 > 75\%$). These improvements are achievable if scenarios are implemented. The first scenario, which referred to water flow in the canal, was found to be satisfactory for Ackers-White (DS and WS) and Brownlie (DS and WS) models. The second scenario, which referred to the suspended sediment, Ackers-White (DS and WS) and Brownlie (DS and WS) and Engenlund-Hansen (DS and WS) models satisfactorily predicted the new situation in the scheme. The third and last scenario referred to

the bed load sediments conditions. Here, Ackers-White (DS) and Brownlie (WS) and Engelund-Hansen (DS and WS) provided better predictions than the rest of the models. From Winters Method, the best fitting model for sediment predictions at CIS, without discriminating scenarios, were given by Ackers-White (DS), Yang (DS), Brownlie (DS and WS) and Engelund-Hansen (DS and WS). These findings if implemented, can help improve the sediment management in the scheme.

5.2. Recommendations

From the findings of this research, the following are recommended:

- i. Regular monitoring is required to minimize canal channel (changes in bathymetric profiles) and inflow factors (water depth and velocity) effects on sediment flux. Potential usage of sediment excluders and regular desiltations in severely affected sites may also be taken into account;
- ii. Temporal trends-dynamics can predict (re)occurrence of sediments, and further investigation is required on the spatial trends-dynamics. Mapping sediment affected areas may reinforce the relevance of the study;
- iii. Determining shear stress threshold for fine sediment deposited in the bed canal may further the scope of this research work; and
- iv. Simulations and scenarios models can be implemented to minimize sedimentation. Engelund-Hansen, Van Rijn 3 and Ackers-White can be favourably used for wet season, whilst Van Rijn 1 and Brownlie, for dry season simulations. Scenarios S1, S2 and S3 can reduce sedimentation burden in the system by manipulating some flexible factors, such as water depth and bed characteristics. Despite well predicting models identified in this work, other models can be researched out to expand this study reach and digital applicative and software be prepared to support managers and researchers.

REFERENCES

- Abhari, M. N., Iranshahi, M., Ghodsian, M., & Firoozabadi, B. (2018). Experimental study of obstacle effect on sediment transport of turbidity currents. *Journal of Hydraulic Research*, *56*(5), 618–629. <https://doi.org/10.1080/00221686.2017.1397778>
- Ackers, P., & Lacey, G. (1992). Gerard Lacey memorial lecture. Canal and river regime in theory and practice "1929-1992". London, United Kingdom. Accessed on 2019 November 21. Retrieved from [1992 gerald lacey memorial lecture. canal and river regime in theory and practice: 1929-92. | semantic scholar](https://www.semanticscholar.org/entry/1992-gerald-lacey-memorial-lecture-canal-and-river-regime-in-theory-and-practice-1929-92)
- Adongo, T. A., Kyei-Baffour, N., Abagale, F. K., & Agyare, W. A. (2020). Assessment of reservoir sedimentation of irrigation dams in northern Ghana. *Lake and Reservoir Management*, *36*(1), 87–105. <https://doi.org/10.1080/10402381.2019.1659461>
- Afan, H. A., El-Shafie, A., Yaseen, Z. M., Hameed, M. M., Wan Mohtar, W. H. M., & Hussain, A. (2015). ANN Based Sediment Prediction Model Utilizing Different Input Scenarios. *Water Resources Management*, *29*(4), 1231–1245. <https://doi.org/10.1007/s11269-014-0870-1>
- Afessa, M. M., & Yosef, B. A. (2019). Impact of irrigation on the water level of Lake Maybar, Northeast Ethiopia. *International Journal of River Basin Management*, *17*(4), 489–506. <https://doi.org/10.1080/15715124.2018.1461105>
- Ahmed, A. S. M., & Sato, S. (2003). A Sheetflow Transport Model for Asymmetric Oscillatory Flows Part I: Uniform Grain Size Sediments. *Coastal Engineering Journal*, *45*(3), 321–337. <https://doi.org/10.1142/S0578563403000786>
- Ait-Sahalia, Y., & Xiu, D. (2019). Principal Component Analysis of High-Frequency Data. *Journal of the American Statistical Association*, *114*(525), 287–303. <https://doi.org/10.1080/01621459.2017.1401542>
- Akasiadis, C., & Georgogiannis, A. (2018). Predicting agent performance in large-scale electricity demand shifting. *Advances in Building Energy Research*, *12*(1), 116–137. <https://doi.org/10.1080/17512549.2017.1325402>
- Akinyemi, S. A., Akinlua, A., Ojo, O. I., Gitari, W. M., Akinyeye, R. O., & Petrik, L. F. (2015). Mineralogy and Mobility Pattern of Trace Metals in Brine Irrigated Dry Disposed Weathered Coal Fly Ash. *Energy Sources, Part A: Recovery, Utilization, and Environmental Effects*, *37*(8), 894–905. <https://doi.org/10.1080/15567036.2011.592904>

- Akkuzu, E., Unal, H. B., Karatas, B. S., Avci, M., & Asik, S. (2008). Evaluation of irrigation canal maintenance according to roughness and active canal capacity values. *Journal of Irrigation and Drainage Engineering*, 134(1), 60-66. [http://doi.org/10.1061/\(ASCE\)0733-9437](http://doi.org/10.1061/(ASCE)0733-9437)
- Aksoy, H., Unal, N. E., Cokgor, S., Gedikli, A., Yoon, J., Koca, K., Inci, S. B., Eris, E., & Pak, G. (2013). Laboratory experiments of sediment transport from bare soil with a rill. *Hydrological Sciences Journal*, 58(7), 1505–1518. <https://doi.org/10.1080/02626667.2013.824085>
- Ali, M., & Sterk, G. (2015). Availability and performance of sediment detachment and transport functions for overland flow conditions. *Hydrological Sciences Journal*, 60(9), 1550–1565. <https://doi.org/10.1080/02626667.2014.948443>
- Ampomah, R. (2014). Sediment Harvesting, Beneficial Use and the Impact of Climate and Land-Use/Land-Cover Change on Sediment Load. (Electronic Thesis or Dissertation). Accessed 2020 June 04. Retrieved from <https://etd.ohiolink.edu/>
- Ancey, C. (2020). Bed load transport: A walk between randomness and determinism. Part 2. Challenges and prospects. *Journal of Hydraulic Research*, 58(1), 18–33. <https://doi.org/10.1080/00221686.2019.1702595>
- Anger, B., Moulin, I., Commene, J.-P., They, F., & Levacher, D. (2019). Fine-grained reservoir sediments: An interesting alternative raw material for Portland cement clinker production. *European Journal of Environmental and Civil Engineering*, 23(8), 957–970. <https://doi.org/10.1080/19648189.2017.1327890>
- Arabameri, A., Pal, S. C., Costache, R., Saha, A., Rezaie, F., Danesh, A. S., Pradhan, B., Lee, S., & Hoang, N.-D. (2021). Prediction of gully erosion susceptibility mapping using novel ensemble machine learning algorithms. *Geomatics, Natural Hazards and Risk*, 12(1), 469–498. <https://doi.org/10.1080/19475705.2021.1880977>
- Asadi, A., Huat, B. B. K., Hanafi, M. M., Mohamed, T. A., & Shariatmadari, N. (2011). Chemico-geomechanical sensitivities of tropical peat to pore fluid pH related to controlling electrokinetic environment. *Journal of the Chinese Institute of Engineers*, 34(4), 481–487. <https://doi.org/10.1080/02533839.2011.576491>
- Asselman, N. E. M. (2000). Fitting and interpretation of sediment rating curves. *Journal of Hydrology*, 234(1), 228-248. Accessed 2017 August 27. Retrieved from www.elsevier.com/locate/jhydrol

- ASTM D4318. 2011. Standard test methods for liquid limit, plastic limit, and plasticity index of soils. West Conshohocken, PA: ASTM International. Accessed 2021 January 17. www.astm.org
- Aydın, D., & Memmedli, M. (2012). Optimum smoothing parameter selection for penalized least squares in form of linear mixed effect models. *Optimization*, 61(4), 459–476. <https://doi.org/10.1080/02331934.2011.574698>
- Bauder, T. A., Waskom, R. M., Sutherland, P. L., & Davis, J. G. (2014). Irrigation Water Quality Criteria. 4. Accessed 2017 March 26. Retrieved from [Irrigation Water Quality Criteria \(mountainscholar.org\)](http://IrrigationWaterQualityCriteria.mountainscholar.org)
- Belal, T., Ghembaza, M. S., & Bellia, Z. (2019). An investigation of the effects of cementation and temperature on the water retention curve of compacted silt. *International Journal of Geotechnical Engineering*, 0(0), 1–11. <https://doi.org/10.1080/19386362.2019.1617953>
- Belaud, G. (1996). Modeling of sediment transport in irrigation canals of Pakistan: examples of application: definition of a simple simulation tool and test on two actual canals of Pakistan: application to management strategies. Accessed 2017 July 16. Retrieved from <https://agris.fao.org/agris-search/search.do?recordID=QL2012000712> and [XVCS : Document 8 \(core.ac.uk\)](http://XVCS.Document8.core.ac.uk)
- Belaud, G., & Baume, J.-P. (2002). Maintaining equity in surface irrigation network affected by silt deposition. *Journal of Irrigation and Drainage Engineering*, 128(5), 316–325. [http://doi.org/10.1016/\(ASCE\)0733-9437](http://doi.org/10.1016/(ASCE)0733-9437)
- Bhattacharyya, P., & Sengupta, D. (2009). Estimation of tool wear based on adaptive sensor fusion of force and power in face milling. *International Journal of Production Research*, 47(3), 817–833. <https://doi.org/10.1080/00207540701403376>
- Blázquez-García, A., Conde, A., Milo, A., Sánchez, R., & Barrio, I. (2020). Short-term office building elevator energy consumption forecast using SARIMA. *Journal of Building Performance Simulation*, 13(1), 69–78. <https://doi.org/10.1080/19401493.2019.1698657>
- Bong, C. H. J., & Liow, C. V. (2019). Hydraulic characteristics of flow through angled baffle-plates in an open channel. *International Journal of River Basin Management*, 0(0), 1–6. <https://doi.org/10.1080/15715124.2019.1653307>

- Borok, A. (2014). Water Quality Standards (Water Quality Standards: Turbidity Technical Review Summary of Sources, Effects, and Issues Related to Revising the Statewide Water Quality Standard for Turbidity, p. 76) [Technical Report]. Oregon Department of Environmental Quality. Accessed 2020 August 05. Retrieved from <https://www.oregon.gov/deq/FilterDocs/TurbidityTechRev.pdf>
- Box, G. E. P. and Jenkins, G. M., Reinsel, G. C., (1994). Time series analysis: forecasting and control, 3rd edition. Prentice Hall, Englewood Cliffs.
- Box, G. E. P., and Jenkins, G. M., (1976). Times series analysis -forecasting and control. Prentice-Hall, Englewood Cliffs.
- Boylan, G. L., & Cho, B. R. (2013). Robust parameter design in embedded high-variability production processes: An alternative approach to mitigating sources of variability. *International Journal of Production Research*, 51(15), 4517–4538. <https://doi.org/10.1080/00207543.2013.774497>
- Branß, T. (2019). Estimation of bed load by tracking supply-limited bedforms. 6. Accessed 2021 May 09. Retrieved from <https://www.marum.de/Binaries/Binary18505/MARIDVI-Branss-Till.pdf>
- Bravo, F., & Grant, J. (2018). Modelling sediment assimilative capacity and organic carbon degradation efficiency at marine fish farms. *Aquaculture Environment Interactions*, 10, 309–328. JSTOR. <https://doi.org/10.2307/26849960>
- BRL Engenharia (Cartographer). (2003). Chókwè Irrigation Map. Hidráulica de Chókwè. E.P. Ministério de Agricultura e Desenvolvimento Rural. Maputo.
- Buffington, J. M., Montgomery, D. R., & Greenberg, H. M. (2004). Basin-scale availability of salmonid spawning gravel as influenced by channel type and hydraulic roughness in mountain catchments. *Canadian Journal of Fisheries and Aquatic Sciences*, 61, 2085-2096. <http://doi.org/10.1139/F04-141>
- Burge, L., Guthrie, R., & Chaput-Desrochers, L. (2014). Hydrological factors affecting spatial and temporal fate of sediment in association with stream crossings of the Mackenzie Gas Pipeline. (Research Document 2014/029). Ottawa, Canada: Fisheries and Oceans Canada, Canadian Science Advisory Secretariat (CSAS). Accessed 2018 July 20. Retrieved from <http://www.dfo-mpo.gc.ca/csas-sccs/csas-sccs@dfo-mpo.gc.ca>

- Cao, Z., Pender, G., & Carling, P. (2006). Shallow water hydrodynamic models for hyperconcentrated sediment-laden floods over erodible bed. *Advances in Water Resources*, 29(4), 546–557. <https://doi.org/10.1016/j.advwatres.2005.06.011>
- Chambal, R. A. (2017, May 17). Stage of the sedimentation in the Chókwè Irrigation Scheme [Presential Interview]. Departamento de Estudos e Projectos de Reabilitação, Direcção de Manutenção e Obras Hidráulicas. Hidráulica de Chókwè. E.P. Chókwè.
- Chan, W. S. (1999). A comparison of some of pattern identification methods for order determination of mixed ARMA models. *Stat Probability Letter* 42(1):69–79. [https://doi.org/10.1016/S0167-7152\(98\)00195-3](https://doi.org/10.1016/S0167-7152(98)00195-3)
- Charnigo, R., Hall, B., & Srinivasan, C. (2011). A Generalized Cp Criterion for Derivative Estimation. *Technometrics*, 53(3), 238–253. <https://doi.org/10.1198/TECH.2011.09147>
- Chauchat, J. (2018). A comprehensive two-phase flow model for unidirectional sheet-flows. *Journal of Hydraulic Research*, 56(1), 15–28. <https://doi.org/10.1080/00221686.2017.1289260>
- Chen, D., Melville, B., Zheng, J., Wang, Y., Zhang, C., Guan, D., & Chen, C. (2021). Pickup rate of non-cohesive sediments in low-velocity flows. *Journal of Hydraulic Research*, 0(0), 1–11. <https://doi.org/10.1080/00221686.2020.1871430>
- Chen, H. L. (2018). Early Prediction of Project Duration: A Longitudinal Study. *Engineering Management Journal*, 30(3), 191–202. <https://doi.org/10.1080/10429247.2018.1483169>
- Chen, X., Wang, J., Zhang, C., Yu, S., Zhou, J., Zhang, N., & Feng, Q. (2018). Biological Mediation of Sediment Erosion: Can We Account for Tidal Effects? *Journal of Coastal Research*, 421–425. JSTOR. <https://doi.org/10.2112/SI85-085.1>
- Chiari, M., Friedl, K., & Rickenmann, D. (2010). A one-dimensional bed load transport model for steep slopes. *Journal of Hydraulic Research*, 48(2), 152–160. <https://doi.org/10.1080/00221681003704087>
- Church, M. (2006). Bed Material Transport and the Morphology of Alluvial River Channels. *Annual Revision of Earth and Planetary Sciences*, 34, 325–354. <http://doi.org/10.1146/annurev.earth.33.092203.122721>
- Church, M., & Hassan, M. A. (2002). Mobility of bed material in Harris Creek. *Water Resources Research*, 38 (11), 1237-1249. <http://doi.org/10.1029/2001WR000753>

- Cislaghi, A., Chiaradia, E. A., & Bischetti, G. B. (2015). A comparison between different methods for determining grain distribution in coarse channel beds. *International Journal of Sediment Research*, (IJSRC54, S1001-6279(16)00003-2). <https://doi.org/10.1016/j.ijsrc.2015.12.002>
- City Population. (2019). Mozambique: Administrative Division (Provinces and Districts)—Population Statistics, Charts and Map. Accessed 2020 December 21. Retrieved from <https://citypopulation.de/en/mozambique/admin/>
- Clayton, J. A., & Pitlick, J. (2007). Spatial and temporal variations in bed load transport intensity in a gravel bed river bend. *Water Resources Research*, 43(W02426). <http://doi.org/10.1029/2006WR005253>
- Coulibaly, P., & Burn, D. H. (2004). Wavelet analysis of variability in annual Canadian streamflows. *Water Resources Research*, 40(3). <https://doi.org/10.1029/2003WR002667>
- Croux, C., García-Escudero, L. A., Gordaliza, A., Ruwet, C., & Martín, R. S. (2017). Robust principal component analysis based on trimming around affine subspaces. *Statistica Sinica*, 27(3), 1437–1459. JSTOR. <https://www.jstor.org/stable/26383263>
- Cui, Y., Booth, D. B., Monschke, J., Gentzler, S., Roadifer, J., Greimann, B., & Cluer, B. (2017). Analyses of the erosion of fine sediment deposit for a large dam-removal project: An empirical approach. *International Journal of River Basin Management*, 15(1), 103–114. <https://doi.org/10.1080/15715124.2016.1247362>
- Das, U. K., Roy, P., & Ghose, D. K. (2019). Modeling water table depth using adaptive Neuro-Fuzzy Inference System. *ISH Journal of Hydraulic Engineering*, 25(3), 291–297. <https://doi.org/10.1080/09715010.2017.1420497>
- de Sousa, L. S. (2012). Does surge flow improve the efficiency of border-check irrigation?: A case study in the Harvey Irrigation Area, southwest of Western Australia. <https://research-repository.uwa.edu.au/en/publications/does-surge-flow-improve-the-efficiency-of-border-check-irrigation>
- Dearnaley, M. P., Spearman, J. R., & Feates, N. G. (1995). *Intercomparison of in-situ particle size and settling velocity measurements* (Technical Report No. SR444; pp. 1–54). HR Wallingford. <https://eprints.hrwallingford.com/364/1/SR444.pdf>
- Decrop, B., Mulder, T. D., Toorman, E., & Sas, M. (2015). New methods for ADV measurements of turbulent sediment fluxes – application to a fine sediment plume.

- Journal of Hydraulic Research*, 53(3), 317–331.
<https://doi.org/10.1080/00221686.2015.1037871>
- Dejen, Z. A. (2015). Hydraulic and Operational Performance of Irrigation Schemes in View of Water Saving and Sustainability: Sugar estates and Community Managed schemes in Ethiopia. (Doctor of Philosophy). Wageningen University and UNESCO-IHE Institute for Water Education, Delft, The Netherlands. (ISBN 978-1-138-02767-1 (Taylor & Francis Group) and ISBN 978-94-6257-169-3 (Wageningen University)). Accessed 2017 August 02. Retrieved from <https://library.wur.nl/WebQuery/wurpubs/482984>
- Delleur, J. W. (2014). Ven Te Chow and Deterministic Hydrology. World Environmental and Water Resources Congress 2014, 733–742.
<https://doi.org/10.1061/9780784413548.076>
- Depeweg, H., & Paudel, K. P. (2003). Sediment transport problems in Nepal evaluated by the SETRIC model. *Irrigation and Drainage*, 52(3), 247–260.
<https://doi.org/10.1002/ird.87>
- Ding, J., Li, J., & Liu, F. (2016). Fast Fourier Transform Accelerated Finite-Difference Delay Modeling Method. *Electromagnetics*, 36(6), 353–365.
<https://doi.org/10.1080/02726343.2016.1207748>
- Ding, Y., & Langendoen, E. J. (2018). Simulation and control of sediment transport due to dam removal. *Journal of Applied Water Engineering and Research*, 6(2), 95–108.
<https://doi.org/10.1080/23249676.2016.1224691>
- Driss, A. A.-E., Harichane, K., Ghrici, M., & Gadouri, H. (2021). Assessing the effect of moulding water content on the behaviour of lime-stabilised an expansive soil. *Geomechanics and Geoengineering*, 0(0), 1–13.
<https://doi.org/10.1080/17486025.2021.1903092>
- Duan, X., Shi, X., Li, Y., Rong, L., & Fen, D. (2017). A new method to calculate soil loss tolerance for sustainable soil productivity in farmland. *Agronomy and Sustainable Development*, 37(2). <http://doi.org/10.1007/s13593-016-0409-3>
- Effler, S. W., & Brooks, C. M. (1998). Gradients and Dynamics in Downward Flux and Settling Velocity in Cannonsville Reservoir. *Lake and Reservoir Management*, 14(2–3), 213–224. <https://doi.org/10.1080/07438149809354332>

- Efthimiou, N., Lykoudi, E., & Karavitis, C. (2017). Comparative analysis of sediment yield estimations using different empirical soil erosion models. *Hydrological Sciences Journal*, 62(16), 2674–2694. <https://doi.org/10.1080/02626667.2017.1404068>
- Einstein, H. A. (1942). Formulae for the transportation of bed load. *Transactions, ASCE*, 107. <https://doi.org/10.1061/TACEAT.0005468>
- El-Amier, Y. A., Zahran, M. A. E.-K., & Al-Mamory, S. H. (2015). Assessment the Physico-Chemical Characteristics of Water and Sediment in Rosetta Branch, Egypt. *Journal of Water Resource and Protection*, 07(13), 1075–1086. <https://doi.org/10.4236/jwarp.2015.713088>
- Elliott, G., Rothenberg, T. J., & Stock, J. H. (1992). Efficient Tests for an Autoregressive Unit Root (No. t0130). *National Bureau of Economic Research*. <https://doi.org/10.3386/t0130>
- Ellison, C. A., Kiesling, R. L., & Fallon, J. D. (2010). Correcting streamflow, turbidity, and suspended sediment concentration in Minnesota’s Wild Rice River. Paper presented at the 2nd Joint Federal Interagency Conference, Las Vegas, Nevada. Accessed 2018 September 12. Retrieved from https://acwi.gov/sos/pubs/2ndJFIC/Contents/8B_Ellison_12_03_09_paper.pdf
- Engelund, F., & Hansen, E. (1967). A monograph on sediment transport in alluvial streams. Technical University of Denmark Østervoldgade 10, Copenhagen K. Accessed 2019 September 14. Retrieved from <https://repository.tudelft.nl/islandora/object/uuid%3A81101b08-04b5-4082-9121-861949c336c9>
- Estabragh, A. R., Amini, A. H., Javadi, A. A., & Kouchakzadeh, M. (2019). Properties of sediments deposited in a fluid with different pH. *Marine Georesources & Geotechnology*, 37(6), 643–650. <https://doi.org/10.1080/1064119X.2018.1471629>
- Estabragh, A. R., Kouchakzadeh, M., & Javadi, A. A. (2019). Treatment of a clay soil deposited in saline water by cement. *European Journal of Environmental and Civil Engineering*, 0(0), 1–17. <https://doi.org/10.1080/19648189.2019.1584769>
- Faghihirad, S., Lin, B., & Falconer, R. A. (2015). Application of a 3D Layer Integrated Numerical Model of Flow and Sediment Transport Processes to a Reservoir. *Water*, 7, 5239-5257. <http://doi.org/10.3390/w7105239>

- Fan, J.-C., Chang, S.-C., Liao, K.-W., Guo, J.-J., Liu, C.-H., Chang, Y.-C., Huang, C.-L., & Yang, C.-H. (2018). The impact of physiographic factors upon the probability of slides occurrence: A case study from the Kaoping River Basin, Taiwan. *Journal of the Chinese Institute of Engineers*, 41(5), 419–429. <https://doi.org/10.1080/02533839.2018.1482236>
- FAO. (2014). Water quality for agriculture. Accessed 2016 April 27. Retrieved from <http://www.fao.org/3/T0234e/T0234E06.htm>
- FAO. (2016). Database of world rivers and their sediment yields. In FAO. ROME: FAO. Accessed 2017 June 15. Retrieved from www.fao.org/aquastat/en/overview/archive/river-sediment-yields
- Feizabadi, J. (2020). Machine learning demand forecasting and supply chain performance. *International Journal of Logistics Research and Applications*, 0(0), 1–24. <https://doi.org/10.1080/13675567.2020.1803246>
- Fent, I., Zech, Y., & Soares-Frazão, S. (2019). Dam-break flow experiments over mobile bed: Velocity profile. *Journal of Hydraulic Research*, 57(1), 131–138. <https://doi.org/10.1080/00221686.2018.1444677>
- Ferrara, C., Martella, F., & Vichi, M. (2019). Probabilistic Disjoint Principal Component Analysis. *Multivariate Behavioral Research*, 54(1), 47–61. <https://doi.org/10.1080/00273171.2018.1485006>
- Fleming, S. W., Lavenue, A. M., Aly, A. H., & Adams, A. (2002). Practical applications of spectral analysis to hydrologic time series. *Hydrological Processes*, 16(2), 565–574. <https://doi.org/10.1002/hyp.523>
- Flynn, R. (2009). Irrigation Water Analysis and Interpretation. New Mexico State University. Accessed 2018 July 11. Retrieved from <https://aces.nmsu.edu/pubs/w/W102.pdf>
- Fujikoshi, Y., Yanagihara, H., & Wakaki, H. (2005). Bias Corrections of some Criteria for Selecting Multivariate Linear Models in a General Nonnormal Case. *American Journal of Mathematical and Management Sciences*, 25(3–4), 221–258. <https://doi.org/10.1080/01966324.2005.10737651>
- Galappatti, G., & Vreugdenhil, C. B. (2010). A depth-integrated model for suspended sediment transport. *Journal of Hydraulic Research*, 23(4), 359–377. <http://doi.org/10.1080/00221688509499345>

- Gao, P. (2008). Understanding watershed suspended sediment transport. *Progress in Physical Geography: Earth and Environment*, 32(3), 243–263. <https://doi.org/10.1177/0309133308094849>
- Gebrehiwot, K. A., Haile, A. M., de Fraiture, C. M. S., Chukalla, A. D., & Embaye, T. G. (2015). Optimizing Flood and Sediment Management of Spate Irrigation in Aba'ala Plains. *Water Resources Management*, 29(3), 833–847. <https://doi.org/10.1007/s11269-014-0846-1>
- Ghomeshi, M., Baher, M. S., & Ehdaei, P. (2019). An experimental study of plunge depth in the case of clear water movement. *International Journal of River Basin Management*, 17(3), 323–332. <https://doi.org/10.1080/15715124.2018.1531420>
- Golui, D., Datta, S. P., Dwivedi, B. S., Meena, M. C., Varghese, E., Sanyal, S. K., Ray, P., Shukla, A. K., & Trivedi, V. K. (2019). Assessing Soil Degradation in Relation to Metal Pollution – A Multivariate Approach. *Soil and Sediment Contamination: An International Journal*, 28(7), 630–649. <https://doi.org/10.1080/15320383.2019.1640660>
- González, C., Richter, D. H., Bolster, D., Bateman, S., Calantoni, J., & Escauriaza, C. (2017). Characterization of bed load intermittency near the threshold of motion using a Lagrangian sediment transport model. *Environmental Fluid Mechanics*, 17, 111–137. <https://doi.org/10.1007/s10652-016-9476-x>
- Goyal, M. K., Sharma, A., & Katsifarakis, K. L. (2017). Prediction of flow rate of karstic springs using support vector machines. *Hydrological Sciences Journal*, 62(13), 2175–2186. <https://doi.org/10.1080/02626667.2017.1371847>
- Graf, W. H., & Cellino, M. (2002). Suspension flows in open channels; experimental study. *Journal of Hydraulic Research*, 40(4), 435–447. <http://doi.org/10.1080/00221680209499886>
- Gu, C., Mu, X., Gao, P., Zhao, G., Sun, W., & Li, P. (2017). Effects of climate change and human activities on runoff and sediment inputs of the largest freshwater lake in China, Poyang Lake. *Hydrological Sciences Journal*, 62(14), 2313–2330. <https://doi.org/10.1080/02626667.2017.1372856>
- Günlü, A., Ercanlı, İ., Şenyurt, M., & Keleş, S. (2019). Estimation of some stand parameters from textural features from WorldView-2 satellite image using the artificial neural

- network and multiple regression methods: A case study from Turkey. *Geocarto International*, 0(0), 1–18. <https://doi.org/10.1080/10106049.2019.1629644>
- Guo, X., Gong, X., Yuan, D., Jiang, G., Cao, J., Lin, Y., Lo, K. F. A., & Chen, C. (2019). Response of drip water temperature to climate variability: A case study in Xiaoyan Cave, southwest China. *Hydrological Sciences Journal*, 64(7), 873–884. <https://doi.org/10.1080/02626667.2019.1608994>
- Gyimah, R. A. A., Gyamfi, C., Anornu, G. K., Karikari, A. Y., & Tsyawo, F. W. (2020). Multivariate statistical analysis of water quality of the Densu River, Ghana. *International Journal of River Basin Management*, 0(0), 1–11. <https://doi.org/10.1080/15715124.2020.1803337>
- Ha, H. J., Choi, S. M., Seo, J. Y., & Ha, H. K. (2018). Erodibility of Sand-Mud Mixed Sediment on the Yeochari Tidal Flat, Gyeonggi Bay, Korea. *Journal of Coastal Research*, 416–420. JSTOR. <https://www.jstor.org/stable/26488251>
- Hamed, K. H., & Ramachandra Rao, A. (1998). A modified Mann-Kendall trend test for autocorrelated data. *Journal of Hydrology*, 204(1), 182–196. [https://doi.org/10.1016/S0022-1694\(97\)00125-X](https://doi.org/10.1016/S0022-1694(97)00125-X)
- Hamilton JD. (1994). *Time Series Analysis*. Princeton University Press: Princeton, NJ; 820 pp. Accessed 2019 November 12. Retrieved from [A.4. Matrix Algebra \(degruyter.com\)](https://www.degruyter.com)
- Hartless, G., Booth, J. G., & Littell, R. C. (2003). Local Influence of Predictors in Multiple Linear Regression. *Technometrics*, 45(4), 326–332. <https://doi.org/10.1198/004017003000000140>
- Haschenburger, J. K. (2003). Partial transport in a natural gravel bed channel. *Water Resources Research*, 39(1), 1020. <http://doi.org/10.1029/2002WR001532>
- Havens, K. E., & Ji, G. (2018). Multiyear oscillations in depth affect water quality in Lake Apopka. *Inland Waters*, 8(1), 1–9. <https://doi.org/10.1080/20442041.2018.1428429>
- Hengade, N., Eldho, T. I., & Ghosh, S. (2018). Climate change impact assessment of a river basin using CMIP5 climate models and the VIC hydrological model. *Hydrological Sciences Journal*, 63(4), 596–614. <https://doi.org/10.1080/02626667.2018.1441531>
- HICEP. (2012). *Perímetro Irrigado do Regadio de Chókwè*. Chókwè: Hidráulica de Chókwè, E. P. – Minitésrio de Agricultura. Maputo.

- Hicks, D. M., Gomez, B., & Trustrum, N. A. (2000). Erosion thresholds and suspended sediment yields, Waipaoa River Basin, New Zealand. *Water Resources Research*, 36(4), 1129–1142. <https://doi.org/10.1029/1999WR900340>
- Hjulstrøm F. (1939) Transportation of debris by moving water, in Trask, P.D., ed., Recent Marine Sediments. A Symposium: Tulsa, Oklahoma, American Association of Petroleum Geologists, Tulsa, Oklahoma, 5–31.
- Hoffmann, T., Hillebrand, G., & Noack, M. (2017). Uncertainty analysis of settling, consolidation and resuspension of cohesive sediments in the Upper Rhine. *International Journal of River Basin Management*, 15(4), 401–411. <https://doi.org/10.1080/15715124.2017.1375509>
- Horton, A. J., Constantine, J. A., Hales, T. C., Goossens, B., Bruford, M. W., & Lazarus, E. D. (2017). Modification of river meandering by tropical deforestation. *Geology*, 45(6), 511–514. <https://doi.org/10.1130/G38740.1>
- Houria, B., Mahdi, K., & Zohra, T. F. (2014). PSO-ANN's based suspended sediment concentration in Ksob basin, Algeria. *Journal of Engineering and Technology Research*, 6(8), 129-136. <http://doi.org/10.5897/JETR2014.0524>
- Hu, M., Xiao, F., & Cheung, H. (2020). Identification of simplified energy performance models of variable-speed air conditioners using likelihood ratio test method. *Science and Technology for the Built Environment*, 26(1), 75–88. <https://doi.org/10.1080/23744731.2019.1665446>
- Hu, P., Han, J., Li, W., Sun, Z., & He, Z. (2018). Numerical investigation of a sandbar formation and evolution in a tide-dominated estuary using a hydro-morphodynamic model. *Coastal Engineering Journal*, 60(4), 466–483. <https://doi.org/10.1080/21664250.2018.1529263>
- Huang, L., Sheng, R., Li, Z., Sun, D., & Yan, N. (2020). Comparison of phosphorus fraction in eutrophic lake sediments from the northern hemisphere. *Chemistry and Ecology*, 36(2), 100–121. <https://doi.org/10.1080/02757540.2019.1699538>
- Hung, M. C., Hsieh, T. Y., Wu, C. H., & Yang, J. C. (2009). Two-Dimensional Nonequilibrium Noncohesive and Cohesive Sediment Transport Model. *Journal of Hydraulic Engineering*, 135(5), 369–382. [https://doi.org/10.1061/\(ASCE\)0733-9429\(2009\)135:5\(369\)](https://doi.org/10.1061/(ASCE)0733-9429(2009)135:5(369))

- Hunt, S., & Jones, H. F. E. (2019). Sediment grain size measurements are affected by site-specific sediment characteristics and analysis methods: Implications for environmental monitoring. *New Zealand Journal of Marine and Freshwater Research*, 53(2), 244–257. <https://doi.org/10.1080/00288330.2018.1553192>
- Ingrassia, S., & Morlini, I. (2005). Neural Network Modeling for Small Datasets. *Technometrics*, 47(3), 297–311. <https://doi.org/10.1198/004017005000000058>
- Instituto Nacional de Estatística (INE). 2019. CENSO 2017. Resultados Definitivos do Resenseamento Geral da População e Habitação. Accessed 2020 December 20. Retrieved from www.ine.gov.mz
- Islam, T. U. (2017). Stringency-based ranking of normality tests. *Communications in Statistics - Simulation and Computation*, 46(1), 655–668. <https://doi.org/10.1080/03610918.2014.977916>
- Iyer, K. K. R., Joseph, J., Lopes, B. C. F. L., Singh, D. N., & Tarantino, A. (2018). Water retention characteristics of swelling clays in different compaction states. *Geomechanics and Geoengineering*, 13(2), 88–103. <https://doi.org/10.1080/17486025.2017.1396363>
- Iyer, K. K. R., Joseph, J., Shetty, R., & Singh, D. N. (2018). Some investigations to quantify hysteresis associated with water retention behaviour of fine-grained soils. *Geomechanics and Geoengineering*, 13(4), 264–275. <https://doi.org/10.1080/17486025.2018.1445872>
- JafariKhasragh, S., Lukovich, J. V., Hu, X., Myers, P. G., Sydor, K., & Barber, D. G. (2019). Modelling Sea Surface Temperature (SST) in the Hudson Bay Complex Using Bulk Heat Flux Parameterization: Sensitivity to Atmospheric Forcing, and Model Resolution. *Atmosphere-Ocean*, 57(2), 120–133. <https://doi.org/10.1080/07055900.2019.1605974>
- Jain, M. K., & Kothyari, U. C. (2000). Estimation of soil erosion and sediment yield using GIS. *Hydrological Sciences Journal*, 45(5), 771–786. <https://doi.org/10.1080/02626660009492376>
- Jaiyeola, A. T., & Adeyemo, J. (2019). Performance comparison between genetic programming and sediment rating curve for suspended sediment prediction. *African Journal of Science, Technology, Innovation and Development*, 11(7), 843–859. <https://doi.org/10.1080/20421338.2019.1587908>

- Jerrett, M., Arain, M. A., Kanaroglou, P., Beckerman, B., Crouse, D., Gilbert, N. L., Brook, J. R., Finkelstein, N., & Finkelstein, M. M. (2007). Modeling the Intraurban Variability of Ambient Traffic Pollution in Toronto, Canada. *Journal of Toxicology and Environmental Health, Part A*, 70(3–4), 200–212. <https://doi.org/10.1080/15287390600883018>
- Jinchi, H., Zhaohui, W., & Eishun, Z. (1993). A study on sediment transport in an irrigation district. Paper presented at the 15th International Congress on Irrigation and Drainage, The Hague, The Netherlands. pp. 1373-1384. Accessed 2018 May 07. Retrieved from <https://www.cabdirect.org/cabdirect/abstract/19946799309>
- Jukić, D., & Denić-Jukić, V. (2004). A frequency domain approach to groundwater recharge estimation in karst. *Journal of Hydrology*, 289(1), 95–110. <https://doi.org/10.1016/j.jhydrol.2003.11.005>
- Jukić, D., & Denić-Jukić, V. (2008). Estimating parameters of groundwater recharge model in frequency domain: Karst springs Jadro and Žrnovnica. *Hydrological Processes*, 22(23), 4532–4542. <https://doi.org/10.1002/hyp.7057>
- Julaia, C. d. S. (2009). Performance assessment of water distribution in large scale irrigation: Case study of Chókwè Irrigation System in Mozambique. (Master of Science). UNESCO-IHE, Institute for Water Education, Delft, The Netherlands. (WSE-HE-LWD-09.05). Accessed 2016 June 21. Retrieved from [Search results for IHE Delft Library \(worldcat.org\)](#)
- Kamble, S. A., Kunjeer, P. S., B, S., & Isaac, N. (2018). Hydraulic model studies for estimating scour cone development during pressure flushing of reservoirs. *ISH Journal of Hydraulic Engineering*, 24(3), 337–344. <https://doi.org/10.1080/09715010.2017.1381577>
- Kansara, S., Parashar, S., & Xue, Z. (2015). Effective Decision Making and Data Visualization Using Partitive Clustering and Principal Component Analysis (PCA) for High Dimensional Pareto Frontier Data. *SAE International Journal of Materials and Manufacturing*, 8(2), 336–343. JSTOR. <https://www.jstor.org/stable/26268720>
- Kaveshnikov, N. T. (1997). Critical state of sediment saturation of a flow in open channels. *Hydrotechnical Construction*, 31(1), 21–26. <https://doi.org/10.1007/BF02767283>
- Kawai, N., Wada, K., Hirano, H., Naganuma, T., Sueyoshi, M., Nakui, H., Saito, I., & Asakura, S. (2003). Critical concentration of dissolved oxygen to form protective iron

- oxides under combined water treatment conditions. *Corrosion Engineering, Science and Technology*, 38(4), 286–290. <https://doi.org/10.1179/147842203225005807>
- Kendall, A. D., & Hyndman, D. W. (2007). Examining Watershed Processes Using Spectral Analysis Methods Including the Scaled-Windowed Fourier Transform. In *Subsurface Hydrology: Data Integration for Properties and Processes* (pp. 183–200). *American Geophysical Union (AGU)*. <https://doi.org/10.1029/171GM14>
- Khan, M. Z., & Ghumman, A. R. (2008). Hydrodynamic modelling for water-saving strategies in irrigation canal. *Irrigation and Drainage*, 57(1), 400–410. <http://doi.org/10.1002/ird.375>
- Khan, S. S., Shareef, H., & Mutlag, A. H. (2019). Dynamic temperature model for proton exchange membrane fuel cell using online variations in load current and ambient temperature. *International Journal of Green Energy*, 16(5), 361–370. <https://doi.org/10.1080/15435075.2018.1564141>
- Khan, S., Sinha, R., Whitehead, P., Sarkar, S., Jin, L., & Futter, M. N. (2018). Flows and sediment dynamics in the Ganga River under present and future climate scenarios. *Hydrological Sciences Journal*, 63(5), 763–782. <https://doi.org/10.1080/02626667.2018.1447113>
- Kiani-Harchegani, M., Sadeghi, S. H., & Asadi, H. (2018). Comparing grain size distribution of sediment and original soil under raindrop detachment and raindrop-induced and flow transport mechanism. *Hydrological Sciences Journal*, 63(2), 312–323. <https://doi.org/10.1080/02626667.2017.1414218>
- Kim, J., Ivanov, V. Y., & Katopodes, N. D. (2013). Modeling erosion and sedimentation coupled with hydrological and overland flow processes at the watershed scale. *Water Research Research*, 49, 5134–5154. <http://doi.org/10.1002/wrcr.20373>
- Kim, K., Suh, Y.-C., Lee, I.-C., Choi, C.-G., & Kim, K. (2019). Changes in Permeability and Benthic Environment of Coastal Sediment based on Calcium Salt Supplier. *Journal of Coastal Research*, 311–315. JSTOR. <https://doi.org/10.2307/26852525>
- Kim, M., Lee, S., Baek, Y. S., Do, J., Lim, H.-S., & Lee, H. J. (2019). In Situ Observations of Ripples on the Surf Zone of a Beach. *Journal of Coastal Research*, 36–40. JSTOR. <https://doi.org/10.2307/26852473>

- Kim, S. D., Jeung, S. J., & Kim, B. S. (2018). Prediction of debris flows in the Korean Oship River based on climate change scenarios. *Geomatics, Natural Hazards and Risk*, 9(1), 703–719. <https://doi.org/10.1080/19475705.2018.1467347>
- Kim, S., Lee, G. S., Kim, D., Hahn, J., & Ryang, W.-H. (2018). Variation of temperature-dependent sound velocity in unconsolidated marine sediments: Laboratory measurements. *Marine Georesources & Geotechnology*, 36(3), 280–287. <https://doi.org/10.1080/1064119X.2016.1277442>
- Kisi, O. (2012). Modeling discharge-suspended sediment relationship using least square support vector machine. *Journal of Hydrology*, 456–457, 110–120. <https://doi.org/10.1016/j.jhydrol.2012.06.019>
- Kouzegaran, S., Shahnazari, H., & Jafarian, Y. (2021). The unsaturated shear strength of calcareous soil in comparison with silicate soil. *Marine Georesources & Geotechnology*, 39(2), 200–218. <https://doi.org/10.1080/1064119X.2019.1692266>
- Kumar, N., Ramanathan, A., Keesari, T., Chidambaram, S., Ranjan, S., Soheb, M., & Tranter, M. (2018). Tracer-based estimation of temporal variation of water sources: An insight from supra- and subglacial environments. *Hydrological Sciences Journal*, 63(11), 1717–1732. <https://doi.org/10.1080/02626667.2018.1526381>
- Kuo, Y.-H., & Kusiak, A. (2019). From data to big data in production research: The past and future trends. *International Journal of Production Research*, 57(15–16), 4828–4853. <https://doi.org/10.1080/00207543.2018.1443230>
- Kuscu, H., Bölüktepe, F. E., & Demir, A. O. (2009). Performance assessment for irrigation water management: A case study in the Karacabey irrigation scheme in Turkey. *African Journal of Agricultural Research*, 4 (2), 124–132. <http://www.academicjournals.org/AJAR> .
- Laanaya, F., St-Hilaire, A., & Gloaguen, E. (2017). Water temperature modelling: Comparison between the generalized additive model, logistic, residuals regression and linear regression models. *Hydrological Sciences Journal*, 62(7), 1078–1093. <https://doi.org/10.1080/02626667.2016.1246799>
- Landgraf, A. J., & Lee, Y. (2020). Generalized Principal Component Analysis: Projection of Saturated Model Parameters. *Technometrics*, 62(4), 459–472. <https://doi.org/10.1080/00401706.2019.1668854>

- Lanzoni, S. (2008). Mathematical modelling of bed load transport over partially dry areas. *Acta Geophysica*, **56**(3), 734–752. <https://doi.org/10.2478/s11600-008-0033-y>
- Lawrence, P. A., Edmund. (1998). Deposition of fine sediments in irrigation canals. *Irrigation and Drainage Systems*, **12**(4), 371–385. <http://doi.org/10.1023/a:1006156926300>
- Lee, S., Kim, J., Choi, B., Kim, G., & Lee, J. (2019). Harmful algal blooms and liver diseases: Focusing on the areas near the four major rivers in South Korea. *Journal of Environmental Science and Health, Part C*, **37**(4), 356–370. <https://doi.org/10.1080/10590501.2019.1674600>
- Lewis, J. (1996). Turbidity-controlled suspended sediment sampling for runoff-event load estimation. *Water Resources Research*, **32**(7), 2299–2310. Retrieved May 11, 2020, from <https://srs.fs.usda.gov/pubs/7806>
- Léziart, T., Rochere, P.-M. D. de la, Cheswick, R., Jarvis, P., & Nocker, A. (2019). Effect of turbidity on water disinfection by chlorination with the emphasis on humic acids and chalk. *Environmental Technology*, **40**(13), 1734–1743. <https://doi.org/10.1080/09593330.2019.1585480>
- Li, B., Su, S., Yuan, H., & Tao, S. (2012). Spatial and temporal variations of AOD over land at the global scale. *International Journal of Remote Sensing*, **33**(7), 2097–2111. <https://doi.org/10.1080/01431161.2011.605088>
- Li, H., Liu, L., Li, M., & Zhang, X. (2013). Effects of pH, Temperature, Dissolved Oxygen, and Flow Rate on Phosphorus Release Processes at the Sediment and Water Interface in Storm Sewer. *Journal of Analytical Methods in Chemistry*, **2013**, e104316. <https://doi.org/10.1155/2013/104316>
- Li, J., Chen, J., & Chen, Z. (2020). Developing an improved composite limit state method for time-dependent reliability analysis. *Quality Engineering*, **0**(0), 1–14. <https://doi.org/10.1080/08982112.2020.1735004>
- Lin, Z. (2018). Characterization of harmonics and multi-charged peaks obtained by Fourier transform ion cyclotron resonance mass spectrometry. *Instrumentation Science & Technology*, **46**(3), 307–315. <https://doi.org/10.1080/10739149.2017.1383270>
- Liu, F., Chen, S., Dong, P., & Peng, J. (2012). Spatial and temporal variability of water discharge in the Yellow River Basin over the past 60 years. *Journal of Geographical Sciences*, **22**(6), 1013–1033. <https://doi.org/10.1007/s11442-012-0980-8>

- Liu, H., & Sato, S. (2005). Laboratory Study on Sheetflow Sediment Movement in the Oscillatory Turbulent Boundary Layer Based on Image Analysis. *Coastal Engineering Journal*, 47(1), 21–40. <https://doi.org/10.1142/S057856340500115X>
- Luo, X., Stefanski, L. A., & Boos, D. D. (2006). Tuning Variable Selection Procedures by Adding Noise. *Technometrics*, 48(2), 165–175. <https://doi.org/10.1198/004017005000000319>
- Ma, Y., & Huang, H. Q. (2016). Controls of channel morphology and sediment concentration on flow resistance in a large sand-bed river: A case study of the lower Yellow River. *Geomorphology*, 264, 132–146. <https://doi.org/10.1016/j.geomorph.2016.03.035>
- Magombeyi, M. S., Taigbenu, A. E., & Barron, J. (2013). Rural poverty and Food insecurity mapping at district level for improved agricultural water management in the Limpopo River Basin. Paper presented at the CGIAR Challenge Program on Water and Food (CPWF). 54pp, Colombo, Sri Lanka. Accessed 2017 June 13. Retrieved from [rural-poverty-and-food-insecurity-mapping-at-district-level-for-improved-agricultural-water-management-in-the-limpopo-river-basin-cgiar-2013.pdf](http://www.gwp.org/publications/pubs/2013/06/rural-poverty-and-food-insecurity-mapping-at-district-level-for-improved-agricultural-water-management-in-the-limpopo-river-basin-cgiar-2013.pdf) (gwp.org)
- Magombeyi, M. S., Taigbenu, A. E., & Barron, J. (2016). Rural food insecurity and poverty mappings and their linkage with water resources in the Limpopo River Basin. *Physics and Chemistry of the Earth, Parts A/B/C*, 92, 20–33. <https://doi.org/10.1016/j.pce.2015.10.020>
- Mahmood Azari, Hamid Reza Moradi, Bahram Saghaian & Monireh Faramarzi (2016) Climate change impacts on streamflow and sediment yield in the North of Iran, *Hydrological Sciences Journal*, 61(1), 123-133, <http://doi.org/10.1080/02626667.2014.967695>
- Mallows, C. L. (2000). Some Comments on Cp. *Technometrics*, 42(1), 87–94. <https://doi.org/10.1080/00401706.2000.10485984>
- Manassis, M., & Constantinos, S. (2003). Conditions Affecting Bromate Formation During Ozonation of Bottled Water. *Ozone: Science & Engineering*, 25(3), 167–175. <https://doi.org/10.1080/01919510390481496>
- Mazumder, B. S., & Ojha, S. P. (2017). Suspension concentration due to combined wave-current flows over waveforms. *ISH Journal of Hydraulic Engineering*, 23(3), 319–330. <https://doi.org/10.1080/09715010.2017.1323316>

- McCave, I. (2006). Winterwerp, J. C. & Van Kesteren, W. G. M. 2004. Introduction to the Physics of Cohesive Sediment in the Marine Environment. Developments in Sedimentology Series no. 56. xiii 466 pp. Amsterdam: Elsevier. ISBN 0 444 51553 4. Geological Magazine, *143*(1), 137-137. Accessed 2020 November 12. Retrieved from <https://doi.org/10.1017/S0016756806211944>
- Mehta, A. J., & Lee, S.-C. (1994). Problems in Linking the Threshold Condition for the Transport of Cohesionless and Cohesive Sediment Grain. *Journal of Coastal Research*, *10*(1), 170–177. <https://www.jstor.org/stable/4298201>
- Mehta, A. J., & Letter, J. V. (2013). Comments on the transition between cohesive and cohesionless sediment bed exchange. *Estuarine, Coastal and Shelf Science*, *131*, 319–324. <https://doi.org/10.1016/j.ecss.2013.07.001>
- Méndez_V., N. J. (1998). Sediment Transport in Irrigation Canals. (Doctor of Philosophy). Wageningen Agricultural University, Balkema, Rotterdam, The Netherland. Accessed 2017 April 10. Retrieved from <https://edepot.wur.nl/193547>
- Merikas, A. G., Merika, A. A., & Koutroubousis, G. (2008). Modelling the investment decision of the entrepreneur in the tanker sector: Choosing between a second-hand vessel and a newly built one. *Maritime Policy & Management*, *35*(5), 433–447. <https://doi.org/10.1080/03088830802352053>
- Miao, C., & Lv, Z. (2020). Nonlinear chemical processes fault detection based on adaptive kernel principal component analysis. *Systems Science & Control Engineering*, *8*(1), 350–358. <https://doi.org/10.1080/21642583.2020.1768173>
- Mohammadi, M. (2020). Principal component analysis for α -stable vectors. *Communications in Statistics - Simulation and Computation*, *0*(0), 1–19. <https://doi.org/10.1080/03610918.2020.1764035>
- Momber, A. W., & Marquardt, T. (2019). Statistical modeling of high-carbon cast-steel particle flow through a blast-cleaning metering system. *Particulate Science and Technology*, *37*(3), 339–346. <https://doi.org/10.1080/02726351.2017.1375054>
- Montgomery, D. R. (2007). Soil Erosion and Agricultural Sustainability. Proceedings of the National Academy of Sciences of the United States of America, *104*(33), 13268–13272. Accessed 2020 October 6. Retrieved from <https://www.jstor.org/stable/25436473>

- Mostern, R. (2016). Sediment and State in Imperial China: The Yellow River Watershed as an Earth System and a World System. *Nature and Culture*, 11(2), 121–147. JSTOR. <https://www.jstor.org/stable/26430616>
- Muema, F. M., Home, P. G., & Raude, J. M. (2018). Application of Benchmarking and Principal Component Analysis in Measuring Performance of Public Irrigation Schemes in Kenya. *Agriculture*, 8(10), 162. <https://doi.org/10.3390/agriculture8100162>
- Mugabe, E. D., Amoda, C. A., & Griffiths, C. L. (2019). Population structure and growth of the beaked clam *Eumarcia pauperula* (Bivalvia, Veneridae) in Maputo Bay, Mozambique. *African Journal of Marine Science*, 41(4), 385–393. <https://doi.org/10.2989/1814232X.2019.1679255>
- Munguambe, E. O., de Sousa, L. S., & Maluana, C. (2013). Comparison of water irrigation efficiency on distributors 8 (D8) and 10 (D10) on the Chókwè Irrigation System, Gaza Province-Mozambique. (Hon. Bachelor). Instituto Superior Politécnico de Gaza, Chókwè.
- Muttashar, W. R., & Bryson, L. S. (2020). Constitutive model for predicting stress-strain behavior of fine-grained sediments using shear-wave velocity. *Marine Georesources & Geotechnology*, 38(8), 896–910. <https://doi.org/10.1080/1064119X.2019.1640815>
- Muttashar, W. R., Bryson, L. S., & Woolery, E. (2019). Determining the effects of depositional processes on consolidation behavior of sediment using shear-wave velocity. *Marine Georesources & Geotechnology*, 37(9), 1032–1043. <https://doi.org/10.1080/1064119X.2018.1524953>
- Mutua, B. M., & Klik, A. (2007). Predicting daily streamflow in ungauged rural catchments: the case of Masinga catchment, Kenya. *Hydrological Sciences Journal*, 52 (2), 292–304. <https://doi.org/10.1623/hysj.52.2.292>
- Mutua, B. M., & Malano, H. M. (2001). Analysis of Manual and Centralised Supervisory Control Operations to Improve Level of Service: A Case Study of Pyramid Hill No 1 Channel, Victoria, Australia. *Irrigation and Drainage Systems*, 15(1), 1–19. <https://doi.org/10.1023/A:1017527118623>
- Myers, G. W., & Tanner, C. R. (1992). Property rights and ecological conservation: The case of state farm divestiture in the Chókwè Irrigation Scheme. Accessed 2016 June 23. Retrieved from [Search results for IHE Delft Library \(worldcat.org\)](#)

- Nawazbhatta, M., Shahid, B.A. & Van Der Velde, E.J. (1996). Using a hydraulic model to prioritize secondary canal maintenance inputs: results from Punjab, Pakistan. *Irrig Drainage Syst* 10, 377–392. <https://doi.org/10.1007/BF01104901>
- Nittrouer, C. A., DeMaster, D. J., Eidam, E. F., Nguyen, T. T., Liu, J. P., Ogston, A. S., & Phung, P. V. (2017). The Mekong Continental Shelf: The Primary Sink for Deltaic Sediment Particles and Their Passengers. *Oceanography*, 30(3), 60–70. JSTOR. <https://www.jstor.org/stable/26201894>
- Nokes, C. R., Bostock, H. C., Strachan, L. J., & Hadfield, M. G. (2019). Hydrodynamics and sediment transport on the North Canterbury Shelf, New Zealand. *New Zealand Journal of Marine and Freshwater Research*, 0(0), 1–20. <https://doi.org/10.1080/00288330.2019.1699584>
- Nowacki, D. J., & Ganju, N. K. (2019). Simple Metrics Predict Salt-Marsh Sediment Fluxes. *Geophysical Research Letters*, 46(21), 12250–12257. <https://doi.org/10.1029/2019GL083819>
- Nyika, J., Onyari, E., Dinka, M., & Mishra, S. (2019). Analysis of particle size distribution of landfill contaminated soils and their mineralogical composition. *Particulate Science and Technology*, 0(0), 1–11. <https://doi.org/10.1080/02726351.2019.1635238>
- Oganesov, A., Vahala, G., Vahala, L., & Soe, M. (2018). Effect of Fourier transform on the streaming in quantum lattice gas algorithms. *Radiation Effects and Defects in Solids*, 173(3–4), 169–174. <https://doi.org/10.1080/10420150.2018.1462364>
- Ogston, A. S., Allison, M. A., McLachlan, R. L., Nowacki, D. J., & Stephens, J. D. (2017). How Tidal Processes Impact the Transfer of Sediment from Source to Sink: MEKONG RIVER COLLABORATIVE STUDIES. *Oceanography*, 30(3), 22–33. JSTOR. <https://www.jstor.org/stable/26201895>
- Oh, J., Choi, J. I., Choi, S. U., & Tsai, C. W. (2017). Physically based probabilistic analysis of sediment deposition in open channel flow. *Journal of Hydraulic Engineering*, 143(5), 04016106. [https://doi.org/10.1061/\(ASCE\)HY.1943-7900.0001269](https://doi.org/10.1061/(ASCE)HY.1943-7900.0001269)
- Ojo, O. I., & Otieno, F. O. A. (2010). Irrigation Canal Simulation Models and its Application to Large Scale Irrigation Schemes in South Africa: A Review (SSRN Scholarly Paper ID 1663073). *Social Science Research Network*. <https://papers.ssrn.com/abstract=1663073>

- Oke, E. O., Araromi, D. O., Jimoda, L. A., & Adeniran, J. A. (2019). Kinetics and neuro-fuzzy soft computing modelling of river turbid water coag-flocculation using mango (*Mangifera indica*) kernel coagulant. *Chemical Engineering Communications*, 206(2), 254–267. <https://doi.org/10.1080/00986445.2018.1483351>
- Olive, D. J., & Hawkins, D. M. (2005). Variable Selection for 1D Regression Models. *Technometrics*, 47(1), 43–50. <https://doi.org/10.1198/004017004000000590>
- Orhan, U., & Kılınç, E. (2020). Estimating soil texture with laser-guided Bouyoucos. *Automatika*, 61(1), 1–10. <https://doi.org/10.1080/00051144.2019.1654283>
- Ortiz, J. D., & Klompaker, A. A. (2015). Turbidity Currents: Comparing Theory and Observation in the Lab. *Oceanography*, 28(3), 220–227. JSTOR. <https://www.jstor.org/stable/24861912>
- Osman, I. S. E. (2015). Impact of improved operation and maintenance on cohesive sediment transport in Gezira Scheme, Sudan. <http://edepot.wur.nl/353547>
- Osman, I. S., Schultz, B., Osman, A., & Suryadi, F. X. (2016). Simulation of Fine Sediment Transport in Irrigation Canals of the Gezira Scheme with the Numerical Model FSED. *Journal of Irrigation and Drainage Engineering*, 142(11), 04016049. [https://doi.org/10.1061/\(ASCE\)IR.1943-4774.0001031](https://doi.org/10.1061/(ASCE)IR.1943-4774.0001031)
- Oss, C. J. van, & Giese, R. F. (2005). Influence of the pH of Water on its Electron-Acceptivity and Donicity. *The Journal of Adhesion*, 81(3–4), 237–244. <https://doi.org/10.1080/00218460590944530>
- Ouellet-Proulx, S., St-Hilaire, A., Courtenay, S. c., & Haralampides, K. a. (2016). Estimation of suspended sediment concentration in the Saint John River using rating curves and a machine learning approach. *Hydrological Sciences Journal*, 61(10), 1847–1860. <https://doi.org/10.1080/02626667.2015.1051982>
- Pal, D., Prasad, S. N., & Römken, M. J. M. (2001). Study of sediment transport in shallow channel flows. Paper presented at the Sustaining the Global Farm.
- Park, J., Jung, E. S., & Park, S. (2017). Input Behavior When Using Two Fingers on a Multi-Touch Device. *International Journal of Human–Computer Interaction*, 33(11), 911–926. <https://doi.org/10.1080/10447318.2017.1300749>
- Parker, G., & Klingeman, P. C. (1982). On why gravel bed streams are paved. *Water Resources Research*, 18(5), 1409–1423. <https://doi.org/10.1029/WR018i005p01409>

- Partheniades, E. (2009). *Cohesive Sediments in Open Channels: Properties, Transport and Applications* (1st Edition). Elsevier. <https://www.elsevier.com/books/cohesive-sediments-in-open-channels/partheniades/978-1-85617-556-2>
- Paudel, K. P. (2010). Role of sediment in the design and management of irrigation canals Sunsari Morang Irrigation Scheme, Nepal. (Doctor of Philosophy). Wageningen University and UNESCO-IHE Institute for Water Education, Delft, The Netherlands. (ISBN 978-0-415-61579-2 (Taylor & Francis Group) and ISBN 978-90-8585-851-5 (Wageningen University)). <https://research.wur.nl/en/publications/role-of-sediment-in-the-design-and-management-of-irrigation-canal>
- Pervukhina, E., Emmenegger, J.-F., Golikova, V., & Osipov, K. (2014). An optimization technique based on a vector autoregression model with state space representation: Application to Ukrainian cargo transport data. *Optimization*, 63(1), 93–108. <https://doi.org/10.1080/02331934.2013.836648>
- Quick, I., König, F., Baulig, Y., Schriever, S., & Vollmer, S. (2019). Evaluation of depth erosion as a major issue along regulated rivers using the classification tool Valmorph for the case study of the Lower Rhine. *International Journal of River Basin Management*. <http://www.tandfonline.com/egertonelibrary/remotexs.co/doi/abs/10.1080/15715124.2019.1672699>
- Rahimi, L., Amanipoor, H., & Battaleb-Looie, S. (2019). Effect of salinity of irrigation water on soil properties (abadan plain, SW Iran). *Geocarto International*, 0(0), 1–20. <https://doi.org/10.1080/10106049.2019.1678678>
- Ramalingam, S., & Chandra, V. (2018). Determination of suspended sediments particle size distribution using image capturing method. *Marine Georesources & Geotechnology*, 36(8), 867–874. <https://doi.org/10.1080/1064119X.2017.1392660>
- Rao, A. R., and Hamed, K. H. (2003). Multi-taper method of analysis of periodicities in hydrologic data. *Journal of Hydrology*, 279, 125–143. [https://doi.org/10.1016/S0022-1694\(03\)00176-8](https://doi.org/10.1016/S0022-1694(03)00176-8).
- Rao, A.R., Hamed, K.H. (1994). Frequency analysis of upper cauvery flood data by L-moments. *Water Resource Manage* 8, 183–201. <https://doi.org/10.1007/BF00877086>.
- Rath, A., & Swain, P. C. (2020). Evaluation of performance of irrigation canals using benchmarking techniques –a case study of Hirakud dam canal system, Odisha, India.

- ISH Journal of Hydraulic Engineering*, 26(1), 51–58.
<https://doi.org/10.1080/09715010.2018.1439777>
- Ravisangar, V., Sturm, T. W., and Amirtharajah, A. (2005). Influence of Sediment Structure on Erosional Strength and Density of Kaolinite Sediment Beds, *J. Hydraul. Engrg., ASCE*, 131(5), 356-365. [https://doi.org/10.1061/\(ASCE\)0733-9429\(2005\)131:5\(356\)](https://doi.org/10.1061/(ASCE)0733-9429(2005)131:5(356))
- Recking, A. (2013). An analysis of nonlinearity effects on bed load transport prediction. *Journal of Geophysical Research*, 118(3), 1264–1281.
<https://doi.org/10.1002/jgrf.20090>
- Recking, A. (2013). Simple Method for Calculating Reach-Averaged Bed-Load Transport. *Journal of Hydraulic Engineering*, 139(1), 70–75.
[https://doi.org/10.1061/\(ASCE\)HY.1943-7900.0000653](https://doi.org/10.1061/(ASCE)HY.1943-7900.0000653)
- Rezaee, L., Moosavi, A. A., Davatgar, N., & Sepaskhah, A. R. (2019). Shrinkage-swelling characteristics and plasticity indices of paddy soils: Spatial variability and their influential parameters. *Archives of Agronomy and Soil Science*, 0(0), 1–21.
<https://doi.org/10.1080/03650340.2019.1706169>
- Riaza, A., Buzzi, J., García-Meléndez, E., Carrère, V., Sarmiento, A., & Müller, A. (2015). Monitoring acidic water in a polluted river with hyperspectral remote sensing (HyMap). *Hydrological Sciences Journal*, 60(6), 1064–1077.
<https://doi.org/10.1080/02626667.2014.899704>
- Robertson, D. M., Juckem, P. F., Dantoin, E. D., & Winslow, L. A. (2018). Effects of water level and climate on the hydrodynamics and water quality of Anvil Lake, Wisconsin, a shallow seepage lake. *Lake and Reservoir Management*, 34(3), 211–231.
<https://doi.org/10.1080/10402381.2017.1412374>
- Rokni, K., Ahmad, A., Solaimani, K., & Hazini, S. (2016). A New Approach for Detection of Surface Water Changes Based on Principal Component Analysis of Multitemporal Normalized Difference Water Index. *Journal of Coastal Research*, 32(2), 443–451. JSTOR. <https://www.jstor.org/stable/43752206>
- Rosenberg, O. I., & Abookasis, D. (2020). Hybrid method combining orthogonal projection Fourier transform profilometry and laser speckle imaging for 3D visualization of flow profile. *Journal of Modern Optics*, 67(13), 1197–1209.
<https://doi.org/10.1080/09500340.2020.1823503>

- Roushangar, K., & Shahnazi, S. (2020). Prediction of sediment transport rates in gravel-bed rivers using Gaussian process regression. *Journal of Hydroinformatics*, 22(2), 249–262. <https://doi.org/10.2166/hydro.2019.077>
- Rovira, A., Alcaraz, C., & Ibáñez, C. (2012). Spatial and temporal dynamics of suspended load at-a-crosssection: The lowermost Ebro River (Catalonia, Spain). *Water Research* (46), 3671 e 3681. <https://doi.org/10.1080/00223131.2019.1651231>
- Salmasi, F., Khatibi, R., & Nourani, B. (2018). Investigating reduction of uplift forces by longitudinal drains with underlined canals. *ISH Journal of Hydraulic Engineering*, 24(1), 81–91. <https://doi.org/10.1080/09715010.2017.1350605>
- Sánchez-Espigares, J. A., Grima, P., & Marco-Almagro, L. (2020). Mosaic normality test. *Communications in Statistics - Theory and Methods*, 0(0), 1–13. <https://doi.org/10.1080/03610926.2020.1734828>
- Santos, B. B. D., Miranda, R. B. D., Estigoni, M. V., Villela, J. M., & Mauad, F. F. (2019). Evaluation of the laser diffraction method for the measurement of suspended sediment concentration in Mogi-Guaçu reservoir (São Paulo, Brazil). *International Journal of River Basin Management*, 17(1), 89–99. <https://doi.org/10.1080/15715124.2018.1446965>
- Schmalz, B., Zhang, Q., Kuemmerlen, M., Cai, Q., Jähnig, S. C., & Fohrer, N. (2015). Modelling spatial distribution of surface runoff and sediment yield in a Chinese river basin without continuous sediment monitoring. *Hydrological Sciences Journal*, 60(5), 801–824. <https://doi.org/10.1080/02626667.2014.967245>
- See, J. C. G., & Porio, E. E. (2015). Assessing Social Vulnerability to Flooding in Metro Manila Using Principal Component Analysis. *Philippine Sociological Review*, 63, 53–80. JSTOR. <https://www.jstor.org/stable/24717187>
- Semenov, M. Y., Marinaite, I. I., Zhuchenko, N. A., Silaev, A. V., Vershinin, K. E., & Semenov, Y. M. (2018). Revealing the factors affecting occurrence and distribution of polycyclic aromatic hydrocarbons in water and sediments of Lake Baikal and its tributaries. *Chemistry and Ecology*, 34(10), 925–940. <https://doi.org/10.1080/02757540.2018.1520848>
- Setiawan, O., Sartohadi, J., Hadi, M. P., & Mardiatno, D. (2020). Infiltration characterization using principal component analysis and K-means cluster analysis on quaternary volcanic landscape at the southern flank of Rinjani Volcano, Lombok Island,

- Indonesia. *Physical Geography*, 41(3), 217–237.
<https://doi.org/10.1080/02723646.2019.1620526>
- Sharif, M., & Kabiri-Samani, A. (2018). Flow regimes at grid drop-type dissipators caused by changes in tail-water depth. *Journal of Hydraulic Research*, 56(4), 505–516.
<https://doi.org/10.1080/00221686.2017.1395370>
- Sharma, S. K., & Ghosh, S. (2016). Short-term wind speed forecasting: Application of linear and non-linear time series models. *International Journal of Green Energy*, 13(14), 1490–1500. <https://doi.org/10.1080/15435075.2016.1212200>
- Shekwa, A., Chirwa, P., Ngulube, E., & Ghebremariam, T. (2017). Productivity, efficiency and costs of manual saw and electric shear pruning operations in *Pinus elliottii* stands of Mpumalanga, South Africa. *International Journal of Forest Engineering*, 28(3), 169–175. <https://doi.org/10.1080/14942119.2017.1337462>
- Shen, Y., Xu, H., & Liu, X. (2019). An alternating minimization method for robust principal component analysis. *Optimization Methods and Software*, 34(6), 1251–1276.
<https://doi.org/10.1080/10556788.2018.1496086>
- Shi, H., Tian, Q., Dai, Q., & Jiang, R. (2008). 1-D Sediment Mathematical Model for Irrigation Canals of the Lower Yellow River. Paper presented at the World Environmental and Water Resources Congress Ahupua'a.
[https://doi.org/10.1061/40976\(316\)470](https://doi.org/10.1061/40976(316)470)
- Simons, D. B., & Şentürk, F. (1992). Sediment Transport Technology: Water and Sediment Dynamics. *Water Resources Publication*.
https://books.google.co.mz/books/about/Sediment_Transport_Technology.html?id=eScptWZAeIC&redir_esc=y
- Soemitro, R. A. A., Adriati, F., Warnana, D. D., Mukunoki, T., Soetanto, R., & Maulana, M. A. (2020). Sediment consolidation in ephemeral river: The effect of applied loading on soil properties and dredging method selection. *International Journal of River Basin Management*, 0(0), 1–10. <https://doi.org/10.1080/15715124.2020.1742135>
- Sofi, I. R., Chuhan, P. P., Sharma, H. K., & Manzoor, J. (2018). Assessment of Physico-Chemical Properties of Water and Sediments of Asan Lake Dehradun, India. *International Journal of Theoretical & Applied Sciences*, 10(1), 68–76.
https://www.researchtrend.net/ijtas/pdf/13_IRFAN_RASHID_SOFI-F.pdf

- Souza, A. T. de, Carneiro, L. A. T. X., Junior, O. P. da S., Carvalho, S. L. de, & Américo-Pinheiro, J. H. P. (2020). Assessment of water quality using principal component analysis: A case study of the Marrecas stream basin in Brazil. *Environmental Technology*, 0(0), 1–10. <https://doi.org/10.1080/09593330.2020.1754922>
- Srinivas, R., Singh, A. P., Dhadse, K., & Garg, C. (2020). An evidence based integrated watershed modelling system to assess the impact of non-point source pollution in the riverine ecosystem. *Journal of Cleaner Production*, 246, 118963. <https://doi.org/10.1016/j.jclepro.2019.118963>
- Stone, M., Mulamoottil, G., & Logan, L. (1995). Grain size distribution effects on phosphate sorption by fluvial sediment: Implications for modelling sediment-phosphate transport. *Hydrological Sciences Journal*, 40(1), 67–81. <https://doi.org/10.1080/02626669509491391>
- Sukhodolov, A. N. (2015). Field-based research in fluvial hydraulics: Potential, paradigms and challenges. *Journal of Hydraulic Research*, 53(1), 1–19. <https://doi.org/10.1080/00221686.2015.1012126>
- Sulaiman, M. S., Sinnakaudan, S. K., Azhari, N. N., & Abidin, R. Z. (2017). Behavioral of sediment transport at lowland and mountainous rivers: A special reference to selected Malaysian rivers. *Environmental Earth Sciences*, 76(7), 300. <https://doi.org/10.1007/s12665-017-6620-y>
- Sun, F., & Ma, R. (2019). Hydrologic changes of Aral Sea: A reveal by the combination of radar altimeter data and optical images. *Annals of GIS*, 25(3), 247–261. <https://doi.org/10.1080/19475683.2019.1626909>
- Sutama, N. H. (2010). Mathematical modelling of sediment transport and its improvement in Bekasi Irrigation System, West Java, Indonesia. (Master of Science). UNESCO-IHE, Institute for Water Education, Delft, The Netherlands. <https://un-ihе.on.worldcat.org/search?databaseList=2897%2C2215%2C2375%2C2375%2C638%2C1847&queryString=Sutama+2010&clusterResults=true>
- Tadesse, A., & Dai, W. (2019). Prediction of sedimentation in reservoirs by combining catchment based model and stream based model with limited data. *International Journal of Sediment Research*, 34(1), 27–37. <https://doi.org/10.1016/j.ijsrc.2018.08.001>

- Tan, Z., Yu, H., Yang, S., Zhu, R., Lu, R., & Han, S. (2020). Fourier-transform ghost imaging with polychromatic light. *Journal of Modern Optics*, 0(0), 1–7. <https://doi.org/10.1080/09500340.2020.1829143>
- Tariq, J. A., & Latif, M. (2010). Improving Operational Performance of Farmers Managed Distributary Canal using SIC Hydraulic Model. *Water Resources Management*, 24(12), 3085–3099. <https://doi.org/10.1007/s11269-010-9596-x>
- Teixeira, P. C., Donagemma, G. K., Fontana, A., & Teixeira, W. G. (2017). Manual de métodos de análise de solo. Brasília, DF: Embrapa, 2017. <http://www.infoteca.cnptia.embrapa.br/handle/doc/1085209>
- Tena, A., Batalla, R. J., & Vericat, D. (2012). Reach-scale suspended sediment balance downstream from dams in a large Mediterranean river. *Hydrological Sciences Journal*, 57(5), 831–849. <https://doi.org/10.1080/02626667.2012.681784>
- Terefe, Y., & Singh, P. (2020). East-bank canal water delivery performance evaluation: Case study of Finchaa Sugar Estate, Ethiopia. *ISH Journal of Hydraulic Engineering*. <http://www.tandfonline.com/egertonelibrary/remotexs.co/doi/abs/10.1080/09715010.2019.1708817>
- Tharkar, A. D., & Mahulikar, S. P. (2019). The Mean Temperature Difference Method for Micro Heat Exchanger Analysis Considering Property Variation. *Heat Transfer Engineering*, 40(8), 605–615. <https://doi.org/10.1080/01457632.2018.1436510>
- Theol, S. A., Jagers, B., Suryadi, F. X., & de Fraiture, C. (2019). The use of Delft3D for Irrigation Systems Simulations: Modelling irrigation systems using Delft3D. *Irrigation and Drainage*, 68(2), 318–331. <https://doi.org/10.1002/ird.2311>
- Thomas, C., Frossard, V., Perga, M.-E., Tofield-Pasche, N., Hofmann, H., Dubois, N., & Lyautey, E. (2019). Lateral variations and vertical structure of the microbial methane cycle in the sediment of Lake Onego (Russia). *Inland Waters*, 9(2), 205–226. <https://doi.org/10.1080/20442041.2018.1500227>
- Uhrich, M. A., & Bragg, H. M. (2003). Monitoring Instream Turbidity to Estimate Continuous Suspended-Sediment Loads and Yields and Clay-Water Volumes in the Upper North Santiam River Basin, Oregon, 1998–2000. Retrieved from Portland, Oregon, USA. <https://pubs.usgs.gov/wri/WRI03-4098/pdf/wri034098.pdf>
- US Department of State Geographer. (2020). Google Earth Pro (Version 2020) [Computer software].

- Van der Wegen, M., BE. Jaffe, & JA. Roelvink. (2011). Process based, morpho-dynamic hindcast of decadal deposition patterns in San Pablo Bay, California, 1856–1887. *Journal of Geophysical Research: Earth Surface*, 116(F2). <https://agupubs.onlinelibrary.wiley.com/doi/abs/10.1029/2009JF001614>
- Van Ledden, M., van Kesteren, W. G. M., & Winterwerp, J. C. (2004). A conceptual framework for the erosion behaviour of sand–mud mixtures. *Continental Shelf Research*, 24(1), 1–11. <https://doi.org/10.1016/j.csr.2003.09.002>
- Van Rijn, L.C., (1993). Principles of Sediment Transport in Rivers, Estuaries and Coastal Seas. Aqua Publications, Amsterdam. [Search results for IHE Delft Library \(worldcat.org\)](#)
- Vargas-Luna, A., Crosato, A., Byishimo, P., & Uijtewaal, W. S. J. (2019). Impact of flow variability and sediment characteristics on channel width evolution in laboratory streams. *Journal of Hydraulic Research*, 57(1), 51–61. <https://doi.org/10.1080/00221686.2018.1434836>
- Varmuza, K. and Filzmoser, P. (2009). Introduction to multivariate statistical analysis in chemometrics. Boca Raton, CRC Press. [\[PDF\] Introduction to Multivariate Statistical Analysis in Chemometrics | Semantic Scholar](#)
- Vericat, D., Batalla, R. J., & Garcia, C. (2006). Breakup and reestablishment of the armour layer in a large gravel-bed river below dams: *The lower Ebro*. *Geomorphology*, 76(1), 122–136. <https://doi.org/10.1016/j.geomorph.2005.10.005>
- Vericat, D.; Batalla, R.J.; Gibbins, C.N. (2008) Sediment entrainment and depletion from patches of fine material in a gravel-bed river: Patch entrainment and depletion. *Water Resource Resource*, 44(11). <https://doi.org/10.1029/2008WR007028>
- Verlicchi, P., & Grillini, V. (2020). Surface Water and Groundwater Quality in South Africa and Mozambique—Analysis of the Most Critical Pollutants for Drinking Purposes and Challenges in Water Treatment Selection. *Water*, 12(1), 305. <https://doi.org/10.3390/w12010305>
- Visser, S. (1996). Canal water distribution at the secondary level in the Punjab, Pakistan: Development of a simplified tool to estimate the canal water distribution at the distributary level. [Master of Science, University of Technology Delft]. The Netherlands. (R-10). <https://1library.net/document/qv1kg2gq-distribution-secondary-pakistan-development-simplified-estimate-distribution-distributary.html>

- Wang, Y., & Aelst, S. V. (2020). Sparse Principal Component Analysis Based on Least Trimmed Squares. *Technometrics*, 62(4), 473–485. <https://doi.org/10.1080/00401706.2019.1671234>
- Wegen, M. van der, Jaffe, B. E., & Roelvink, J. A. (2011). Process-based, morphodynamic hindcast of decadal deposition patterns in San Pablo Bay, California, 1856–1887. *Journal of Geophysical Research: Earth Surface*, 116(F2). <https://doi.org/10.1029/2009JF001614>
- Wei, K., Zhang, J., & Qin, S. (2019). Experimental and Numerical Assessment into Frequency Domain Dynamic Response of Deep water Rigid-Frame Bridge. *Journal of Earthquake Engineering*, 0(0), 1–24. <https://doi.org/10.1080/13632469.2019.1684402>
- Wei, Y., Jiao, J., Zhao, G., Zhao, H., He, Z., & Mu, X. (2016). Spatial – temporal variation and periodic change in streamflow and suspended sediment discharge along the mainstream of the Yellow River during 1950 - 2013. *CATENA*, 140, 105 - 115. <https://doi.org/10.1016/j.catena.2016.01.016>
- West, H. G., & Myers, G. W. (1996). A Piece of Land in a Land of Peace? State Farm Divestiture in Mozambique. *The Journal of Modern African Studies*, 34(1), 27–51. <https://doi.org/10.1017/S0022278X00055191>
- White, R.W., & Day, T.J. (1982) Transport of graded gravel bed material. In *Gravel-Bed Rivers*; Hey, J.C., Bathurst, J.C., Thorne, C.R., Eds.; *John Wiley*: Hoboken, NJ, USA; pp. 181–223.
- Widjaja, J., Paichit, S., Kamonboon, J., & Wongjaren, J. (2020). Handheld pocket-size Fourier transform profilometry using projector-enabled smartphone. *The Imaging Science Journal*, 68(2), 69–75. <https://doi.org/10.1080/13682199.2020.1738068>
- Wilcock, P., Pitlick, J., & Cui, Y. (2009). *Sediment Transport Primer Estimating Bed-Material Transport in Gravel-Bed Rivers* (General Technical Report No. 226; p. 78). U.S. Department of Agriculture, Forest Service, Rocky Mountain Research Station. Accessed on 12/04/2017. https://www.researchgate.net/publication/252141249_Sediment_Transport_Primer_Estimating_Bed-Material_Transport_in_Gravel-Bed_Rivers
- Wilcock, R. J., McDowell, R. W., Quinn, J. M., Rutherford, J. C., Young, R. G., & Depree, C. V. (2020). Dynamics of phosphorus exchange between sediment and water in a

- gravel-bed river. *New Zealand Journal of Marine and Freshwater Research*, 0(0), 1–21. <https://doi.org/10.1080/00288330.2020.1741402>
- William L., Peacock and L., Peter Christensen L., Chapter 15: Interpretation of Soil and Water Analysis, pp. 115-120. Accessed 2020 December 3. Retrieved from <http://iv.ucdavis.edu/files/24409.pdf> ,
- World Meteorological Organization (WMO). (2012). Limpopo River Basin: a proposal to improve the Flood Forecasting and Early Warning System. Retrieved from http://www.wmo.int/pages/prog/hwrrp/chy/chy14/documents/ms/Limpopo_Report.pdf
- Wu, F.-C., & Chou, Y.-J. (2003). Simulation of gravel-sand bed response to flushing flows using a two-fraction entrainment approach: Model development and flume experiment. *Water Resources Research*, 39(8). <https://doi.org/10.1029/2003WR002184>
- Wu, K., Liu, S., Sun, W., Zhang, G., & Li, Z. (2018). Temperature effects and heat transfer in granular soils by discrete element modeling of CPT. *European Journal of Environmental and Civil Engineering*, 0(0), 1–22. <https://doi.org/10.1080/19648189.2018.1548740>
- Wu, W., Wang, S. S. Y., & Jia, Y. (2000). Nonuniform sediment transport in alluvial rivers. *Journal of Hydraulic Research*, 38(6), 427-434. <https://doi.org/10.1080/00221680009498296>
- Wu, X., Xiang, X., Chen, X., Zhang, X., & Hua, W. (2018). Effects of cascade reservoir dams on the streamflow and sediment transport in the Wujiang River basin of the Yangtze River, China. *Inland Waters*, 8(2), 216–228. <https://doi.org/10.1080/20442041.2018.1457850>
- Xiao, Y., Yang, F. S., Zhou, Y. J., & Chen, W. S. (2015). 1-D numerical modeling of the mechanics of gravity-driven transport of fine sediments in the Three Gorges Reservoir. *Lake and Reservoir Management*, 31(2), 83–91. <https://doi.org/10.1080/10402381.2015.1010026>
- Xie, G., Qian, Y., & Yang, H. (2019). Forecasting container throughput based on wavelet transforms within a decomposition-ensemble methodology: A case study of China. *Maritime Policy & Management*, 46(2), 178–200. <https://doi.org/10.1080/03088839.2018.1476741>
- XLSTAT (2020) statistical and data analysis solution. Addinsoft. New York, USA. <https://www.xlstat.com>.

- Xu, Shihe. (2019). Extraction and quantitative analysis of water, sediment, soil and biosolids for trace-level trimethylsilanol. *International Journal of Environmental Analytical Chemistry*, 100(3), 268–281. <https://doi.org/10.1080/03067319.2019.1636041>
- Xu, Z., & Zhang, Y. (2020). Uniqueness problem and growth property for Fourier transform of functions in the upper half-space. *Applicable Analysis*, 0(0), 1–8. <https://doi.org/10.1080/00036811.2020.1729357>
- Yang, Z., and Han, D. (2006), Derivation of Unit Hydrograph Using a Transfer Function Approach, *Water Resources Research*, 42(1). <https://doi.org/10.1029/2005WR004227>
- Yao, P., Hu, Z., Su, M., Chen, Y., & suying, O. (2018). Erosion Behavior of Sand-silt Mixtures: The Role of Silt Content. *Journal of Coastal Research*, 1171–1175. JSTOR. <https://www.jstor.org/stable/26488402>
- Yarar, A. (2014). A Hybrid Wavelet and Neuro-Fuzzy Model for Forecasting the Monthly Streamflow Data. *Water Resources Management*, 28(2), 553–565. <https://doi.org/10.1007/s11269-013-0502-1>
- Ye, Z. (2012). Erosion Threshold and Erosion Rate of Seabed Sediments. The University of Western Australia. Accessed 2021 February 11. Retrieved from <https://research-repository.uwa.edu.au/en/publications/erosion-threshold-and-erosion-rate-of-seabed-sediments>
- Yokoyama, K., & Kitada, T. (2019). Generalized formulation of extended cross-section adjustment method based on minimum variance unbiased linear estimation. *Journal of Nuclear Science and Technology*, 56(1), 87–104. <https://doi.org/10.1080/00223131.2018.1531078>
- Yokoyama, K., Yamamoto, A., & Kitada, T. (2018). Dimension-reduced cross-section adjustment method based on minimum variance unbiased estimation. *Journal of Nuclear Science and Technology*, 55(3), 319–334. <https://doi.org/10.1080/00223131.2017.1397563>
- Yu, G., & Lim, S.-Y. (2003). Modified Manning formula for flow in alluvial channels with sand-beds. *Journal of Hydraulic Research*, 41(6), 597–608. <https://doi.org/10.1080/00221680309506892>
- Yu, J., Qin, X., Larsen, O., & Chua, L. H. C. (2014). Comparison between Response Surface Models and Artificial Neural Networks in Hydrologic Forecasting. *Journal of*

- Hydrologic Engineering*, 19(3), 473–481. [https://doi.org/10.1061/\(ASCE\)HE.1943-5584.0000827](https://doi.org/10.1061/(ASCE)HE.1943-5584.0000827)
- Yurekli, K., & Ozturk, F. (2003). Stochastic Modeling of Annual Maximum and Minimum Streamflow of Kelkit Stream. *Water International*, 28(4), 433–441. <https://doi.org/10.1080/02508060308691721>
- Zahidi, I., Yusuf, B., Cope, M., Mohamed, T. A., & Shafri, H. Z. M. (2018). Effects of depth-varying vegetation roughness in two-dimensional hydrodynamic modelling. *International Journal of River Basin Management*, 16(4), 413–426. <https://doi.org/10.1080/15715124.2017.1394313>
- Zakhem, B. A., Al-Charideh, A., & Kattaa, B. (2017). Using principal component analysis in the investigation of groundwater hydrochemistry of Upper Jezireh Basin, Syria. *Hydrological Sciences Journal*, 62(14), 2266–2279. <https://doi.org/10.1080/02626667.2017.1364845>
- Zamprognò, B., Reisen, V. A., Bondon, P., Cotta, H. H. A., & Neyval C. Reis, J. (2020). Principal component analysis with autocorrelated data. *Journal of Statistical Computation and Simulation*, 0(0), 1–19. <https://doi.org/10.1080/00949655.2020.1764556>
- Zhang, G., Tang, L., Liu, Z., Zhou, L., Liu, Y., & Jiang, Z. (2020). Machine-learning-based damage identification methods with features derived from moving principal component analysis. *Mechanics of Advanced Materials and Structures*, 27(21), 1789–1802. <https://doi.org/10.1080/15376494.2019.1710308>
- Zhang, N., Zhu, W., He, H., Lv, Y., & Wang, S. (2017). Experimental study on settling velocity of soil particles in dredged slurry. *Marine Georesources & Geotechnology*, 35(6), 747–757. <https://doi.org/10.1080/1064119X.2016.1236862>
- Zhang, Y.-K., & Schilling, K. (2004). Temporal scaling of hydraulic head and river base flow and its implication for groundwater recharge. *Water Resources Research*, 40(3). <https://doi.org/10.1029/2003WR002094>
- Zhang, Z., Zhang, C., Huang, Z., Yi, X., Zeng, H., Zhang, M., & Huang, M. (2018). Residue levels and spatial distribution of phthalate acid esters in water and sediment from urban lakes of Guangzhou, China. *Journal of Environmental Science and Health, Part A*.

<http://www.tandfonline.com/egertonelibrary/remotexs.co/doi/abs/10.1080/10934529.2018.1530539>

- Zheng, G., Shao, L., Guo, X., & Zhang, J. (2020). Investigation of the mechanical behaviour of an unsaturated soil mixture using a digital image measurement system. *European Journal of Environmental and Civil Engineering*, 24(8), 1051–1067. <https://doi.org/10.1080/19648189.2018.1442258>
- Zhu, C., Liu, X., Shan, H., Zhang, H., Shen, Z., Zhang, B., & Jia, Y. (2018). Properties of suspended sediment concentrations in the Yellow River delta based on observation. *Marine Georesources & Geotechnology*, 36(1), 139–149. <https://doi.org/10.1080/1064119X.2017.1328715>
- Zorndt, A. C., & Schlurmann, T. (2019). Sources of uncertainty in estuarine climate impact modeling. *Journal of Applied Water Engineering and Research*, 7(1), 37–47. <https://doi.org/10.1080/23249676.2017.1355756>

APPENDICES

A: Selected Photographs







B: The Velocity-Area Method of Streamflow Measurement

B.1. Flow measurement (current metering)

Flow measurements at the intake and offtake were performed using current meters, every once a week, with aim to determine average discharges in the entire study period. Seven readings were taken for same number of points, with three repetitions, in order to determine the daily average discharge. Water discharges of the canals were computed using the Mean section method. In this method, canal cross section was divided into a number of verticals, at which water depths and depth-averaged velocities were measured. The flow (q) between any two adjacent verticals was given by a product of the width between verticals (W), the mean of water depths of two adjacent verticals and the mean of the average velocities over those two verticals (Figure B.1). The total discharge (Q) at the section was determined as a sum of the discharges in each sub section.

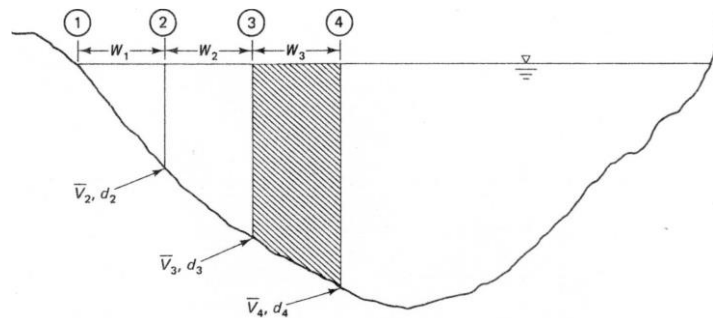


Figure B.1: Mean section method of flow determination in open channels

$$Q = \sum_{x=1}^n W_x \times \left(\frac{\bar{v}_x + \bar{v}_{x+1}}{2} \right) \times \left(\frac{y_x + y_{x+1}}{2} \right) \quad (\text{B.1})$$

Where,

Q = total discharge (m^3/s)

W = width between two adjacent verticals (m)

\bar{v} = depth-averaged velocity (m/s)

y = flow depth, and (m)

x = the number of verticals (-).

B.2. Measurement and determination of mean velocity in a vertical

Current meters measure the velocity of flowing water at a point. The measurement of discharge in a river or channel stream requires the determination of mean velocity for each sampling vertical across the measuring section. If the flow in the stream is not turbulent it can be assumed that the velocity distribution in a vertical is close to the regular typical “ideal”

form, as given in Figure B.2. A number of methods are in use to define the mean velocity in a vertical and the choice of method will depend primarily on the depth in vertical but also on the width of the stream and the accuracy required. The mean velocity in a vertical is normally obtained by measuring velocity at one, two or three points and thereafter applying a correct averaging procedure. The methods provide reliable estimates of mean velocity if the vertical velocity distribution is regular and close to the typical velocity profile.

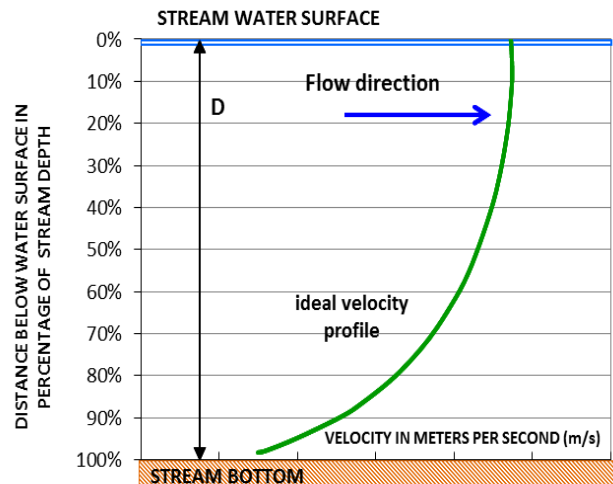


Figure B.2: Typical “ideal” water flow velocity in canal. Source: Perzyna, 2016.

B.2.1. One-Point Method

Velocity observations were taken at each vertical by setting the current meter at 0.6 of the depth below the surface (see Figure B.3). The observed value is considered as the mean velocity in the vertical. This method is generally used in shallow streams and when water depth in vertical is less than 1.0 m.

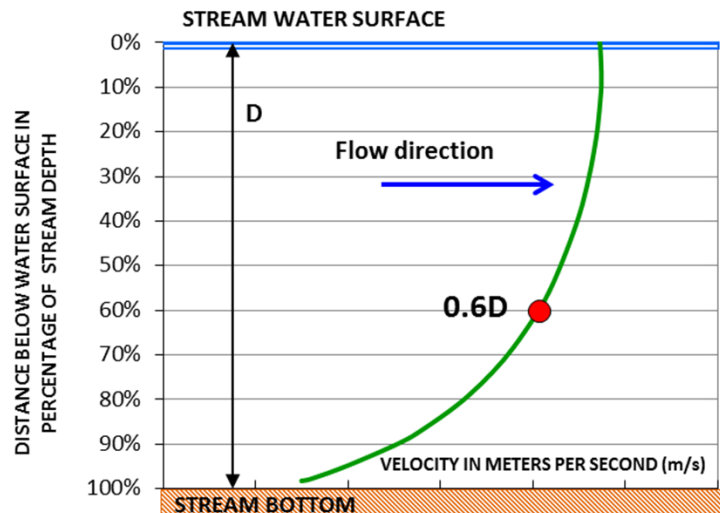


Figure B.3: One-point method of velocity measurement. Source: Perzyna, 2016.

One-point method is the least accurate, and it is preferable to use two points in the vertical. However it is often necessary to use this method owing to depth limitations.

B.2.2. Two point Method

Velocities should be measured at 0.2 and 0.8 of the depth below the surface. The average of the two values is taken as the mean velocity in the vertical. This method is generally used when water depth in vertical is more than 1.0 m (see Figure B.4).

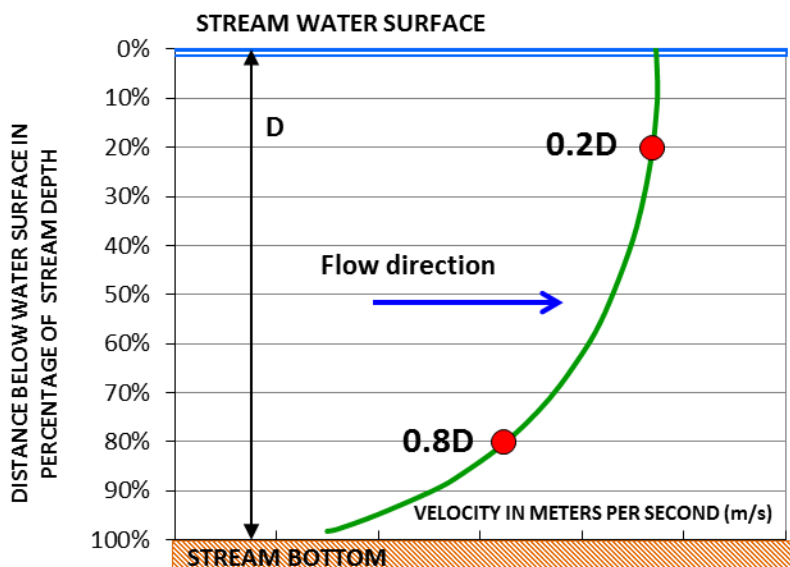


Figure B.4: Two-point method of velocity measurement. Source: Perzyna 2016

B.2.3. Three point method

Velocities should be measured at 0.2, 0.6, and 0.8 of the depth below the surface. The mean velocity in the vertical is calculated by first averaging the 0.2 and 0.8 measurements and then averaging the result with the 0.6 value (see Figure B.5). Usually, the three point method is used when velocity in the vertical varies much and differs from the classical velocity profile.

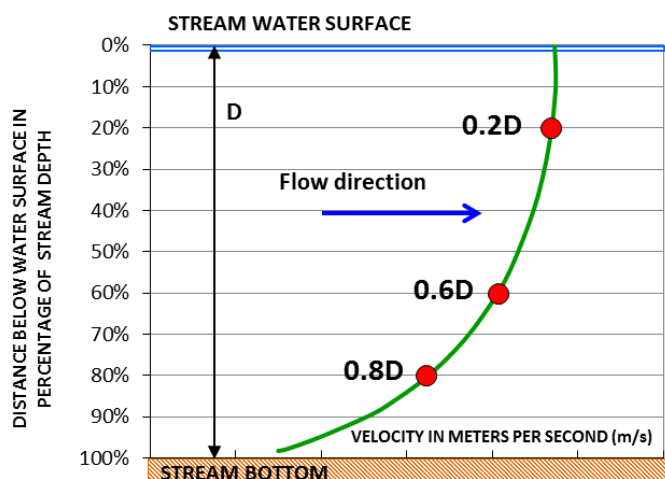


Figure B.5: Three-point method of velocity measurement. Source: Perzyna, 2016

In the table B.1 is presented the equations used in calculation of the mean velocity and respective water depths, for one, two and three points.

Table B.1: Salient features of the three velocity measurement methods.

Method of measurement	Calculation of mean velocity in vertical	Water depth limits
One point	$V_{mean} = V_{0.6 \times D}$ (E.2)	0.1 – 1.0 m
Two points	$V_{mean} = \frac{V_{0.2 \times D} + V_{0.8 \times D}}{2}$ (E.3)	>1.0
Three points	$V_{mean} = \frac{V_{0.2 \times D} + V_{0.6 \times D} + V_{0.8 \times D}}{4}$ (E.4)	>1.0

Note: Some sources refer to a depth 0.75 m as a limit for the 0.6 method.

B.3. Discharge Calculation by Mid-Section Method

After finishing velocity measurement calculation of the total stream discharge was performed. The first calculation of discharge was carried out by the gauging team at the streamflow measurement site. To calculate the discharge, the mid-section method is adopted. This method has been widely adopted in USA and other countries as a standard computation procedure for the current meter streamflow measurements. The mid-section method of discharge calculation assumes that the mean velocity in each vertical represents the mean velocity in a subsection (segment). The mean velocity in each vertical is determined by one of the methods described in the B2 section of this Appendix. For each vertical the segment area extends laterally from half the distances from the preceding vertical to half the distance to the next vertical and from the water surface to the sounded depth in the vertical. When using the mid-section method it is needed to calculate discharge separately for each subsection and thereafter to sum up the individual subsection's discharges to obtain the total river or channel discharge.

Figure B.4. shows diagrammatically the measurement cross-section of a river. The cross-section is defined by observation (measurement) verticals at locations 1, 2, 3, 4, . . . , n. At each location, the depths are sounded with the wading rod and the velocities are sampled by current meter to obtain the mean of the vertical distribution of velocity. The partial discharge is now computed for any subsection as:

$$q_i = v_i \times \left[\frac{(L_i - L_{i-1})}{2} + \frac{(L_{i+1} - L_i)}{2} \right] \times d_i = v_i \times \left[\frac{(L_{i+1} - L_{i-1})}{2} \right] \times d_i \quad (\text{B.2})$$

Where:

q_i = discharge through partial section (segment) i ,

v_i = mean velocity in vertical i ,

L_i = distance from initial point to vertical i ,

L_{i-1} = distance from initial point to preceding vertical,

L_{i+1} = distance from initial point to next vertical,

d_i = depth of water at vertical i .

The procedure is slightly different for the first and the last segments in cross-section. The main difference is in the determination of the widths. Because at the beginning (first) and the end (last) subsections there is no preceding or following vertical, the width becomes one-half the distance from the edge (bank) to the first vertical or from the last vertical to the edge

(bank). For the first segment (1) shown shaded blue in Figure B.6 the discharge is computed as:

$$q_i = v_1 \times \left[\frac{L_2 - L_1}{2} \right] \times d_1 \quad (\text{B.3})$$

Where,

q_i = discharge through segment 1,

v_1 = mean velocity in vertical 1,

L_1 = distance from initial point to vertical i,

L_2 = distance from initial point to precedint vertical,

d_1 = depth of water at vertical 1 (at start of bank water edge).

And for the end of bank water edge:

$$q_n = v_n \times \left[\frac{L_n - L_{(n-1)}}{2} \right] \times d_n$$

(B.4)

Where:

q_n = discharge through segment n ,

v_n = mean velocity in vertical n ,

$L_{(n-1)}$ = distance on the tape corresponding to location of vertical $n-1$,

$L_{(n)}$ = distance on the tape corresponding to location of vertical n ,

d_n = depth of water at vertical n (at the end bank water edge).

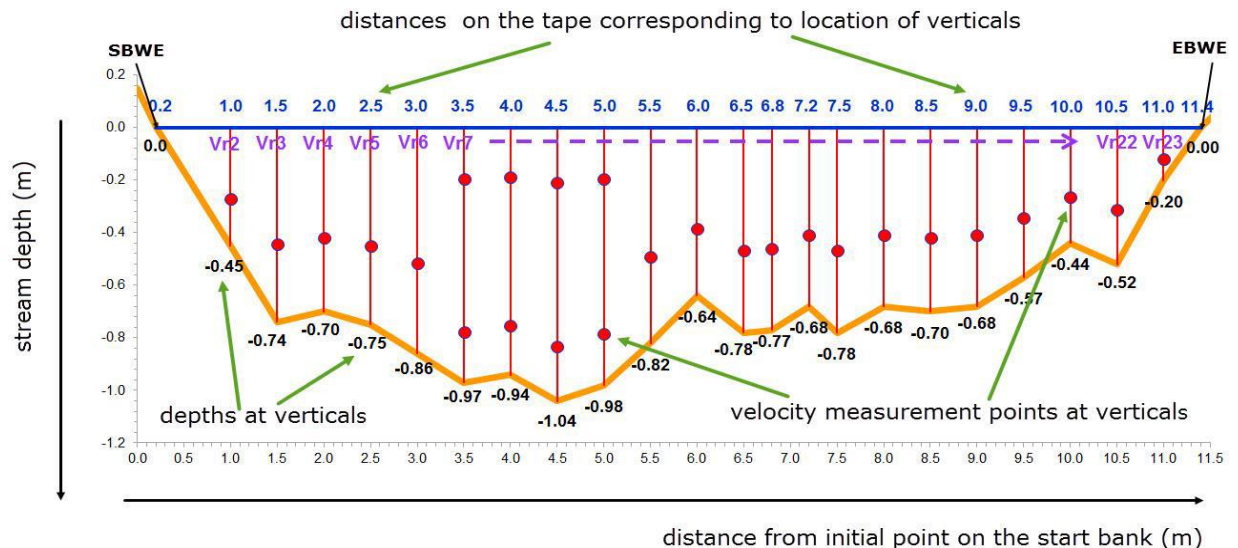


Figure B.6: Reference graph for the computation example of discharge

C: Chókwè Irrigation Canal Reaches and Cross-Sections

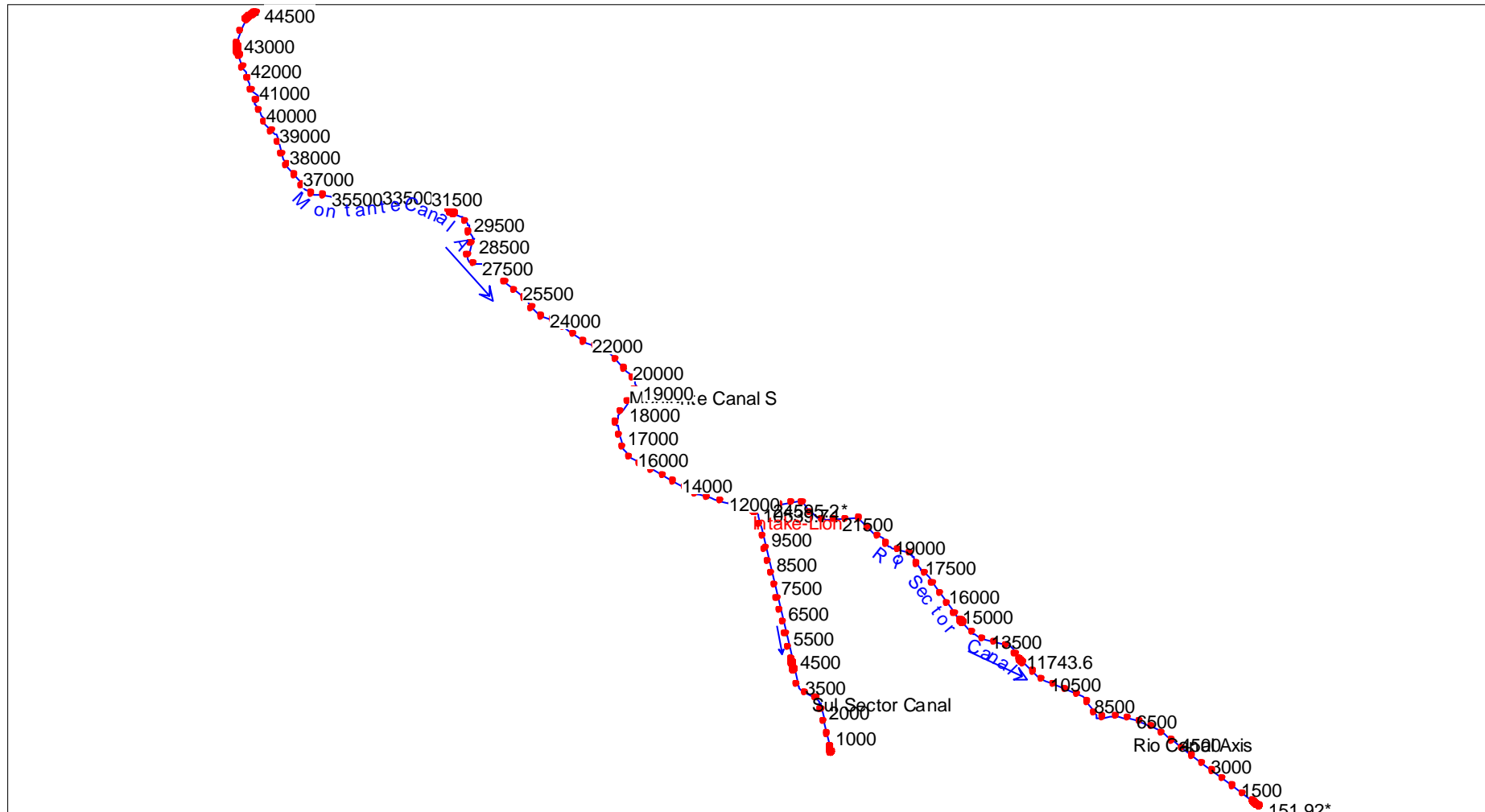


Figure C.1: Canal section geometry representing reaches and flow direction based on HEC-RAS modelling

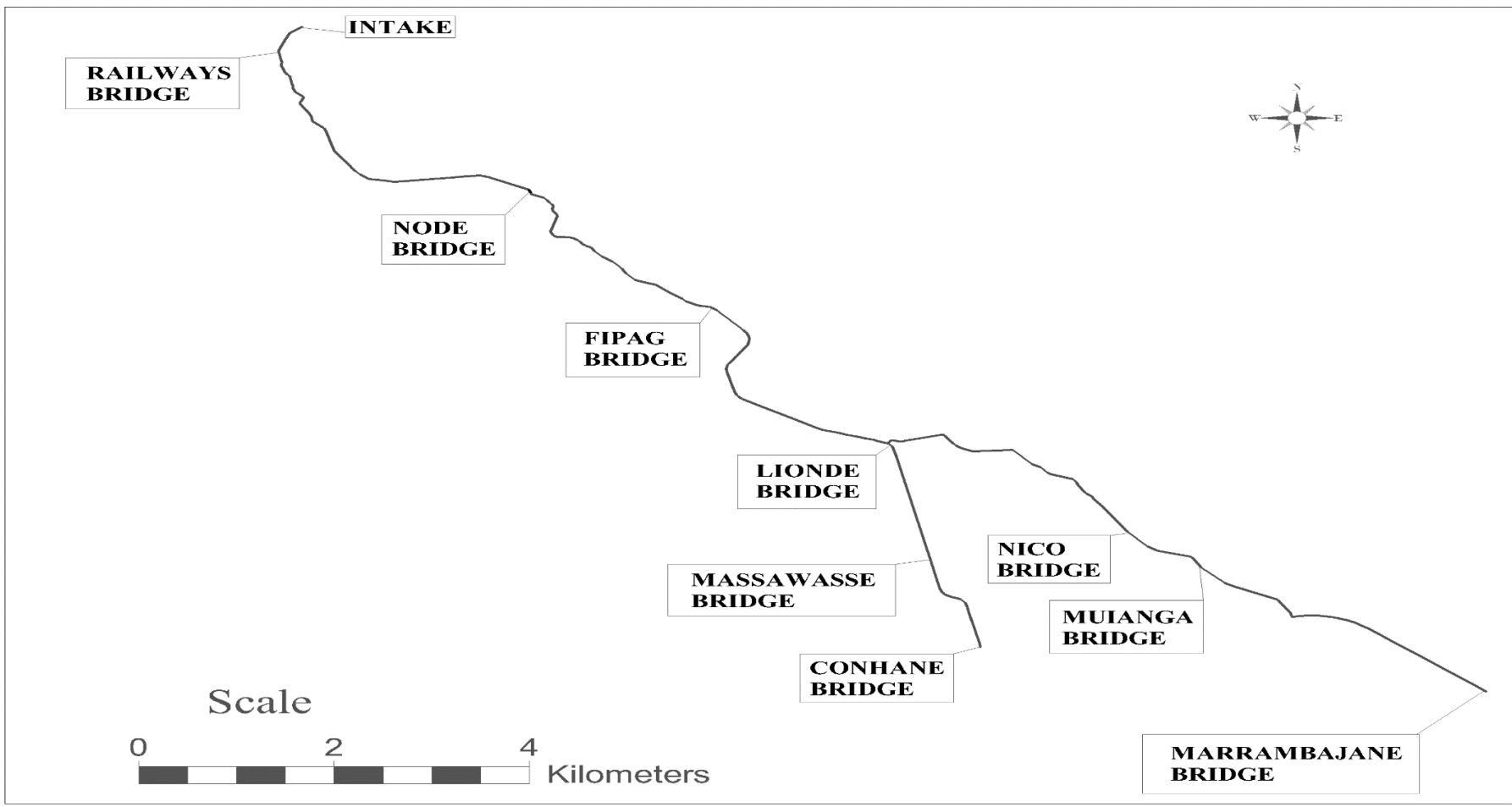
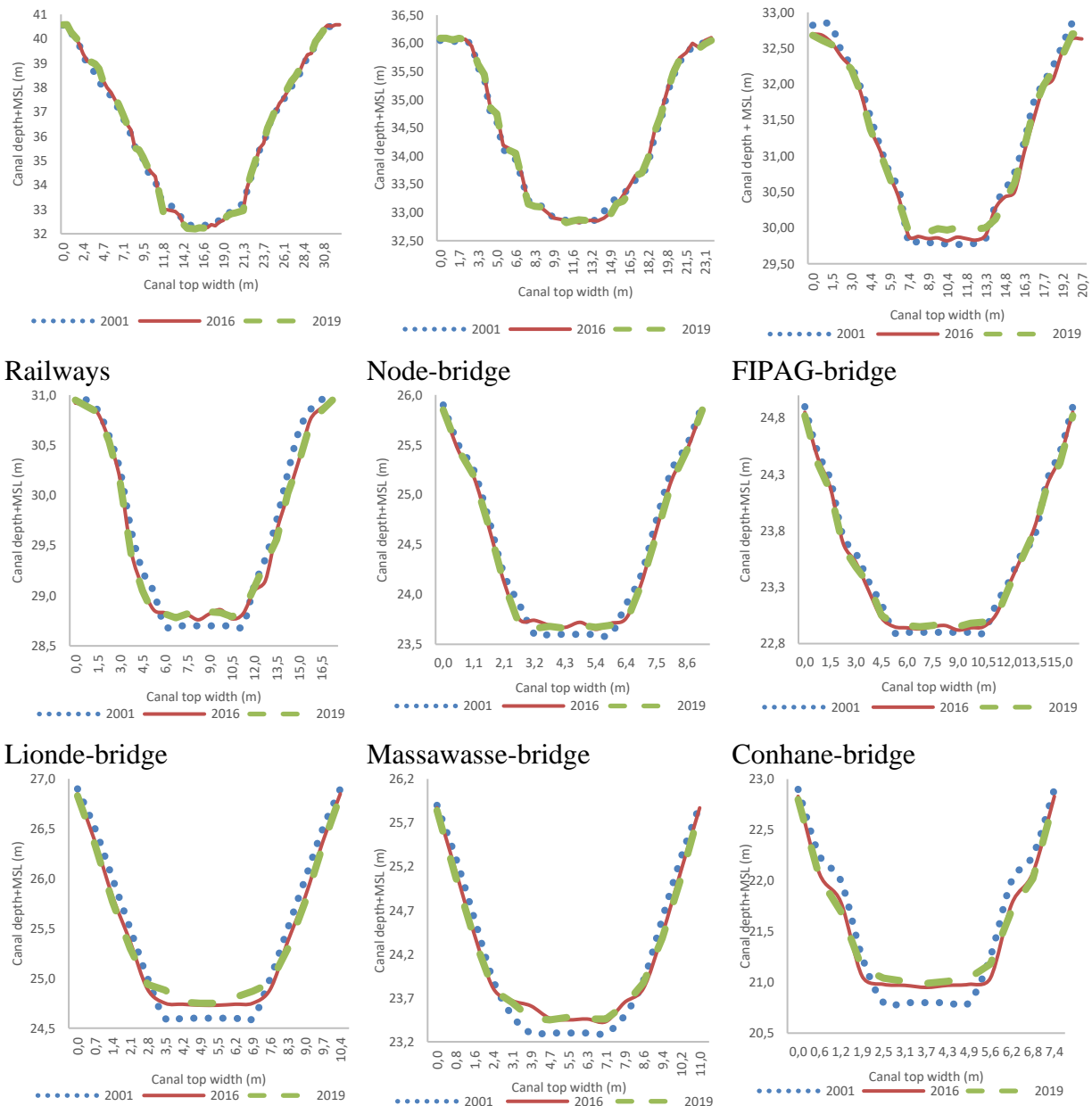


Figure C.2: Canal section geometry representing reaches and flow direction

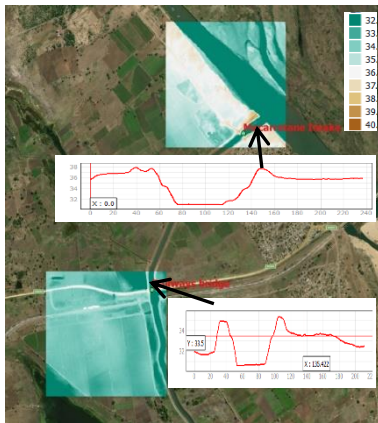


Figure C.3: Fieldwork Sampling Stations

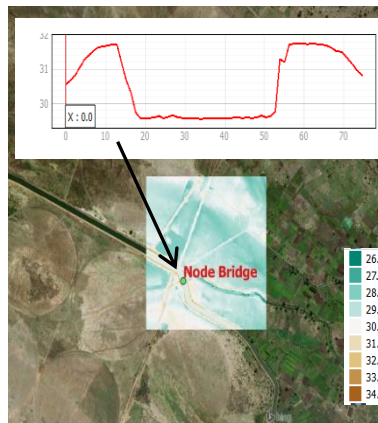
Source: Chókwè Irrigation Scheme. 24°39'15.87"S and 33°09'53.95"E. Google Earth. August 16, 2019. June 20, 2020.



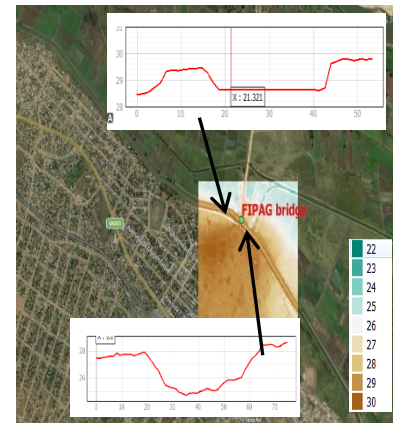
Nico-bridge Muianga-bridge Marrambajane-bridge
Figure C.4: Cross sections (a-i) for different stations for the years 2001, 2016 and 2019



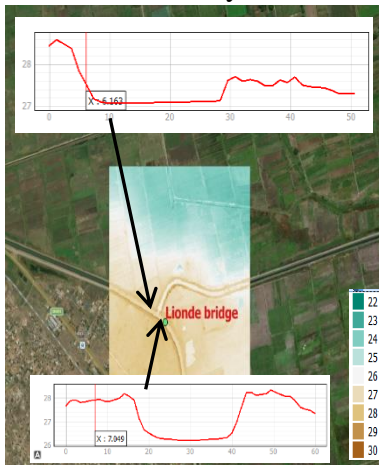
Intake and Railways



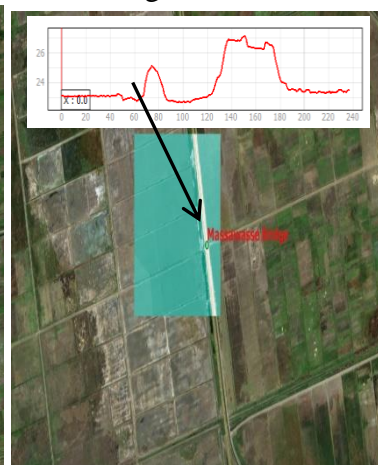
Node-bridge



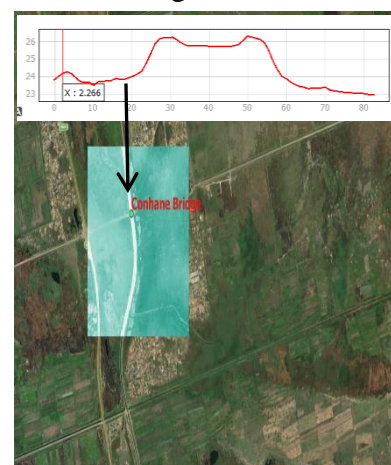
FIPAG-bridge



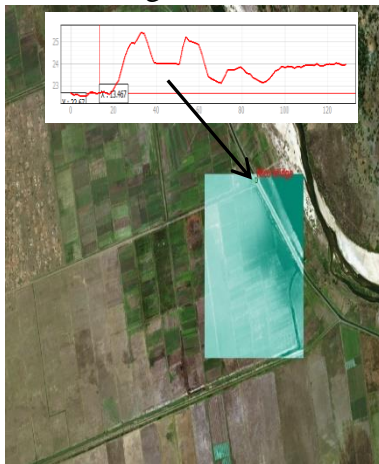
Lionde-bridge



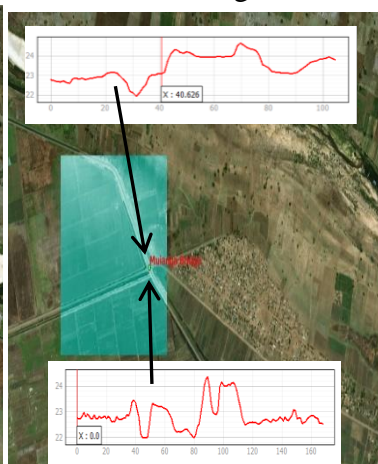
Massawasse-bridge



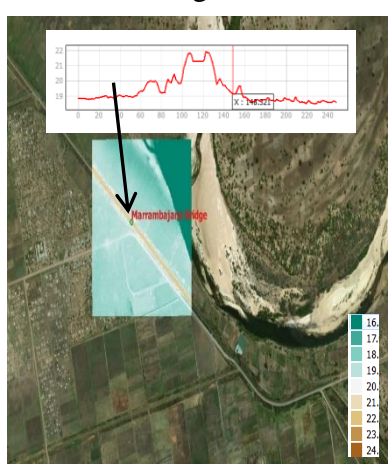
Conhane-bridge



Nico-bridge



Muianga-bridge



Marrambajane-bridge

Figure C.5: Canal cross sections (a-i) for different reaches and sampling stations taken from LiDAR in 2019. Source: Google Earth Pro

Table C1: Chemistry Analysis for Sediment Samples Collected During DS

Parameters	Units	Sampling Stations							
		Railways-Node	FIPAG	Lionde	Massawasse	Conhane	Nico	Muianga	Marrambajane
		Mean±SD (Min-Max) CV (%)							
Water Depth	m	3.75±1.11 (1.30-4.60) 29.53	3.46±0.16 (3.20-3.70) 4.52	2.32±0.18 (2.18-2.72) 7.92	2.04±0.30 (1.77-2.65) 14.58	1.51±0.15 (1.20-1.70) 9.64	2.18±0.11 (1.96-2.28) 4.84	2.23±0.06 (2.15-2.30) 2.65	1.96±0.17 (1.70-2.20) 8.77
Na ⁺	mg/L	0.85±0.59 (0.55-2.30) 69.19	0.64±0.13 (0.48-0.85) 19.76	0.64±0.17 (0.48-0.96) 26.05	0.59±0.19 (0.37-0.97) 32.4	0.76±0.19 (0.61-1.16) 24.67	0.86±0.88 (0.42-3.04) 102.17	0.61±0.11 (0.47-0.81) 18.43	0.65±0.15 (0.41-0.91) 22.54
K ⁺	mg/L	2.11±0.63 (1.56-3.02) 29.70	1.98±0.76 (0.80-3.30) 38.19	1.57±0.65 (0.74-2.86) 41.31	2.22±1.06 (1.37-4.38) 47.64	2.12±1.10 (1.49-4.77) 52.17	1.81±0.45 (1.21-2.40) 24.94	1.92±0.30 (1.55-2.34) 15.4	1.89±0.22 (1.48-2.25) 11.54
Ca ²⁺ +Mg ²⁺	mg/L	0.05±0.01 (0.03-0.06) 20.29	0.04±0.01 (0.03-0.06) 21.75	0.03±0.01 (0.02-0.04) 18.55	0.04±0.01 (0.02-0.05) 25.86	0.03±0.01 (0.02-0.05) 27.53	0.05±0.02 (0.03-0.08) 34.03	0.04±0.01 (0.03-0.05) 21.77	0.05±0.01 (0.03-0.05) 17.29
Sum-Value	mg/L	3.02±0.70 (2.19-3.91) 23.28	2.66±0.81 (1.41-4.18) 30.63	2.25±0.69 (1.41-3.61) 30.7	2.85±1.05 (1.85-5.02) 37.04	2.91±1.26 (2.25-5.95) 43.18	2.72±1.17 (1.87-5.49) 43.05	2.56±0.30 (2.24-2.99) 11.57	2.59±0.20 (2.12-2.73) 7.83
SAR	(-)	5.56±3.84 (3.10-14.81) 69.04	4.61±1.27 (3.23-6.90) 27.46	5.47±1.56 (3.87-7.64) 28.54	4.48±1.30 (2.36-6.72) 29.12	6.01±2.07 (4.01-9.81) 34.35	5.71±5.61 (2.90-19.47) 98.27	4.47±1.15 (3.36-6.61) 25.72	4.37±1.17 (2.62-6.42) 26.84
ESP	%	27.65±13.40 (15.27-58.85) 48.47	25.68±7.94 (18.43-40.69) 30.92	30.25±9.37 (18.55-46.06) 30.95	22.52±9.12 (12.05-38.12) 40.52	27.48±5.21 (19.40-34.18) 18.95	28.40±12.35 (15.11-55.39) 43.5	23.86±4.63 (18.54-29.54) 19.41	25.19±5.43 (15.01-33.28) 21.54
Electric Conductivity (EC)	dS/m	0.22±0.14 (0.10-0.53) 63.00	0.22±0.10 (0.11-0.40) 43.61	0.24±0.09 (0.12-0.40) 37.03	0.18±0.06 (0.12-0.30) 35.79	0.19±0.06 (0.12-0.30) 29.06	0.25±0.09 (0.13-0.40) 35.42	0.28±0.13 (0.11-0.54) 46.15	0.21±0.06 (0.12-0.29) 30.96
Plasticity Index	%	33.31±7.62 18.96-45.70 22.87	34.12±7.12 (22.56-41.40) 20.88	28.22±8.64 (17.57-39.00) 30.61	22.11±7.22 (15.14-32.47) 32.66	23.05±8.68 (15.02-42.79) 37.64	39.63±6.69 (31.31-50.70) 16.88	33.68±5.63 (25.56-41.33) 16.73	40.37±6.11 31.24-49.70 15.13
Soil classification		Sodic	Saline-sodic	Saline-sodic	Saline-sodic	Saline-sodic	Sodic	Saline-sodic	Saline-sodic
Sediment condition		Floculation and Dispersion	Floculation	Floculation	Floculation	Floculation	Floculation and Dispersion	Floculation	Floculation

Table C2: Chemistry Analysis for Sediment Samples Collected During WS

Parameters	Units	Sampling Stations							
		Railways-Node	FIPAG	Lionde	Massawasse	Conhane	Nico	Muianga	Marrambajane
		Mean±SD							
		(Min-Max)							
CV (%)									
Water Depth	m	2.91±0.44	3.32±0.66	2.32±0.18	2.21±0.07	1.85±0.08	2.27±0.06	2.34±0.15	1.88±0.21
		(2.20-3.80)	(1.90-3.73)	(1.95-2.50)	(2.12-2.34)	(1.70-1.91)	(2.20-2.35)	(2.06-2.54)	(1.55-2.16)
		15.19	20.04	7.65	3.32	4.5	2.87	6.28	11.34
Na ⁺	mg/L	0.09±0.04	0.06±0.03	0.04±0.02	0.04±0.03	0.05±0.02	0.05±0.02	0.04±0.02	0.06±0.02
		(0.05-0.15)	(0.03-0.11)	(0.02-0.07)	(0.02-0.08)	(0.03-0.08)	(0.02-0.09)	(0.02-0.07)	(0.03-0.10)
		40.27	41.11	44.84	64.14	49.36	51.72	60.13	41.23
K ⁺	mg/L	0.15±0.10	0.22±0.09	0.12±0.06	0.13±0.05	0.13±0.06	0.15±0.06	0.12±0.06	0.18±0.08
		(0.06-0.38)	(0.08-0.37)	(0.07-0.23)	(0.06-0.18)	(0.06-0.21)	(0.10-0.27)	(0.05-0.21)	(0.10-0.37)
		65.57	41.98	46.62	36.57	45.47	38.71	49.68	45.62
Ca ²⁺ +Mg ²⁺	mg/L	0.05±0.02	0.05±0.02	0.03±0.01	0.03±0.01	0.03±0.01	0.02±0.00	0.03±0.01	0.04±0.01
		(0.03-0.09)	(0.03-0.08)	(0.02-0.04)	(0.02-0.06)	(0.02-0.04)	(0.01-0.02)	(0.02-0.05)	(0.02-0.05)
		41.32	37.07	29.49	53.68	28.24	13.23	41.18	22.09
Sum-Value	mg/L	0.30±0.11	0.33±0.10	0.19±0.07	0.20±0.07	0.21±0.07	0.21±0.05	0.19±0.08	0.27±0.09
		(0.17-0.52)	(0.14-0.49)	(0.12-0.31)	(0.10-0.28)	(0.13-0.30)	(0.15-0.32)	(0.09-0.31)	(0.17-0.45)
		35.54	31.5	33.99	36.13	32.5	26.54	43.57	31.51
SAR	(-)	0.60±0.25	0.41±0.22	0.37±0.16	0.34±0.21	0.39±0.20	0.49±0.26	0.34±0.23	0.42±0.20
		(0.35-0.97)	(0.19-0.76)	(0.20-0.56)	(0.12-0.72)	(0.23-0.77)	(0.21-1.00)	(0.14-0.81)	(0.21-0.85)
		40.90	53.24	42.34	63.14	50.72	52.72	68.44	47.58
ESP	%	32.70±13.00	19.24±7.20	23.01±9.72	18.45±6.60	23.09±8.37	22.00±10.40	20.08±8.84	20.79±7.98
		(15.50-57.91)	(9.22-29.29)	(14.76-40.94)	(11.70-30.19)	(10.99-33.06)	(11.93-39.78)	(11.02-36.84)	(9.91-35.27)
		39.75	37.43	42.26	35.76	36.27	47.24	44.02	38.39
Electric Conductivity (EC)	dS/m	0.19±0.07	0.19±0.06	0.14±0.03	0.13±0.05	0.14±0.05	0.12±0.03	0.19±0.08	0.28±0.21
		(0.12-0.32)	(0.12-0.31)	(0.10-0.20)	(0.09-0.24)	(0.06-0.21)	(0.09-0.18)	(0.12-0.36)	(0.12-0.75)
		37.42	33.04	21.93	35.76	34.67	25.56	41.55	76.33
Plasticity Index	%	34.12±6.53	34.37±4.12	33.09±4.99	19.81±4.95	23.90±5.70	30.93±8.76	34.28±14.04	41.33±2.92
		26.67-45.02	(28.54-42.01)	(26.64-40.93)	(14.17-29.04)	(16.78-33.43)	(17.51-40.68)	(18.93-54.08)	(38.43-46.90)
		19.13	11.98	15.07	24.98	23.87	28.32	40.95	7.06
Soil classification		Sodic	Saline-sodic	Saline-sodic	Saline-sodic	Saline-sodic	Sodic	Saline-sodic	Saline-sodic
Sediment condition		Flocculation	Flocculation	Flocculation	Flocculation	Flocculation	Flocculation	Flocculation	Flocculation

D: T-Student Test and PCA Analysis

D.1. T-Student Test

Table D.1: Summary statistics for t-test.

Variable	Observations	Obs. with missing data	Obs. without missing data	Minimum	Maximum	Mean	Std. deviation
2016	340	0	340	29,201	41,025	35,168	2,718
2019	340	0	340	29,961	41,478	36,058	2,239

t-test for two independent samples / Two-tailed test:

95% confidence interval on the difference between the means:
 [-1,265; -0,515]

Difference	-0,890
t (Observed value)	-4,660
t (Critical value)	1,963
DF	678
	<0,000
p-value (Two-tailed)	1
alpha	0,050

Test interpretation:

H0: The difference between the means is equal to 0.

Ha: The difference between the means is different from 0.

As the computed p-value is lower than the significance level $\alpha=0,05$, one should reject the null hypothesis H0, and accept the alternative hypothesis Ha.

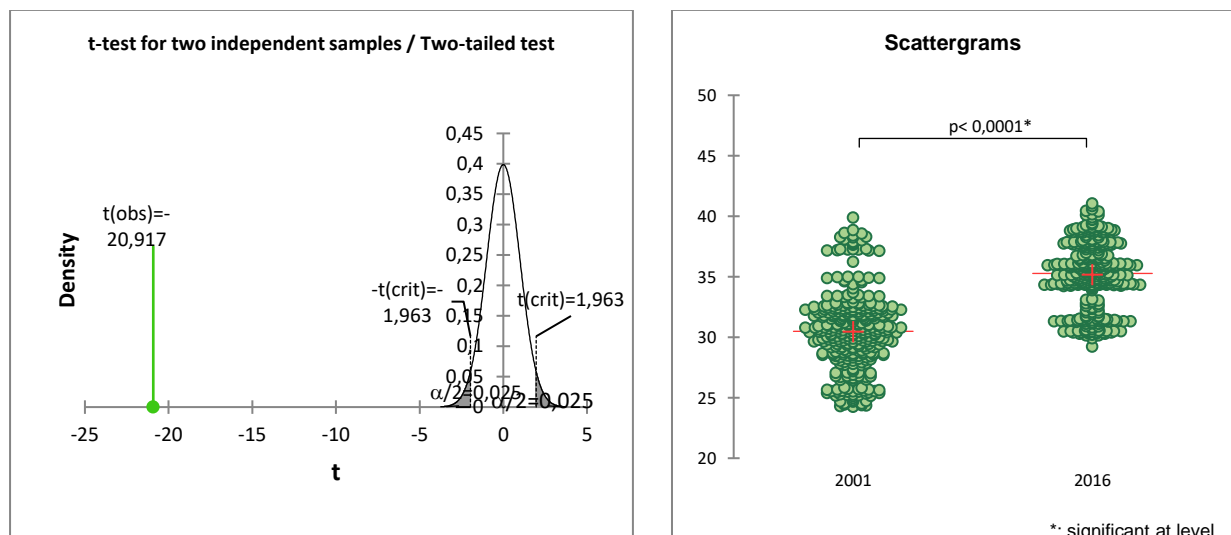


Figure D.1: T-Student test density and scattergrams

D.2. PCA Correlation matrices

Table D.2: PCA correlation matrix (Pearson)(n) for the Canal Channel Factors-DS

Variables	Q	WD	CD	SV	CSS	PI	EC	ESP	SAR	Na ⁺	K ⁺	Ca ²⁺ + Mg ²⁺
Q	1	0,416	0,313	-0,080	0,225	0,240	0,123	0,050	0,044	0,284	0,061	0,377
WD	0,416	1	0,879	-0,217	0,348	0,284	0,286	0,014	-0,273	-0,065	-0,088	0,221
CD	0,313	0,879	1	-0,279	0,337	0,279	0,155	0,114	-0,062	0,233	0,090	0,427
SV	-0,080	-0,217	-0,279	1	-0,276	-0,216	0,095	-0,753	-0,585	-0,509	0,298	-0,104
CSS	0,225	0,348	0,337	-0,276	1	0,958	0,538	0,181	-0,238	0,169	-0,498	0,610
PI	0,240	0,284	0,279	-0,216	0,958	1	0,514	0,124	-0,200	0,288	-0,415	0,733
EC	0,123	0,286	0,155	0,095	0,538	0,514	1	0,208	-0,042	0,031	-0,618	0,073
ESP	0,050	0,014	0,114	-0,753	0,181	0,124	0,208	1	0,799	0,584	-0,623	-0,109
SAR	0,044	-0,273	-0,062	-0,585	-0,238	-0,200	-0,042	0,799	1	0,777	-0,125	-0,068
Na ⁺	0,284	-0,065	0,233	-0,509	0,169	0,288	0,031	0,584	0,777	1	0,048	0,571
K ⁺	0,061	-0,088	0,090	0,298	-0,498	-0,415	-0,618	-0,623	-0,125	0,048	1	0,248
Ca ²⁺ + Mg ²⁺	0,377	0,221	0,427	-0,104	0,610	0,733	0,073	-0,109	-0,068	0,571	0,248	1

Values in bold are different from 0 with a significance level alpha=0,05

Table D.3: PCA correlation matrix (Pearson)(n) for the Canal Channel Factors-WS

Variables	Q	WD	CD	SV	CSS	PI	EC	ESP	SAR	Na ⁺	K ⁺	Ca ²⁺ + Mg ²⁺
Q	1	0,368	0,329	-0,360	0,049	0,057	0,004	0,564	0,441	0,460	-0,178	0,246
WD	0,368	1	0,998	-0,471	0,199	0,201	0,026	0,295	0,407	0,601	0,528	0,728
CD	0,329	0,998	1	-0,471	0,214	0,216	0,039	0,236	0,364	0,563	0,558	0,721
SV	-0,360	-0,471	-0,471	1	-0,748	-0,688	-0,501	-0,315	-0,518	-0,518	-0,507	-0,441
CSS	0,049	0,199	0,214	-0,748	1	0,958	0,703	0,140	0,408	0,340	0,522	0,228
PI	0,057	0,201	0,216	-0,688	0,958	1	0,780	0,179	0,322	0,375	0,499	0,344
EC	0,004	0,026	0,039	-0,501	0,703	0,780	1	0,057	0,166	0,372	0,565	0,481
ESP	0,564	0,295	0,236	-0,315	0,140	0,179	0,057	1	0,841	0,828	-0,108	0,422
SAR	0,441	0,407	0,364	-0,518	0,408	0,322	0,166	0,841	1	0,864	0,265	0,434
Na ⁺	0,460	0,601	0,563	-0,518	0,340	0,375	0,372	0,828	0,864	1	0,444	0,809
K ⁺	-0,178	0,528	0,558	-0,507	0,522	0,499	0,565	-0,108	0,265	0,444	1	0,685
Ca ²⁺ + Mg ²⁺	0,246	0,728	0,721	-0,441	0,228	0,344	0,481	0,422	0,434	0,809	0,685	1

Values in bold are different from 0 with a significance level alpha=0,05

Table D.4: PCA correlation matrix (Pearson)(n) for the Inflow Factors-DS

Variables	Q	WD	T	WV	SSC	EC	TDS	TURB	pH	Na ⁺	K ⁺	Ca ²⁺
Q	1	0,416	-0,113	0,984	0,321	0,270	0,360	-0,541	0,102	-0,041	-0,014	0,100
WD	0,416	1	-0,316	0,409	0,010	0,811	0,863	-0,252	-0,046	-0,191	-0,091	-0,016
T	-0,113	-0,316	1	-0,059	0,378	-0,627	-0,581	-0,364	-0,266	-0,486	-0,496	-0,099
WV	0,984	0,409	-0,059	1	0,403	0,201	0,331	-0,623	0,132	-0,109	-0,098	0,146
SSC	0,321	0,010	0,378	0,403	1	-0,397	-0,241	-0,377	-0,465	-0,152	-0,136	-0,422
EC	0,270	0,811	-0,627	0,201	-0,397	1	0,885	0,043	0,010	0,174	0,242	-0,044
TDS	0,360	0,863	-0,581	0,331	-0,241	0,885	1	0,097	0,160	0,204	0,249	-0,001
TURB	-0,541	-0,252	-0,364	-0,623	-0,377	0,043	0,097	1	0,011	0,626	0,615	-0,307
pH	0,102	-0,046	-0,266	0,132	-0,465	0,010	0,160	0,011	1	-0,252	-0,358	0,905
Na ⁺	-0,041	-0,191	-0,486	-0,109	-0,152	0,174	0,204	0,626	-0,252	1	0,982	-0,551
K ⁺	-0,014	-0,091	-0,496	-0,098	-0,136	0,242	0,249	0,615	-0,358	0,982	1	-0,625
Ca ²⁺	0,100	-0,016	-0,099	0,146	-0,422	-0,044	-0,001	-0,307	0,905	-0,551	-0,625	1

Values in bold are different from 0 with a significance level alpha=0,05

Table D.5: PCA correlation matrix (Pearson)(n) for the Inflow Factors-DS

Variables	Q	WD	T	WV	SSC	EC	TDS	TURB	pH	Na ⁺	K ⁺	Ca ²⁺
Q	1	0,368	-0,293	0,918	-0,361	-0,480	-0,450	0,851	0,592	0,163	0,110	-0,465
WD	0,368	1	-0,427	0,290	-0,488	-0,319	-0,286	0,492	0,521	0,860	0,393	0,374
T	-0,293	-0,427	1	-0,070	0,955	0,640	0,648	-0,350	-0,152	-0,369	0,113	0,171
WV	0,918	0,290	-0,070	1	-0,094	-0,523	-0,485	0,896	0,521	0,170	0,325	-0,334
SSC	-0,361	-0,488	0,955	-0,094	1	0,581	0,586	-0,390	-0,142	-0,363	0,068	0,134
EC	-0,480	-0,319	0,640	-0,523	0,581	1	0,998	-0,773	-0,146	-0,321	-0,469	0,015
TDS	-0,450	-0,286	0,648	-0,485	0,586	0,998	1	-0,742	-0,105	-0,302	-0,464	0,005
TURB	0,851	0,492	-0,350	0,896	-0,390	-0,773	-0,742	1	0,414	0,417	0,510	-0,122
pH	0,592	0,521	-0,152	0,521	-0,142	-0,146	-0,105	0,414	1	0,148	-0,195	-0,406
Na ⁺	0,163	0,860	-0,369	0,170	-0,363	-0,321	-0,302	0,417	0,148	1	0,561	0,582
K ⁺	0,110	0,393	0,113	0,325	0,068	-0,469	-0,464	0,510	-0,195	0,561	1	0,737
Ca ²⁺	-0,465	0,374	0,171	-0,334	0,134	0,015	0,005	-0,122	-0,406	0,582	0,737	1

Values in bold are different from 0 with a significance level alpha=0,05

Table D.6: PCA factor loadings for the canal channel Factors-DS

	F1	F2	F3	F4	F5	F6	F7	F8
Q	0,432	-0,175	0,389	0,105	0,644	0,452	0,001	0,031
WD	0,521	-0,442	0,190	0,692	-0,020	-0,037	-0,035	-0,121
CD	0,581	-0,289	0,423	0,535	-0,144	-0,266	0,119	0,093
SV	-0,570	-0,580	-0,104	-0,216	0,390	-0,271	0,234	0,006
CSS	0,814	-0,365	-0,279	-0,242	-0,181	0,123	-0,010	0,140
PI	0,808	-0,361	-0,190	-0,392	-0,130	0,062	-0,005	-0,078
EC	0,516	-0,211	-0,585	0,035	0,402	-0,380	-0,197	0,025
ESP	0,544	0,779	-0,208	0,180	-0,001	0,026	0,139	0,046
SAR	0,233	0,928	0,172	-0,028	0,170	-0,153	-0,041	0,009
Na+	0,579	0,544	0,450	-0,323	0,127	-0,205	0,036	-0,057
K+	-0,463	-0,196	0,823	-0,132	-0,041	-0,123	-0,172	0,076
Ca2+ + Mg2+	0,620	-0,330	0,489	-0,503	-0,078	-0,075	0,048	-0,037
Eigenvalue	3,988	2,864	2,025	1,444	0,852	0,600	0,164	0,063
Variability (%)	33,236	23,869	16,872	12,032	7,100	5,003	1,363	0,525
Cumulative %	33,236	57,104	73,977	86,009	93,109	98,112	99,475	100,000

Table D.7: PCA factor loadings for the canal channel Factors-WS

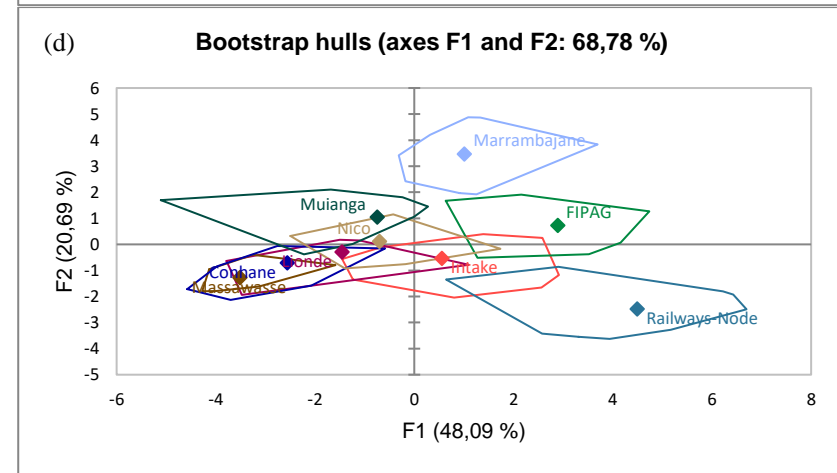
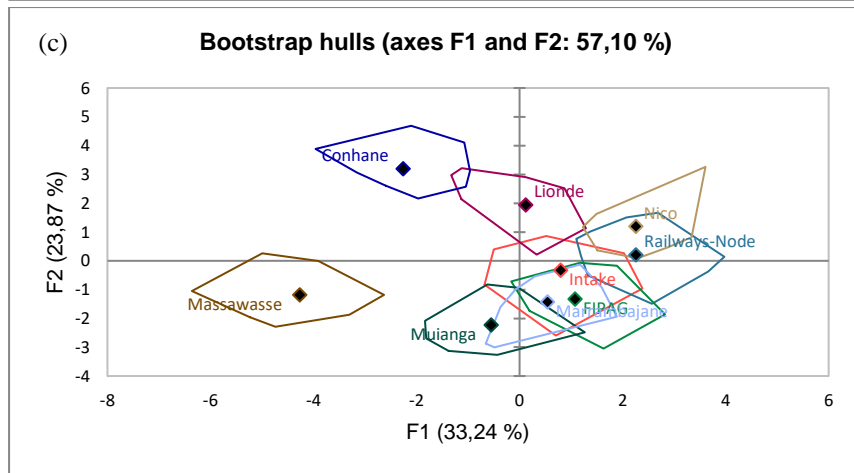
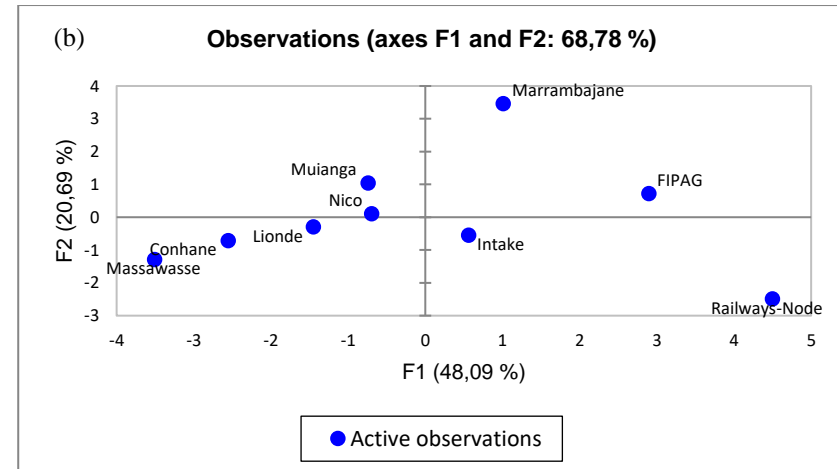
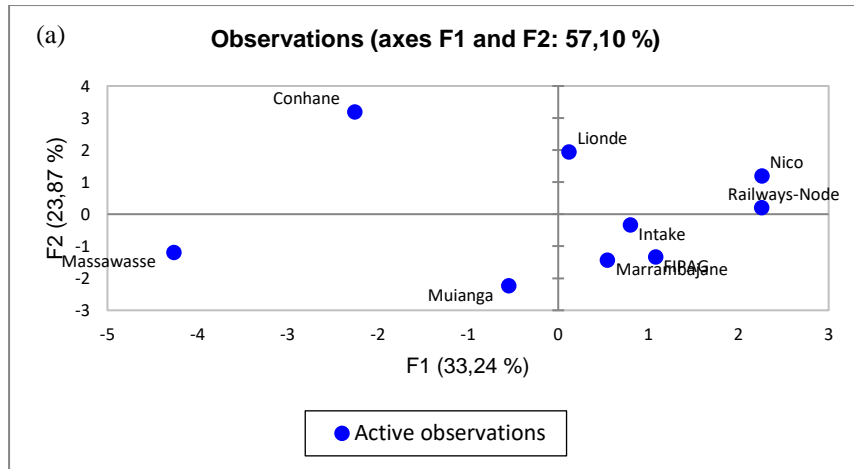
	F1	F2	F3	F4	F5	F6	F7	F8
Q	0,417	-0,539	-0,323	0,434	0,443	-0,123	0,172	-0,047
WD	0,724	-0,340	0,534	0,226	-0,059	0,129	0,015	0,059
CD	0,711	-0,291	0,574	0,238	-0,061	0,129	0,019	0,049
SV	-0,791	-0,234	0,135	-0,374	0,073	0,266	0,291	-0,006
CSS	0,662	0,622	-0,270	0,223	-0,181	0,097	0,099	0,009
PI	0,674	0,623	-0,250	0,132	-0,004	0,261	0,017	-0,095
EC	0,562	0,654	-0,168	-0,237	0,390	-0,010	0,021	0,140
ESP	0,571	-0,563	-0,530	-0,199	-0,062	0,142	-0,107	-0,034
SAR	0,732	-0,346	-0,402	-0,150	-0,345	-0,137	0,138	0,058
Na+	0,876	-0,337	-0,145	-0,312	0,002	-0,004	0,003	0,004
K+	0,667	0,408	0,491	-0,216	-0,099	-0,250	0,144	-0,090
Ca2+ + Mg2+	0,811	-0,134	0,351	-0,336	0,264	0,038	-0,114	-0,062
Eigenvalue	5,771	2,483	1,729	0,878	0,596	0,300	0,190	0,053
Variability (%)	48,090	20,692	14,412	7,317	4,966	2,497	1,582	0,444
Cumulative %	48,090	68,782	83,194	90,511	95,477	97,974	99,556	100,000

Table D.8: PCA factor loadings for the Inflow Factors-DS

	F1	F2	F3	F4	F5	F6	F7	F8
Q	0,193	0,733	0,428	-0,447	-0,099	0,093	0,157	-0,012
WD	0,542	0,655	0,127	0,481	0,114	0,057	-0,024	-0,110
T	-0,791	-0,056	0,304	0,222	-0,182	0,440	-0,056	0,024
WV	0,108	0,773	0,436	-0,440	-0,030	0,069	0,023	-0,002
SSC	-0,345	0,117	0,801	-0,051	0,456	-0,095	-0,056	0,052
EC	0,820	0,391	-0,100	0,335	-0,159	-0,067	0,066	0,135
TDS	0,819	0,460	-0,067	0,203	0,134	0,193	-0,129	0,010
TURB	0,439	-0,731	-0,301	-0,032	0,293	0,241	0,196	-0,009
pH	-0,063	0,392	-0,787	-0,401	0,186	0,143	-0,064	0,056
Na+	0,667	-0,573	0,190	-0,403	-0,076	0,041	-0,141	0,038
K+	0,716	-0,553	0,259	-0,310	-0,100	0,021	-0,059	-0,073
Ca2+	-0,297	0,531	-0,754	-0,230	0,002	-0,057	-0,048	-0,050
Eigenvalue	3,670	3,549	2,520	1,305	0,444	0,344	0,121	0,046
Variability (%)	30,587	29,574	21,002	10,872	3,701	2,868	1,010	0,386
Cumulative %	30,587	60,161	81,162	92,034	95,735	98,604	99,614	100,000

Table D.9: PCA factor loadings for the Inflow Factors-WS

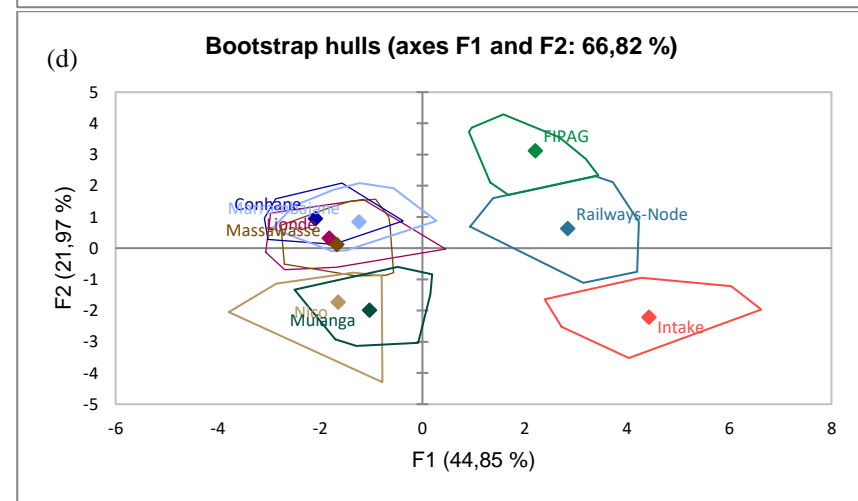
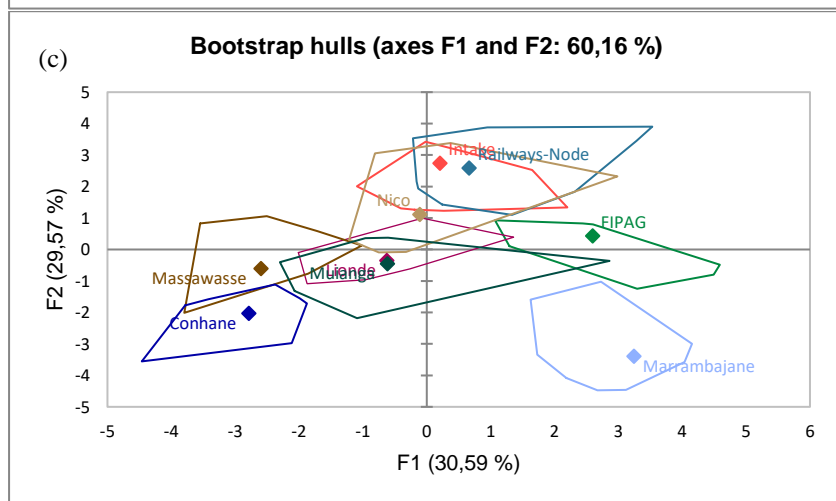
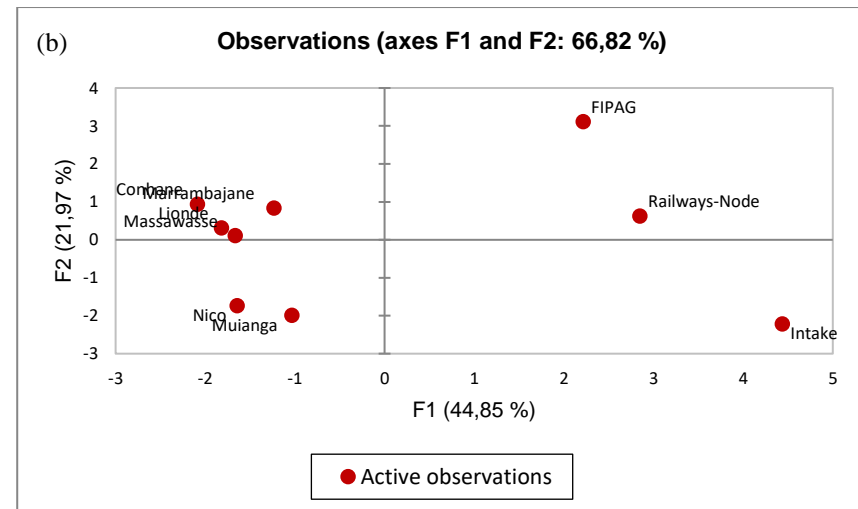
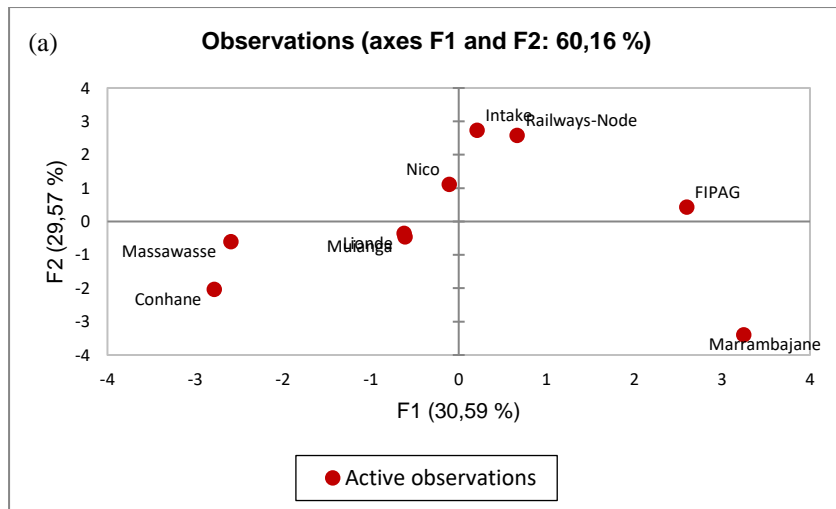
	F1	F2	F3	F4	F5	F6	F7	F8
Q	0,760	-0,490	0,306	0,074	-0,254	-0,093	-0,084	-0,056
WD	0,668	0,380	0,024	0,630	0,035	-0,081	0,039	0,046
T	-0,646	0,042	0,754	-0,059	0,034	-0,055	0,069	-0,020
WV	0,722	-0,370	0,554	-0,093	-0,122	0,050	-0,042	0,083
SSC	-0,656	0,028	0,704	-0,108	0,174	0,172	-0,043	0,003
EC	-0,855	-0,058	0,161	0,437	-0,218	-0,040	-0,006	-0,015
TDS	-0,831	-0,070	0,193	0,467	-0,215	-0,032	0,021	0,021
TURB	0,921	-0,105	0,313	-0,143	-0,093	0,013	0,116	-0,020
pH	0,451	-0,466	0,238	0,596	0,406	-0,044	-0,017	-0,025
Na+	0,569	0,643	0,019	0,417	-0,125	0,267	-0,005	-0,033
K+	0,437	0,710	0,453	-0,298	0,009	-0,102	-0,002	-0,015
Ca2+	-0,046	0,979	0,130	0,032	0,038	-0,124	-0,064	0,005
Eigenvalue	5,382	2,637	1,907	1,475	0,396	0,152	0,035	0,016
Variability (%)	44,850	21,974	15,893	12,289	3,302	1,268	0,295	0,130
Cumulative %	44,850	66,824	82,716	95,006	98,307	99,575	99,870	100,000



For Dry Season

For Wet Season

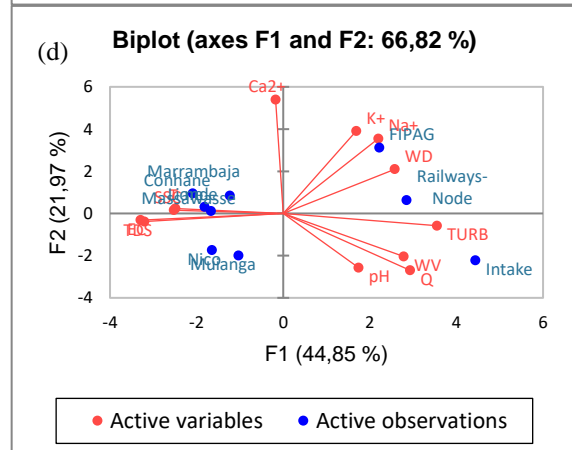
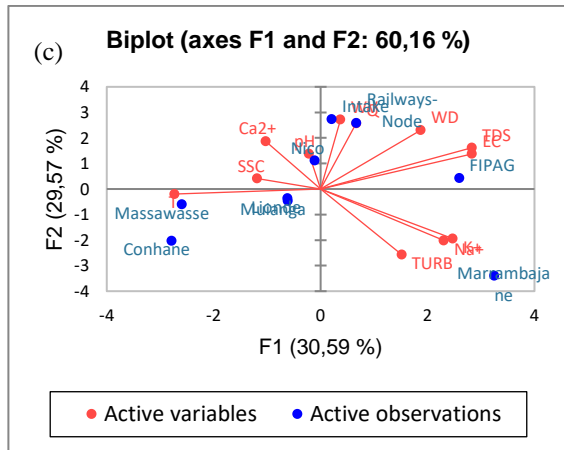
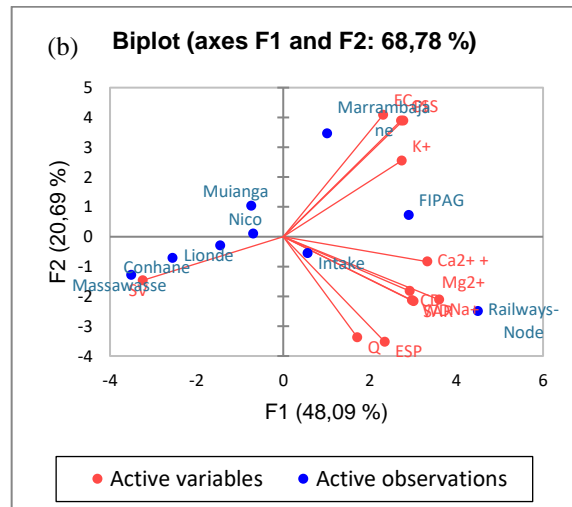
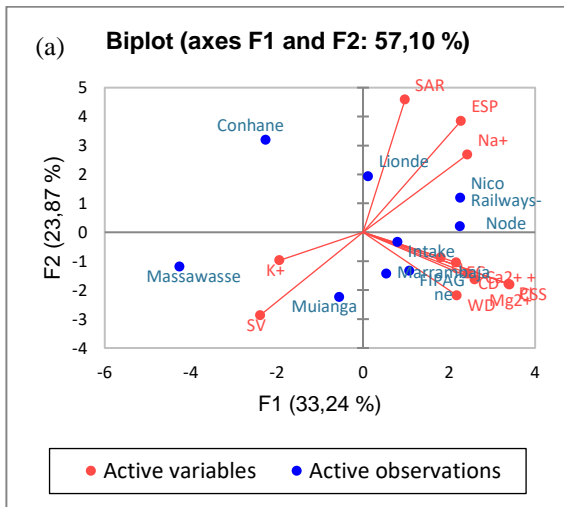
Figure D.2: PCA Analysis for Observations (a&b) and Bootstrap Hulls (c&d) for Canal Channel Factors at DS and WS



For Dry Season

For Wet Season

Figure D. 3: PCA Analysis for Observations (a&b) and Bootstrap Hulls (c&d) for Inflow Factors at DS and WS



For Dry Season

For Wet Season

Figure D. 4: PCA Analysis for Biplots of Canal (a&b) and Inflow (c&d) Factors for DS and WS

E: Sediment Budget Analysis

A sediment budget summarises the balance of inputs and outputs for a defined system (such as an irrigation canal, river stream, estuary or coastal embayment) and time period. This helps determine if a system has an overall surplus (accretion) or deficit (erosion) of material. If the accretion and erosion figures are equal, then the system is considered to be in balance/equilibrium. In its most basic form, the sediment budget equation can be written as follows:

$$\Delta Q_s = Q_{sTotal_Inputs} - Q_{sTotal_Outputs}$$

(E.1)

Where:

$$Q_{sTotal_Inputs} = \text{Total sediment inputs}$$

$$Q_{sTotal_Outputs} = \text{Total sediment outputs}$$

$$\Delta Q_s = \text{Net change in sediment volume within the system}$$

The choice of volume or mass as a base unit is likely to relate to the type of system being investigated. Firstly, definition of changes in volume within the defined area to give a balance. This is applicable to non-cohesive (that is, sand and shingle) shores, where suspended sediment concentrations are low and material types remain similar. Secondly, definition of exchanges in mass to and from the water column to give a mass balance. This is more straightforward in relation to systems with cohesive (that is, muddy) or mixed sediments, large suspended sediment concentrations and higher degrees of variability in the sediment dynamics within the system, as is the case with the Chókwè Irrigation Scheme, for example.

F: Normality Test

Table F.1: Summary for Water discharge:

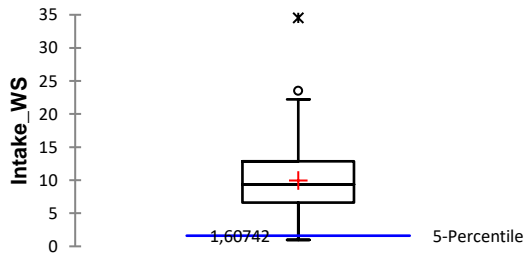
Variable\Test	Shapiro-Wilk	Anderson-Darling	Lilliefors	Jarque-Bera
Intake_WS	<0.0001	0.003	0.018	<0.0001
Intake_DS	0.000	0.003	0.039	0.001
Node_WS	0.100	0.020	0.000	0.938
Node_DS	0.000	0.009	0.003	<0.0001
FIPAG_WS	0.002	0.000	0.000	0.085
FIPAG_DS	<0.0001	<0.0001	0.001	0.000
Lionde_WS	0.084	0.079	0.087	0.285
Lionde_DS	0.076	0.175	0.564	0.309
Massawasse_WS	0.015	0.073	0.395	0.290
Massawasse_DS	<0.0001	<0.0001	0.007	<0.0001
Conhane_WS	0.001	0.001	0.027	0.061
Conhane_DS	<0.0001	<0.0001	<0.0001	<0.0001
Nico_WS	<0.0001	<0.0001	<0.0001	<0.0001
Nico_DS	<0.0001	<0.0001	0.000	<0.0001
Muianga_WS	<0.0001	<0.0001	<0.0001	<0.0001
Muianga_DS	<0.0001	0.000	0.023	<0.0001
Marrambajane_WS	<0.0001	<0.0001	<0.0001	0.022
Marrambajane_DS	0.000	0.001	0.023	0.086

Table F.2: Summary for Sediment discharge:

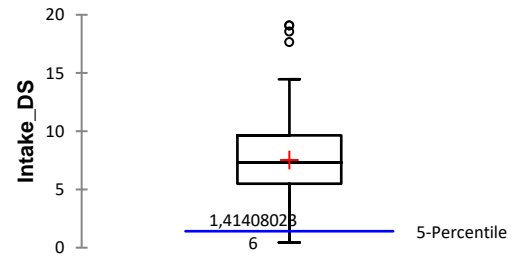
Variable\Test	Shapiro-Wilk	Anderson-Darling	Lilliefors	Jarque-Bera
Sed_Intake_WS	<0.0001	0.003	0.018	<0.0001
Sed_Intake_DS	0.000	0.003	0.039	0.001
Sed_Offtake_WS	<0.0001	<0.0001	<0.0001	0.022
Sed_Offtake_DS	0.000	0.001	0.023	0.086

Boxplots for water discharge

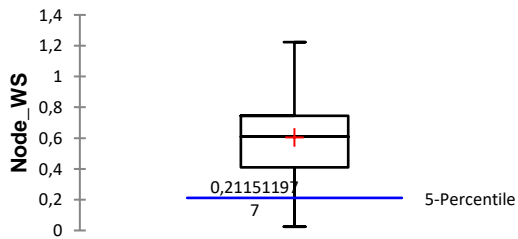
Box plot (Intake_WS)



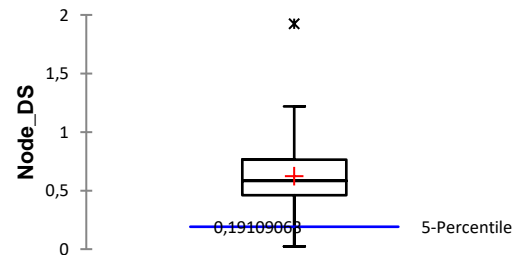
Box plot (Intake_DS)



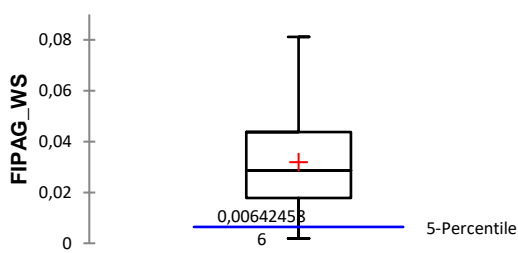
Box plot (Node_WS)



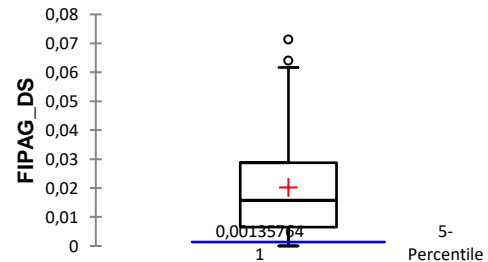
Box plot (Node_DS)



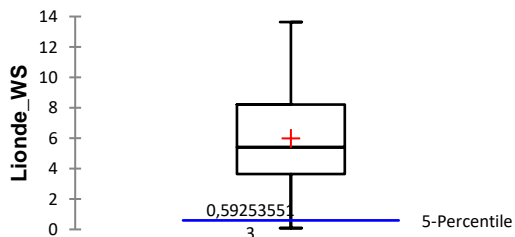
Box plot (FIPAG_WS)



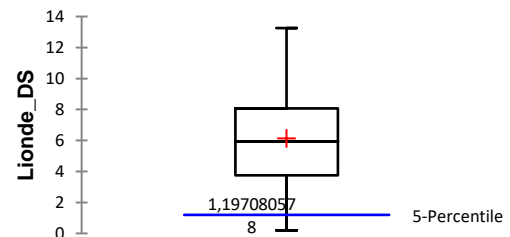
Box plot (FIPAG_DS)



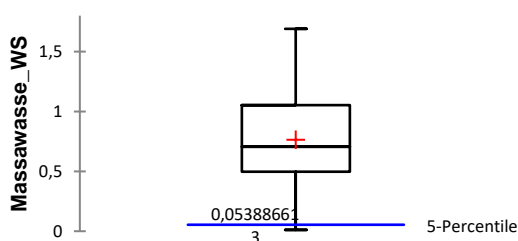
Box plot (Lionde_WS)



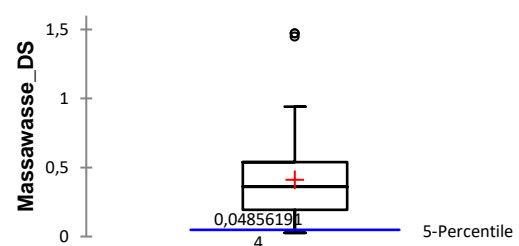
Box plot (Lionde_DS)



Box plot (Massawasse_WS)



Box plot (Massawasse_DS)



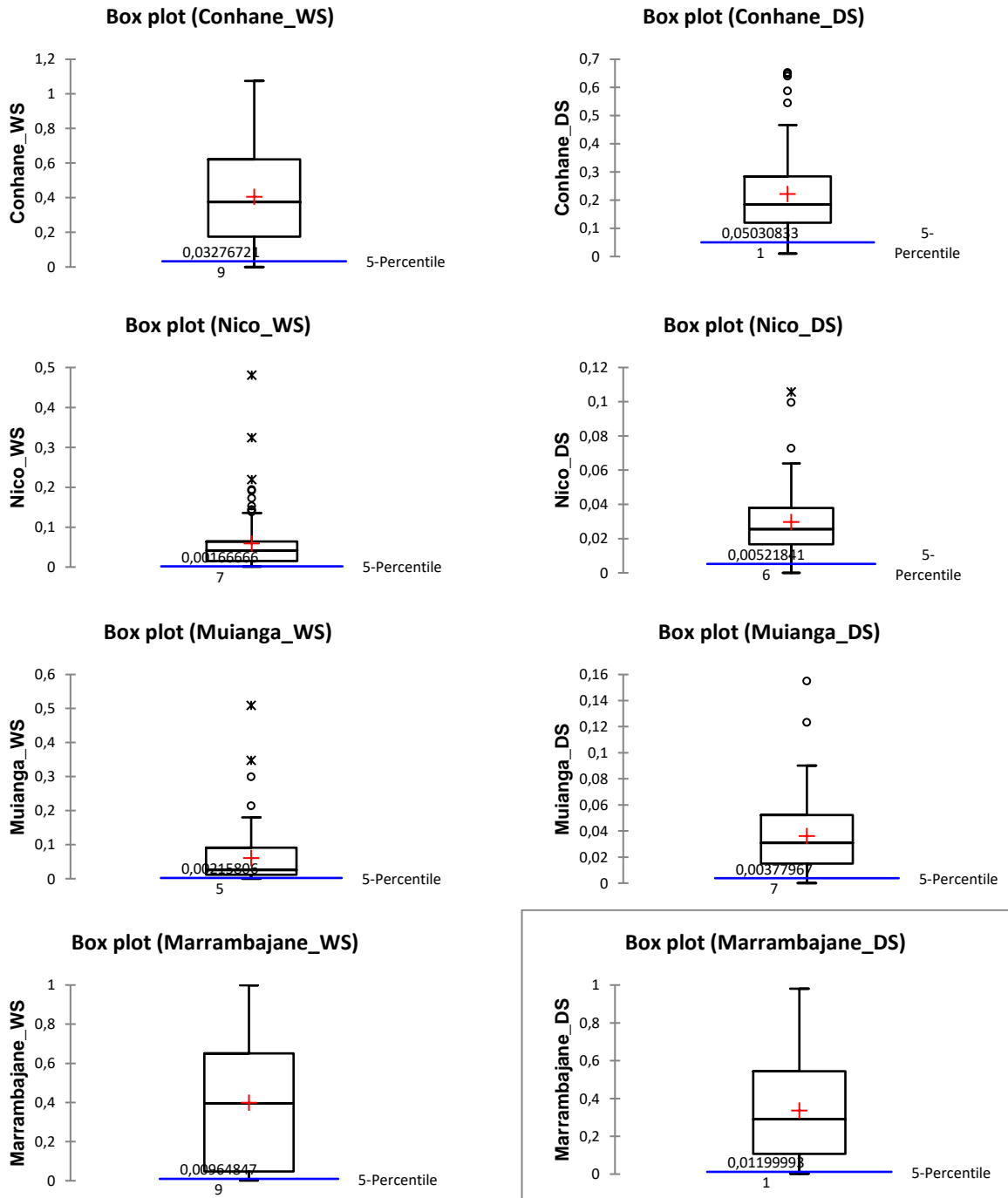
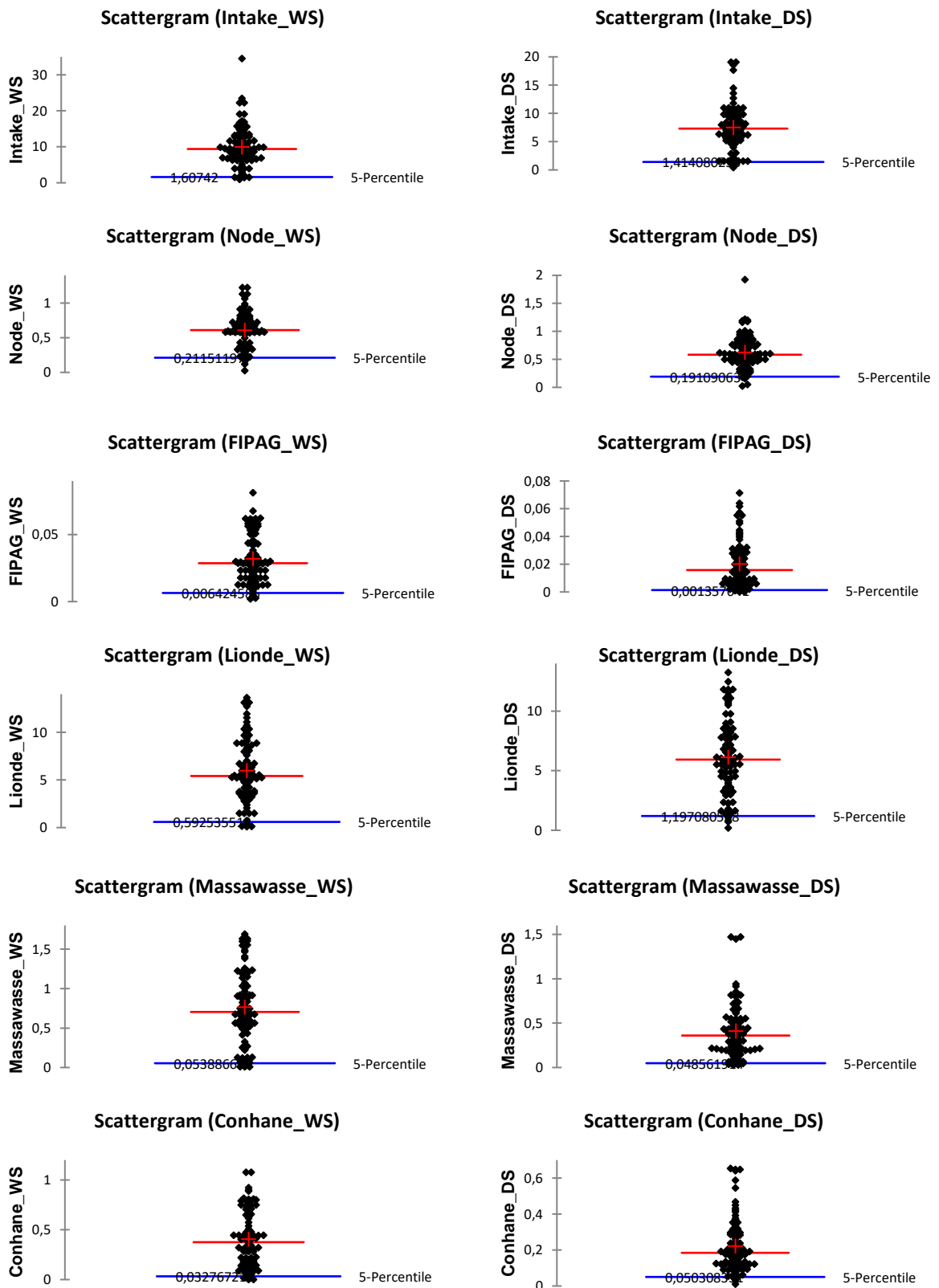


Figure F.1: Boxplots for water discharge dataset.

Scattergrams for water discharge



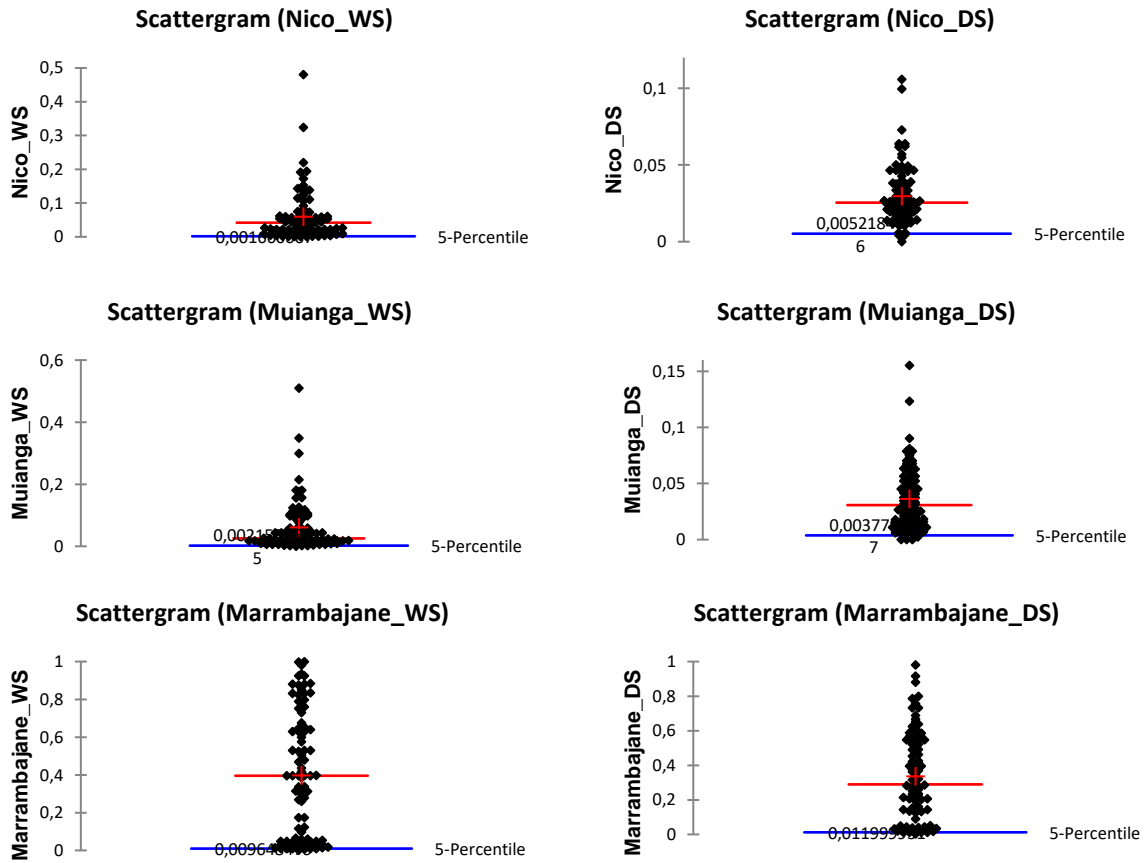


Figure F.2: Scattergrams for water discharge dataset.

Boxplots for sediment discharge

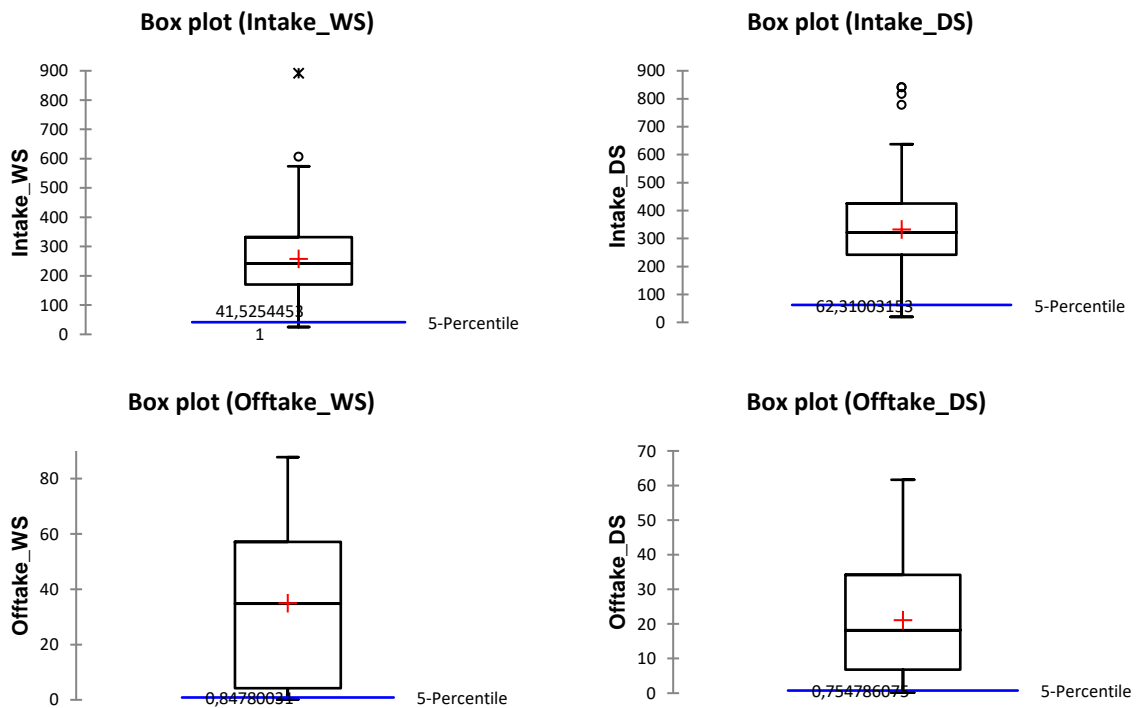


Figure F.3: Boxplots for sediment discharge dataset.

Scatterplots for sediment discharge

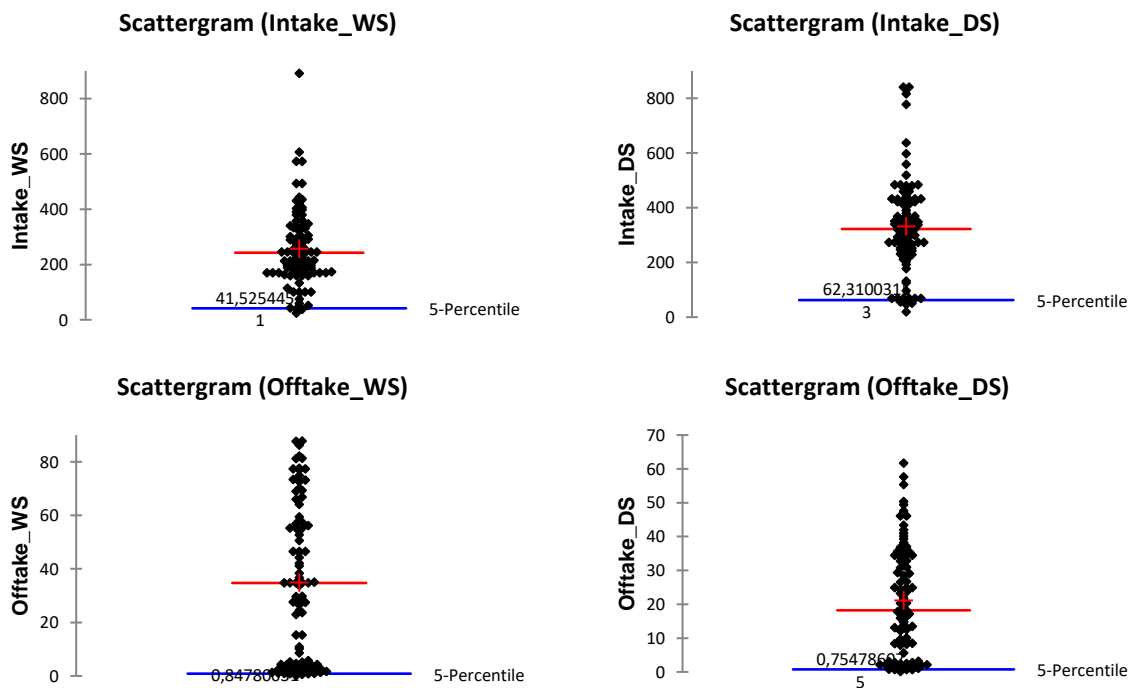


Figure F.4: Scattergrams for sediment discharge dataset.

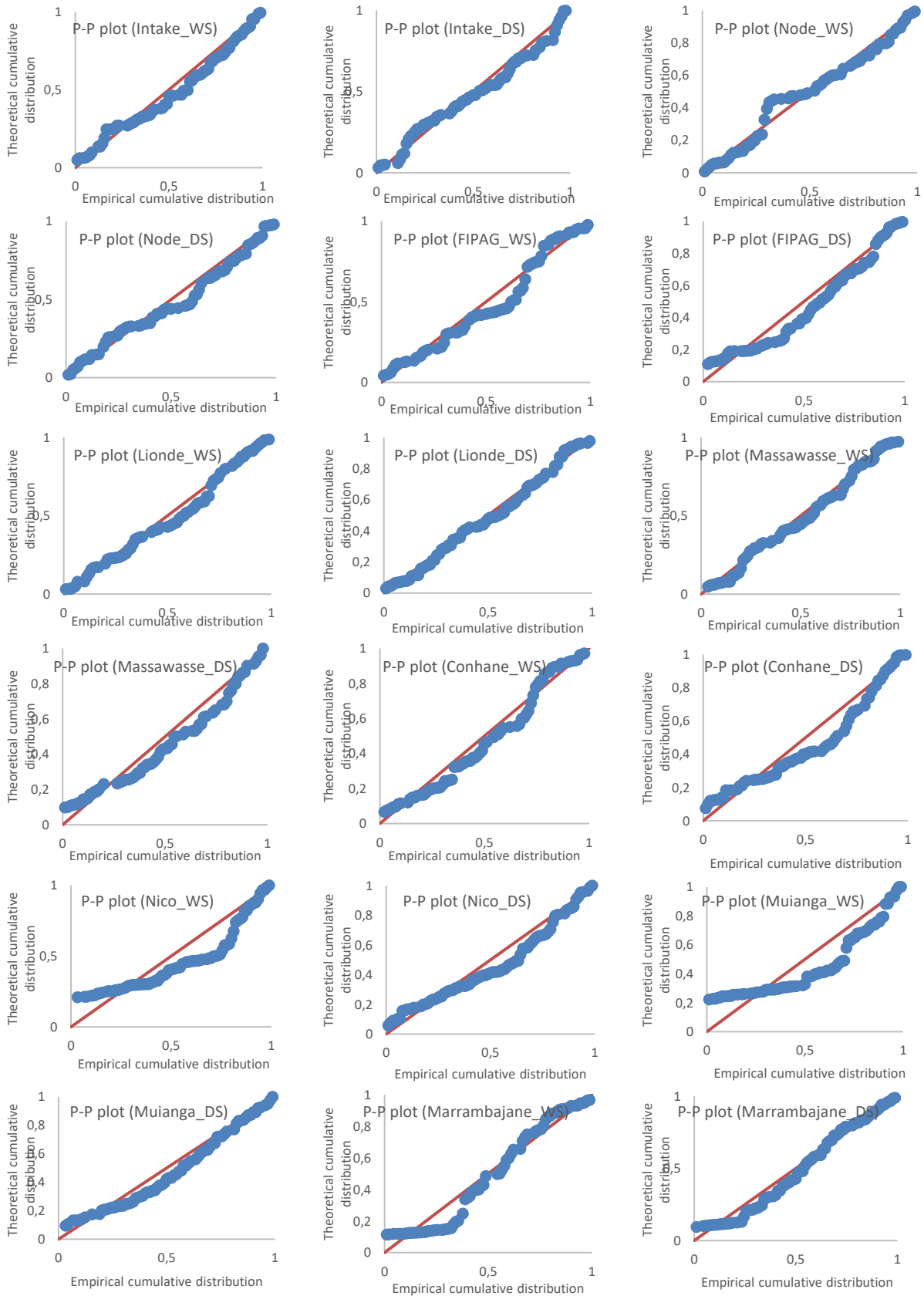


Figure F.5: Normal P-P plots for the water discharge data set.

Normal P-P plots for sediment discharge

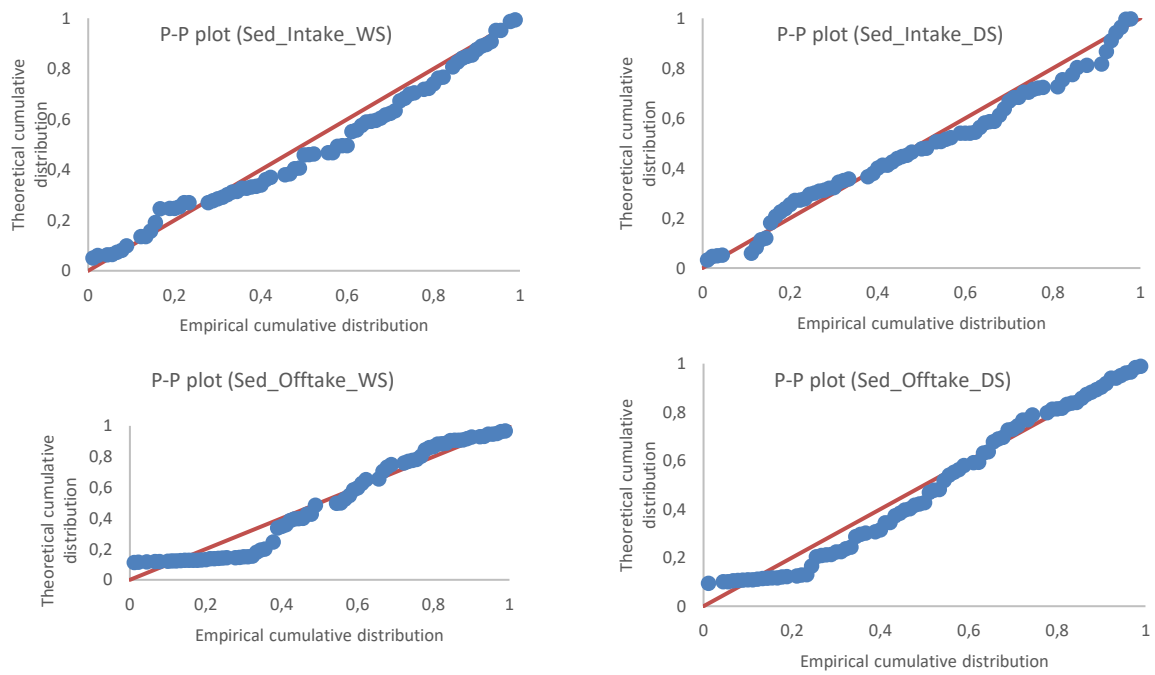


Figure F.6: Normal P-P plots for sediment discharge data set.

G. ARIMA and MANN-KENDALL tests

Table G1: Dickey-Fuller Test for Stationarity Assessment of Water Discharge Dataset Relevant for ARIMA Model

Variable	Minimum	Maximum	Mean	Std. deviation	Tau (Obs. Value)	Tau (Crit. Value)	p-value	alpha	Observation
Intake_WS	970.978	34535.081	10010.585	5517.649	-2.288	-3.409	0.417	0.05	Serie is Not Stationary
Intake_DS	444.573	19080.549	7552.784	3876.104	-3.053	-3.409	0.113	0.05	Serie is Not Stationary
Node_WS	24.194	1223.260	603.749	247.331	-4.303	-3.409	0.004	0.05	Serie is Stationary
Node_DS	23.250	1925.340	625.056	291.639	-3.855	-3.409	0.016	0.05	Serie is Stationary
FIPAG_WS	1.935	81.154	32.004	17.721	-3.286	-3.409	0.067	0.05	Serie is Not Stationary
FIPAG_DS	0.000	71.309	20.169	16.582	-1.802	-3.409	0.681	0.05	Serie is Not Stationary
Lionde_WS	116.976	13637.708	6047.020	3158.961	-3.752	-3.409	0.021	0.05	Serie is Stationary
Lionde_DS	193.692	13255.000	6159.642	3181.423	-3.092	-3.409	0.104	0.05	Serie is Not Stationary
Massawasse_WS	10.845	1690.010	772.036	451.413	-3.092	-3.409	0.104	0.05	Serie is Not Stationary
Massawasse_DS	26.597	1470.257	407.927	301.142	-2.587	-3.409	0.268	0.05	Serie is Not Stationary
Conhane_WS	0.000	1074.922	408.729	272.897	-3.388	-3.409	0.053	0.05	Serie is Not Stationary
Conhane_DS	10.267	653.000	217.651	144.372	-1.461	-3.409	0.819	0.05	Serie is Not Stationary
Nico_WS	0.968	480.844	58.683	72.815	-3.162	-3.409	0.089	0.05	Serie is Not Stationary
Nico_DS	0.000	105.784	29.919	19.034	-3.020	-3.409	0.121	0.05	Serie is Not Stationary
Muianga_WS	0.000	509.104	59.987	80.077	-4.103	-3.409	0.008	0.05	Serie is Stationary
Muianga_DS	0.000	155.037	36.116	27.704	-4.588	-3.409	0.001	0.05	Serie is Stationary
Marrambajane_WS	1.527	998.759	393.470	328.281	-3.117	-3.409	0.099	0.05	Serie is Not Stationary
Marrambajane_DS	2.291	980.485	335.683	256.894	-3.403	-3.409	0.051	0.05	Serie is Not Stationary

WS=Wet season

DS=Dry season

Table G2: Adopted Structure and Parameters of ARIMA Model for Water Discharge at CIS Based on AIC

Variable	Model Identification	Model Structure		AIC
		AR (<i>p</i>)	MA (<i>q</i>)	
Intake_WS	ARIMA (3,1,5)	-0.373; 0.067; -0.065	-0.456; 0.095; -0.168; -0.185; 0.043	508.509
Intake_DS	ARIMA (2,1,3)	-0.080; 0.239	-0.424; -0.455; -0.048	431.226
Node_WS	ARMA (2,0,2)	0.371; 0.529	0.268; -0.086	16.582
Node_DS	ARMA (1,0,1)	0.936	-0.538	53.315
FIPAG_WS	ARIMA (2,1,1)	-0.128; -0.082	-0.336	-433.628
FIPAG_DS	ARIMA (1,0,2)	0.990	-0.432; 0.033	-462.863
Lionde_WS	ARMA (1,0,2)	0.987	-0.713; 0.055	424.263
Lionde_DS	ARIMA (2,1,3)	-0.004; 0.205	-0.408; -0.384; -0.094	408.291
Massawasse_WS	ARIMA (2,0,2)	0.469; 0.482	0.080; -0.435	101.235
Massawasse_DS	ARIMA (3,1,3)	-0.821; -0.203; 0.385	0.349; -0.461; -0.667	12.206
Conhane_WS	ARIMA (3,1,0)	-0.433; -0.145; -0.227	0.000	29.828
Conhane_DS	ARIMA (3,2,2)	0.106; -0.282; -0.094	-1.712; 0.718	-79.387
Nico_WS	ARIMA (2,1,1)	-0.109; -0.427	-0.145	-228.627
Nico_DS	ARIMA (1,1,0)	-0.358	0.000	-403.075
Muianga_WS	ARMA (1,0,0)	0.559	0.000	-173.737
Muianga_DS	ARMA (1,0,0)	0.814	0.000	-371.113
Marrambajane_WS	ARIMA (1,0,0)	0.880	0.000	13.145
Marrambajane_DS	ARIMA (1,0,0)	0.894	0.000	-36.484

Test performed at confidence intervals of 95%

Optimization at Likelihood (Convergence = 0.00001 / Iterations = 500)

Table G3: Mann-Kendall Test for Water Discharge Trends for Both Seasons from 2004-2005 to 2018-2019 Period

Sampling station	Season	Data period	Kendall's tau	S	Var (S)	p-value (Two-tailed)	alpha	Sen's slope			Sen's Intercept			Significant Trend	Trend Tendency
								Slope	Lower bound (95%)	Upper bound (95%)	Intercept	Lower bound (95%)	Upper bound (95%)		
Intake	Wet	2004-	0.201	801	292934	0.139	0.05	0.001	0.000	0.002	-33.423	-48.34	-17.76	No	
	Dry	2018	0.238	948	240327	0.053	0.05	0.001	0.000	0.001	-29.701	-38.77	-18.33	No	
Node	Wet	2004-	0.027	107	175056	0.800	0.05	0.000	0.000	0.000	0.404	-2.87	1.05	No	
	Dry	2018	-0.136	-542	124308	0.125	0.05	0.000	0.000	0.000	1.868	1.226	2.638	No	
FIPAG	Wet	2004-	-0.022	-89	138757	0.813	0.05	0.000	0.000	0.000	0.045	0.005	0.093	No	
	Dry	2018	0.105	419	257889	0.410	0.05	0.000	0.000	0.000	-0.045	-0.083	-0.003	No	
Lionde	Wet	2004-	0.236	944	220382	0.045	0.05	0.001	0.000	0.001	-26.340	-34.92	-17.473	Yes	Increasing
	Dry	2018	0.217	869	246839	0.081	0.05	0.001	0.000	0.001	-25.726	-32.99	-15.914	No	
Massawasse	Wet	2004-	0.089	355	180426	0.405	0.05	0.000	0.000	0.000	-0.906	-2.41	0.425	No	
	Dry	2018	0.227	907	197864	0.042	0.05	0.000	0.000	0.000	-1.759	-2.40	-1.116	Yes	Increasing
Conhane	Wet	2004-	0.064	254	137904	0.496	0.05	0.000	0.000	0.000	-0.343	-1.153	0.376	No	
	Dry	2018	0.126	502	168236	0.222	0.05	0.000	0.000	0.000	-0.403	-0.775	-0.075	No	
Nico	Wet	2004-	-0.290	-1161	397295	0.066	0.05	0.000	0.000	0.000	0.516	0.393	0.665	No	
	Dry	2018	0.084	336	99476	0.288	0.05	0.000	0.000	0.000	-0.019	-0.064	0.021	No	
Muianga	Wet	2004-	-0.219	-877	181831	0.040	0.05	0.000	0.000	0.000	0.446	0.285	0.621	Yes	Decreasing
	Dry	2018	-0.170	-681	161245	0.090	0.05	0.000	0.000	0.000	0.206	0.134	0.266	No	
Marrambajane	Wet	2004-	-0.388	-1549	579754	0.042	0.05	0.000	0.000	0.000	4.367	3.732	5.202	Yes	Decreasing
	Dry	2018	-0.486	-1946	1056049	0.058	0.05	0.000	0.000	0.000	4.626	4.091	5.133	No	

* The hydrologic year in Mozambique starts in September/October at the second semester of the year and ends up in August/September of following year. Therefore, where 2004 is stated, this means that the hydrologic year is 2004-2005, and 2018-2019.

**Test interpretation:

Null hypothesis (H_0): There is no trend in the series; Alternative hypothesis (H_a): There is a trend in the series.

When the computed p-value is *greater* than the significance level $\alpha=0.05$, one cannot reject the null hypothesis H_0 . And when the computed p-value is *lower* than the significance level $\alpha=0.05$, one should reject the null hypothesis H_0 , and accept the alternative hypothesis H_a .

Table G4: Mann-Kendall Test for Sediment Disch. Trend at Intake and Offtake for Both Seasons for the 2004-2005 to 2018-2019 Period

Sampling station	Season	Data period	Mann-Kendall's tau	S	Var (S)	p-value (Two-tailed)	alpha	Sen's slope			Sen's Intercept			Significant Trend	Trend Tendency
								Slope	Lower bound (95%)	Upper bound (95%)	Intercept	Lower bound (95%)	Upper bound (95%)		
Intake	Wet	2004-2018	0.201	801	293	0.139	0.05	0.027	0.007	0.046	-863	-1249	-459	No	Increasing
	Dry		0.238	948	240	0.053	0.05	0.041	0.016	0.061	-1309	-1708	-808	No	Increasing
Offtake	Wet	2004-2018	-0.388	-1549	580	0.042	0.05	-0.009	-0.012	-0.006	383	328	457	Yes	Decreasing
	Dry		-0.496	-1939	1056	0.058	0.05	-0.007	-0.008	-0.005	291	257	322	No	

* The hydrologic year in Mozambique starts in September/October at the second semester of the year and ends up in August/September of following year. Therefore, where 2004 is stated, this means that the hydrologic year is 2004-2005, and 2018-2019.

**Test interpretation:

Null hypothesis (H_0): There is no trend in the series;

Alternative hypothesis (H_a): There is a trend in the series.

When the computed p-value is *greater* than the significance level $\alpha=0.05$, one cannot reject the null hypothesis H_0 . And when the computed p-value is *lower* than the significance level $\alpha=0.05$, one should reject the null hypothesis H_0 , and accept the alternative hypothesis H_a .

H. Scenarios Formulation for Sediment Deposition in CIS

Table H.1: Performance criteria for sediment scenarios of Ackers and White method-all 3 reaches

Models	Season	Series	Training											Validation					
			R ²	Adj. R ²	MSE	RMSE	MAPE	DW	Cp	AIC	SBC	PC	Press	Q ²	R ²	MSE	RMSE	MAPE	Q ²
Ackers-White (3 R)	DS	Actual	0,997	0,997	0,000	0,000	0,599	0,162	2,000	-303,491	-301,602	0,004	0,000	0,996	1,000	0,000	0,000	0,591	0,000
		Scenario 1	0,997	0,996	0,000	0,007	0,651	0,163	2,000	-185,905	-184,016	0,004	0,001	0,995	1,000	0,000	0,009	0,640	0,000
		Scenario 2	0,997	0,996	0,000	0,011	0,651	0,163	2,000	-169,621	-167,732	0,004	0,003	0,995	1,000	0,000	0,014	0,640	0,000
	WS	Actual	0,558	0,502	9,062	3,010	2325,050	1,139	2,000	23,810	24,415	0,664			1,000	36,928	6,077	363,654	
		Scenario 1	0,627	0,581	2,733	1,653	848,495	1,090	2,000	11,824	12,429	0,559			1,000	9,645	3,106	183,382	
		Scenario 2	0,758	0,728	1,773	1,332	186,602	0,996	2,000	7,496	8,101	0,363			1,000	5,146	2,268	69,431	

Where: 3 R = all three reaches

Table H.2: Performance criteria for sediment scenarios of Brownlie method-Intake-Lionde reach

Models	Season	Series	Training											Validation					
			R ²	Adj. R ²	MSE	RMSE	MAPE	DW	Cp	AIC	SBC	PC	Press	Q ²	R ²	MSE	RMSE	MAPE	Q ²
Brownlie 1 (Intake-Lionde Reach)	DS	Actual	0,80	0,78	0,69	0,83	11,54	0,41	2,00	-4,49	-2,82	0,26	15,16	0,70	1,00	1,35	1,16	17,91	0,00
		Scenario 1	0,80	0,78	0,14	0,38	11,54	0,41	2,00	-31,17	-29,50	0,26	3,15	0,70	1,00	0,28	0,53	17,91	0,00
		Scenario 2	0,80	0,78	19,81	4,45	11,54	0,41	2,00	52,63	54,30	0,26	436,32	0,70	1,00	38,71	6,22	17,91	0,00
	WS	Actual	0,73	0,71	9,02	3,00	11,96	0,70	2,00	32,64	33,92	0,36			1,00	5,35	2,31	11,82	
		Scenario 1	0,73	0,71	3,58	1,89	11,96	0,70	2,00	19,68	20,95	0,36			1,00	2,12	1,46	11,82	
		Scenario 2	0,73	0,71	2,15	1,47	11,96	0,70	2,00	12,55	13,82	0,36			1,00	1,27	1,13	11,82	

Table H.3: Performance criteria for sediment scenarios of Brownlie method-Lionde-Conhane reach

Models	Season	Series	Training											Validation					
			R ²	Adj. R ²	MSE	RMSE	MAPE	DW	Cp	AIC	SBC	PC	Press	Q ²	R ²	MSE	RMSE	MAPE	Q ²
Brownlie 2 (Lionde-Conhane Reach)	DS	Actual	0,76	0,74	0,91	0,96	11,95	0,38	2,00	0,34	2,01	0,31	19,71	0,65	1,00	0,67	0,82	11,77	0,00
		Scenario 1	0,76	0,74	0,20	0,45	11,95	0,38	2,00	-25,47	-23,80	0,31	4,32	0,65	1,00	0,15	0,38	11,77	0,00
		Scenario 2	0,76	0,74	26,43	5,14	11,95	0,38	2,00	57,54	59,21	0,31	569,95	0,65	1,00	19,28	4,39	11,77	0,00
	WS	Actual	0,84	0,83	1,52	1,23	7,26	0,39	2,00	7,66	8,94	0,21			1,00	10,34	3,22	14,30	
		Scenario 1	0,84	0,83	0,00	0,01	7,26	0,39	2,00	-128,84	-127,56	0,21			1,00	0,00	0,03	14,30	
		Scenario 2	0,84	0,83	0,00	0,03	7,26	0,39	2,00	-99,28	-98,00	0,21			1,00	0,01	0,07	14,30	

Table H.4: Performance criteria for sediment scenarios of Brownlie method-Lionde-Marrambajane reach

Models	Season	Series	Training											Validation					
			R ²	Adj. R ²	MSE	RMSE	MAPE	DW	Cp	AIC	SBC	PC	Press	Q ²	R ²	MSE	RMSE	MAPE	Q ²
Brownlie 3 (Lionde-Marrambajane Reach)	DS	Actual	0,68	0,66	0,38	0,61	10,72	0,80	2,00	-14,70	-13,03	0,40	8,98	0,49	1,00	0,25	0,50	7,52	0,00
		Scenario 1	0,68	0,66	0,08	0,29	10,72	0,80	2,00	-40,78	-39,12	0,40	1,94	0,49	1,00	0,05	0,23	7,52	0,00
		Scenario 2	0,68	0,66	13,35	3,65	10,72	0,80	2,00	45,93	47,60	0,40	317,95	0,49	1,00	8,70	2,95	7,52	0,00
	WS	Actual	0,85	0,84	1,47	1,21	7,58	0,37	2,00	7,25	8,53	0,20			1,00	10,29	3,21	14,22	
		Scenario 1	0,85	0,84	0,00	0,01	7,58	0,37	2,00	-129,24	-127,97	0,20			1,00	0,00	0,02	14,22	
		Scenario 2	0,85	0,84	0,00	0,01	7,58	0,37	2,00	-141,99	-140,71	0,20			1,00	0,00	0,02	14,22	

Table H.5: Performance criteria for sediment scenarios of Van Rijn method-all 3 reaches

Models	Season	Series	Training											Validation					
			R ²	Adj. R ²	MSE	RMSE	MAPE	DW	Cp	AIC	SBC	PC	Press	Q ²	R ²	MSE	RMSE	MAPE	Q ²
Van Rijn (All Reaches)	DS	Actual	0,43	0,41	0,81	0,90	63,22	0,66	2,00	-3,70	-1,18	0,66	26,07	0,23	1,00	0,96	0,98	97,82	0,00
		Scenario 3	0,43	0,41	20340,32	142,62	61,92	0,66	2,00	259,85	262,36	0,66	658037,38	0,24					
	WS	Actual	0,53	0,51	0,00	0,00	48,14	0,53	2,00	-262,59	-260,32	0,55			1,00	0,00	0,01	42,59	
		Scenario 3	0,54	0,51	0,03	0,18	46,43	0,53	2,00	-77,33	-75,06	0,55			1,00	0,45	0,67	41,34	

Table H.6: Performance criteria for sediment scenarios of Engelund-Hansen method-Intake-Lionde reach

Models	Season	Series	Training											Validation					
			R ²	Adj. R ²	MSE	RMSE	MAPE	DW	Cp	AIC	SBC	PC	Press	Q ²	R ²	MSE	RMSE	MAPE	Q ²
Engelund-Hansen 1 (Intake-Lionde Reach)	DS	Actual	0,98	0,98	0,01	0,11	41,50	0,09	2,00	-107,11	-104,67	0,02	0,37	0,98	1,00	0,01	0,08	5,21	0,00
		Scenario 1	0,98	0,98	0,00	0,03	41,50	0,09	2,00	-166,04	-163,61	0,02	0,03	0,98	1,00	0,00	0,02	5,21	0,00
		Scenario 2	0,98	0,98	0,00	0,04	41,50	0,09	2,00	-153,86	-151,42	0,02	0,06	0,98	1,00	0,00	0,03	5,21	0,00
		Scenario 3	0,98	0,98	0,00	0,03	41,50	0,09	2,00	-172,38	-169,94	0,02	0,03	0,98	1,00	0,00	0,02	5,21	0,00
	WS	Actual	0,98	0,98	0,11	0,33	41,87	0,18	2,00	-47,47	-45,29	0,02			1,00	0,13	0,35	30,13	
		Scenario 1	0,98	0,98	0,37	0,61	41,87	0,18	2,00	-19,94	-17,75	0,02			1,00	0,44	0,66	30,13	
		Scenario 2	0,98	0,98	0,31	0,56	41,87	0,18	2,00	-23,78	-21,60	0,02			1,00	0,37	0,61	30,13	
		Scenario 3	0,98	0,98	0,15	0,39	41,87	0,18	2,00	-40,07	-37,89	0,02			1,00	0,18	0,42	30,13	

Table H.7: Performance criteria for sediment scenarios of Engelund-Hansen method-Lionde-Conhane reach

Models	Season	Series	Training											Validation					
			R ²	Adj. R ²	MSE	RMSE	MAPE	DW	Cp	AIC	SBC	PC	Press	Q ²	R ²	MSE	RMSE	MAPE	Q ²
Engelund-Hansen 2 (Lionde-Conhane Reach)	DS	Actual	0,99	0,98	0,00	0,04	39,40	0,09	2,00	-162,54	-160,11	0,02	0,04	0,98	1,00	0,00	0,05	6,53	0,00
		Scenario 1	0,99	0,98	0,00	0,03	39,40	0,09	2,00	-178,97	-176,53	0,02	0,02	0,98	1,00	0,00	0,04	6,53	0,00
		Scenario 2	0,99	0,98	0,00	0,05	39,40	0,09	2,00	-150,36	-147,92	0,02	0,06	0,98	1,00	0,00	0,07	6,53	0,00
		Scenario 3	0,99	0,98	0,00	0,03	39,40	0,09	2,00	-166,79	-164,35	0,02	0,03	0,98	1,00	0,00	0,05	6,53	0,00
	WS	Actual	0,98	0,98	0,13	0,36	35,07	0,20	2,00	-43,11	-40,93	0,02			1,00	0,22	0,47	49,60	
		Scenario 1	0,98	0,98	0,45	0,67	35,07	0,20	2,00	-15,58	-13,40	0,02			1,00	0,77	0,88	49,60	
		Scenario 2	0,98	0,98	0,38	0,62	35,07	0,20	2,00	-19,42	-17,24	0,02			1,00	0,65	0,80	49,60	
		Scenario 3	0,98	0,98	0,20	0,44	35,07	0,20	2,00	-33,88	-31,70	0,02			1,00	0,34	0,58	49,60	

Table H.8: Performance criteria for sediment scenarios of Engelund-Hansen method-Lionde-Marrambajane reach

Models	Season	Series	Training											Validation					
			R ²	Adj. R ²	MSE	RMSE	MAPE	DW	Cp	AIC	SBC	PC	Press	Q ²	R ²	MSE	RMSE	MAPE	Q ²
Engelund-Hansen 3 (Lionde-Marrambajane Reach)	DS	Actual	0,98	0,98	0,00	0,06	37,87	0,12	2,00	-135,81	-133,37	0,02	0,12	0,98	1,00	0,01	0,09	6,69	0,00
		Scenario 1	0,98	0,98	0,00	0,02	37,87	0,12	2,00	-196,43	-194,00	0,02	0,01	0,98	1,00	0,00	0,03	6,69	0,00
		Scenario 2	0,98	0,98	0,00	0,02	37,87	0,12	2,00	-184,25	-181,82	0,02	0,02	0,98	1,00	0,00	0,04	6,69	0,00
		Scenario 3	0,98	0,98	0,00	0,01	37,87	0,12	2,00	-212,36	-209,92	0,02	0,01	0,98	1,00	0,00	0,02	6,69	0,00
	WS	Actual	0,98	0,98	0,03	0,18	39,95	0,13	2,00	-73,46	-71,28	0,02			1,00	0,06	0,25	7,95	
		Scenario 1	0,98	0,98	0,11	0,34	39,95	0,13	2,00	-45,93	-43,75	0,02			1,00	0,22	0,47	7,95	
		Scenario 2	0,98	0,98	0,10	0,31	39,95	0,13	2,00	-49,77	-47,59	0,02			1,00	0,18	0,43	7,95	
		Scenario 3	0,98	0,98	0,03	0,18	39,95	0,13	2,00	-74,50	-72,32	0,02			1,00	0,06	0,24	7,95	

Table H.9: Performance criteria for sediment scenarios of Van Rijn method-all 3 reaches

Models	Season	Series	Training											Validation					
			R ²	Adj. R ²	MSE	RMSE	MAPE	DW	Cp	AIC	SBC	PC	Press	Q ²	R ²	MSE	RMSE	MAPE	Q ²
Yang 1 (Intake-Lionde Reach)	DS	Actual	1,00	1,00	0,00	0,00	0,00					0,00	0,00	1,00	1,00	0,00	0,00	0,00	0,00
		Scenario 1	1,00	1,00	0,00	0,00	0,00					0,00	0,00	1,00	1,00	0,00	0,00	0,00	0,00
		Scenario 2	1,00	1,00	0,00	0,00	0,00					0,00	0,00	1,00	1,00	0,00	0,00	0,00	0,00
	WS	Actual	1,00	1,00	0,00	0,00	0,00					0,00			1,00	0,00	0,00	0,00	
		Scenario 1	1,00	1,00	0,00	0,00	0,00					0,00			1,00	0,00	0,00	0,00	
		Scenario 2	1,00	1,00	0,00	0,00	0,00					0,00			1,00	0,00	0,00	0,00	

Table H10: Statistics models for Linear Regression simulations

Model	Season	Variables	Goodness of fit statistics														
			Obs.	SW	DF	R ²	Adj.R ²	MSE	RMSE	MAPE	DW	Cp	AIC	SBC	PC	Press	Q ²
Ackers-White	DS	q _s (m ² /s) vs	26	26	24	0.62	0.61	209260	457.5	1329.8	0.16	2.0	320.5	323.0	0.44	6379843	0.52
	WS	y (m)	26	26	24	0.65	0.63	207282	455.3	1350.8	0.13	2.0	320.2	322.7	0.41	6196296	0.56
Brownlie	DS	q _s (ppm) vs	19	19	17	0.77	0.75	1118,3	33.4	11.3	0.36	2,0	135.3	137.1	0.29	26905,9	0.67
	WS	Rh (m)	19	19	17	0.72	0.71	1197,9	34.6	12.0	0.43	2.0	136.6	138.5	0.34	30441,4	0.59
Engelund - Hensen	DS	q _s (m ³ /s.m)	27	27	25	0.98	0.98	0.0	0.1	39.1	0.08	2.0	-115.8	-113.3	0.02	0.4	0.98
	WS	vs y (m)	27	27	25	0.99	0.99	0.0	0.1	21.6	0.09	2.0	-122.6	-120.0	0.02	0.3	0.98
Van Rijn ₁	DS	u* (m/s) vs	28	28	26	0.75	0.74	0.0	0.0	6.6	0.21	2.0	-271.1	-268.4	0.28	0.0	0.69
	WS	y (m)	28	28	26	0.74	0.73	0.0	0.0	7.0	0.21	2.0	-269.8	-267.1	0.30	0.0	0.67
Van Rijn ₂	DS	q _b (m ² /s) vs	28	28	26	0.47	0.45	0.8	0.9	67.9	0.37	2.0	-3.9	-1.2	0.61	27.0	0.33
	WS	y (m)	28	28	26	0.48	0.46	0.8	0.9	76.5	0.38	2.0	-3.9	-1.2	0.60	27.6	0.32
Van Rijn ₃	DS	q _b (m ² /s) vs	21	21	19	0.93	0.92	0.0	0.2	22.1	0.70	2.0	-65.9	-63.9	0.09	1.8	0.83
	WS	u* (m/s)	21	21	19	0.94	0.94	0.0	0.2	19.9	0.44	2.0	-67.2	-65.1	0.06	1.3	0.90
Yang	DS	q _s (ton/sm)	8	8	6	1.00	1.00	0.0	0.0	0.0	-	-	-	-	0.00	0.0	1.00
	WS	vs y (m)	8	8	6	1.00	1.00	0.0	0.0	0.0	-	-	-	-	0.00	0.0	1.00

Where: Obs=observations; SW=Sum of weights; DF=degree of freedom; R²=coefficient of determination; Adj.R²=adjusted coefficient of determination; MSE=Mean Square Error; RMSE=Root Mean-Square Error; MAPE = Mean Absolute Percentage Error; DW=Durbin-Watson statistic; Cp=Mallows coefficient; AIC=Akaike's Information Criterion; SBC=Schwarz's Bayesian Criterion; PC=Amemiyas's Prediction Criterion; Press= Prediction error sum of squares; Q²= the fraction of total variation of dependent variables that can be predicted by a component; y=water depth (m); q_{s (AW)} =Total sediment transport per unit width (m²/s); q_{s (BRO)} =Total sediment discharge (ppm); q_{s (EH)} =Total sediment discharge (m³/s.m); q_{b (VR)} =Bed load transport (m²/s); u*= Critical bed shear velocity related to grains (m/s); q_{s (YAN)} =Total load transport (m²/s); and vs=versus or plotted against.

I. The Main Assumptions for the Scenarios Applications

For the best scenarios application, there were considered some assumptions such as that: the inflowing sediment characteristics (size and concentration) were kept constant for simulations and non-erosion conditions in the initial bottom level was allowed or considered. Previously sediment deposit was the sole aspect taken into consideration that could be entrained during simulations; the side slopes were stable and not erodible; conditions of the initial roughness of the canal(s) were explained by a single roughness on the wetted perimeter; weed infestation was only taken into account for roughness parameter; roughness conditions of variations in time could be observed due to variations of the inflows, occurrence of bed forms on the bottom and obstruction by weed infestation (in case of its occurrence); the water level at the downstream-end of the main canal was kept constant; the water level at the downstream-end of internal reaches was governed by the hydraulic conditions either by a flow control structure or by the water level of the downstream reach; the sediment transport capacity of the water flow and the actual sediment load were referred to in terms of equilibrium concentration and actual concentration of sediment respectively. The concentration is expressed in ppm (parts per million) as the weight of sediment per unit volume of the water-sediment mixture.

J: ARIMA's ACF, PACF, ACFR and PACFR and PACFR

Intake Station

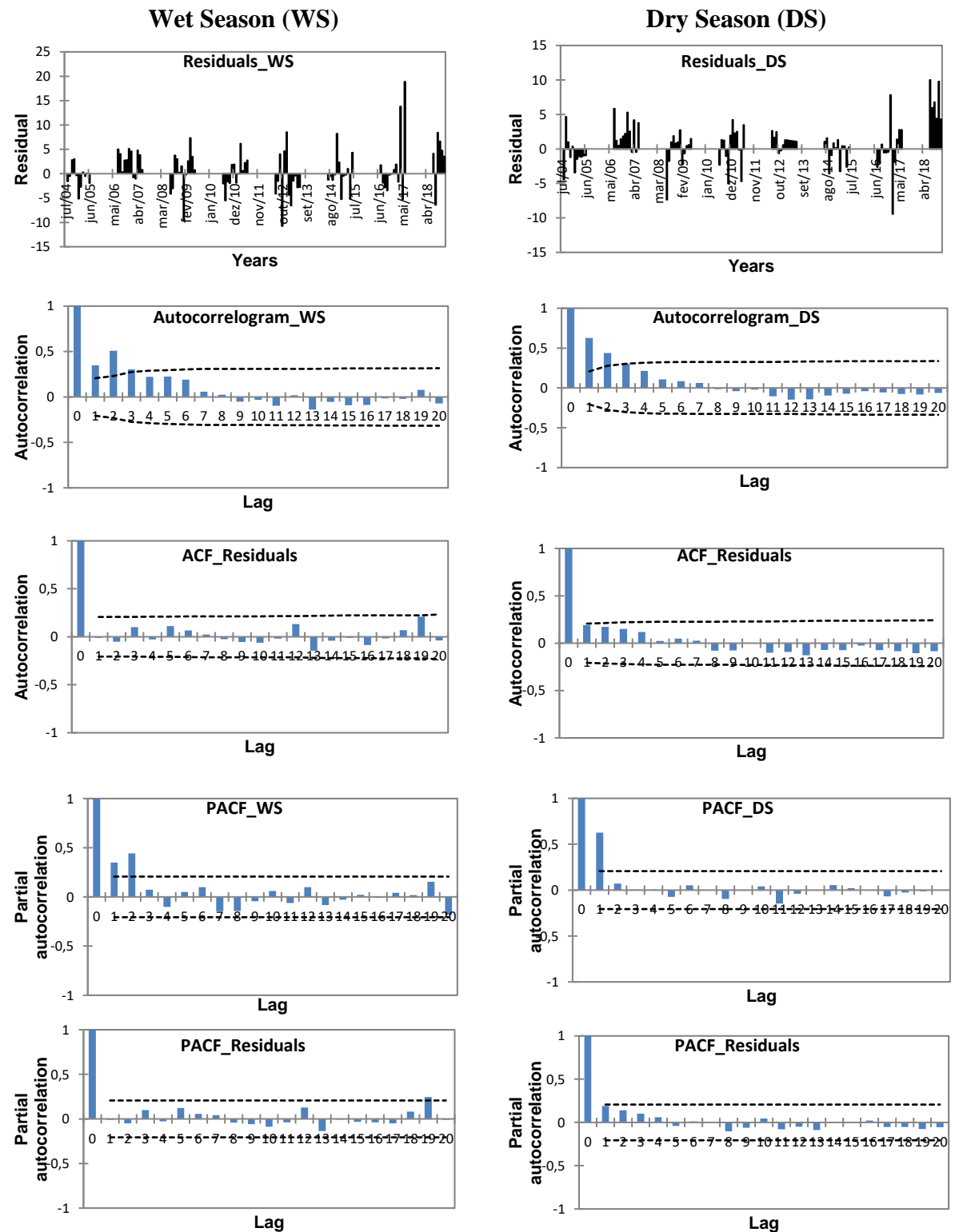


Figure J.1: ACF, PACF, ACFR and PACFR for the Intake station for DS and WS.

Node Station

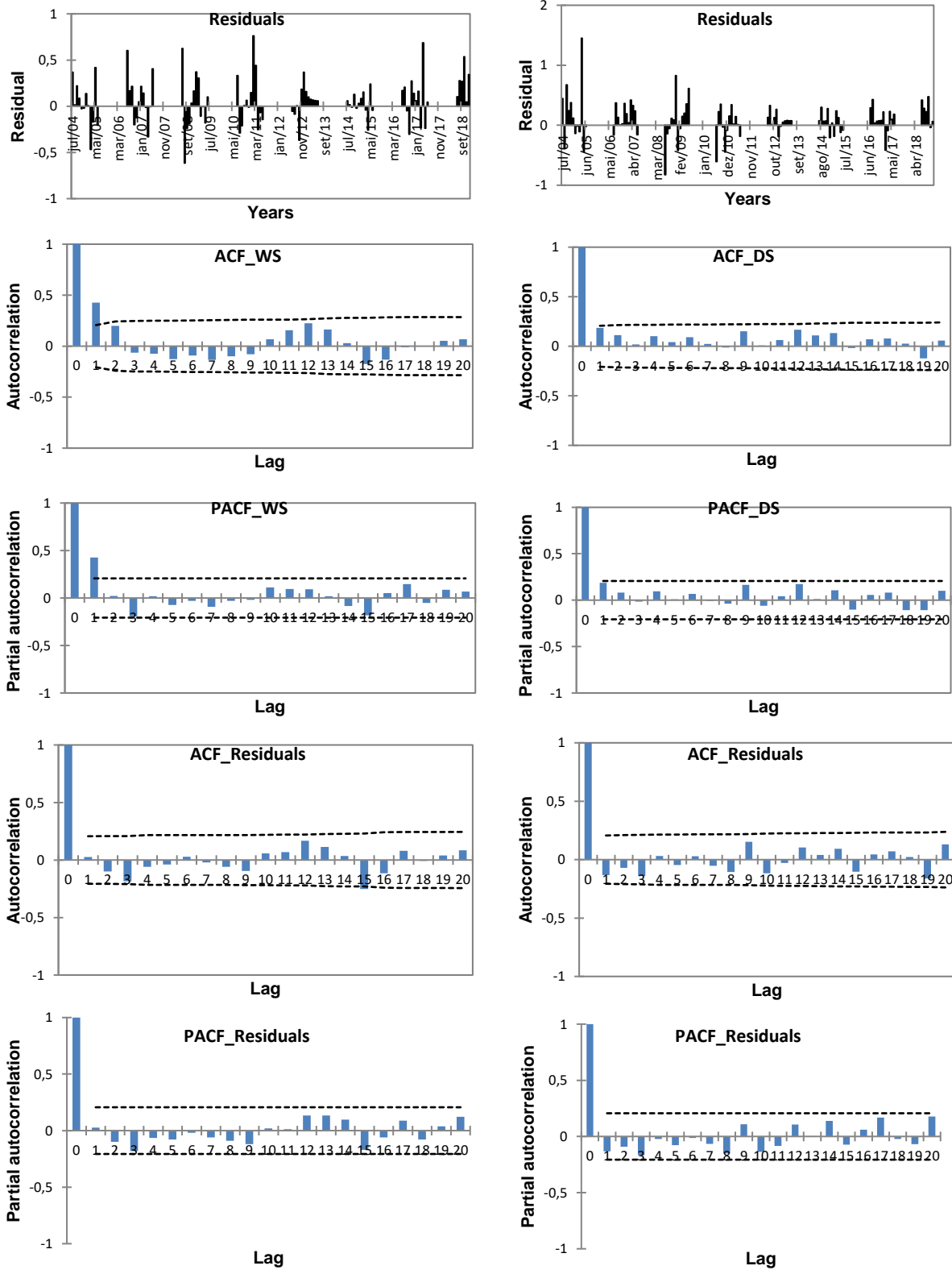


Figure J.2: ACF, PACF, ACFR and PACFR for the Node station for DS and WS.

FIPAG Station

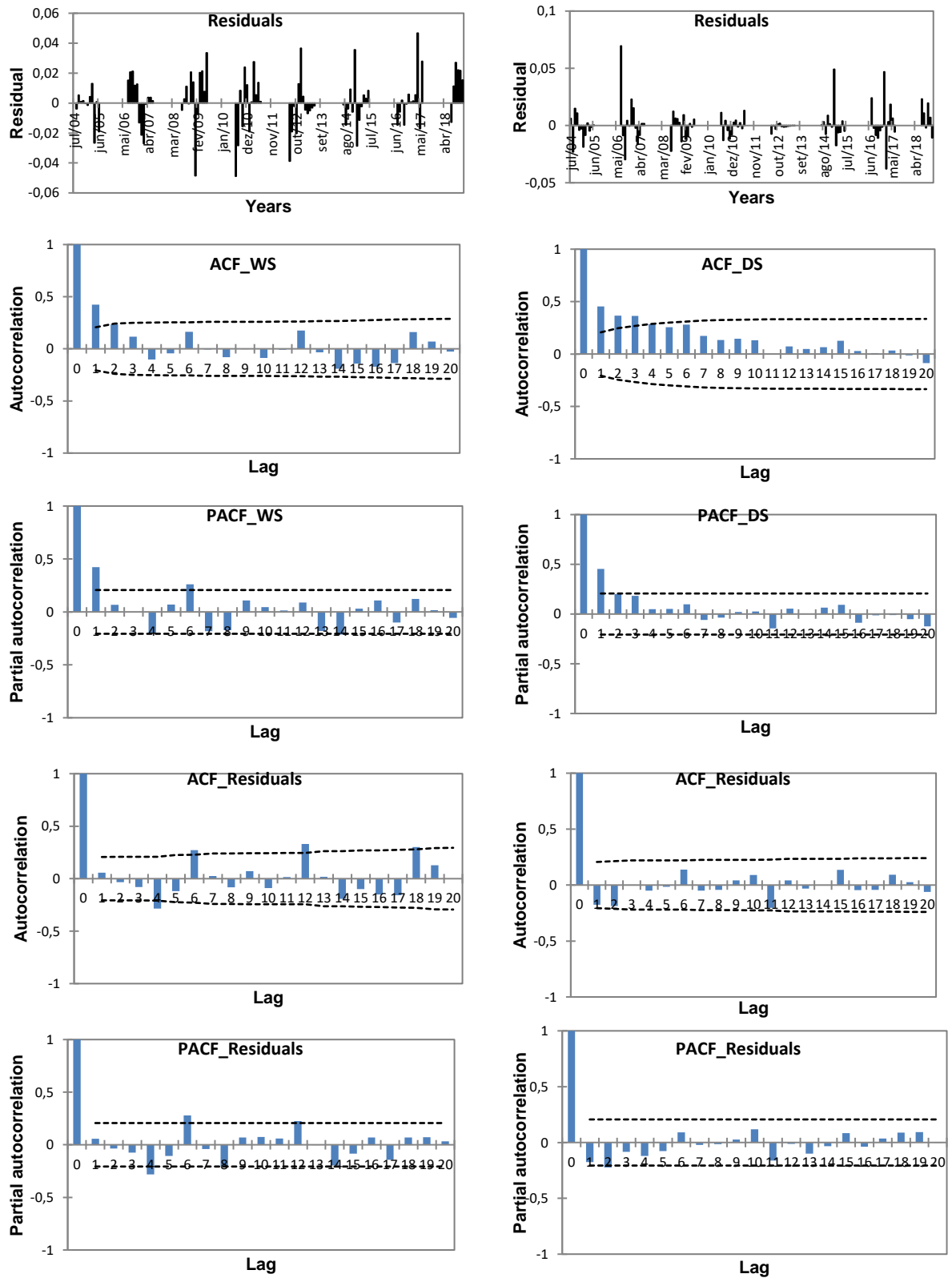


Figure J.3: ACF, PACF, ACFR and PACFR for the FIPAG station for DS and WS.

Lionde Station

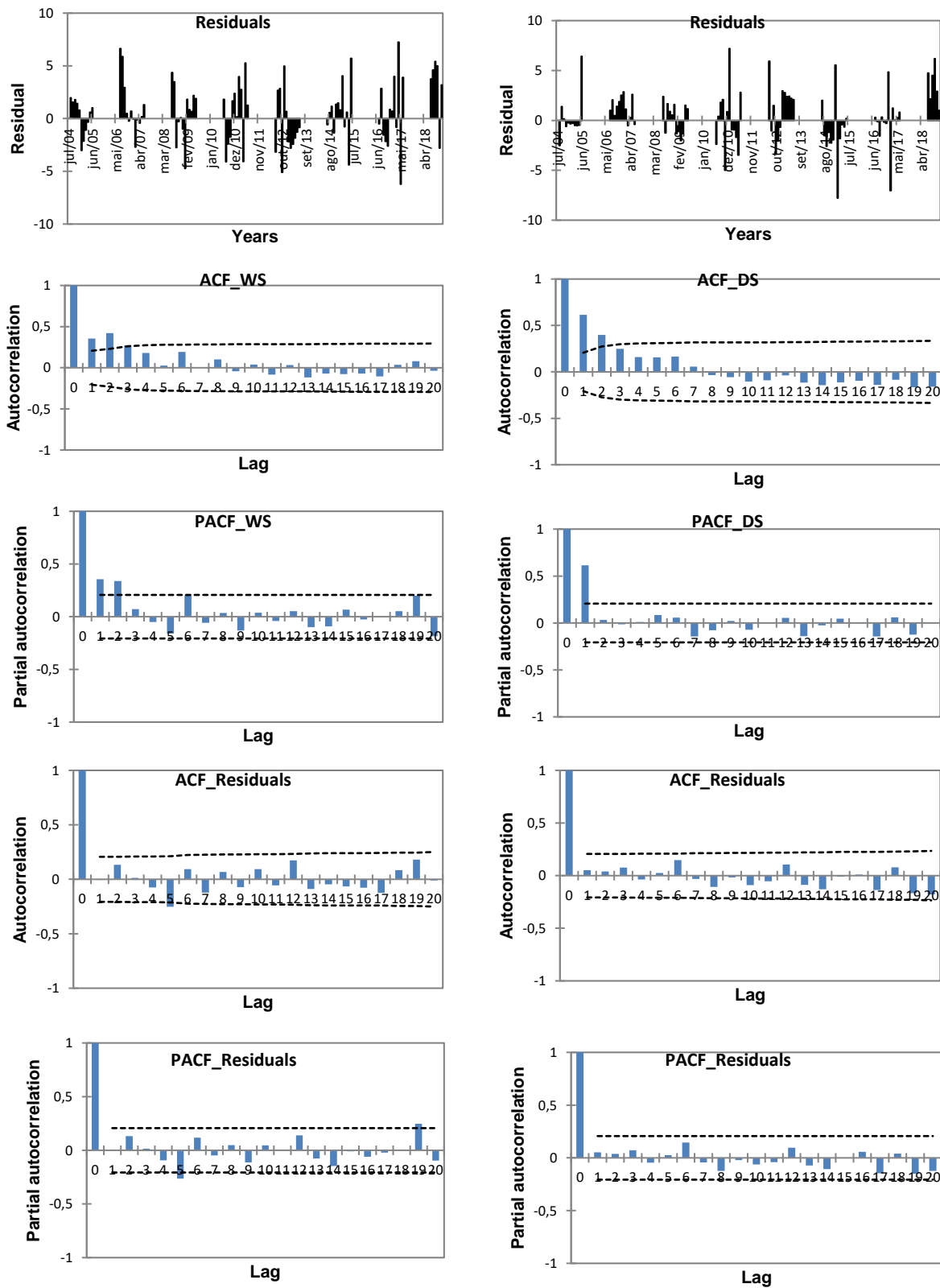


Figure J.4: ACF, PACF, ACFR and PACFR for the Lionde station for DS and WS.

Massawasse Station

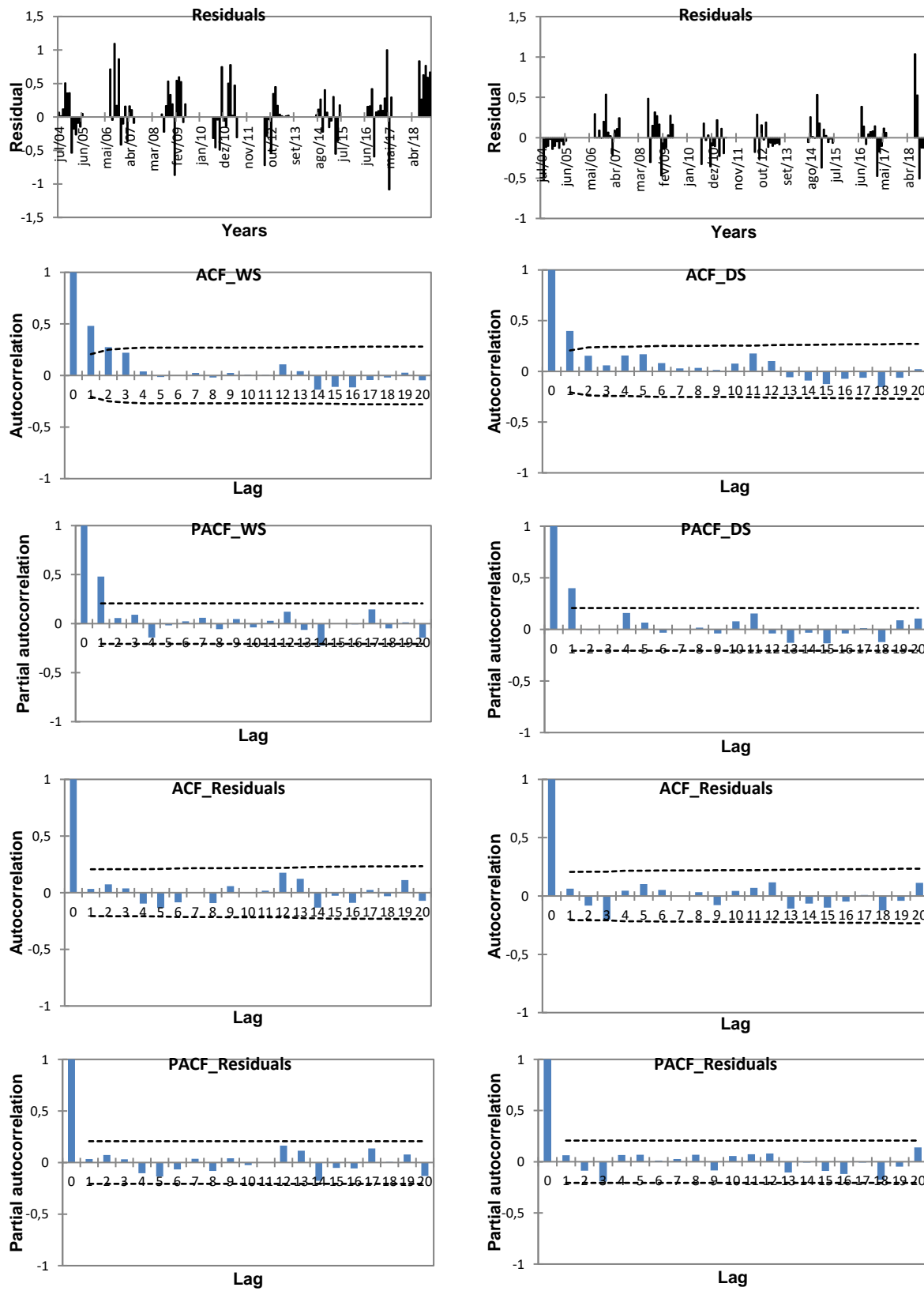


Figure J.5: ACF, PACF, ACFR and PACFR for the Massawasse station for DS and WS.

Conhane Station

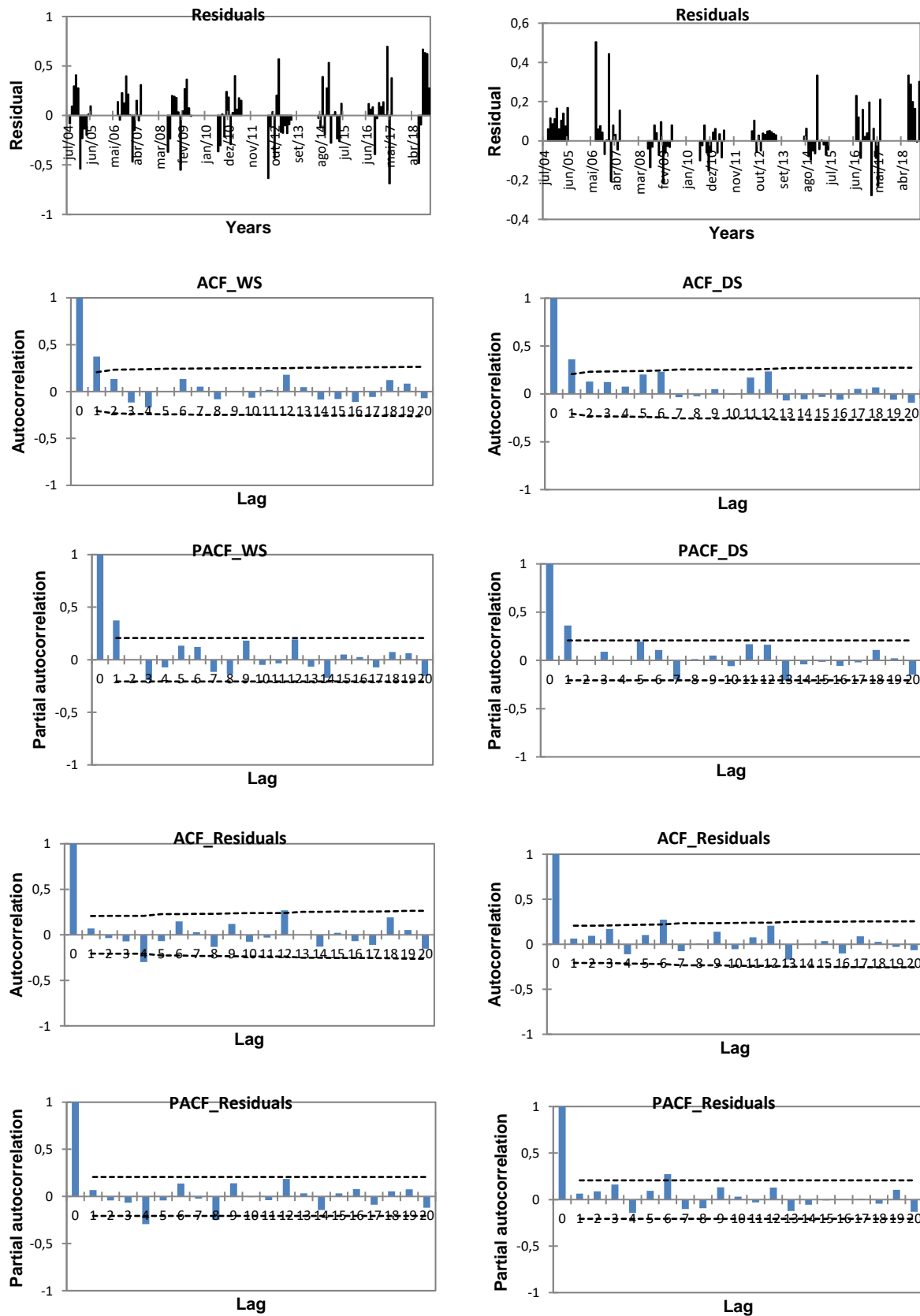


Figure J.6: ACF, PACF, ACFR and PACFR for the Conhane station for DS and WS.

Nico Station

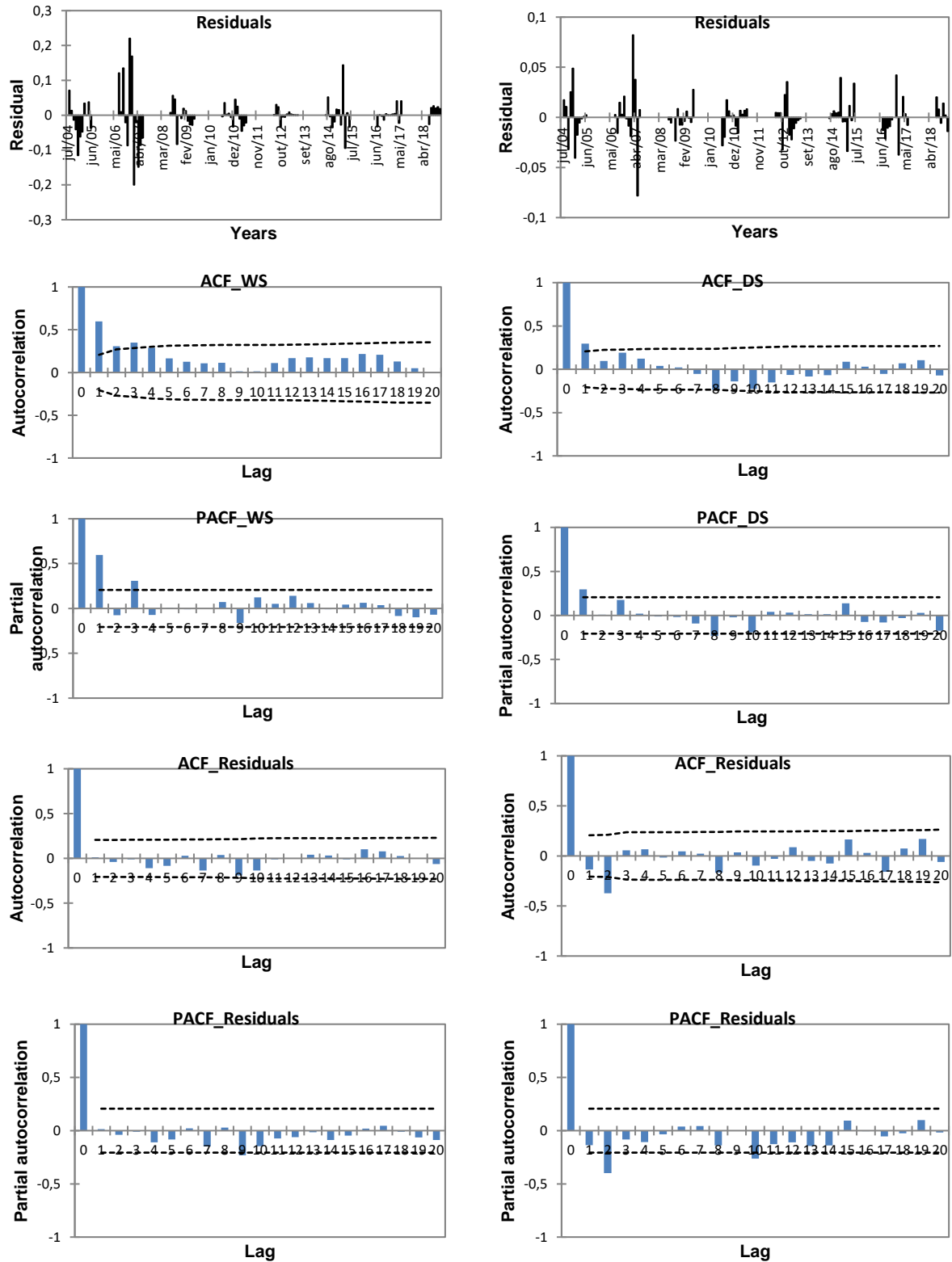


Figure J.7: ACF, PACF, ACFR and PACFR for the Nico station for DS and WS.

Muianga Station

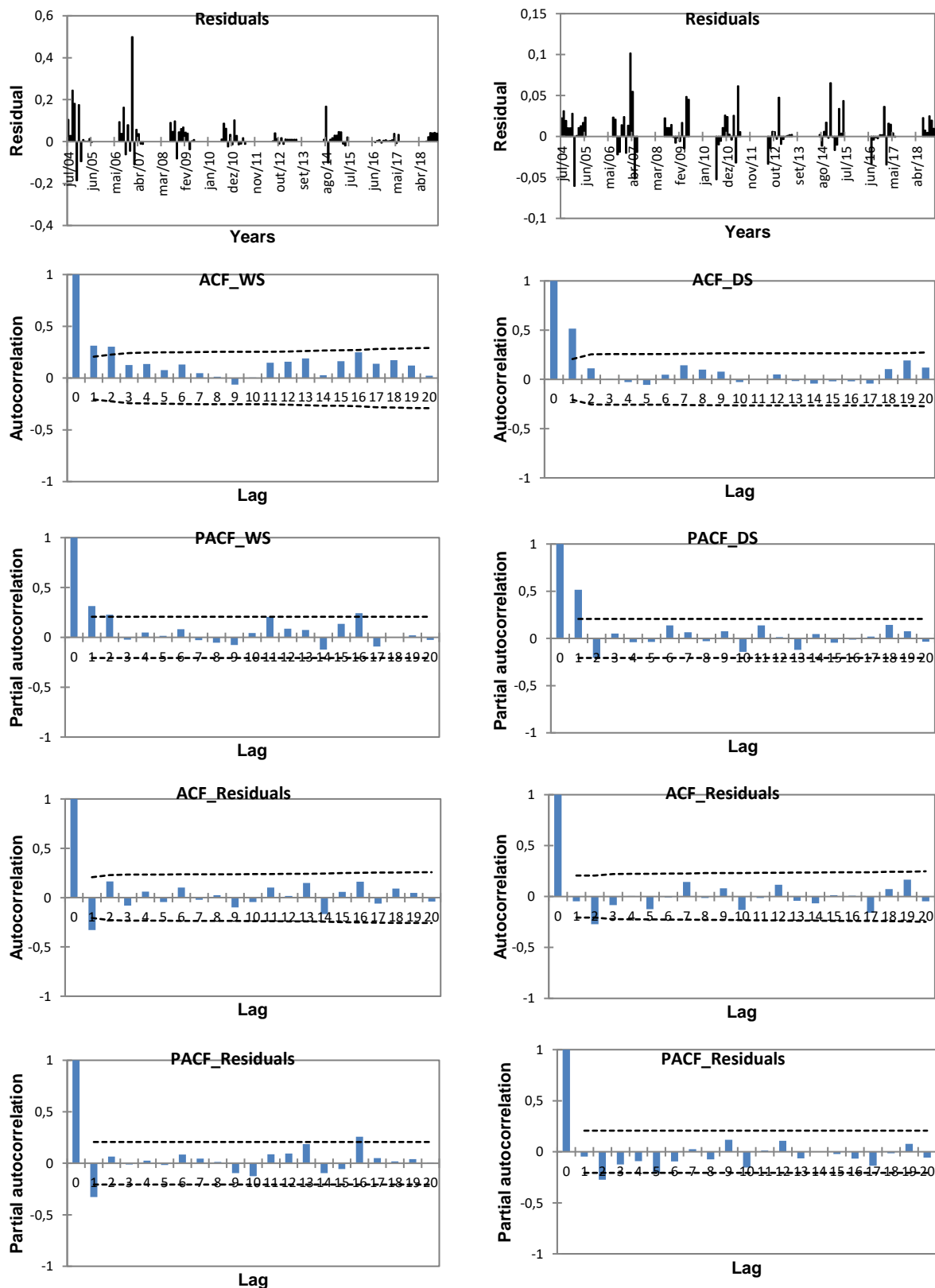


Figure J.8: ACF, PACF, ACFR and PACFR for the Muianga station for DS and WS.

Marrambajane Station

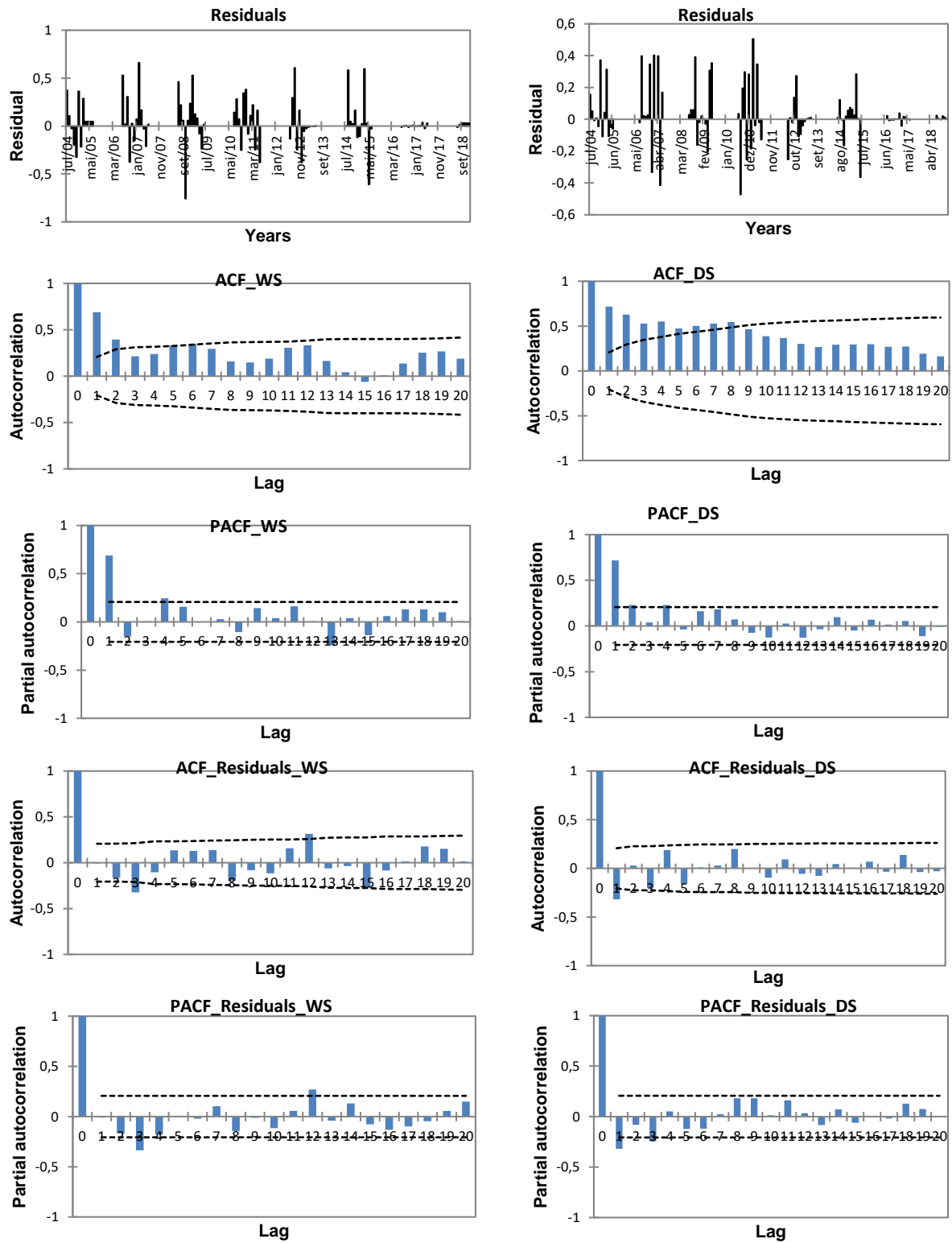


Figure J.9: ACF, PACF, ACFR and PACFR for the Marrambajane station for DS and WS.

K: Atterberg Test Procedures

Atterberg Limits testing is widely used in the design stage of construction to ensure that the soils being used exhibit the proper consistency to support structures even as their moisture levels change. Soils for engineering use are often classified based on properties relative to foundation support or how they might perform under pavements and in earthworks. In the early 1900s, the Swedish chemist Albert Atterberg developed a classification system and method with which these states of consistency could be determined. His methods were later defined by Arthur Casagrande. The method is based on the determination of the water content at distinct transitions between different states of soil consistency. These transitions are defined as shrinkage limit, plastic limit, and liquid limit, and collectively are referred to as Atterberg limits. The liquid limit and plastic limit tests are the most commonly used of the Atterberg limits tests. The values for these limits are dependent on various soil parameters (e.g., particle size, specific surface area of the particles that are able to attract water molecules).

Geotechnical classification systems are designed to make it easy to equate field observations to estimates of engineering properties. As moisture content of a fine-grained, clay-like soil increases, it goes through four distinct states of consistency: solid, semi-solid, plastic, and liquid. Each stage is defined by significant changes in strength, consistency and behavior. As a hard, rigid solid in the dry state, fine grained soil becomes a crumbly (friable) semisolid when certain moisture content, or shrinkage limit, is reached. This soil will also begin to swell as shrinkage limit is exceeded. Increasing the water content beyond the soil's plastic limit will transform it into a plastic mass, which causes additional swelling. The soil will remain in this plastic state until its liquid limit is exceeded, which causes it to transform into a viscous liquid that flows when jarred. These limits can be determined with the three tests that make up the Atterberg limits tests. They are Shrinkage limit, Plastic limit and Liquid limit.

Knowledge of these values helps in foundation design of structures and to predict behavior of soils in fills and embankments. The values derived from Atterberg limit tests can contribute to estimates of shear strength, permeability, settlement and the identification of potentially expansive soils.

The Atterberg limits for different types of fine-grained soils can vary greatly. For example, Illite exhibits a shrinkage limit of 15% to 17% depending on particle sizes, while its plastic limit is typically 24% to 52%, and its liquid limit is typically 30% to 110%. Kaolinite exhibits a shrinkage limit of 25% to 29% depending on particle sizes, while its plastic limit is typically 30% to 40%, and its liquid limit is typically 35% to 72%.

A common way to describe expansive soils is through plasticity index values. The plasticity index refers to the range of plastic properties a soil exhibits at varying levels of water content. The plasticity index is essentially the difference between liquid limit and plastic limit values. Clay loam has a plasticity index of 10-20% and is referred to as a medium plastic soil. Silty clay has a plasticity index of 20-35% and is considered a highly plastic soil. Very high plasticity soils have a plasticity index of over 35% and contain a predominance of clay.

Liquid Limit

The liquid limit (ASTM D4318) is defined as the water content at which the behavior of a clayey soil changes from plastic to liquid. However, the transition from plastic to liquid behavior is gradual over a range of water contents, and the shear strength of the soil is not actually zero at the liquid limit. The precise definition of the liquid limit is based on standard test procedures described below.

The original liquid limit test developed by Atterberg involved mixing a pat of clay in a round-bottomed porcelain bowl of 10–12cm diameter. A groove was cut through the pat of clay with a spatula, and the bowl was then struck many times against the palm of one hand. Casagrande subsequently standardized the apparatus and the procedure to make the measurement more repeatable.

Soil is placed into the metal cup portion of a liquid limit device and a groove is cut down its center with a standardized tool of 2 mm (0.079") width. The cup is repeatedly dropped 10 mm onto a hard rubber base at a rate of 120 blows per minute, during which the groove closes up gradually as a result of the impact. The number of blows for the groove to close is recorded.

The moisture content at which it takes 25 drops of the cup to cause the groove to close over a distance of 12.7mm (0.50") is defined as the liquid limit. The test is normally run at several

moisture contents, and the moisture content which requires 25 blows to close the groove is interpolated from the test results. The test method also allows running the test at one moisture content where 20 to 30 blows are required to close the groove; then a correction factor is applied to obtain the liquid limit from the moisture content.

Plastic Limit

Water content at the change from a plastic to a semisolid state is known as the plastic limit. The plastic limit test (ASTM D4318) is done by rolling out a small thread of soil on a flat, non-porous surface. If the soil is at a moisture content where its behavior is plastic, the thread will retain its shape down to a very narrow diameter. As the moisture content falls due to evaporation, the thread will begin to break apart at larger diameters. The sample can then be re-molded and the test repeated. The plastic limit is defined as the moisture content where the thread breaks apart at a diameter of 3.2mm (about 0.125"). A soil is considered non-plastic if a thread cannot be rolled out down to 3.2 mm at any moisture possible.

Shrinkage Limit

The shrinkage limit (ASTM D4943) is defined as the point where the water content of the soil will not result in any more volume reduction. This test is much less commonly used than the liquid and plastic limit tests. Humboldt offers the H-4254 Shrinkage Limit Set for performing this test.

L. Letter of Authorization for Field Data Collection



HIDRÁULICA DE CHÓKWÈ, E. P.

Chókwè, 15th April 2021

TO WHO IT MAY CONCERN,

This is to confirm that **Mr. Lateiro Salvador de Sousa**, holder of National ID Card No. 110100436740I, issued on the 15th of December 2020, in Maputo, a **PhD candidate of EGERTON UNIVERSITY, Njoro Main Campus-Nakuru, in Kenya**, has been permitted to conduct research in the Chókwè Irrigation Scheme, under HICEP management, on the topic related to:

ASSESSMENT OF TEMPORAL TREND-DYNAMICS OF WATER FLOW AND SEDIMENT FLUX FOR CHÓKWÈ IRRIGATION SCHEME IN GAZA PROVINCE, MOZAMBIQUE

for which will collect samples and relevant data related to water flow and sediment flux at nine (9) sampling stations, located in the Montante, Sul and Rio sectors. The list of permitted data are related to canal hydraulics (length, width, depth, slope, regulators), water flow, water quality, maps and shape files, sediment load (suspended and bed) and other hydraulic related information relevant to the topic.

This permit is valid for the above research and other related topics for a period of 5 years, starting from 2018 and ending in December 2023.

Chairman of the Board of Administrators

(Soares Almeida Xirinda, PhD)

M. Published Articles

M.1. First Publication





AgriEngineering



Review

Assessment of Water Flow and Sedimentation Processes in Irrigation Schemes for Decision-Support Tool Development: A Case Review for the Chókwè Irrigation Scheme, Mozambique

Lateiro Salvador de Sousa ^{1,*} , Raphael Muli Wambua ², James Messo Raude ³  and Benedict Mwavu Mutua ⁴

¹ Faculty of Agriculture, Instituto Superior Politécnico de Gaza, Campus Politécnico de Lionde, 711226 Chókwè-Gaza Province, Mozambique

² Department of Agricultural Engineering, Egerton University, 20115 Nakuru, Kenya; wambuarm@gmail.com

³ Soil, Water & Environmental Engineering Department, Jomo Kenyatta University of Agriculture & Technology, 00200 Nairobi, Kenya; ramesso@jkuat.ac.ke

⁴ Division of Planning, Research and Innovation, Kibabii University, 50200 Bungoma, Kenya; bmmutua@kibu.ac.ke

* Correspondence: lateirodesousa@gmail.com; Tel.: +258-823-047-052 or +258-844-739-021

Received: 16 January 2019; Accepted: 28 February 2019; Published: 6 March 2019



Abstract: Water flow and sedimentation processes have been significantly erratic at the Chókwè Irrigation Scheme (CIS) and have affected its hydraulic performance. Given its expansion there is need to understand these processes taking place on-site and along the channels of the scheme. CIS being the biggest project of its kind in Mozambique requires proper management of water flow and sedimentation processes. Therefore, the effect of water flow, sediment transport and deposition parameters on the performance of the CIS is needed. In order to determine the effect of spatial and temporal water flow and sediment distribution trends along the irrigation canals, there is need to establish a correlation between these parameters. Determining the influence of water flow velocity on sediment settling rate at different depths along the canal reaches is important in managing the CIS. In addition, a developed decision-support tool to predict sediment deposition is required. For this reason, it is therefore crucial to carry out a timely assessment of water flow and sedimentation processes in CIS in a review concept. From the current review, some gaps that exist for more focused research on Chókwè Irrigation Scheme have been identified. In this regard therefore, there is need to develop an effective support tool for managing water flow and sediment deposition along the canal reaches with a view to increasing crop production in CIS.

Water Flow and Sediment Flux Forecast in the Chókwè Irrigation Scheme, Mozambique

Lateiro Salvador De Sousa^{1*}, Raphael Muli Wambua², James Messo Raude³,
Benedict Mwavu Mutua⁴

¹Division of Agriculture, Instituto Superior Politécnico de Gaza, Campus Politécnico de Lionde, Chókwè-Gaza Province, Mozambique

²Department of Agricultural Engineering, Egerton University, Nakuru, Kenya

³Soil, Water & Environmental Engineering Department, Jomo Kenyatta University of Agriculture & Technology, Nairobi, Kenya

⁴Division of Planning, Partnerships, Research and Innovation, Kibabii University, Bungoma, Kenya

Email: *lateiro.sousa@ispg.ac.mz, raphael.wambua@egerton.ac.ke, ramesso@jkuat.ac.ke, bmmutua@kibu.ac.ke

How to cite this paper: De Sousa, L.S., Wambua, R.M., Raude, J.M. and Mutua, B.M. (2020) Water Flow and Sediment Flux Forecast in the Chókwè Irrigation Scheme, Mozambique. *Journal of Water Resource and Protection*, 12, 1089-1122.
<https://doi.org/10.4236/jwarp-2020.1212065>

Received: November 15, 2020

Accepted: December 28, 2020

Published: December 31, 2020

Copyright © 2020 by author(s) and Scientific Research Publishing Inc. This work is licensed under the Creative Commons Attribution International License (CC BY 4.0).
<http://creativecommons.org/licenses/by/4.0/>



Open Access

Abstract

This study sought to forecast water flow and sediment flux in the scheme as potential contributions for improved management in the Chókwè Irrigation Scheme (CIS). Fieldwork data was collected during dry (DS) and wet (WS) seasons. Flow measurement was performed at 9 stations using a calibrated flow meter OTT C31. Water flow and sediment flux from 2004 to 2019 were used. Hydrodynamic forecast simulations were performed using Mann-Kendall test and ARIMA model for determination of temporal trends. Findings suggest higher values during DS for water discharge and sediment flux. Mann-Kendall test for sediment discharge trends was not significant at 95% significance level, except for the Offtake in WS. ARIMA test for the sediment discharges, at the Intake, for DS and WS, sediments were well described by the ARIMA model and gave a good result for the sediments. Good fit between the observed and the predicted ARIMA model was found. ARIMA model for sediment discharge at CIS based on AIC has a good fit for AR ($p = 1$), whereby, at the Intake the ARIMA p-value was 0.822 and 0.932, for WS and DS, respectively. Whilst in the Offtake, the ARIMA p-value was 0.877 and 0.893, respectively. These results can be used to improve the CIS management, both for water flow and sediment flux.

Keywords

Water Flow, Sediment Flux, Mann-Kendall Test, ARIMA Model, Chókwè Irrigation Scheme

M.3. Third Publication

Journal of Sedimentary Environments
<https://doi.org/10.1007/s43217-021-00058-3>

ORIGINAL ARTICLE



Cohesive and non-uniform sediment characteristics in the unlined canal of Chókwè Irrigation Scheme, Mozambique

Lateiro Salvador de Sousa¹ · Raphael M. Wambua² · James M. Raude³ · Benedict M. Mutua⁴

Received: 4 January 2021 / Revised: 5 April 2021 / Accepted: 12 April 2021
© The Author(s), under exclusive licence to Springer Nature Switzerland AG 2021

Abstract

This study sought to characterise sediments in the unlined canal in Chókwè Irrigation Scheme (CIS), during dry (DS) and wet (WS) seasons. Laboratory analysis were performed on the sediment's soluble extracts for pH, turbidity, total dissolved solids (TDS), sodium, calcium, magnesium, and potassium concentrations. Atterberg tests and particle size distribution (PSD) were also investigated for all sediment samples collected in the CIS main canal. Results suggest acceptable water pH and turbidity in both seasons. The concentration of TDS was found to be 250 and 300 ppm for the DS and WS, respectively. Sodium was the most predominant element in water and sediment samples, followed by potassium and calcium. The Liquid Limit, Plasticity Limit and Plasticity Index were 52%, 20% and 32%, respectively. A mean of 2.960 N/m² was obtained for the critical shear stress of erosion. The main particle size in bedload sediments which were classified as saline were silt, fine sand, and clay. Overall, CIS is characterized by the occurrence of cohesive and varied degrees of uniformity in the sediments grain size. Considering the physicochemical properties of the canal bed sediments as an accurate representation of